NASA TECHNICAL TRANSLATION

NASA TT F-522

NASA TT F-522

TECH LIBRARY KAFB, NM
0069025

LOAN COPY: RETURN TO
AFWL (WLIL-2)
KIRTLAND AFB, N MEX

LIQUID METALS

P. L. Kirillov, V. I. Subbotin, and P. A. Ushakov, Editors

Atomizdat, Moscow, 1967

NATIONAL AERONAUTICS AND SPACE ADMINISTRATION • WASHINGTON, D. C. • MAY 1969

TECH LIBRARY KAFB, NM
0069025
NASA TT F-522

LIQUID METALS

By P. L. Kirillov, V. I. Subbotin, and P. A. Ushakov, Editors

Translation of "Zhidkiye Metally."
Atomizdat, Moscow, 1967

NATIONAL AERONAUTICS AND SPACE ADMINISTRATION

For sale by the Clearinghouse for Federal Scientific and Technical Information
Springfield, Virginia 22151 – CFSTI price $3.00

Page intentionally left blank

TABLE OF CONTENTS

	Page
List of Symbols, Standard Throughout the Book	vii
Foreword	viii
Part One	1
Heat Transfer in Round, Annular and Square Channels	
Study of Heat Transfer in Liquid Metals in Round Pipes (V. D. Talanov and P. A. Ushakov)	1
Heat Transfer with Liquid Metal in a Vertical Pipe with Low Peclet Numbers (N. A. Ampleyev, P. L. Kirillov, V. I. Subbotin and M. Ya. Suvorov)	8
Heat Transfer of Sodium and a Sodium-Potassium Alloy in Short Vertical Pipes by Combined Convection (L. G. Volchkov, M. K. Gorchakov, P. L. Kirillov and F. A. Kozlov)	28
Taking into Account Longitudinal Heat Flows when Measuring the Average Temperature of Fluids in Pipes and Heat Exchanges for Low Peclet Numbers (M. K. Gorchakov)	40
Statistical Characteristics of Turbulent Temperature Fluctuations in Fluid Flows (V. P. Bobkov, M. Kh. Ibragimov and V. I. Subbotin)	53
Statistical Characteristics of Temperature Fluctuations in Heat Exchanger Walls Attendant to High Thermal Fluxes (M. Kh. Ibragimov, V. I. Merkulov and V. I. Subbotin)	71
Heat Transfer in Turbulent Flow of Fluids in Square Ducts (M. Kh. Ibragimov, Yu. M. Rabotyashnik, G. I. Sabelev, V. I. Sidirov and V. I. Subbotin)	82
Fluid Dynamics in an Annular Space with Longitudinal Ribs (Yu. D. Levchenko, V. I. Subbotin, P. A. Ushakov and A. V. Sheynina)	100
Effect of Eccentricity on Heat Transfer to Liquid Metals in Annular Spaces (V. I. Subbotin, V. D. Talanov and P. A. Ushakov)	108
Transfer of Heat in Turbulent Flows of Fluids in Annular and Plane Spaces (N. I. Buleyev, V. A. Mosolova and L. D. Yel'tsova)	120

Experimental Study of Heat Transfer From a Flat Horizontal Surface to Sodium by Free Convection (A. P. Kudryatsev, D. M. Ovechkin, D. N. Sorokin, V. I. Subbotin and A. A. Tsyganok) 130

Part Two

Heat Transfer and Fluid Dynamics of Intricately-Shaped Passages

Approximate Thermal Simulation of Cylindrical Fuel-Element Rods (P. A. Ushakov) 136

Heat Transfer From Loosely-Spaced [Fuel] Rod Clusters to Liquid Metal Flowing in the Axial Direction (A. V. Zhukov, V. I. Subbotin and P. A. Ushakov) 149

Experimental Study of Temperature Fields of Fuel Elements, Using Models (A. V. Zhukov, L. K. Kudryatseva, Ye. Ya. Sviridenko, V. I. Subbotin, V. D. Talanov and P. A. Ushakov) 170

Heat Transfer in the Intertubular Space of Liquid-Metal Heat Exchanges (P. L. Kirillov and M. Ya. Suvorov) 190

Analysis of the Applicability of Average Heat-Transfer Coefficients in Heat-Exchanger Design (P. A. Ushakov) 200

Resistance to Axial Flow of Fluids Past Rod Clusters (A. V. Sheynina) 207

Velocity Distribution in a Cell Formed by a Densely-Packed Cluster of Rods (Yu. D. Levchenko, V. I. Subbotin, P. A. Ushakov and A. V. Sheynina) 220

Calculation and Experimental Study of Velocity Fields in Intricately-Shaped Passages (M. Kh. Ibragimov, I. A. Isupov and V. I. Subbotin) 231

Part Three

Boiling and Condensation of Metals

Electronically-Heated Setup for the Study of Heat Transfer From Boiling Metals by Free Convection (A. A. Ivashkevich, A. P. Kudryavtsev, D. M. Ovechkin, D. N. Sorokin, V. I. Subbotin and A. A. Tsyganok) 248

Transfer of Heat From Sodium Boiling in a Large Vessel (A. P. Kudryavtsev, D. M. Ovechkin, D. N. Sorokin, V. I. Subbotin and A. A. Tsyganok) 265

Experimental Study of Critical Thermal Fluxes in Sodium Boiling in a Large Vessel (A. P. Kudryavtsev, D. M. Ovechkin, D. N. Sorokin, V. I. Subbotin and A. A. Tsyganok) 281

Mean Temperature Difference in Low-Pressure Vapor Generators and Condensers (P. L. Kirillov) 287

Transfer of Heat From Condensing Sodium Vapor (N. B. Bakulin, M. N. Ivanovskiy, V. P. Sorokin, V. I. Subbotin and B. A. Chulkov) 294

Part Four

Techniques of Work With Liquid Metals

Corrosion Resistance of Construction Materials to Sodium (V. V. Zotov, B. A. Nevzorov and Ye. V. Umnyashkin) 300

Determination of the Oxygen Content of Sodium and of the Sodium-Potassium Alloy by Vacuum Distillation (I. B. Dmitryeva, F. A. Kozlov and E. K. Kuznetsov) 318

The Cock-Type Indicator as an Instrument for Detecting Admixtures in Sodium (F. A. Kozlov, E. K. Kuznetsov and V. I. Subbotin) 324

Effect of Admixtures on the Electric Resistance of Molten Lithium (M. N. Arnol'dov, M. N. Ivanovskiy, V. I. Subbotin and B. A. Shmatko) 336

The Use of Hot Traps for Removing Oxygen From Sodium (F. A. Kozlov and E. K. Kuznetsov) 340

Maximum Permissible Leakage in a Sodium-to-Water Steam Generator (N. N. Ivanovskiy and F. A. Kozlov) 357

Some Problems of Operation and Design of Liquid-Metal Loops (A. V. Drobyshev, V. A. Kurov and I. T. Filipov) 360

Heat Exchangers of Experimental Liquid-Metal Loops (V. A. Kurov and V. F. Men'shikov) 368

Study of Velocity Fields by the Electromagnetic Method (N. N. Turchin and R. V. Shumskiy) 377

Electromagnetic A-C Pump for Liquid Metals Rated at 120 m^3/hour (Ye. M. Avilova, T. V. Doktorova, N. I. Marin and V. A. Povsten') 385

Electromagnetic Screw Pump for Pumping of Liquid Metals (Ye. M. Avilova, Ye. L. Ivanter, N. I. Marin and V. A. Povsten') 389

Hydrostatic Bearings in Sodium Pumps (N. N. Aristarkhov, Yu. Ye. Bagdasarov, Yu. L. Kulikov, Ye. N. Larin, M. S. Pinkhasik, A. A. Rineyskiy and B. S. Tymosh) 392

Flowmeter for Measuring Large Liquid-Metal Flows (N. L. Loginov) 403

Time Needed for Melting Cylindrical [Metal] Volumes (V. M. Selivanov, N. M. Trebina and V. I. Sharypin) 406

Frozen Sodium Seals (A. V. Drobyshev, Yu. I. Likhachev and I. M. Saratov) 412

Appendices

I. Calculations of Heat Transfer in Liquid Metals 437

II. Corrosion Resistance and Temperature Limit of Utilization of Certain Construction Materials in a Sodium Flow 446

Abstracts 448

LIST OF SYMBOLS, STANDARD THROUGHOUT THE BOOK

$Nu = \alpha d/\lambda$	Nusselt number
$Pe = wd/a$	Peclet number
$Pr = v/a$	Prandtl number
$Gz = Pe\ d/l$	Grätz number
$Re = wd/v$	Reynolds number
$Gr = \beta l^3 \Delta tg/v^2$	Grashof number
$Bi = \alpha d/\lambda_w$	Biot number
$q,\ q_w$	Specific heat load
$Ra = GrPr$	Rayleigh number
α	Heat-transfer coefficient
v	Thermal conductivity coefficient
C_p	Specific heat
γ	Specific weight
a	Coefficient of thermal diffusivity
v	Kinematic viscosity
μ	Dynamic viscosity
β	Coefficient of volumetric expansion
g	Acceleration of gravity
d	Tube diameter
F	Heat transfer area
t	Temperature, ° C
Δt_α	Mean temperature difference, °C

FOREWORD

The production of atomic [nuclear] power may become an important branch of the national economy and satisfy to a substantial degree the requirements for electric power and heat, provided that economic nuclear power generation stations are constructed, in particular those using fast-neutron reactors. Such reactors, because of their physical characteristics, make it possible to utilize almost all the uranium, as compared with the negligible part of this element which is utilized by thermal neutron reactors; in addition, thorium can be used in fast-neutron reactors. These remarkable properties increase the supplies of utilizable nuclear fuel to such an extent that it becomes entirely possible to set up a large atomic [nuclear] power producing system on a "country-wide" scale, and provided with fuel for long periods of time. Hence, the development of fast-neutron reactors is one of the primary goals of the nuclear power technology.

The optimal heat transfer agent in these reactors is liquid sodium, due to the favorable combination of properties such as the nuclear-physical, thermophysical and corrosion, as well as because of its comparatively low cost. While the use of liquid sodium has little effect on the nuclear properties of reactors, it permits the removal of large specific quantities of heat (500-1000 kw per liter in the active zone of the reactor).

One can expect that the sodium temperature at the reactor outlet will be 500-650° C, which will make it possible to obtain steam of sufficiently high pressures to operate the power station at high efficiency.

Studies in the field of thermal physics and technology of sodium, study of thermal processes in active zones, in reactor reflectors, heat exchangers, steam generators and other equipment are tasks of paramount importance, Successful solution of these tasks is closely tied to the development of fast-neutron reactor technology.

In the Physics and Power Institute, where the development of fast-neutron reactors is regarded as a major task, a large group of investigators has been working for several years on the thermal physics and technology of liquid metal heat transfer agents. Some results of this work are published in the present collection.

Studies in this field already permit the practical utilization of liquid metal heat transfer agents on an appreciable scale. This is attested to by the successful operation for many years of the BR-5 experimental fast-neutron reactor. The content of the present collection reflects the level of research work in this field.

The problems of thermal physics of real active zones and reflectors of reactors as well as of impurity removal from the liquid metals, development of

of standard technologies and corrosion studies of structural materials are being successfully solved. They serve as a basis for optimism as to the feasibility of developing efficient electric power stations employing fast-neutron reactors within the next few years.

A.I. Leypunskiy

CUT ALONG THIS LINE

FOLD LINE

NATIONAL AERONAUTICS AND SPACE ADMINISTRATION
WASHINGTON, D.C. 20546

OFFICIAL BUSINESS

POSTAGE AND FEES PAID
NATIONAL AERONAUTICS & SPACE ADMINISTRATION

NATIONAL AERONAUTICS AND SPACE ADMINISTRATION
CODE USS-T
WASHINGTON, D.C. 20546

NASA TTF No.
522

FOLD LINE

CUT ALONG THIS LINE

NATIONAL AERONAUTICS AND SPACE ADMINISTRATION

TECHNICAL TRANSLATION EVALUATION

Budget Bureau No. 104-R037
Approval Expires: Sept. 30, 1969

TO:
THE USERS OF THIS TRANSLATION →

NASA TTF NO. 522

MAINTAINING THE QUALITY OF NASA TRANSLATIONS REQUIRES A CONTINUOUS EVALUATION PROGRAM. PLEASE COMPLETE AND MAIL THIS FORM TO AID IN THE EVALUATION OF THE USEFULNESS AND QUALITY OF THE TRANSLATING SERVICE.

THIS PUBLICATION *(Check one or more)*

- ☐ FURNISHED VALUABLE NEW DATA OR A NEW APPROACH TO RESEARCH.
- ☐ VERIFIED INFORMATION AVAILABLE FROM OTHER SOURCES.
- ☐ FURNISHED INTERESTING BACKGROUND INFORMATION.
- ☐ OTHER *(Explain)*: _____

FOLD LINE FOLD LINE

TRANSLATION TEXT *(Check one)*

- ☐ IS TECHNICALLY ACCURATE.
- ☐ IS SUFFICIENTLY ACCURATE FOR OUR PURPOSE.
- ☐ IS SATISFACTORY, BUT CONTAINS MINOR ERRORS.
- ☐ IS UNSATISFACTORY BECAUSE OF *(Check one or more)*:
  - ☐ POOR TERMINOLOGY.
  - ☐ NUMERICAL INACCURACIES.
  - ☐ INCOMPLETE TRANSLATION.
  - ☐ ILLEGIBLE SYMBOLS, TABULATIONS, OR CURVES.
  - ☐ OTHER *(Explain)*: _____

FOLD LINE FOLD LINE

REMARKS

FROM	DATE

NOTE: REMOVE THIS SHEET FROM THE PUBLICATION, FOLD AS INDICATED, STAPLE OR TAPE, AND MAIL. NO POSTAGE NECESSARY.

NASA Form 1332 AUG 66 GPO 915-777

CUT ALONG THIS LINE

CUT ALONG THIS LINE

ANNOTATION

This collection presents results of original studies performed during the last few years at the Physics and Power Institute of the State Committee for Utilization of Atomic Energy.

The collection contains theoretical and experimental solutions of problems of convective heat transfer, pertaining to the flow of liquid metals in ducts of various shapes. Of particular importance are ducts formed by the cluster of round rods, since this is the most prevalent form of fuel elements in active zones of nuclear reactors.

This book considers problems of heat transfer and fluid flow attendant to fluid flow past clusters of round rods in the longitudinal direction, as well as problems of boiling and condensation of metals. It presents techniques of working with liquid metals, methods for removing impurities from them, methods of impurity control, problems of corrosion and the experience in operating various kinds of equipment used in experimental facilities of the Physics and Power Institute.

This collection illuminates problems of design of facilities employing liquid metals. It presents recommendations on calculating the heat transfer in liquid metals and a summary of physical properties, which were used in analyzing the experimental results.

The materials in this collection can be used extensively for the development of facilities in which liquid metals are used as heat transfer agents.

PART ONE

HEAT TRANSFER IN ROUND, ANNULAR AND SQUARE CHANNELS

STUDY OF HEAT TRANSFER IN LIQUID METALS IN ROUND PIPES

V. D. Talanov and P. A. Ushakov

Investigations have been carried out at the Physics and Power Institute concerned with the heat transfer to mercury flowing inside tubes made of nickel and stainless steel, as well as with heat transfer to a sodium-potassium alloy flowing /9*

*Numbers in the margin indicate pagination in the foreign text.

inside a copper tube [1]. The experimentally obtained data for different conditions were in good agreement with each other and are described by the following [empirical] formula

$$Nu = 4.3 + 0.025Pe^{0.8}. \quad (1)$$

Using data for sodium, whose Prandtl number is much lower than that corresponding to mercury or to the sodium-potassium alloy, it was recommended in [1] to calculate the heat transfer to liquid metals in tubes by using the formula

$$Nu = 5 + 0.025Pe^{0.8}. \quad (2)$$

The sodium-potassium alloy wets the copper surface well, while the surface of stainless steel is not wetted by this low-temperature alloy. This was experimentally confirmed.

To obtain data on heat transfer between the stainless steel wall and the sodium-potassium alloy two series of tests were performed. In them use was made of an eutectic alloy (22%Na +78%K) at a temperature not above 100°C [2]. Before pouring the alloy into the circuit, it was passed through a wire-gauze filter and the oxides were continuously removed by a cold trap. The oxygen content of the alloy, which was determined by a distillate sampling device, varied from $3 \cdot 10^{-4}$ to 10^{-3}% by weight. The design of the testing tube is shown in Fig. 1. The calibrated tube from 1Kh18N9T stainless steel, 19.5 mm in diameter and with a wall thickness of 0.4 mm, was plated by a copper layer of about 7.8 mm by the zone melting method. The entrance flow stabilization segment comprised 20d, the heating length was about 940 mm (about 50d). The pipe was provided at its ends with mixing chambers in which the mixed mean temperature of the sodium-potassium coolant was measured. The outlet mixing chamber is removed from the end of the heated segment by approximately 10d.

To measure the pipe wall temperature six thermocouples, two of which could be moved along the entire heated segment, were built into the copper shell. The movable thermocouples were placed in copper capillaries 1.5/0.6 mm in diameter, inserted at a distance of 2.4 mm from the heat transfer surface and placed in longitudinal slots in diametrically opposite sides of the pipe. The slots and the copper plates by which the capillaries were calked were rounded off along the radii of the latter, which improved the thermal contact between the capillaries and the copper shell. In addition, when inserted into the pipe wall, the capillaries were soldered with tin. /10

The movable thermocouples were made from copper and constantan wires 0.09 in diameter, pulled through a capillary from 1Kh18N9T steel 0.5/0.3 mm in diameter, and welded to it at one end. The thermocouples were moved automatically by means of a device consisting of an electric motor, speed reducer, cam, Maltese-cross type gear and a drum on which the driving cable was wound. On each revolution of the gear the thermocouples moved through 20 mm. The time

elapsed between the thermocouple motions (~30 secs) was sufficient to stabilize their readings and for making the necessary measurements.

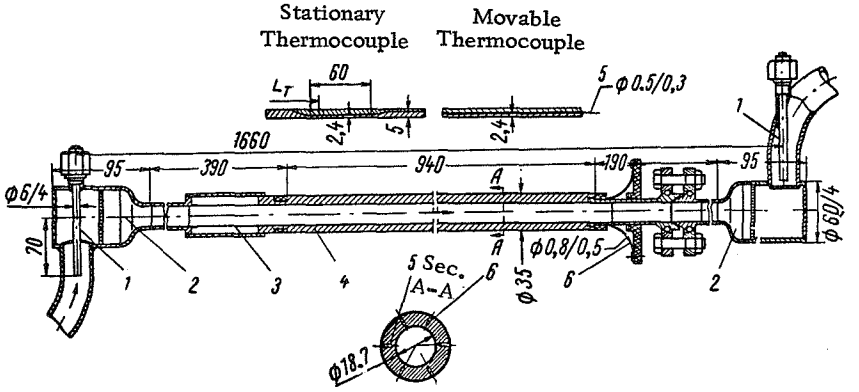

Figure 1. Schematic Diagram of the Test Pipe. 1) Thermocouple Sleeve; 2) End Chamber; 3) Stainless Steel Pipe; 4) Copper Shell; 5) Movable Thermocouples; 6) Stationary Thermocouples

In order to check the readings of the movable thermocouples, use was made of four [additional] thermocouples, which were built into the wall at distances of 440, 540, 640 and 740 mm from the beginning of the heated segment. The distance from the junctions of these thermocouples to the heat-transfer surface was 2.4 mm. The copper capillary served as one of the thermocouple electrodes, while the other was Kopel wire in alundum insulation. Preliminary tests produced good agreement in the readings of the movable and the stationary thermocouples, hence the main measurements were made by using the former.

The test pipe was heated by a band-type nichrome heater with a cross section of 6 x 0.25 mm insulated by an organic silicon compound and micanite. Heat losses to the surrounding medium were reduced to a minimum by the thermo-insulation and by a compensating heater, which was automatically adjusted by a system of thermometers and devices. The power of the heater was adjusted by the AOSK-25/0.5 transformer and was measured by class 0.5 astatic instruments. The thermocouple emfs were measured by R-2/1 semiautomatic potentiometers. The flow of rate of the sodium-potassium alloy was measured by magnetic flowmeters and on the basis of the heat content of the alloy flowing in the test pipe (calorimetric method). /11

The double-wall pipe was made as follows. A calibrated pipe from the 1Kh18N9T stainless steel was placed coaxially into a thin-walled cylindrical shell to which it was then welded at the bottom, and [then] copper rings were inserted into the annual space [thus formed]. The entire structure was suspended from a molybdenum wire pulled through an auxiliary copper tube, the upper end of which was rigidly connected to the structure, while the lower end was placed on a washer fastened to the molybdenum wire.

The structure was subjected to zonal melting in a small shaft-type furnace. As the copper rings, and after them the auxiliary copper tube, melted, the structure lowered itself under its own weight. The heating zone thus moved along the length of the pipe in the upward direction and after leaving the furnace it was cooled by natural convection of the surrounding air. After the section was copper plated in this manner the external steel shell was removed on a lathe.

The experimental specimens exhibited good diffusion bonding of the copper with the stainless steel. Penetration of stainless steel components into the copper and vice versa was observed at the boundary between the two metals, i.e., a transition layer was formed several tens of microns thick.

In order to determine the magnitude of the effective temperature correction for the depth of the thermocouple insertion experiments were performed using water in a range of Reynolds numbers from 18,000 to 600,000. Comparison of the data thus obtained with the results of experiments conducted with a copper tube in which the correction for the depth of thermocouple insertion is small showed that the formation of the transition layer between the steel and the copper attendant to the melting of the latter is equivalent to reducing the thickness of the steel wall by 67 microns. If we assume that the effective wall thickness of the internal steel pipe is 0.333 mm, then the data for water obtained with this two-metal pipe and with copper tube segments are in agreement to within ± 6%.

Moving the thermocouples along the test section made it possible to determine the temperature distribution at the heat transfer surface along the length of the passage. Characteristic temperature distributions for two Peclet numbers are shown in Fig. 2. The temperatures of the sodium-potassium alloy in any cross section were found by linear interpolation of the heat-transfer agent's temperature /12 at the pipe inlet and outlet.

The results of experiments concerned with determining the stabilized values of the Nusselt numbers as a function of the Peclet numbers for the two series of tests are shown in Tables 1 and 2, as well as in Fig. 3. The same figure shows the previously obtained [1] data, results obtained in [3] and curves obtained by using formulas

$$Nu = 7 + 0.025Pe^{0.8}; \quad (3)$$

$$Nu = 5.2 + 0.025Pe^{0.8}; \quad (4)$$

$$Nu = 5 + 0.014Pe^{0.8} \quad (5)$$

recommended in [4] and [5], as well as those obtained by using Eq. (1).

The good agreement between experimental data for mercury and for the sodium-potassium alloy, which were passed through pipes of various materials, show that the effect of the thermal contact resistance is of no importance under the conditions considered. The results we have obtained again confirmed the hypothesis on

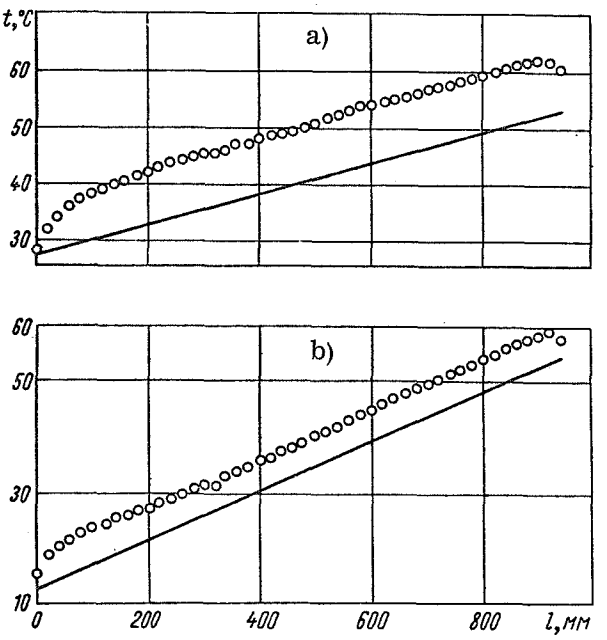

Figure 2. Temperature Distribution Along the Length of the Pipe for Pe = 796, q = $109 \cdot 10^3$ kcal/m^2-hour (a) and Pe = 163, q = $39 \cdot 10^3$ kcal/m^2-hour (b). The Circles Show the Temperature of the Heat Transfer Surface, the Line Denotes the Temperature of the Sodium-Potassium Alloy.

TABLE 1. Heat Transfer Experiments Using a Sodium-Potassium Alloy in a Stainless Steel Pipe

$q \times 10^{-3}$, kcal/m^2-hr	$(t_w - t_f)$, °C	Re × 10^{-3}	Pe	Nu	$q \times 10^{-3}$, kcal/m^2-hr	$(t_w - t_f)$, °C	Re × 10^{-3}	Pe	Nu
17.12	2.9	3.22	80	5.7	62.3	6.0	35.4	797	10.0
21.8	3.5	3.69	93	6.0	46.7	4.5	29.1	830	10.1
15.6	2.3	4.23	95	6.4	101.2	8.6	41.1	945	11.2
15.6	2.8	4.53	104	5.4	101.2	7.85	57.2	1217	12.3
19.45	2,9	5.46	122	6.4	101.2	7.3	68.1	1770	13.2
31.18	4.7	5.25	133	6.3	101.2	6.0	102	2250	16.2
20.2	3.1	6.43	144	6.2	101.2	5.3	121	2800	18.2
38.9	5.8	6.46	170	6.4	101,2	5.4	137	3080	18.0
54.5	8.4	8.33	216	6.2	101,2	4.9	149.6	3290	19.8
49.8	7.0	8.28	208	6.8	101.2	4.5	161	3700	21.7
54.5	7.4	9.55	266	7.2	101,2	3.7	209.5	4610	25.8
49.8	6.5	17.0	408	7.3	101.2	3.4	244.5	5470	28.5
49.8	5.6	25.2	605	8.5	101.2	2.9	278	6490	33.1
109.0	10.2	29.3	796	10.3					

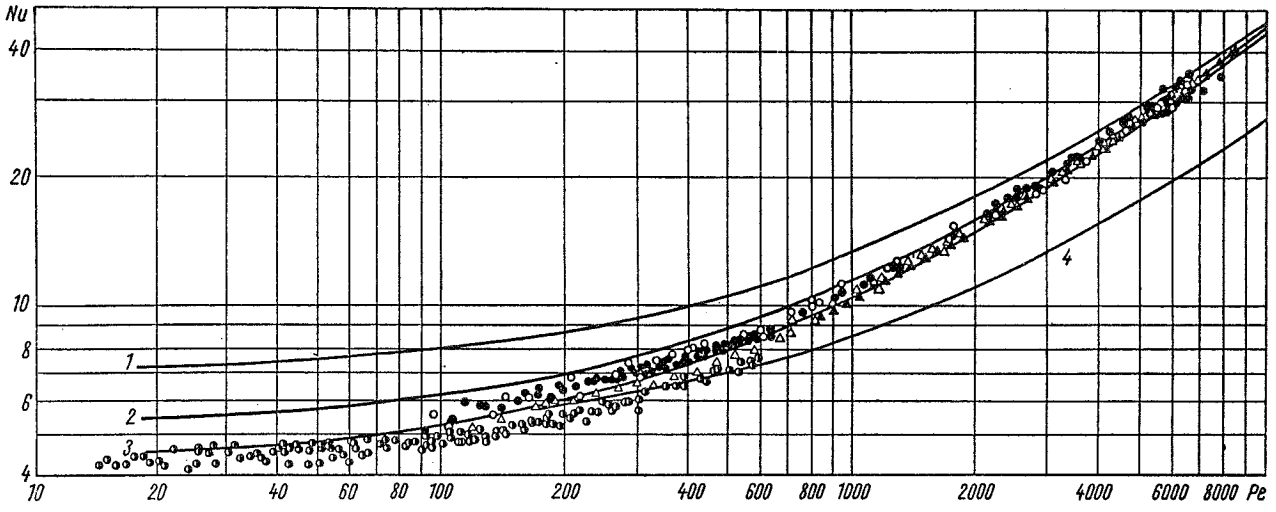

Figure 3. Data on Heat Transfer in Liquid Metals Flowing in Round Pipes for $0.02 \leq Pr \leq 0.03$. 1, 2, 3, 4 Are Curves Obtained by Eqs. (3) and (4), (1) and (5), Respectively; the White and Black Triangles Pertain to Tests Using Mercury in Nickel and Stainless Steel Pipes, Respectively [1]; the Black Circles are for Tests With the Na-K Alloy in a Copper Pipe [1]; the Half-Shaded Circles Show Experimental Data for Mercury [3]; the White Circles Show the Results of the Two Series of Tests With the Na-K Alloy in a Stainless Steel Pipe.

TABLE 2. Results of Control Tests Using the Sodium-Potassium Alloy for a Stainless Steel Pipe

Pe	Nu	Pe	Nu	Pe	Nu	Pe	Nu
134	6.2	692	8.9	1290	11.7	1995	14.5
172	6.2	700	9.4	1290	12.6	2065	14.2
309	7.2	733	9.9	1445	12.9	2320	17.0
462	8.3	881	11.1	1480	12.6	2630	19.1
537	8.3	891	10.4	1570	13.5	2920	17.0
550	8.7	1000	10.2	1585	12.3	5290	27.6
631	8.9	1000	11.9	1780	14.5	6160	31.6
669	9.0	1100	11.0	1820	14.8		

the negligible effect of the thermal contact resistance on heat transfer provided the oxides of the liquid metal are in the dissolved state. /13

The experimental data for $0.02 \leqslant Pr \leqslant 0.03$ are situated somewhat lower than the curve obtained in Eq. (2) and, together with data of [3], can be approximated by Eq. (1). As the Prandtl numbers are made smaller, the Nusselt numbers increase with the Peclet numbers held constant, which follows, for example, from calculations made by Buleyev, which are quoted in [1]. Hence, heat transfer in liquid metals (as well as in sodium, $Pr \approx 0.005$) flowing through pipes should be calculated by Eq. (2). The loss of accuracy when using this equation will not exceed 10% even for low (~100) Peclet numbers.

REFERENCES

1. Subbotin, V.I., et al.: Inzhenerno-fizicheskiy zhurnal, Vol. VI. No. 4, 16 (1963). /15
2. Subbotin, V.I., et al.: Vliyaniye ekstsentrisiteta na teploobmen zhidkikh metallov v kol'tsevom zazore [Effect of Eccentricity on the Heat Transfer in Liquid Metals in an Annual Space], Present collection, p. 108.
3. Petukhov, B.S. and Yushin, A.Ya.: Doklady AN SSSR, 136, 6 (1960).
4. Lyon, R.: Chem. Eng. Progr., 47, 2, 75 (1951).
5. Kutateladze, S.S., et al.: Zhidkometallicheskiye teplonositeli [Liquid-Metal Heat Transfer Agents]. Moscow, Atomizdat, 1958.

HEAT TRANSFER WITH LIQUID METAL IN A VERTICAL PIPE AT LOW PECLET NUMBERS

N. A. Ampleyev, P. L. Kirillov, V. I. Subbotin
and M. Ya. Suvorov

Heat transfer with liquid metal in pipes has been thoroughly studied during the last fifteen years. At present a large amount of experimental data has been accumulated and the main governing relationships needed for practical calculations have been, for the most part, clarified. Still remaining unclear are the more complex cases of heat transfer (combined forced and free convection) and the physicochemical processes at the liquid-solid metal interface. The most general solution of heat transfer in a round pipe with q = const has been given by Lyon [1]

$$\frac{1}{\mathrm{Nu}} = 2\int_0^1 \frac{\left(\int_0^\xi u\xi\, d\xi\right)^2}{1+\varepsilon\frac{\varepsilon_M}{\nu}\mathrm{Pr}}\, d\xi. \tag{1}$$

In order to evaluate this integral, in addition to the velocity distribution $u(\xi)$, one must also know the quantity $\frac{\varepsilon_M}{\nu} = \frac{\tau/\mu}{du/dy} - 1$, i.e., the expression which is calculated by differentiating the velocity distribution, and ϵ, the ratio of coefficients of turbulent transfer. The work of E. V. Nomofilov was directed at investigating the relationship

$$\varepsilon\frac{\varepsilon_M}{\nu} = f(\mathrm{Re},\ y). \tag{2}$$

Other theoretical solutions reduce, in one way or another, to the evaluation of Eq. (1), upon making use of Eq. (2).

The first experiments on the heat transfer in liquid metals [2] were more or less roughly qualitative in character, and their accuracy was not too high. The large number of experiments [performed since], [3, 4] have resulted in the following [empirical] formulas

$$\mathrm{Nu} = 3 + 0.014\mathrm{Pe}^{0.8}, \tag{3}$$

$$\mathrm{Nu} = 5 + 0.0021\mathrm{Pe}. \tag{4}$$

When performing these experiments the metal was not specially purified, and its purity was not checked. In experiments with pure metals, higher heat transfer coefficients were obtained, and these are given by the expression /16

$$Nu = 5 + 0.014Pe^{0.8}. \quad (5)$$

The difference in the Nusselt numbers obtained by the above expression and by Eq. (3) was attributed to the so-called thermal contact resistance at the boundary between the wall and the liquid metal. The nature of this resistance, despite experiments performed to clarify it, remained unclear for a long time. The majority of hypotheses have not been verified experimentally or the results of subsequent experiments were contradictory (effect of wettability, gas, etc.). In addition, some investigators attributed to contact resistance any data having values below those which at that time were considered as standard, though these values were quite possible either results of experimental inaccuracies or procedural errors.

The thermal contact resistance to an alkaline metal flowing in a pipe, was recently investigated as well as the conditions leading to its appearance on the heat transfering surface [6]. One can conclude from these experiments that the Nusselt numbers calculated by Eq. (3) apparently, corresponds to the maximum value of the thermal contact resistance produced by impurities suspended in the heated coolant. The maximum value of this resistance is determined by the thickness and structure impurities which precipitate on the wall, and depends on the rate of flow of the liquid metal but does not depend on the impurity content in the flowing metal.

In order to eliminate the effect of the thermal contact resistance on the results of heat-transfer experiments, a method was developed which makes it possible to measure the temperature fields in the liquid stream. The results of experiments performed by using this method have yielded higher heat transfer coefficients than those given by Eqs. (3) and (4) and were in close agreement with Lyon's formula

$$Nu = 7 + 0.025Pe^{0.8}, \quad (6)$$

which is obtained by evaluating the integral in Eq. (1) with attendant use of the Nikuradze velocity distribution on the assumption that $\varepsilon = 1$. It is possible to give a definitive physical meaning to the formula

$$Nu = Nu_0 + APe^{0.8} \quad (7)$$

if we regard the expression $Nu_0(Re)$ as the value of the Nusselt number when $Pr = 0$. In this case the values of Nu_0 which characterize the heat transferred by conduction only will not be constant, but will depend on the velocity

distribution, i.e., on the Reynolds number. The second term in Eq. (7) will reflect the contribution made by turbulent heat transfer.

Various authors have obtained close results for Nu_0 [7]; it may be assumed approximately, with an error of 10%, that /17

$$Nu_0 = 8\frac{\bar{w}}{w_{max}}. \quad (8)$$

It is known, that for laminar flow $\bar{w}_{min}/w_{max} = 0.5$ and this expression thus yields Nu = 4. As is known, the theoretical value is 4.36, as this was substantiated experimentally in [8]. On the other hand, other experiments have yielded higher (Nu = 7) as well as lower (Nu = 0.6) values [9-12].

The opinions to the effect that the high heat coefficients obtained in papers [9] and [13] were due to the fact that the heat transfer was measured in a section with unsteady heat transfer ($l = 5d$) is incorrect. In this case, if there is no experimental error, $Nu/Nu_\infty = 1.15$-1.2 and then Nu should be not more than about 5, but not 7 or 8 as was obtained in [9] and [13]. Consequently, the 50% difference remains unexplained.

The opinion that the low heat transfer coefficients in the region of low Peclet numbers are due to improper determination of the average temperature of the liquid, which is caused by not taking into account longitudinal heat leakages along the wall and the heat transfer agent [14] and [15], is only partially correct. The experiments performed by Johnson are in doubt from the point of view of methodology due to the distortion of the temperature field and the heat fluxes by transverse slots in the test section. However, the same results were obtained in a copper pipe [10], which did not have slots and which was cooled by a sodium-potassium alloy. Consideration of longitudinal heat fluxes in the fluid does not make a large contribution, since the Nusselt numbers still differ by a factor of two when Pe = 25.

Analysis of data on measured temperature fields expressed in the dimensionless form [11] has made it possible to approximately establish the experimental temperature distribution a stream of liquid metal and to use this distribution to set up the interpolational formula

$$Nu = 5 + 0.025Pe^{0.8}$$

or

$$Nu = 4.36 + 0.343Pe_*^{0.8}, \text{ where } Pe_* = \frac{v_* d}{\nu}.$$

The theoretical results obtained in [16] are practically identical with the above results.

Reference [17] describes approximate calculations of heat transfer to the inlet part of a pipe during flow of a liquid metal. It has been determined that the length of the thermal stabilization segment becomes larger with an increase in the Reynolds number. The values of the Nusselt number were estimated in a wide range of Reynolds and Prandtl numbers. Deissler [18] has analyzed the effect (on the heat transfer) of the length of thermal stabilization, of Re and Pr, the shape of the channel, and the initial velocity distribution. As a result it was shown that at Pr = 0.01 and a given l/d, the ratio Nu_{loc}/Nu_{∞} for parallel plates /18
is somewhat lower than for pipes. At high Reynolds numbers and a given l/d, the ratio Nu_{loc}/Nu_{∞} becomes smaller with an increase in the Prandtl number. For low Reynolds numbers the changes are more complex. Ratio Nu_{loc}/Nu_{∞} first decreases and then, with an increase in the Prandtl number, increases somewhat. Results of calculations performed in [17] show that fully developed heat transfer starts as early as at a distance of less than 10d.

N. S. Kondrat'yev has studied heat transfer ($l/d = 17.4,\ 8.4$) attendant to the flow of the lead-bismuth eutectic alloy [12]. The results of his experiments can be approximated by the expression

$$\frac{Nu}{Nu_{loc}} = \varepsilon_l = 4.6\left(\frac{l}{d}\right)^{-0.4},\quad \frac{l}{d} \ll 30.$$

Kondrat'yev has not detected the effect of the Reynolds number on the length of the thermal section. By comparing the experimental data obtained by various authors it follows from [4] that, when $l/d \geq 30$, the effect of the inlet section has little influence on the average heat transfer, while for short pipes it is recommended to introduce the coefficient ε_l which takes this effect into account:

$$\varepsilon_l = 1.72\left(\frac{d}{l}\right)^{0.16}.$$

It was discovered in [19] by measuring the temperature distribution in the inlet section of the pipe that stabilization of local values of the heat transfer coefficient takes place at a distance of less than 10d when the flow is hydordynamically stabilized at Pe = 50-1500. On the other hand, Isakoff and Drew [20] found that the heat transfer coefficient is not stabilized even at a length of 58d and it is by 12% higher than the values obtained at a distance of 138d from the pipe inlet. Similarly, Subbotin et al. [21] have determined the local coefficients of heat transfer for $Pr \approx 0.02$ in the thermal stabilization section ($l/d = 5$, 10 and 15) at $Pe = 10^4 - 2\cdot 10^5$.

Stabilization of heat transfer in the range of Re under study took place practically at $l/d = 15$. At distance $l/d = 5$ the heat transfer coefficient was by 20-40% higher than the stabilized values. The disagreement between the experimentally obtained values of ε_l and those obtained theoretically in [17] is as high as 30%.

The length of the thermal stabilization section and $\varepsilon_l = Nu_{loc}/Nu_\infty$ increase, according to [17], with an increase in the Reynolds number. The heat transfer coefficients obtained by measuring the wall temperature are lower than those obtained on the basis of the measured temperature distribution. The length of the thermal stabilization section and the magnitude of ε_l in this case are smaller; the coefficient is equal to ten and does not depend on the rate of flow of the metal. This difference is attributed to the effect of the thermal contact resistance.

The local Nusselt numbers for Re = $7.1 \cdot 10^3$, $3.4 \cdot 10^4$, $1.6 \cdot 10^5$ and $7.2 \cdot 10^5$ in a round pipe were determined numerically in [22]. It follows from the results /19
of calculations that the length of the thermal stabilization section (Pr = 0.025) increases as the Peclet number is increased from 10 to 3000 and decreases when the latter number is increased further.

In the present paper an attempt is made to clarify the cause of the disagreement between results obtained experimentally at low Peclet numbers and the theoretical value of Nu = 4.36. We have set out to determine the length of the initial thermal [stabilization] section as a function of the Peclet number for turbulent flow.

Figure 1 shows the schematic diagram of the circulation circuit made from 1Kh18N9T stainless steel pipes with an a-c electromagnetic volute pump, providing a delivery rate of up to 10 m^3/hour. The metal in the circuit is circulated through the test section and an alloy-water heat exchanger. The alloy is pressurized from tank 1 into tank 4 and into the circuit by means of an inert gas and flows through a mesh filter made of several layers of nickel wire mesh. Measuring tank 7 was provided for calibrating the flowmeters. The oxides are continuously removed from the alloy by cold traps. The oxide content is monitored by a float indicator and a distillation sampler [23]. The flow rate of the sodium-potassium alloy is measured by a magnetic flowmeter combined with the R2/1 potentiometer and is adjusted by valves.

The test section (Fig. 2) consists of a 2700 mm long copper pipe with an /21
inside diameter of 50 mm and wall thickness of 5 mm. The pipe is connected to mixing chambers by flanges employing a ball-and-socket joint. The mechanism for moving the thermocouple and a rubber packing gland, which is fastened by a connector nut, is placed on the top chamber cover. Longitudinal grooves 3 mm deep are milled in the pipe wall and chromel-alumel thermocouples are placed in them. The hot junctions of the thermocouples are calked by copper wedges, and the electrodes are provided with alundum insulation. The copper pipe is insulated by micanite 0.2-0.3 mm thick, on which is placed a nichrome heater from wire 3.5 mm in diameter with a pitch of 4 mm; then asbestos insulation, thermometers and compensating heaters were placed over the pipe, in this order (see Fig. 2).

When measuring heat transfer (Pe < 100) we have discovered appreciable heat losses at the section from the end of the heater to the mixing chamber, for which reason we have placed thermometers there. The heater was made in two sections, each 1 meter long. The electric power used by the heaters was measured by a set of class 0.5 instruments. The thermocouple emf was measured by the PPTN-1 potentiometer, together with the M 21/4 mirror galvanometer.

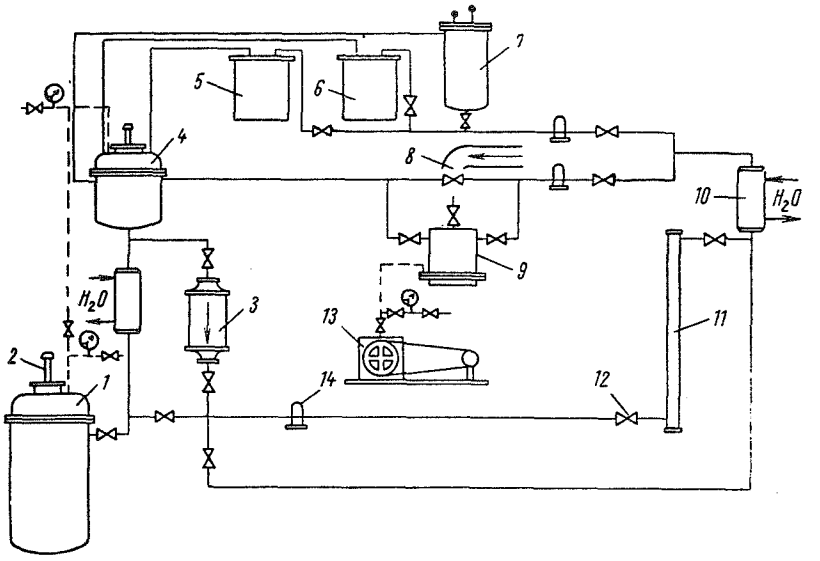

Figure 1. Schematic of Experimental Setup. 1) Filling Tank; 2) Level Meter; 3) Electromagnetic Pump; 4) Pump Tank; 5) Toluene-Cooled Cold Trap; 6) Water-Cooled Cold Trap; 7) Tank for Calibrating the Electromagnetic Flowmeter; 8) Float Indicator; 9) Sample Taker; 10) Heat Exchanger; 11) Test Section; 12) Valve; 13) VN-2 Vacuum Pump; 14) Electromagnetic Flowmeter.

The temperature distribution in the metal flow was measured by a movable /22 thermocouple (Fig. 3). The frame of the mechanism is pipe 11, which has been lead out from the metal flow through a packing gland, and the thermocouple is moved in the longitudinal direction by a jack-type mechanism. The main components of the mechanism used for moving the thermocouple in the lateral direction are a rod with an inclined slit (wedge) and a probe with a shank and axle. When the rod is moved in the longitudinal direction, the shank which is inserted into the inclined slit moves across the pipe. The thermocouple which is fastened to the other side of the axis, then also moves across the flow. Pipe 12 is moved relative to pipe 11 by another jack, which imparts motion to the rod. The shank and the entire inside cavity of pipe 11 are protected by a bellows from penetration by the metal. The chromel-alumel wires are welded hermetically to the end of the probe, pass inside of flexible insulation through the probe, shank and pipe 12, and are lead out to the outside. The movement of the end of the probe (of the thermocouple) in the transverse direction is recorded by an indicator, which bears on the pullbar, which is connected to pipe 12. The movement along the pipe was measured by a ruler (with scale division of 1 mm). The thermocouple was calibrated by comparing the displacement of its end part with the indicator readings. The thermocouple junction thickness is 0.7 mm. The probe was centered in the pipe by means of a guiding bushing, into which three guiding blades have been inserted.

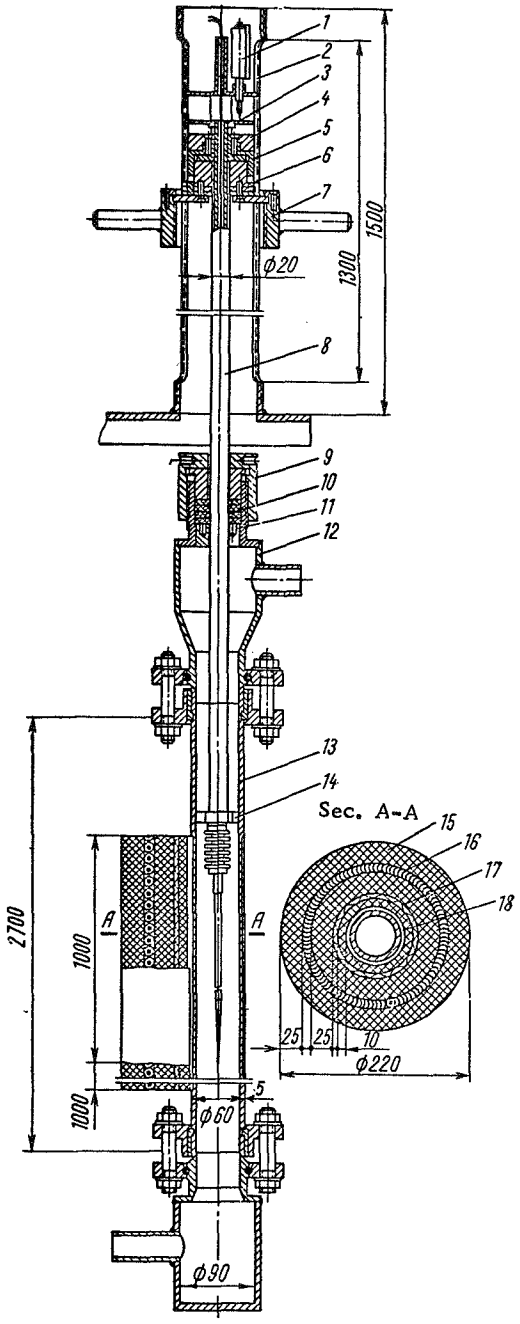

Figure 2. Test Section.
1) Indicator; 2) Pipe 202 mm in Diameter; 3) Plate; 4) Graduated Circle; 5) and 9) Connector Nuts; 6) Support; 7) Triple-Thread Nut; 8) Movable Thermocouple; 10) Packing Gland; 11) Pipe Union; 12) Mixing Chamber; 13) Copper Pipe; 14) Guide Bushing; 15) Asbestos Insulation; 16) Compensating Heater; 17) Thermometer; 18) Insulation (Mica).

Methodology Used in the Experiments and in Analyzing the Experimental Data

Before starting the experiments the sodium-potassium alloy was filtered through the cold trap. When doing this the sampling device was periodically started up. After an oxygen concentration of $3 \cdot 10^{-3}$-$5 \cdot 10^{-4}$% by weight was reached, the given flow rate of the alloy through the test section was established and the heaters were started up. After the wall temperature was measured, the temperature in the alloy flow (28 points) was taken. The density of measurements was the highest in the region closest to the wall. The measurements were made with the thermocouple moving from the center to the wall. Here, for more reliable temperature readings at the wall, the thermocouple was moved until two consecutive temperature measurements were identical. The bending of the thermocouple (0.5-1 mm) which is inevitable [under these circumstances] did not go past the limits of the device's flexibility.

The theoretical power was calculated as an average

$$\overline{Q} = \frac{Q_{el} + Q_{th}}{2}.$$

The disagreements in the thermal balance magnitude did not basically exceed 3-7%. The heat transfer coefficient was determined by two methods: 1) from the temperature distribution of the wall along the length of the section and of the temperature

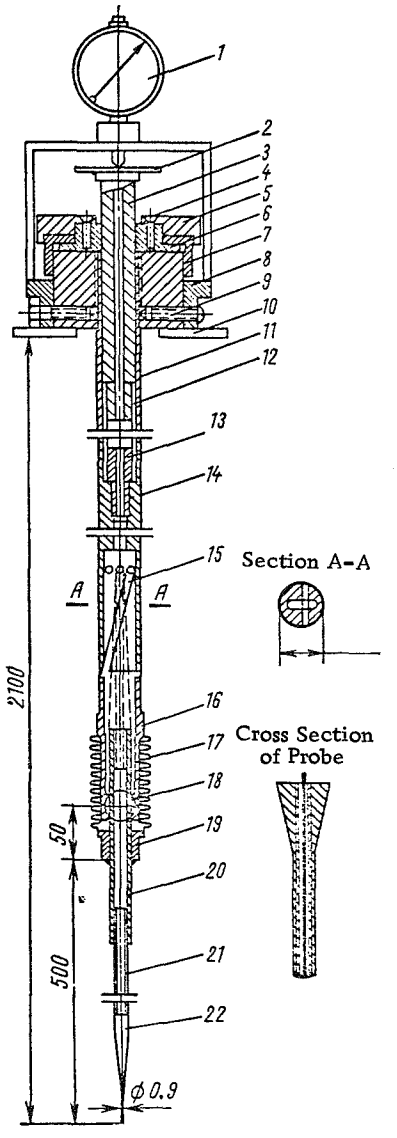

Figure 3. Movable Thermocouple. 1) Indicator; 2) Plate; 3) Pullbar; 4) Bolt; 5) Graduated Circular; 6) Bushing; 7) Nut; 8) Support; 9) Spline; 10) Washer; 11) Pipe With Diameter of 20 x 2 mm; 12) Pipe With Diameter of 16 x x 1 mm; 13) Reducing Adapter; 14) Wedge; 15) Shank; 16) Rim; 17) Bellows; 18) Axle; 19) Ring; 20) Pipe With Diameter of 10 x x 2 mm; 21) Pipe With Diameter of 6 x 1 mm; 22) End Pieces.

of the liquid in the mixing chambers and 2) from the temperature distribution in the alloy flow. The heat transfer coefficient was calculated from the expression:

$$\alpha = \frac{\bar{q}}{(\bar{t}_w - \bar{t}_f)}, \qquad (9) \quad /23$$

where

$$\bar{q} = \frac{\bar{Q}}{\pi d_{in} l};$$

here ($\bar{t}_w$ - t_f) is the difference of temperatures at the inside surface of the wall and the average calorimetric temperature of the liquid, averaged over the length. This difference was determined on the basis of the temperature distribution of the wall along the length of the pipe and the readings of the thermocouples used to measure the alloy's temperature at the inlet and exit from the heated section. The temperature drop in the wall was determined by the ordinary formulas

$$\Delta t_3 = \frac{\bar{q} d_{in} \ln \frac{d_{ext}}{d_{in}}}{2\lambda_w}. \qquad (10)$$

The temperature of the alloy at the inlet and outlet of the heated section was determined by taking into account the heat lost in the flow stabilization section and from the end of the heater to the mixing chamber

$$\bar{t}_{inl} = t_{mch.} - \Delta t, \quad \bar{t}_{out} = t_{mch.} + \Delta t_{los}$$

The heat losses were determined from the formula

$$Q_{los} = \frac{\lambda_{as} F \cdot 10^3}{\delta_{th} 40 \cdot 10^{-3}} \Delta E.$$

The average liquid temperature $\bar{t}_f$ was determined upon taking into account the flow of heat in the liquid and the wall $t_f = \bar{t}_{mch.} + \delta t$

$$\delta t = \frac{1}{c_p \gamma w} \left\{ \lambda_f + \lambda_w \left[\left(\frac{d_{ext}}{d_{in}} \right)^2 - 1 \right) \right\} \frac{d\bar{t}}{dx},$$
$$\frac{dt}{dx} = \frac{4q}{c_p \gamma d_{in}}. \qquad (11)$$

According to the second method the wall temperature was found by extrapolating the temperature distribution to the wall's surface. Here the convergence was checked with the boundary condition

$$\left.\frac{dt}{dr}\right|_{r=r_0} = -\left.\frac{\bar{q}}{\lambda_f}\right|_{r=r_0}.$$

The average temperature of the liquid metal could have been found from the expression

$$\bar{t}_f = \frac{\int_0^1 t_i \frac{w_i}{\bar{w}}\, dz}{\int_0^1 \frac{w_i}{\bar{w}}\, dz}, \text{ where } z = \left(1-\frac{r_i}{r_0}\right)^2. \tag{12}$$

In calculating $\bar{t}_f$ the integration was replaced by summing. We shall now consider in more detail the selection of the velocity distribution for calculating this temperature. As was shown in [18], there is no difference in $\bar{t}_f$ and, consequently, also in the Nusselt numbers, if it is assumed that the turbulent flow is governed by Karman's logarithmic velocity distribution /24

$$\begin{array}{ll} 0<y^+<5 & u^+=y^+ \\ 5<y^+<30 & u^+=5\ln y^+-3{,}05 \\ 30<y^+ & u^+=2{,}5y^++5{,}5 \end{array} \tag{13}$$

or by the power law

$$\frac{w_i}{\bar{w}} = \frac{(2+a)(1+a)}{2}\left(1-\frac{r_i}{r_0}\right)^a; \quad a=f(\mathrm{Re}). \tag{14}$$

Expressions (13) and (14) are suitable for developed turbulent flow. For laminar flow with Re < 2300 it would have been natural to use the parabolic expression for the velocities

$$\frac{w_i}{\bar{w}} = 2\left[1-\left(\frac{r_i}{r_0}\right)^2\right]. \tag{15}$$

However, Eqs. (13-15) are suitable only for an isothermal flow. When the liquid is heated or cooled the velocity distribution changes. In addition, turbulent flow ensues with lower Reynolds numbers as a result of acceleration or turbulization of the flow, which is brought about by natural convection. The velocity distribution in a nonisothermal laminar flow has been analyzed in [24]. The parameter which characterizes the natural convection intensities is the quantity

$$Z = r_0 \sqrt{\frac{g\beta \mathrm{Pr}}{\nu^2} \cdot \frac{dt}{dx}}. \tag{16}$$

The curve of $\mathrm{Re}_{cr} = f(Z)$, according to data of [24] is shown in Fig. 4.

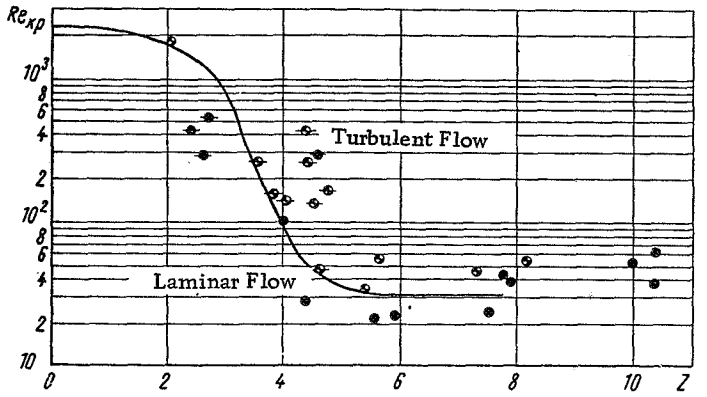

Figure 4. The Critical Reynolds Number as a Function of Z.

In our experiments Z varied from 5 to 10. Figure 4 shows that under the circumstances we always had turbulent flow. Hence, strictly speaking, the use of the expression for the velocity distribution given in [24] is also incorrect /25

$$\frac{w_i}{w} = \frac{Z}{2}\left[\frac{ber\,(Z')\,i\,bei\,(Z) - ber\,(Z)\,bei\,(Z')}{bei'\,(Z)\,bei\,(Z) + ber'\,(Z)\,ber\,(Z)}\right]; \tag{17}$$

$$Z = r_0 \sqrt[4]{\frac{g\beta \mathrm{Pr}}{\nu^2}\frac{\partial t}{\partial x}}\quad ber\,(Z) = \mathrm{Re}\left[J_0(Z\sqrt{i})\right]$$

$$bei\,(Z) = -\mathrm{Im}\left[J_0(Z\sqrt{i})\right]$$

$$Z' = r_i \sqrt{\frac{g\beta \mathrm{Pr}}{\nu^2}\frac{\partial t}{\partial x}}\quad ber'\,(Z) = -\mathrm{Re}\left[\sqrt{i}\,J_1(Z\sqrt{i})\right]$$

$$bei'\,(Z) = \mathrm{Im}\left[\sqrt{i}\,J_1(Z\sqrt{i})\right]$$

Re denotes the real part; Im denotes the imaginary part; $J_0 J_1$ is a Bessel function.

The velocity distribution obtained by Deissler [25, 26] for heat transfer in a round pipe was calculated by considering the viscosity only along the pipe cross section, and hence is suitable only for gases. Ber [27] has calculated the velocity field in a round pipe with heat transfer in a flow of fluid. To determine the velocity for Re < 2300 Gorchakov [28] has suggested to use the energy equation

$$w_i = \frac{1}{r_i}\frac{dt}{dr}\left[r_i(\varepsilon_q + a)\frac{dt}{dr}\right]\frac{1}{dt/dx}. \tag{18}$$

It may be assumed in the first approximation that 1) $\varepsilon_q = \varepsilon_M$ and 2) that the turbulent viscosity in the flow

$$\frac{\varepsilon_m}{\nu} = 0.4\frac{\vartheta_* r_0}{\nu}\xi(1-\xi) \text{ [26]},$$
$$\varepsilon_m = \varepsilon_q = 0.4 v_* r_0 \xi(1-\xi),$$
$$\varepsilon_q = b\xi(1-\xi).$$

Differentiating Eq. (18) we get

$$w_i = \frac{1}{Ar_0^2}\left\{\frac{1}{\xi}(a + 2b\xi - 3b\xi^2)\times\right.$$
$$\left.\times\frac{dt}{d\xi} + (a + b\xi + b\xi^2)\frac{dt^2}{d\xi^2}\right\}, \tag{19}$$

where

$$A = \frac{dt}{dx} = \text{const}.$$

The first and second derivatives of the temperature were determined graph- /26
ically from the experimental temperature curves in the sodium-potassium flow. It was thus found that $W_i = f(\xi)$. In the region next to the wall W_i was found by interpolation. After the velocity distribution has been interpolated, the value thus obtained was computed with the measured value of $\overline{W}$ and the difference did not exceed 10%. In this manner we have found the approximate distribution of $W_i/\overline{W} = f(\xi)$ for Re < 2300 in a nonisothermal flow. Using this distribution we have calculated the Nusselt number. Figure 5 shows the velocity distribution obtained by differentiation for Z = 5 and 9 and the theoretically calculated curves from [24].

Results

The results of studies, expressed in terms of similarity criteria, are shown in Figs. 6 and 7. The experimental data for laminar flow gave values of Nu > 4.36. This divergence from the theoretical value is due to the effect of natural convection. Consequently, also in previously performed work this difference, whenever observed, is attributable to precisely this circumstance.

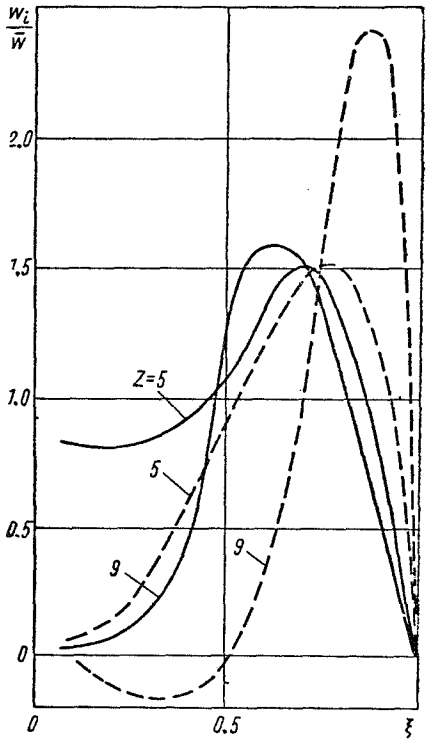

Figure 5. Velocity Distribution According to Data of [24] (Dashed Line) and That Found Graphically (Solid Line).

The measured temperature distribution in the flow of the sodium-potassium alloy has shown that the actual temperature is higher than the mixed mean, which is determined in the mixing chamber. Figure 8 shows the temperature distribution in the wall and in the liquid along the length where heat transfer takes place (Pe = 10, Re = 400). As can be seen from the figure, the actual temperature of the alloy is higher than the temperature given by the straight line drawn through points obtained in the mixing chamber $t_{mch.}$, which is usually assumed in calculating heat transfer coefficients for q = const. This temperature increase is satisfactorily taken into account by the formula presented in [14].

The length of the initial thermal [stabilization] section for Pe < 100 is about $l_0/d \approx 1$. The sharp drop in the heat transfer (in the Nusselt numbers) in the above range of Peclet numbers obtained in [10] is due to the fact that in analyzing the results no consideration was given to heat losses from the end of the heated section at the exit to the mixing chamber. This is attested to by a recalculation of one of the regimes. The lower-than-average Nusselt numbers obtained in [15] have been produced, as was shown in [8], by distortion of the thermal flux which was brought about by the transverse grooves in the test sections. /28

The heat transfer, which was determined by two methods yielded close results for Pe < 100, which points to the absence under the conditions at hand (oxygen content in the sodium-potassium alloy of $3 \cdot 10^{-3}$ -$5 \cdot 10^{-4}$% by weight) of appreciable thermal contact resistances.

The local value of the Nusselt number at different distances from the inlet is shown in Fig. 9. Using these experimental points we have found the averaging

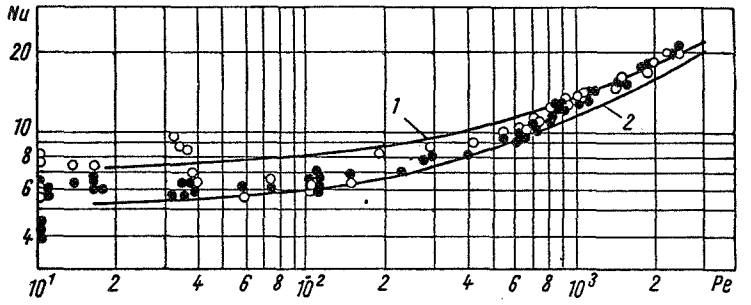

Figure 6. Experimental Data Using the Coordinates lg Nu = f(lg Pe). 1) $Nu = 7 + 0.025\ Pe^{0.8}$; 2) $Nu = 5 + 0.025\ Pe^{0.8}$; the White Circles Denote the Temperature Distribution in the Flow of the Sodium-Potassium Alloy; the Black Circles Denote the Same in the Wall.

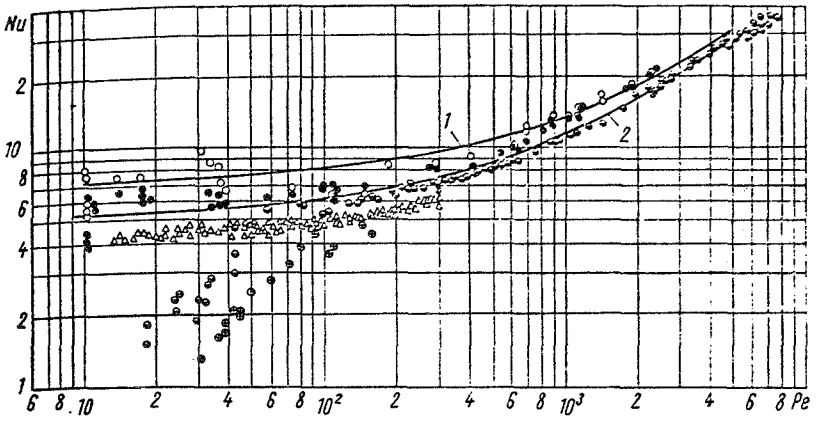

Figure 7. Results of Heat Transfer Experiments in a Pipe. 1) $Nu = 7 + 0.025\ Pe^{0.8}$; 2) $Nu = 5 + 0.025\ Pe^{0.8}$; the Black Circles Denote Curves of Temperature Distribution in the Wall; the White Circles Denote the Same in the Sodium-Potassium Alloy; the Triangles Are for Data of [8], the Half-Blackened Circles are for Data of [10] and the Crossed Circles Are for Data of [15]

curves and calculated the coefficients $\varepsilon_l = Nu_{loc}/Nu_{\infty}$, which characterize the increase in the heat transfer at the inlet section of the pipe. Figure 10 compares the experimental results with those calculated theoretically in [22]. The length of the initial thermal [stabilization] section was here determined from the

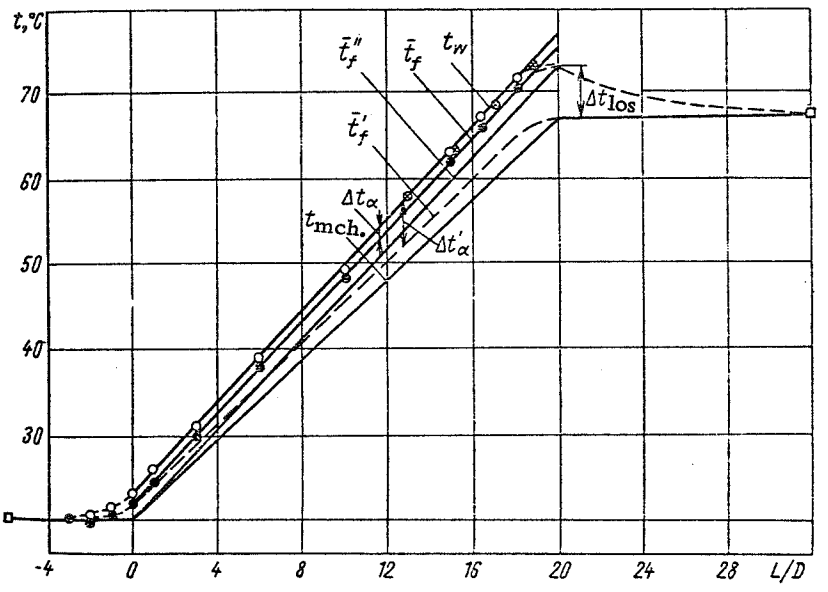

Figure 8. Characteristic Temperature Distributions Along the Length of the Test Section. $\bar{t}_f''$ is the Temperature, Calculated by Taking Into Account Heat Losses, but Without Accounting for Heat Flow in the Longitudinal Direction; t_w Is the Wall Temperature; $t_{mch,}$ is the Temperature Without Consideration of Heat Losses and the Longitudinal Flow of Heat; $\bar{t}_f'$ is the Temperature Calculated by Considering the Longitudinal Flux, But Without Taking Into Account the Heat Losses; $\bar{t}_f$ Is the Temperature Calculated by Taking Into Account the Longitudinal Flux and the Heat Losses; the Crossed Circles Denote the Wall Temperature Measured by Thermocouples Inserted in the Wall; the Squares Denote the Temperature in the Mixing Chamber; the Black Circles Show the Liquid Temperature Measured by the Movable Thermocouple; the White Circles Denote the Wall Temperature.

distribution of Δt_α along the length of the pipe. It follows from Figs. 10 and 11 that this length and the coefficient ε_l first increase with an increase in the velocity, and then decrease. Qualitatively this phenomenon is in agreement with results obtained in [18] and [22]. Stabilization of heat transfer in the range of Peclet numbers under study takes place at $l/d \leq 15$.

The experimental data (Fig. 12) lie below the theoretical curve obtained in [25]. The lower values of Nusselt numbers, as compared with those calculated theoretically, are, in the opinion of the authors, due to an increase in parameter Z. /30

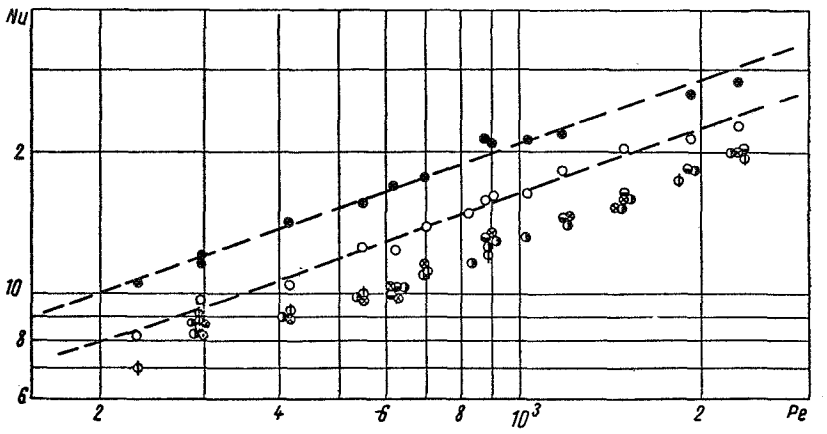

Figure 9. Local Nusselt Numbers for Cross Sections Situated at Different Distance l/d.

1 3 6 10 15 16.5

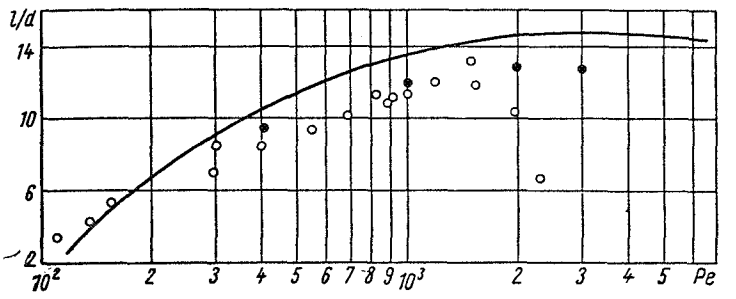

Figure 10. Length of the Initial Thermal [Stabilization] Section as a Function of the Peclet Numbers. The White Circles Denote Data Obtained by the Present Authors; the Black Circles Are for Experimental Data Obtained in [21]; the Calculations Are From [22].

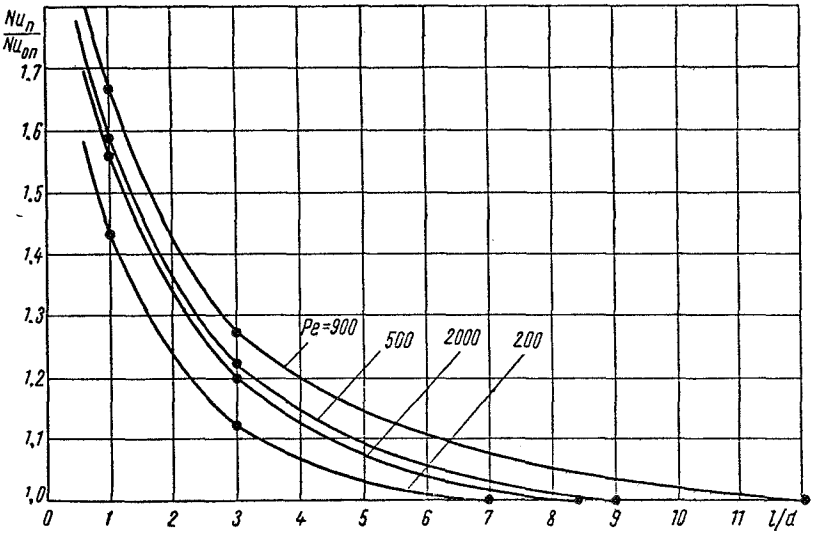

Figure 11. Change in the Relative Heat Transfer at the Inlet Section of the Pipe. The Black Circles Denote Data Obtained by the Present Authors.

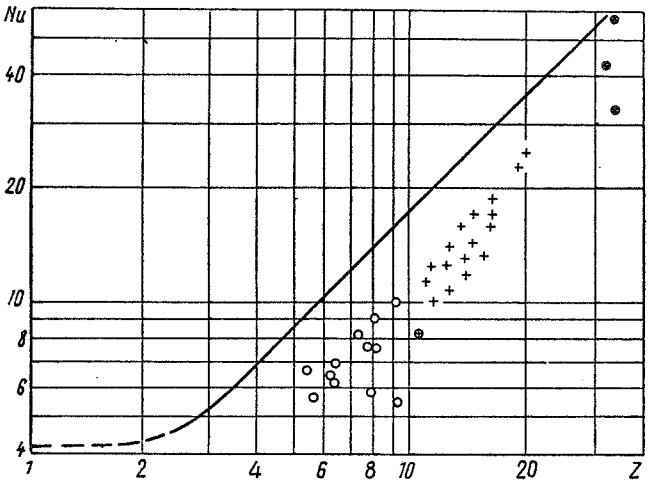

Figure 12. Comparison of Experimental Data With the Theoretical Curve of [24]. The White Circles Denote Results Obtained by the Present Authors; the Black Circles Are for Data Due to Gorchakov; the Crosses Denote Results Obtained in [28].

As was shown, when natural convection arises, the flow becomes turbulent even with Re = 400. Hence, the turbulent Z will be somewhat lower (ν becomes greater) and the experimental points will be displaced to the left. A more detailed study of this problem is presented in [28].

NOTATION

l length of heated section

r_0 pipe radius

y distance from wall

Q heater rating

E thermocouple emf

G flow rate

m number of junctions in thermometer [thermocouple]

δ thermometer [thermocouple] thickness

ε_q turbulent heat transfer coefficient

ε_M	turbulent momentum transfer coefficient
$\varepsilon = \varepsilon_q / \varepsilon_M$	ratio of turbulent transfer coefficients
$\varepsilon_l = Nu_{loc}/Nu_\infty$	ratio of the local Nusselt number and of that stabilized along the length
$\bar{\varepsilon}_l = \overline{Nu}/Nu_\infty$	average ratio

Dimensionless quantities

$y^+ = y\ v^*/\nu$	distance from wall
$\xi = r/r_0$	distance from center

Subscripts /31

in	internal side
ext	external side
f	fluid
W	wall
loc, i	local value
-(bar)	average value
el	electrical
th	thermal, pertaining to the thermometer [thermocouple]
∞	at infinity from the inlet
los	pertaining to losses
inl	pertaining to the inlet
out	pertaining to the outlet
as	asbestos
max	maximum value
mch	mixing chamber

fl pertaining to the flow stabilization section

cr critical, i.e., corresponding to transition from laminar to turbulent flow

REFERENCES

1. Lyon, R. N.: Chem. Eng. Progr. 47, 75 (1951).
2. Styrikovich, M. A. and Semenovker, I. Ye.: Zhurnal eksperimental'noy i teoreticheskoy fiziki, 10, 1324 (1940).
3. Mikheyev, M. A., et al.: In the book Reaktorostroyeniye i teoriya reaktorov [Reactor Building and Theory]. page 139. Moscow, Published by Academy of Sciences of the USSR (Report of the Soviet Delegation to the Internal Conference on the Peaceful Uses of Atomic Energy, Geneva, 1955).
4. Kutateladze, S. S., et al.: Zhidkometallicheskiye teplonositeli [Liquid-Metal Heat Transfer Agents]. Atomizdat, Moscow, 1958.
5. Dwyer, O. E.: A. I. Ch. E. Journal, 9 (2), 261 (1963); Nucl. Sci. Eng., 15, 336 (1963).
6. Ivanovskiy, M. N., et al.: Kontaktnoye termicheskoye soprotivleniye pri turbulentnom techenii zhidkikh metallov [Thermal Contact Resistance in the Turbulent Flow of Liquid Metals]. In print.
7. Kirillov, P. L.: Teplofizika vysokikh temperatur, 1 (1), 102 (1963).
8. Petukhov, B. S. and Yushin, A. Ya.: Doklady AN SSSR. 136 (6), page 132, 1961.
9. Pirogov, M. S.: Teploenergetika, No. 3, 62 (1961).
10. Subbotin, V. I., et al.: Issledovaniye teploodachi pri techenii zhidkikh metallov v trubakh [Study of Heat Transfer in Liquid Metal Flows in Pipes]. Inzhenerno-fizicheskiy zhurnal, 6, No. 4, 16 (1963).
11. Kirillov, P. L.: Atomnaya energiya, 13, No. 5, 481 (1962).
12. Kondrat'yev, N. S.: In the collection, Voprosy teploobmena [Problems of Heat Transfer] 96. Published by the Academy of Sciences of the USSR. Moscow, 1959.
13. Pirogov, M. S.: Atomnaya energiya, 8, No. 4, 367 (1960).
14. Trefethen, L. M.: Trans. ASME, 78 (6), 1207 (1956).
15. Johnson, H.: Trans. ASME, 75 (6), 1191 (1953).
16. Buleyev, N. I.: Teploperedacha, Published by the Academy of Sciences of the USSR, 64, 1962.
17. Poppendiek, H. F.: Nucl. Sci. Eng, 5 (6), 390 (1959).
18. Deissler, R. G.: Trans. ASME, 77, No. 8 (1955).
19. Kirillov, P. L., et al.: Atomnaya energiya, 6, No. 4, 382 (1959).
20. Isakoff, S. E. and Drew, T. B.: General Discussion on Heat Transfer, 405 (1951).
21. Subbotin, V. I., et al.: Atomnaya energiya, 13, No. 2, 155 (1962).
22. Buleyev, N. I., et al.: Teplofizika vysokikh temperatur, 4, No. 4, page 540, 1966.
23. Dmitriyeva, I. B., et al.: Opredeleniye soderzhaniya kisloroda v natrii i splave natriy-kaliy metodom vakuumnoy distillatsii [Determination of the Oxygen Content of Sodium and of a Sodium-Potassium Alloy by Vacuum Distillation].

24. Brown, W. G.: VDI-Forschungsheft, 480 (1960).
25. Deissler, R. G.: Trans. ASME, 76, (1), 73 (1954).
26. Deissler, R. G.: NACA TN 2242, 3145 (1954).
27. Ber, L. E.: Izvestiya AN SSSR, OTN, No. 11, page 77, 1957. /32
28. Gorchakov, M. K., et al.: Teplootdacha natriya i splava natriy-kaliy v korotkikh vertikal'nykh trubakh pri smeshannoy konvektsii [Heat Transfer of Sodium and of a Sodium-Potassium Alloy in Short Vertical Pipes by Combined Convection]. Article following this one in the present collection.

HEAT TRANSFER OF SODIUM AND A SODIUM-POTASSIUM ALLOY IN SHORT VERTICAL PIPES BY COMBINED CONVECTION

L. G. Volchkov, M. K. Gorchakov, P. L. Kirillov and F. A. Kozlov

Heat transfer with liquid metal by combined convection (forced and natural) /32 is studied because of the need to design heat exchanger apparatus, particularly, cold traps for oxides of alkaline metals. Data on this topic are not available, with the exception of individual remarks [1] to the effect that on parallel convection (when forced and natural convection proceed in the same direction) the heat transfer coefficient increases substantially. The published results of theoretical [2-5] and experimental [6-10] studies using liquids with $Pr > 1$ do not satisfactorily clarify the problem of heat transfer with liquid metals by combined convection. The qualitative pattern of the fluid flow and heat transfer for combined convection can be observed in [2], which solves the problem for laminar stabilized flow with $q_w = \text{const}$. Subsequently the results of these calculations will be compared with experimentally obtained data.

The heat transfer was studied at test sections - recuperators* - with the following basic parameters:

Section number	1	2	3
Central tube diameter, d, mm	102	68	135
Length of heat transfer section, $l_{h.t}/d$	5	5	5
Central tube length, l/d	8	8	8
Wall material	Copper	1Kh18N9T steel	Copper
Wall thickness, mm	6.0	1.2	5.0
Width of annular space δ, mm	5.0	6.0	7.5
Heat transfer agent	Na and Na—K	Na	Na

*[Translator's Note: Also called regenerators].

Section number	1	2	3
Range of Peclet numbers under study	7.5—130 (Na) 3.6—350 (Na—K)	4.8—150	3.1—150
Range of Z under study	15.8—21.5 (Na) 19—29 (Na—K)	10.5—17	19—26

At test section No. 1 (external surface of the annular space) we have installed thermocouples, the design of which (similar to that described in [6]) made it possible to measure the temperature along the pipe cross section at the entire heat-transfer section. At section No. 2 (see Fig. 1) the movable thermocouple could be used to measure the temperature distribution only at the center of the heat transfer section. The thermocouples at section No. 3 were placed both on the heat transfer and on the external wall. Except for this the sections differ from one another only by inconsequential details. This design of the test sections makes it possible to safely reach a thermal flux density of $3 \cdot 10^5$ kcal/m^2-hour using a low-capacity adjustable cooler on the line connecting the outlet of the center pipe with the inlet into the annular space. In addition, this simplifies the necessary measurements. /33

The experimental sections were placed in sequence on a multipurpose test stand, provided with a cold trap for oxides, oxide content indicator and a measuring tank for calibration of the flowmeters. The manner in which the test section with its main elements was connected to the circuit is shown in Fig. 2.

Experience of our work has shown that, in spite of the presence of a gas separator, gas accumulated at the inlet part of the center pipe, decreasing the mean heat transfer (a part of the surface was not wetted by the metal). An additional blow-down line was constructed for continuous removing this gas. The experiments were performed using pure metal with a continuously operating oxide trap. The oxygen content of the metal was determined only before performing a series of experiments; it comprised $5 \cdot 10^{-4}$% by weight.

When steady flow was established we have recorded at least three times the following data: metal flow rate, temperature at the inlets and outlets of the center pipe and of the jacket, readings of thermocouples which covered the entire surface of the test section. The heat losses through the surface of the [test] section because appreciable for moderate metal flow rates and at high temperatures, hence the real temperature was always calculated for each point.

To calculate the heat transfer coefficient we have used the difference δt between the metal's temperature at the inlet of the center pipe and at its exit, as well as the mean temperature difference Δt_{theo} between the pipe's outlet and the inlet into the annular space, with a correction for heat lost through the outside surface of the annular space. The theoretical heat transfer coefficient K_{theo} /35

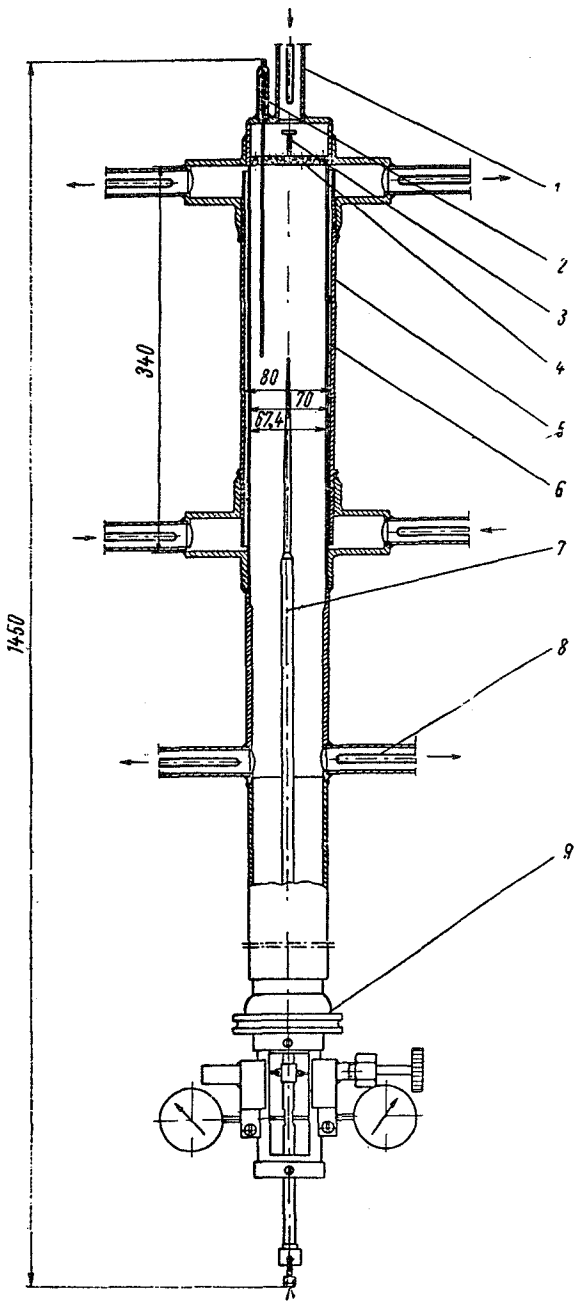

Figure 1. Design of No. 2 Test Section. 1) Inlet Connecting Stub; 2) Pocket (Capillary); 3) Recoiling Mushroom; 4) Wire Mesh; 5) Jacket; 6) Heat-Transfer Wall; 7) Movable Thermocouple; 8) Pocket With Thermocouple; 9) Mechanism for Moving the Thermocouple Probe.

(without giving consideration to heat flow along the axis) was found from the expression

$$K_{\text{theo}} = \frac{C\,(\alpha_{\text{th}}\gamma)_{l=\Gamma}\cdot\delta t}{\pi\, dl_{\text{h. t}}\,\Delta_{\text{theo}}} \qquad (1)$$

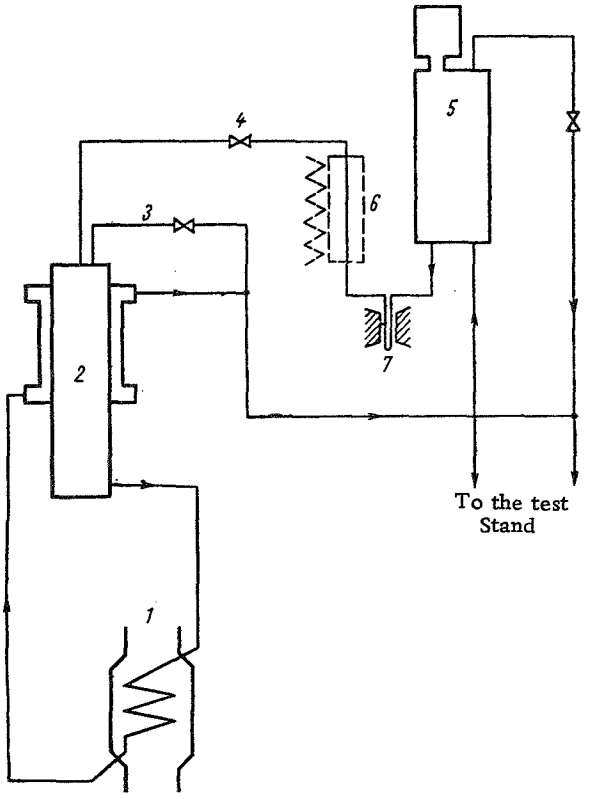

Figure 2. Schematic Diagram Showing How the Test Section Was Connected to the Main Circuit. 1) Cooler; 2) Test Section; 3) Blow-Down Line; 4) Regulating Valve; 5) Gas Trap; 6) Heating Section; 7) Electromagnetic Pump, Partially Adjusting the Flow Rate Through the Section.

The actual heat transfer coefficient for the center pipe was found from the relationship

$$\alpha = \frac{1}{\frac{1}{K} - \frac{d}{\lambda_w} \ln \frac{d_1}{d} - \frac{d}{d_1 \alpha_g}}, \qquad (2)$$

The relationship between K_{theo} and K was found by a method presented in [11] (Fig. 3, a and b). The error of the correction increases highly with a reduction in the Peclet number. Hence K and α were not calculated for very low Pe. The pattern of the experimental points for K_{theo} points to the appreciable role /36

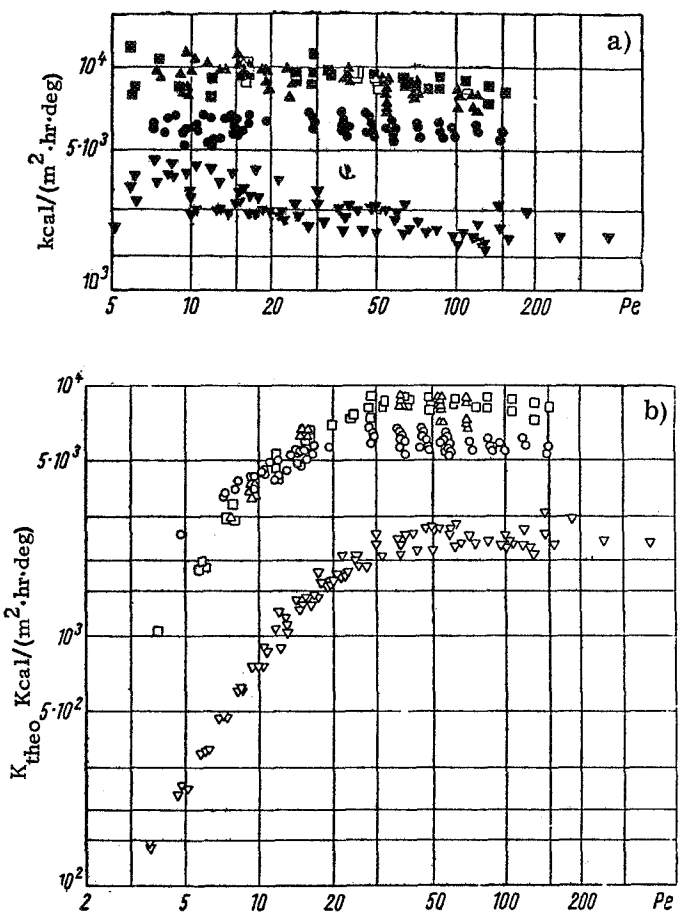

Figure 3. Values of K (a) and K_{theo} (b), the Heat Transfer Coefficients, at the Test Sections. a) ▲ - Section No. 1 (Sodium); ▼ - the Same (Sodium-Potassium Alloy); ● - Section No. 2 (Sodium); ■ - Section No. 3 (Sodium); b) △, ▽, ○, □ - Corresponding Values of K_{theo}.

of longitudinal heat fluxes in the greater part of Peclet numbers under study, in particular in the sodium-potassium alloy. Calculations of K made with moderate Peclet numbers yielded the expected result, i.e., heat transfer by combined convection improves with a reduction in Pe.

We wish to note two factors bearing on heat transfer with very low Peclet numbers. On the one hand, the experimental study under these circumstances is made difficult by the fact that it is necessary to take into account longitudinal heat fluxes and due to technical difficulties (maintaining the flow rate, taking the heat losses into account). On the other hand, the smaller Pe, the lower the experimental accuracy which is acceptable for making design calculations. In fact, /37

for specified inlet and outlet passage temperature and for a given fluid flow rate the actual thermal flux through the wall will be expressed as [12]

$$\mathrm{Nu}_{\text{theo}} = \frac{\mathrm{Nu}}{1+\frac{4\mathrm{Nu}}{\mathrm{Pe}^2}(1+\varphi)}.$$

With a reduction in the Peclet number the $\mathrm{Nu}_{\text{theo}}$ becomes increasingly less dependent on Nu, and when

$$\frac{4\mathrm{Nu}}{\mathrm{Pe}^2}(1+\varphi) \gg 1 \qquad \mathrm{Nu}_{\text{theo}} \approx \frac{\mathrm{Pe}^2}{4(1+\varphi)}.$$

Since Nusselt numbers attendant to parallel combined convection are high, the above factors have the most direct bearing on the results obtained.

The data on heat transfer in the annular gap for very low Peclet numbers, needed for calculating α have not been published. However, extrapolation of the available [13], [14] data to the needed range of Pe, is apparently permitted, just as in the case of a round pipe. Reference [15] presents a study of the heat transfer by mercury flowing in a pipe up to the laminar regime and it shows that the heat transfer is practically unchanged for Pe < 100. The extrapolated data can be only used when one is assured of the absence of natural convection in the annual space. (Estimates which were made show that this condition is satisfied.) According to [13], [14] the heat transfer in an annular space heated from one side [only] is described by the expression

$$\mathrm{Nu} = 4.9 + 0.0175\mathrm{Pe}^{0.8}.$$

The thermocouples built into the wall of section No. 3 could not as yet be used to find the heat transfer coefficient in the annular space due to low-frequency temperature pulsations.

The data on heat transfer obtained for parallel combined convection were analyzed in coordinates Nu(Z), where $Z = \frac{d}{2}\sqrt[4]{\frac{g\beta}{\nu a}\cdot\frac{\partial t}{\partial x}}$ is a parameter which fully describes the fluid flow and heat transfer in the steady-state laminar flow [2]. The use of Z for analyzing heat transfer in the nonstabilized region is not entirely correct. But since the accuracy of experimental data is such that it is [anyway] impossible to take into account the effect of the Reynolds and Prandtl numbers, as well as other factors, Z was found to be the most suitable parameter for purposes of analysis. Figure 4 shows Nu(Z) for stabilized laminar flow (solid line) [2]. The results could also have been analyzed in the coordinates Nu(Cr/ /Re), but this would not have reduced the scatter of points and would have introduced additional inconvenience in using the data. To find Z it is necessary /38

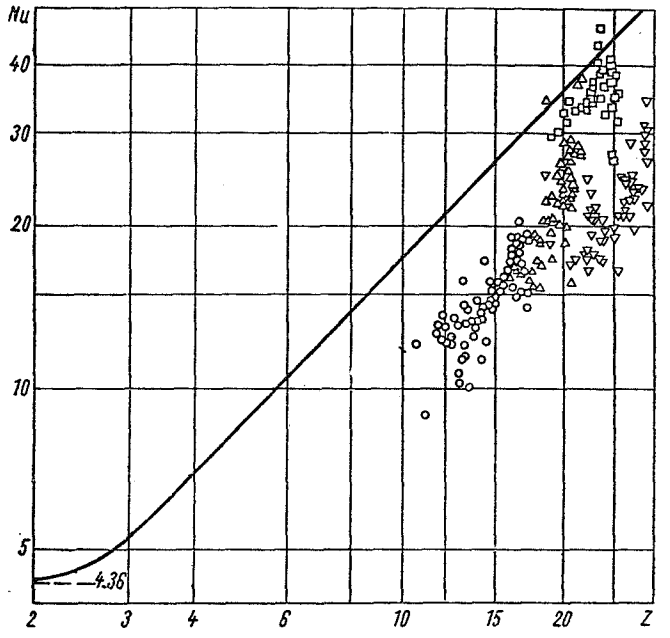

Figure 4. Nusselt Numbers for Parallel Combined Convection. △ - Section No. 1 (Sodium); ▽ - Same as Above (Sodium-Potassium Alloy); ○ - Section No. 2 (Sodium); □ - Section No. 3 Sodium.

to know the liquid's properties and the temperature gradient along the length, [while] for calculating Cr and Re one must know the rate of flow of the fluid and the mean temperature difference. In the presence of longitudinal heat fluxes the calculation of t requires several approximations.

It can be seen from Fig. 4 that there exists a relationship for Nu(Z) which is similar to that taking place in a laminar flow with parallel combined convection, i.e., Nu increases with an increase in Z, remaining, however, below the laminar curve.

The unusual location of points may be explained as follows. In a purely laminar flow the effect of the natural on the forced convection is expressed as follows: the fluid layers closest to the wall of the pipe are imparted high velocities, while in the center the velocity is reduced. Hence, the mean temperature difference between the wall and the fluid drops, while Nu increase. Turbulence makes the velocity distributions more flat, the velocity maximum near the wall becomes "washed out" to a certain degree. In other words, the increase in turbulence acts in the same direction as a reduction in Z. If we analyze the structure of parameter Z derived for laminar flow, then it becomes possible to qualitatively estimate the effect of turbulence on the relationship between Nu and Z. As is known, in turbulent flow $\nu_{h.t} = \nu_{h.t}(Re)$ and $a_{h.t} = a_{h.t}(Re)$; here always $\nu_{h.t} > \nu$ and $a_{h.t} > a$. It is seen from this that Z for turbulent flow calculated on the basis of the molecular values of ν and a is always higher than some actual $Z_{h.t}$ which is a function of Re and Pr. Thus, relating the experimentally obtained values of Nu from a real turbulent flow to parameter Z calculated on the basis of properties of laminar flow one should expect that the Nusselt numbers will lie below the line corresponding to heat transfer in laminar flow. /39

The accuracy of the data obtained ($\Delta K_{theo}/K_{theo} = 11\,6.5\%$) does not allow one to follow quantitatively the effect of the magnitudes of Pr, Re and $\bar{t}$ on the Nusselt numbers. Qualitatively it is possible to observe the heat transfer as a function

of Re (or Pe): at each section the heat transfer coefficient depends on the Reynolds numbers for the same Z. The higher Re, the lower the Nusselt number. The contribution made by the pipe's diameter is also noticeable, i.e., for sodium the heat transfer coefficient in the region at hand depends weakly on d and we get that $Nu \approx d$.

Points obtained in the sodium-potassium alloy are situated somewhat lower. This apparently is due to the fact that the turbulent component of thermal conductivity of the alloy is higher than that of sodium. Hence, when using the coordinates Nu(Z) the points for the alloy fall below those for sodium, although the values of the Nusselt numbers are situated at the same level. We can use the following relationship to describe the experimental points obtained for sodium

$$Nu = 0.34Z^{1.4}.$$

The Nusselt numbers for the alloy are situated by 40% lower.

At section No. 2 we have obtained data on the heat transfer attendant to oppositely directed [counterflow] combined convection (Fig. 5). In laminar flow described in [2] the Nusselt numbers become lower in this case for $Z = 0\text{-}3$, while when $Z > 3$ the flow is unstable. In our experiments we have not noticed a dependence on Z, since the turbulence of the flow was quite appreciable. The effect of natural convection is obvious, i.e., the lower the Peclet number, the lower the heat transfer rate. The increase in Nu with increasing Peclet numbers to values above $Nu = 5 + 0.025\ Pe^{0.8}$ is due to the fact that the section is short ($l_{h.t}/d = 5$) and a turbulizing mesh has been installed at the inlet.

Figures 6 and 7a and b show the temperature distributions recorded under different conditions. The not too high smoothness of the distributions is due to the low-period temperature pulsations in the flow. For accurate reading of a single point of the distribution with small Peclet numbers it is necessary to average these pulsations over a large time interval (up to 10 minutes). The most minor variations in the flow conditions distort the results of temperature readings. Hence, the temperature distributions are only qualitatively correct. We note that, unlike the ordinary pattern, the temperature distributions at the beginning of the heat transfer section are here always greater than in the following sections (see Fig. 6). It is seen from Fig. 7b that, for the same average velocity, the shape of the temperature distribution is highly affected by the thermal flux at the wall. At the same time the heat transfer coefficients does not vary appreciably ($Nu \sim \sqrt[4]{\delta t}$). When the average velocity of the liquid is reduced, the drop in the temperature distribution becomes larger, it widens. At very low velocities the distribution becomes flat. Qualitatively this is similar to the behavior of the temperature distribution for laminar combined convection [2]. /41

The thermocouples installed on the jacket of section No. 1 and on the heat transferring wall of section No. 3 made it possible to determine the trend in the average temperature along the length of the section. The temperature variation in the jacket wall along the length remains linear except for very small Peclet

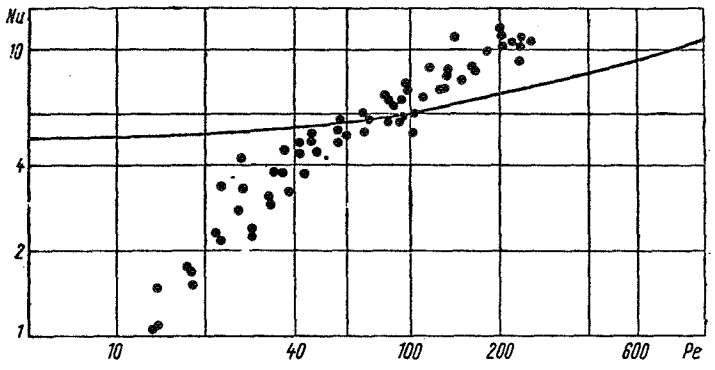

Figure 5. Nusselt Numbers for Oppositely Directed [Counterflow] Combined Convection. ● - Section No. 2 (Sodium); Solid Line - Curve of

$$Nu = 5 + 0.025\ Pe^{0.8}.$$

numbers, when the heat lost through the lateral surface of the jacket results in an appreciable increase in the mean temperature difference between the passages. Linearity in the temperature trend of the jacket to such an extent shows that the heat transfer coefficient (and consequently also the heat transfer in the passages) does not vary too much along the length of the section. This fact justifies the applicability of the method for taking into account longitudinal heat fluxes to the analysis of preliminary results, which is presented in [11].

The only insignificant variation in K along the length may be attributed to the species of the fluid flow with combined convection (return flow of fluid in the center of the pipe).

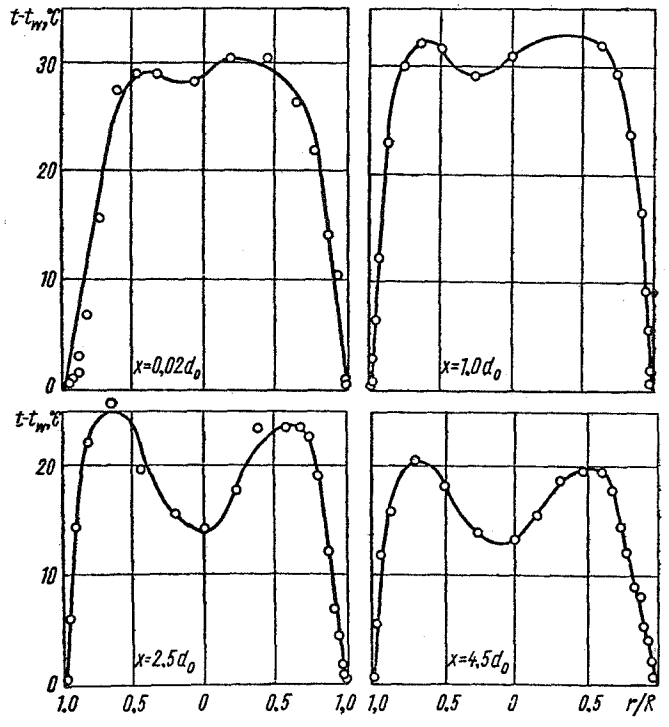

Figure 6. Temperature Distributions in Section No. 1 at Different Distances From the Inlet (Sodium).

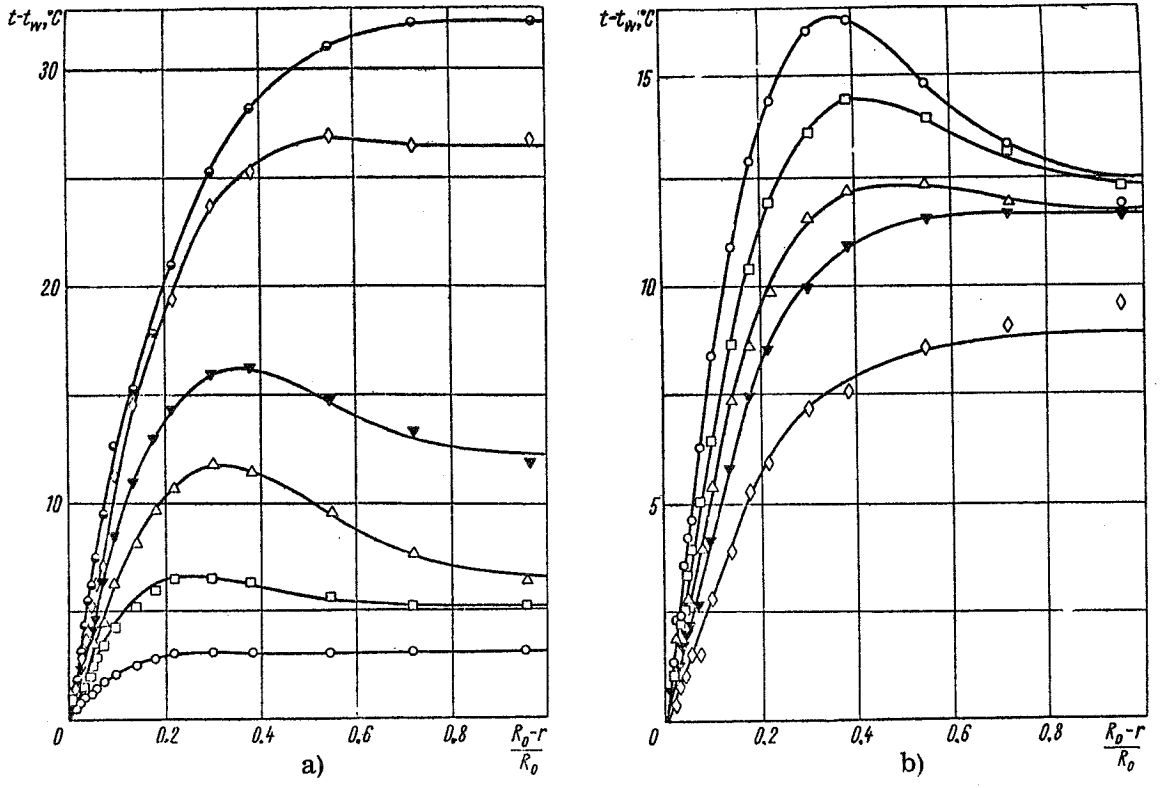

Figure 7. The Temperature Distribution in Section No. 2 as a Function of:

a) - Average Velocity of the Liquid Metal;

w, mm/sec — Re

○ — 82 — 15 600;
△ — 27 — 4700;
· — 55 — 9900;
□ — 9,1 — 1500;
▼ — 36 — 6300;
○ — 4,6 — 740

b) - the Heating in the Section ($Re = 7 \cdot 10^3$):

δt, °C

○ — 224;
▼ — 99;
□ — 180;
◇ — 80;
△ — 144;

Results

1. In the region of Peclet numbers and Z under study the heat transfer of sodium and of the sodium-potassium alloy on parallel combined convection is appreciably higher (and on counterflow it may be lower) than the heat transfer with forced convection only.

2. The heat transfer coefficient (and consequently also the heat transfer) in short ducts of experimental sections varies little along the length, which is shown by the linear temperature variation of the section's surface.

3. The study of heat transfer in the region of low Peclet numbers is difficult. At the same time, it is possible to use for practical purposes data the less accurate the lower Pe and the higher Nu and φ.

4. The qualitative picture of the behavior of the temperature fields in the sections is in agreement with theoretical predictions made on the basis of the solution to the problem of stabilized laminar flow [2].

5. Despite the small variation in the heat transfer coefficient in short ducts its dependence on the duct length remains unclear.

NOTATION

$l_{h.t}$	length of the heat transfer section	/43
l	total length of center pipe	
x	longitudinal distance	
$\bar{t}$	average temperature of liquid in the center pipe, °C	
δt	difference between the liquid temperature at the inlet and outlet of the center pipe, °C	
Δt_{theo}	theoretical value of the liquid-to-liquid mean temperature difference in the heat exchanger, °C	
G	flow rate of liquid through the test section	
φ	ratio of the longitudinal conductivities of the pipe wall and of the liquid in the pipe	

REFERENCES

1. Subbotin, V.I., et al.: Teplofizika vysokikh temperatur, 1, No. 3 (1963).
2. Brown, W.G. and Grassman, P.: Forsch. Geb. Ingenieurwesens, 25, No. 3, pages 69-78 (1959).
3. Ber, L.E.: Izvestiya AN SSSR, OTN, No. 6, page 25, 1962.
4. Ostroumov, G.A.: Svobodnaya konvektsiya v usloviyakh vnutrenney zadachi [Free Convection Under Conditions of the Internal Problem]. Gostekhizdat, Moscow-Leningrad, 1952.
5. Hanratty, T.J., Rosen, E.M. and Kabel, R.L.: Industr. and Engng Chem., No. 5., 1958.
6. Brown, W.G.: VDI-Forschungsheft, 480, 1960.
7. Watzinger, A. and Johnson, D.G.: Forsch. Geb. Ingenieurwesens, 10, No. 4, pages 182-196 (1939).
8. Wetjen K.A.: Chem.-Ingr.-Techn., 26, No. 8/9 (1954).
9. Alad'yev, I.T., et al.: Izvestiya AN SSSR, OTN, 1951.
10. Petukhov, B.S. and Nol'de, L.D.: Teploenergetika, No. 1, 72 (1959).
11. Gorchakov, M.K.: Uchet prodol'nykh peretechek tepla pri izmerenii sredney temperatury zhidkosti v trubakh i teploobmennikakh pri malykh chislakh Pekle [Taking Into Account Longitudinal Heat Fluxes When Measuring the Average Temperature of Fluids in Pipes and Heat Exchangers for Low Peclet Numbers]. Article immediately following this in the present collection.
12. Trefethen, L.: Trans. ASME, 78, No. 6, pages 1207-1212 (1956).
13. Subbotin, V.I., et al.: Atomnaya energiya, 9, No. 6, 461 (1960).
14. Harrison, W.B. and Menke, J.R.: Trans. ASME, 71, No. 7, pages 797-804 (1949).
15. Yushin, A.Ya, et al.: Izvestiya vuzov. Energetika, No. 7, pages 79-85 (1961).

TAKING INTO ACCOUNT LONGITUDINAL HEAT FLOWS WHEN MEASURING THE AVERAGE TEMPERATURE OF FLUIDS IN PIPES AND HEAT EXCHANGES FOR LOW PECLET NUMBERS

M. K. Gorchakov

It is assumed in the study of heat transfer with $q_w = \text{const}$ that the real mean /43
temperature of the liquid in the duct varies linearly from $t\big|_{X=0} = t\big|_{X=-\infty}$ to $t\big|_{X=L} = t\big|_{X=\infty}$, i.e., $t = t_{theo}$ ($X = 0$ and $X = L$ pertain to the start and end of the heated section). However, for low Peclet numbers the axial heat fluxes result in the fact that t differs from t_{theo} by some value δt. If this difference is not taken into account in analyzing the experimental data and in calculating heat ex- /44
change devices, this can produce erroneous results. The authors of [1-5] had as their purpose finding the average temperature of the liquid in the presence of longitudinal flows of heat. Expressions were found for δt for heat transfer in hydrodynamically stabilized laminar flow and stabilized heat transfer in any flow. It turns out that these data are insufficient for analyzing experimental data obtained in the study of heat transfer in the recuperating part of cold traps of alkaline metal oxides. The heat transfer conditions are quite varied: a short double-tube heat exchanger (see figure), heat transferring wall with an appreciable longitudinal conductivity, and the velocity and temperature fields are interrelated, and only their qualitative picture is clear; heat transfer coefficients in both passages are significant.

Below we attempt to find a relationship between the actual mean tempera- /45
ture of the fluid t and its theoretical value t_{theo} in tubes with $q_w = \text{const}$ and in heat exchangers with identical flow rates in both passages.

The effect of longitudinal flows of heat on the mean temperatures of the fluids in passages of a real heat exchanger is a complex problem, although in principle solvable. By considering separately the following principal problems and then combining the results thus obtained it is practically possible to achieve the same results: 1) behavior of the mean temperature of the liquid in the general case of nonstabilized heat transfer in the presence of longitudinal heat fluxes; 2) dependence of δt on the shape of the inlet and outlet parts of the passage; 3) the value of $\delta t_{h.e}$ in two-dimensional flows in the passages of a counterflow heat exchanger without taking into account the conductivity of the heat transferring wall; 4) taking into account the latter conductivity; 5) the dependence of $\delta t_{h.e}$ in the heat exchanger on the changes in the heat transfer coefficient and of the mean temperature difference along the length of the passages.

As a result of consideration of these problems it is possible to obtain a method for introducing corrections for longitudinal fluxes of heat for calculations of the mean temperature of the fluid in passages with q_w = const and in heat exchangers.

1. The temperature distribution in a nonstabilized flow in a pipe is given by the expression

$$\gamma c_{theo}\left[w(x, r)\frac{\partial\Theta}{\partial x}+v(x, r)\frac{\partial\Theta}{\partial r}\right]=\frac{1\partial}{r\,\partial r}\left\{r[\lambda+\lambda_T(x, r)]\frac{\partial\Theta}{\partial r}\right\}+\lambda\frac{\partial^2\Theta}{\partial x^2}, \quad (1)$$

if it is assumed that the physical properties of the liquid are constant, while the turbulent component of the thermal conductivity is small in comparison with the molecular component. Since we are interested only in the behavior of the mean temperature of the liquid in the presence of longitudinal heat fluxes, it is possible to obtain the required result by averaging Eq. (1) over the pipe cross section. Multiplying it by $2\pi r dr$ and integrating both parts from $r = 0$ to r_0, we get

$$\gamma c_{theo} F w\frac{\partial t}{\partial x}=F\lambda\frac{\partial^2 t}{\partial x^2}-2\pi r_0 q, \quad (2)$$

where $q = -\lambda(\partial\Theta/\partial r)_{r=r_0}$ is the thermal flux at the wall. It is clear from this that the character of the heat transfer does not affect the distribution of the mean fluid temperature along the length of the duct. In any case this distribution can be found from the simple equation of balance (2).

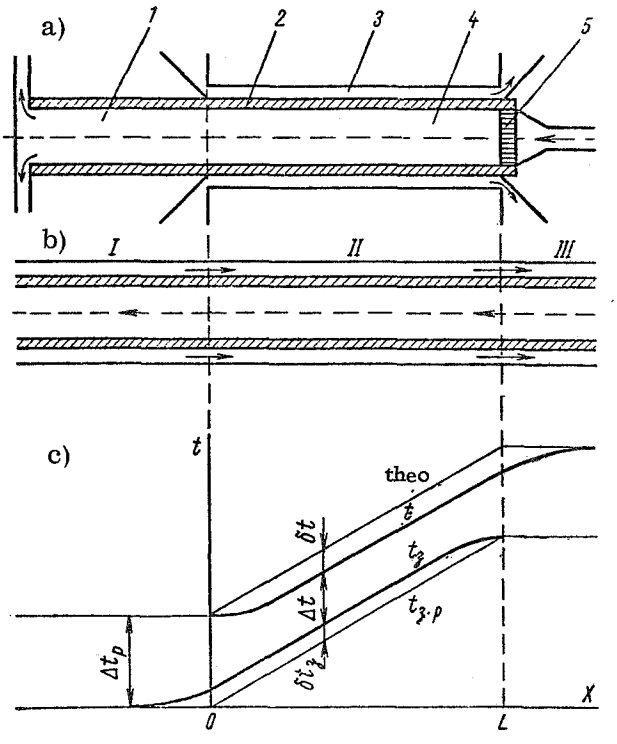

Change in Mean Fluid Temperatures in Heat Transfer Passages. a) Heat Exchanger Design [1) Mixing Chamber; 2) Heat Transferring Wall; 3) Annular Space; 4) Center Passage; 5) Inlet Screen]: b) Schematic Replacing the Actual Heat Exchanger When Finding $\delta t_{h.e.} = t + \delta t_{sp}$ (I, II and III Are Heat Transfer Zones); c) Curve Showing Variations in t and t_{theo} in [Simplified] Circuit b.

Consideration of a specific problem with q_w = const, without taking into account the wall conductivity, [4], yields the expression

$$\delta t=\frac{4qd}{\lambda Pe^2}[1-e^{-Pe(L-X)}] \quad (3)$$

when $0 \leq X \leq L$

$$\overline{\delta t} = \frac{1}{L}\int_0^L \delta t\, dX = \frac{4qd}{\lambda \mathrm{Pe}^2}\left[1 - \frac{1}{\mathrm{Pe}\,L}\left(1 - e^{-\mathrm{Pe}\,L}\right)\right]. \tag{4}$$

If $\mathrm{Pe} \cdot L > 6$, then /46

$$\delta t = \frac{4qd}{\lambda \mathrm{Pe}^2}\left(1 - \frac{1}{\mathrm{Pe}L}\right). \tag{5}$$

2. When working with short passages without hydrodynamic stabilization sections it is important to know the effect exerted by inlet and outlet devices on the magnitude of δt for small Peclet numbers. The heat transfer coefficient at the initial section definitely depends on the shape of the inlet, and in some cases also on the shape of the outlet (in the case of intensive effect of natural convection) [sic]. This dependence on the shapes of the inlet and outlet can be clarified by solving the following problem.

Let the passage in the zone $0 \leq X \leq L$ in which heat transfer takes place have a cross section F_{II}, cross section F_I for $X < 0$ (narrowing down the fluid-passing cross section by means of a grid with low-thermal conductivity in which case $F_I < F_{II}$, or its expansion in the form of a chamber in which case $F_I > F_{II}$), and cross section F_{III} when $X > L$. In this case we shall write Eq. (2) for zones I, II and III

$$\left.\begin{aligned}
&\lambda F_{\mathrm{I}} \frac{\partial^2 t_{\mathrm{I}}}{\partial x^2} - w_{\mathrm{I}} F_{\mathrm{I}} c_{\mathrm{theo}} \gamma \frac{\partial t_{\mathrm{I}}}{\partial x} = 0,\\
&\lambda F_{\mathrm{II}} \frac{\partial^2 t_{\mathrm{II}}}{\partial x^2} - w_{\mathrm{II}} F_{\mathrm{II}} c_{\mathrm{theo}} \gamma \frac{\partial t_{\mathrm{II}}}{\partial x} + 2\pi r_0 q = 0,\\
&\lambda F_{\mathrm{III}} \frac{\partial^2 t_{\mathrm{III}}}{\partial x^2} - w_{\mathrm{III}} F_{\mathrm{III}} c_{\mathrm{theo}} \gamma \frac{\partial t_{\mathrm{III}}}{\partial x} = 0.
\end{aligned}\right\} \tag{6}$$

Boundary conditions

$$\left.\begin{aligned}
&X = -\infty, \quad t_{\mathrm{I}} = 0;\\
&X = 0, \quad t_{\mathrm{I}} = t_{\mathrm{II}}, \quad \lambda F_{\mathrm{I}} \frac{\partial t_{\mathrm{I}}}{\partial x} = \lambda F_{\mathrm{II}} \frac{\partial t_{\mathrm{II}}}{\partial x};\\
&X = L, \quad t_{\mathrm{II}} = t_{\mathrm{III}}, \quad \lambda F_{\mathrm{II}} \frac{\partial t_{\mathrm{II}}}{\partial x} = \lambda F_{\mathrm{III}} \frac{\partial t_{\mathrm{III}}}{\partial x};\\
&X = \infty, \quad t_{\mathrm{III}} = \mathrm{const}.
\end{aligned}\right\} \tag{7}$$

Reducing Eqs. (6) to the dimensionless form and making use of the fact that $w_I F_I = w_{II} F_{II} = w_{III} F_{III}$, we can get expressions for the mean temperature by zones:

$$t_I = \frac{4qd}{\lambda Pe^2}(1 - e^{-Pe\,L})\, e^{\frac{F_{II}}{F_I} Pe\, X}, \tag{8}$$

$$t_{II} = \frac{4qd}{\lambda Pe} X + \frac{4qd}{\lambda Pe^2}[1 - e^{-Pe\,(L-X)}], \tag{9}$$

$$t_{III} = \frac{4qd}{\lambda Pe} L. \tag{10}$$

It can be seen from Eq. (9) that the shapes of the inlet and outlet parts of the passage do not affect the mean temperature in the heat transfer zone. In the section before heat transfer starts the reduction in δt as $X \to -\infty$ depends on the relationship between F_{II} and F_I; this factor should be taken into account when placing the pickup measuring the temperature of the fluid at the inlet. It is thus clear that $\delta t = t - t_{theo}$ in the heat exchanger zone can be calculated without consideration of the internal structure of the flow and without taking into account the specific end devices. /47

3. The above simplifies the analysis of heat exchangers to the extreme. For finding the distribution of mean temperatures and of δt_{theo} the actual heat exchanger can be replaced by a simplified arrangement (see Fig. 1b and c), since only the heat transferring zone is of interest. Assuming that K, the heat transfer coefficient, is constant along the length and treating the wall through which heat transfer takes place simply as a thermal resistance, it is possible to write a system of equations describing the trend of the mean temperature in both passages in all the zones. For this it is necessary to replace q = const in Eq. (2) by the expression $K(t - t_{sp})$. In zones I and II K = 0, in zone II

$$K = \frac{1}{\frac{1}{\alpha} + \frac{d}{\alpha_3 d_1} + \frac{d}{2\lambda} \ln \frac{d_1}{d}}. \tag{11}$$

The subscript II is dropped for convenience when writing equations in the dimensionless form.

Zone I

$$\frac{\partial^2 t_{spI}}{\partial X^2} - \frac{Pe}{\varkappa} \frac{\partial t_{spI}}{\partial X} = 0, \tag{12}$$

$$\frac{\partial^2 t_I}{\partial X^2} + \mathrm{Pe}\frac{\partial t_I}{\partial X} = 0. \tag{13}$$

Zone II

$$\frac{\partial^2 t_{sp}}{\partial X^2} - \frac{\mathrm{Pe}}{\varkappa}\frac{\partial t_{sp}}{\partial X} + \frac{4\mathrm{Nu}_k}{\varkappa}(t - t_{sp}) = 0, \tag{14}$$

$$\frac{\partial^2 t}{\partial X^2} + \mathrm{Pe}\frac{\partial t}{\partial X} - 4\mathrm{Nu}_k(t - t_{sp}) = 0. \tag{15}$$

Zone III

$$\frac{\partial^2 t_{sp_{III}}}{\partial X^2} - \frac{\mathrm{Pe}}{\varkappa}\frac{\partial t_{sp_{III}}}{\partial X} = 0, \tag{16}$$

$$\frac{\partial^2 t_{III}}{\partial X^2} + \mathrm{Pe}\frac{\partial t_{III}}{\partial X} = 0. \tag{17}$$

Boundary conditions

$$\left.\begin{aligned} &X = -\infty \;\; t_I = \mathrm{const}, \;\; t_{spI} = 0; \\ &X = 0 \;\; t_I = t, \;\; t_{spI} = t_{sp}, \;\; \frac{\partial t_I}{\partial X} = \frac{\partial t}{\partial X}, \;\; \frac{\partial t_{spI}}{\partial X} = \frac{\partial t_{sp}}{\partial X}; \\ &X = L \;\; t = t_{III}, \;\; t_{sp} = t_{sp_{III}}, \;\; \frac{\partial t}{\partial X} = \frac{\partial t_{III}}{\partial X}, \;\; \frac{\partial t_{sp}}{\partial X} = \frac{\partial t_{sp_{III}}}{\partial X}; \\ &X = \infty \;\; t_{III} = t_0, \;\; t_{sp_{III}} = \mathrm{const}. \end{aligned}\right\} \tag{18}$$

Solving simultaneously Eqs. (12)-(17) with the above boundary conditions yields a system of algebraic equations with 12 unknown constants of integration. Since the arrangement assumed to represent the heat exchanger yields the correct trend of mean temperatures only in the heat transfer zone, it makes sense /48 only to find the four unknowns, which enter into the description of t and t_g. Due to the cumbersomeness of intermediate calculations only the expressions for the heat transfer zone are presented here

$$t_{sp} = C_1\frac{1}{\beta_1^2}e^{\beta_1 X} + C_2\frac{1}{\beta_2^2}e^{\beta_2 X} + C_3 X + C_4, \tag{19}$$

$$t = C_1\left(\frac{1}{\beta_1^2} + P\right)e^{\beta_1 X} + C_2\left(\frac{1}{\beta_2^2} + Q\right)e^{\beta_2 X} + C_3\left(\frac{\mathrm{Pe}}{4\mathrm{Nu}_k} + X\right) + C_4, \tag{20}$$

$$\beta_{1,2} = \mathrm{Pe}\frac{1-\varkappa}{2\varkappa} \pm \sqrt{\left(\mathrm{Pe}\frac{1+\varkappa}{2\varkappa}\right)^2 + 4\mathrm{Nu}_h \frac{1+\varkappa}{\varkappa}},$$

$$P = \frac{\varkappa}{4\mathrm{Nu}_h}\left(\frac{\mathrm{Pe}}{\varkappa\beta_1} - 1\right),$$

$$Q = \frac{\varkappa}{4\mathrm{Nu}_h}\left(\frac{\mathrm{Pe}}{\varkappa\beta_2} - 1\right),$$

$$C_1 = \frac{t_0}{H}[(1 + Q\beta_2^2) - e^{\beta_2 L}]. \qquad (21)$$

The value of H is not presented, since it is very cumbersome and it is not needed for calculating the theoretical expressions.

$$C_2 = \frac{t_0}{H}[e^{\beta_1 L} - (1 + P\beta_1^2)],$$

$$C_3 = \frac{t_0}{H}[(1 + P\beta_1^2)\, e^{\beta_2 L} + (1 + Q\beta_2^2)\, e^{\beta_1 L}] \cdot \frac{1}{\beta_1\beta_2},$$

$$C_4 = C_1\left(\frac{\varkappa}{\mathrm{Pe}\beta_1} - \frac{1}{\beta_1^2}\right) + C_2\left(\frac{\varkappa}{\mathrm{Pe}\beta_2} - \frac{1}{\beta_2^2}\right) + C_3\frac{\varkappa}{\mathrm{Pe}},$$

$$\Delta t_{\mathrm{theo}} = (t - t_{\mathrm{sp}})|_{X=-\infty} =$$

$$= C_1\left(P + \frac{\varkappa}{\mathrm{Pe}\beta_1}\right) + C_2\left(Q + \frac{\varkappa}{\mathrm{Pe}\beta_2}\right) + C_3\left(\frac{\mathrm{Pe}}{4\mathrm{Nu}_h} + \frac{\varkappa}{\mathrm{Pe}}\right),$$

$$\frac{K}{K_p} = \frac{\Delta t_p}{\overline{(t - t_{\mathrm{sp}})}} = 1 + \frac{\overline{\delta t}}{\overline{\Delta t}} = 1 + \omega_{L,\,\mathrm{h.e.}} \qquad (22)$$

If $e^{\beta_1 L} \gg 1$ and $e^{\beta_2 L} \ll 1$, we have

$$1 + \omega_{L,\,\mathrm{h.e.}} = \frac{\left(Q + \frac{\varkappa}{\mathrm{Pe}\beta_2}\right)\beta_2 - (1 + Q\beta_2^2)\left(\frac{\mathrm{Pe}}{4\mathrm{Nu}_h} + \frac{\varkappa}{\mathrm{Pe}}\right)}{\frac{1}{L}[(1 + Q\beta_2^2)\, P - Q] - (1 + Q\beta_2^2)\frac{\mathrm{Pe}}{4\mathrm{Nu}_h}}. \qquad (23)$$

When $L \to \infty$

$$\omega_{L,\,\mathrm{h.e.}}|_{L\to\infty} = \omega_T = \frac{y_2}{\frac{\mathrm{Pe}^2}{4\mathrm{Nu}_h\varkappa}\, y_2(y_2 - 1) - 1}, \qquad (24)$$

where y_2 is found from the expression

$$y_{1,2} = 1 - \frac{\beta_{1,2}\varkappa}{\mathrm{Pe}} = 0{,}5\,(1 + \varkappa)\left[1 \mp \sqrt{1 + \frac{4\mathrm{Nu}_h}{\mathrm{Pe}^2} \cdot \frac{4\varkappa}{1+\varkappa}}\right]. \qquad (25)$$

Calculations using Eq. (24) yield the expression /49

$$\omega = \frac{4\mathrm{Nu}_k}{\mathrm{Pe}^2}(1+\varkappa). \tag{26}$$

Substituting the above expression into Eq. (23), we will get a simpler formula for a heat exchanger of arbitrary length

$$1+\omega_{L,} = \frac{1+\omega}{1-\frac{y_1}{\beta_1 L}-\frac{\omega}{y_2\beta_2 L}}. \tag{27}$$

The above expression can be used to calculate K/K_{theo} for a heat exchanger in which the longitudinal thermal flux along the intermediate wall is negligible as compared with the flux along the fluid in both passages.

4. If the wall is conducting in the longitudinal direction, the situation is much more complicated. The problem of the behavior of mean temperatures in the passages of heat exchangers cannot as yet be solved exactly. However for moderate φ and for heat exchangers of moderate length it is apparently possible to use results obtained on the following assumptions: a) the longitudinal conductivity of the wall is regarded as an additional conductivity of the fluid in the passages; b) in the statement of the problem the heat exchanger's passages do not in any way differ from one another, except for the difference in the area of the flow passing cross sections. Hence the conductivity of the wall is divided between the passages in proportion to their cross sections, i.e., $\varphi = \varphi_1 + \varphi_2$,

$$\varphi_1 = \frac{\varkappa}{1+\varkappa}\varphi, \quad \varphi_2 = \frac{1}{1+\varkappa}\varphi.$$

On these assumptions we write Eqs. (14) and (15) in the form

$$\frac{\partial^2 t_{sp}}{\partial X^2} - \frac{\mathrm{Pe}}{\varkappa+\varphi_1}\cdot\frac{\partial t_{sp}}{\partial X} + \frac{4\mathrm{Nu}_k}{\varkappa+\varphi_1}(t-t_{sp}) = 0, \tag{28}$$

$$\frac{\partial^2 t}{\partial X^2} + \frac{\mathrm{Pe}}{1+\varphi_2}\frac{\partial t}{\partial X} - \frac{4\mathrm{Nu}_k}{1+\varphi_2}(t-t_{sp}) = 0. \tag{29}$$

Similar changes will take place also in the expressions for zones I and III; the boundary conditions retain their form. The form of the solution of the new system of equations remains the same

$$\frac{K}{K_{\text{theo}}} = 1 + \omega_{L,\ \text{h.e.}\ \varphi} = \frac{1+\omega_{\text{h.e.}\ \varphi}}{1-\frac{y_{\varphi 1}}{\beta_{\varphi 1}L}\frac{\omega_{\text{h.e.}\ \varphi}}{y_{\varphi 2}\beta_{\varphi 2}L}} = \frac{1+\omega_{\text{h.e.}\ \varphi}}{1+\xi_{\text{h.e.}}}, \tag{30}$$

$$y_{\varphi 1,\ 2} = \frac{1+\varkappa}{2}\left[1 \mp \sqrt{1+4\omega_{\text{h.e.}\varphi}\frac{\varkappa}{(1+\varkappa)^2}}\right], \tag{31}$$

$$\beta_{\varphi 1,\ 2} = (1-y_{\varphi 1,\ 2})\frac{1+\varkappa}{(1+\varkappa+\varphi)\varkappa}\cdot \text{Pe}, \tag{32}$$

$$\omega_{\text{h.e.}\varphi} = \omega_{L,\ \text{h.e.}\ \varphi}|_{L\to\infty} = \frac{4\text{Nu}_k}{\text{Pe}^2}(1+\varkappa+\varphi). \tag{33}$$

The use of the above set of equations is convenient when calculating K_{theo} on the basis of a known K. /50

When analyzing experimental data the calculations proceed in the opposite direction, K is unknown, it can be found by successive approximations. However, it is more convenient to use the relationships obtained by solving the problem of variation in the mean temperatures in the reduced representation of a heat exchanger in which a constant thermal flux through the wall is assumed. This problem, together with the assumptions made for finding Eqs. (30-33), makes it possible to consider each passage separately with a part of the wall, i.e., the problem of a heat exchanger with q_w = const consists of two problems about passages with q_w = const, similar to expression (6), where λF_{II} should be replaced by $\lambda F_{II} + \lambda_w F_w(1/1+\varkappa)$ for the center passage and by $\lambda F_{II} + \lambda_w F_w(\varkappa/1+\varkappa)$ for the annular space. The expressions for $\delta\bar{t}$ and $\delta\bar{t}_{sp}$ found under these circumstances make it possible to find the relationship between the actual and theoretical heat transfer coefficients.

$$\alpha = \frac{\alpha_{\text{theo}}}{1-\frac{4\alpha_{\text{theo}}d}{\lambda\text{Pe}^2}\left(1+\frac{\varphi}{1+\varkappa}\right)\left[1-\frac{1+\varkappa+\varphi}{(1+\varkappa)\,\text{Pe}\,L}\left(1-e^{-\frac{(1+\varkappa)\text{Pe}L}{1+\varkappa+\varphi}}\right)\right]}, \tag{34}$$

$$\alpha_a = \frac{\beta_{sp\,\text{theo}}}{1-\frac{4\alpha_{sp}p d_1}{\lambda\text{Pe}^2}\varkappa\left(1+\frac{\varphi}{1+\varkappa}\right)\left[1-\frac{\varkappa(1+\varkappa+\varphi)}{(1+\varkappa)\,\text{Pe}L}\left(1-e^{-\frac{(1+\varkappa)\text{Pe}L}{(1+\varkappa+\varphi)\varkappa}}\right)\right]}. \tag{35}$$

Substituting the two above expressions into Eq. (11), we get

$$K_q = \frac{K_{\text{theo}}}{1 - \frac{4K_{\text{theo}}d}{\lambda \text{Pe}^2}(1+\varkappa+\varphi)\cdot\xi_q}, \tag{36}$$

where

$$\xi_q = 1 - \frac{1+\varkappa+\varphi}{(1-\varkappa)^2 \text{Pe}L}\left[1 - e^{-\frac{(1+\varkappa)\text{Pe}L}{1+\varkappa+\varphi}} + \varkappa^2\left(1 - e^{-\frac{(1+\varkappa)\text{Pe}L}{(1+\varkappa+\varphi)\varkappa}}\right)\right], \tag{37}$$

or, in other words (calculating $K_{q,\ \text{theo}}$ on the basis of K)

$$K_{q,\ \text{theo}} = \frac{K}{1+\omega_{\tau,\ \varphi}\xi_q}. \tag{38}$$

In principle $K_{q,\ \text{theo}}$ obtained from the above expression and K_{theo} obtained from Eq. (30) have different values, which difference disappears with an increase in L and Pe.

Practically for calculating K on the basis of K_{theo} it is sufficiently convenient to use the expression

$$K = \frac{K_{\text{theo}}}{1 - \frac{4K_{\text{theo}}d(1+\varkappa+\varphi)}{\lambda \text{Pe}^2\psi}\xi_q}, \tag{39}$$

where /51

$$\psi = \frac{\omega_{\text{h.e.}\ \varphi}\xi_q}{\omega_{L,\ \text{h.e.}\ \varphi}}. \tag{40}$$

The magnitude of Ψ can be calculated for a specific heat exchanger by assuming values of Nu_k. Numerical calculations show that for a specific heat exchanger Ψ depends little on Nu_k, varying appreciably (by several percents) with changes in the Peclet number.

5. Since all of the preceding analysis was performed on the assumption that the heat transfer coefficients remain unchanged along the length of the passages, it is necessary to examine the behavior of $\overline{\delta t}$ and $\overline{\delta t}_{\text{h. e}}$ for the case when they are

variable. In a duct with a thin wall, when q_w = const, $\overline{\delta t}$ obviously is independent of changes in α along the length. Approximately (without taking into account the effect of heat leakages in the wall at the ends of the heat supply section) the same may be claimed also for a wall with an appreciable longitudinal thermal conductivity.

The behavior of mean temperatures in heat exchanger passages, as well as $\overline{\delta t}_{theo}$ and $\overline{K}/\overline{K}_{theo}$ are affected by changes in the heat transfer coefficient along the length, as well as by the heat losses through the outside surface, since $q_w(X) = K(X) \cdot \Delta t(X)$. Also here it is possible to analyze both passages of the heat exchanger separately [system of Eqs. (6)], with $q_w = q(X)$.

Since in order to estimate the effect of q(X) on $\overline{\delta t}$ it is necessary to know the specific relationship governing the former quantity, it therefore makes sense to consider only one passage without the conducting wall. Solving Eqs. (6) with boundary conditions (7) for a variable q_w in the heat transfer zone we get

$$t_x = \frac{4d}{\lambda \mathrm{Pe}} \left[\int_0^X q(X)\, dX + e^{\mathrm{Pe}X} \int_X^L q(X)\, e^{-\mathrm{Pe}X}\, dX \right], \tag{41}$$

$$\delta t_x = \frac{4d}{\lambda \mathrm{Pe}} e^{\mathrm{Pe}X} \int_X^L q(X)\, e^{-\mathrm{Pe}X}\, dX. \tag{42}$$

If information on q(X) is available it is possible to calculate δt_X and $\overline{\delta t}_X$ for both passages making up the heat exchanger and, upon using Eq. (11), to find $\overline{K}_X/K_{X,\,theo}$. However, this is apparently not needed since the difference between $\overline{\delta t}_X$ and $\overline{\delta t}$ found from Eq. (3), with $q = \overline{q(X)}$, is found to be quite moderate. In fact, let $q(X) = q_0 + bX$, $\overline{q(X)} = q_0 + 0.5bL$, then

$$\delta t_x = \frac{4d}{\lambda \mathrm{Pe}^2} \left[\left(q_0 + b \frac{\mathrm{Pe}L + 1}{\mathrm{Pe}} \right) (1 - e^{-\mathrm{Pe}(L-X)}) - b(L - X) \right], \tag{43}$$

$$\overline{\delta t}_x = \frac{4d}{\lambda \mathrm{Pe}^2} \left\{ \left(q_0 + b \frac{\mathrm{Pe}L + 1}{\mathrm{Pe}} \right) \left[1 - \frac{1}{\mathrm{Pe}L} (1 - e^{-\mathrm{Pe}L}) \right] - \frac{bL}{2} \right\}. \tag{44}$$

The difference between $\overline{\delta t}_X$ and $\overline{\delta t}$ can be seen from the following expression /52
(for $e^{-Pe \cdot L} \ll 1$)

$$\frac{\overline{\delta t}_X}{\overline{\delta t}} - 1 = \frac{\frac{bL}{2}\left(\frac{1}{PeL} - \frac{2}{Pe^2L^2}\right)}{\left(q_0 + \frac{bL}{2}\right)\left(1 - \frac{1}{PeL}\right)}.$$

For $q_0 = 0$ we have

$$\frac{\overline{\delta t}_X}{\overline{\delta t}} - 1 = \frac{1 - \frac{2}{PeL}}{PeL - 1}. \qquad (45)$$

Thus, even when the thermal flux varies appreciably along the length of the passage, the $\overline{\delta t}$ (and consequently also $\overline{K}/\overline{K}_{theo}$) calculated on the basis of the average magnitude of the flux does not produce appreciable errors if the product Pe· L is not very small. In the presence of a conducting wall the following correction should be introduced: Pe· L in Eq. (45) should be replaced by Pe· L/ $1 + \varphi$.

Results

1. In the case of q_w = const the displacement of the actual mean temperature relative to its theoretical value does not depend on the shape of the velocity distribution and on velocity variations along the length of the passage.

2. The shape of the passage ahead of and past the heat transfer section does not affect δt

3. Finding the distribution of mean temperatures in the heat exchanger passages in the case of a low-conductivity wall and with a constant K yields a method for finding K/K_{theo}.

4. Upon making certain assumptions it is possible to find a method for taking into account the longitudinal conductivity of the heat conducting wall when calculating K/K_{theo}.

5. The use of the average thermal flux for finding $\overline{K}/\overline{K}_{theo}$ does not yield, under certain conditions, appreciable errors even when the thermal flux varies highly along the length of the passage.

6. The use of the above results in analyzing experimental data of [6] for not too low Peclet numbers has yielded expected results.

NOTATION

$\Theta(x, r)$	temperature of a point, °C
δt	difference between the actual mean temperature in a passage and the theoretical value brought about by longitudinal heat fluxes, $\delta t_{h.e} = \delta t + \delta t_{sp}$, °C
Δt	actual mean temperature difference, $\Delta t = t - t_{sp}$ for a heat exchanger, °C
ω	relative difference in the fluid's temperature due to longitudinal heat fluxes, averaged over the length
x	longitudinal coordinate /53
r	current radius
r_0	radius of pipe, $d = 2r_0$
d_1	internal diameter of the annular space
d_{sp}	[representative] flow diameter of the annular space
l	length of the heat conducting part of passage or heat exchanger
$\varkappa = F_{sp}/F$	ratio of cross sectional areas of the heat exchanger passages
$\varphi = F_w\lambda_w/F\cdot\lambda$	ratio of longitudinal conductivities of the heat conducting wall and of the fluid in the main passage
$v(x, r)$, $w(x, r)$	transverse and longitudinal components of the flow velocity in a point
$Nu_k = Kd/\lambda$	Nusselt number calculated for the heat transfer coefficient

Dimensionless quantities

$X = x/d$, $R = r/r_0$, $L = l/d$ are the longitudinal coordinate, radius and length of the heat conducting section, respectively.

Subscripts

theo	theoretical value
w	wall
sp	space
L	arbitrary length of the heat conducting section
h.e	heat exchanger
q	constant thermal flux on the wall
x	variable thermal flux on the wall

REFERENCES

1. Labuntsov, D. A.: Doklady AN SSSR, 118, No. 6, 1118 (1958).
2. Genin, L. G.: Teplofizika vysokikh temperatur, 1, No. 2, 247-253 (1963).
3. Pirogov, M. S.: Zhidkiye metally [Liquid Metals], page 94, Gosatomizdat, Moscow, 1963.
4. Trefethen, L.: Trans. ASME, 78, No. 6, 1207 (1956).
5. Petukhov, B. S. and Yushin, A. Ya.: Doklady AN SSSR, 136, No. 6, 1321 (1961).
6. Volchkov, L. G., et al.: Teplootdacha natriya i splava natriy-kaliy v korotkikh vertikal'nykh trubakh pri smeshannoy konvektsii [Heat Transfer of a Sodium and a Sodium-Potassium Alloy in Short Vertical Pipes by Combined Convection]. Article in present collection immediately preceding the above.

STATISTICAL CHARACTERISTICS OF TURBULENT TEMPERATURE FLUCTUATIONS IN FLUID FLOWS

V. P. Bobkov, M. Kh. Ibragimov and V. I. Subbotin

A characteristic feature of turbulent flow is the disorderliness, randomness /53
of motion which results in random variations in the velocity, pressure, tempera- /54
ture, etc., in time and space. Statistical averaging of instantaneous values makes it possible to separate the steady part of the velocity and temperature fields. The irregular part of turbulent flow can be described by statistical methods. Total statistical description of turbulent motion is sufficiently complex and requires extensive information on the values of the correlation and spectral tensors, on the probability distribution, etc. New experimental data in the field will make it possible to more fully represent the mechanism of turbulence processes and to create a physically substantiated statistical theory of fluid flow and heat transfer, free of artifical prerequisite conditions and assumptions.

At present many works have been published on the statistical nature of turbulent flow [1], [2]. All publications support the idea that it is necessary to measure experimentally the following specific quantities:

1) Averaged velocity and temperature fields, their dependence on the physical parameters of the fluid and on the Reynolds number. Experimental work which was performed makes it possible to qualitatively estimate the magnitude of the turbulent transfer of momentum and heat for different fluids in different flows; 2) root mean square values of the velocity and temperature fluctuations, reflecting the intensity of the process; 3) spectral densities of the fluctuations; 4) space-time correlation coefficients in one and more points of the flow; 5) probability distribution at various time instants and in different points of the flow.

The existing statistical theories make use of average statistical characteristics. Only time averaging is practically possible in experiments. The relationship between the average statistical values and values averaged with respect to time is established by the ergodic theorem. In hydrodynamics this theorem is not theoretically proved, however, experiment data show that it can be used in the study of hydrodynamic phenomena [2]. The validity of the ergodic theorem for temperature fluctuations is proven in [3].

Under conditions of constant heat transfer, the velocity and temperature fluctuations are steady-state random functions. Such a function can be represented as a system of random quantities, i.e., of ordinates of a random function during specified, sufficiently small time intervals. Consequently, the study of statistical characteristics of stationary random functions can be reduced to the study of a system of random quantities making use in the process of the probability theory theorem.

This circumstance will be used in the present article for obtaining the distribution function and other statistical characteristics.

The empirical information on the statistical characteristics of turbulent flow in ducts is not too extensive. The available experimental data pertain mainly to /55
turbulent fluctuations of velocities in the flow of air or water [4-9]. No systematic information is available on the statistical characteristics of turbulent temperature fluctuations, although, obviously, only the study of temperature fluctuations and of the statistical relationship between them and the velocity fluctuations will make it possible to clarify the mechanism of turbulent heat transfer.

The present article presents results of measurements of certain statistical characteristics of temperature fluctuations in turbulent flow of various fluids with highly different thermal conductivities (water, mercury, lead).

Methods of Measurements, Apparatus

The measurements were performed in a round pipe 52.2 mm in diameter at a distance of 30 diameters from the start of the heated section and of 40 diameters from the pipe inlet. The temperature in the flow were measured by chrome-alumel thermocouples with an external diameter of 0.3 and 0.5 mm. They were fastened in a special probe. Reference [3 and 4] depict the layouts of the section, probes and microthermocouples. The test pipe was held vertically. The thermal flux was produced by a band-type electric heater, which was double wound on the pipe to reduce electromagnetic interference in the thermocouple circuit. The fluid was lead into the pipe past the elbow in the loop. A part of experiments with mercury was performed with a grid, consisting of a steel plate 3 mm thick with holes 2.5 mm in diameter, forming a square lattice with a hole-to-hole distance of 4 mm at the pipe inlet. These experiments have shown that the measurements were performed under conditions of hydrodynamic and thermal stabilization of the flow.

To measure and automatically calculate the root mean square values of the temperature fluctuations and the correlation coefficients we have used the 46K1 correlometer (analog computer) and special amplifiers with a transmission band of from 0.15 to 200 cps. The oscillograms of turbulent temperature fluctuations were recorded on 35-mm film by means of the MPO-2 oscillograph. This information was used for determining the probability density distributions and other statistical characteristics.

In measuring turbulent temperature fluctuations one most know how the inertia, relationship between the specific heats of the thermocouple and the turbulent flow and distortions of the structure of the turbulent flow by the thermocouple in the point under measurement effect the experimental results. The effect of the inertia on the measurement of fluctuations can be estimated by considering the effect of the latter on the root mean square values of the temperature fluctuations, if the spectral function of fluctuations and the time constant of the temperature under the specified conditions of heat transfer between the thermocouple junction and the medium are known.

If we replace the stationary random function by a stationary linear system, each of the ordinates of its spectrum will be multiplied by the square of the modulus of the transient function of the system for the corresponding frequency [11], [12]. /56

$$S_1(\omega) = |\Phi(i\omega)|^2 S_0(\omega). \tag{1}$$

The transient function for a thermocouple can, in the first approximation, be represented as a purely aperiodic component [13], i.e.,

$$\Phi(i\omega) = \frac{1}{\sqrt{(T_T\omega)^2+1}} e^{-i\,\mathrm{arctg}\,T_T\omega}. \tag{2}$$

Multiplying both sides of Eq. (1) by $d\omega$ and using Eq. (2) and integrating, we will get the dispersion of the real (undistorted) signal

$$D = 2\int_0^\infty S_1(\omega)\,[(T_T\omega)^2+1]\,d\omega. \tag{3}$$

Thus, in order to find the real value of the temperature fluctuation intensity, it is necessary to know the measured spectral density and T_{th}, the thermocouple's time constant which, in general, depends not only on the dimensions of the junction and its thermophysical properties, but also on the conditions of heat transfer between the fluid and the thermocouple junction.

The inertia was studied separately. Numerical values of the time constant were obtained (experimentally) for different thermocouples under unequal conditions of heat transfer between the thermocouple junction and the surrounding medium. It was found that for the thermocouple 0.5 mm in diameter the time constant does not exceed 0.04 secs (when wetted with water flowing at 0.2 m/sec); for a thermocouple 0.3 mm in diameter it was not more than 0.01 secs (when wetted with water flowing at 1 m/sec). It is natural that when wetted with mercury and lead the heat transfer in the junction is very high and the time constant will be even smaller [14]. Preliminary results [3-11] have shown that $S_1\omega$, the spectral function of temperature fluctuations has a value close to unity as early as at a frequency of 10 cps, which attests to the negligible energy which is carried by the higher frequencies (above 10 cps). Calculations using Eq. (3) have shown that for frequencies from 0 to 10 cps the error produced by the inertia in measuring the temperature fluctuation intensity does not exceed 1% for thermocouples 0.5 and 0.3 mm in diameter. The measured fluctuation intensities obtained by different thermocouples do not differ. Equation (3) is suitable for estimating the correction only in the case when T_{th}, the time constant, does not vary with time, i.e., when the coefficient of heat transfer between the junction and the fluid is constant. An estimate of the effect of unsteadiness on the heat transfer has shown that the

heat transfer coefficient under conditions of our experiment differs little from the steady-state coefficient [14].

The effect of the distortions introduced by the thermocouples was estimated indirectly: the intensities of fluctuations in the given point of the flow (center of pipe) were measured with the thermocouples situated at different distances from one another (Fig. 1); it was found that σ_t, does not change. This, apparently, can /57 be explained as follows: the temperature fluctuations in the given point are determined mainly by the turbulent field in the preceding, rather than in the given section of the pipe. The second thermocouple also had no effect on the probability distribution function.

It is known that the accuracy in determining the turbulent characteristics depends on the averaging time τ. Reference 15 recommends formulas for selecting the time interval over which τ is to be integrated for a given experimental accuracy. An estimate made using these formulas has shown that in the case of $\tau = 5$ min (maximum integration time of the correlometer) the error in determining second-order moment is not more than 2%. The oscillograms which were obtained are recordings over time intervals from 15 secs to 2 mins. When $\tau = 15$ secs the maximum error due to the fact that the integration time is finite should comprise not more than 45%. Actually it turned out to be much lower. Comparison of results obtained by the correlometer and of those produced by analysis of the oscillograms shows that they agree satisfactorily. It is natural that the error in measuring moments of higher order for the same integration time.

Intensity of Temperature Fluctuations

The intensity of temperature fluctuations was measured for the flow of water /58 (Re = 16,000), mercury (Re from 5,000 to 125,000) and lead (Re from 30,000 to 216,000). Experimental data for water (thermal flux density $2.3 \cdot 10^4$ watts/m^2) and mercury (for fluxes from $1.16 \cdot 10^4$ up to $2.3 \cdot 10^4$ watts/m^2) were obtained by using the correlometer; for lead (for fluxes from $1.8 \cdot 10^4$ to $3.1 \cdot 10^4$ watts/m^2) they were obtained by analysis of the temperature fluctuation oscillograms. Here the time pace was 0.01 secs, which enabled us to satisfactorily reproduce the fluctuation oscillograms up to frequencies of the order of 10 cps [16]. The measurements were made over the entire pipe cross section (from the pipe axis to contact with the wall).

To determine the manner in which the intensity of temperature fluctuations depends on the thermal flux density, we have performed experiments (for mercury) with Re = 16,000 and thermal fluxes of $1.2 \cdot 10^4$, $1.8 \cdot 10^4$ and $2.3 \cdot 10^4$ watts/m^2. It was found that the intensity σ_t, is proportional to the thermal flux density.

The manner in which the dimensionless fluctuation intensity varies for mercury and water for Re = 16,000 over the pipe cross section is shown in Fig. 2.

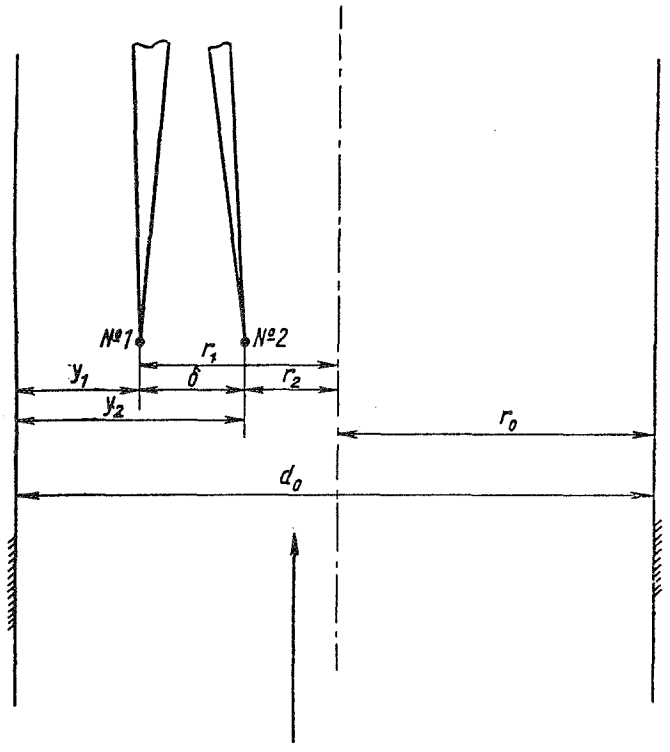

Figure 1. Location of Thermocouples in the Pipe. No. 1 and No. 2 are Thermocouples.

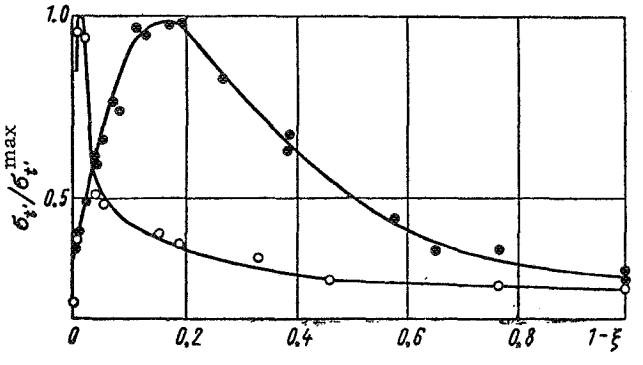

Figure 2. Intensity of Temperature Fluctuations for Re = 16,000 Where the White Circles Denote Water, While the Black Circles are for Mercury.

The fluctuation intensity curves have a maximum for water near the very wall, when while those for mercury and lead are at maximum at [some] distance from it. This is due to the fact that the temperature distribution in the main body of the flow for a fluid with large Reynolds numbers is simplified and changes highly near the wall, while for liquid metals the mean temperature distribution is represented by a flat-curve over the entire flow cross section.

The maximum relative fluctuation intensity for mercury changes in a complex manner with an increase in Re (Fig. 3), i.e., first it increases rapidly, reaching a maximum when Re $\approx$ 20,000, and then decreases smoothly. The fluctuation intensity curve /59 tends to zero as Re approaches the critical value, since the temperature fluctuations produced by natural convection are of such a low frequency that they are not within the transmission band of the amplifier. Experimental data for lead were obtained with Re > 20,000. Here we were able to observe the section in which the fluctuation rate drops with an increase in the Reynolds number.

The above behavior of the fluctuation intensity with an increase in the Reynolds number is due to the interaction of two factors acting in opposite directions. First, the turbulence is still developing in the transition region of the flow, the velocity fluctuations increase with an increase in Re, and consequently,

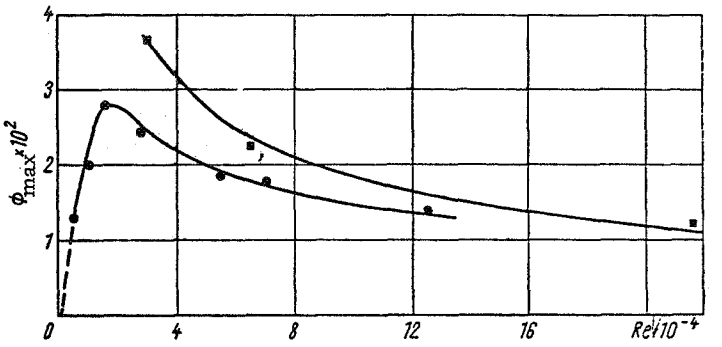

Figure 3. Maximum Intensity of Temperature Fluctuations as a Function of Re. The Squares Denote Lead, the Circles are for Mercury.

the temperature fluctuations increase also. Secondly, the maximum mean temperature difference in the fluid drops with an increase in the Reynolds number. This should result in reducing the temperature fluctuation intensity. The latter quantity thus changes depending on the relative strength of the two aforementioned factors. In the transition region the effect of the first factor predominates with an increase in Re, while when Re is higher than 20,000 the second factor predominates.

The above behavior of the fluctuation intensity with changes in Reynolds numbers was observed almost over the entire cross sectional area of the pipe. The fluctuation intensity increases continuously with an increase in Re to 70,000, then some drop in the fluctuation intensity is observed. For lead and mercury the distance between the point of maximum fluctuation intensity and the wall first increases rapidly with an increase in Re, and then this increase slows down. The fluctuation intensity curve becomes more flat with an increase in the Reynolds number.

Analyzing the experimental data for the three above heat transfer agents we have found general quantitative laws governing the behavior of the temperature fluctuations. The first governing relationship is a satisfactory generalization of experimental data for the maximum value of the fluctuation intensity and the distance between this maximum point and the wall. Figure 4 shows the curve of $\sigma_{t_1}/\sigma_{t_1}^{max}$ as a function of y/y_{max} for all the heat transfer agents (the Prandtl numbers differ by a factor of 300) obtained for the Reynolds numbers and thermal fluxes at hand. The observed scattering of points is within the limits of experimental error. The generalization attest to the similarity between temperature fluctuation intensity curves as a function of y_{max}. The second relationship pertains to the generalization of the dependence of the maximum fluctuation intensity and of the distance between this maximum and the wall for different Reynolds and Prandtl numbers (Fig. 5). The experimental points for mercury and lead can be generalized satisfactorily in logarithmic coordinates.

/61

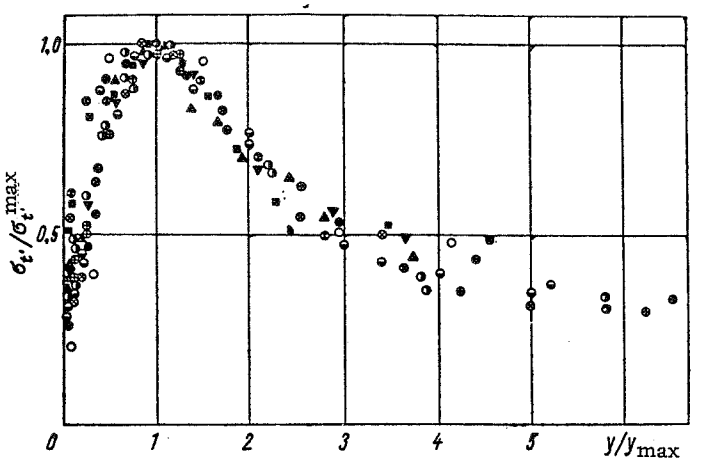

Figure 4. Fluctuation Intensity Curves.

○ — Re = 16,000 (for water); ● — Re = 30,000; ▲ — Re = 64,000; ■ — Re = 216,000 (for mercury); ⊕ — Re = 10,000; ◑ — Re = 16,000; ◒ — Re = 28,000; ⊗ — Re = 55,000; ▼ — Re = 70,000; □ —Re = 125,000 (for mercury);

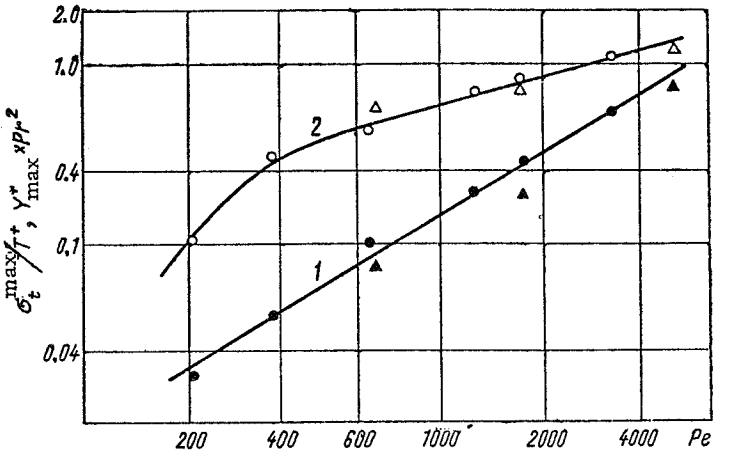

Figure 5. Curves Showing $Y^+_{max} \cdot Pr$ (1) and $\sigma^{max}_{t'}/T^+$ (2) as a Function of the Peclet Number. ○ and ● are for Mercury; △ and ▲ are for Lead.

The above generalization shows that the observed inhomogeneity of the temperature fluctuation intensities over the pipe's radius disappears gradually with an increase in the average velocity, and the fluctuation intensity maximum becomes degenerate. This means that the turbulent flow tends to an isotropic flow with an increase in the Reynolds number.

Spatial Correlation Coefficients and Scales of Temperature Disturbances

Spatial correlation coefficients $R_{1\cdot 2}$ are major statistical characteristics of turbulent flow. Study of these coefficients between velocity fluctuations in the flow gives an idea of the scales of velocity disturbances, making it possible to estimate the structure of the eddies [2]. Similarly, $R_{1\cdot 2}$ between temperature fluctuations in two points of the flow determine the dimensions of the temperature disturbances; changes in these dimensions with a change in the character of the flow for fluids with different Prandtl numbers provide us with some idea on the character of the velocity fluctuations.

It is known [1] that $R_{1\cdot 2}$ between random quantities of the same kind of two points of the turbulent flow has the following properties. It varies within the limits of ± 1. When the distance between the points is reduced, $R_{1\cdot 2}$ goes to unity, which denotes a tendency to functional relationship between the fluctuations in the two points. When the distance between the points is increased, $R_{1\cdot 2}$ goes to zero. For independent random stationary processes $R_{1\cdot 2}$ is equal to zero, which is known from the probability theory [17]. For random stationary processes with normal distributions the converse is also true. The fact that the correlation coefficient is zero does not mean that there is no statistical relationship (in general).

When the distance between two points is reduced, the first derivative of the correlation coefficient (with respect to space) tends to zero, while the second derivative has a finite value when $\delta = 0$. The correlation curves for sufficiently small δ are parabolic [1]. This property is due to the fact that $R_{1\cdot 2}$ varies symmetrically with respect to δ near $\delta = 0$. Upon expanding the correlation coefficient in a Taylor series, we will obtain the following relationship for sufficiently small δ:

$$R_{1\cdot 2} = 1 - \frac{\delta^2}{\lambda_0^2}, \qquad (4)$$

where λ_0 is a microscale, characterizing the average size of the dissipation eddies. /62

Except for these general properties it is impossible to analytically determine the shape of the curve for anisotropic flow. In each particular case the character of the curve is determined by the specific conditions: geometry of the passage, rate of flow, properties of the fluid, degree of stabilization, the fluctuating quantities which are measured (velocity, temperature, concentration, pressure, etc.).

We have studied the correlation coefficient for the flow of water (Re = 16,000) and mercury (Re = 10,000-125,000). The movement of thermocouples during measurements is shown diagramatically in Fig. 1. Thermocouple No. 1 was placed at a given point in the flow, while thermocouple No. 2 was moved relative to the first

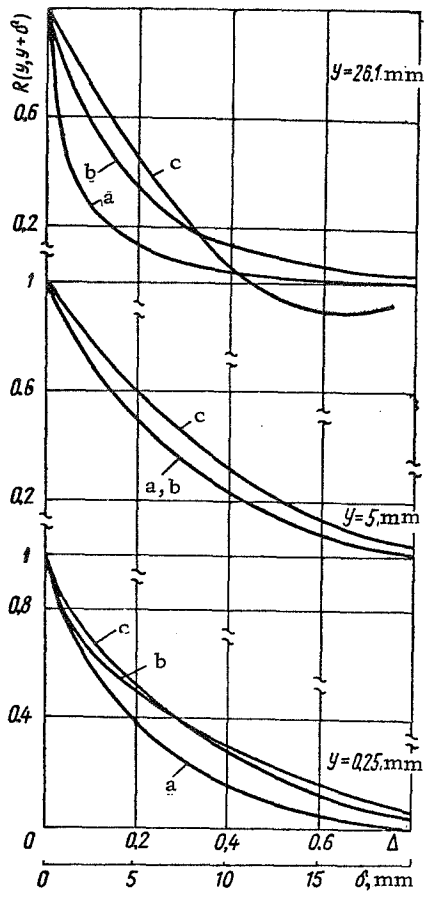

Figure 6. Correlation Coefficients for Mercury for Different Reynolds Numbers. a) Re = 10,000; b) Re = = 28,000; c) Re = 125,000.

along the pipe's diameter in the direction of the axis of the flow. The distance between the thermocouples was varied from 0.5 mm (contact) to 20 mm. These experiments were performed without a screen at the inlet.

For each flow mode curves of $R_{1\cdot 2}$ were obtained for different positions of thermocouple No. 1 [from the center of the pipe up to contact with the wall (Figs. 6 and 7)]. For mercury the correlation coefficient varies appreciably as thermocouple No. 1 is moved along the pipe's radius and it depends on the Reynolds number. In the center of the pipe, for low Reynolds numbers, the correlation coefficient goes more rapidly to zero with an increase in the distance between the two thermocouples, than for high Re. Consequently, as the Reynolds number in the center of the pipe is increased the size of the disturbances increases. For the case when one of the thermocouples is in contact with the wall curves of the correlation coefficient change little with an increase in Re, while as the thermocouple is moved away from the wall, the change in $R_{1\cdot 2}$ with changes in the Reynolds number becomes increasingly more perceptible. This shows that the correlation relationships in the region close to the wall do not change when Re > 10,000 which, apparently, is due /63 to the limiting effect of the wall, while the center of the flow the character of the correlation coefficient, and consequently also, the structure of the eddies, changes with an increase in Re. Self-similarity ensures only for Reynolds numbers in excess of 30,000. The curves of the correlation coefficient are sufficiently smooth (without sharp bends), but with a sharp drop near $\delta = 0$, which points to the presence of a continuous wide spectrum of eddies in the flow. For mercury at high Reynolds numbers we have noticed the existence of regions with negative correlation coefficients (see Fig. 6). For lower values of Re negative regions were not observed in the explicit form (with δ varied from 0.5 to 20 mm), although the curves do have a tendency to such values.

The fact that velocity fluctuations must have negative correlation coefficients was proven in [17]. The existence of negative regions of correlation coefficients

also for temperature fluctuations can be proven similarly. From the fact that the flow and the heat transfer take place under steady-state conditions we have

$$\int_0^{r_0} (\bar{t} + t')\, r\, dr = \text{const} = \int_0^{r_0} \bar{t} r\, dr, \tag{5}$$

consequently, at each time instant

$$\int_0^{r_0} t' r\, dr = 0. \tag{6}$$

Multiplying both parts of the above expression t'_y, we get

$$t'_c \int_0^{r_0} t' r\, dr = 0, \tag{7}$$

where t'_c is the magnitude of the temperature fluctuations in the center of the pipe, which is independent of radius r. Thus, putting t'_c under the integral sign and averaging it with respect to time, we get

$$\int_0^{r_0} (\bar{t}'_c t')\, r\, dr = 0; \tag{8}$$

since $\bar{t}'_c t' = \sigma_{t'_c} \sigma_{t'} R_{t'_c t'}$, it follows that

$$\sigma t'_c \int_0^{r_0} \sigma_{t'} R_{t'_c t'} r\, dr = 0 \tag{9}$$

or

$$\int_0^{r_0} \sigma_{t'} R_{t'_c t'} r\, dr = 0. \tag{10}$$

/64

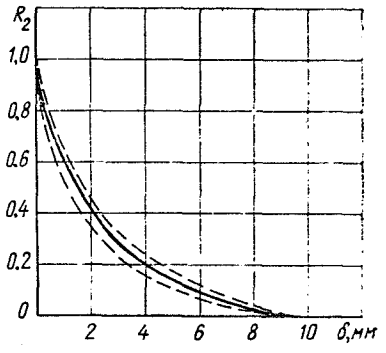

Figure 7. Correlation Coefficient for Water with ξ = = 0-0.99, Re = 16,000.

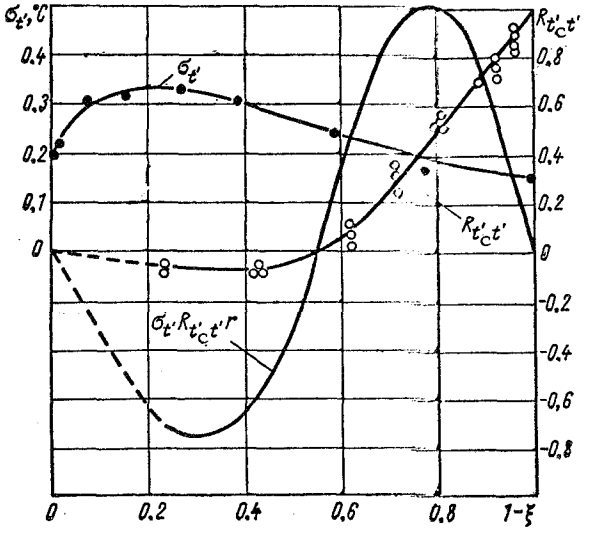

Figure 8. Experimental Substantiation of Eq. (10).

The validity of the above expression is substantiated by experimental data on the correlation coefficient and by the root-mean-square value of temperatures [18]. Figure 8 shows $R_{t'_c t'} \sigma_{t'} r$ as a function of the dimensionless radius of the pipe for Re = 125,000. The areas of the positive and negative regions coincide satisfactorily with one another. Similarly this kind of relationship can also be observed for other, lower Reynolds numbers (in particular, for water). However, for lower Reynolds numbers in order to satisfy Eq. (10) very small negative $R_{t'_c t'}$ are required (less than 0.04), since a large difference in the fluctuation intensity is observed in the center of the pipe and at its wall. Hence these values cannot always be observed due to measurement errors.

Satisfaction of Eq. (10) means that the measurements of $\sigma_{t'}$ and $R_{t'_c t'}$ in the experiments were of sufficient accuracy. The physical meaning of the negative correlation coefficients consists in the presence of regions with reversed flows, hence negative correlation coefficients are produced by the main pulsating motion and do not describe the scales of the disturbances.

For water with Re = 16,000 /65 the character of the curves for correlation coefficients differ little over the pipe's cross section, with the exception of a region near the wall where a weaker variation in R_r was observed than in the center of the flow.

We have not discovered parabolic segments in the correlation coefficient curves near $\delta = 0$. Apparently, our thermocouples are not capable to directly determine the microscale of the temperature disturbances.

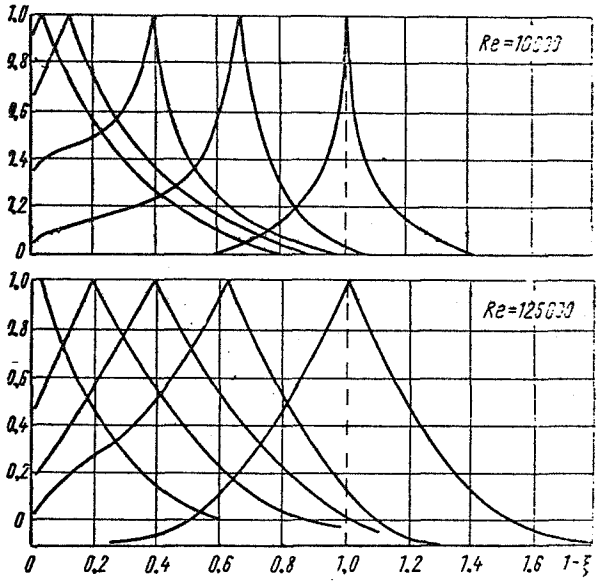

Figure 9. Correlation Coefficients for Different Directions of Motion of Thermocouple No. 2.

If the ratio of the macro- and microscales for the temperature fluctuations has the same order as that for the velocity fluctuations [1]

$$\frac{L}{\lambda_0}=\frac{\sigma_t\cdot\lambda_0}{\nu}, \qquad (11)$$

then λ_0 for our conditions should be about 0.1 mm. A quantity of this magnitude can obviously not be detected by the microthermocouples we have used.

For all the Reynolds numbers we have noted that the correlation coefficients are not the same when δ varies in the positive and negative directions. The coefficients are symmetrical only along the pipe's axis. The lack of symmetry becomes less pronounced with an increase in the Reynolds number (Fig. 9).

In determining the scales of the disturbances the problem arises of analyzing the experimental data on the basis of correlation coefficients. Strictly speaking, a calculation using the expression /66

$$L_r=\int_0^\infty R(y;\ y+\delta)\,d\delta, \qquad (12)$$

is valid [only] for a normal joint distribution of random functions, which describe the temperature fluctuations in two points of the flow. Our preliminary calculations have shown that this distribution is close to normal in the center of the flow. A certain deviation from normal distribution exists near the wall, in particular of low Re. No recommendations exist on calculating the scale of disturbance for a non-normal joint distribution. However, it may be assumed that disregarding higher-order moments which are brought about by a not too large deviation from a normal joint distribution will have little effect on the scales of disturbances. On the other hand, the use of Eq. (12) is apparently not entirely logical, since it does not take into account features produced by the nearness of the wall and by the correlation curves. In addition, this expression assumes that, within the limits of the transverse dimensions of the passage and at the wall, $R_{1\cdot 2}$ reaches a zero value (for δ_0). It also takes into account negative regions of the correlation

coefficient, which unjustifiably reduces the scales of disturbances. In another method for determining the scales of disturbances [5], using the expression

$$L_r = \int_0^{\delta} R\left(y - \frac{\delta}{2};\ y + \frac{\delta}{2}\right) d\delta \tag{13}$$

it is assumed that the correlation coefficient varies symmetrically to both sides of the given point of the flow along the radius of the pipe. Allowing for the fact that $R_{1\cdot 2}$ does not vary symmetrically, we propose another method for obtaining L_2, using the formula

$$L_r = \frac{L_{r+} + L_{r-}}{2}, \tag{14}$$

where

$$L_{r+} = \int_0^{\delta_0} R(y;\ y+\delta)\, d\delta \text{ and } L_{r-} = \int_0^{\delta_0} R(y;\ y-\delta)\, d\delta.$$

Integration with respect to δ_0 means that the region with negative correlation coefficients R_r is disregarded. For comparison we have calculated the microscales of temperature fluctuations using Eqs. (12) and (14). The region of negative correlation coefficients was not taken into account in these calculations; it was assumed that $R_{1\cdot 2}$ at the wall becomes zero, since there is no turbulent transfer at this point, although naturally, temperature fluctuations produced by thermal conductivity do penetrate it. Results of calculations for mercury and water for Re = 16,000 and 125,000 are presented in Fig. 10. It can be seen from the figure that L_r near the wall depends appreciably on the selected method of calcula- /67
tions. The first method gives a maximum value of L_r, since in this case we do not use the condition for which $R_{1\cdot 2}$ at the wall is zero (integration takes place into the flow). The second method yields the lowest values of L_r due to the fact that the effect of the zero condition at the wall is extended to the center of the flow. The third method yields intermediate values. In the center of the flow all the three methods give the same size of temperature disturbances, since the structure of the flow is close to homogeneous.

Figure 12 also shows values of L_r obtained for water flowing with Re = = 16,000. Data for water have been calculated from Eq. (13). In the center of the pipe and near the wall the scales of temperature disturbances are the same, but in

the region where L_r has its maximum, for the case of mercury they turned out to be somewhat higher than for water. It is possible that this is a result of the effect of thermophysical properties of the [different] liquids. The scales of temperature disturbances for mercury as a function of Re, obtained from Eq. (14), are shown in Fig. 11. The greater the distance from the wall, the more does the scale vary as a function of the Reynolds number. The scale reaches its full size for large Re in the center of the flow, but not at the wall. In the immediate vicinity of the wall the scale does not change with an increase in the Reynolds number (for Re > 10,000). This is due to the fact that near the wall the scale of turbulent disturbances is limited by the presence of the latter. /68

Probability Distribution for Temperature Fluctuation Amplitudes

We have studied the one-dimensional probability distributions for water, mercury and lead. This study consisted in checking the hypothesis on the normal distribution of the temperature fluctuations in a given point in the flow, the deviation from which was checked by constructing rectified diagrams [17]. Figure 12 shows the rectified [linearized] diagrams for mercury at Re = 28,000 for different distance from the wall. It was noted that the experimental points agree with the straight line describing the normal distribution only in the center of the flow. The closer to the wall the larger the deviation from the normal distribution; in addition, the character of this deviation changes. Qualitative study of this deviation has shown that the distributions under study are somewhat asymmetrical and have an excess, which is characterized by third-and fourth-order moments, respectively. Deviations from the normal distribution are not too large and they are ordered. It is known that these distributions can be smoothed out according to the Charlier distribution [19] (a particular case of which is the normal distribution), which is expressed as

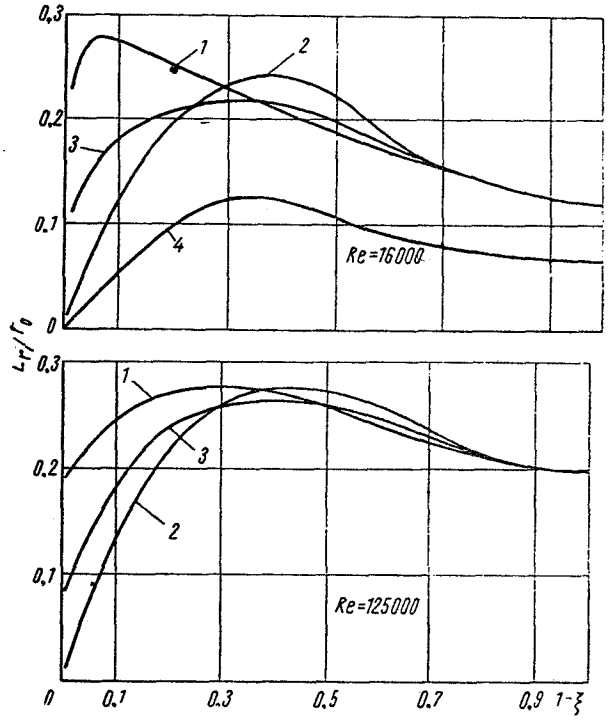

Figure 10. Scales of Temperature Disturbances. 1) Equation (12); 2) Equation (13); 3) Equation (14) (Mercury); 4) Equation (13) (water).

$$n_i = \frac{N_0 h}{\sigma_{t'}} \Phi_d \left[1 + \frac{A}{6}(t'^3 - 3t') + \frac{E-3}{24}(t'^4 - 6t'^2 + 3)\right].$$

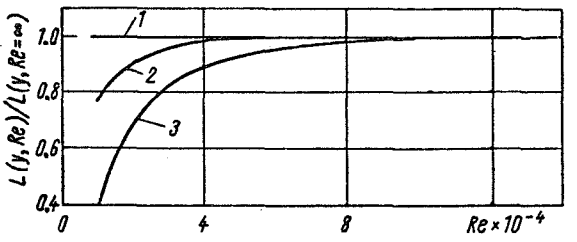

Figure 11. Scales of Temperature Disturbances as a Function of the Reynolds Number. 1) y = = 1 mm; 2) y = 5 mm; 3) y = r_0 = = 26.1 mm.

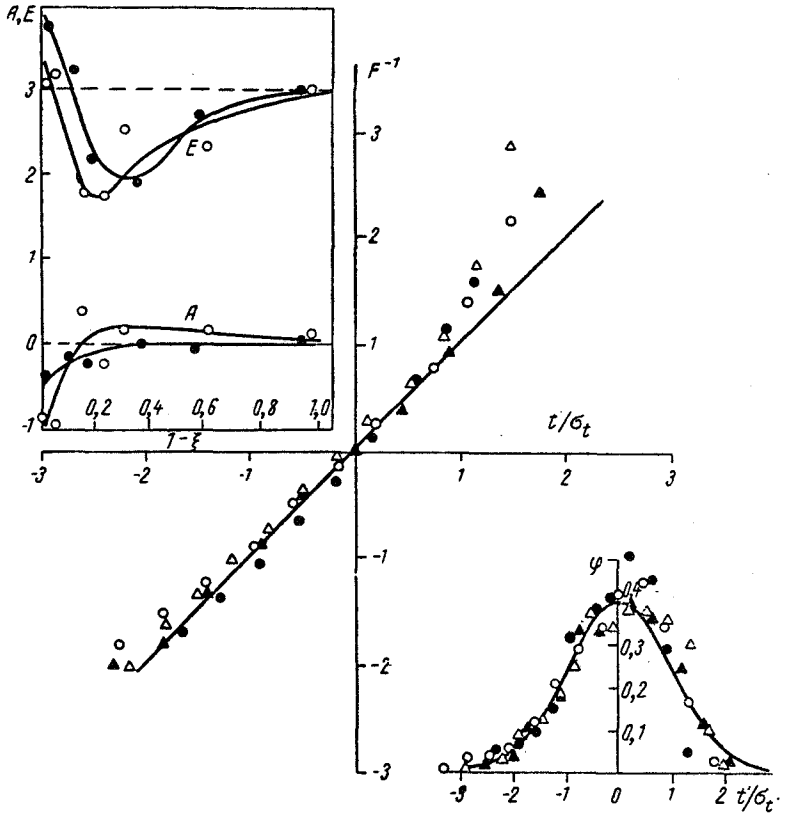

Figure 12. Probability Distribution Density, Linearized Diagrams and Parameters of Temperature Fluctuation Distributions for the Flow of Mercury.

y, mm	Re	
	2.8·10⁴	1.25·10⁵
0.25 4	○ △	● ▲

Then we have determined the parameters of the above distribution and we have followed their variations along the pipe's cross section. Figure 12 shows

variations of parameters A and E over the pipe's cross section for two different Reynolds numbers for mercury. As the pipe wall is approached, the excess as well as the asymmetry change. In conclusion it may be stated that near the wall the probability of the appearance of large positive temperature fluctuations decreases, while that of small fluctuations increases. Scatter of points in the direction of cooling (the main body of the flow cooler than the wall) have a distribution close to normal (see Fig. 14). The coefficients of excess and of asymmetry also change /70

NOTATION

r_0	pipe radius
y	distance from wall
δ	distance between thermocouples
y_{max}	position of the maximum temperature fluctuation intensity
t'	temperature fluctuation, ° C
t'_c	temperature fluctuation in the center of the pipe, ° C
$\sigma_{t'}$	temperature fluctuation intensity, ° C
$\sigma_{u'}$	fluctuation intensity of the velocity in the transverse direction
u^+	rate of friction
D	dispersion
$R_{1\cdot 2}$	correlation coefficient
R_2	spatial correlation coefficient in the radial direction
L_r	microscale of temperature fluctuations over the pipe's radius
ω	angular frequency
$S_0(\omega), S_1(\omega)$	real and measured densities of the spectral function, respectively
$\Phi(i\omega)$	transient function
T_{th}	thermocouple time constant

τ time

n_i frequency of appearance of fluctuations in the given range of values;

$$\sum_{i=1}^{\infty}$$

d probability density of the normal distribution

A coefficient of asymmetry

E coefficient of excess

Dimensionless Quantities

$\Delta = \delta / r_0$ distance between thermocouples

$y^t = y \cdot u^t / \nu$ distance from the wall

$\xi = r / r_0$ radius

$\Phi = \sigma_{t'} \cdot \lambda / q_0 r_0$ temperature fluctuation intensity

REFERENCES

1. Khintse, I.O.: Turbulentnost' [Turbulence]. Fizmatgiz, Moscow, 1963.
2. Townsend, A.A.: Struktura turbulentnogo potoka s poperechnym sdvigom [Structure of Turbulent Flow with Shear], Izdatel'stvo inostrannoy literatury [translated from English], 1959.
3. Subbotin, V.I., et al.: Teplofizika vysokikh temperatur, No. 1 (1964).
4. Velikanov, M.A.: Dinamika ruslovykh potokov [Dynamics of Channel Flows], 1, Moscow, 1954.
5. Minskiy, Ye.M.: Turbulentnost' ruslovogo potoka [Turbulence of Channel Flow]. Gostekhizdat, Moscow, 1953. /71
6. Taylor G.J.: Proc. Roy. Soc. A., 135 (1932).
7. Fage A.: Philos. Mag., 7, 21 (1936).
8. Laufer, J.: NACA, Report-1053 (1951).
9. Laufer, J.: NACA, Report-1174 (1953).
10. Subbotin, V.I., et al.: Teploenergetika, No. 3 (1962).
11. Venttsel', Ye.S.: Teoriya veroyatnosti [Theory of Probability]. Fizmatgiz, Moscow, 1962.
12. Pugachev, V.S.: Teoriya sluchaynykh funktsii [Theory of Random Functions]. Fizmatgiz, Moscow, 1957.

13. Solodovnikov, V. V.: Osnovy avtomaticheskogo regulirovaniya [Fundamentals of Automatic Control]. Gostekhizdat, Moscow, 1954.
14. Bobkov, V. P., et al.: Teploenergetika, No. 5 (1965).
15. Opredeliniye parametrov sluchaynykh protsessov [Determination of the Parameters of Random Processes]. Collection of articles under the editorship of V. I. Chaykovskiy. Gostekhizdat, Kiev, 1962.
16. Harley, N. and Buch, K.: Introduction to the Theory of Probability and to Mathematical Statistics [translated from English], 1951.
17. Taylor, G. J.: Proc. Roy. Soc. A., 537, (1936).
18. Bobkov, V. P., et al.: Teplofizika vysokikh temperatur, No. 5 (1965).
19. Romanovskiy, L. Ya.: Primeneniye matematicheskoy statistiki v opytnom dele (Utilization of Mathematical Statistics in the Performance of Experiments]. Gostekhizdat, Moscow, 1947.

STATISTICAL CHARACTERISTICS OF TEMPERATURE FLUCTUATIONS IN HEAT EXCHANGER WALLS ATTENDANT TO HIGH THERMAL FLUXES

M. Kh. Ibragimov, V. I. Merkulov and V. I. Subbotin

Under conditions of steady-state turbulent heat transfer temperature fluctuations arise in heat conducting walls [1], [2]. The cause of these fluctuations is the disorderly, random motion of a part of the fluid (eddies) in the turbulent flow. In a nonisothermal flow of a fluid, when the temperature has a gradient over the flow cross section, the motion of an eddy from one layer to another results in temperature fluctuations. When moving, the more energetic eddies penetrate up to the wall of the duct, producing rapid temperature changes in it. The majority of the eddies does not reach the wall, it breaks up in the region close to the wall, producing in it temperature fluctuations which by thermal diffusivity are transported to the wall of the duct. It is obvious that the maximum temperature fluctuation at the heat conducting surface of the wall may be equal to Δt_{α}. However, the probability of the fact that eddies from the center part of the flow will reach the wall is very small, since the integral scales of the temperature disturbances in turbulent flow is smaller than the transverse dimensions of the duct [3]. As a result of this, the maximum amplitude of temperature fluctuations in the wall should be lower than the mean temperature difference. /71

The amplitude of the temperature fluctuations in the layer near the wall and in the wall proper is damped exponentially; here the degree of damping depends on the frequency of fluctuations and on the thermal diffusivity of the fluid and the wall /72

$$\frac{A_x}{A_m} = e^{-x\sqrt{\frac{\pi \cdot n}{a}}}, \qquad (1)$$

where A_m and A_x are the amplitudes of the temperature fluctuations at the point of origin and at a distance x from that point, and n is the frequency of fluctuations, cps. Consequently, the fluctuation intensity and the spectral composition of the temperature fluctuations will vary depending on the thickness of the wall and will be determined by the behavior of the fluctuations in the fluid region adjoining the wall.

Heat exchange apparatus operate at very high mean temperature differences. Hence, studies of temperature fluctuations in the wall are performed with attendant high heat fluxes, since in this case even very high frequency fluctuations have large amplitudes and may penetrate the channel's wall still retaining a sufficiently high intensity. It can be expected that not only the fluctuation intensity increase with an increase in the thermal flux, but also the contribution

of high-frequency fluctuations, which are more dangerous from the point of view of thermal fatigue stresses.

As a result of temperature fluctuations thermal stresses alternating at high rates appear in the wall of the channel. Their effect on the fitness of devices at high thermal fluxes is apparently substantial and should be taken into account in strength calculations. These additional thermal stresses are particularly dangerous when the heat conducting wall contains microcracks, deep, slots, etc., which produce stress concentrations [2]. The magnitude of the thermal stresses is determined by the magnitude of temperature disturbances in the wall of the channel, i.e., by the values of the spatial correlation coefficients of temperature fluctuations in two different points of the channel's wall.

This article presents some statistical characteristics (the intensity and the cross-correlation function) of temperature fluctuations in the wall of a double-tube heat exchanger. The same heat transfer agent (liquid metal) was pumped through both heat exchanger passages, at a different temperature.

Experimental Setups and Methods of Measurement

The heat exchanger was made from 1Kh18N9T steel with inner tube diameters of 25 x 2.5 mm and outer tube diameters of 42 x 3 mm. The manner in which the heat exchanger was connected to the circulation loop, when the heat transfer agent flow rate in both parts of the heat exchanger was the same, made it possible to perform the experiments under conditions close to that of constant thermal flux, passing through the heat conducting wall and directed into the annular space [space between the tubes]. The heat transfer took place over an l length $l_{h.e} = 900$ mm [$l_{h.e}/d_1 = 43$, $l_{h.e}/(D_1 - d_2) = 82$]. /73

Nine chromel-alumel microthermocouples were inserted into the inner tube wall at a given cross section along the heat exchanger length i.e., at a distance of 185 mm from the heat transfer agent inlet into the intertubular space; the diameter of the outer hood of each thermocouple being 0.5 mm. The thermocouples were metallized in slots 0.6 mm deep, milled in the tube wall. The centers of thermocouple junctions were situated at a depth of 0.35 mm from the outer surface of the tube at specified distances along the circumference (Fig. 1).

The heat exchanger was operated on the principle of counterflow (see Fig. 1). In order to reduce the effect of inlet conditions and to improve the mixing of the liquid metal in the heat exchanger, provisions were made for three mixing chambers, two of which were placed at the points where the liquid metal enters and leaves the intertubular space, and one at the point where the metal leaves the inner tube. Bushings for measuring the average temperatures of the liquid metals were inserted in the supply and discharge pipes of the heat exchanger. Temperature expansions in the heat exchanger were compensated for by a dish-type compensator, made from 1Kh18N9T stainless sheet steel 1.5 mm thick. In order to provide for a large temperature difference between the liquid metal flowing in the inner and outer passages of the heat exchanger, a heating section and /74

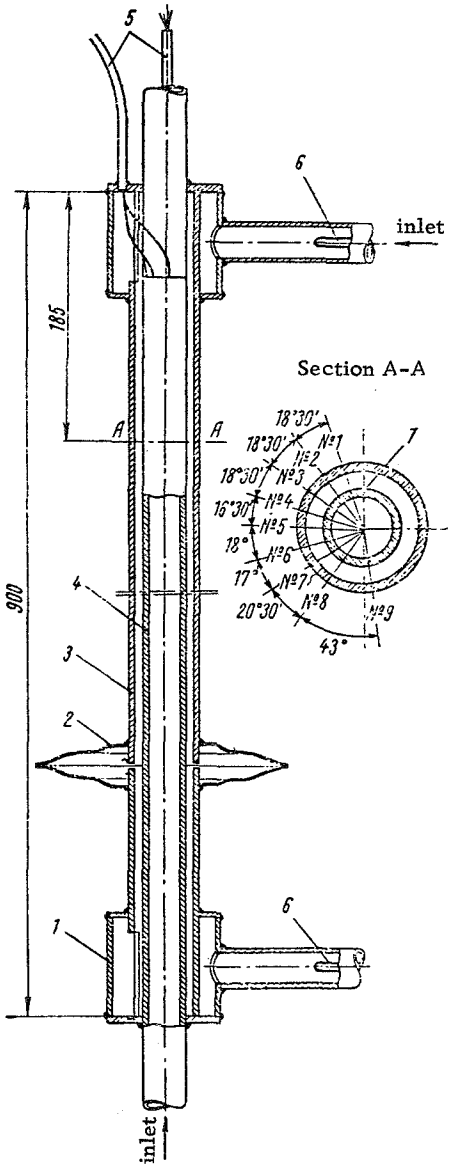

Figure 1. General View of Test Section and the Location of Microthermocouples. 1) Mixing Chamber; 2) Compensator; 3) Outer Jacket; 4) Heat-Conducting Tube; 5) Tubes for Removing the Thermocouple from the Section; 6) Thermocouple hood; 7) Thermocouple Beads [??] in the Wall of the Heat Conducting Tube.

a cooling device were installed in the circulation loop. The liquid metal was heated by passing electric current through the heating section. The heat generated by the cooling device was absorbed by water. The flow rate in the loop was measured by a magnetic flowmeter and was checked on the basis of the heat balance at the heating section. For this purpose appropriate thermocouples in hoods were placed at the heating section and in the loop.

The temperature fluctuations in the heat-conducting wall of the heat exchanger were recorded by the EPP-09 high-speed automatic potentiometer with an upper scale limit of 1, 2.5 and 5 millivolts, as well as by the MPO-2 loop oscillograph. The temperature fluctuations were recorded on the diagram tape of the EPP-09 potentiometer with a speed of 6 mm/sec; the loop oscillograph recording was on a 35-mm moving picture film with a speed of 10 mm/sec using the No. 5 loop. The statistical characteristics of the temperature fluctuations were calculated automatically by the 46K1 correlometer using special amplifiers with a transmission band of 0.18-300 cps [5]. The arrangement used for measuring the temperature fluctuations in the wall is shown in Fig. 2.

From the common point of the /75
switch [presumably PMT, DBL] the signal of all the thermocouples was fed through tumbler switch TS-1 either to the input of amplifier A2 or to the circuit of potentiometer EPP-09. The thermocouple was connected directly to the input terminals of amplifier A1, bypassing switch PMT. The amplified thermocouple signal could be directed either to the correlometer or to the MPO-2 loop oscillograph. The magnitude of the temperature fluctuations was monitored by means of cathode oscillograph EO-7. In the experiments, alongside with measuring the temperature fluctuations, we have also recorded the

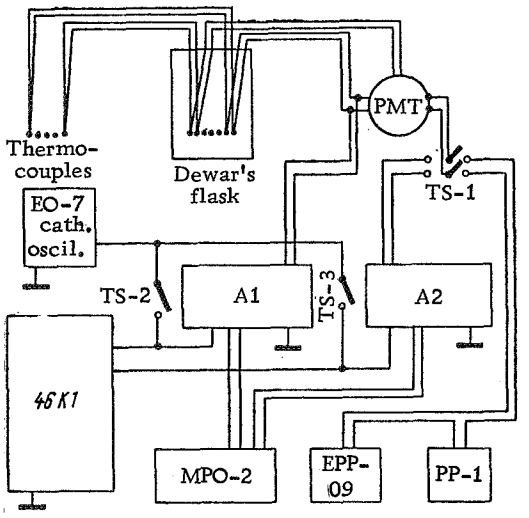

Figure 2. Measuring Arrangement. A1 and A2 are Amplifiers; MPO-2 is a Loop Oscillograph; EPP-09 and PP--1 are Potentiometers; 46K1 is a Correlometer; TS-1, TS-2 and TS-3 are Tumbler Switches; PMT is a Twenty-Point Switch.

constant component of all the thermocouples, by moving tumbler switch TS1 into the appropriate position, in which the common point of switch PMT was connected with the circuits of potentiometers EPP-09 and PP-1. All the thermocouple connecting lines were screened, the screen was grounded at the point where the thermocouples left the test section.

The goal of the experiment was to study the behavior of temperature fluctuation in one point in the wall, as well as the correlations between the fluctuations of two points. To study the behavior of the low-frequency components of the process, the temperature fluctuations were recorded on the diagram tape of the EPP-09 during 10-30 minutes, while for the high-frequency components of the process they were recorded on the moving-picture film of the MPO-2 oscillograph during 4-5 min. The correlometer was used to determine the root-mean-square values of the temperature fluctuations in two points of the wall σ_{t_i} and σ_{t_k} and the correlation coefficients in these points

$$R_{t_i' t_k'} = \frac{t_i' t_k'}{\sigma_{t_i} \sigma_{t_k}} . \qquad (2)$$

The integration time was 5 min; the fluctuation characteristics in each experiment were measured 3-4 times and their average was used in calculations. To check the changes in the correlation coefficients for symmetry, we have picked thermocouple No. 5 as the base thermocouple, since it occupies the middle position between the nine thermocouples inserted into the tube wall. The average thermal flux, referred to the inner surface of the heat-conducting pipe, was calculated from the heat balance equation

$$\bar{q} = \frac{G c_p \gamma \Delta t}{F} \text{ watts/m}^2. \qquad (3)$$

The experiments were performed for the following Reynolds number ranges: in the inner tube Re_{tube} = 41,900-196,000; in the intertubular space $Re_{i.s}$ 10,700-

49,800. Under these conditions the thermal flux varied within the limits of $q = 170 \cdot 10^3 - 600 \cdot 10^3$ watts/m.

The difference in the average mixed temperatures of the heat transfer agents in both heat exchanger passages or the total mean temperature difference between the two liquid metal flows comprised $\Delta t_n = 140\text{-}250°$. If we take into account the temperature drop in the wall, then the total mean temperature difference between the fluid and the wall for both heat exchanger passages is /76

$$\Delta t_{\alpha_{dot}} = \Delta t_{\alpha_{tube}} + \Delta t_{\alpha_{i.s.}} = 70 \div 160° \text{ C}.$$

Experimental Results

Temperature fluctuations in the wall of a duct is a complex random process and the statistical characteristics of this process are determined by many factors. For example, the root-mean-square value of the fluctuations is a factor of the following quantities

$$\sigma_t = f(\bar{q}, \text{ Re, Pr, } a_w, \Phi, R_c \text{ etc.}). \qquad (4)$$

Our experiments show that the intensity of temperature fluctuations in the wall increases linearly with an increase in the thermal flow or of the mean temperature difference with a constant heat transfer coefficient. Figure 3 shows the curve of $\sigma_t = f(\bar{q})$. The thermal flux varied within the limits of $\bar{q} = (170\text{-}600) \cdot 10^3$ watts/m^2.

Since the fluctuation intensity depends on the rate of flow (Reynolds number), i.e., on the degree of turbulization of the flow and on the magnitude of the mean temperature difference between the fluid and the wall, one should expect that function $\sigma_t = f(\text{Re})$ will have a maximum. This is due to the fact that no temperature fluctuations in the wall take place in laminar flow, while in a developed turbulent flow (as a result of reduction in Δt_α) the fluctuation intensity will also become lower with an increase in Re. Consequently, σ_t should have a maximum in some range of Reynolds numbers. This assumption was confirmed by our experiment (Fig. 4). The dimensionless expression $\Psi = \sigma_t \cdot \lambda_w / \bar{q} \cdot (D_1 - d_2)$, characterizing the fluctuation intensity, is plotted off on the ordinate axis of Fig. 4a, while the ratio of the fluctuation intensity to the mean temperature difference in the intertubular space /77

$$\frac{\sigma_t}{\Delta t_{\alpha_{i.s.}}} = \Psi \text{Nu}_{i.s.} \frac{\lambda_{fl.}}{\lambda_w}.$$

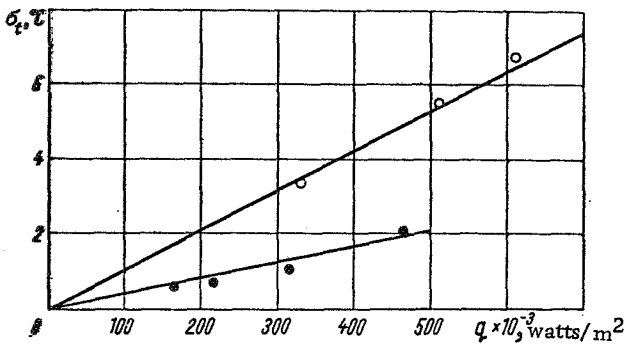

Figure 3. The Intensity of Temperature Fluctuations as a Function of the Thermal Flux. o - $Re_{tube} = 80,300$ (Flow With Unstable R_c); ● - $Re_{tube} = 196,000$.

is plotted off on the ordinate axis of Fig. 4b. The above fluctuation intensity maximum is situated in the range of $Re_{i.s} \simeq$ $\simeq 18,000$. This apparently is valid only for a given heat exchanger geometry; the maximum for other designs may appear with different Reynolds numbers. Knowing the magnitude of σ_t it is possible to estimate the value of the maximum peak to peak amplitude of temperature fluctuations. For example, for a normal distribution of fluctuation amplitudes, the maximum peak-to-peak amplitude can be $5\sigma_t$ (the probability of this occurrence is 1.5%).

The simplest frequency characteristic of a random process is the average frequency

$$n_{av} = \frac{N}{2T}, \tag{5}$$

where N is the number of temperature fluctuation extrema and T is the period. The average frequency in our experiments was within the limits of 1-4 cps. It should be noted that frequency n_{max} of temperature fluctuations which makes the greatest contribution to the intensity at which the process takes place will be lower than n_{av}.

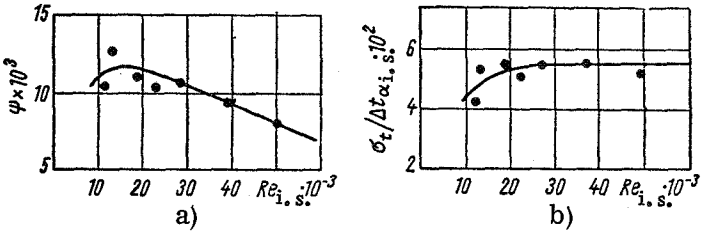

Figure 4. The temperature Fluctuation Intensity as a Function of the Reynolds Number. a) Generalization of $\Psi = \sigma_t \lambda_w / q \cdot D_1 - d_2$ as a Function of the Reynolds Number; b) $\sigma_t / \Delta t_{\alpha\, i.s}$ as a Function of the Reynolds Number.

In analyzing the values of σ_t in the wall one must remember that the thermocouples recorded the superposition of two, independent random processes of temperature fluctuations from the direction of the intertubular space as well as from the direction of the inner tube. In this sense the ratio $\sigma_t/\Delta t_{\alpha_{i.s}}$ is somewhat arbitrary. However, the thermocouple junctions are situated closer to the intertubular space, hence the thermocouples read primarily the temperature fluctuations which penetrate the wall from the direction of the intertubular space, which can be shown by calculating the damping of fluctuations in the wall, using Eq. (1). It is known, [3], that in turbulent flow of a fluid in a pipe (d = 52.2 mm, /78
Re = 10^5), the temperature fluctuation of maximum intensity have a frequency n_{max} = 0.8 cps. Consequently, if we pick n_{max} = cps as the fundamental frequency, then we get the following pattern of reduction in the amplitude of fluctuations as a function of increase in the wall thickness

x, mm	0.1	0.5	1.0	1.5	2.0	2.5
A_x/A_m	0.923	0.681	0.445	0.295	0.197	0.133

Figure 5 shows the correlation coefficients over the angle of the heat conducting wall. The two correlation curves, i.e., $R_t(-\delta_\varphi) = R_t(\delta_\varphi)$, are in good agreement, hence we have constructed for each flow regime a joint curve of correlation coefficients, which drop sufficiently rapidly to zero and even become negative. The shape of the correlation curve depends on the Reynolds number.

The correlations in the wall reflect the dimensions of the turbulent disturbances in the fluid flow region near the wall. Hence, the behavior of the variation in the correlation coefficient can supply information on the structure of turbulent disturbances near the wall. A sharp drop in $R_t(\delta_\varphi)$ in the wall points to the fact that the temperature fluctuations are produced by turbulent eddies of sufficiently small size. The higher the Reynolds number, the faster does the /79
correlation coefficient reach zero, consequently, the smaller the size of the eddies in the region near the wall. The latter, apparently, have a specific orientation: their rotational motion takes place along the axis of the tube. Hence, after some distance δ_{φ_0}, commensurable with the maximum dimensions of the eddies, the correlation coefficients take on negative values (see Fig. 5). When the Reynolds number becomes smaller the correlation reduces at a lower rate, which points to the increase in size of the maximum eddies in the region near the wall. It is interesting to note that there is a maximum to the size of the largest eddies, which can be seen from the behavior of the variation in δ_{φ_0} as a function of the Reynolds number (Fig. 6). Eddies in the region near the wall are of maximal size when $Re_{i.s} \simeq 18,000$, i.e., when σ_t has its maximum. This shows that the main contribution to the intensity of temperature fluctuations is made by large-scale turbulent disturbances.

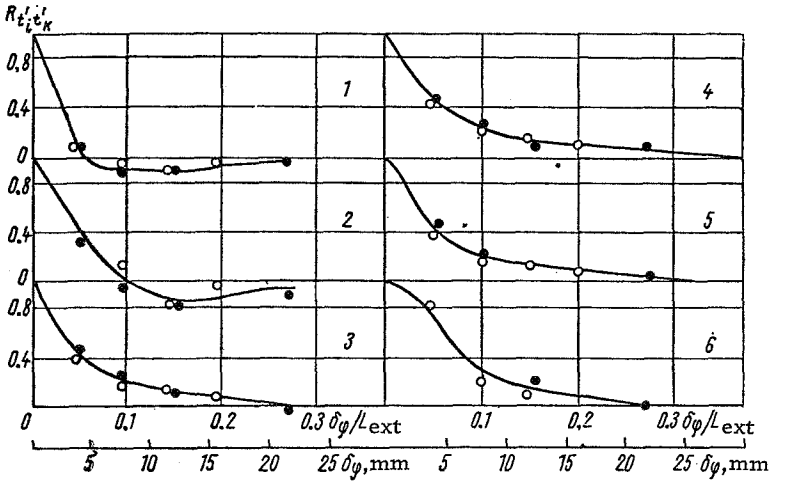

Figure 5. The Correlation Coefficients $R_t(-\delta_\varphi)$ (●), $R_t(\delta_\varphi)$(○) as a Function of the Reynolds Number.

Curve	Re_{tube}	Curve	Re_{tube}
1	196,000	4	80,300
2	116,000	5	58,500
3	96,700	6	41,900

A sharp drop in the correlation curve is observed in region of large Re_{tube} (80,300–196,000) when $\delta_\varphi \to 0$, which points to the existence of a wide range of eddy sizes in the region near the wall (see Fig. 5). For $Re_{tube} = 41,900$ and 58,500, the correlation curve has a smoother character as $\delta_\varphi \to 0$, which is due to the predominance of eddies of the same size in the region near the wall, since the smallest eddies disappear, while the size of the large eddies is reduced.

By analogy with the turbulence scale for temperature fluctuations in the wall we can introduce integral scales of temperature disturbances which are calculated from the expression

$$L_{\delta_\varphi} = \int_0^{\delta_{\varphi 0}} R(\delta_\varphi)\, d\delta_\varphi. \qquad (6)$$

Figure 6 shows the curve of the scale of temperature disturbances in the wall, referred to the external diameter of the heat conducting wall, which differs little from the length of the circumference at which the centers of the thermocouple junctions are located. Consequently, the magnitude of scale L_{δ_φ} increases with a reduction in Re. However, we have not observed an explicit /80

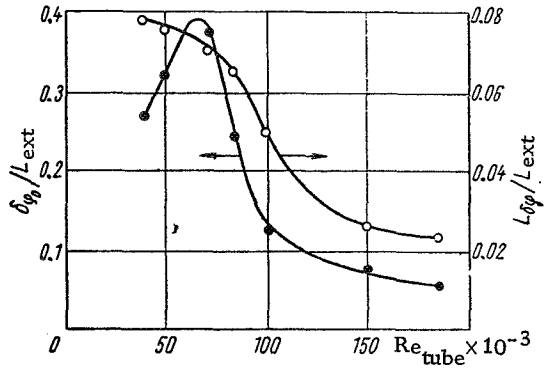

Figure 6. The Curve of $\delta_{\varphi_0} / L_{ext}$ = = f(Re) (●) and $L_{\delta_\varphi} / L_{ext}$ = f(Re) (○), the Scale of Temperature Disturbances in the Wall, as a Function of the Reynolds Number.

maximum in the curve of L_{δ_φ}, as was the case of δ_{φ_0}, since at the smallest Reynolds numbers the size of the largest eddies decreases, and the smallest eddies disappear. Hence, the integral scale remains approximately constant.

It was noted in [2] that the state of the heat conducting surface exerts an appreciable effect on the behavior of the temperature fluctuations in the wall. In our experiment we have obtained additional information on this problem. The behavior of temperature fluctuations with Re_{tube} = 116,000, if there is no R_c on the heat conducting surface is shown in Fig. 7a. When R_c is present, the statistical characteristics of temperature fluctuations change sharply (the amplitude and frequency of the fluctuations are reduced appreciably). The appearence of R_c is accompanied by an increase in the average wall temperature. For example, for a thermal flux of $5 \cdot 10^5$ watts/m^2 the wall temperature increased as a result of the appearance of R_c by 100-120° C, while the fluctuation intensity was reduced by a factor of 3-3.5. When R_c disappears, the temperature state of the wall returns to the previous level and the fluctuation intensity increased to its previous magnitude. This effect of R_c on the temperature fluctuations in the wall is recorded on the diagram of the EPP-09 instrument and shown in Fig. 7b. When R_c is unstable, the temperature fluctuations brought about by the turbulent disturbance [turbulence] have superimposed upon them additional sharp temperature bursts, which may be as high as 70° C when $\bar{q}$ = 590,000 watts/m^2 (see Fig. 7c). Calculations made using Eq. (1) show that a sufficiently thin oxide film up to 0.1 mm thick is capable of reducing the temperature fluctuation amplitude at a frequency of 1 cps several-fold.

/81

Our experiments, which were performed using a heat exchanger of a given design with fixed dimensions, are [of necessity] partial in character. The amplitude and frequency spectrum of temperature fluctuations in the wall will depend appreciably on the dimensions of the passage in which the heat transfer agent flows. For the same Reynolds numbers we have: the smaller the dimenions of the passage, the higher the frequency and the smaller the amplitude of the fluctuations. Hence analysis of additional variable thermal stresses which arise in the wall due to temperature fluctuations should be performed so as to take into account the specific features of the given heat exchanger.

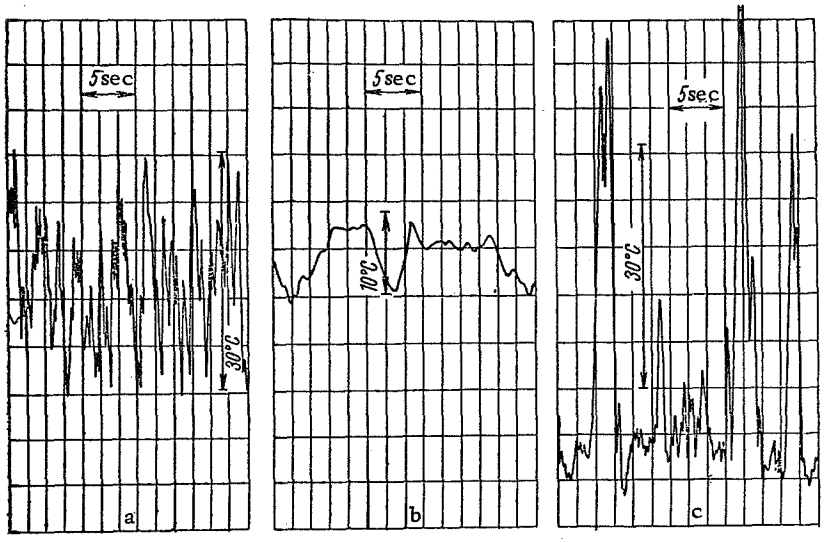

Figure 7. Record of Temperature Fluctuations Made by the EPP-09 Instrument for Re_{tube}=116,000, $\bar{q}$=590,000 watts/m^2 in the Absence of R_c (a), With a Stable R_c (b) and With an Unstable R_c (c).

NOTATION

$l_{h.e}$ length of heat exchanger

d_1, d_2 internal and external diameter of the heat-conducting tube

D_1 internal diameter of the heat exchanger shell

t'_i, t'_k temperature fluctuations in points i and k of the heat-conducting tube, ° C

$\sigma_{t_i}, \sigma_{t_k}$ root-mean-square values of temperature fluctuations in the wall, ° C

$R_{t'_i t'_k}$ coefficient of correlation between random processes in points i and k of the heat conducting wall

G flow rate of heat transfer agent

Δt heating of the heat transfer agent in the test section, ° C

Φ characteristic linear dimension

L_{δ_φ} integral scale of temperature disturbances in the wall with respect to angle φ

δ_{φ_0} distance from the point of intersection of the curve of the cross-correlation function with the abscissa axis

L_{ext} length of the circumference along the external diameter

tube and i.s subscripts of parameters pertaining to the tube or to the inter-tubular space

R_c thermal contact resistance

REFERENCES

1. Subbotin, V.I., et al.: Teploenergetika, No. 3 (1962).
2. Subbotin, V.I., et al.: Atomnaya energiya, 18, No. 5, 527 (1965).
3. Subbotin, V.I., et al.: Teplofizika vysokikh temperatur, No. 1 (1964).
4. Sveshnikov, A.A.: Prikladnyye metody teorii sluchaynykh funktsii [Applied Methods of the Theory of Random Functions]. Sudpromgiz, Leningrad, 1961.
5. Bobkov, V.P., et al.: Teplofizika vysokikh temperatur, No. 4 (1965).

HEAT TRANSFER IN TURBULENT FLOW OF FLUIDS IN SQUARE DUCTS

M. Kh. Ibragimov, Yu. M. Rabotyashnik, G. I. Sabelev,
V. I. Sidirov and V. I. Subbotin

The fluid dynamics in rectangular ducts have been extensively analyzed in several publications [1-3]. The problems of heat transfer in turbulent fluid flow have not been studied to such an extent. While publications on the flow of fluids in rectangular ducts describe studies not only of the average, but also of local characteristics of turbulent flow (distribution of velocities, turbulent stresses), then in the majority of publications devoted to the study of heat transfer in rectangular ducts present data only on average heat transfer coefficients [4-8]. /82

The boundary conditions in many of these studies were close to conditions of constant wall temperature along the duct perimeter. To calculate the heat transferred to the heat transfer agents with $Pr \geq 1$ it is recommended to use the same formulas which are used for heat transfer in round pipes, and to use the hydraulic diameter as the characteristic dimension. However, this method is not always justified. As was shown in [9-11], the use of the hydraulic diameter does not yield satisfactory results for liquid-metal heat-transfer agents. For example, for liquid metals flowing in rectangular ducts the heat transfer coefficients calculated on the basis of the hydraulic diameter become smaller by almost two-fold, if the duct is heated from one side rather than from two. In calculating high thermal flux heat exchangers it is necessary to know not only the average heat transfer coefficients, but also the local distribution of heat fluxes and temperatures on the heat conducting surface and in the duct walls [11, 12].

Below are presented results obtained in the study of heat transfer in a square duct in turbulent flow of water and mercury. We have studied the temperature fields in the wall and in the fluid, as well as the statistical characteristics of turbulent temperature fluctuations.

Methods Used in the Experiments

Experiments with heat transfer in water were performed in an open-circuit setup. The water flow rate was kept constant by using a 125-liter supply tank. It was provided by a filter for removing impurities. The rate of flow of water in the circuit was adjusted by a valve and measured by an RS-7 rotameter. The experiments with mercury were performed in a closed circuit, with the mercury circulated through it by a centrifugal pump. The mercury flow rate was adjusted by a valve and was measured by a Venturi tube used in combination with the DT-50 differential manometer. Brand R-3 mercury, which was filtered before being circulated, was used in the experiment. /83

The test section consisted of a square duct, installed in the circuit in the vertical position, with a cross section of 30 x 30 mm, wall thickness of 6 mm and 1800 mm long (Fig. 1). The experimental section had at its inlet a chamber for equalizing the velocity distribution, while at the outlet it was provided by a mixing chamber. In both chambers were installed thermocouples in sleeves, used for measuring the temperature of the fluid at the inlet and outlet from the test section. The outlet chamber was provided by a probe for measuring the temperature in the fluid flow. The inside surface of the duct was machined to finish class $\nabla 5$. The distance between walls 2 and 4 (see Fig. 1b) was $30^{+0.19}_{-0.08}$ mm, while the distance between walls 1 and 3 was $30^{+0.34}_{-0.10}$ mm. Wall 4 was used as the basic wall for measuring the temperature distribution.

The heat was supplied to the test section by four electric heaters of the plate type, made from 30 mm wide 1Kh18N9T steel, conforming to the width of the flow cross section of the duct, 0.1 mm thick and 1100 mm long (see Fig. 1b). Each heater was fastened to a square textolite rod and was pressed to the duct by clamp screws, fastened in steel columns. A layer of mica about 0.1 mm thick was placed between the heater and the duct wall. The current and voltage at the heaters were measured by class 0.5 astatic instruments. The heaters could be started up in any combinations. The experiments were performed with the duct heated from four sides, with a heater corner (walls 1 and 4), with heating two opposite walls (walls 2 and 4) and with heating one wall (wall 4).

The temperature distribution in wall 4 was measured at three different distances from the point where heating started: 1000, 1020 and 1040 mm (which corresponded to distances from the inlet of 1645, 1665 and 1685 mm) by 27 microthermocouples, 9 of which were built into each of the cross sections (see Fig.1c). These thermocouples were made from copper and constantan wires 0.09 and 0.10 mm in diameter, coated by Viniflex insulation and placed over the external side of wall 4 into slots 0.1 mm wide and 0.1-0.15 mm deep at an angle of 75° to the duct axis. The hot junction of the thermocouples were welded to the bottom of the slot in such a manner that the junctions of all the nine thermocouples would be situated in a plane perpendicular to the duct axis. The wall temperature was measured differentially, referring it to the temperature of the heat transfer agent leaving the duct. The thermocouple readings were measured by ar R-2/1 potentiometer with a sensitivity limit of 0.01 millivolts. The temperature distribution in the wall of the square duct was measured under steady conditions in the zone of stabilized heat transfer. The distance from the duct inlet to the second cross section (see Fig. 1) is $l/d_h = 56$, while from the start of the heated section it is /85 $l/d_h = 34$.

The temperature in the water and mercury flows were measured by a thermocouple probe (Fig. 2). The copper-constantan thermocouple was made from wires 0.09 and 0.10 mm in diameter with Viniflex insulation, welded together with the capillary. The 0.25 mm diameter thermocouple which is obtained in this manner was placed at a distance of 5 mm from the edge of the cone. The probe was moved along the duct cross section by means of two mutually perpendicular micrometer screws, which made it possible to position the probe at any point in the duct with a precision to within 0.02 mm. In order to reduce the effect

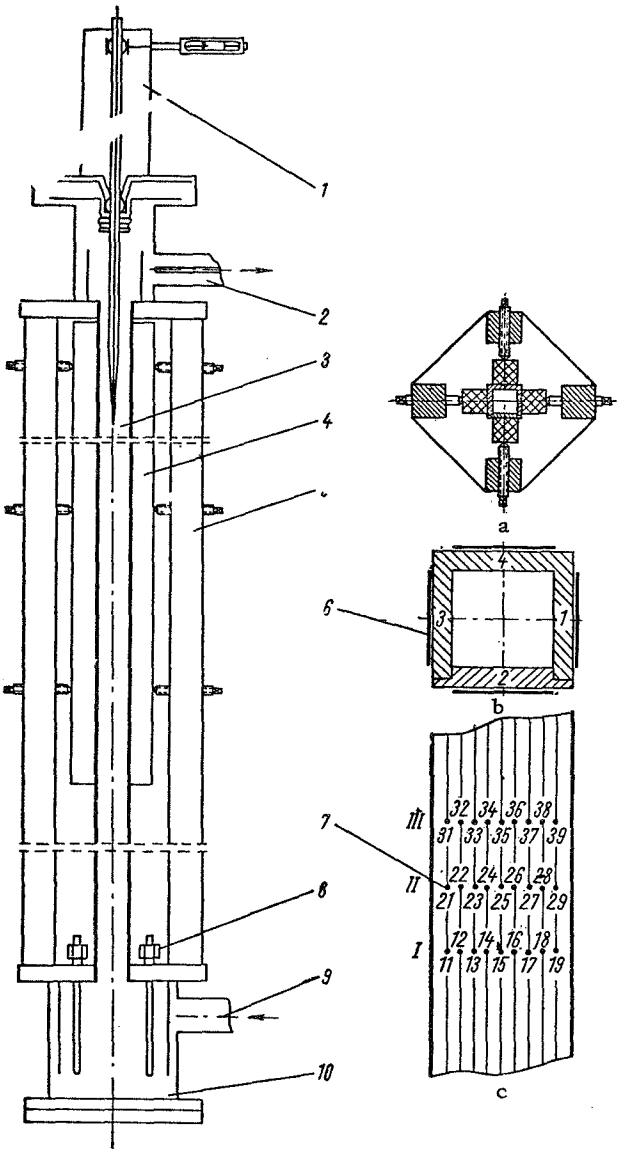

Figure 1. Schematic Diagram of the Test Section. 1) Thermocouple Probe; 2) Outlet Pipe; 3) Square Duct; 4) Textolite Bar; 5) Column; 6) Electric Heater; 7) Thermocouples Built Into the Wall; 8) Inlet Thermocouple; 9) Inlet Pipe; 10) Inlet Chamber. a) Cross Section of Test Section; b) Cross Section of Square Duct (1, 2, 3 and 4 are the Numbers of the Walls); c) Location of Hot Junctions of Thermocouples at the Outer Surface of the Duct (I, II and III are Sections in Which the Termocouples Have Been Inserted); 11-19; 21-29 and 31-39 are Thermocouples Numbers.

of free play, the probe in our experiments was moved in one direction only, i.e., from the center of the duct toward the walls.

The temperature in the water and mercury flows was measured under steady conditions in the region with thermal and fluid flow stability. The moving thermocouple was connected differentially with a thermocouple placed at the outlet from the test section. To obtain average temperatures in each point of the flow, the thermocouple readings were continuously recorded on the diagram tape of the EPP-09 potentiometer with a scale of 0-1 mv during 40-60 secs. The PPTN-1 low-resistance potentiometer, which provided the compensating voltage was installed in series with the EPP-09. The readings of the thermocouple which were obtained for a given probe position were average with respect to time, and these quantities were used to plot graphs of temperature distributions in the flow in various planes along lines perpendicular to the wall. The primary temperature used for analysis of experimental data was the mixed average temperature of the flow in the cross section in which the movable thermocouple moved. The physical parameters of the water were those in [13], while for mercury the parameters of [14] were used.

When measuring the temperature fluctuations the thermocouple signal was fed to an amplifier with a transmission band from 0.18 to

200 cps and an amplification factor of 10^5, equipped with a noise silencer (damping factor of 10^4). The amplified signal was fed either to the MPO-2 loop oscillograph, or to the 46K1 correlometer [15]. The latter could be used to measure the root-mean-square value of temperature fluctuations, the averaging time of which is 5 mins. In addition, the thermocouple readings were recorded by the loop oscillograph on a motion picture film. The time marks were recorded simultaneously on the film. The thermocouple readings were recorded for 60-70 secs in each experiment.

The Heat Transfer and the Temperature Distribution in the Wall of a Square Duct

The results obtained by measuring the temperature distribution at the outer surface of the wall of a square duct are presented in Figs. 3a and b. As can be seen, the temperature of the outer surface of a heat conducting wall is not constant along the perimeter. The temperature distribution when the duct is heated from four sides has the form of a symmetrical curve with two maxima, situated at a distance of about 0.7 y/a from the center line of the duct wall. The shape of the distributions we have obtained depends, naturally, on the velocity distribution in the duct, on the shape, dimensions and thermal conductivity of the duct wall.

It can also be seen from Fig. 3 that, when the duct is heated from four sides, there are observed on the outer surface of the wall temperature minima in zones /88
directly adjoining the duct's corners. These minima are produced by the fact that the heaters are narrower than the outer duct surface [being heated]. The fact that a non-heated, heat conducting section was situated at the end boundary of the heater reduced the thermal resistance of the corner zone and, consequently, resulted in dropping the temperature of the outer surface of the duct. The temperature distribution on the inner, heat conducting wall of the duct, when heated from four sides, will not be identical with the distribution shown in Figs. 3a and b. The temperature maxima at the outer surface for the same amount of heating will be in the corners of the duct. This was substantiated experimentally by measuring the temperature fields in the fluid in the same square duct.

We note that the temperature distributions obtained in the three cross sections (see Fig. 3a) are practically identical with one another. The small differences between them and the slight asymmetricity can be ascribed to bending or displacement of the heater's band, as well as to the fact that it was not uniformly pressed to the duct. The shape of temperature curves on heating from one and two sides is highly affected by the heat flowing along the side, nonheated walls, which in these cases act as cooling ribs.

Curves obtained on heating from two and one side, shown in Figs. 3a and b have a temperature minimum in the corner of the duct. In the given duct the lateral, unheated wall had a relatively high thermal conductivity (9 ~ 10 watts/m-degree). But, as is shown in [12], even if the lateral wall has a thermal conductivity

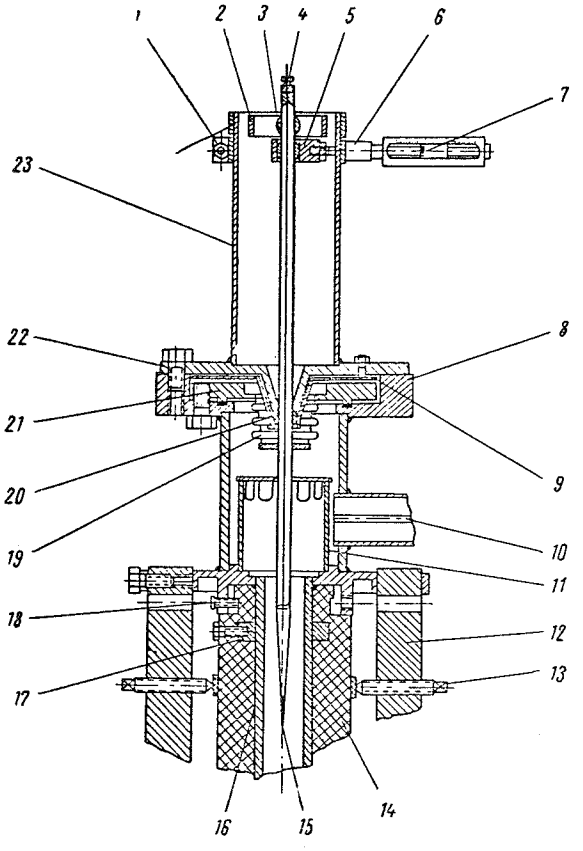

Figure 2. Construction of the Thermocouple Probe. 1) Clamping Ring; 2) X-axis Guide; 3) Ball; 4) Packing Gland; 5) Y-axis Guide; 6) Sleeve; 7) Micrometer Screw; 8) Mixing Chamber Housing; 9) Clamping Cone; 10) Thermocouple Well; 11) Mixing Unit; 12) Column; 13) Heater-Clamping Screw; 14) Textolite Bar; 15) Tube With Thermocouple; 16) Heater; 17) Current-Carrying Heater End Pieces; 18) Adjusting Screws; 19) Bellows-Type Packing; 20) Hinge; 21) Air-Tight Flange; 22) Top Flange; 23) Cup.

of ~ 0.1 watts/m-degrees, the thermal flux to it is so appreciable, that the temperature of the heated wall in a corner of a duct heated from two or one side is lower than its temperature in the central region. The shape of Curve 2 (see Fig. 3a), drawn for heating the corner, reflects the peculiar features of Curves 1 and 3 and is intermediate between them. Curve 2 shows to what distance along the duct's perimeter the effect of these heat leakages on the wall temperature extends.

Up to now we have considered only the shape of the temperature curves. We now compare these curves with the average mean temperature differences, which can be done to estimate the effect of the liquid's thermal conductivity on the heat transfer. For the simplest case, when the fluid flows between two parallel plates, it was shown by Seban [10] that the heat transfer coefficient will be affected by the heating method (i.e., whether the duct is heated from one or two sides) for liquids with $Pr \ll 1$; if, however, $Pr \gtrsim 1$, then the heat transfer coefficient is practically independent of the heating method. Experiments on heat transfer in slot-type and rectangular ducts confirm the fact that the number of sides heated has an effect on the heat transfer coefficient in the case of a liquid metal heat transfer agent [11]. This effect of the Prandtl number on the heat transfer coefficient is a result of the fact that in liquid metals the temperature distribution /89 varies smoothly over the duct cross section, and hence, it depends on the heating conditions of the second wall. In ordinary, low-conductivity fluids the entire temperature drop which determines the heat transfer coefficient is concentrated in the layer near the wall and it is almost unaffected by the heating conditions at the other wall. Let us now compare the results obtained with water and mercury heated from one and two sides (see Figs. 3a and b). While Curves 3 and 4 (water) are practically identical, then Curve 4

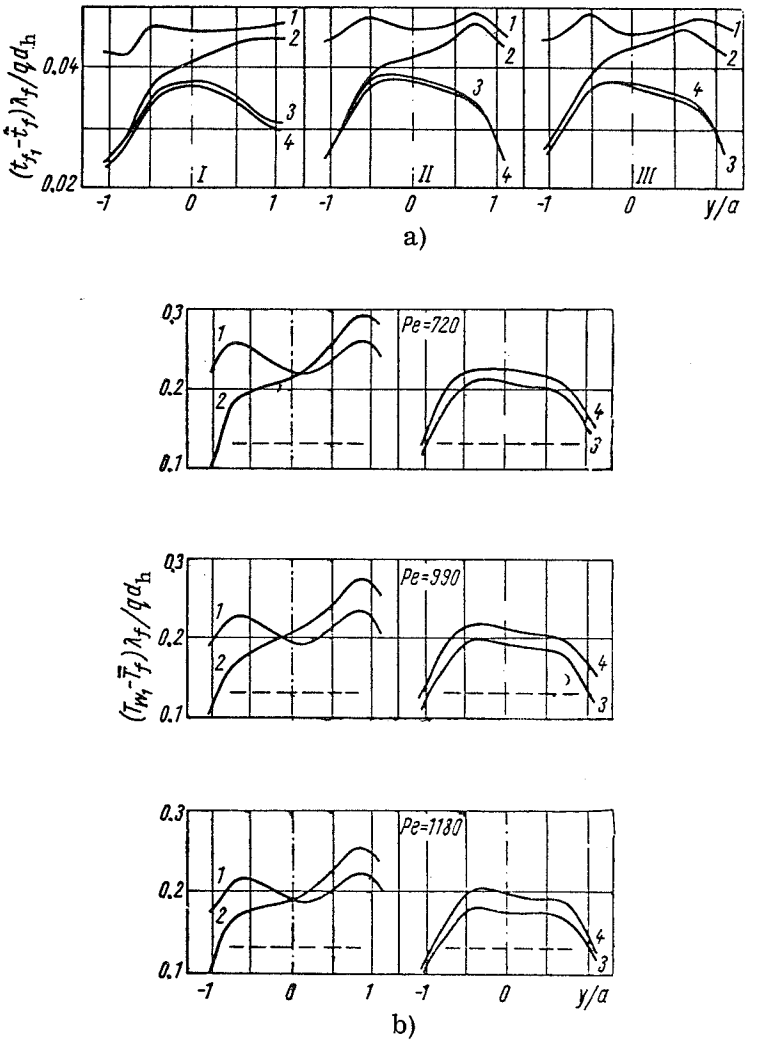

Figure 3. Temperature Distribution on the Outer Surface of a Wall of a Square Duct When Heat is Transferred to Water (Re = 4910) (a) and to Mercury (b). 1) Heating From Four Sides; 2) Heating a Corner; 3) Heating From Two Sides; 4) Heating From One Side. The Dimensionless Distance From the Center Line of the Duct Wall has Been Laid off on the Abscissa Axis, While the Dimensionless Temperature of the Wall has Been Laid off on the Ordinate Axis. The Roman Numerals Denote Numbers of Duct Sections (a). All the Curves of (b) Pertain to the Second Cross Section.

(one sided heating) in experiments with mercury lies noticeably higher than Curve 3. It can be seen from Fig. 3b that the average mean temperature difference for

heating from one side is higher than that for heating from two sides. Fig. 3a shows that, in experiments with water, the heating method does not have this effect on the heat transfer, although in some cases one may observe also a drop in the temperature of the outer, heated wall, produced by increased heat leakage due to the increased effective length of the cooling rib.

Comparison of Curves 1 and 2 (see Figs. 3a and b) shows that, for heat transfer to mercury, the total mean temperature difference in the corner of a duct heated at the corner is higher than for heating from four sides. This increase in the mean temperature difference for two-sided heating as compared with heating from four sides can be ascribed to the same effect of the heating method on the heat transfer as is observed in slot-type ducts. In this case heating from four sides can be regarded as twice heating from two sides. Thus, a reduction in the portion of the heated perimeter on heat transfer in liquid metals increases the mean temperature difference, while the presence of heat flux leakages over the unheated, conducting walls can result in reducing it. In some cases these effects may compensate for one another and the average heat transfer coefficient may not be dependent on that portion of the heated perimeter.

On Fig. 3b are drawn dashed lines the ordinate of which corresponds to the average mean temperature difference over the thickness of the duct wall. The difference between the ordinates of the dashed line and one of the curves for any value of y/a yields an arbitrary value 1/Nu in the given point on the perimeter.

Figures 4a and b show curves of Nusselt numbers as a function of the fluid flow rate attendant to heat transfer to water and mercury. The values of Nusselt numbers were determined from the expression

$$\mathrm{Nu} = \frac{2qa}{\left(\bar{t}_w - \frac{qb}{\lambda_w} - \bar{t}_f\right)\lambda_f}.$$

The Nusselt numbers obtained should be regarded as [somewhat] arbitrary. Figure 4a (line 1-2-3) shows the dependence of Nu on the Reynolds number for nonmetal liquids, which is used for calculating the heat transfer coefficients in round pipes [5]. Segment 1-2 corresponds to transient flow, while Segment 2-3 corresponds to the formula

$$\mathrm{Nu} = 0.021\mathrm{Re}^{0.8}\mathrm{Pr}^{0.43}\left(\mathrm{Pr}_f/\mathrm{Pr}_w\right)^{0.25}.$$

The straight line in Fig. 4b was obtained from a formula used for calculating the heat transfer to liquid metals in round pipes [16] /90

$$\mathrm{Nu} = 5 + 0.025\mathrm{Pe}^{0.8}.$$

The spread of experimental points in Figs. 4a and b can be attributed to two factors: effect of the thermal conductivity of the fluid and of heat flux leakages along the duct's wall on the mean temperature difference for different methods of heating.

Temperature Fields in the Flow of a Fluid

Results obtained by measuring the temperature in the flow of water and mercury are shown in Figs. 5-10. It can be seen from these figures that the temperature distributions for the case of mercury are smoother than for water. As is the case with pipes, the main part of the temperature drop is concentrated in the region near the wall within the limits of $y/a = 0.9-1.0$. As the Reynolds number becomes larger the width of this region is reduced (see Fig. 5a). For mercury the effect of the flow velocity on the temperature distributions at $Re = (16-45)\cdot 10^3$ is weak (see Fig. 5b). /92

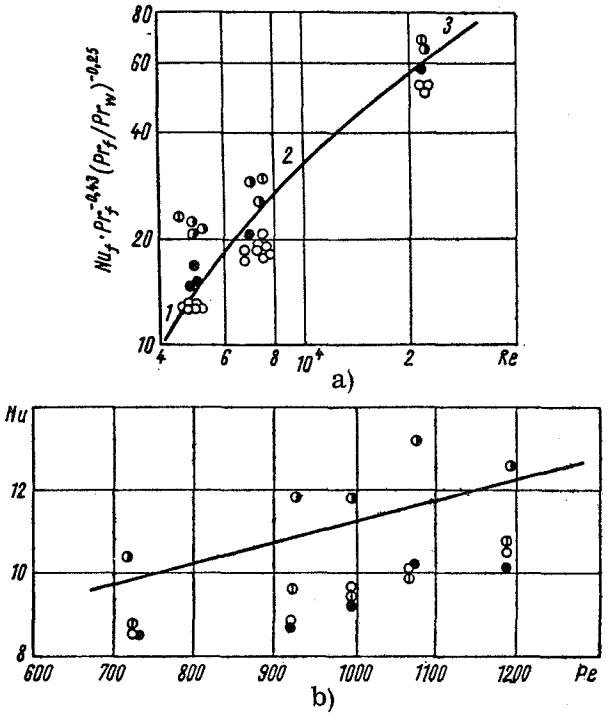

Figure 4. Heat Transfer in a Square Duct to Water (a) and Mercury (b) for Different Heating Conditions. ○ - Heating From Four Sides; ◑ - Heating From Two Sides; ◐ - - Heating From One Side; ● - Heating the Corner.

The shapes of temperature distributions in different duct cross sections for heat transfer to water are not the same. While for the temperature distribution with $x/a = 0$ the minimum is in the center of the duct, then for the remaining distributions the temperature minimum is displaced toward the wall and is situated within the limits of $y/a = 0.6-0.8$ (see Fig. 6a). In heat transfer to mercury the temperature distributions in the [various] duct cross sections have no inflections and the minima are situated at $y/a = 0$. It is remarkable that in the flow region near the wall the slopes of the temperature curves differ appreciably in different cross sections. The maximum slopes of temperature curves in this region in the case of water are observed in the cross section $x/a = 0.90$, and they become smaller as one moved from this cross section to the center of the duct and to the corner region (see Fig. 6a). In the case of mercury the maximum temperature curve slopes are observed in the center zone and become smoothly smaller as one comes closer to the duct's corner (see Fig. 6b). The

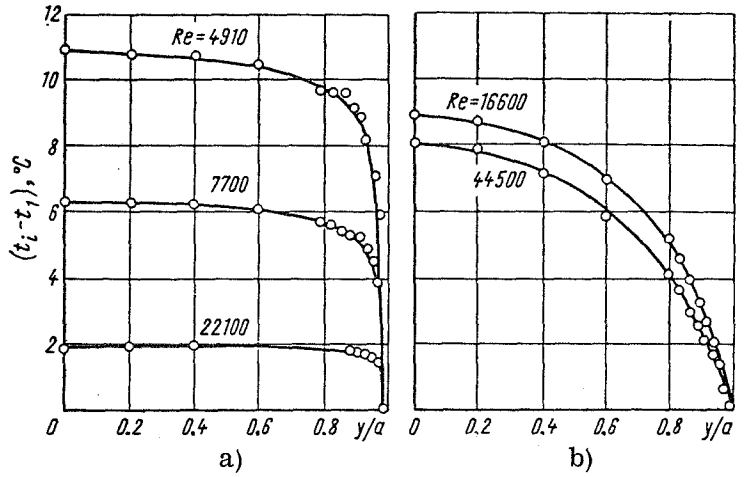

Figure 5. Temperature Distributions in a Square Duct for x/a = 0 and for Heating From Four Sides for Water (a) and for Mercury (b); t_1 is the Temperature of the Fluid When y/a = 0.99.

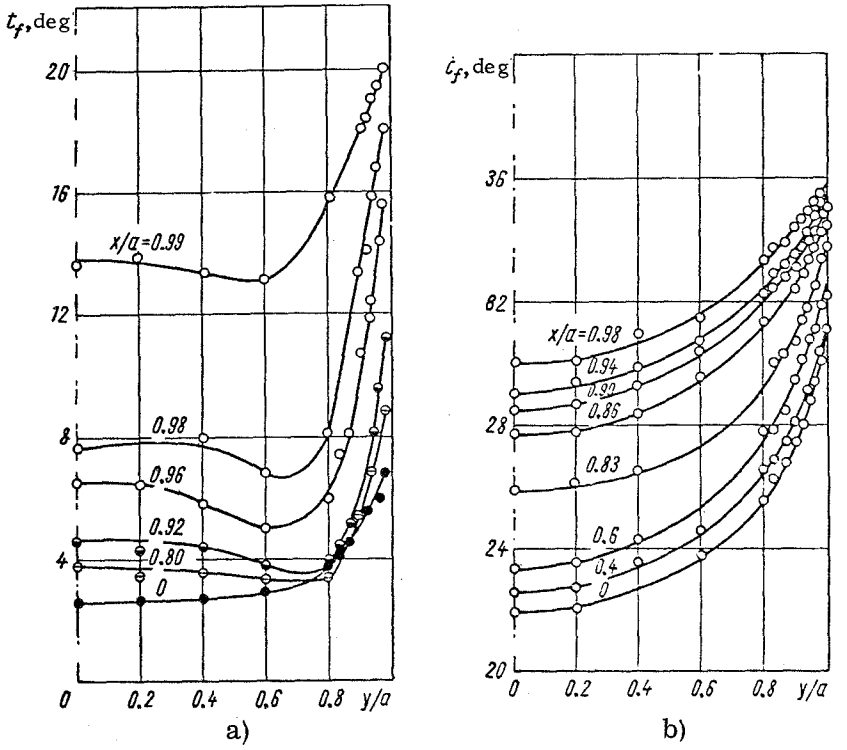

Figure 6. Temperature Distributions in Different Flow Cross Sections for Heating From Four Sides for Water (a) (Re = 4910) and Mercury (b) (Re = 16,600).

reduction in the slope of the temperature curve at x/a = 0 can be attributed to the effect of secondary flows, directed from the heat-conducting surface to the center of the duct [3]. As was shown experimentally, the secondary flows in a square duct occupy the entire duct cross section. The fluid is carried by the secondary flows along a diagonal from the center to the corner of the duct, and then the secondary flow flows along the wall and then from the center region of the wall to the center of the duct. When x/a = 0, the direction of the secondary flow coincides with the direction of the thermal flux. Consequently, the secondary flow in this point should assist in reducing the temperature gradient. The effect of the secondary flows on the temperature distribution in the flow of water is particularly noticeable by the distortion of isotherms in Figs. 7 and 8. All figures display the characteristic inflection of the isotherms in the direction of the duct's corner.

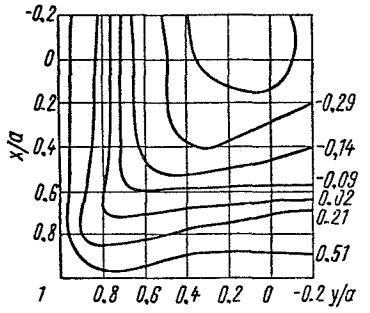

Figure 7. Isotherms in the Flow of Water in a Square Duct Heated From Four Sides for Re = 7700.

As can be seen from Fig. 9, the shape of isotherms in the flow of mercury differs appreciably from the shape of isotherms obtained in the flow of water. It is obvious that for such highly-conducting fluids as mercury, the effect of secondary flows on the shape of temperature fields is much smaller. When the heat is supplied asymmetrically (see Figs. 8 and 9) the temperature distribution in the fluid flow is affected by heat leakages along the heat conducting walls of the duct. The effective area of heat transfer is found to be larger and is not equal to the area of the heater. The behavior of isotherms near the unheated wall points to the fact that a part of /93
the heat supplied by the heater flows along the conducting walls and is transferred from them to the flow of the fluid. The quantity of heat which is transferred to the fluid by the unheated walls, and the shape of the temperature fields depend on the heat transfer coefficient, dimensions of the duct, thermal conductivity and wall thickness. In particular, it follows from Fig. 9 that in the case of heating from one and two sides the temperature of the fluid in the corners of the duct is lower than the temperature in the middle part of the wall and, consequently, the fluid and the wall in the corners of the duct are not overheated.

The high thermal conductivity of mercury, secondary flows and thermal fluxes through the wall result in the fact that the maximum temperature of the heat conducting surface is situated not in the corner of the duct, but in the center of the duct wall. Such a temperature distribution naturally depends on the boundary conditions at the outer surface. If the heater is wider than the width of the flow cross section of the duct and the heat transfer at the outer surface is nonuniform, for example, high heat transfer density in the corner of the duct, /94
then the temperature maximum of the heat conducting surface may be found to be in the corner of the duct.

We wish to note the following: in a square duct heated from four sides the isotherm corresponding to the average mixed temperature of mercury in a given

cross section is situated at a distance y/a and x/a $\sim$ 0.7, which coincides with the location of a similar isotherm in a pipe (for liquid metals).

Statistical Characteristics of Turbulent Temperature Fluctuations

Figure 10 shows oscillograms of temperature fluctuations in the flow of water in a duct heated from four sides with a specific thermal flux of q $\approx$ 15,000 watts/m^2 and Re = 4910. To the left of each oscillogram is shown the temperature scale. To the right are given the coordinates of the probe and its location is noted by a dot. It can be seen from the oscillogram that the characteristics of the fluctuation curve differ from one another in the different points of the duct's cross section. First, while in the central zone of the duct one observes high-frequency temperature fluctuations with a relative moderate amplitude ($\sim$1° C) (see Fig. 10a), /95 then in the region adjoining to the duct wall (x/a = 0, y/a = 0.98), the temperature fluctuations are as high as 10° C and their frequency is lower. In the very corner of the duct the fluctuation frequency is even lower (see Fig. 10c). Secondly, the oscillogram (see Fig. 10c) does not exhibit high-frequency components of the spectrum. This shows that only large-scale fluctuations are capable of entering the corner region. And, finally, the oscillograms in the corner of the duct are not symmetrical with respect to the time-average temperature in the given point of the flow, which can be seen from Fig. 10 and from other oscillograms which were obtained with higher water flow rates. The same asymmetry has been observed also in experiments with mercury. It consists in the fact that the temperature curve has peaks directed primarily in one direction away from the average temperature. For the region near the wall they are directed in the direction of smaller temperatures, while for the center region they are directed in the direction of higher temperatures. Apparently these peaks are produced when the center of a turbulent disturbances passes through the thermocouple. If the thermocouple is situated in a region adjoining the wall, then the peaks are produced by cold portions of the fluid which arrives from the center of the duct. In the central region of the flow the temperature peaks are brought about by the /96 passing of hot portions of the fluid, carried from the wall to the center of the flow through the thermocouple junction.

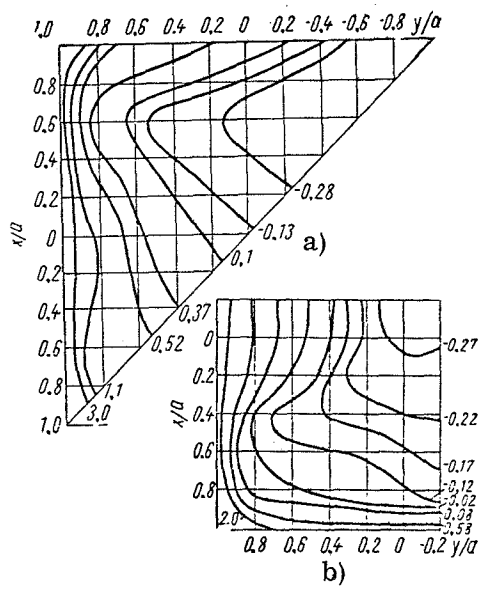

Figure 8. Isotherms in the Flow of Water in a Square Duct. a) Heating the Corner, Re = 4910; b) Heating From Two Sides (the Left Wall is Heated), Re = 4910.

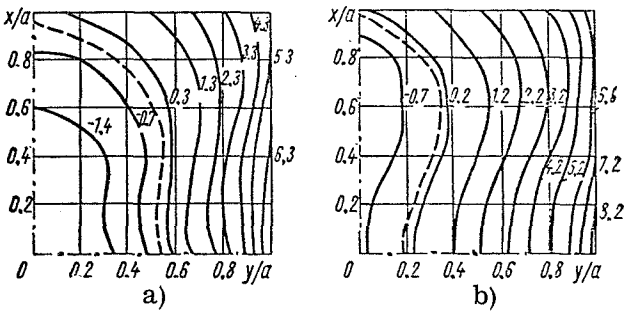

Figure 9. Isotherms in the Flow of Mercury in a Square Duct. a) Heating From Two Sides, Re = 28,400; b) Heating From One Side; Re = 28,200.

A more complete picture of the distribution of temperature fluctuations in different cross sections of the square duct was obtained using the correlometer. The results obtained by measuring the root-mean-square values of temperature fluctuations in water flowing in a square duct are shown in Figs. 11-13a. Figure 11 shows the curve of σ_t, the root-mean-square values of temperature fluctuations along lines parallel to axis Y. The parameter of these curves is the distance from the center of the duct along axis X.

The distribution of σ_t over the cross section of a square duct is shown more graphically in Fig. 12. The lines of this figure correspond to the locus of points with a constant root-mean-square temperature fluctuation of the flow. The parameter of curves in Fig. 12 is σ_t. As can be seen from Figs. 11 and 12, the distribution of σ_t over the duct cross section is quite complex. In the center part and at the walls σ_t has a minimum; the maxima are situated at the axial lines of the square at a distance of $\sim$14.5 mm (y/a = 0.97) from the center of the duct. At the wall σ_t increases very sharply. As x/a becomes larger (see Fig. 11) the maxima are reduced smoothly and move away from the wall of the duct. They move farthest away in the corner region. In the center region of the flow, when x/a and y/a $\leq$ 0.5, the magnitudes of σ_t are practically constant. In regions with 0.5 < x/a < 0.9 and 0.5 < y/a < 0.9 the curves of constant values of σ_t have a peculiar shape: at the axial lines these curves are displaced toward the center of the duct, while in the corner region they are extended along the bisectrix into the corner of the duct.

The shape of curves σ_t = const attests to the presence of secondary flows in the square duct. Let us examine the distribution of σ_t along the line y/a = = 0.8. The lines of σ_t = const for x/a = 0.6 are displaced to the center of the duct. The location of these displacements is the same as the maximum value of the normal velocity component of the secondary flow [3]. Lines σ_t = 0.7 and 0.9 for y/a = 0.3 conversely, are displaced toward the wall of the duct. The region of minimal σ_t for x/a $\approx$ 0.8 is identical with the location of the eddy of the secondary flow, where the normal components of the secondary flow velocity are at minimum. We thus notice a correspondence between the magnitudes of normal components of secondary flows and the magnitude of σ_t. /97

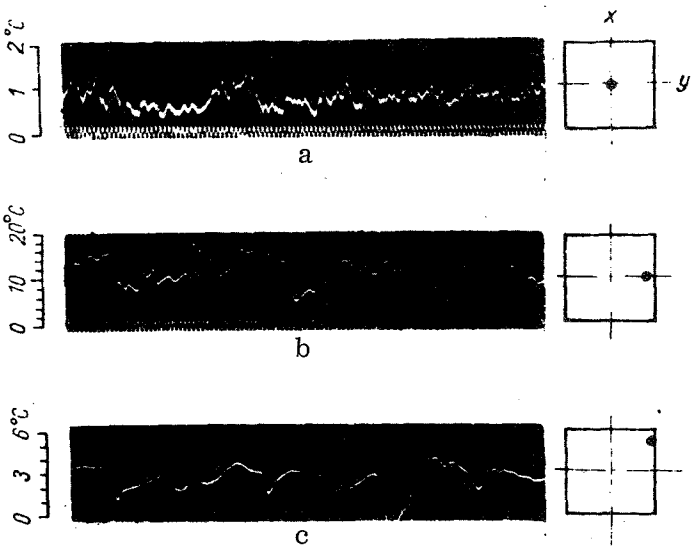

Figure 10. Oscillograms of Temperature Fluctuations in Water Flowing in a Square Duct. a) x = 0, y = 0; b) x = 0, y = 14.75 mm; c) x = 13 mm; y = 14.4 mm; Time Scale is 1 sec.

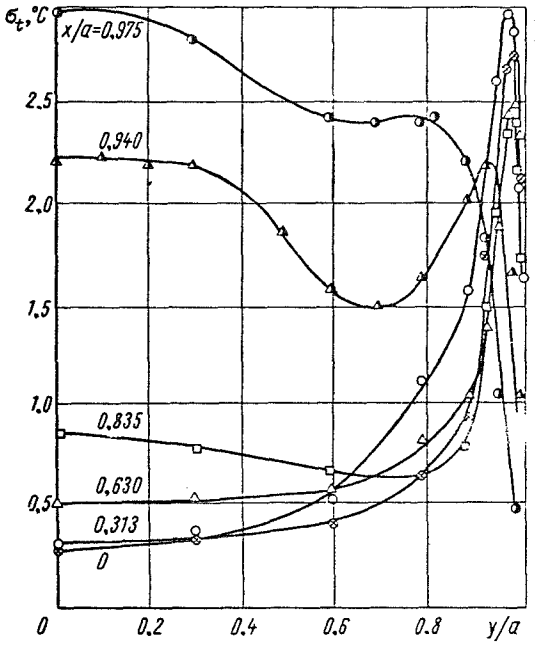

Figure 11. Curves of σ_t the Root-Mean-Square Values of Temperature Fluctuations in Different Cross Section of a Flow of Water, R=4910.

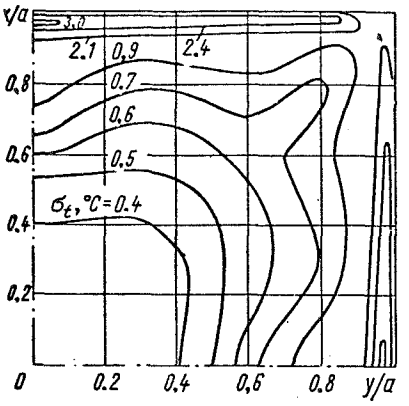

Figure 12. Distribution of Curves of Constant σ_t in the Cross Section of a Duct in the Flow of Water, Re = 4910.

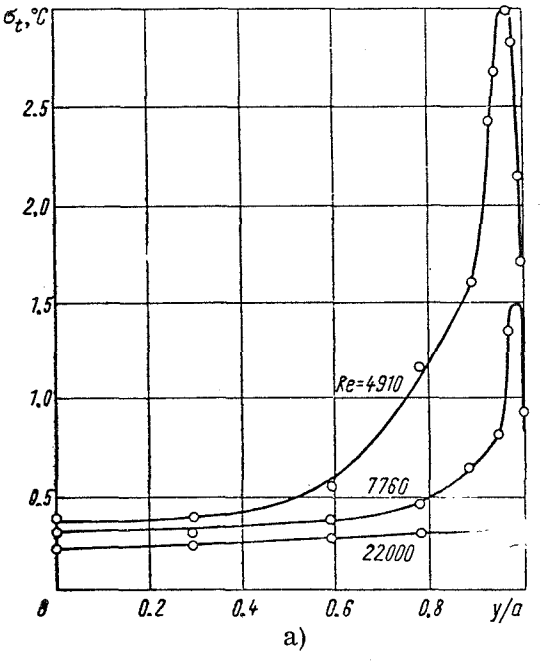

a)

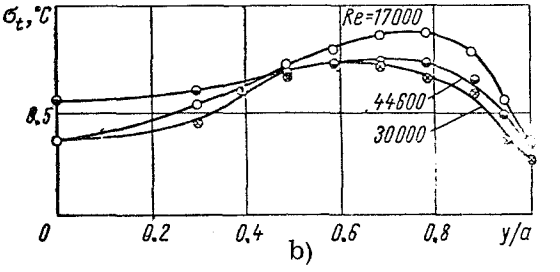

b)

Figure 13. Distributions of σ_t in a Square Duct Heated From Four Sides With a Flow of Water (a) and Mercury (b) for Different Reynolds Numbers.

Figure 13 shows the change in σ_t (determined at the same thermal flux) along the center line of the duct (x/a = 0) for different flow rates of water and mercury in a square duct. As Re is increased from 4910 to 22,000, the central region in which σ_t is practically constant, extends from y/a = 0.5 to y/a = 0.9 and the magnitude of σ_t becomes increasingly uniform over the duct's cross-section. The shape of the curves is no longer self-similar. The absence of a peak in the σ_t curve in the region near the wall at Re = 22,100 is produced by the relatively large dimensions of the pickup. The maximum of σ_t is located near the laminar sublayer, the thickness of which at the above Reynolds number is about 0.1 mm. Hence a thermocouple with an outer diameter of 0.25 mm is situated outside the region of maximum values of σ_t and, in addition, may appreciabley distort these readings.

/98

We wish to note that Figs. 11-13 display only the amplitude characteristics of the fluctuations. The frequency characteristics of the fluctuations, as was already shown, differ in different regions in the duct. Judging by the oscillograms, the closer the point to the wall and to the corner of the duct, the greater the contribution of low-frequency components. The average frequency of fluctuations, determined from the oscillograms of Fig. 10 as half of the number

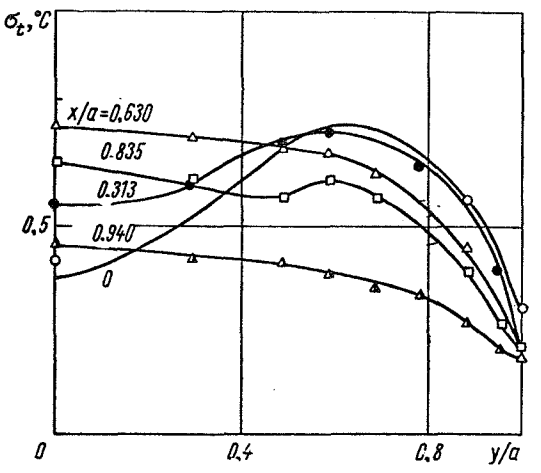

Figure 14. Distributions of the Root-Mean-Square Value of σ_t, the Temperature Fluctuation, in Different Cross Sections in a Flow of Mercury, Re = 30,400.

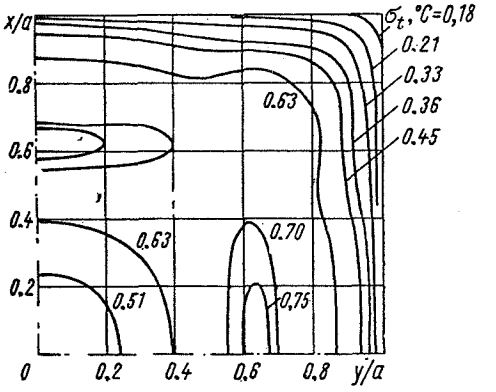

Figure 15. Distribution of Lines σ_t = const in the Cross Section of a Square Duct for Mercury, Re = 30,400.

of extrema of the temperature curve per second, was found to be 6.7, 2.8 and 0.9 cps for the central region, region near the wall and the duct's corner, respectively. The fluctuation characteristics for mercury were determined using the same equipment as for water.

Figure 14 shows values of σ_t along lines parallel to axis Y. Figure 15 shows lines of constant σ_t, constructed on the basis of curves of Fig. 14. It follows from these figures that the root-mean-square values of temperature fluctuations for mercury are distributed smoother than in experiments with water. The maximum of σ_t is also located on the axial lines of the cross section, but it is displaced appreciably from the wall of the duct to the center, i.e., /99
y for σ_{max} for Re = 30,400 is 9 mm (y/a = 0.6). This change in the distribution of σ_t with an increase in the thermal conductivity of the liquid [when water is replaced by mercury, DBL] agrees with a hypothesis stating that the amplitude of the turbulent temperature fluctuations is proportional to the product of the mixing path and the gradient of the average temperature [17]. In liquids with high thermal conductivities the temperature gradient exists in the entire interval from the wall to the center of the duct, while when heat is transferred to water the main temperature drop is observed near the wall. Hence, the magnitude of $\sigma_{t\,max}$, which is obtained in experiments with water is located at the wall of the duct, while that obtained with mercury is displaced to the center of the duct. The shape of curves of constant σ_t obtained in experiments with mercury differs from similar curves obtained with water (see Fig. 15). In the mercury experiments the effect of secondary flows on the σ_t field is also smaller, i.e., curves of σ_t = = 0.45, 0.36, etc., are extended in the direction of the duct's corner. This again

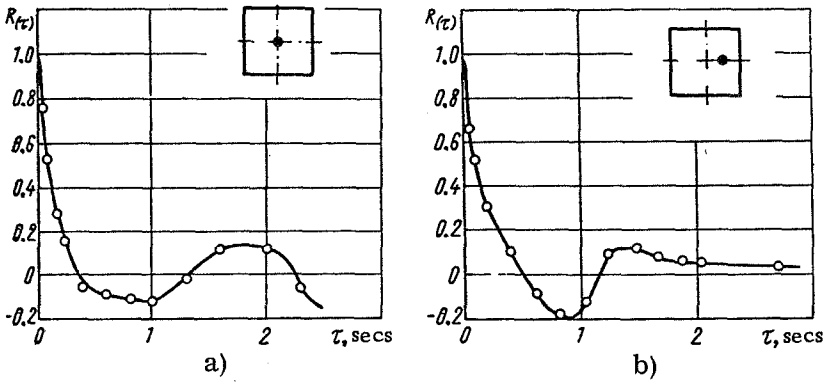

Figure 16. Normed Autocorrelation Function in the Center of a Turbulent Flow of Water in a Square Duct Heated From Four Sides; Re = 4910; a) x/a = 0, y/a = 0; b) x/a = 0; y/a = 0.8.

confirms the fact that in liquid metals with high thermal conductivity the effect of secondary flows on the heat transfer becomes lower. The effect of the average velocity within the given limits of variation in Re does not have a substantial effect on the magnitude of σ_t (see Fig. 13b). Comparing Figs. 11 and 13 we note that the magnitudes of σ_t in the center of the duct in experiments with water and mercury are close to one another by absolute magnitude. The magnitude of σ_t was measured with a specific thermal flux of q = 15,000 watts/m^2 provided by heaters on heating from four sides. When the Reynolds number is increased the magnitude of σ_t over a large part of the duct cross section in the flow of mercury becomes greater than for water

The magnitude of σ_t and the average frequency of fluctuations do not fully /100 characterize the temperature fluctuations. An important characteristic is the probability that the fluid in the given point of the flow will have a given temperature. We have used the oscillograms to determined the distribution of the probability of temperature fluctuation amplitude, which is in good agreement with a normal distribution of random variables. Since the points examined are situated in different regions of the duct's cross section (for example, at the wall and at the corner of the duct) it may be assumed that in the first approximation the probability distribution of amplitudes of the temperature fluctuations conforms to the normal distribution for a large part of the cross section of the square duct.

Figures 16a and b show the normed autocorrelation function (correlation coefficient) in two points of a flow of water, calculated from the expression

$$R_\tau = \frac{t'(0) \cdot t(\tau)}{\overline{t'^2}}.$$

In the main body of the flow (see Fig. 16) the correlation coefficient decreases rapidly to zero; on further increase in τ, the time shift, function $R(\tau)$ fluctuates about zero and is gradually damped out. The life of the temperature disturbance, determined by the first intersection between the curve of R_τ and the abscissa axis is 0.35 and 0.55 secs. The life of a turbulent disturbances can be used to determine its dimensions. The characteristic dimension of a temperature disturbance in the axial direction is $L_1/a = \tau \cdot \bar{u}/a = 6$ (when Re = 4910), i.e., it is appreciably greater than the cross sectional dimensions of the duct.

Results

Our experimental work shows that for accurate calculation of temperature field in rectangular ducts it is insufficient to have relationships used for calculating heat transfer in round pipes. This is true for liquid metal, as well as for ordinary, low-thermal-conductivity, heat transfer agents. /101

The fact that secondary flows have an appreciable effect on the heat transfer process in a square duct was proven experimentally. This was demonstrated by the characteristic distribution of the wall temperature, by the specific shape of the mean temperature distributions and of the temperature fluctuation intensity in the fluid flow.

The existing semi-empirical theory of heat transfer do not at all take into account the contribution of secondary flows, hence, these theories should be corrected accordingly.

The heat transfer in a square duct, in addition to secondary flows, is also affected by heat fluxes through the wall, which depend on the duct geometry, thickness and thermal conductivity of the wall, which is a characteristic feature of all nonround channels. Hence, for accurate calculations of nonround ducts from the point of view of fluid flow as well as from the point of view of heat transfer one must examine each specific geometry and solve the problem on taking into account all the factors which affect the temperature field.

NOTATION

t_{f_1} temperature of fluid at the duct inlet, ° C

t_{w_1} temperature at the outer surface of the wall, ° C

t_{w_2} temperature at the inner surface of the wall, ° C

G flow rate of heat-transfer agent

σ_t root-mean-square value of temperature fluctuations, °C

x, y current coordinates (the coordinate origin is in the center of the duct)

a half-width of the flow cross section

b wall thickness

d_h hydraulic diameter of the duct

REFERENCES

1. Nikuradze J.: Ingenieur-Archiv, 1, 306 (1930).
2. Laufer J.: NACA T N-2133, 1950.
3. Brundrette E. and Baines, W. D.: J of Fluid Mech., 19, 3 (1964).
4. Bailey, A. and Cope, W. F.: Aeronaut. Res. Comm. (Great Britian), Techn. Rept., 43, 199 (1933).
5. Mikheyev, M. A.: Osnoy teploperedachi [Fundamentals of Heat Transfer]. Gosenergoizdat, Moscow, 1949.
6. Kays, W. M.: Techn. Rept. 14 Dept. Mech. Engng., Stranford University, Calif., (1959).
7. Tsarenko, N. V.: Izvestiya Kievskogo politekhnecheskogo instituta, 17, 143 (1956).
8. Lubarsky, B. and Kaufman, S.: NACA, Report., No. 1270 (1956),
9. Novikov, I. I. and Voskresenskiy, K. D.: Prikladnaya termodinamika i teploperedacha [Applied Thermodynamics and Heat Transfer]. Gosatomizdat, Moscow, 1961.
10. Seban, R. A.: Trans. ASME, 72, 789 (1950).
11. Subbotin, V. I., et al.: Teploenergetika, No. 9 (1961).
12. Novotny, I. L., et al.: E. R. I. Eckert A. I. Ch. E. Journal, v. 10, No. 4 p. 466-470 (1964). /102
13. Teplofizicheskiye svoystva veshchestv [Thermophysical Properties of Substances]. Handbook, under the editorship of N. B. Vargaftik. Gosenergoizdat, Moscow, 1956.
14. Nikol'skiy, N. A., et al.: In the collection "Voprosy teploobmena" [Problems of Heat Transfer]. Published by the Academy of Sciences of the USSR, Moscow, 1959.
15. Bokov, V. P., et al.: Teplofizika vysokikh temperatur, 3, No. 5 (1965).
16. Subbotin, V. I., et al.: Teplofizika vysokikh temperatur, 3, (1965).
17. Subbotin, V. I., et al.: Teploenergetika, No. 3 (1962).

FLUID DYNAMICS IN AN ANNULAR SPACE WITH LONGITUDINAL RIBS

Yu. D. Levchenko, V. I. Subbotin, P. A. Ushakov and A. V. Sheynina

To reduce the quantity of the coolant in the active zones of reactors, the coolant annuli should be narrow. However, in this case the production tolerances for the geometric dimensions become comparable with the dimensions of the coolant annulus proper. This can result in appreciable eccentricities, which cause redistribution of coolant velocities, and consequently, also cause the appearance of temperature variations along the perimeter of fuel cells. The present paper presents the study of a narrow ($d_1/d_2 = 0.895$) coolant annulus with three longitudinal spacing ribs (Fig. 1). It considers a concentric duct and ducts with relative eccentricities $\varepsilon = 0.5$ and 1 (the limiting case). /102

The test section was made of a pipe ($d_2 = 95$ mm) made from 1Kh18N9T steel with a dural rod ($d_1 = 85$ mm) placed inside it. The pipe and the rod formed an annular slot 1900 mm long and with $d_1/d_2 = 0.895$, $\delta = d_2 - d_1/2 = 5$ mm. Brass spacing ribs were inserted into longitudinal slots, milled on the surface of the rod. In the experiments we have used three rods, one of which had identical ribs, which were used to keep it concentrical with the outer tube. The dimensions of the ribs of the two remaining rods were selected so as to provide for eccentricities of 0.5δ and δ. We have examined the displacement of the rod in the direction of one of the ribs only. At the inlet to the test section was placed a mixing header with a mesh for equalizing the velocity distribution. Along the surfaces of the central replaceable rods were milled slots into which six capillaries 2 mm in diameter from 1Kh18N9T steel were inserted and fastened by the quick-setting "Stynscryl" plastic, after which the surface was carefully smoothed out. Holes in the capillaries (0.5 mm) for measuring the static pressure were provided in cross sections situated at distances of 500 and 1000 mm from the inlet. Static pressure pickups have also been provided at the outer tube at a distance of 150-200 from one another over the length of the tube. /103

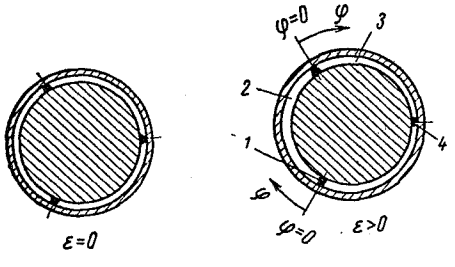

Figure 1. Cross Section of Test Section. 1) Large Rib; 2) Wide Annulus Segment; 3) Narrow Annulus Segment; 4) Small Rib.

Moving the inner rod [off-center] (see Fig. 1) forms three cells, two of which have the same geometry ("narrow" cells), and one has a different cross section ("wide" cell). The basic parameters of the test section are given in Table 1.

TABLE 1. Basic Parameters of Test Section

Designation	$\varepsilon = 0$	$\varepsilon = 0,5$		$\varepsilon = 1$	
		1	2	1	2
How cross section of cell, mm^2	459	346	648	254	878
Hydraulic diameter of cell d_h, mm	9.20	7.30	13.0	5.40	17.0

NOTE: The numbers 1 and 2 refer to the narrow and wide cells, respectively.

The construction of the test stand has been described in [1]. The pressure drops were measured by U-shaped glass differential manometers using distilled water. The temperature of the water was varied from 6 to 80°C in order to extend the range of Reynolds numbers. Depending on the pressure drops the differential manometers were filled with mercury, tetrabromoethane, carbon tetrachloride and chlorobenzene. The rate of flow of the water through the test section was measured by calibrated venturi tubes. Moderate (less than $2\ m^3$/ /hour) water flow rates were determined by measuring tanks. The water temperature was monitored by copper resistance thermometers and the temperature of the surrounding air was measured by mercury thermometers.

The friction resistance coefficients λ were determined on the basis of the measured pressure drops for the concentric spaces. For eccentric spaces this was not possible, since in this case the flow rate distribution among the cells is unknown. The experiments have shown that for a concentric space the pressure drops in the cells do not differ by more than 5%. To reduce the time needed for measurements, the measurements for small water flow rates were made in one cell only. /104

The velocity distributions were measured in cells of eccentric annular spaces. The experiments were performed on an air stand, the construction of which is described in [2]. The local velocities were measured by a glass Pitot tube (with an external diameter of 0.2 mm and an internal diameter of 0.12 mm) in the duct outlet cross section. The static pressure was measured through a hole 0.8 mm in diameter in the wall of the outer tube. The Pitot tubes were positioned and moved in two mutually perpendicular directions by a coordinate spacer with a sensitivity of 0.05 mm. The pressure drops were measured by a U-shaped differential

manometer, filled with alcohol. The air flow rate through the model was kept constant by monitoring it by the pressure drop over a 600 mm long section.

The theoretical limiting error in measuring λ, the friction coefficients in water was 5-10%, which includes the errors in the geometric dimensions, water flow rates and pressure drops. The accuracy in measuring local velocities in the air was 1.5-2%, while that of measuring the friction coefficients λ was 7%. The velocity distributions in the cells of eccentric annular spaces were also determined analytically, using the method due to Deissler and Taylor [3]. The original data used in the calculations were: working medium - water at 18°C, pressure gradient $dp/dl = 238$ kg/m^2 - m).

The measured friction coefficients in the concentric space are shown in Fig. 2. The experimental data for laminar flow are in good agreement with the theoretical formula obtained for annular passages without ribs [4]-[6] /105

$$\lambda = \Psi\left(\frac{d_2}{d_1}\right)\frac{64}{\mathrm{Re}}, \tag{1}$$

where $\mathrm{Re} = \bar{u}d_h/\nu$ and d_h is the equivalent hydraulic diameter of the passage, taking into account the ribs;

$$\Psi = \frac{\left(\frac{d_2}{d_1}-1\right)^2 \ln\frac{d_2}{d_1}}{\left[\left(\frac{d_2}{d_1}\right)^2+1\right]\ln\frac{d_2}{d_1}-\left[\left(\frac{d_2}{d_1}\right)^2-1\right]}.$$

For a round pipe $\Psi = 1$, while for a flat slot $\Psi = 1.5$. For our case

$$\lambda \approx \frac{96}{\mathrm{Re}}.$$

Calculations using Eq. (1), derived for a round pipe, naturally yields values of λ on the lower side. Equation (1) is in good agreement with experimental data obtained in [4] for $d_1/d_2 = 0.212$-0.838.

Transition from laminar to turbulent flow is observed at Re = 2300-2400. The experimental data for turbulent flow are in agreement with the well-known formulas for round pipes due to Blasius (2) and Nikuradse (3)

$$\lambda = 0.316\mathrm{Re}^{-0.25}; \tag{2}$$

$$\lambda = 0.0032 + 0.221\mathrm{Re}^{-0.237}. \tag{3}$$

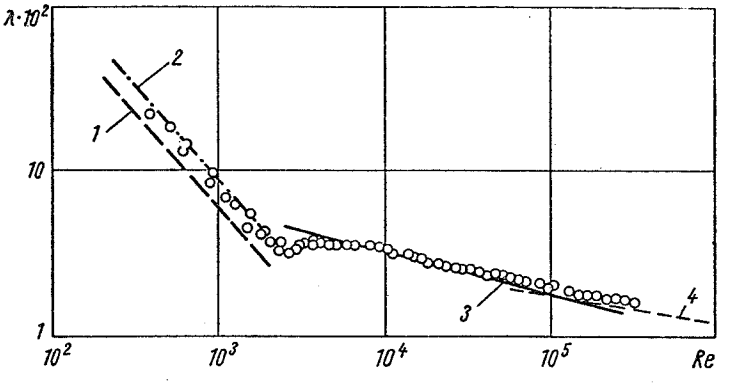

Figure 2. Friction Coefficients for a Concentric Annular Passage With Longitudinal Ribs. 1) and 2) Calculated From Eq. (1) for $\psi = 1$ and 1.5 Respectively; 3) and 4) Calculated Using Eqs. (2) and (3) Respectively; the Circles Denote Experimental Results.

Consequently, if we take the hydraulic diameter as the characteristic dimension, then the hydraulic resistance in the thin concentric annular space with three longitudinal ribs can be calculated by using formulas for round tubes in turbulent flow and by formulas for ribless annular passages in laminar flow.

The characteristic velocity distributions and the isotachs [equal-velocity lines] obtained experimentally with an eccentricity of $\varepsilon = 1$ are shown in Fig. 3. These data were used for constructing the dimensionless velocity distributions

$$\left(\frac{u}{\bar{u}}\right) = f\left(\frac{y}{y_{max}}\right),$$

where u is the local velocity, $\bar{u}$ is the average velocity for the cell under study, y is a coordinate measured from the surface of the rod along a normal and y_{max} is the width of the annulus for a given angle φ.

Comparing the measured distributions of velocity $u/\bar{u}$ with those calculated by the Deissler-Taylor method for two eccentricities show that they agree in the majority of cases. The slight disagreement which is observed near the rib ($\varphi = 6°$) is due to the fact that the calculations for regions near the ribs are not too accurate.

For each angle φ we found the average velocity /108

$$\overline{U}_\varphi = \overline{\left(\frac{u}{\bar{u}}\right)}_\varphi = \frac{\int_0^{y_{max}} \frac{u}{\bar{u}}(R_1+y)\,dy}{\int_0^{y_{max}} (R_1+y)\,dy} = \frac{\int_0^{y_{max}} \frac{u}{\bar{u}}(R_1+y)\,dy}{y_{max}\left(R_1+\frac{y_{max}}{2}\right)}. \qquad (4)$$

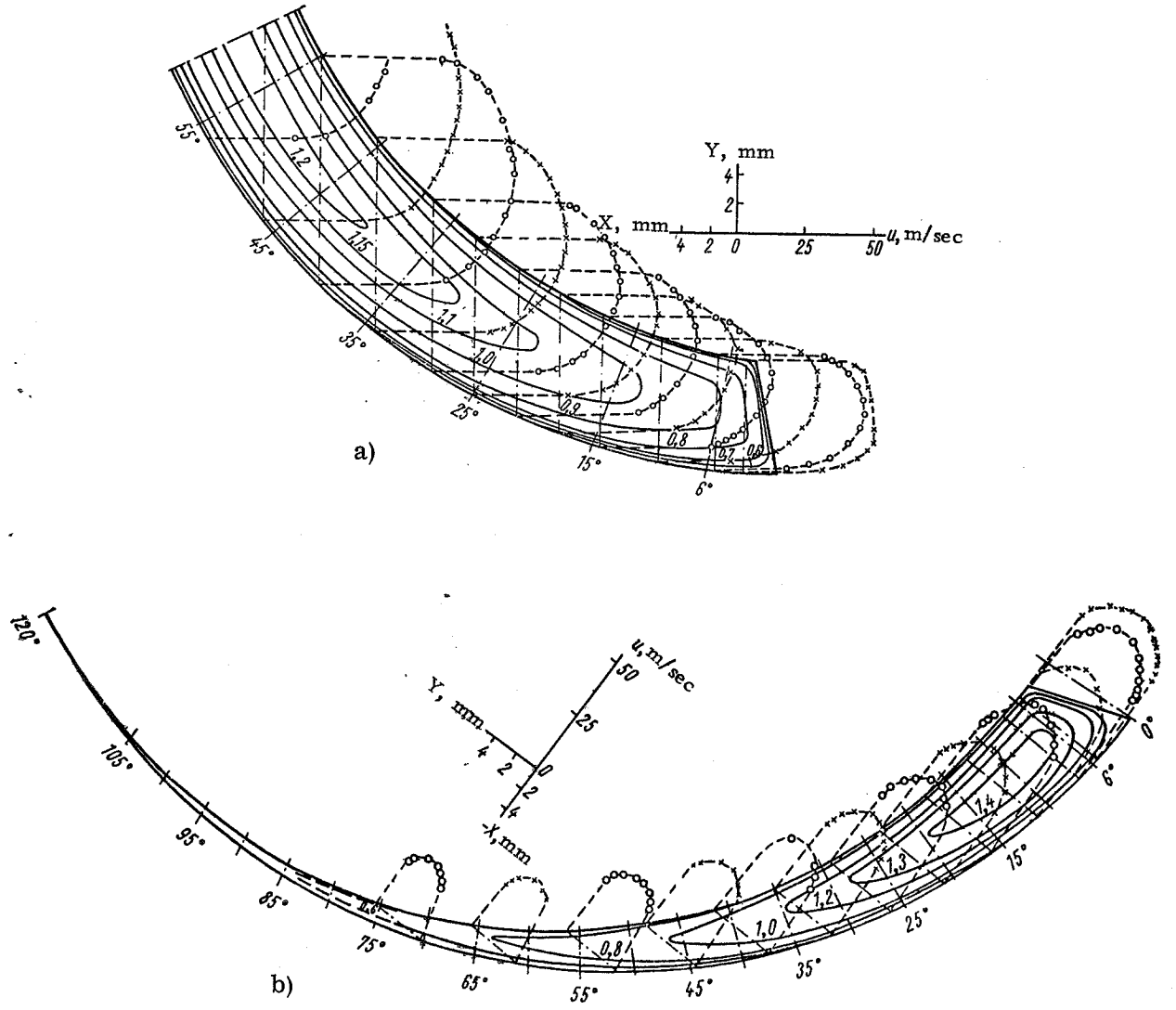

Figure 3. Distribution of Velocities $u/\bar{u}$ in the Wide (a) and Narrow (b) Cells for $\epsilon = 1$.

The curve of U_φ as a function of φ is shown in Fig. 4, from which it follows that the average velocity in the direction of the normal in the wide cell depends little on the eccentricity, while in the region of $20 < \varphi < 100°$ it practically does not vary along the perimeter and is approximately equal to the average velocity in the cell. The picture observed in narrow cells is different. When $\varepsilon = 0.5$ U_φ varies from 1.2 for $\varphi = 15°$ to 0.7 for $\varphi = 110°$, i.e., by approximately a function of 1.7. Velocity $\bar{U}_\varphi$ varies even more rapidly in the case of $\varepsilon = 1$. In this case the experimental data could be obtained only for a part of the narrow cell ($\varphi \leq 65°$), since the comparatively small dimensions of the passage made it impossible to perform measurements in the region of minimal spaces. Analytical calculations were also made only for $\varphi \leq 85°$. The values of U_φ obtained theoretically and experimentally are close to one another (see Fig. 4).

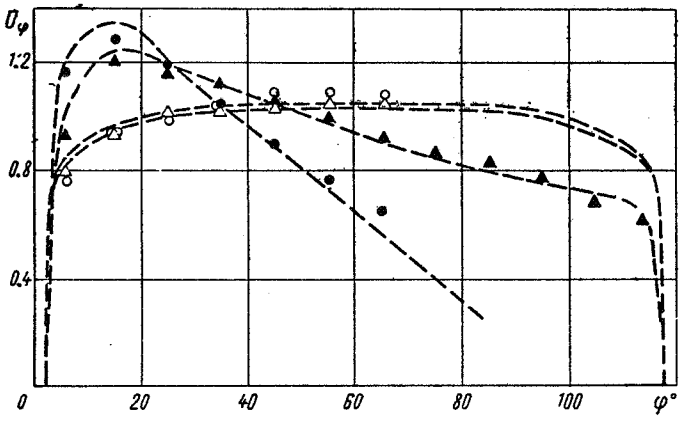

Figure 4. Distribution of Relative Velocity, U_φ over angle φ ∆ and ▲ are Experimental Data for the Wide and Narrow Cells, Respectively, when $\varepsilon = 0.5$; ○ and ● Denote the Same for $\varepsilon = 1$; the Dashed Line Shows Theoretical Results.

The average velocities in the cells found by graphical integration and the measured pressured gradiants dp/dl were used to calculate the Reynolds numbers and the friction coefficients λ (Table 2). In was assumed in these calculations that the pressure gradients in all the cells are the same (238 kg/m^2-m). /109
However, it was established experimentally that the pressure gradients in the cells differ (see Table 2), which apparently is due to the effect of local resistances to flow at the cell inlets and outlets. This phenomenon is one of the causes for the differences between the calculated and experimentally obtained values of $\bar{u}_2/\bar{u}_1$, shown in Table 2.

If we make a correction to take into account the differences in dp/dl, then the theoretical values of $u_2/\bar{u}_1$ will be: 1.37 for $\varepsilon = 0.5$ and 1.73 for $\varepsilon = 1$. Then the maximum difference between the theoretical and experimentally obtained results will not exceed 10% even for $\varepsilon = 1$. Figure 5 compares the values of λ (see /110
Table 2). Lines were drawn through the experimental and theoretical points on the assumption that for all the cells the friction coefficients are proportional to $Re^{-0.25}$. When $\varepsilon = 0.5$ the theoretical and experimental values for the wide cell are in agreement with one another and conform to Eq. (2) for a round pipe, while

TABLE 2. Experimental and Theoretical Data

Parameters	ε = 0,5				ε = 1,0			
	Experi.		Theoret.		Experi.		Theoret.	
	1	2	1	2	1	2	1	2
t_w, °C	—	—	18	18	—	—	18	18
t_{air}, °C	32	31	—	—	31	31	—	—
$\bar{u}$, m/sec	41.1	55.6	1.03	1.51	35.8	56.6	1.01	1.83
Pressure gradient, dp/dl, kg/m^2·m	343	308	238	238	255	236	238	238
Re·10^{-3}	18.6	44.9	7.2	18.7	12.1	60	5.12	29.5
λ·10^2	2.52	2.19	3.27	2.7	1.82	2.12	2.47	2.38
Ratio of the average velocities in the wide and narrow cells, $\bar{u}_2/\bar{u}_1$	1.35		1.46		1.58		1.81	
Ratio of the fluid flow rates in the cells, Q_2/Q_1	2.52		2.73		5.46		6.26	

NOTE: 1 and 2 denote the narrow and wide cells, respectively.

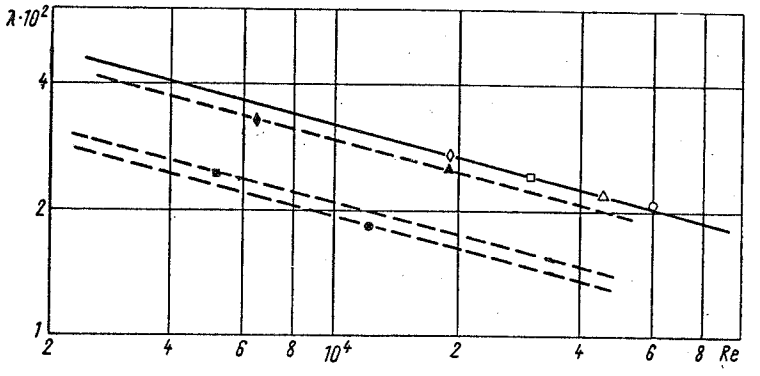

Figure 5. Friction Coefficients λ for Cells of Eccentric Annular Spaces.

	Calculated	Experiment
ε = 0.5	◇ ◆	△ ▲
ε = 1.0	□ ■	○ ●

in the narrow cell they are situated by 6% lower. For an eccentricity of $\varepsilon = 1$ the data for the wide cell are also in agreement with Eq. (2). At the same time the data for the narrow cell are by approximately 40% lower than values of obtained by Eq. (2).

Thus, our experiments and calculations have shown that the approximate method due to Deissler and Taylor [3] can be used for practical calculations of distributions of velocity and of frictional resistance coefficients of narrow eccentric passages.

REFERENCES

1. Sheynina, A. V.: Gidravlicheskoye soprotivleniye puchkov sterzhney v osevom potoke zhidkosti [Resistance to Flow of Clusters of Rods in an Axial Flow]. Present collection.
2. Ibragimov, M. Kh. and Isupov, I. A.: Raschet i eksperimental'noye issledovaniye poley skorosti v kanale slozhnoy geometrii [Calculation and Theoretical Study of Velocity Fields in an Intricately Shaped Passage]. Present collection.
3. Deisler, R. G. and Taylor, M. F.: Reactor Heat Transfer Conference of 1956, TID-7529/Pt 1/, Book 2, 416, 1957.
4. Koch, R. and Feind, K.: Chem. Ingr. Techn., 30, No. 9, 577 (1958).
5. Walker, Y. E., et al.: A. I. Ch. E. Journal, vol. 3, No. 4, 484 (1957).
6. Idel'chik, I. Ye.: Spravochnik po gidravlicheskim soprotivleniyam [Handbook on Resistances to Fluid Flows] p. 58. Gosenergoizdat, Moscow-Leningrad, 1960.

EFFECT OF ECCENTRICITY ON HEAT TRANSFER TO LIQUID METALS IN ANNULAR SPACES

V. I. Subbotin, V. D. Talanov and P. A. Ushakov

The coolant annulus which is formed by a fuel-element rod and the tube in /111
which it is placed is one of the versions of ducts used in reactors with liquid metal cooling. When the fuel element is displaced (an eccentricity is formed) the symmetry of the flow past the fuel rod is disturbed, producing temperature variations along the rod's perimeter, local overheating, additional thermal stresses, etc.

The use of spacing ribs only partially alleviates the above shortcomings. Perceptible eccentricities may appear due to geometric tolerances of the passage even when these ribs are used. In addition, the presence of the ribs produces additional temperature bursts beneath the ribs and alongside them, similar to those already observed [1]. The eccentricities have a particularly appreciable effect on thin coolant annuli, in which the geometric tolerances are commensurable with the dimensions of the annulus proper.

The present paper describes the effect of spacing ribs and eccentricities on the temperature field of the surface of the heat-conducting tube which is cooled by liquid metal flowing in the narrow annulus ($D/d_2 = 1.12$). The experiments were performed with the Na-K alloy (22% Na and 78% K) using a setup consisting of a closed circuit made from 1Kh18N9T steel with a volute electromagnetic pump [2], providing an alloy flow rate of about 10 m^3/hour at a pressure of about 4 kg/cm^2. The heat was carried away from the stand in a double-tube kind of heat exchanger, through a double wall with an intermediate contact layer made of lead. A small part of the coolant was continuously circulated through a cold oxide trap, which was cooled through a double wall. The oxides content in the circuit was monitored by a distillation sampler, the sample collected which was subsequently analyzed.

The test duct (Fig. 1) has been made so as to make it possible to rotate the center tube through any specified angle directly during the measurements. The annulus was formed by a jacket with internal diameter D = 76 mm, wall thickness of 3 mm and an internal tube with $d_1 = 2R_1 = 64$ mm and $d_2 = 2R_2 = 68$ mm. Thus the width of the coolant annulus was 4 mm; the electric heater of the inner tube was made from 3 mm nichrome wire in the form of a spiral. To prevent short-circuiting the coils, the spiral was first oxidized by heating it in air. In addition, the nichrome wire was coated by a thin layer of an alundum-orthophosphoric oxide /112
mixture. The spital is insulated from the internal surface of the tube by an organic silicon compound $\sim$ 0.6 mm thick. One end of the heater is attached to the

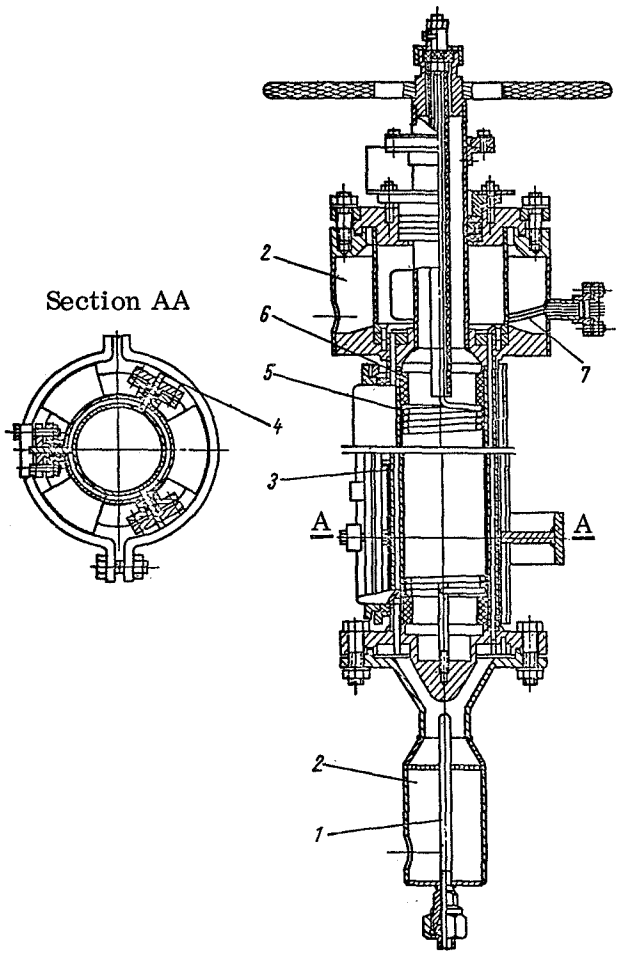

Figure 1. Structure of the Experimental Duct. 1) Thermocouple in a Sleeve; 2) Mixing Headers; 3) Jacket; 4) Slat-Shaped Ribs; 5) Nichrome Heater; 6) Inside Tube; 7) Thermocouples for Measuring the Temperature Distribution of the Coolant at the Duct's Exit.

housing, while the other has a potential over it. The power which was supplied to the heater from the AOMK-100/0.5 transformer was measured by class 0.5 meters. This heater design provides $q \simeq \text{const}$ at the inner surface of the tube. The heated duct length was $l_0 = 675$, out of a total length l of 755 mm.

The inside tube may be positioned concentrically or eccentrically by means of replaceable end grids and slat-shaped centering ribs 4 mm thick in the following manner. The ribs are placed into longitudinal slots milled in the outer tube and are packed by vacuum rubber. In all the cases the inside tube is displaced relative to the jacket in the direction of one of the ribs. The angles are read from the axis of this rib. The flow cross section of the duct (upon reducing the area of the ribs) was 856 mm^2, and the hydraulic diameter was $d_h = 7.58$ mm. /113

The temperature of the heat-conducting surface was measured by 12 copper constantan thermocouples, situated at different distances from the duct inlet. The thermocouple wires in Viniflex insulation were placed into steel capillaries with dimensions of 0.5/0.3 mm. The latter together with the thermocouple wires were inserted into the wall of the inside tube by calking and metallizing.

The temperature of the Na-K alloy at the duct's inlet and outlet was measured by thermocouples located in the mixing headers. In addition, at the point where the coolant left the duct we also measured the temperature distribution of the coolant along the perimeter of the annulus, for which we have used thermocouples in capillaries placed each 15° along the perimeter.

All the components of the test duct in contact with the coolant were made from 1Kh18N9T stainless steel. The test duct was placed on the stand in the vertical position, and the liquid metal flowed from the bottom upward. The experiments were performed for coolant temperatures from 40 to 100°C. The average thermal conductivity coefficients were: for the wall $\lambda_w = 13.2$ kcal/m-hour-degree, for the Na-K alloy $\lambda_f = 19.5$ kcal/m-hour-degree. The oxygen content of the alloy did not exceed 10^{-3} % by weight.

As was shown by the experiments, bursts in the temperature of the heat-conducting surface are observed near the ribs in the concentric annulus. The dimensionless variations in the temperature of the concentric annulus for the region with stable heat transfer is shown in Fig. 2a. The magnitude of the variations depends to a large extent on the Peclet number, which was calculated on the basis of the average velocity and of the d_h calculated upon subtracting the rib area. As the Peclet number is made large the region of elevated temperatures near the rib narrows down somewhat. This, apparently, is due to the effect exerted by the higher turbulization of the flow in high-velocity coolants. In the range of Peclet numbers used the dependence of the temperature nonuniformity on the Peclet number can be approximately described by a power law. In logarithmic coordinates this relationship is expressed by straight lines (see Fig. 2b).

The variations in the temperature along the perimeter of the heat-conducting surface of eccentric annuli with ribs for $l/d_h \approx 79$ are shown in Fig. 3. The Peclet numbers have been calculated on the basis of the average coolant velocity and of the hydraulic diameter of the annulus, upon subtracting the rib area. Temperature bursts at points with $\varphi = 120°$ correspond to the rib locations. In the region with the minimum annulus width ($\varphi = 0$) the temperature increase is basically produced not by the ribs, but rather by over-heating of the coolant in the narrow parts of the eccentric annulus. The temperature nonuniformity in eccentric annuli is much greater than that produced by the ribs. /114

The temperature distributions for eccentric smooth annuli behave in approximately the same way as the distribution for ribbed annuli, with the exception of the local temperature bursts beneath the ribs. In the region of low Pe (transient and laminar flows) the temperature nonuniformity for a smooth passage is less dependent on the Peclet number than for large Pe. A similar trend was observed also in experiments in a ribbed annulus with a relative eccentricity of $x = 0.5$.

Comparing experimental data obtained for ribbed and ribless annuli we see that the temperature variations over the perimeter of the central heat-conducting tube for low Peclet numbers ($20 < Pe < 80$) in both cases is approximately the same (Fig. 4). As Pe is increased, the temperature variations in the ribless annulus reduce much faster than in a ribbed space. Apparently the ribs interfere with the intermixing of the coolant and make tagential flows of heat in the coolant more difficult. /116

The temperature variations over the perimeter of the inner tube is determined basically by the difference in the amounts of heat absorbed by the coolant in the narrow and wide parts of the eccentric annuli (Fig. 5). It can be seen that the

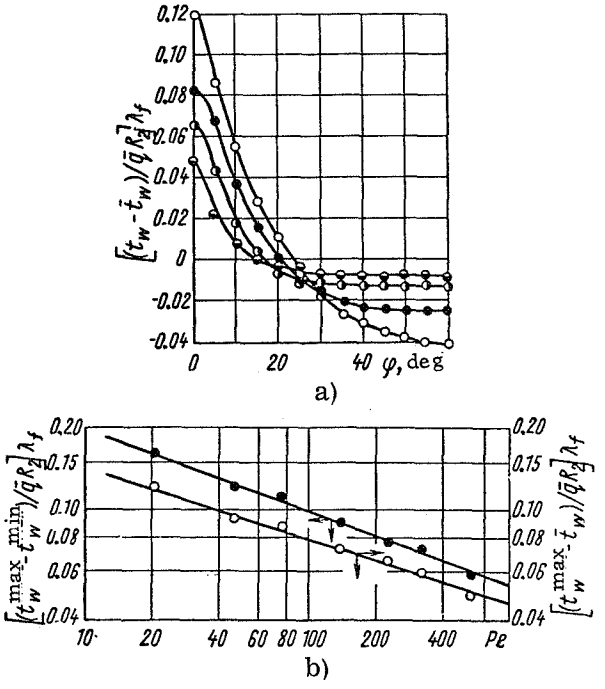

Figure 2. Stabilized Values of Temperature Nonuniformity in a Concentric Annulus With Ribs. ○, ●, ◐ and ◒ are Results of Experiments With Pe = 21, 75, 223 and 540, Respectively.

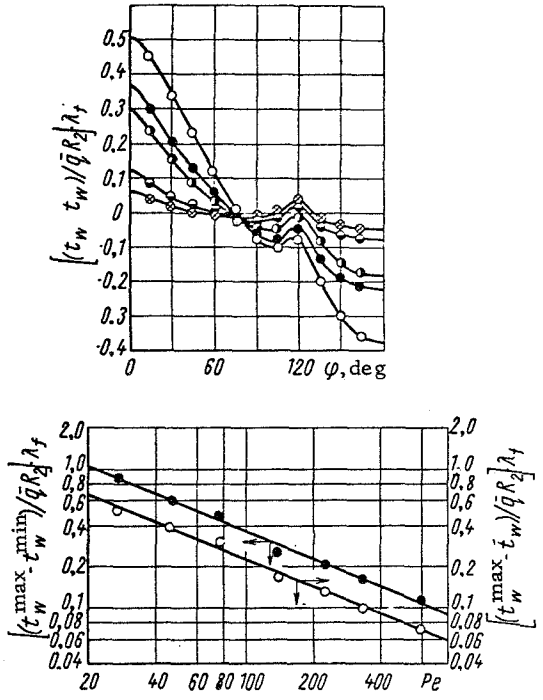

Figure 3. Variations in the Temperature of a Ribbed Annulus With an Eccentricity of x = 0.25. ●, ○, ◑, ◒ and ⊗ are Experimental Results for Pe = 26, 49, 78, 236 and 559, Respectively.

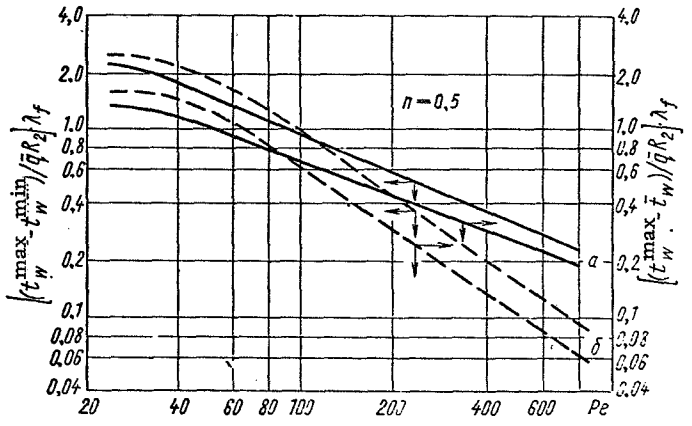

Figure 4. Variations in the Temperature of Ribbed (a) and Smooth (b) Eccentric Annuli.

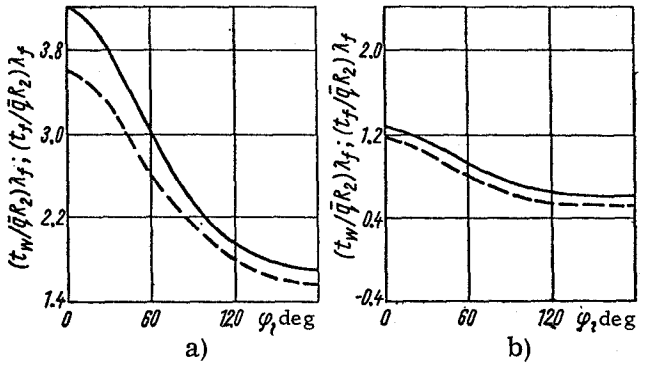

Figure 5. Temperature Distributions in the Wall (Solid Line) and in the Fluid (Dashed Line) in a Ribless Annulus With an Eccentricity x = 0.5 and with $l/d_h = 75$, Obtained for Pe = 27 (a) and Pe = 147 (b).

local mean temperature differences between the wall and the coolant are much smaller than the total temperature variation, and the curves describing the temperature distributions in the fluid and in the wall are approximately equidistant. A similar pattern is observed also in ribbed annuli.

The temperature distributions we have found were used to calculate the distributions of the thermal fluxes along the tube perimeter [3]

$$T_w \simeq \overline{T}_w + \sum_{k=1}^{n} a_k \cos k\varphi, \quad (1)$$

$$\frac{q}{\bar{q}} \simeq 1 - \sum_{k=1}^{n} a_k k \varepsilon_k \cos k\varphi, \quad (2)$$

where $T_w = \frac{t_w}{qR_2}\lambda_f$ is the dimensionless local temperature of the wall in the section at hand, $\overline{T}_w$ is the value of T_w averaged over the perimeter, a_k is a coefficient of the Fourier series describing the temperature distribution, q and $\bar{q}$ are the local specific thermal flux and the flux averaged over the perimeter; ε_k is a parameter characterizing the design and properties of the fuel rod [3].

$$\varepsilon_k = \frac{\lambda_w}{\lambda_f}\frac{1-\xi_1^{2k}}{1+\xi_1^{2k}}, \quad \xi_1 \equiv \frac{R_1}{R_2}. \quad (3)$$

Since the heat conducting tube had a relatively small wall thickness ($\delta/R_2 = R_2 - R_1/R_2 = 0.059$), which made thermal fluxes over its perimeter difficult, the variation in the distribution of thermal fluxes $q/\bar{q}$ was [only] moderate. We present an example. For a coolant annulus with Pe = 82, $l/d_h = 75$ and with an eccentricity of x = 0.5 we found /117

$$T_w - \bar{T}_w \approx 0.572 \cdot \cos\varphi + 0.217 \cdot \cos 2\varphi + 0.0715 \cdot \cos 3\varphi + 0.020 \cdot \cos 4\varphi + 0.0177 \cos 5\varphi + 0.006 \cdot \cos 6\varphi;$$

$$\frac{q}{\bar{q}} \approx 1 - (0.024 \cos\varphi + 0.036 \cos 2\varphi + 0.0266 \cos 3\varphi + 0.013 \cos 4\varphi + 0.018 \cos 5\varphi + 0.0086 \cdot \cos 6\varphi).$$

When $\varphi = 0$, the magnitude of $q/\bar{q}$ differs from unity by approximately 10-13% and at the remaining angles it does so by not more than 5%. Consequently, the thermal flux over a major part of the tube's perimeter is close to the average thermal flux.

The experiments have shown that for eccentricities of $x \geq 0.25$ the heat transfer does not become stabilized as far as $\sim 80\,d_h$ (Fig. 6). It may be assumed that the section of thermal stabilization will become larger with an increase in Pe. Thus the data obtained for eccentric annuli pertain [only] to the inlet section.

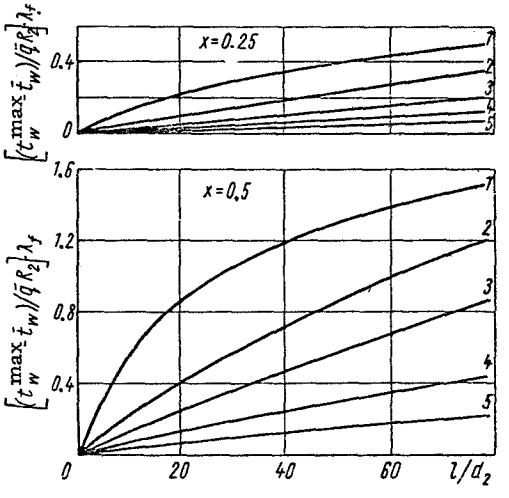

Figure 6. Changes in Temperature Variations Along the Length of Ribless Eccentric Annuli. 1, 2, 3, 4 and 5 are Curves for Pe = 26, 54, 80, 143 and 234, Respectively.

The temperature variations in ribbed eccentric annuli is more dependent on the Peclet numbers than in concentric annuli. In the first case the temperature variation is produced primarily by the eccentricity, while in the second case it is due to local temperature bursts in the vicinity of ribs. It should be emphasized that we are here comparing the temperature variations as a function of the Peclet number for the inlet section in eccentric spaces with these variations for a stabilized region of heat transfer in a concentric passage. It is logical to assume that for the stabilized heat transfer region /118 the temperature variation in eccentric annuli will depend less on the Peclet number than for the inlet section.

The curves of Nu as a function of the Peclet number for different l/d_h are shown in Figs. 7 and 8. The Nusselt numbers were calculated from the expression

$$Nu = \frac{\bar{q} d_k}{(\bar{t}_w - \bar{t}_f)\lambda_f},$$

where $\bar{t}_w$ and $\bar{t}_f$ are the average temperatures of the wall and the fluid for the value of l/d_h at hand. The Peclet numbers have been calculated on the basis of the average coolant velocity. The hydraulic diameter was found for the ribbed annuli upon subtracting the rib area, and for ribless passages it was found from the expression $(d_h)_{sm} = d_2 - d_1$.

Data on the average heat transferred by concentric annular spaces for stabilized heat transfer are presented in Fig. 9. On the same figure are drawn curves obtained from Lyon's semiempirical formulas quoted in [4]

$$Nu = 4.9 + 0.0175 \cdot Pe^{0.8} \quad (4)$$

and from those given in [5]

$$Nu = 5.1 + 0.02 \cdot Pe^{0.8}. \quad (5)$$

The experimental data for a ribless annulus are higher than values obtained from the above formulas by not more than 15% at large Peclet numbers. When Pe is reduced this difference becomes smaller. Previously published data for mercury are also in satisfactory agreement with Eqs. (4) and (5), [5]. The presence of ribs reduces the values of Nu calculated by taking into account temperature bursts beneath the ribs and near them by an average of 25%. /119 /120

On the basis of the results we have obtained, we may claim the following. First, the variation in the coolant temperature over the width of a concentric annulus is small in comparison with the temperature variation over the passage's perimeter (see Fig. 5). Secondly, for values of l/d_h used in this investigation, the heat transfer does not become stabilized. Tangential thermal fluxes in a narrow space with a coolant and in the thin wall of the heat conducting tube are moderate for the inlet section, which is attested to by the weak change in the thermal flux along the perimeter of the passage and the close-to-linear dependence of the temperature variation on l/d_h (see Fig. 6). Let us now consider the problem of temperature variations under the following assumption; 1) the heat transfer agent temperature is constant over the width of the annular space and is equal to the wall temperature, but it varies over the perimeter, i.e., $t_w = t_f = t = f(\varphi)$;

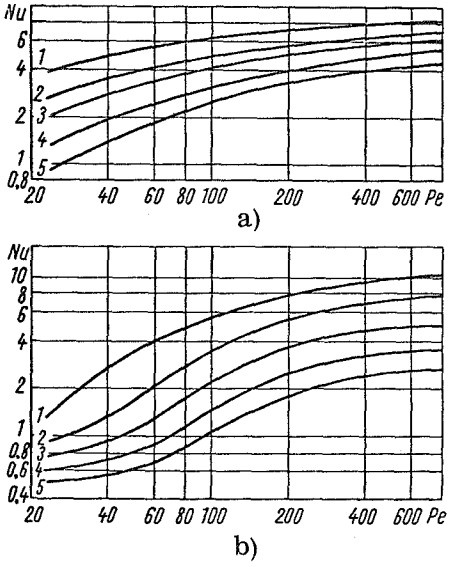

Figure 7. Nusselt Numbers as a Function of Pe for Ribbed Annuli With an Eccentricity of x = 0.25 (a) and x = 0.5 (b). 1, 2, 3, 4 and 5 are for l/d_h = 6, 13, 26, 52 and 79, Respectively.

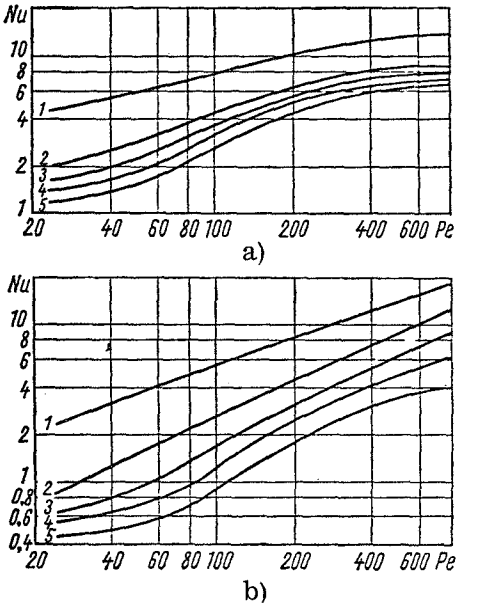

Figure 8. Nusselt Numbers as a Function of Pe for Ribless Annuli With an Eccentricy of x = 0.25 (a) and x = 0.5 (b). 1, 2, 3, 4 and 5 are for l/d_h = 6, 18, 25, 50 and 75, Respectively.

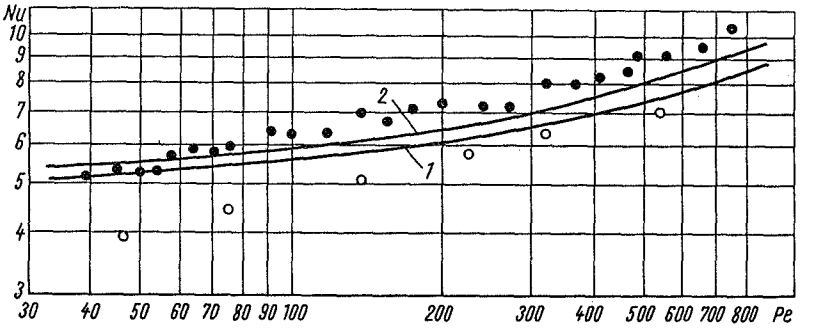

Figure 9. Average Heat Transfer in Concentric Annular Spaces for Stabilized Heat Transfer. ● and ○ Denote Experimental Data for a Ribless and Ribbed Annuli, Respectively; 1 and 2 Correspond to Calculations by Eqs. (4) and (5), Respectively.

2) no tangential heat fluxes take place in the fluid or wall; 3) on the heat conducting surface the specific thermal flux is the same in all points (q = const); 4) the flow is hydrodynamically stable.

The thermal balance of an elementary volume of the coolant, bounded by angle $d\varphi$, height dx and the passage's walls can be written as

$$qR_2 d\varphi\, dx = \frac{\partial t}{\partial x} dx \cdot U_\varphi\, d\omega\, C_p \gamma,$$

where U_φ is the average velocity through the elementary area;

$$d\omega = \frac{r_m^2 - R_2^2}{2} d\varphi; \qquad r_m = R_2 + y,$$

where y is the distance between the walls of the passage along the normal to the surface of the inside tube and R_2 is the outer radius of the inside tube. Transforming we get

$$\frac{\partial T}{\partial X} = \frac{2}{\mathrm{Pe} \frac{U_\varphi}{\bar{U}} \left(\frac{R_2}{d_h}\right) \left[\left(\frac{r_m}{R_2}\right)^2 - 1\right]}, \tag{6}$$

where $\bar{U}$ is the coolant velocity, averaged over the entire passage

$$T \equiv \frac{t\lambda_f}{qR_2}; \qquad X \equiv \frac{x}{R_2}.$$

Integrating Eq. (6) and transforming, we get

$$T = \frac{8(A-1)^2 Z}{\mathrm{Pe}\,\mu(2+\mu)} \cdot \frac{\bar{U}}{U_\varphi}, \tag{7}$$

where $\mu \equiv y/R_2$; $A = D/2R_2$ is the ratio of the diameters of the outside and inside tubes and $Z = x/d_h$ is a dimensionless coordinate along the passage.

To find the velocity distribution we assume, by analogy with [6] that the d'Arcy formula is valid for each elementary area $d\omega$, if for the characteristic /121

length we take twice the space 2y (local hydraulic diameter), and for the characteristic velocity we take the average velocity (U_φ) in the elementary area

$$\frac{dp}{dx}=\frac{\xi}{2y}\cdot\frac{\rho U_\varphi^2}{2}.$$

For the entire annulus $dp/dx = \bar{\xi}/2y\cdot\frac{\rho U_\varphi^2}{2}$. Assuming that the local and average coefficients of frictional resistance ξ and $\bar{\xi}$ are described by the same law, for example, by the Blasius formula $\xi = 0.316/Re^{0.25}$, we will get from the last two equations

$$\frac{U_\varphi}{\bar{U}}=\left(\frac{y}{\bar{y}}\right)^n=\left(\frac{\mu}{A-1}\right)^n, \tag{8}$$

where $n = 0.715$. If we assume that $\xi \simeq \bar{\xi}$, as this was done in [6], then $n = 0.5$. The velocity distribution calculated from Eq. (8) with $n = 0.715$ is in satisfactory agreement with experimental data obtained in [7].

Finally, from Eqs. (7) and (8) we get

$$T=\frac{8z}{Pe}\cdot\frac{(A-1)^{2.715}}{\mu^{1.715}(2+\mu)}. \tag{9}$$

Despite the large number of assumptions made, analytical calculations using Eq. (9) yield satisfactory results, which is attested to by Table 1. Consequently, the assumptions we have made [do] reflect the heat transfer process at the inlet section of the annular space under study. /122

The above experimental data were obtained for a uniform heat supply to the inner surface of the inside tube of the passage ($q \approx$ const at R_1). However, these data are just as valid for the case of uniform heat generation in the wall of the tube (q_v = const at $R_1 \leq r \leq R_2$), which was shown, for example, in [3]. In fact, the temperature field of the heat transfer surface does not depend on the method by which the tube is heated (q = const at R_1 or q_v = const in the wall), since the tangential heat fluxes are determined solely by the relative thickness and thermal conductivity of the tubes's wall under identical conditions in the fluid. The similarity parameter ε_k characterizing the properties and dimension of the tube is in both cases described by Eq. (3).

The inside tube used in the experiments can be regarded as thin-walled [3], since the magnitude of ε_k/k depends little on the number of the harmonic (k) of the

TABLE 1. Comparison of Results Calculated From Eq. (9) With Experimental Data for Ribless Eccentrical Annular Spaces

Eccentricity x		0.25			0.5		
Peclet numbers		79	234	568	82	234	558
$\frac{t_w^{max}-t_w^{min}}{\bar{q}R_2}\lambda_f$	Calculated	0,420	0,140	0,058	1,18	0,41	0,17
	Obtained experi.	0,364	0,112	0,045	1,30	0,38	0,15
Maximum disagreement, %		19	25	29	10	10	13

TABLE 2. Values of the Similarity Parameter ε_k for $\lambda_w/\lambda_f = 0.677$ and $\lambda_w\delta/\lambda_f R_2 = 0.0398$

Number of harmonic, k	1	2	3	4	5	6
ε_k obtained from Eq. (3)	0,0410	0,0808	0,1205	0,1590	0,1965	0,2330
ε_k/k	0.0410	0,0404	0,0402	0,0398	0,0393	0.0388

Fourier series, which can be seen from Table 2. Then it is possible to transform parameter ε_k to the simpler form

$$\varepsilon_k \simeq \frac{\lambda_w \delta}{\lambda_f R_2}, \quad \delta \equiv R_2 - R_1. \tag{10}$$

In our case $\varepsilon_k = 0.398$, hence the results obtained in the experiments are valid for passages in which the parameters of the thin-walled inside tubes satisfy the conditions

$$\frac{\lambda_w \delta}{\lambda_f R_2} \simeq 0{,}04; \quad \mathrm{Pr} \ll 1.$$

The method of approximate thermal simulation presented in [3] makes it possible to use the data we have obtained for calculating a given group of fuel element rods.

REFERENCES

1. Stein, R. and Begell, W.A.I.Ch.E. Journal, vol. 4, No. 2, 127 (1958).
2. Marin, N.I., et al.: Atomnaya energiya, 18, 3, 239 (1965).
3. Ushakov, P.A.: Priblizhennoye teplovoye modelirovaniye tsilindricheskikh teplovydelyayushchikh elementov [Approximate Thermal Simulation of Cylindrical Fuel Elements]. First article in Part II of present collection.
4. Harrison, W. and Menke, J.: Trans. ASME, 71, 797 (1949). /123
5. Subbotin, V.I., et al.: Atomnaya energiya, 9, 4, 310 (1960).
6. Khabakhpasheva, Ye.M. and Korsun, A.S.: In the collection Zhidkiye metally [Liquid Metals], page 34, Gosatomizdat, Moscow, 1963.
7. Levchenko, Yu.D., et al.: Gidrodinamika v kol'tsevom zazore s prodol'nymi rebrami [Fluid Dynamics in an Annular Space With Longitudinal Ribs]. Article immediately preceding this one in the present collection.

TRANSFER OF HEAT IN TURBULENT FLOWS OF FLUIDS IN ANNULAR AND PLANE SPACES

N. I. Buleyev, V. A. Mosolova and L. D. Yel'tsova

This article presents calculations of temperature fields and heat transfer /123
coefficients for turbulent flows of fluids in annular and plane spaces. Use is made here of integral approximations for turbulent thermal conductivity coefficients [1].

The calculated Nu_1 and Nu_2, corresponding to one-sided internal or external heating of the fluid flow are represented in the form of functions of parameters Re, Pr and $\Theta = a_1/a_2$, where a_1 and a_2 are the radii of the inner and outer tubes, forming the space, respectively.

The calculated heat transfer coefficients for several fluids are compared with the available experimental data.

Statement of the Problem

Let us consider the steady temperature regime in a turbulent flow of a fluid in a space with the specified thermal fluxes q_1 and q_2 at the walls of the passage. The starting equation of the heat influx in the given case can be written in the form [1]

$$w\frac{\partial T}{\partial z}=\frac{1}{r}\frac{\partial}{\partial r}\left\{r\left(t+\varepsilon_t\right)\frac{\partial T}{\partial r}\right\}, \tag{1}$$

where

$$\varepsilon_t\left(M_0\right)=0{,}20L_0\int_{-\infty}^{\infty}F\left(\eta\right)f_0\left(q\eta\right)f_1\left(\lambda q\eta\right)G\left(\eta\right)d\eta, \tag{2}$$

and also

$$\eta=\frac{r-r_0}{042L_0},\quad F\left(\eta\right)=\begin{cases}L\left|\frac{\partial w}{\partial r}\right| & \text{when } \gamma_*>25\\ 0 & \text{when } \gamma_*\leqslant 25,\end{cases}$$

$$G\left(\eta\right)=\frac{1}{2}\left|\eta\right|e^{-\frac{1}{2}\eta^2},\quad f_0\left(x\right)=e^{-|x|},$$

$$f_1(x)=\frac{1}{|x|}(1-e^{-|x|}),$$ /124

$$q=\frac{75}{\gamma_*}\cdot\frac{L_0}{L},\quad \gamma_*=\frac{L^2}{\nu}\left|\frac{\partial w}{\partial r}\right|$$

$$\lambda=\begin{cases}0.8+0.2\left(\frac{k}{\nu}\right)^{0.67} & \text{when} \quad \frac{k}{\nu}>1,\\ 1 & \text{when} \quad \frac{k}{\nu}\leqslant 1.\end{cases}$$

Here T is the temperature of the fluid, ν, k and ε_t are the coefficients of molecular viscosity, molecular and turbulent thermal diffusivity respectively and L is the turbulence scale.

For calculating the coefficient ε_t using Eq. (1) we restrict ourselves by the dimensionless integration interval $-2.4 < \eta < 2.4$, i.e., by the interval $|r-r_0|\leq L_0$ [1]. The quadrature formulas for ε_t will have the form

$$\varepsilon_t(M_0)=0{,}20L_0\{0{,}15[D(-0{,}4)+D(0{,}4)]+$$
$$+0{,}23[D(-1{,}2)+D(1{,}2)]+0{,}12[D(-2,0)+D(2,0)]\},$$

where

$$D(\eta)=F(\eta)\cdot f_0(q\eta)\cdot f_1(\lambda q\eta).$$

To determine L in a cross section of a rectilinear passage of infinite length, [1] has suggested the approximation

$$\frac{1}{L(M)}=\frac{1}{2}\int_0^{2\pi}\frac{1}{l}\,d\varphi, \tag{3}$$

where $l(\varphi)$ is the distance between the point in question M to the perimeter of the passage cross section in the variable direction φ.

In Eqs. (1)-(3) we change to the dimensionless variables

$$\left.\begin{aligned}&\xi=\frac{r}{a_2},\quad \Theta=\frac{a_1}{a_2},\quad y=\frac{\xi-\Theta}{1-\Theta},\quad U=\frac{w}{v_*},\\ &\Phi=\frac{\tilde{a}v_*}{\nu},\ \mathrm{Re}=\frac{2\tilde{a}\bar{w}}{\nu}=2\bar{U}\Phi,\quad \zeta=\frac{8}{\bar{U}^2},\end{aligned}\right\} \tag{4}$$

where $\tilde{a}=a_2-a_1$, and $v_*^2=\frac{\tilde{a}}{2}\cdot\frac{1}{\rho}\left|\frac{\partial p}{\partial z}\right|=\frac{\zeta}{8}\bar{w}^2$.

For a duct with an annular cross section Eq. (3) for the turbulence scale L(M), making use of the notation of Eq. (4), yields the following results [2]

$$\frac{L}{a_2-a_1}=\frac{1}{B}(1-y)\,y, \tag{5}$$

where /125

$$B(\xi,\ \Theta)=\frac{1}{1+\xi}\frac{\zeta-\Theta}{1-\Theta}\left[2E\left(\xi,\frac{\pi}{2}\right)-E(\xi,\lambda)\right]+$$

$$+\frac{\Theta}{\xi+\Theta}\frac{1-\xi}{1-\Theta}\left[\frac{1-\Theta^2}{1-\xi^2}+\frac{\Theta}{\xi}H\left(\frac{\Theta}{\xi}\right)\right],$$

$$\sin\lambda=\frac{\Theta}{\xi},$$

$$E(k,\varphi)=\int_0^{\varphi}\sqrt{1-k^2\sin^2\alpha}\,d\alpha,$$

$$H(k)=\int_0^{\pi/2}\frac{\cos^2\alpha\cdot d\alpha}{\sqrt{1-k^2\sin\alpha}}.$$

The values of function $B(\xi,\Theta)$ are close to unity.

For the case of a plane space of width h, Eq. (3) takes on the simple form

$$\frac{L}{h}=(1-y)\,y, \tag{6}$$

where $y = l/h$ and l is the distance between variable point M and one of the plates forming the space.

To eliminate $\partial T/\partial z$ from Eq. (1) we use the balance equation, which is obtained by interating Eq. (1) along the radius from a_1 to a_2

$$c\rho\,(a_2^2-a_1^2)\,w\frac{\partial T}{\partial z}=2\,(a_1q_1+a_2q_2). \tag{7}$$

Substituting the value of $\partial T/\partial z$ from the above expression into Eq. (1), and using the notation of Eq. (4), we get

$$\frac{1}{\xi}\frac{\partial}{\partial y}\left\{\zeta\left(\frac{k}{\nu}+\frac{\varepsilon_t}{\nu}\right)\frac{\partial T}{\partial y}\right\}=\frac{2}{1-\Theta^2}\cdot\Phi\times\frac{\Theta q_1+q_2}{c\rho v_*}\cdot\frac{U}{\overline{U}}. \tag{8}$$

From the point of view of mathematics it is sufficient to examine only the case of heat supply from one side, since for the case of two-sided heating with arbitrary relationships between fluxes q_1 and q_2 the solution for temperature T can be represented in the form of a linear superposition of solutions for the case of only inside and only outside heat supplies.

Equation (8) was solved by a numerical method. Here coefficient ε_t was calculated from Eq. (2) using the field of velocities w obtained in [1].

Results of Calculations

Table 1 present the results of calculating the dimensionless temperatures /126

$$\Psi_i = \frac{c\rho v_* (T_1 - T)}{q_1}$$

in the flow of fluid in the space for a given constant thermal flux q_1 at the internal wall of the space and the dimensionless temperatures

$$\Psi_2 = \frac{c\rho v_* (T_2 - T)}{q_2}$$

for a given thermal flux q_2 at the inner wall of the space. Here T_1 and T_2 are the temperatures of the inner and outer walls of the space, respectively.

If we introduce the concepts

$$\mathrm{Nu}_1 = \frac{2\tilde{a} q_1}{\lambda (T_1 - \bar{T})} = \frac{2\Phi \cdot \mathrm{Pr}}{\bar{\Psi}_1} \quad \text{and} \quad \mathrm{Nu}_2 = \frac{2\tilde{a} q_2}{\lambda (T_2 - \bar{T})} = \frac{2\Phi \cdot \mathrm{Pr}}{\bar{\Psi}_2}$$

for the corresponding cases of heating from one side, then the following can be said about the results of calculations of Nu_1 and Nu_2 in annular spaces. First of all, the calculated Nu_1 are greater than Nu_2. As parameter Θ becomes larger, /127 the difference in the calculated values of the above two Nusselt numbers, naturally, decreases (Table 1). For a specified value of Θ the relative difference between Nu_1 and Nu_2 is reduced with an increase in the Reynolds number. There exists a tendency toward the reduction in the relative difference between Nu_1 and Nu_2 with an increase in the Prandtl number.

TABLE 1. Calculated Average Temperatures $\bar{\Psi}_1$ and $\bar{\Psi}_2$ and of Nu_1 and Nu_2 in Spaces With the Flow of Fluid Heated From One Side

		$\Theta=0.5$			$\Theta=0.8$			$\Theta=1$		
Pr	$Re\cdot10^{-3}$	9.30	46.7	219	9.22	47.5	221	14.1	69.6	322
0.025	$\bar{\Psi}_1$	2.24	5.68	9.55	2.44	5.99	10.0			
	$\bar{\Psi}_2$	2.57	6.29	10.4	2.56	6.17	10.2	3.22	7.14	10.9
	Nu_1	7.00	11.0	26.2	6.52	10.6	25.4			
	Nu_2	6.11	9.94	24.1	6.21	10.3	24.9	6.89	12.6	32.6
0.8	$\bar{\Psi}_1$	18.2	21.7	24.2	19.6	22.7	24.5			
	$\bar{\Psi}_2$	20.4	23.0	25.4	20.8	23.5	25.4	21.5	24.2	26.2
	Nu_1	27.6	92.2	331	26.0	89.5	332			
	Nu_2	24.6	87.0	316	24.5	86.5	320	33.0	117	434
10	Ψ_2							76.2	72.5	73.6
	Nu_2							116	490	1930

Figures 1 and 2 show the temperature distributions calculated in fluid flows in spaces with $\Theta = 0.5$-1 at different values of the Reynolds number and with the heat supplied to the fluid from one side. For the selected dimensionless variables, $\tilde{a}$, Nu and Re the calculated Nu_2 for the space are lower as compared with the Nusselt numbers calculated for a pipe with the same Re, particularly numbers increase rapidly when Θ is increased from 0 to 0.5. When Θ is increased from 0.5 to 1, but with the Reynolds number kept constant, the calculated Nu_2 remain practically constant.[1]

For spaces with $\Theta = 0.5$-1 for $5\cdot10^3 < Re < 5\cdot10^5$ the calculated Nu_2 differ from the Nusselt numbers for a pipe by approximately 25% in the case of fluids

[1]Reference [3] presents calculations for Nu_1 and Nu_2 in annular spaces for fluid flows with low Prandtl numbers, there the values of ε_t needed for the calculations were calculated on the basis of the latest measurements of the fields of velocities w in the spaces. All that has been said above about Nu_1 and Nu_2 calculated in the present article for fluids with $Pr \leq 1$ is in satisfactory agreement with results of calculations of [3].

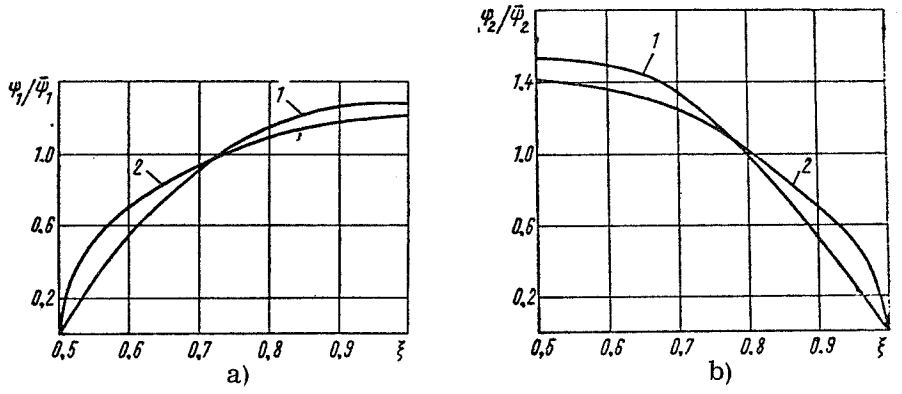

Figure 1. Calculated Temperature Distributions in the Flow of a Fluid in a Space With the Heat Supplied Through the Inside (a) and the Outside (b) Wall; Ⓗ = 0.5, Pr = 0.025; Curves 1 and 2 are for $Re = 9.3 \cdot 10^3$ and $Re = 2.2 \cdot 10^5$.

with low Prandtl numbers and by 10-15% for gases (Fig. 3). In the case of fluids /128
with Pr = 10 the calculated values of Nu_2 for the space practically do not differ from the Nusselt numbers for a pipe at the same Re.

The values of Nu_2 calculated for liquid metals with Ⓗ = 0.5-1 can be approximated by the expression

$$Nu = 5.0 + 0.020Pe^{0.8}. \quad (9)$$

For gas flowing in spaces with Ⓗ = 0.5-1 the following expression will be approximately valid

$$Nu = 0.018Re^{0.8} \cdot Pr^{0.4}. \quad (10)$$

The structure of interpolation formulas (9) and (10) has been made traditional purposely, for convenience in comparing results obtained in the present paper with results for a pipe and spaces from other publications. Equation (9) yields somewhat higher values of Nusselt numbers than that given in [4] and of almost identical with the equation presented in [5].

For known values of functions $\Psi_1(\xi)$ and $\Psi_2(\xi)$ the distributions of temperature T in the flow of a fluid heated from both sides with an arbitrary relationship between fluxes Q_1 and Q_2 can be calculated by the following formula (Fig. 4).

$$c\rho v_* (T_2 - T) = q_2 \Psi_2(\xi) + q_1 [\Psi_1(\xi) - \Psi_1(1)]. \quad (11)$$

Table 2 presents the calculated values of the average dimensionless temperature $\overline{\Psi} = c\rho v_* (T_2 - T/q_2$ and of $Nu^* = 2\Phi \cdot Pr/\overline{\Psi}$ in the flow of a fluid in a plane space with symmetrical heat supply from two sides. The values of Nu* obtained for the plane space can be related to the Nusselt numbers obtained on heating from one side by the following approximate expression

$$Nu^* = 8{,}6 + [1{,}50 - 0{.}15 \lg (1 + 100Pr)] (Nu - 5{.}0) \qquad (12)$$

which is valid for fluids with Pr = 0-10. When > 10 it may be assumed that Nu* = = Nu.[2]

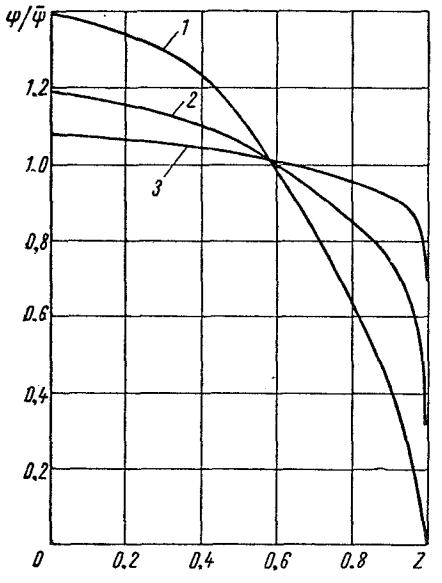

Figure 2. Temperature Distributions Calculated in the Flows of Various Fluids in a Flat Space (Θ = 1) With Heat Supplied From One Side; Re = $= 6.96 \cdot 10^4$; Curves 1, 2, 3 are for Pr = 0.025, 0.8 and 10, Respectively.

TABLE 2. Calculated Average Temperatures $\overline{\Psi}$ and Nu* in the Flow of a Fluid in a Plane Space With the Fluid Heated Symmetrically From Two Sides

Pr		10^4 Re		
		1.41	6,96	32,2
0.025	$\overline{\Psi}$	1,89	4,42	7.41
	Nu*	11,7	20,1	47.8
0,8	$\overline{\Psi}$	16,5	19,3	22,6
	Nu*	43,0	147	503
10	$\overline{\Psi}$	6967	68,5	69.6
	Nu*	128	519	2040

Figure 5 compares the calculated Nu and Nu* for flows of liquid metals in a plane space with experimental data of [7]. As can be seen from this figure, the theoretical and experimental results are in good agreement. The calculated Nusselt numbers for the flow of gas in a plane space are in good agreement with results obtained by Doroshchuk, [8]. On the other /130

[2] The results provided by Eqs. (9), (10) and (12) were obtained by the authors earlier, when using the arrangement suggested in [6] for calculating the velocity and temperature fields in the passage. Equations (10) and (12) are presented in [7].

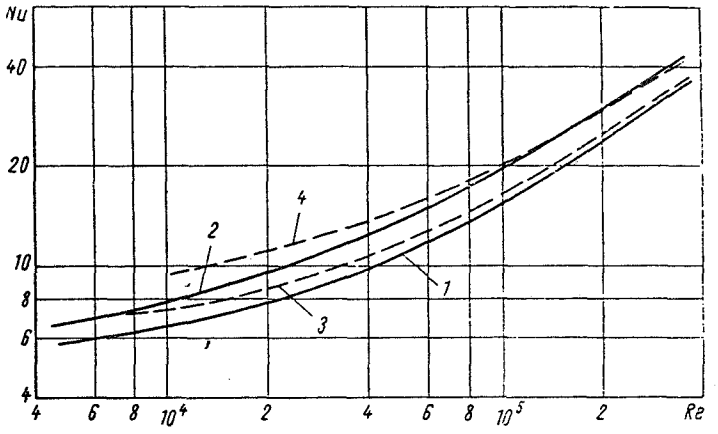

a)

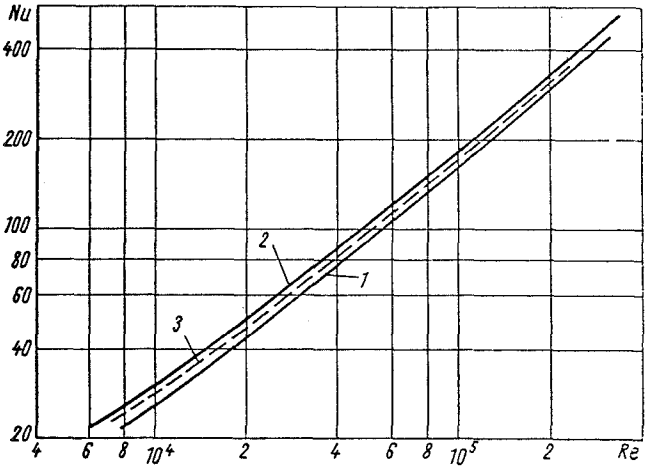

b)

Figure 3. Calculated Nusselt Numbers for a Flow of Fluid in a Space With Heat Supplied From One Side; Pr = 0.025 (a), Pr = 0.8 (b). 1) Ⓗ = 0.5-1 (Heating From the Outside; 2) Ⓗ = 0 (Round Pipe); 3) Ⓗ = 0.5 (Heating From the Inside); 4) Ⓗ = 0.2 (Heating From the Inside).

hand, the calculated heat transfer attendant to the flow of fluid in a space with Pr = 10 are in agreement with measurements made by Mikheyev and others [9] /131
pertaining to the small difference between Nu_1 and Nu_2, as well as with respect to bringing these numbers close to the Nusselt numbers in a pipe for the same Reynolds numbers.

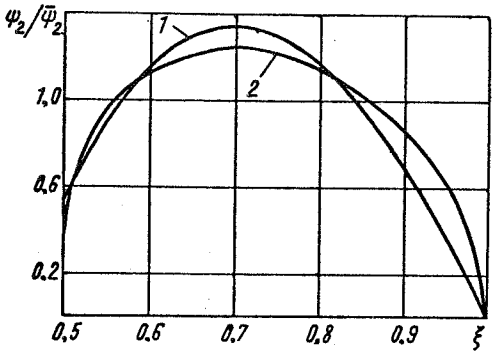

Figure 4. Temperature Distributions Calculated in the Flow of a Fluid in a Gap Heated From Two Sides; ⊛ = 0.5; $q_1/q_2 = 1$, Pr = = 0.025; Curves 1 and 2 are for $Re = 9.3 \cdot 10^3$ and $Re = 2.2 \cdot 10^5$.

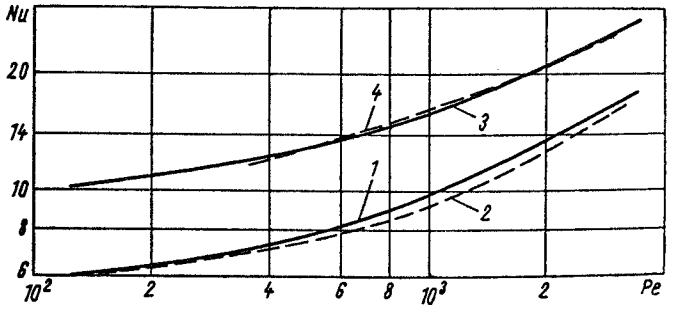

Figure 5. Calculated Nusselt Numbers for Flows of Liquid Metals in a Plane Space; the Experimental Data are That of [7]. 1) and 2) are Values Obtained Theoretically and Experimentally, Respectively, for Heating From One Side; 3) and 4) are Values Obtained Theoretically and Experimentally, Respectively, for Symmetrical Heating From Two Sides.

REFERENCES

1. Buleyev, N.I.: Teoreticheskaya model' turbulentnogo obmena v trekhmernom potoke zhidkosti [Theoretical Model of Turbulent Transfer in a Three-Dimensional Flow of Fluids]. Report presented at the 3rd International Conference on Peaceful Uses of Atomic Energy. Geneva, 1964.
2. Buleyev, N.I.: Teoreticheskaya model' mekhanizma turbulentnogo obmena v potokakh zhidkosti [Theoretical Model of the Mechanism of Turbulent Transfer in Flows of Fluids]. In the collection Teploperedacha [Heat Transfer]. Published by the Academy of Sciences of the USSR, Moscow, 1962.
3. Dwyer, O.E. and Tu, P.S.: Nucl. Sci. Engng, 15, No. 1 (1963).
4. Harrison, W.B. and Menke, J.R.: Trans. ASME, 71, 797 (1949).
5. Seban, R.A.: Trans. ASME, 72, 789 (1950).

6. Buleyev, N.I.: Raspredeleniye skorosti i temperatury v turbulentnom potoke zhidkosti v krugloy trube [Velocity and Temperature Distributions in the Turbulent Flow of a Fluid in a Pipe]. In the collection Voprosy teploobmena [Problems Heat Transfer]. Published by the Academy of Sciences of the USSR, Moscow, 1959.
7. Subbotin, V.I., et al.: Atomnaya energiya, 9, No. 4 (1960).
8. Doroshchuk, V.Ye. and Frid, F.P.: Energomashinostroyeniye, No. 11 (1959).
9. Averin, Ye.K., et al.: In the collection Teploperedacha i teplovoye modelirovaniye [Heat Transfer and Thermal Simulation], page 138. Published by the Academy of Sciences of the USSR. Moscow, 1959.

EXPERIMENTAL STUDY OF HEAT TRANSFER FROM A FLAT HORIZONTAL SURFACE TO SODIUM BY FREE CONVECTION

A. P. Kudryatsev, D. M. Ovechkin, D. N. Sorokin,
V. I. Subbotin and A. A. Tsyganok

The experiments described in this article were performed in order to compare the levels of heat transfer on boiling [1], [2] and free convection. In addition, they were of independent interest since we know of only two publications devoted to the study of heat transfer from a horizontal surface to liquid metals under free convection conditions, [3] and [4]. /131 /132

Reference 3 concerns itself with heat transfer from sodium, which gives up its heat to a flat round plate from stainless steel 203 mm in diameter which is located approximately 3 mm below the free level of the sodium, which is contained in a tank 760 mm in diameter. The sodium was heated by furnaces situated outside the tank. The experiments were performed with sodium temperatures in the range of 140-350°C. On the basis of experimental data it was found in [3] that

$$\mathrm{Nu} = 0.262\,(\mathrm{Gr}\cdot\mathrm{Pr}^2)^{0.35}. \qquad (1)$$

The characteristic dimension in the above expression is the diameter of the plate. On the basis of the power of $(\mathrm{Gr}\cdot\mathrm{Pr}^2)$ in the above expression, it is assumed in [3] that the heat transfer took place in the turbulent region.

Experiments with mercury situated between two horizontal chromium plated (electroplated) copper plates are described in [4]. Here use was made of plates 134 mm in diameter held at distances of 35 and 66.5 mm from one another. The lower plate was heated while the top plate was cooled. The data thus obtained can be expressed thus

$$\mathrm{Nu} = 0.069\,(\mathrm{Gr}\cdot\mathrm{Pr})^{1/3}\cdot\mathrm{Pr}^{0.074}. \qquad (2)$$

The characteristic dimension here was the distance between the plates.

Our experiments were performed with flat horizontal surfaces from 1Kh18N9T stainless steel 38 mm in diameter, which was heated by electron bombardment. The heat transfer surface was placed in a work tank from stainless steel 165 mm in diameter. The sodium level above the surface was about 150 mm. Chromel-alumel thermocouples, which measured the temperatures of the heat conducting wall were placed in protective capillaries from 1Kh18N9T

stainless steel 0.8 x 1.5 mm in diameter, which were then covered by molten copper under a vacuum (thermocouple wire diameter 0.2 mm). The temperature of the sodium was measured by chromel-alumel thermocouples placed in a sleeve (thermocouple wire diameter 0.5 mm), the beads of which were located by ~ 60 mm above the heat conducting surface. Such an arrangement is also described in [5].

We have measured the temperature differences between the wall and the liquid and the temperature of the sodium, as well as the temperature fields in the latter using a moving thermocouple. The readings of the thermocouples, including the movable one, which was connected differentially with the stationary thermocouple, were recorded continuously by EPP-09 potentiometers (1 sec) and were also measured intermittently by the R-2/1 potentiometer. We have performed four series of test. In all of them the sodium was held under inert gas pressure of about 2 atm absolute. The regime of the heat transfer agent (laminar or turbulent) was determined on the basis of temperature fluctuations recorded by the movable thermocouple and by the thermocouples in the wall.

Results of Experiments for the Turbulent Region

$q \cdot 10^{-6}$ kcal/(m^2 · hr)	Δt, degs.	t_l, degs.	$q \cdot 10^{-6}$, kcal/(m^2 · hr)	Δt, degs.	t_l, degs.
1 Series			2 Series		
			0.77	80.2	300
0.74	89.9	254	1.12	105	324
1.51	140	281	1.53	135	419
1.12	120	294	3 Series		
0.74	99.4	518	0.72	80.6	481
0.69	94.2	572	0.93	101	518
1.08	133	634	1.11	121	555
0.71	86.1	660	1.31	138	592
1.52	146	680	1.50	150	621
0.95	114	682	4 Series		
0.70	86.3	694	0.71	74.5	550
0.70	95.4	699	1.06	107	690
1.00	127	719	1.46	136	733
1.43	139	734			

For thermal fluxes below $0.7 \cdot 10^6$ kcal/m^2-hour neither the movable thermocouple, situated near the wall, nor the thermocouples built into the wall recorded any temperature fluctuations. When the heat fluxes were made large, both the movable and the stationary thermocouples record temperature fluctuations. At a distance of more than approximately 15 mm from the heat conducting surface no temperature fluctuations have been observed for thermal fluxes of up to $1.5 \cdot 10^6$ kcal/m^2-hour. The presence of fluctuations shows that the fluid flow at the heated surface is turbulent. For thermal fluxes of $(0.7\text{-}0.9) \cdot 10^6$ kcal/m^2--hour, which correspond to transition from the laminar to turbulent heat transfer

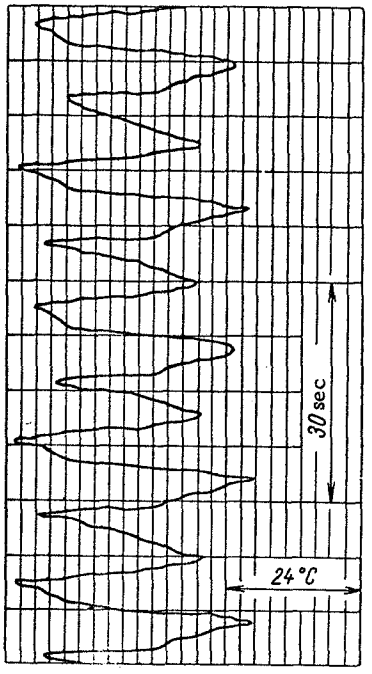

Figure 1. Record of the Readings of the Movable Thermocouple, Touching the Wall.

regime, the Grashof number is about 10^8, which agrees with data obtained by Fedynskiy [6], who has found that transition from laminar to turbulent flow takes place at $Gr > 1.5 \cdot 10^8$, irrespective of the Prandtl number. Figure 1 shows a recording of the readings of the movable thermocouple in contact with the wall for $q = 0.95 \cdot 10^6$ kcal/m^2-hour and $t_1 = 682°C$.

Figure 2 displays temperature distributions in the sodium obtained by the movable thermocouple for three values of the thermal flux. The dashed line denotes the position of the center of the movable thermocouple's junction at the instant it touches the wall. The heat transfer coefficients α, calculated on the basis of the temperature differences between the wall and the liquid and on the basis of the temperature measured by the movable thermocouple in the liquid next to the wall, with subsequent extrapolation of the temperature to the wall, are in satisfactory agreement. For example, α determined by the temperature difference for thermal flux values of $(0.35, 0.95, 1.53) \cdot 10^6$ kcal/m-hour comprise $6.75 \cdot 10^3$, $8.35 \cdot 10^3$ and $11.3 \cdot 10^3$, respectively, while α determined from the temperature distributions constructed in Fig. 2 comprise, respectively, $7.96 \cdot 10^3$, $8.64 \cdot 10^3$ and $13.3 \cdot 10^3$ kcal/m-hour-degree. /134

It is recommended in [6], on the basis of analysis of differential equations, that the experimental data on heat transfer by free convection of liquid metals be processed in the coordinates $Nu - Cr \cdot Pr^2$, i.e., without giving consideration to the viscosity. Using these coordinates we have constructed (Fig. 3) the experimental curves for the turbulent region. These points have a scatter of ±15% about averaging curve 1, which represents the relationship

$$Nu = 0.38 (Gr \cdot Pr^2)^{1/3}. \quad (3)$$

The characteristic temperature here is the temperature of the fluid far from the wall. If the wall temperature is taken as the characteristic temperature, then the results will differ by approximately 4.6%, since the temperature difference between the wall and the liquid metal in our experiments did not exceed 150°C. The physical properties of sodium used in the calculations are those given in [7] and [8]. The diameter of the heat conducting surface (38 mm) was taken as the characteristic dimension.

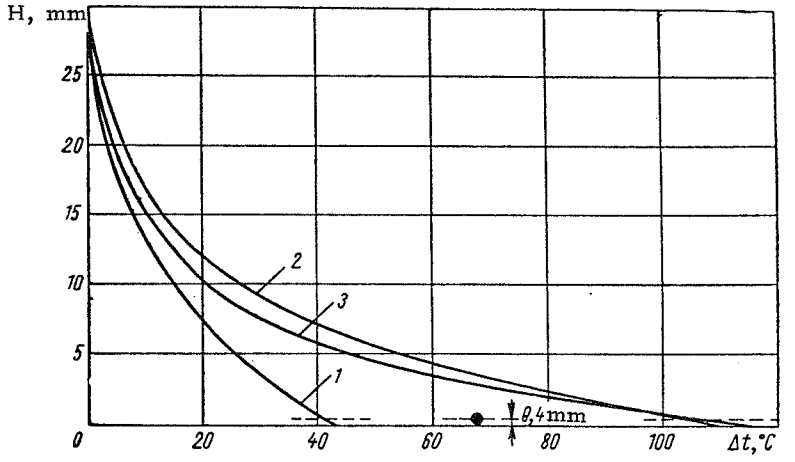

Figure 2. Temperature Distributions for Sodium, Constructed on the Basis of Readings of the Movable Thermocouple. The Dashed Line Denotes the Position of the Center of the Junction of the Movable Thermocouple at the Instant When the Latter is in Contact With the Wall.

Curve 1 = $0.35 \cdot 10^6$; Curve 2 = $0.95 \cdot 10^6$;
Curve 3 = $1.53 \cdot 10^6$ kcal/m^2-Hour.

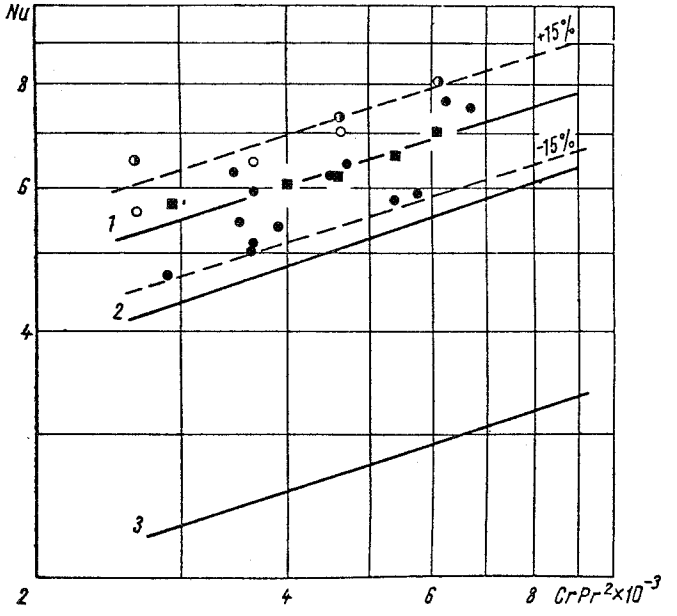

Figure 3. Experimental Data on Heat Transfer. Test Series: ● - First; ○ - Second; ■ - Third; ◑ - Fourth. 1) Obtained From Eq. (3); 2) Obtained From Eq. (1); 3) Obtained From Eq. (4).

Reference [6] recommends to use the following formulas for heat transfer calculations in liquid metals by free convection under turbulent and laminar regimes

$$\mathrm{Nu} = 0.16 \left(\frac{\mathrm{Gr} \cdot \mathrm{Pr}^2}{1 + \mathrm{Pr}} \right)^{1/3}, \tag{4}$$

$$\mathrm{Nu} = 0.67 \left(\frac{\mathrm{Gr} \cdot \mathrm{Pr}^2}{1 + \mathrm{Pr}} \right)^{1/4} \tag{5}$$

Line 3 of Fig. 3 was obtained by using Eq. (4). If the Nusselt numbers are calculated from Eqs. (4) and (5) at a sodium temperature of 500°, then Eq. (4) yields Nusselt numbers approximately two-fold smaller than Eq. (5) for a Grashof number of about 10^8 ($\mathrm{Gr} \cdot \mathrm{Pr}^2 \sim 2.5 \cdot 10^3$), which corresponds to transition to turbulent flow. Equations (4) and (5) yield identical values of the Nusselt number only when $\mathrm{Gr} \sim 10^{12}$. Consequently, Eq. (4) is incorrect. /136

Equation (5) is in satisfactory agreement with Eq. (3) when $\mathrm{Gr} \cdot \mathrm{Pr}^2 = 2.5 \cdot 10^3$, i.e., at the start of the turbulent heat-transfer region. In the interval of $\mathrm{Gr} \cdot \mathrm{Pr}^2$ of about from $2.5 \cdot 10^3$ to $8 \cdot 10^3$ Eq. (1) (line 2) yields values of Nu by about 25% lower than Eq. (3). If the values of α are calculated from Eq. (2) for the turbulent region [$q > 0.7\ 10$ kcal/m^2-hour], then they lie by about 20% lower than the average value of data obtained by us. Equation (5) is in satisfactory agreement with our experimental points obtained with low thermal fluxes, i.e., in the laminar region (points not shown).

It thus may be assumed that Eqs. (1)-(3) reflect the level of heat transfer to liquid metals by free convection in the turbulent region, while Eq. (5) is valid for laminar flow.

REFERENCES

1. Subbotin, V.I., et al.: Teploperedacha v elementakh reaktorov, okhlazhdayemykh zhidkim metallom [Heat Transfer in Reactor Elements Cooled by Liquid Metals]. Report presented at the 3rd International Conference on the Peaceful Uses of Atomic Energy. Geneva, 1964.
2. Kudryatsev, A.P., et al.: Teplootdacha pri kipenii natriya v bol'shom ob"yeme [Heat Transfer From Boiling Sodium in a Large Volume]. Part III of present collection.
3. Donald, M. and Conolly T.: Nucl. Sci. Engng, 8, No. 5 (1960).
4. Globe, S. and Dropkin, D.: Trans. ASME, 81, 24—30 (1959).
5. Ivashkevich, A.A., et al.: Ustanovka s elektronnym obogrevom dlya issledovaniya teploobmena pri kipenii metallov v usloviyakh svobodnoy konvektsii [Setup with Electronic Heating for the Study of Heat Transfer From Boiling Metals By Free Convection]. Part III of present collection.

6. Kutateladze, S.S., et al.: Zhidkometallicheskiye teplonositeli [Liquid-Metal Heat Transfer Agents]. Atomizdat, Moscow, 1958.
7. Vargaftik, N.B.: Spravochnik po teplofizicheskim svoystvam gazov i zhidkostey [Handbook of Thermophysical Properties of Gases and Liquids]. Fizmatgiz, Moscow, 1963.
8. Zhidkometallicheskiye teplonositeli [Liquid-Metal Heat Transfer Agents]. A.Ye. Sheyndlin, Editor, translated from English. Foreign Lit. Pub. House, Moscow, 1958.

PART TWO

HEAT TRANSFER AND FLUID DYNAMICS OF INTRICATELY-SHAPED PASSAGES

APPROXIMATE THERMAL SIMULATION OF CYLINDRICAL FUEL-ELEMENT RODS

P. A. Ushakov

In reactors with liquid-metal cooling use is made most frequently of fuel /137
rods (fuel elements), arranged either in the form of regular triangular or square lattices, or placed in clusters or one-by-one in separate ducts. The geometry of the passages created by the rod clusters or of the individual ducts is responsible for the appearance of variations in the temperature over the fuel rod periphery. This variation produces additional thermal stresses, i.e., local overheating, which reduces the reliability of the fuel elements.

The lack of uniformity in the fuel element temperature, all other conditions remaining equal, is due to the thermal conductivity and on the dimensions of its /138
component parts, i.e., the fissionable-material core, protective jackets, contact layers, etc. All this should be taken into account in thermal simulation of fuel elements.

Let us consider a fuel rod with three shells [jackets]. The more elementary fuel elements are particular cases of the above. Let us assume that ideal thermal contacts exist between the shells, between the rod and the first shell, as well as between the outer shell and the coolant; the physical parameters of the system are constant and do not depend on the temperature, the fluid is incompressible and does not change its state of aggregation, the effect of natural convection is negligible and the heat generation in the rod is uniform.

We now analyze equations for laminar flow of the fluid assuming that the similarity criteria which will be thus found are valid also for turbulent flow which, on the average, is steady with respect to time. On these assumptions the equation of motion for the fluid

$$\frac{dg}{R_4}\frac{1}{\mathrm{Re}}\nabla^2\mathbf{W} - \operatorname{grad}\varepsilon_u - (\mathbf{W}, \operatorname{grad})\,\mathbf{W} = 0. \qquad (1)$$

Equation for the heat propagation through the fluid

$$\frac{dg}{R_4}\frac{1}{\mathrm{Pe}}\nabla^2 T_f - (\mathbf{W}\operatorname{grad} T_f) = 0. \qquad (2)$$

The temperature fields in the fuel rod and in the shells are described, respectively, by the Poisson and Laplace equations

$$\nabla^2 T_0 + 2\frac{\lambda_f}{\lambda_0}\frac{1}{\xi_1^2} = 0, \tag{3}$$

$$\nabla^2 T_1 = 0, \quad \nabla^2 T_2 = 0, \quad \nabla^2 T_3 = 0. \tag{4}$$

The boundary conditions

$$\left.\begin{aligned} &\text{when } \xi = 0 \quad \frac{\partial T_0}{\partial \xi} = 0; \\ &\text{when } \xi = \xi_1 \quad T_0 = T_1; \ \frac{\partial T_0}{\partial \xi} = \frac{\lambda_1}{\lambda_0}\frac{\partial T_1}{\partial \xi}; \\ &\text{when } \xi = \xi_2 \quad T_1 = T_2; \ \frac{\partial T_1}{\partial \xi} = \frac{\lambda_2}{\lambda_1}\frac{\partial T_2}{\partial \xi}; \\ &\text{when } \xi = \xi_3 \quad T_2 = T_3; \ \frac{\partial T_2}{\partial \xi} = \frac{\lambda_3}{\lambda_2}\frac{\partial T_3}{\partial \xi}; \end{aligned}\right\} \tag{5}$$

$$\text{when } \xi = 1 \quad T_3 = T_f; \ \frac{\partial T_3}{\partial \xi} = \frac{\lambda_f}{\lambda_3}\frac{\partial T_f}{\partial \xi}. \tag{6}$$

Here we have used the notation /139

$W = \frac{\omega}{\bar{u}}$; $T_i = \frac{t_i \lambda_f}{\bar{q} R_4}$; $\xi = \frac{r}{R_4}$, $\xi_i = \frac{R_i}{R_4}$; $\bar{q} = q_v \frac{R_1^2}{2R_4}$ is the specific thermal flux at the heat-conducting surface (when $\xi = 1$), d_h is the equivalent hydraulic diameter of the passage, and $\varepsilon_u = \Delta p/\rho \bar{u}^2$ is the Euler number, which is a function of Re. The remaining notation is shown in Fig. 1.

Analyzing Eqs. (3) and (4) and boundary conditions (5) we can find a relationship between the temperature distribution and the distribution of thermal fluxes over the perimeter of the outer shell [jacket] of the fuel element ($\xi = 1$)

$$T_w = \bar{T}_w + \sum_{k=1}^{\infty} a_k \cos k\varphi, \tag{7}$$

$$\frac{q}{\bar{q}} = 1 - \sum_{k=1}^{\infty} k a_k \varepsilon_k \cos k\varphi, \tag{8}$$

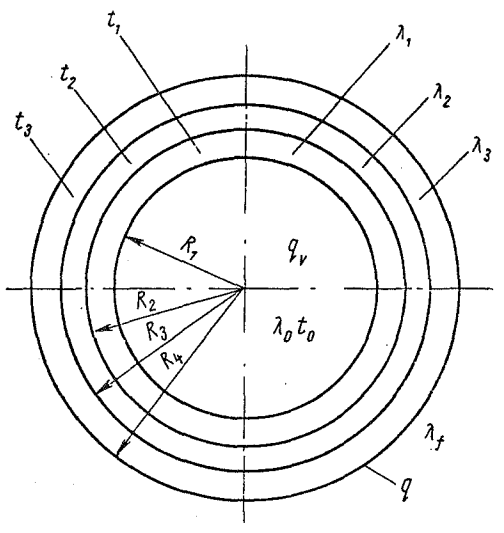

Figure 1. Schematic of a Fuel Rod [Cross Section] With Three Shields [Jackets].

$T_w \equiv T_3(\varphi, 1, Z)$, where Z is a dimensionless distance along the passage and φ is an angle, measured over the rod's perimeter. Without detriment to generality of the problem, we may assume that the functions being considered are even and thus to drop the sine terms in the series.

Parameter ε_k which characterizes the thermophysical properties of the fuel element can be found analytically. The Fourier series coefficients can be represented in the form

$$a_k = \frac{2}{\pi}\int_0^{\pi} T_3(\varphi, 1, Z)\cos k\varphi\, d\varphi = \frac{2}{\pi}\int_0^{\pi} T_f(\varphi, 1, Z)\cos k\varphi\, d\varphi.$$

The specific thermal flux is related to the temperature gradient of the fluid

$$\frac{q}{\bar{q}} = -\left.\frac{\partial T_f}{\partial \xi}\right|_{\xi=1},$$

hence we can write Eqs. (7) and (8) in the form

$$T_f(\varphi, 1, Z) = \overline{T_f}(1, Z) + \sum_{k=1}^{\infty}\left[\frac{2}{\pi}\int_0^{\pi} T_f(\varphi, 1, Z)\cos k\varphi\, d\varphi\right]\cos k\varphi, \tag{9}$$

$$-\left.\frac{\partial T_f}{\partial \xi}\right|_{\xi=1} = 1 - \sum_{k=1}^{\infty} k\varepsilon_k\left[\frac{2}{\pi}\int_0^{\pi} T_f(\varphi, 1, Z)\cos k\varphi\, d\varphi\right]\cos k\varphi. \tag{10}$$

From the above two equations, together with Eqs. (1) and (2) we get the criterial equation for geometrically similar channels

$$T_f(\varphi, \xi, Z) = f(\varphi, \xi, Z, \mathrm{Re}, \mathrm{Pe}, \varepsilon_k). \tag{11}$$

We now find ε_k. The solution of the [above] system of equations for the fuel element is most conveniently represented in the form of a sum of two solutions /140

$$T_i(\varphi, \xi, Z) = \Theta_i(\xi, Z) + \Psi_i(\varphi, \xi, Z), \tag{12}$$

where Θ is a solution which takes into account heat generation in the core at constant temperature along the perimeter of the outer shell $\xi = 1$: $\Theta(1, Z) = \overline{T}_w(Z)$, while Ψ is a solution for the case when there is no heat generation in the rod, but the temperature varies over the perimeter of the outer shell, i.e., when $\xi = 1$: $\Psi(\varphi, 1, Z) = \sum_{k=1}^{\infty} a_k(Z) \cos k\varphi$.

Solutions for $\Theta(\xi, Z)$

$$\left.\begin{aligned}
\Theta_0 &= \overline{T}_w + \frac{\lambda_f}{\lambda_3}\ln\frac{1}{\xi_3} + \frac{\lambda_f}{\lambda_2}\ln\frac{\xi_3}{\xi_2} + \frac{\lambda_f}{\lambda_1}\ln\frac{\xi_2}{\xi_1} + \frac{1}{2}\frac{\lambda_f}{\lambda_0}\left[1-\left(\frac{\xi}{\xi_1}\right)^2\right];\\
\Theta_1 &= \overline{T}_w + \frac{\lambda_f}{\lambda_3}\ln\frac{1}{\xi_3} + \frac{\lambda_f}{\lambda_2}\ln\frac{\xi_3}{\xi_2} + \frac{\lambda_f}{\lambda_1}\ln\frac{\xi_2}{\xi};\\
\Theta_2 &= \overline{T}_w + \frac{\lambda_f}{\lambda_3}\ln\frac{1}{\xi_3} + \frac{\lambda_f}{\lambda_2}\ln\frac{\xi_3}{\xi};\\
\Theta_3 &= \overline{T}_w + \frac{\lambda_f}{\lambda_3}\ln\frac{1}{\xi}.
\end{aligned}\right\} \tag{13}$$

Solutions for $\Psi(\varphi, \xi, Z)$ have the form

$$\left.\begin{aligned}
\Psi_0 &= \sum_{k=1}^{\infty} H_k \xi^k \cos k\varphi;\\
\Psi_1 &= \sum_{k=1}^{\infty} (A_k \xi^k + B_k \xi^{-k}) \cos k\varphi;\\
\Psi_2 &= \sum_{k=1}^{\infty} (C_k \xi^k + D_k \xi^{-k}) \cos k\varphi;\\
\Psi_3 &= \sum_{k=1}^{\infty} (E_k \xi^k + F_k \xi^{-k}) \cos k\varphi.
\end{aligned}\right\} \tag{14}$$

The coefficients found from the boundary conditions are

$$\begin{aligned}
H_k &= N_k \xi_2^{2k} \xi_3^{2k} (1+m_1)(1+m_2)(1+m_3);\\
A_k &= N_k \xi_2^{2k} \xi_3^{2k} (1+m_2)(1+m_3);\\
B_k &= N_k \xi_1^{2k} \xi_3^{2k} m_1 (1+m_2)(1+m_3);
\end{aligned}$$

$$C_k = N_k \xi_3^{2k} (1 + m_3) (\xi_1^{2k} m_1 m_2 + \xi_2^{2k});$$
$$D_k = N_k \xi_2^{2k} \xi_3^{2k} (\xi_1^{2k} m_1 + \xi_2^{2k} m_2) (1 + m_3);$$
$$E_k = N_k [\xi_2^{2k} m_3 (\xi_1^{2k} m_1 + \xi_2^{2k} m_2) + \xi_3^{2k} (\xi_1^{2k} m_1 m_2 + \xi_2^{2k})];$$
$$F_k = N_k [\xi_2^{2k} \xi_3^{2k} (\xi_1^{2k} m_1 + \xi_2^{2k} m_2) + \xi_3^{2k} \xi_3^{2k} m_3 (\xi_1^{2k} m_1 m_2 + \xi_2^{2k})],$$

where /141

$$\frac{1}{N_k} = \frac{1}{a_k} [\xi_2^{2k} (\xi_3^{2k} + m_3) (\xi_1^{2k} m_1 + \xi_2^{2k} m_2) +$$
$$+ \xi_3^{2k} (1 + \xi_3^{2k} m_3) (\xi_1^{2k} m_1 m_2 + \xi_2^{2k})],$$
$$m_1 = \frac{\lambda_1 - \lambda_0}{\lambda_1 + \lambda_0}; \quad m_2 = \frac{\lambda_2 - \lambda_1}{\lambda_2 + \lambda_1}; \quad m_3 = \frac{\lambda_3 - \lambda_2}{\lambda_3 + \lambda_2}; \quad -1 \leqslant m \leqslant 1.$$

The relative thermal flux at the surface of the outer shell

$$\frac{q}{\bar{q}} = -\frac{\lambda_3}{\lambda_f} \frac{\partial T_3}{\partial \xi}\Big|_{\xi=1} =$$
$$= 1 - \sum_{k=1}^{\infty} a_k \left[\frac{\partial}{\partial \xi} \frac{\lambda_3}{\lambda_f} (E_k \xi^k + F_k \xi^{-k}) \right] \cos k\varphi \text{ where } \xi = 1.$$

Resorting to Eq. (8), we get

$$\varepsilon_k = \frac{\lambda_3}{\lambda_f} (E_k - F_k) =$$
$$= \frac{\lambda_3 \xi_2^{2k} (m_3 - \xi_3^{2k}) (\xi_1^{2k} m_1 + \xi_2^{2k} m_2) + \xi_3^{2k} (1 - m_3 \xi_3^{2k}) (\xi_1^{2k} m_1 m_2 + \xi_2^{2k})}{\lambda_f \xi_2^{2k} (m_3 + \xi_3^{2k}) (\xi_1^{2k} m_1 + \xi_2^{2k} m_2) + \xi_3^{2k} (1 + m_3 \xi_3^{2k}) (\xi_1^{2k} m_1 m_2 + \xi_2^{2k})}. \quad (15)$$

The requirement that ε_k = idem can be rigorously satisfied for any harmonics (any values of k) only on the condition that simplexes $\xi_1, \xi_2, \xi_3, \lambda_1/\lambda_0, \lambda_2/\lambda_1, \lambda_3/\lambda_2, \lambda_f/\lambda_3$ have the same values in nature and on the model. This requirement also follows directly from the system of starting equations and boundary conditions (3-9).

The creation of thermal models of fuel elements with volumetric heat generation and with ideal thermal contacts between the layers under laboratory conditions is very difficult. The above difficulties can be eliminated by using approximate thermal simulation. This will somewhat reduce the accuracy of the results.

The substance of the latter consists in replacing the fuel rod with shells by some equivalent tube, at the inner surface of which we in one way or another

satisfy the conditions: q = const or t = const along the perimeter. To be able to select the dimensions and the thermal conductivity of the equivalent tube it is necessary to know approximately the behavior of the temperature distribution over the perimeter of the fuel element under study, i.e., the fundamental harmonic of the Fourier series which describes the temperature distribution. In some cases it is possible to guess this harmonic. For example, for cluster of fuel rods arranged in a regular triangular lattice the fundamental harmonic is $k_0 = 6$, for a square lattice $k_0 = 4$, while for an eccentric annulus $k_0 = 1$, [1-4], When it is difficult to guess the fundamental harmonic, one must resort to successive approximations. Let us assume that in experiments with the model we have obtained the distribution of the dimensionless variation in the temperature /142

$$\Delta T_w = (T_w - \overline{T}) \approx \sum_{k=1}^{n} a_k \cos k\varphi, \tag{16}$$

and on the basis of these data we have calculated the distribution of thermal fluxes in the model

$$\frac{q}{\overline{q}} \simeq 1 - \sum_{k=1}^{n} a_k k \, (\varepsilon_k)_{\text{mod}} \cos k\varphi. \tag{17}$$

Had the distribution of thermal fluxes on the surface of the fuel element been the same as in the model, then the variation in the fuel element temperature would have been described by the expression

$$\Delta T_w^* = (T_w - \overline{T}_w)^* \simeq \sum_{k=1}^{n} a_k \frac{(\varepsilon_k)\text{mod}}{(\varepsilon_k)\text{f. e.}} \cos k\varphi. \tag{18}$$

In the case w' en the effective thermal conductivity in the model is lower than that of the fuel element, which corresponds to the case of $(\varepsilon_k)_{\text{mod}} < (\varepsilon_k)_{\text{f. e}}$, the experimental value of ΔT_w will be on a high side. On the other hand, the lack of uniformity of thermal fluxes over the perimeter will turn out to be weaker for the model than in the fuel element, while the lack of uniformity ΔT_w^* will be on the lower side as compared with the actual lack of uniformity in the fuel element's temperature. For the opposite case of $(\varepsilon_k)_{\text{mod}} > (\varepsilon_k)_{\text{f. e}}$, ΔT_w^* will yield higher than actual, while ΔT_w will yield lower than actual values of variations in the fuel element's temperature.

The true value of the variation in the fuel element's temperature will lie between values obtained on the basis of experiments performed with the model

given by Eq. (16) and those calculated on the assumption of $q/\bar{q}$ = idem, which is the basis of Eq. (18). Approximately this can be defined as the root-mean-square value

$$(\Delta T_w)_{\text{true}} \approx \frac{\Delta T_w + \Delta T_w^*}{2} = \frac{1}{2} \sum_{k=1}^{n} a_k \left[1 + \frac{(\varepsilon_k)\text{mod}}{(\varepsilon_k)\text{f.e.}} \right] \cos k\varphi.$$

If the divergence between ΔT_w and ΔT_w^* exceeds the desirable accuracy, then the experiments are repeated using a model the parameters of which have been appropriately adjusted. The average temperature of the heat-conducting surface depends much less on the design of the fuel element than the variation in the temperature. This is attested to experimental data presented in [1-3]. Assuming, by analogy with a round tube, that the Reynolds number for liquid metal can be approximately eliminated from criterial Eq. (11), we get

$$T_f(\varphi, \xi, Z) \simeq f(\varphi, \xi, Z, \text{Pe}, \varepsilon_{k_0}). \tag{19}$$

In approximate thermal simulation the goal is to obtain approximate similitude of temperature fields of the fluids, and consequently also, of the heat-conduction surfaces. Knowing the temperature field of the heat-conducting surface /143 it is not difficult to find the temperature field inside the fuel element using Eqs. (13) and (14).

The condition that q = const at the surface to which heat is supplied to the model can be satisfied, for example, by using electric heaters. In some experiments use was made of heaters made in the form of coils from nichrome wire and insulated from the tube walls by a thin layer of organic silicon. The condition that t = const over the inner perimeter can, apparently be created by pressing or soldering copper rings inside the tubes.

Let us consider some particular fuel element designs. The value of ε_k for a single-shell element is obtained from Eq. (15) by setting $\xi_1 = \xi_2 = \xi_3 = \xi_0$ and $\lambda_3 = \lambda_w$

$$\varepsilon_k = \frac{\lambda_w}{\lambda_f} \frac{1 - m\xi_0^{2k}}{1 + m\xi_0^{2k}}, \tag{20}$$

where $m = \lambda_w - \lambda_0 / \lambda_w + \lambda_0$; $\xi_0 = R_1/R_2$, while R_1 and R_2 are the inner and outer radii of the shell, respectively.

If the rod has a thick shell, i.e., if $\xi_0^{2k} \ll 1$, then the temperature field (T_w) of the heat conducting surface is practically independent of the thermal

conductivity (λ_0) of the heat-generating rod (of the boundary conditions at the inner surface of the shell).

If the thermal conductivities of the rod and the shell are approximately the same, i.e., $\lambda_0 \approx \lambda_w$, then the temperature field of the heat-conducting surface (T_w) practically does not depend on the shell thickness, which also follows from the solution of Eq. (12). In fact, the temperature level of the fuel element is determined by the function Θ, while the temperature distribution over the perimeter is given by the function Ψ, which is independent of the radius of the heat-generating volume (ξ_0).

The above cases are equivalent to a heat-generating rod without a shell or to a tube with sufficiently thick walls with internal heat supply. The simulation conditions here become much simpler

$$\left(\frac{\lambda_w}{\lambda_f}\right)_{\text{f.e.}} = \left(\frac{\lambda_w}{\lambda_f}\right)_{\text{mod}};\ (\xi_0^{2k})_{\text{mod}} \ll 1. \tag{21}$$

It is easy to simulate fuel elements in which the thermal conductivities of the rod and of the shell differ highly. When $\lambda_0 \ll \lambda_w$ ($m \approx 1$), we get from Eq. (20)

$$\varepsilon_k \simeq \frac{\lambda_w}{\lambda_f} \cdot \frac{1-\xi_0^{2k}}{1+\xi_0^{2k}}, \tag{22}$$

and when $\lambda_0 \gg \lambda_w$ ($m \simeq -1$)

$$\varepsilon_k \simeq \frac{\lambda_w}{\lambda_f} \frac{1+\xi_0^{2k}}{1-\xi_0^{2k}}. \tag{23}$$

These fuel elements are simulated by tubes in which we impose on the inner surface the conditions q = const (22) or t = const (23) over the perimeter.

We shall assume that the fuel element has a very thin shell, i.e., that /144
$\delta \ll R_2$ (δ is the shell thickness), while the value of m is moderate. Expanding ξ_0^{2k} in a binomial series, we get

$$\xi_0^{2k} = \left(1-\frac{\delta}{R^2}\right)^{2k} \simeq 1 - 2k\frac{\delta}{R^2} + \ldots.$$

It follows from Eq. (20) that

$$\varepsilon_k \simeq \frac{\lambda_w}{\lambda_f} \frac{1-m\left(1-2k\frac{\delta}{R_2}\right)}{1+m\left(1-2k\frac{\delta}{R_2}\right)} \simeq \frac{\lambda_w}{\lambda_f}\frac{1-m}{1+m} = \frac{\lambda_0}{\lambda_f}, \tag{24}$$

i.e., the effect of the shell can be disregarded. The criteria for shell thinness in the given case is the fact that ε_k depends little on k, the number of the harmonic.

If the thermal conductivities of the rod and the shell of a fuel element with a thin-walled shell differ, i.e., the fuel elements are equivalent to thin-walled tubes with q = const or t = const, then

$$\varepsilon_k \approx \frac{\lambda_w}{\lambda_f} \frac{1-1+2k\frac{\delta}{R_2}}{1+1-2k\frac{\delta}{R_2}} \approx k\frac{\lambda_w\delta}{\lambda_f R_2} \tag{25}$$

for $\lambda_0 \ll \lambda_w$ or

$$\varepsilon_k \simeq \frac{\lambda_w}{\lambda_f} \frac{1+1-2k\frac{\delta}{R_2}}{1-1+2k\frac{\delta}{R_2}} \simeq \frac{1}{k}\frac{\lambda_w R_2}{\lambda_f\delta} \tag{26}$$

for $\lambda_0 \gg \lambda_w$. In these cases simulation becomes appreciably simpler and reduces to selecting tubes and liquid-metal heat-transfer agents, which satisfy the conditions

$$\frac{\lambda_w\delta}{\lambda_f R_2} = \text{idem and} \frac{\lambda_w R_2}{\lambda_f\delta} = \text{idem}$$

for q ≈ const and t ≈ const, respectively, at the inner surface of the tubes.

Methods of approximate thermal simulation can be used in generalizing experimental data and for solving problems by the method of thermal-electric analogy.

Let us consider some examples of approximate simulation. For this we use experimental data obtained with a Na-K solution ($\lambda_w/\lambda_f = 0.695$) for rods packed closely in a square arrangement, [2], an eccentric annulus [4] and for a rod placed inside a hexagonal jacket [5]. The fuel-element models are tubes heated from within by electric coils (q ≈ const at R_1). The values of ξ_0 for the /147

equivalent fuel elements in all the cases were assumed to be 0.92, which corresponds to a jacket thickness of $\delta = 0.4$ mm and an outer radius of $R_2 = 5$ mm. The ratio of thermal conductivities λ_w/λ_f for fuel elements arranged in a closely packed square in one case is assumed to be 1.25 while in the other it is 0.416. These values of the ratio of thermal conductivities are obtained for cases when the fuel element jacket is made from ferritic-pearlitic steel ($\lambda_w \approx 25$ kcal/m-hour-degree), while the coolants are the Na-K alloy ($\lambda_f \approx 20$ kcal/m-hour-degree) or sodium ($\lambda_f \approx 60$ kcal/m-hour-degree), respectively.

For fuel elements corresponding to annuli and for those located in the corner of the shield, we have considered two cases

$$\frac{\lambda_w}{\lambda_f} = 0.416 \text{ and } \frac{\lambda_w}{\lambda_f} = 0.2.$$

The value $\lambda_w/\lambda_f = 0.2$ is not encountered and is used in the calculations only in order to extend the range within which the fuel element parameters are varied.

The values of $m = \lambda_w - \lambda_0/\lambda_w + \lambda_0$ for the equivalent fuel elements were found from the expression

$$\left(\frac{\lambda_w}{\lambda_f}\,\frac{1-m\xi_{s0}^{2k_0}}{1+m\xi_{s0}^{2k_0}}\right)_{\text{f. e.}} = (\varepsilon_{k_0})_{\text{mod}}$$

with the condition that for dense square packing $k_0 = 4$, while for the two other cases $k_0 = 1$.

The main parameters of the models and of the fuel elements being simulated are tabulated in Table 1, which also lists the values of coefficients of the Fourier series (a_k) obtained by analyzing experimental data for the models.

The calculated parameters ε_k and the temperature variations ΔT_w and ΔT_w^* calculated from Eqs. (16), (18) and (20) are shown in Figs. 2-4. Despite the fact that the values of $(\varepsilon_k)_{\text{mod}}$ and $(\varepsilon_k)_{\text{f. e}}$ differ appreciably when $k \neq k_0$, /148
the [temperature] variations of the model and the fuel elements in the dense packing arrangement do not differ significantly (see Fig. 2). A somewhat greater difference between ΔT_w and ΔT_w^* is observed for the annulus (see Fig. 3) and for the corner rod (see Fig. 4), since in these cases the values of $(\varepsilon_k)_{\text{mod}}$ and $(\varepsilon_k)_{\text{f. e}}$ differ more appreciably and, in addition, the character of curves describing the temperature field is more complicated.

The sought value of temperature variations is estimated as the arithmetic mean of ΔT_w and ΔT_w^*.

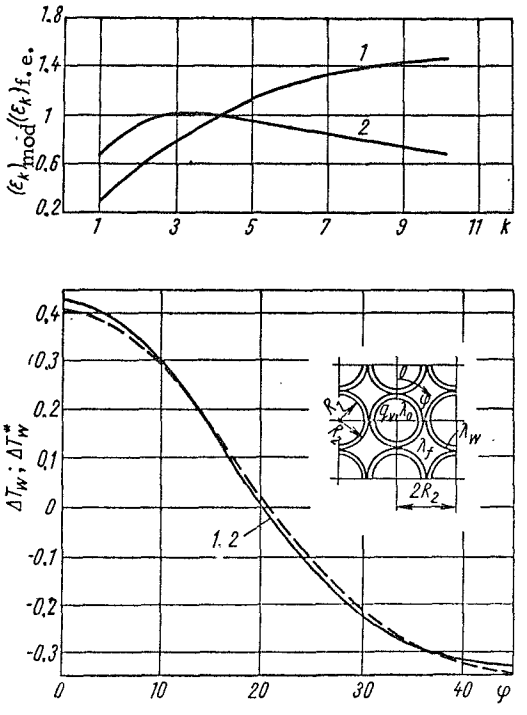

Figure 2. Fuel Rods Densely Packed in a Square Arrangement. 1 and 2 are the Values of $(\varepsilon_k)_{mod}/(\varepsilon_k)_{f.e}$ and ΔT_w^* for Type 1 and 2 Fuel Elements; the Dashed Line Denotes the Value of ΔT_w.

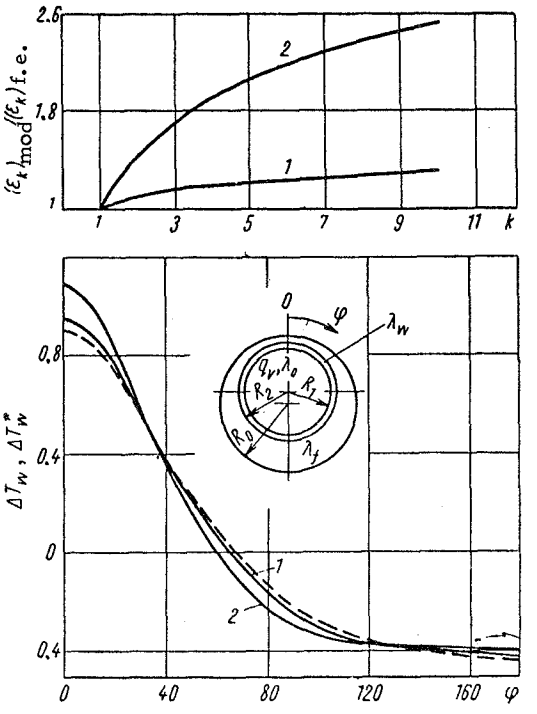

Figure 3. Annulus With $R_0/R_2 = 1.11$ With an Eccentricity of 0.5 (for Notation see Fig. 2).

TABLE 1. Basic Parameters of Models and Fuel Elements

Type of passage	a_1	a_2	a_3	a_4	a_5
Formed by rods packed densely in a square arrangement	—	—	—	0.362	—
Annulus with an eccentricity of 0.5	0.572	0.217	0.0715	0.02	0.0177
Corner rod, triangular lattice	2.12	1.10	—0.27	—0.187	0.154

TABLE 1. (Concluded)

a_6	a_8	Pe	$\xi_{0,\text{mod}}$	Type 1 fuel element		Type 2 fuel element	
				m	$\frac{\lambda_w}{\lambda_f}$	m	$\frac{\lambda_w}{\lambda_f}$
—	0.041	100—500	0.773	0.778	1.25	—0.246	0,416
0,006	—	82	0,942	0.970	0,416	0,772	0.20
0.021	—	23	0,933	0,937	0,416	0,722	0.20

The error in determining [these] values

$$(\Delta T_w)_{\max}=\frac{t_w^{\max}-\bar{t}_w}{\bar{q}R_2}\lambda_f \text{ and } (\Delta T_w)_{\max}-(\Delta T_w)_{\min}=\frac{t_w^{\max}-t_w^{\min}}{\bar{q}R_2}\lambda_f,$$

which we denote by N and M respectively, are presented in Table 2.

TABLE 2. Errors in Determining the Variations in Temperature, %

Type of passage	Type 1 fuel element		Type 2 fuel element	
	N	M	N	M
Space formed by densely packed rods	1	1	2	1
Annulus	2	1	10	5
Corner rod	1	6	4	9

As can be seen from this table, the accuracy of simulation in the above cases does not, go past the precision limits of experiments of this class. This does not, however, mean that any fuel element can be simulated with the same accuracy. All depends on the relationship between the parameters of the fuel rod elements and the limitations in the selection of heat transfer agents and structural materials for the models.

The methods of approximate thermal simulation presented in this article are used successfully in the study of active [cores] zones of reactors with liquid-metal cooling.

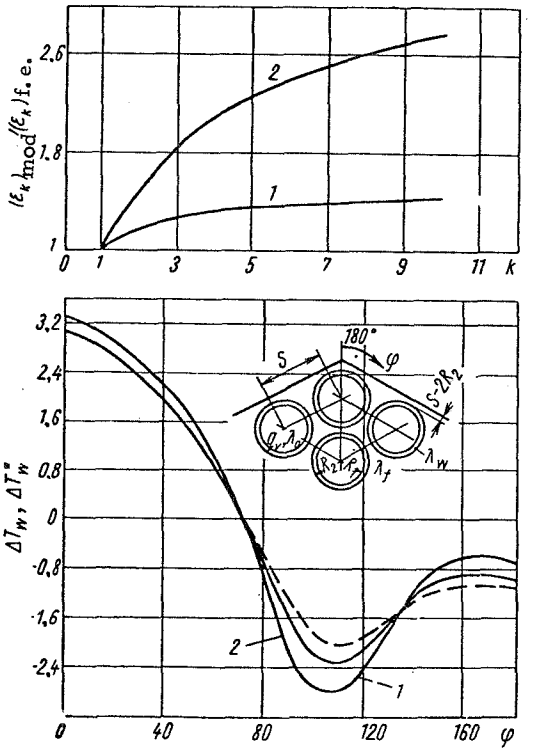

Figure 4. Corner Rod in a Triangular Lattice With $s/2R_2 = 1.04$ (for Notation see Fig. 2).

REFERENCES

1. Subbotin, V.I. et al.: Atomnaya energiya, 9, 6, 461 (1960).
2. Subbotin, V.I. et al.: Atomnaya energiya, 13, 2, 162 (1962).
3. Subbotin, V.I. et al.: Teplos"yem v elementakh reaktorov s zhidkometallicheskim okhlazhdeniyem [Heat Removal in Elements of Liquid-Metal-Cooled Reactors]. Report read to the 3rd International Conference on Peaceful Uses of Atomic Energy, Geneva, 1964.
4. Subbotin, V. I. et al.: Vliyaniye ekstsentrisiteta na teploobmen zhidkikh metallov v kol'tsevom zazore [Effect of the Eccentricity on Heat Transfer to to Liquid Metals in an Annular Space]. Part I of present collection.
5. Zhukov, A. V. et al.: Eksperimental'noye issledovaniye na modelyakh poley temperatury teplovydelyayushchikh elementov [Experimental Studies of Temperature Fields of Fuel Elements, Using Models]. Part II of present Collection.

HEAT TRANSFER FROM LOOSELY-SPACED [FUEL] ROD CLUSTERS TO LIQUID METAL FLOWING IN THE AXIAL DIRECTION

A. V. Zhukov, V. I. Subbotin and P. A. Ushakov

The present article considers the transfer of heat from loosely-spaced [fuel] rod clusters in which the temperature variation over the rod perimeters is small and the heat transfer coefficients depend little on the fuel element design (jacket thickness, thermal conductivity of the fissionable material and the jacket). /149

Analyzing the differential equations describing the processes taking place in the fissionable material, fuel element jackets and the coolant, together with the appropriate boundary conditions, we can find the needed similarity criteria which define the temperature fields and the average heat transfer in the rod clusters.

$$\frac{t_w - \bar{t}_w}{\bar{q}R_2}\lambda_f = f_1\left(\frac{l}{d_h},\ x,\ \varphi,\ \xi,\ \frac{\lambda_0}{\lambda_f},\ \frac{\lambda_w}{\lambda_f},\ \mathrm{Re},\ \mathrm{Pr}\right),$$

$$\mathrm{Nu} = f_2\left(\frac{l}{d_h},\ x,\ \xi,\ \frac{\lambda_0}{\lambda_f},\ \frac{\lambda_w}{\lambda_f},\ \mathrm{Re},\ \mathrm{Pr}\right).$$

Parameters ξ, λ_0/λ_f and λ_w/λ_f which characterize the fuel element design have their greatest effect on the temperature fields and on the average heat transfer in densely-packed fuel-element clusters ($x = 1$), when maximum temperature variations are observed over the perimeter of the latter, [1-6]. In clusters with $x \geq 1.1$ the temperature variations over the perimeter of the fuel elements are moderate and the above parameters have little effect on the average Nusselt number. In this case the Nusselt numbers calculated by using the hydraulic diameter depend primarily on the physical properties and the flow regime of the coolant as well as on the value of x.

Basic information on investigations concerned with heat transfer to liquid metals in loosely packed rod clusters is presented in Table 1. Figure 1 depicts the cross sections of clusters used in these studies.

The authors of [7-9] have used seven-tube clusters with spacers fastened to a cylindrical shell. The tubes were heated internally so as to provide q_w = const at the inner surface. The center tubes from St. 3 or copper were equipped with thermocouples embedded into longitudinal slots near the heat conducting surface. These tubes could be rotated through any angle. As a rule, the total heat supplied to the coolant by the clusters was the quantity measured. In individual cases the temperature was measured at the outlets from the central cells of the cluster. The dependence of Nusselt numbers on the relative spacing

TABLE 1. Characteristics of Test Sections and Experimental Conditions [7-13]

Designation	Reference and year of publication								
	[7]					[8]	[9]	[10]	[10–13]
	1956	1958	1958	1959	1962	1963	1964	1961	1961–1964
Coolant	Liquid metals with Pr = 0.025-0.036					Na		Hg	Hg, the Na-K alloy
Material of the heat-conducting surface	Carbon steel				1Kh18N9T Steel, St. 3 Steel	Cu		Cu, nickel- or chromium-plated surfaces	
Method of heat supply	Heating by passing current through an inside tubular heater							Electric heating by nichrome coils	
Number of thermocouples on the center tube	4	7	6	5	12			9	
Description of thermocouples and the manner in which they are attached	Chromel-alumel thermocouple wires 0.18-0.3 mm in diameter in two-passage porcelain tubes along the inner surface or in metal capillaries 1.0 × 0.15 mm in diameter along the outer surface with subsequent metallizing or electroplating of the surface							Copper and constant thermocouple wires 0.127 mm in diameter in a capillary 1.09 × × 0.74 mm in diameter	
Method for determining the temperature in the center cells	Calculated theoretically		Calculated theoretically and measured	Calculated theoretically	Measured			—	
Description of thermocouples used for measuring the liquid's temperature in the center cells	—				Chromel-alumel thermocouple wires 0.18 mm in diameter in capillaries 1.0 × 0.15 mm in diameter			—	

Coolant velocity V, m/sec		0.18—1.0	0.16—2.02	0.9—0.59	0.0488—0.61	
Re · 10^{-3}		10—48	3.8—57	4.3—28	8—80	7.5—200
Peclet number	500—1800	300—1450	30—345	28—172	190—1700	150—4000
Prandtl number	0.036—0.025	$3 \cdot 10^{-2}$	$(72—57) \times 10^{-4}$	$64 \cdot 10^{-4}$	0.016—0.021	~0.02
Coolant temperature, t_f, °C		200—250	210—310	220—270	49—127	~38
Thermal flux, q, kcal/m^2 · hour	$(50—100) \cdot 10^3$				36 700	$(66.5—100) \cdot 10^3$
Metal purity, oxygen content by weight, %	was not checked	$2.4 \cdot 10^{-4}$	$1.7 \cdot 10^{-2}$			

d_1, mm	17							7.6
d_2, mm	22						12.7	12.7
$x = \frac{S}{d_2}$	1.14		1.3		1.2	1.5	1.38	1.75
L, mm	600		685		1510	1240		1712
l_0, mm	500		600		1050	700	1016	1370
Limits of rotation of center tube, φ, degrees	—10 — +35	—10 — +70	—10 — +50	held at 30°	0-360° in steps of 30°	0 — 360	was not rotated	

TABLE 1. (Concluded)

Designation	Reference and year of publication										
	[7]				[8]	[9]	[10]	[10–13]			
	1956	1958	1958	1959	1962	1963	1964	1961	1961–1964		
hydraulic diameter of cluster d_h^{cl}, mm					11.43			13.85	30.2		
Hydraulic diameter of center cells d_h, mm	9.57		18.9		13.0		32.6	13.85	30.2		
Inside diameter of shell D, mm	96		92		83			86.2	100.6		
l/d_h	30—100								4—46		

of the rods was not established [8], [9]. To calculate average Nusselt numbers in clusters with x = 1.2-1.75 [8] recommends the empirical formula

$$Nu = 6 + 0.006Pe$$
$$\text{for } 30 \leqslant Pe \leqslant 4000 \text{ and } Re > 10^4. \quad (1)$$

In [10-13] use was made of clusters consisting of 13 and 19 heated tubes, held in a cylindrical shell. The shell diameter was selected so as to keep the hydraulic diameters of the cluster and of the central cells equal to one another. Thermocouples were embedded into longitudinal slots on the surface of the copper center element. This element was chromium or nickel plated in order to obtain, respectively, a mercury-wetted or nonwetted surface. The coolant temperature in the cells of the test section was not measured, and the center tube was not rotated during the study of temperature fields. /154

Dwyer and Tu [14] have analytically calculated the heat transfer coefficients in rod clusters with $1.3 \leq x \leq 3.0$. The method used in calculations was based on replacement of the hexagonal boundary around the rod cluster [apparent error, should be rod cluster/cluster of rods, DBL] by an equivalent circle. The calculations were thus reduced to solving the problem of heat transfer in annular passages. The velocity distribution was calculated by the method due to Rothfus [15]. The final formula used in calculations has the form [12, 13].

$$\mathrm{Nu} = 6.66 + 3.126x + 1.184x^2 + 0.0155\,(\bar{\psi}\,\mathrm{Pe})^{0.86},$$
$$10^2 \leqslant \mathrm{Pe} \leqslant 10^4;\ 1.3 \leqslant x \leqslant 3.0. \qquad (2)$$

The effective dissimilarity factor for the turbulent heat transfer and the momentum are determined, according to Dwyer's estimated, by the expression

$$\bar{\psi} = 1 - \frac{1.82}{\mathrm{Pr}\left(\frac{\varepsilon_v}{\nu}\right)^{1.4}_{\max}}.$$

A solution similar to that given in Eq. (2) was obtained by Friedland and Bonilla [16], using data obtained by Knudsen and Katz [17] on the velocity distribution in annular passages

$$\mathrm{Nu} = 7 + 3.8x^{1.52} + 0.027x^{0.27}\,(\bar{\psi}\,\mathrm{Pe})^{0.8},$$
$$1.38 \leqslant x \leqslant 10. \qquad (3)$$

Equations (2) and (3) yield close results and show that, when the hydraulic diameter is used in analysis, the Nusselt numbers in the clusters depend on the relative spacing of the rod lattice.

Experimental Clusters and Methods Used in the Experiments

Experiments using mercury were performed on three identical stands (Fig. 2), while those using the Na-K alloy were performed on the setup described in [18]. The mercury (brand R_3) and the Na-K alloy were circulated by centrifugal pumps with an approximate delivery of up to 10 m^3/hour with a pressure of about 18 kg/cm^2 and with a delivery of 150 m^3/hour at a pressure of about 6 kg/cm^2, respectively. Impurities were continuously removed from the coolants during operation in the following manner: the mercury was filtered through suede, while the impurities from the Na-K alloy were removed in cold traps. The mercury flow rate was measured by precalibrated Venturi tubes connected to U-shaped differential manometers, while the flow rate of the alloy was measured by electromagnetic flowmeters. The coolant flow rates were adjusted by bellows-type valves. All the components of the test stands were made from 1Kh18N9T steel.

Experiments with mercury were performed using clusters with x = 1.10, 1.20, 1.30, 1.40 and 1.50. The clusters were made up of seven heated tubes and twelve rods installed into appropriately shaped displacers [1]. Experiments /155
with the Na-K alloy were performed using a cluster with x = 1.15, consisting of

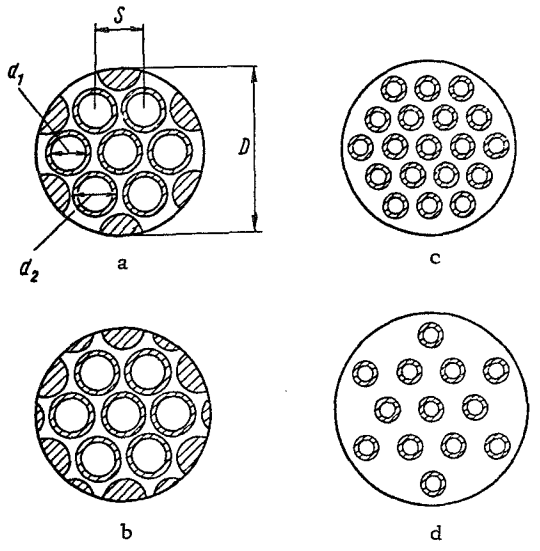

Figure 1. Sections Through Clusters Used in [7-9] (a and b) and [10] and [11] (c and d).

	d_1, mm	d_2, mm	D, mm	S/d_2
a	17	22	92, 83	1,2—1,5
b	17	22	96	1.14
c	7,6	12.7	86	1,38
d	7.6	12,7	101	1,75

37 heated tubes contained in a hexagonal shell [18]. The tubes were heated internally by nichrome coils, which provided $q_w \simeq$ const at their inner surfaces. The coils were insulated from the walls by a layer of electric insulation ~ 0.3-0.4 mm thick. The center tubes were equipped with 12 thermocouples placed in capillaries from 1Kh18N9T steel with an outer diameter of 0.5 mm. The thermocouple wires were made from copper and constantan in chlorovinyl insulation (for experiments with mercury) and from chromel, kopel and alumel in alundum and organic silicon insulation (experiments with the Na-K alloy). The thermocouple wire diameters were 0.08 mm, and the junctions were calked at the tube surface.

The center tube was inserted into the cluster by means of a packing gland, which made it possible to rotate it through any angle without disturbing the operating mode of the setup. The thermocouple capillaries were held hermetically in the packing gland in a round bore made in the wall of the tube and filled with the AKR-7 plastic. The coolant temperature was measured at the outlet from each cell by thermocouples in capillaries 0.5 or 0.8 mm in diameter, as well as in the cluster headers by thermocouples in sleeves.

Table 2 shows the main geometric dimensions of the test clusters. The clusters had a moderate number of heated tubes, hence, the temperature field of the coolants over the cluster cross section was nonuniform due to the effect of nonheated displacers and jackets. The experimental data was analyzed on the basis of the coolant temperatures in the center cells; in this manner they can be used for thermal calculations for clusters with a large number of heat-producing rods (for an infinite lattice). We have also studied the temperature field of the surface of the center tube with the coolant flowing at different velocities. Here the temperature of the medium at the inlet into the cluster and the thermal flux were maintained constant. The tube was rotated from $\varphi = 0°$ to $\varphi = 360°$ in steps of 5-10° for clusters with x = 1.1 and 1.15 and in steps of 30 and 60° for clusters with x = 1.2, 1.3, 1.4 and 1.5. The mean temperature differences between the wall and the fluid were measured at different distances from the inlet. /156

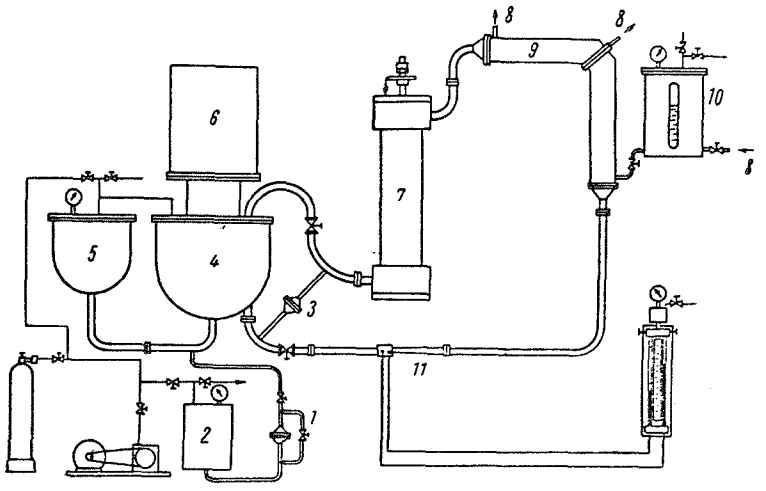

Figure 2. Schematic Diagram of the Setup for Mercury Experiments. 1) Filter; 2) Montejus; 3) Filter; 4) Pump Tank; 5) Mercury Tank; 6) Pump; 7) Heat Exchanger; 8) Water Inlet and Outlet; 9) Cooler; 10) Damping Tank; 11) Flowmeter.

The stabilized heat transfer coefficients were calculated from the expression $\alpha = \bar{q}/\vartheta$. For clusters with x = 1.1 the temperature variation over the perimeter of the center tube was estimated. Here the thermocouple readings were averaged and reduced to the reduced angles $\varphi = 0$, 5, 10, 20 and 30°. /157

In analyzing the experimental results the values of the physical parameters of 1Kh18N9T steel, of the mercury and of the Na-K alloy were taken from [19] and [20]. In some cases temperature fluctuations of the heat-conducting surface and of the coolant were recorded. For this purpose use was made of the EPP-09 rapid-acting, single-point electron potentiometers with a scale of 1 mV and requiring 1 sec in order for the carriage to traverse the entire scale. Sections through the clusters are shown in Fig. 3.

Experimental Results

Fluctuations in the temperature of the heat conducting surface and of the coolant were observed in experiments using clusters with small relative spacings ($x \simeq 1.1$). To reduce the resistance to flow, a grid, with a large flow cross section, approximately equal to the flow cross section of the cluster, was placed at the cluster inlet. Here particularly high temperature fluctuations were observed in the center cells. The amplitudes of these fluctuations became smaller with an increase in the coolant velocity. The temperature fluctuations in the wall of the center tube increased as the distance from the start of the heating zone became larger.

TABLE 2. Main Geometric Dimensions of Test Clusters

Designation and units	Numerical values							
Relative spacing of rods, $x = S/2R_2$	1.1	1.1	1.15	1.15	1.2	1.3	1.4	1.5
Tube length L, mm	770	495	750		891	770	891	770
Distance from the butts of tubes to the start of the heated zone, l_{st}, mm	30	40			50	40	50	40
Length of heated zone, l_0, mm	710	445	690		800	700	800	700
Outer diameter of tubes, $d_2 = 2R_2$, mm	17.6		17		17.6		16	17.6
Inner diameter of tubes, $d_1 = 2R_1$, mm	13.6		13	15.4	13.6		12.5	13.6
Flow cross section of the cell ω, mm^2	40.7		52.06		71.5	105.4	117.5	180
Flow cross section of the cluster Ω, mm^2	978		4300		1720	2530	2820	4314
Hydraulic diameter of a cell in the cluster, $d_h = 4\omega/p$, mm	5.9		7.80		10.3	15.2	18.6	26.1

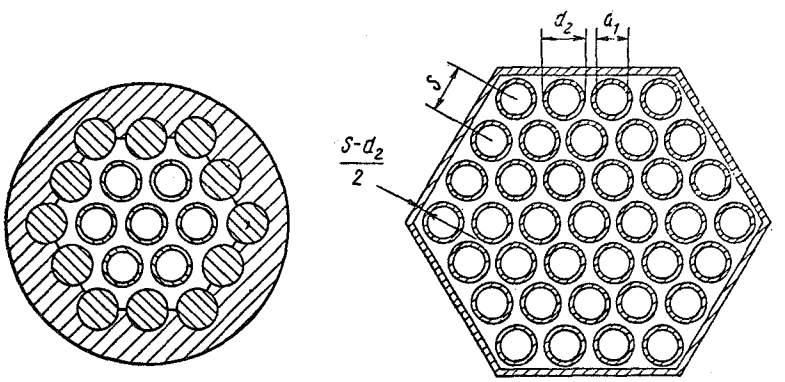

Figure 3. Sections Through Experimental Clusters.

Temperature fluctuations observed in the cluster with x = 1.1 are produced by fluctuations in the flow rates of the coolant in the cells, while the total flow rate through the cluster remains constant. In addition, the temperature fluctuations are brought about by the temperature gradient over the cluster cross sections. Experiments show that heating of the shell of the above cluster with x = = 1.1 practically does not affect the temperature fluctuations in the center cells. /158 The fluctuations in the coolant temperature in extreme cells do increase in this case.

Thus, the main cause for temperature fluctuations in this case is the lack of stability in the [individual] flow rates and, consequently, in the quantity of heat transferred to the coolant in cells of the cluster. After the inlet resistance has been increased, the temperature fluctuations dropped appreciably.

Another picture was observed in clusters with a less tight spacing of tubes ($x \geq 1.2$), where the coolant temperature fluctuations were at maximum in the intermediate, rather than the center cells. Apparently, this is due to intermixing of hot and cold fluid streams within the cluster's cells. In experiments with a cluster with x = 1.2 the flow cross section of the cluster was by a factor of 2.5-3 larger than the line cross section of the inlet centering grid.

Temperature fluctuations were also studied in experiments with the Na-K alloy using a cluster with x = 1.24 consisting of 37 heated tubes (Fig. 4). For the same coolant velocity the fluctuations in the temperature of the heat-conducting surface increase with an increase in the distance from the start of the heated section. The behavior of temperature fluctuations as a function of the rate of flow of the Na-K alloy is remarkable. When the alloy flow is turbulent (Re = 5200) and $q = 15,500$ kcal/m^2-hour the temperature fluctuations $t_{max} - t_{min}$ comprised about 0.3°C, while when Re = 3470 they reached the maximum (approximately 1°C). When the velocity was reduced further the fluctuations decreased. Finally, in a purely laminar flow (Re = 740) the fluctuations practically disappeared. The behavior of temperature fluctuations in the Na-K alloy in the center cells was similar.

The behavior of changes in the fluctuations shown in Fig. 4 can be explained as follows. An increase in the fluctuations over the length of the cluster is due to an increase in the amount of heat transferred to the coolant in the cells. Low-frequency fluctuations at high Reynolds numbers apparently are produced by a certain amount of instability in the flow rates of the coolant through the cells which, in its turn, is brought about by the conditions at the inlet into the cluster, by the less than uniform operation of the pump, as well as by variations in the power supply. High-frequency fluctuations with a low amplitude are apparently related to the turbulent flow velocity fluctuations, which disappear in laminar flow. Maximum temperature fluctuations naturally take place in transient flow.

Thus, the magnitude of fluctuations in rod clusters depends on the inlet conditions and on the resistance of the inlet grid. When the inlet is smooth and the dynamic resistance at the inlet is low as compared with the resistance to the flow of fluid of the grid and the cluster, the temperature fluctuations are primarily determined by the flow turbulence. They become larger with an increase in the thermal load. In reactors operated under high thermal loads fluctuations

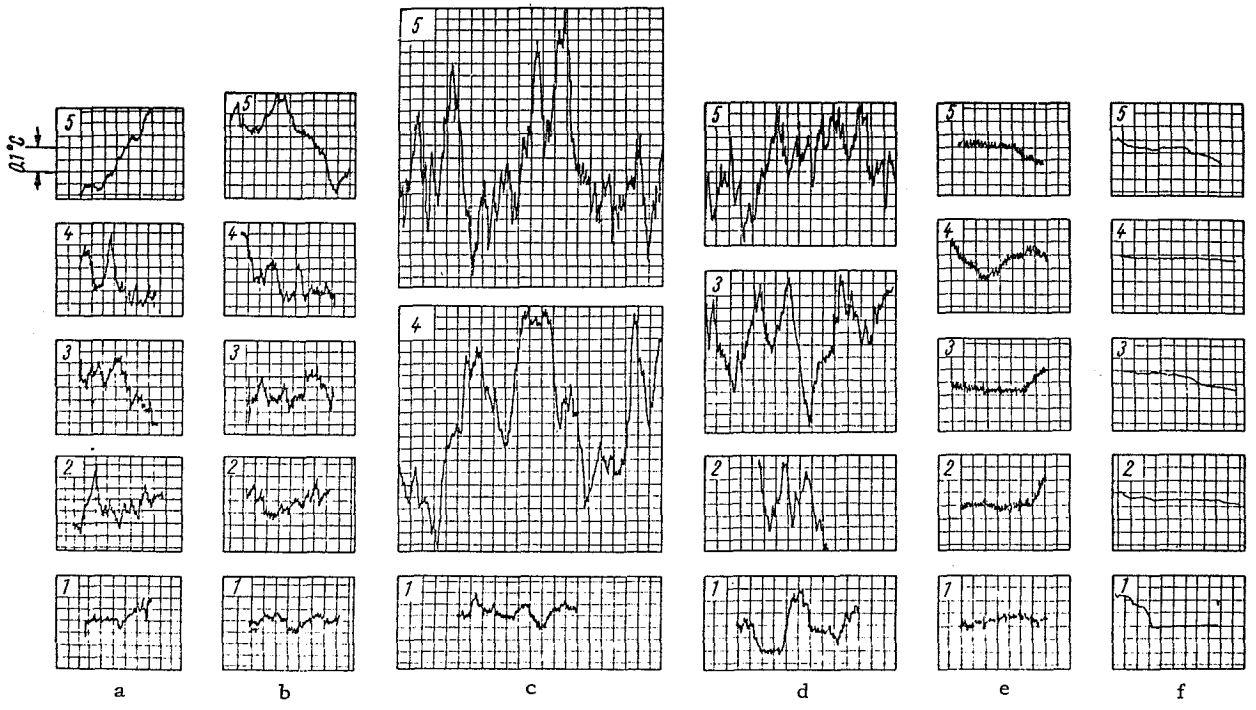

Figure 4. Fluctuations in the Wall and Coolant Temperatures in a Cluster With x = 1.24.

	w, m/sec	Re	Pe		w, m/sec	Re	Pe
a	0.348	5200	157	d	0.178	2840	78
b	0.281	4250	125	e	0.047	920	19.3
c	0.224	3470	99	f	0.03	740	11.6

Fluctuations in the wall temperature of the center tube

	1	2	3	4
l/d_h	0	20	27	47.5

5) fluctuations in the coolant temperature in center cells.

in the temperature of the heat-conducting surface and of the coolant may reduce the operating reliability of the fuel elements. From this point of view it is undesirable to have flow transition (from turbulent to laminar) of the coolant in a reactor, for which the temperature fluctuations are at maximum. /160

A characteristic temperature distribution over the perimeter of center tubes of clusters with x = 1.1 and 1.5 (original data) is shown in Fig. 5. For x = 1.1 temperature bursts are observed in narrow spots of the cells, (φ = 0, 60, 120°, etc.) produced by coolant overheating in these places. However, the effect of the above variability is compensated for by the effect produced by the bending of tubes of the cluster, which results in redistribution of the coolant flow rates among the individual cells, as a result of which the amount of heat transferred to the coolant in different cells is nonuniform. Hence, the variability in the temperature due to the bending of tubes is increased as the section at hand is taken further away from the inlet and reduction in the coolant velocity (i.e., increasing the quantity of heat transfer).

For tightly-packed clusters (x = 1-1.1) the temperature difference ($t_w - t_f$) varies over the perimeter much less than the wall temperature, since the behavior of temperature distributions in the wall and in the coolant are approximately the same. This follows from analysis of experimental data.

Starting with the condition of ΔP = idem for all the cells and assuming that the friction coefficient $f \approx Re^{-0.25}$ we can write an expression for the rate of flow by volume of the coolant through a cell of the cluster

$$V = \frac{\omega^{\frac{3}{1.75}}}{p^{\frac{1.25}{1.75}}}.$$

The relative variation of the wall temperature

$$\frac{\delta t_w}{t_w} \approx d \ln (t_f + \vartheta).$$

Hence, we get

$$\frac{\delta t_w}{\delta \vartheta} = \frac{\delta t_f}{\delta \vartheta} + 1. \qquad (4)$$

Increase in the coolant temperature in a cell when q_w = const

$$(t_f - t_0) = \frac{qlp}{C_p \gamma V} \approx \left(\frac{p}{\omega}\right)^{\frac{3}{1.75}} \cdot p. \qquad (5)$$

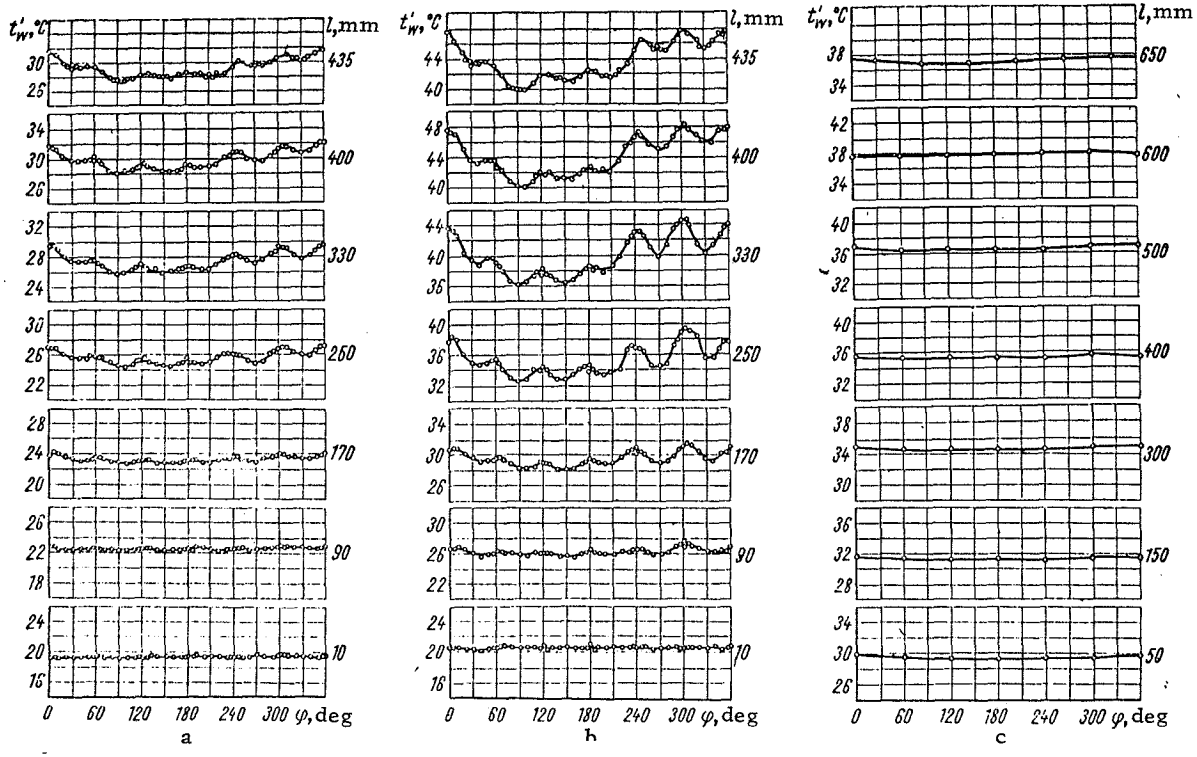

Figure 5. Distribution of Temperature Over the perimeter of Center Tubes of Clusters. a) and b) for x = 1.1, q = 50,000 kcal/m^2-hour and W = 10.4 and 0.43 m/sec; c) for x = 1.5, q = 43,400 kcal/m^2-hour and W = 0.46 m/sec.

Making use of the above expression, we get

$$\frac{\delta t_f}{\vartheta} = \frac{\delta (t_f - t_0)}{\vartheta} \approx \frac{12}{1.75} \cdot \frac{l}{d_h} \cdot \frac{\mathrm{Nu}}{\mathrm{Pe}} \left(\frac{dp}{p} - \frac{\delta \omega}{\omega} \right); \qquad (6)$$

The variation in the thermal flux over the perimeter of the tubes, which is due to the difference in the amount of heat imparted to the coolant in the different cells does not exceed 4%. Hence, it may be assumed approximately that q = const.

In this case /162

$$\frac{\delta \vartheta}{\vartheta} \approx \frac{\delta \alpha}{\alpha}.$$

To find $\delta\alpha/\alpha$ on the basis of experimental results we have assumed that $\alpha \approx W^{0.45}$. Then

$$\alpha \approx \left(\frac{V}{\omega} \right)^{0,45} \approx \left(\frac{\omega}{p} \right)^{-\frac{1.25 \cdot 0.45}{1.75}}.$$

We write the relative variation of the mean temperature difference

$$\frac{\delta \vartheta}{\vartheta} = -\frac{\delta \alpha}{\alpha} = \frac{1.25 \cdot 0.45}{1.75} \left(\frac{dp}{p} - \frac{\delta \omega}{\omega} \right). \qquad (7)$$

It follows from the above expression and from Eqs. (4) and (6) that

$$\frac{\delta t_w}{\delta \vartheta} \approx \frac{12}{1.25 \cdot 0.45} \cdot \frac{l}{d_h} \cdot \frac{\mathrm{Nu}}{\mathrm{Pe}} + 1. \qquad (8)$$

For a cluster with x = 1.1, q = 50,000 kcal/m^2-hour, W = 0.43 m/sec and l = = 400 mm, we get

$$\frac{\mathrm{Nu}}{\mathrm{Pe}} \approx 10^{-2}; \quad \frac{l}{d_h} = 68; \quad \frac{\delta t_w}{\delta \vartheta} \approx \frac{12 \cdot 0.68}{1.25 \cdot 0.45} + 1 = 15.$$

Thus the variation in the wall temperature (δt_w) is approximately by a factor of 15 greater than the variation in the mean temperature differences (δ).

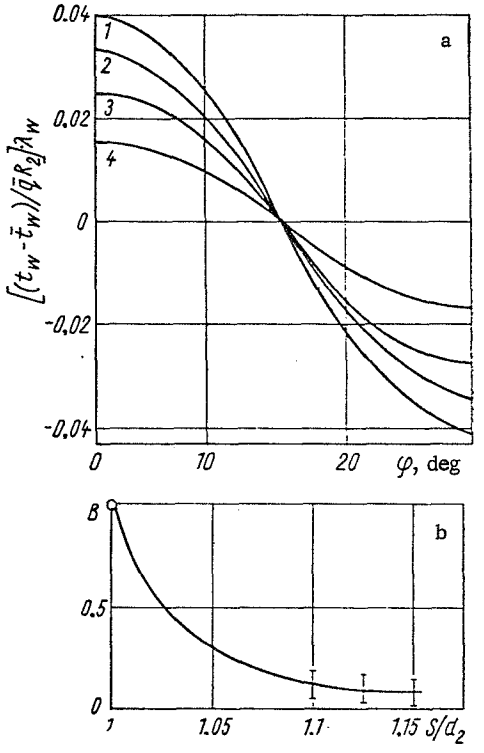

Figure 6. Dimensionless Temperature Distribution in a Cluster With x = 1.1 (a), and the Effect of the Rod Spacing on Variations in the Thermal Flux (b). 1, 2, 3 and 4 are for W = 0.12, 0.24, 0.66 and 1.04 m/sec Respectively; 1 = 400 mm; B is a Coefficient in Eq. (10).

For clusters with a large relative spacing the effect of tube bends is only moderate, while temperature variations with a period of 60°, which is due to the cell's geometry is negligible (See Fig. 5).

Figure 6a shows a periodic temperature variation obtained in experiments for a cluster with x = 1.1. The temperature distribution over the tube perimeter is close to the sinusoidal /163

$$\frac{t_w - \bar{t}_w}{\bar{q}R_2}\lambda_w \simeq A\cos 6\varphi. \qquad (9)$$

The moderate difference in the values of A for two clusters with x = 1.1 for the same coolant velocities are within the limits of experimental error (Table 3).

The distribution of thermal fluxes over the tube perimeter can be found by using the solution to the problem of thermal conductivity of a tube in the cluster presented in [1].

$$\frac{q}{\bar{q}} = 1 - B\cos 6\varphi, \qquad (10)$$

where

$$B = 6A\cdot\frac{1-\xi^{12}}{1+\xi^{12}}.$$

The temperature variation in a cluster with x = 1.1 is moderate and for the range of velocities under study is by a factor of 5-10 smaller than in a densely packed cluster of rods [1, 2]. This is not dangerous from the point of view of fuel element overheating. For example, for fuel elements, the equivalent thermal conductivity of which is equal to the thermal conductivity of tubes of the clusters under study ($\lambda_w \approx 14$ kcal/m-hour-degree), the temperature fluctuation $t_w - \bar{t}_w$ recalculated for $q = 10^6$ kcal/m^2-hour comprises not more than ≈10-15°C. Coefficient B [Eq. (10)] as a function of the relative spacing x is shown in Fig. 6b. The variation in thermal fluxes and, consequently, also in the temperatures decreases rapidly with an increase in x. In experiments with clusters with x = = 1.15 these fluctuations were practically nonexistent even when the coolant flow was laminar.

TABLE 3. Numerical Values of Coefficients A in Eq. (9) for Clusters With x = 1.1

$l_0 = 710$ mm						
W, m/sec	0.42	0.49	0.60	0.85	1.04	1.2
A	0.025	0.020	0.015	0.013	0.0115	0.0101

$l_0 = 445$ mm								
W, m/sec	0.12	0.24	0.31	0.43	0.52	0.66	0.83	1.04
A	0.038	0.032	0.032	0.026	0.0247	0.0175	0.016	0.0137

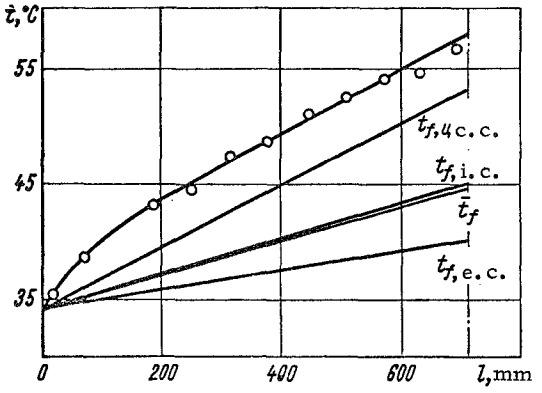

Figure 7. Temperature Distribution Over the Length of a Cluster With x = = 1.1 When W = 0.42 m/sec and q = = 25,200 kcal/m^2-hour. $t_{t.c.c}$, $t_{fi.c}$ and $t_{f\ e.c}$ are the Average Mixed Temperatures of Mercury at the Inlet From the Center, Intermediate and Extreme Cells, Respectively; t_f is the Average Mixed Temperature of Mercury in the Header, the Circles Denote the Temperature of the Wall of the Center Tube.

Figure 7 shows a characteristic distribution of the temperature over the length of a cluster. The coolant temperature in the center, intermediate and extreme cells is different. If /164 the characteristic temperature in this case is t_f, the average coolant temperature over the entire cluster cross section, rather than $t_{f,cent.cell}$, then the mean temperature differences between the wall and the coolant will come out to be much greater. This again emphasizes the importance of taking into account the variation in the coolant temperature over the cross section /165 of clusters with a moderate number of rods (tubes). The manner in which the heat transfer varies over the length of the clusters is shown in Fig. 8. Stabilization of heat transfer in loosely-packed clusters ensures with lower values of l/d_h, than in tightly-packed ones. This can be explained as follows. First, the formation of the velocity and temperature distributions in tightly-packed clusters is made difficult by the narrow parts of the cells. Secondly,

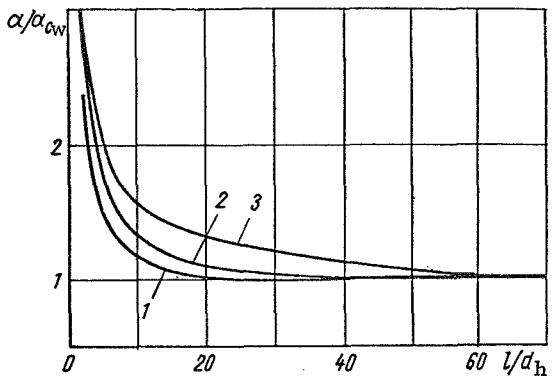

Figure 8. Variation in Heat Transfer Over the Length of Clusters. 1) x = 1.4, 1.5; 2) x = 1.2, 1.3; 3) x = 1.1 (l_0 = 445 and 710 mm).

the hydraulic diameter, which is by convention used as the characteristic dimension becomes appreciably larger with an increase in the relative spacing.

It is interesting to note that, for the same flow velocity of the mercury and the same tube diameters, the relative spacing practically does not affect the magnitude of α (Fig. 9). For this reason the experimental data in terms of similarity criteria calculated on the basis of the outer diameter of tubes /166 (the tube diameters in all the clusters are the same, see Table 1), for $1.1 \leq x \leq 1.5$ are in good agreement with one another can be expressed as (Fig. 10)

$$Nu = 0.58\,Pe_d^{0.45}, \qquad (11)$$

where d_2, the outer diameter of the tube is taken as the characteristic dimension. When using this approach in analyzing the experimental data, the data obtained using mercury and the Na-K alloy in developed turbulent flow are in good agreement with one another. The experimental points can be approximated by Eq. (11) with a scatter not exceeding ±15%.

If, in Eq. (11), we take the hydraulic diameters of the center cell as the characteristic linear dimension, then it will take on the form

$$Nu = 0{,}58\,(1{,}1x^2 - 1)^{0.55} \cdot Pe^{0.45}.$$
$$1{,}1 \leqslant x \leqslant 1.5;\ 400 \leqslant Pe \leqslant 4000. \qquad (12)$$

Figure 11 compares experimental and theoretical data obtained by various authors, [8], [9] and [13]. The data of [10] obtained with a cluster with x = 1.38 were not used since they should be regarded as qualitative [only]. The above reference notes an appreciable effect of the cluster's geometry and bends of the rods on their temperature fields. The reproducibility of experiments when replacing the working tubes in the cluster with x = 1.38 was poor. It can be seen that the experimental data of [3] break up into smooth distributions for each of the relative rod spacings (x). This behavior of points is not observed in experimental data of [8] and [9].

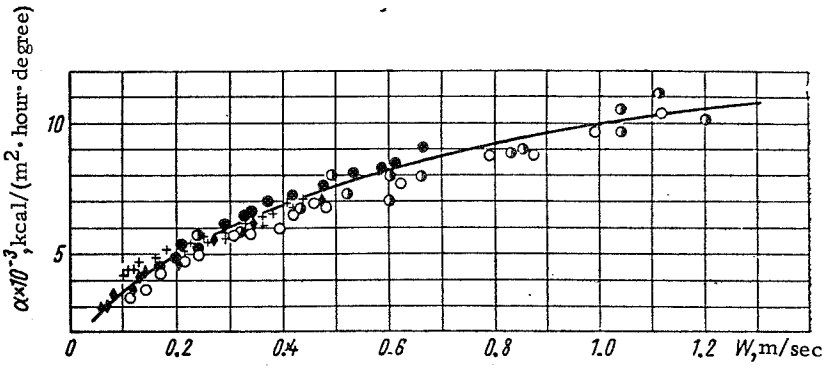

Figure 9. Heat Transfer Coefficients as a Function of the Mercury Velocity. ◑, ●, ○, + and ◆ Denote Clusters With x = 1.1, 1.2, 1.3, 1.4 and 1.5 Respectively $d_2 \approx 17$ mm. A) kcal/m^2-hour-degree.

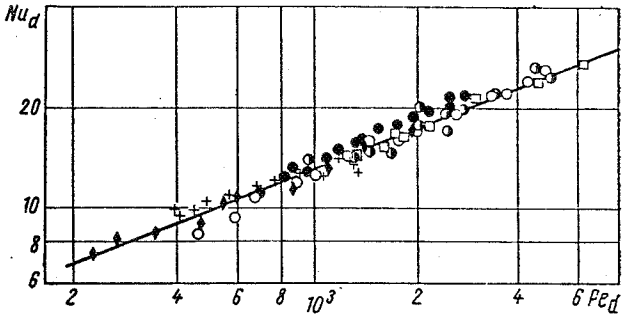

Figure 10. Curve of $Nu_d = f(Pe_d)$ Obtained by Using the Outer Diameter of Tubes as the Characteristic Dimension. □ - Cluster With x = 1.15 (d_1 = 15.4 mm, d_2 = 17 mm) for the Na-K alloy; ◑, ●, ○, + and ◆ are Clusters With x = 1.1, 1.2, 1.3, 1.4 and 1.5, Respectively for Mercury.

Figure 11 displays dashed curves of Nu = f(Pe), calculated by Dwyer. The theoretical curve D for the cluster with x = 1.75 was taken from [13], the theoretical curves, C, B and A for clusters with x = 1.5, 1.20 and 1.1 have been taken from the article by Dwyer, devoted to analytical calculation of heat transfer to liquid metals flowing in relatively tightly packed rod clusters. As can be seen, the results of these calculations show that the Nusselt numbers depend appreciably on the relative spacing of the rods. Thus, when $Pe = 10^3$ the calculated Nusselt numbers in clusters with x = 1.1 and 1.75 differ by approximately 60%. The numerical values of the theoretical relationships Nu = f(Pe) in clusters with x = = 1.2 and 1.10 lie above the corresponding experimental data for turbulent flow by 60% on the average.

Of great interest are heat transfer in rod clusters in the laminar flow of the coolant. The distributions of temperature and of the thermal fluxes over the perimeter of the fuel elements, as well as the average Nusselt numbers in laminer flow can be calculated analytically. Reference [21] presents a corresponding solution for the boundary condition t_w = const over the perimeter of the fuel elements. The Nusselt numbers have been calculated primarily for loosely-spaced

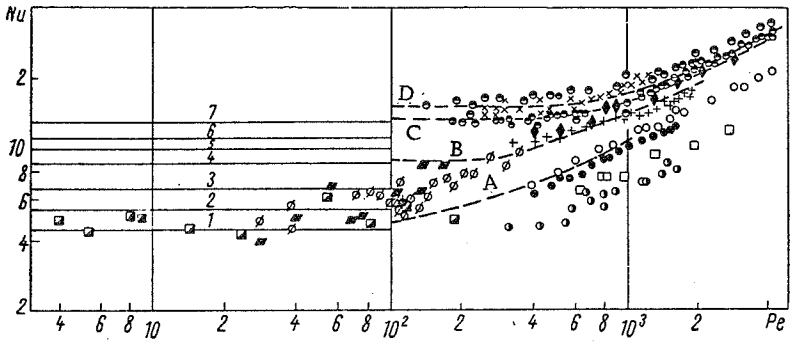

Figure 11. Curves of Nu = f(Pe) Using the Hydraulic Diameter as the Characteristic Dimension. 1, 2, 3, 4, 5, 6 and 7 are Calculated Values of Nusselt Numbers for Laminar Flow in Clusters With x = 1.1, 1.15, 1.2, 1.3, 1.4, 1.5 and 1.75, Respectively, [4]. ◪ and □ are Clusters With x = 1.15 (d_1 = = 13 mm, d_2 = 17 mm, d_1 = 15.4 mm, d_2 = 17 mm, Respectively) for the Na-K Alloy; ◑, ◍, ○, + and ◆ are Clusters With x = 1.1, 1.2, 1.3, 1.4 and 1.5, Respectively for Mercury; ⊖ and x Denote a Cluster With x = 1.75 Using Mercury and the Na-K Alloy, Respectively, [13]; ø and ◆ are Clusters With x = 1.2 and 1.5, Respectively, for Sodium, [8] and [9], A, B, C and D are Curves Obtained Theoretically by Dwyer, [13], for Clusters With x = 1.1, 1.2, 1.5 and 1.75, Respectively.

clusters ($x \geq 1.1$). Reference [4] gives a general analytical solution of thermal conductivity and heat transfer equations in the fissionable material, jacket and coolant for any boundary condition. The Nusselt numbers have been calculated for clusters with x = 1-1.5 for two limiting boundary conditions t_w = const and q_w = const. This solution proves that the boundary conditions and the relative rod spacing have an appreciable effect on the average Nusselt numbers. The solid lines in Fig. 11 are for theoretically calculated values of Nusselt numbers for laminar flow, taken from [4]. The Nusselt numbers for clusters with x = 1.1, 1.15 and 1.2 were obtained by taking into account the properties of the tubes (wall thickness and its thermal conductivity), used in the experiments. The values of Nusselt numbers for these clusters lie between the limiting values of Nusselt numbers calculated on the basis of the boundary conditions q_w = const and t_w = const over the perimeter of the tubes. Since in clusters with x = 1.2 the properties of the tube have almost no effect on the temperature fields and on the heat transfer, the theoretical values of Nusselt numbers for q_w = const and t_w = const are equal to one another.

The average heat transfer in laminar flow of the Na-K alloy was studied using a cluster with x = 1.15, consisting of 37 heated tubes 17 x 2 mm in diameter.

The methods used for performing the experiments and processing the data were the same as in the study of heat transfer in turbulent flow. However, in the region with very low Peclet numbers, when large temperature gradients and, consequently, axial thermal fluxes through the coolant and in the wall were appreciable, appropriate corrections were introduced into the mean temperature difference between the wall and the coolant for the region with stabilized heat transfer, using the formula /168

$$\Delta\vartheta = \frac{\frac{\Delta t}{t_0}\left(1+\frac{\lambda_w\omega_w}{\lambda_f\omega_f}\right)\cdot d_r}{\mathrm{Pe}}, \qquad (13)$$

where Δt is the increase in the coolant temperature, ω_w and ω_f are the cross sectional areas of the tube and of the coolant flow, respectively.

As can be seen from Fig. 11, the experimental points for laminar flow in a cluster with x = 1.15 are clustered about Nu ≈ 5, which does not depend on the Peclet numbers. This value of the Nusselt number is shown in Fig. 12 for comparison with the corresponding results obtained theoretically in [4]. This figure also displays average values of Nusselt numbers for laminar flow in clusters with x = = 1.2, 1.5 and 1.75, taken from [8], [9] and [13]. The value of Nu for the cluster with x = 1.5 [9] lies below the corresponding theoretically obtained value by approximately a factor of 2.7. In clusters with x = 1.1, 1.2, 1.3, 1.4 and 1.5 experimental data were also obtained on the average heat transfer for the transient (from turbulent to laminar) flow of mercury (up to Re ≈ 3500). However, these data turned out to be on the lower side as compared with theoretically calculated Nusselt numbers for laminar flow.

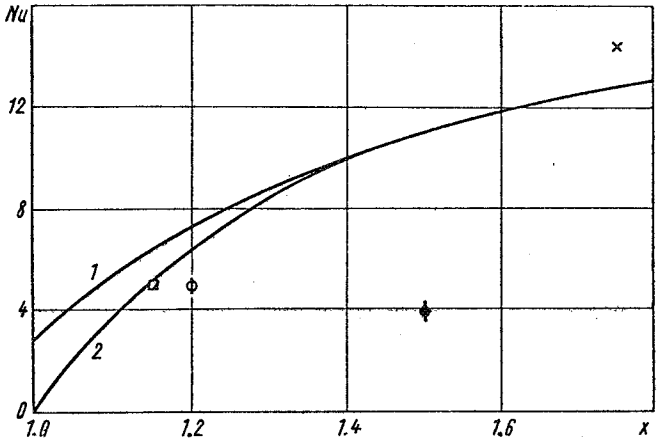

Figure 12. Comparison of Experimental Data on Nusselt Numbers With the Analytically Obtained Relationships of Nu = f(x) for Laminar Flow, Taken From [4]. 1) t_w = const; 2) q_w = = const, Over the Perimeter of Fluid Element (for Notation see Fig. 11).

This may be ascribed to the fact that the design of clusters with x = 1.1, 1.2, 1.3, 1.4 and 1.5 did not sufficiently satisfy the features peculiar to /169

heat transfer in laminar flow.[1] One may note the following features of heat transfer of laminar flow in fuel element clusters: 1) an extended temperature distribution at the outlet of the center cells, due to the insufficient rate of coolant intermixing; 2) axial and radial thermal fluxes, which increase with a reduction in the Peclet number; 3) reconstruction of the velocity distribution over the cross section of the cluster in the case of transient flow; 4) presence of large temperature gradients over the heated length, which is responsible for the appreciable effect of errors in determining the location of the start and end of the heated section. All this makes difficult the experimental determination of the average mixed temperature of the coolant in the center cells of the cluster and as the end results reduces the accuracy of experimental data on the average Nusselt numbers.

The experimental data obtained with clusters with x = 1.1, 1.2, 1.3, 1.4 and 1.5 in turbulent flow should, when extrapolated to the region of low Peclet numbers, join the corresponding theoretical values of Nusselt numbers for laminar flow. From this point of view it makes sense to generalize the data presented in [5], which yield continuous curves of Nu = f(Pe) for turbulent, transient and laminar flows of the coolant.

The empirical formula (12) can be used for calculating Nusselt numbers for developed turbulent flow. It should not be extrapolated to region where Pe < 400.

NOTATION

t_0 coolant temperature at the inlet to the cluster, °C

$\lambda_0, \lambda_w, \lambda_f$ thermal conductivities of the fissionable material, fuel-element jacket and the coolant, respectively

ε_ν turbulent viscosity

V volumetric flow rate of coolant

$d_2 = 2R_2$ outer diameter of tube

$d_1 = 2R_1$ inner diameter of tube

S distance between tube centers

P wetted (which is the same as heated) perimeter of the cell angle of rotation of the center tube

φ deflection angle of central tube

---

[1] The design of the clusters was developed to determine temperature field and heat transfer in developed turbulent flow of the coolant.

Dimensionless Quantities

$x = S/2R_2$ relative rod spacing

$\xi = R_1/R_2$ relative wall thickness of the tube

REFERENCES

1. Subbotin, V.I., et al.: Atomnaya energiya, 9, 6, 461 (1960). /170
2. Ushakov, P.A., et al.: Atomnaya energiya, 13, 2, 162 (1962).
3. Subbotin, V.I., et al.: Teplootdacha v elementakh reaktora okhlazhdayemykh zhidkim metallom Heat Transfer in Elements of Liquid-Metal Cooled Reactors]. Report presented at the 3rd International Conference on Peaceful Uses of Atomic Energy. Geneva, 1964.
4. Ibragimov, M.Kh. and Zhukov, A.V.: Atomnaya energiya, 18, 6, 630 (1965).
5. Ibragimov, M.Kh. and Zhukov, A.V.: Atomnaya energiya, 20, 5, 425 (1966).
6. Buleyev, N.I., et al.: Teplofizika vysokikh temperatur, 2, 5, 749 (1964).
7. Borishanskiy, V.M. and Firsova, E.V.: In the collection Zhidkiye Metally [Liquid Metals]. Gosatomizdat, Moscow, 1963.
8. Borishanskiy, V.M. and Firsova, E.V.: Atomnaya energiya, 14, 6, (1963).
9. Borishanskiy, V.M. and Firsova, E.V.: Atomnaya energiya, 16, 5, (1964).
10. Friedland, A.J., et al.: Trans. ASME, III, 526 (1961).
11. Nimmo, B. and Dwyer, O.E.: Trans. ASME, 312 (1965).
12. Maresca, M.W. and Dwyer, O.E.: Trans. ASME, 86, 180 (1964).
13. Dwyer, O.E. and Lyon, R.N.: USA report No. 225 presented to the 3rd International Conference on Peaceful Uses of Atomic Energy, Geneva. 1964.
14. Dwyer, O.E.: T u P.S. Chem. Engng Progr. Sympos. Series, v56, 30 (1960).
15. Rothfus, R.R., et al.: A.I. Ch. E. Journal, 4, 240 (1958).
16. Friedland, A.I. and Bonilla, C.F.: A.I. Ch. E. Journal, 7, No. 1 (1961).
17. Knudsen, J.G. and Katz, D.L.: Proceedings of the Midwest Conference on Fluid Dynamics, University of Illinois, Urbana, III, 1950, 175-203.
18. Zhukov, A.V., et al.: Eksperimental'noye issledovaniye na modelyakh poley temperatury teplovydelyayushchikh elementov [Experimental Study of Temperature Fields of Fuel Elements, Using Models]. Article immediately following this one in the present collection.
19. Neymark, B.Ye.: Teploenergetika, 3, (1955).
20. Nikol'skiy, N.A., et al.: In the collection Voprosy teploobmena [Problems of Heat Transfer, pp. 193-199]. Published by the Academy of Sciences of the USSR. 1959.
21. Sparrow, E.M., et al.: Trans. ASME, 415 (1961).

EXPERIMENTAL STUDY OF TEMPERATURE FIELDS OF FUEL ELEMENTS, USING MODELS

A. V. Zhukov, L. K. Kudryatseva, Ye. Ya. Sviridenko, V. I. Subbotin, V. D. Talanov and P. A. Ushakov

The active zones and side screens of reactors frequently consist of hexagonal fuel-element holders in which the cylindrical fuel elements are placed in a regular triangular lattice. To prevent the fuel elements from buckling and to eliminate the attendant temperature variations, the fuel elements are held at fixed distances from one another by winding spiral fins on the shell; the height of the fins is equal to the minimum space between the elements or to half of this distance. In the first case the fuel elements are in "rib-to-shell" contact, while in the second the contact is "fin-to-fin." The peripheral fuel elements contact by their fins the fuel holder wall in either case. /170

The reliability of reactor operation depends to a large extent on the conditions under which the heat is removed from the fuel-element surfaces, i.e., on the temperature regimes of the latter. Heat transfer in clusters of smooth rods, arranged in a regular, infinite alternating pattern was studied previously for a wide range of variation in the relative spacings $1 < x < 1.5$. The results of these studies are presented in [1] and [2]. /171

The characteristic features of heat transfer from finned fuel elements held in hexagonal assemblies are produced by the fact that the peripheral fuel elements are situated near a flat wall and by the fact that all the fuel elements are finned. The peripheral elements in the fuel-element holders at hand are not cooled uniformly over the perimeter due to the difference in the configuration of the spaces surrounding them. Various quantities of the coolant flow through the different spaces and hence, the temperature of the coolant differs appreciably over the perimeter of the fuel elements. The fact that the fuel elements are finned can promote the intermixing of the coolant over the cross section of the fuel-element holder, which improves the conditions for heat transfer. On the other hand, the presence of fins produces local increases in the temperature of fuel-element cladding.

Liquid metals have relative high thermal conductivity coefficients and low coefficients of specific heat per unit volume. They are characterized by high heat-transfer coefficients and high temperature rises in the coolant flowing in passages. Hence, the temperature distribution in fuel-element surfaces is determined basically by the local temperature gains of the coolant, rather than by the local heat-transfer coefficients.

Temperature fields of fuel elements under different conditions of heat transfer (centrally and peripherally located fuel elements) were investigated at the Physics and Power Institute. The experiments were performed on a stand (Fig. 1) consisting of two main loops [one] with sodium and [the other] with a

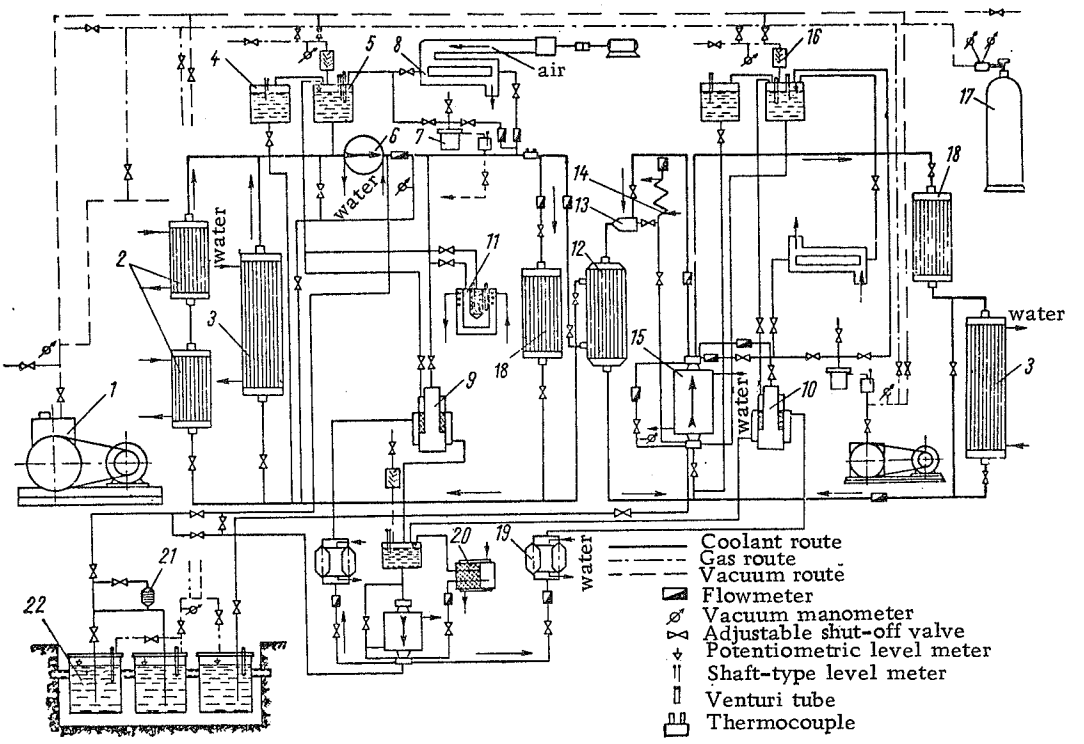

Figure 1. Schematic Diagram of the Experimental Stand. 1) Vacuum Pump; 2), 3) and 19) Cooler; 4) Measuring Tank; 5) Breathing Tank; 6) Centrifugal Pump; 7) Sampler; 8) Air Cooler; 9), 10), 11) and 20) Traps; 12) Inter-Circuit Heat Exchanger; 13) Mixing Tank; 14) Heating Loop; 15) Electromagnetic Pump; 16) Vapor Trap; 17) Gas Bottle; 18) Test Section; 21) Filter; 22) Drain Tank.

sodium-potassium alloy (22% Na + 78% K). The sodium was circulated by an electromagnetic, and the sodium-potassium alloy by a centrifugal pump providing a pressure of about 6 kg/cm^2 for a coolant flow rate of about 150 m^3/hour. The impurities were removed from the coolant by cold traps cooled by sodium-potassium alloy provided from an auxiliary loop. The oxygen content of the coolants was measured by distilling a coolant sample with subsequent chemical analysis of the residue. The heat removal in the circuits was brought about in metal-to-water heat exchangers, built with a double wall with a graphite interlayer (for high temperature) or with an interlayer from Wood's metal (for low temperatures). Bellows-type valves were used in the sodium-potassium loop, while valves with frozen-sodium seals were used in the sodium loop. All the components of the stand were made from 1Kh18N9T steel. The experiments with the sodium-potassium alloy were performed using models of four types.

Model No. 1, consisting of 37 tubes assembled in a triangular array with a relative spacing x = 1.15 and placed in a hexagonal shell is shown in Figs. 2 and 3. The tubes were heated by nichrome coils so as to give q = const at the

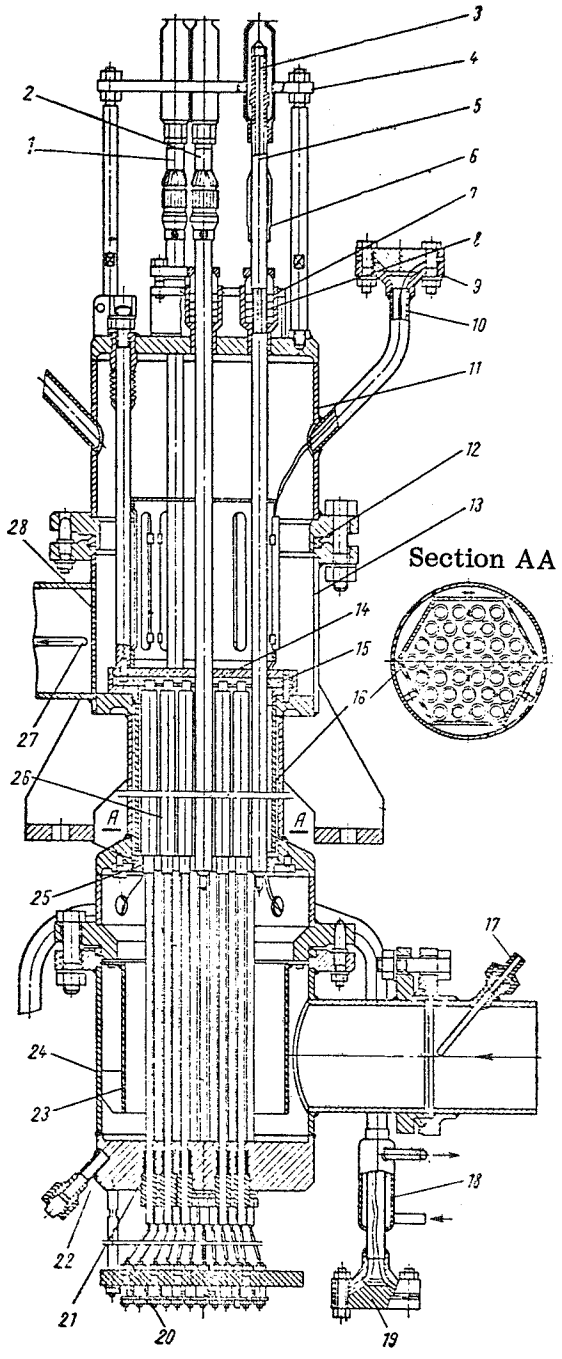

Figure 2. Overall View of Model No. 1 (Smooth Tubes). 1, 2, 5, 7 and 8) Tubes With Thermocouples and Packing Glands; 3) and 20) Terminal Blocks; 4) [Retaining] Plank; 6, 9, 10 and 19 Packing and Fastening of Thermocouples; 11, 12, 13, 23 and 24), Headers With Packings and Repellers; 14 and 28) Grating With Thermocouples and Mixing Header; 15 and 25) Gratings; 16) Shell; 17 and 27) Thermocouples; 18) Cooler; 21) Packing Gland; 22) Connecting Stub; 26) Heated Tubes.

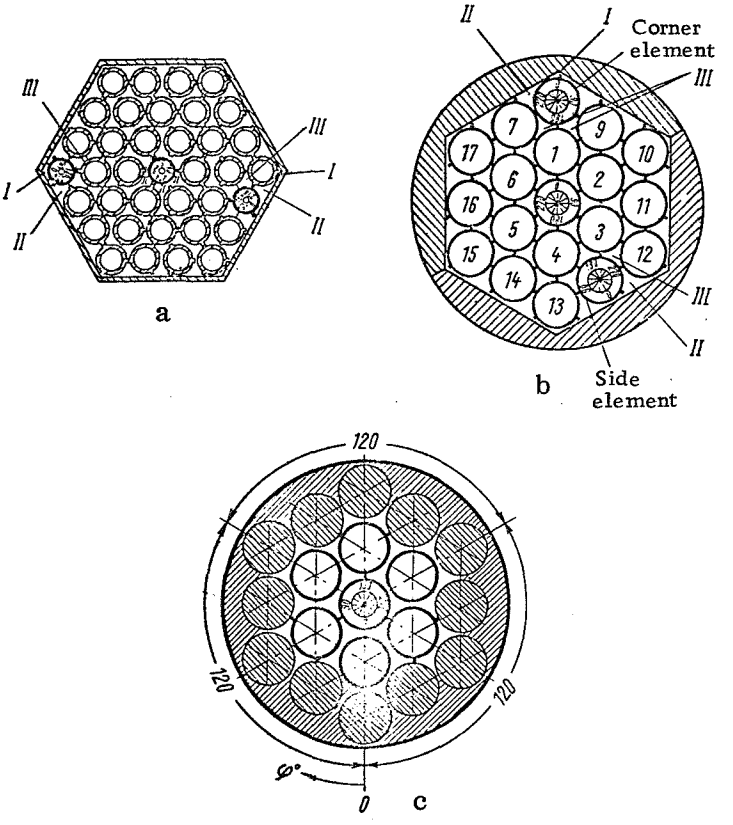

Figure 3. Sections Through Models. a), b) and c) are Models No. 1 (With Ribbed Tubes), No. 3 and 4, Respectively; I, II and III are Numbers of Intertubular Spaces [Cells].

inner surface. The center, side and corner tubes were equipped with 12 thermocouples each, placed in capillaries with an external diameter of 0.5 or 0.8 mm. These tubes are held in ribbed holders, in close contact with the tube surfaces. Using these holders it is possible to rotate the tubes without disturbing the circuit's mode of operation. The remaining 34 tubes had fins spot welded to them. The height of the ribs was half the size of the narrow space between the tubes. In addition, this model was also studied in the finless version.

Model 2 is basically of the same design, except that it consists if 37 smooth tubes with a relative spacing x = 1.24. This model was used to study the temperature fields in the center and corner tubes.

Model No. 3, consisting of 19 tubes assembled in a triangular array with relative spacing x = 1.04 and placed in a hexagonal shell, is shown in Fig. 3b. /175
The tubes were held at fixed distances by spiral fins, the height of which was equal to the size of the narrow intertubular space (the ribs were in contact with the surfaces of neighboring tubes and of the shell walls). The center, a side and

a corner tube were made so that they can be rotated. The temperature at the tubes surfaces was measured by thermocouples in protective capillaries with an outer diameter of 0.3 mm.

Model No. 4 (Fig. 3c) consists of seven heated tubes, twelve rods and a specially-shaped spacers, placed in a cylindricals shell. The tubes and the rods are arranged in a regular triangular array with a relative spacing of x = = 1.04. Three side heated tubes and three displacing rods have three fins each, while the remaining tubes and spacers are smooth. Thus, the fins are in contact with the surfaces of the smooth tubes and of the spacing rods. The center tube is made so that it can be rotated. In its surface were embedded 12 thermocouples in protective capillaries with an outer diameter of 0.5 mm.

The temperature of the fluid at the outlet from each cell and in the headers was measured in each model, for which purpose we used thermocouples in capillaries with an outer diameter of 0.8 or 0.5. The geometric characteristics of the models are presented in Table 1.

TABLE 1. Geometic Characteristics of Models

Designation	Model			
	№ 1	№ 2	№ 3	№ 4
Outer diameter of tubes d_2, mm	17	17	17.6	17.6
Inner diameter of tubes d_1, mm	13	13	16.4	13.6
Relative lattice spacing, x	1.15	1.24	1.04	1.04
Heated length l_0, mm	690	730	700	700
Distance between end lattices L, mm	750	785	770	770
Cross sectional area of rib, mm^2	1.8×1.2	—	0.8×0.8	0.8×0.75
Windind pitch of each rib, mm	750	—	1500	1500

Side Elements

The temperature variations were determined over the perimeter of a side tube, located near a flat wall. Figure 4 presents experimental results obtained with model No. 1. The temperature minimum is observed in the region adjoining the shell ($\varphi = 0°$), while the maximum took place at $\varphi = 180°$. This behavior can be attributed to the difference in the temperature gains of the coolant in spaces II and III, surrounding the side tube (see Fig. 3a and Table 2).

Figure 5 shows the results of approximately calculated relationships between the average velocities (W_{II}/W_{III}), volume flow rates (V_{II}/V_{III}) and temperature gains of the coolant ($\Delta t_{II}/\Delta t_{III}$) in spaces [cells] II and III as a function of the relative tube spacing for clusters with hexagonal holders (models No. 1 /178

TABLE 2. Geometric Characteristics of Spaces [Cells] I, II and III of Clusters of Smooth Tubes

Designation	General expression	Model	
		№ 1, $x = 1.15$	№ 2, $x = 1.24$
Area of flow cross section of the cell			
I	$\Omega_I = \frac{\pi d_2^2}{48}\left(\frac{2\sqrt{3}}{\pi}x^2 - 1\right)$, mm²	8.676	13.1
II	$\Omega_{II} = \frac{\pi d_2^2}{8}\left(\frac{4}{\pi}x^2 - 1\right)$, mm²	77.60	109
III	$\Omega_{III} = \frac{\pi d_2^2}{8}\left(\frac{2\sqrt{3}}{\pi}x^2 - 1\right)$, mm²	52.06	79
Wetted perimeter of cell			
I	$P_I = \frac{\pi d_2}{12}\left(\frac{2\sqrt{3}}{\pi}x + 1\right)$, mm	10.2	10.5
II	$P_{II} = \frac{\pi d_2}{2}\left(\frac{2x}{\pi} + 1\right)$, mm	46.2	47.8
III	$P_{III} = \frac{\pi d_2}{2}$, mm	26.7	26.7
Heated perimeter of cell			
I	$P_{0_I} = \frac{\pi d_2}{2}$, mm	8.91	8.91
II	$P_{0_{II}} = \frac{\pi d_2}{2}$, mm	26.8	26.8
III	$P_{0_{III}} = \frac{\pi d_2}{2}$, mm	26.8	26.8
Hydraulic diameter of cell			
I	$d_{h_I} = \frac{d_2\left(\frac{2\sqrt{3}}{\pi}x^2 - 1\right)}{\frac{2\sqrt{3}}{\pi}x + 1}$, mm	4.4	3.4
II	$d_{h_{II}} = \frac{d_2\left(\frac{4}{\pi}x^2 - 1\right)}{\frac{2}{\pi}x + 1}$, mm	9.16	6.71
III	$d_{h_{III}} = \left(\frac{2\sqrt{3}}{\pi}x - 1\right)d_2$, mm	11.8	7.80

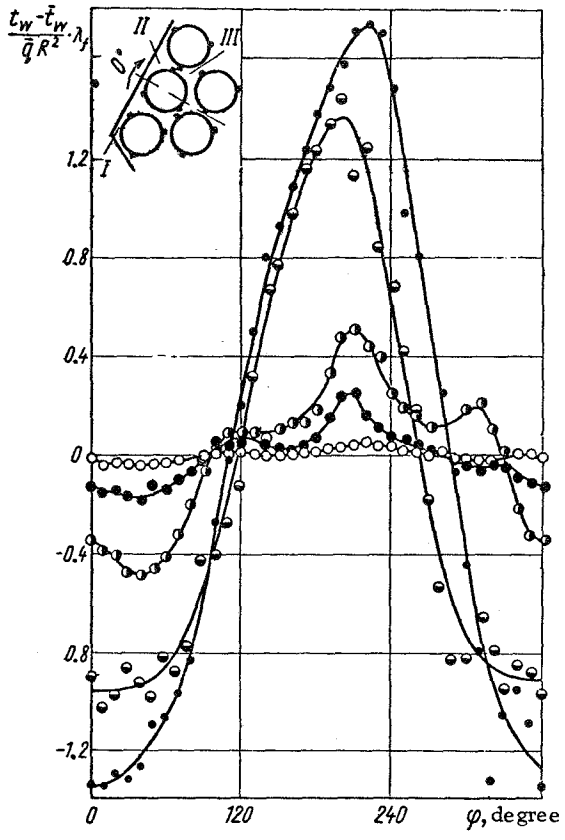

Figure 4. Temperature Variation in a Ribbed Side Tube of Model No. 1.

	W, m/sec	Re	Pe
○	8.65	77 300	2550
●	2.37	19 800	594
◑	0.95	8 830	234
◒	0.196	2 345	45.5
•	0.072	878	16.7

and No. 2 with smooth tubes). The calculations were made for turbulent and laminar flows of the coolant on the assumption that between the cells the coolant does not become intermixed and exchange of heat does not take place [between its individual streams], while the pressure drop in all the cells is identical

$$\Delta P = \lambda \frac{\rho L W^2}{2 d_h} = \text{idem.} \qquad (1)$$

The calculations were performed for three cases.

1. Turbulent flow with $\mathrm{Re} > 10^5$. In this case it may be assumed that the friction coefficient does not depend on the geometry of the cells (λ = idem). It follows from Eq. (1) that the average velocity of the coolant in the cell is

$$W \sim d_h^{0.5}. \qquad (2)$$

2. Turbulent flow with $10^4 \leq \mathrm{Re} \leq 10^5$. In this case it may be assumed that

$$\lambda = \frac{0.3164}{\mathrm{Re}^{0.25}}, \text{ while } W \sim d_h^{0.714}. \qquad (3)$$

3. Laminar flow. In this case /179

$$\lambda = \frac{A}{\mathrm{Re}}, \qquad (4)$$

Where A is a coefficient which depends on the shape of the passage. From Eq. (1) we get that

$$W \sim \frac{d_h^2}{A}. \qquad (5)$$

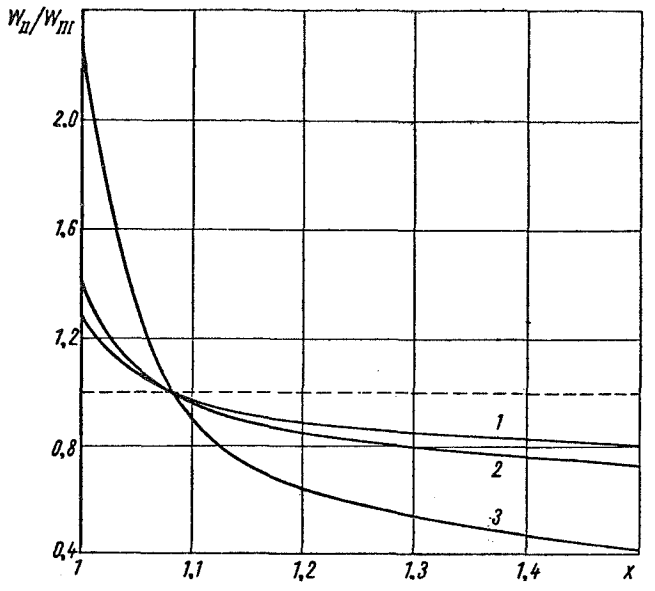

a

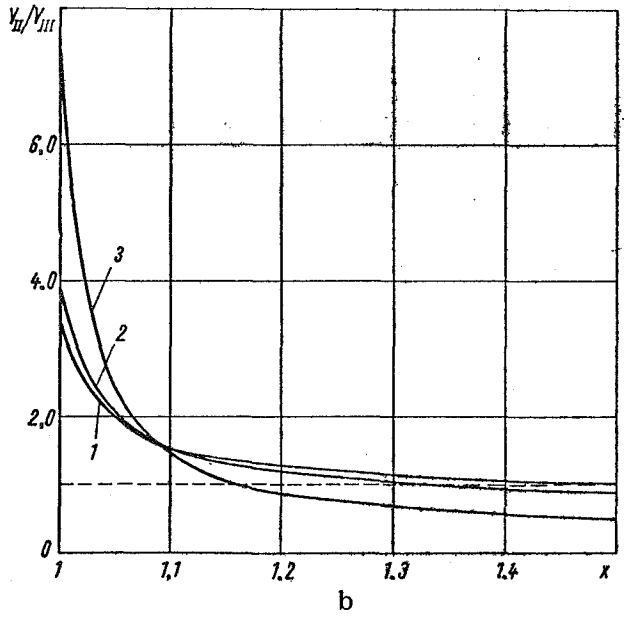

b

Figure 5. Caption on Following Page.

It is assumed that coefficients A are the same for the side and center cells.

As can be seen from Fig. 5, the theoretical relationships between the velocities, volume flow rates and temperature gains of the coolant in cells II and III depend to a large extent on the relative spacing of the rods in the holder. When x is changed, the minimum distance between the peripheral elements and the flat wall change also. This produces a change in the relationship between the flow cross section of cells II and III. The latter circumstance results, in the final count, to redistribution of velocities, flow rates and temperature gains of the coolant in the above cells.

For model No. 1 with smooth tubes (x = 1.15) the theoretical estimates are

$$\frac{W_{II}}{W_{III}} = 0.90; \quad \frac{V_{II}}{V_{III}} = 1.37; \quad \frac{\Delta t_{II}}{\Delta t_{III}} = 0.75.$$

As can be seen, the temperature gain the coolant in cells II is by 25% lower than that in cell III, which is precisely the circumstance responsible for the temperature variation over the perimeter of the side tube. These theoretical estimates should be regarded as approximate, but useful for qualitative clarification of the character of temperature fields over the perimeter of the side tube obtained in the experiments.

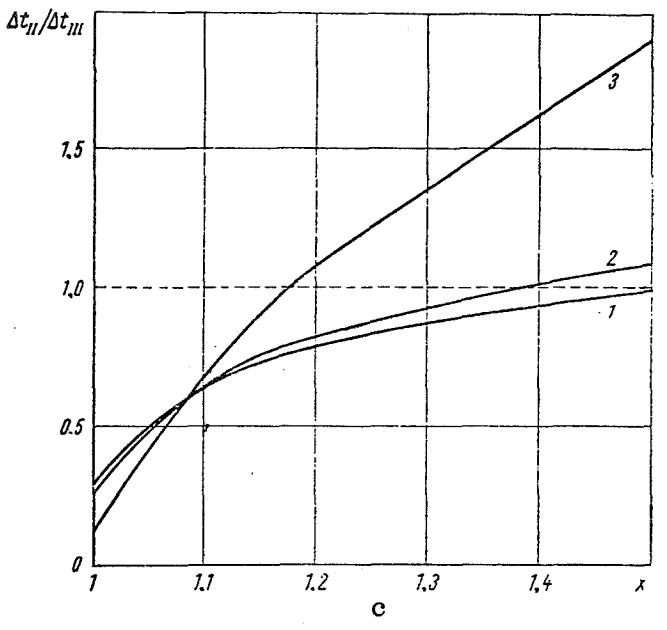

Figure 5. Calculated Values of W_{II}/W_{III} (a); V_{II}/V_{III} (b); $\Delta t_{II}/\Delta t_{III}$ (c) for Cells II and III of Models No. 1 and No. 2 With Smooth Tubes. 1) Turbulent Flow With $Re < 10^5$; 2) Same as Above With $10^4 \leq Re \leq 10^5$; 3) Laminar Flow.

It can be seen from Fig. 4 that, at relatively high Peclet numbers, local distortions of the temperature distribution are observed, which are due to the presence of fins. At low Pe this effect disappears, however, the overall temperature variation increases sharply. In the absence of fins the wall temperature varies over the perimeter smoothly at all Peclet numbers.

Analysis of experimental data shows that for a wide range of Peclet numbers ($100 < Pe < 4000$), the presence of fins does not sharply reduce the temperature variations in the side-element wall. Some peculiar features of the behavior of temperature variations can be observed in the laminar and transient flows of the coolant. For the model with smooth tubes in the range $20 < Pe < 80$ ($800 < Re < 3000$) one observes maxima in the temperature variations $[t_w^{max} - t_w^{min}/\bar{q} \cdot R_2] \cdot \lambda_f$ (Fig. 6). For a cluster of finned tubes these maxima are not as pronounced and are somewhat displaced into the region of lower Peclet numbers. An exception are the initial sections ($l/d_h < 30$). As the rate of flow becomes lower, the temperature gains, and /181 consequently, also the variations in the temperature of the peripheral elements, increase. This increase cannot be infinite, due to heat transfer between the cells, which is proportional to the difference in temperature gains. In low-velocity regions an effect is exerted by natural convection, which aids in intermixing the coolant and reducing the temperature variations, hence, a maximum in the temperature variations is observed at certain Peclet numbers. The lower temperature variations observed in finned tubes in this region are attributed to the fact that the ribs aid in intermixing the coolant.

In laminar flow the effect of the ribs is, apparently, moderate, while the development of natural convection in a cluster of finned tubes is more difficult as compared with this phenomenon in a cluster of smooth tubes. Hence, the variations in the temperature of the side finned tube in laminar flow is found to be somewhat greater than for a smooth tube (see Fig. 6).

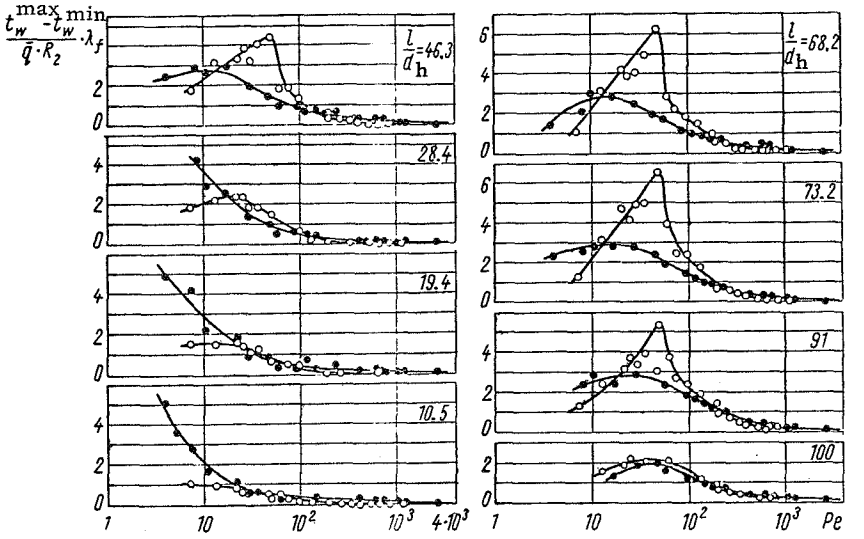

Figure 6. Curve of the Maximum Variation in the Temperature of a Side Tube of Model No. 1 as a Function of the Peclet Number. o and ● Denote Points Obtained for the Smooth and Ribbed Tubes, Respectively.

In the experiments (particularly with the cluster of smooth tubes of model No. 1) we have observed the following: in transient flow the temperature distribution of the coolant at the outlet from the cluster varies in such a manner /182
that the coolant has its maximum temperature gain not at the center of the cluster, but near its periphery (Fig. 7). Here the average temperature of the peripheral tube exceed the average temperature of the center tube, while the temperature variation over its perimeter reaches a maximum. These effects disappear at higher and lower Peclet numbers.

It is assumed that the above anomalies in the temperature fields are due to the redistribution of the rates of flow of the coolant among the cells of the cluster attendant to transition from turbulent to laminar flow. This redistribution is produced by the fact that such a transition takes place primarily in the peripheral cells, in which the velocity of the coolant (see Fig. 5a) and the hydraulic diameters (see Table 2), and consequently, also the Reynolds numbers are lower than in the center cells. Here the flow in the center zone still remains turbulent. Using Eq. (1) we can write

$$\frac{W_{II}}{W_{III}} = \sqrt{\frac{\lambda_{\tau_{III}}}{\lambda_{\pi_{II}}}} \cdot \sqrt{\frac{d_{h_{II}}}{d_{h_{III}}}}, \qquad (6)$$

where $\lambda_{t\,III}$ and $\lambda_{t\,II}$ are the coefficients of resistance of cells III (turbulent flow) and cells II (laminar flow). It can be seen that at the instant of transition from /184

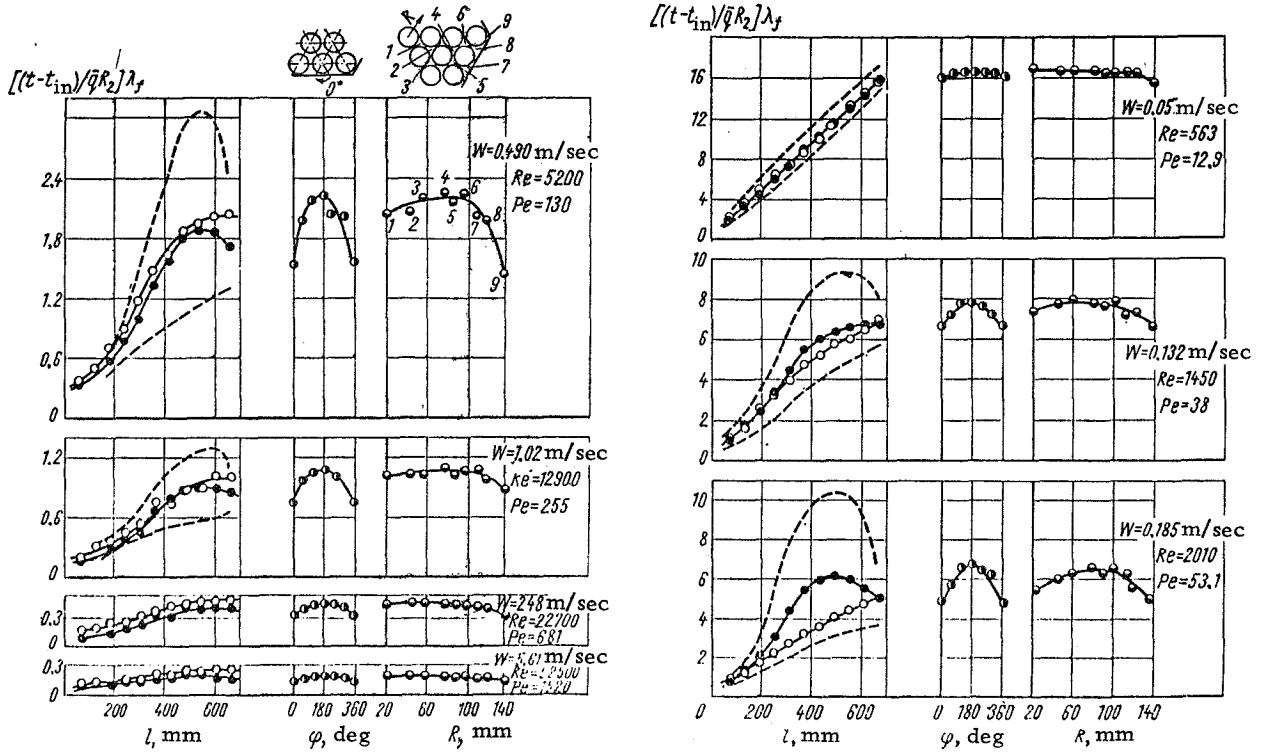

Figure 7. Temperature Fields in a Cluster of Smooth Tubes of Model No. 1. ● and ○ Denote the Average Temperatures of the Walls of the Side and Center Elements, Respectively; the Dashed Lines Shown the Maximum and Minimum Temperatures of the Wall of the Side Tube; ◑ Denotes the Temperature of the Coolant Around a Side Tube at the Outlet From the Cluster; ◒ Denotes the Temperature of the Coolant Over the Radius of the Cluster.

turbulent to laminar flow an additional velocity drop, by a factor of $\sqrt{\lambda_{t\,III}/\lambda_{t\,II}}$ takes place in cells II, for which reason the flow of the coolant moves into the center of the cluster.

The reduction in the average temperature and in the temperature variation of the peripheral tube toward the end of the heated section (see Fig. 7) is apparently due to the turbulizing effect of the upper butt grid and due to redistribution of velocities about it.

In the finned tubes cluster all the above effects were less pronounced, since in this case the redistribution of the flow rates was weaker due to the smaller differences in the hydraulic diameters of cells II and III ($d_{h\,II} = 6$ mm, $d_{h\,III} = 6.5$ mm).

Figure 8 shows changes in the temperature variations in side tubes of model No. 1 with ribbed tubes (x = 1.15) as a function of the length l/d_h of the heated section for the range 200 < Pe < 1000. For this range of changes in Pe the temperature variations became stabilized. In the region of large Peclet numbers (1000-500) this ensued at length $l/d_h \approx 60$, while for lower Pe (400-200) this took place at $l/d_h \approx 80$-90.

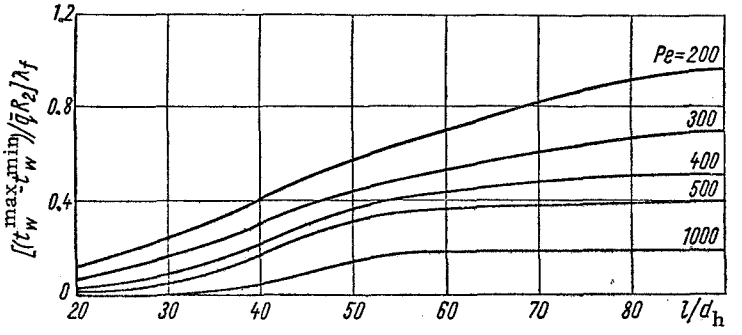

Figure 8. Curves of the Maximum Variation in the Temperature of a Side Tube of Model No. 1 as a Function of the Length of the Heated Section.

The temperature variation over the perimeter of a side tube of model No. 3 (x = 1.04) behaves in approximately the same manner as in experiments with x = 1.15. However, the temperature maxima in the wall in this case are displaced to the points where the side tube comes close to tubes 3 and 4 ($\varphi = 210$ and 150°, see Fig. 3b). Temperature minima correspond to cells in which the coolant is relatively underheated, which is due to the smaller spaces between the tubes as compared with model No. 1.

For the same Peclet numbers the magnitude of the temperature variation in the side tube of model No. 3 exceed appreciably the temperature variation in

a side tube of model No. 1 for the following reasons. First, the relative spacing of tubes in model No. 3 ($x = 1.04$) is appreciably smaller than in model No. 1 ($x = 1.15$), which interferes with intermixing of the coolant between the cells. Second, the relative distance from the peripheral elements to the flat shell in model No. 3 is greater than in No. 1. Hence, the variations in the coolant flow rates, and, consequently, also in the temperature between the different cells of model No. 3 is more appreciable. This corresponds to results of qualitative calculations shown in Fig. 5. Third, the relative wall thickness of tubes of model No. 3 is lower than in model No. 1. This interferes with tangential heat fluxes and produces an additional temperature variation as compared with tubes of model No. 1.

The temperature variations over the heated length of the side tube of model No. 3 did not become stabilized. This circumstance is apparently attributable to the lesser intermixing of the coolant between cells II and III as compared with model No. 1.

Corner Elements

The temperature fields of the corner elements were studied using models No. 1, 2 and 3. The tubes of models No. 1 and 2 were smooth, while those of model No. 3 were ribbed. The results of measurements are shown in Figs. 9-11. It can be seen from Fig. 9 that in clusters of smooth tubes with $x = 1.15$ and $l/d_h = 76$ the maximum temperature in the wall of a corner tube is observed in the region adjoining the corner of the shell, while the minimum temperature is observed in the opposite part of the tube's perimeter. There are no explicit temperature jumps at points where the tube comes closest to the shell. The temperature behaves similarly in the corner element of model No. 2 ($x = 1.24$). Apparently, in fuel element clusters with $x = 1.15$ and 1.24 the minimum distance between the shell and the surface of the corner tube, which is equal in models No. 1 and 2 to half of the space between the tubes (height of the fin) is entirely sufficient to eliminate appreciable overheating of the coolant. The wall temperature at points close to neighboring tubes does not increase either. As was shown [2], a variation in the wall temperature virtually does not exist in clusters of fuel elements arranged in a regular infinite array with a relative spacing $x > 1.1$.

We should note the rather insignificant minima in the wall temperature of the corner tube in the region of $\varphi = 90$ and 270°, which are observed in experiments with model No. 1 at high Reynolds numbers (see Fig. 9). These minima are due to the fact that the coolant flowing in cell II is cooler than that flowing in cell III. At low Reynolds (Peclet) numbers (for example, $Re = 760$) these minima do not exist.

The variations in the temperature of corner tubes of model No. 1 are appreciably lower than the corresponding temperature variation of side tubes in the range of Re(Pe) under study. The shape of the curve of maximum variation in the wall temperature of a corner tube $(t_w^{max} - t_w^{min}/\bar{q} \cdot R_2)\lambda_f$ as a function of

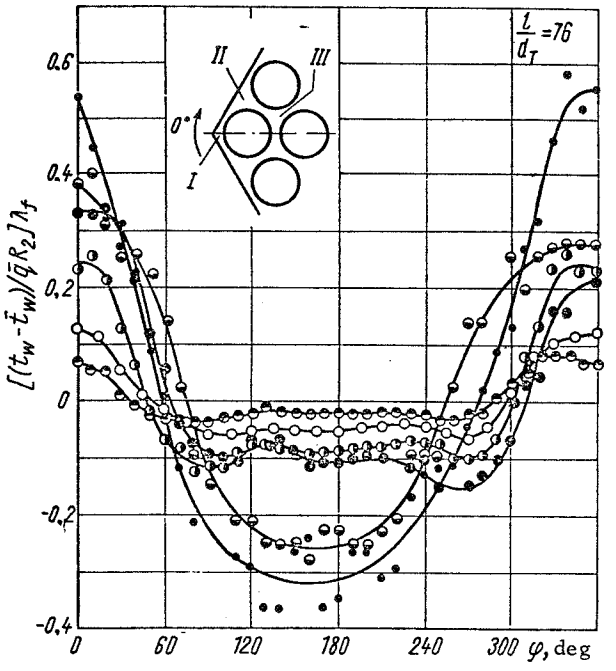

Figure 9. Temperature Variations of a Smooth Corner Tube of Model No. 1.

	W, m/sec	Re	Pe
◓	2.71	28 300	616
○	2,48	19 900	609
◑	1.26	13 750	283
●	0.498	4 620	117
•	0.083	760	19.4
◒	0.029	339	6.4

Pe is approximately the same as for side tubes. However, the maxima in the temperature variations for the corner tubes are less pronounced. /187

The manner in which the wall temperature changes along the perimeter of a corner tube of model No. 3 for $l/d_h = 145$ is shown in Fig. 10. The wall temperature in this case changes in a different manner than in corner elements of models No. 1 and 2. The temperature maximum is observed at the point where it is close to tube 1 (φ = =180°, see Fig. 3b), the temperature minima occur in cells in which the coolant is relatively underheated. This behavior is attributable to the fact that the relative spacing between the corner elements of model No. 3 and the shell is by a factor of two greater than in models No. 1 and 2.

Figure 11 shows changes in the maximum variations in the temperature of corner and side tubes of model No. 3 as a function of the Peclet number at $l/d_h = 145$ and 180. The temperature variation of the corner and side tubes for $l/d_h = 145$ is approximately the same for the same Peclet numbers in the range $20 < Pe < 200$ under study. However, for the given value of l/d_h thermal stabilization ensues only for the corner tube. Hence, as l/d_h increases, the temperature variation in the side tube is increased somewhat.

It is seen from Fig. 11 that the curve of temperature variations as a function of Pe for the corner and side tubes of model No. 3 has no maxima. In a cluster of fuel elements with x = 1.04 heat transfer between the cells, as well as natural convection are more difficult than in clusters with x = 1.15 and 1.24. This is responsible

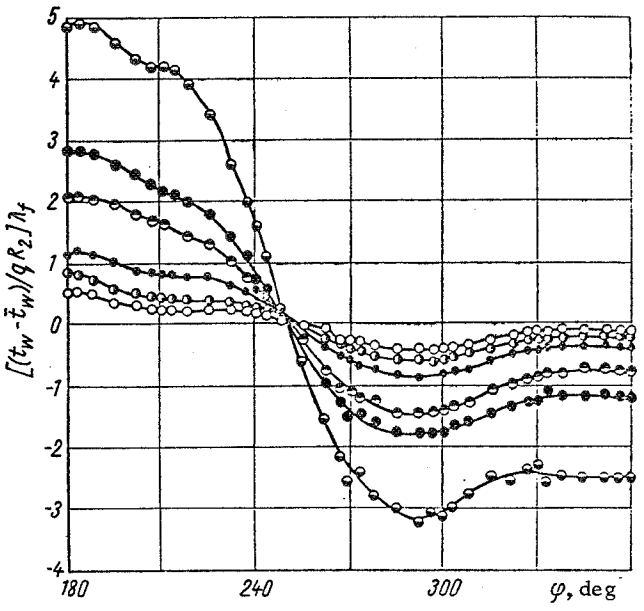

Figure 10. Variations in the Temperature of a Corner Tube of Model No. 3.

	Pe		Pe
◒	8	●	68
◉	23	◑	108
◓	32	○	166

for the continuous increase in the maximum [temperature] variation $(t_w^{max} - t_w^{min}/\bar{q} \times R_2)\lambda_f$ of the corner and side tubes of model No. 3 with a reduction in the Peclet numbers in the range $20 < Pe < 200$. Maxima in this case are apparently displaced into the region of lower Peclet numbers.

Center Elements

Study of the temperature fields of a finned center tube of model No. 1 has shown that the wall temperature under the fins increases. As can be seen from Fig. 12, the maxima in the wall temperature which are observed /189 in the vicinity of the fins are more or less the same for large Re. As the Reynolds numbers are reduced the temperature field is no longer symmetrical. The temperature disturbances induced by the fins extend to an appreciable part of the tube's perimeter. This effect is not as yet sufficiently clear. However, it may be assumed that it is due to a certain deviation of the fins from the nominal dimensions, not entirely identical contact between individual fins and the tube surface, as well as to an increase in the laminar layer near the wall with a reduction in Re.

Following are the values of the Nusselt numbers averaged over the perimeter of the center tube of model No. 1 in the region of stabilized heat transfer:

Pe	1150	1000	835	693	553	228	166	111	54.3	27.3	9.93	7.65	4.71	3.72
Nu	10.2	9.44	8.56	7.22	6.55	5.46	5.68	3.80	5.17	5.07	5.15	4.64	6.00	3.20

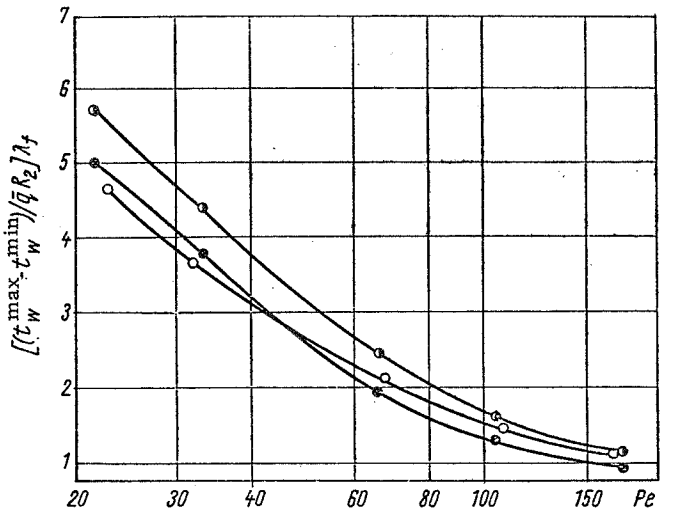

Figure 11. Maximum Temperature Variation in the Corner and Side Tubes of Model No. 3 as a Function of the Peclet Number. ◑ - Side Tube, $l/d_h = 180$; ● - Same as Above for $l/d_h = 145$; ○ Denotes a Corner Tube With $l/d_h = 145$.

The above Nusselt and Peclet numbers have been calculated by means of the following expression

$$\mathrm{Nu} = \frac{\bar{q} d_h}{(\bar{t}_w - \bar{t}_f)\lambda_f}; \qquad \mathrm{Pe} = \frac{W d_h}{\lambda_f} C_p \gamma, \tag{7}$$

where d_h is the hydraulic diameter calculated by subtracting the area occupied by the ribs, $\bar{t}_w$ is the temperature of tube's surface, averaged over the perimeter and calculated by taking into account the temperature increase beneath the ribs; $\bar{t}_f$ is the average temperature of the coolant in the section at hand and q is the specific thermal flux, calculated for a smooth tube. /190

Figure 13 shows experimental data for stabilized Nusselt numbers for a model with x = 1.15 (finned tubes), as well as the curve of Nu = f(Pe), calculated for a cluster with x = 1.15 (smooth tubes) using a generalized relationship obtained in [3]. Comparison of experimental data with this curve is rather arbitrary, however, it follows from it that the fins of tubes of the model with x = = 1.15 does not result in an appreciable change in Nu as compared with the smooth version of tubes, if the Nusselt and Peclet numbers are calculated from Eqs. (7). The appreciable scatter in the experimental data for laminar flow should be regarded as a natural phenomenon, since the experimental accuracy in this region is only moderate.

Results of studies of the temperature field of the center tube of model No. 3 (x = 1.04) are presented in Fig. 14. The temperature distribution over the perimeter of the center tube is determined primarily by the configuration of the cells. When fins are positioned in narrow parts of the cells, the additional increase in the temperature variation comprises about 5-10% of the average variation. The distributions of thermal fluxes over the perimeter were found by solving the problem of thermal conductivity and on the basis of results obtained by measuring the temperature distribution.

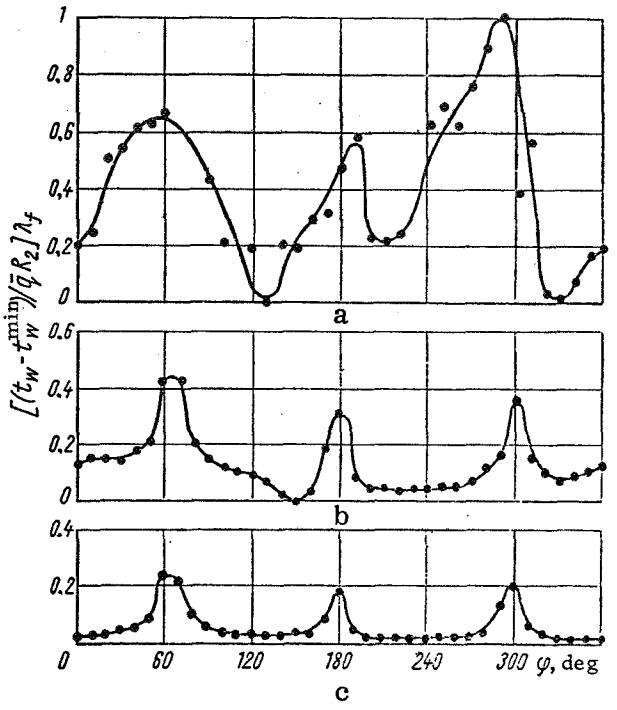

Figure 12. Variation in the Temperature of a Finned Center Tube of Model No. 1.
a) W = 1.54 m/sec, Re = 14,400, Pe = 366;
b) W = 2.37 m/sec, Re = 20,600, Pe = 601;
c) W = 4.02 m/sec, Re = 32,330; Pe = 1030.

The dependence of the temperature variation of the center element on the Peclet number for $20 < Pe < 300$ is described by the formula

$$\frac{t_w^{max} - \bar{t}_w}{\bar{q}R_2}\lambda_f = 1.5\,Pe^{-0.32}. \qquad (8)$$

The values of the Nusselt numbers in the region with stabilized heat transfer for the center element of model No. 3 are as follows: /192

Pe	22	33	66	106	175
Nu	1.26	1.62	2.90	4.60	5.90

The strong dependence of the Nusselt on the Peclet number (the power of Pe being about 0.75, as compared with clusters of smooth tubes (the Peclet number here 0.45) is remarkable and is apparently brought about by the fins.

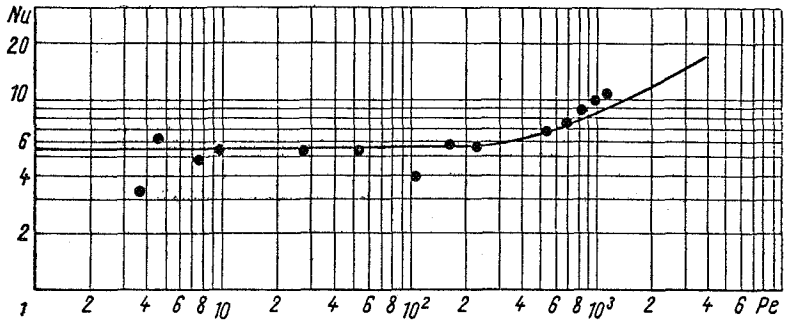

Figure 13. Values of Nusselt Numbers in the Stabilized Heat-Transfer Region of Model No. 1. The Black Dots Represent Data Obtained on a Model With Finned Tubes; the Solid Line is the Curve of Nu = f(Pe) for a Cluster of Smooth Tubes.

Results of studies of the temperature field of the center tube of model No. 4 are presented in Figs. 15 and 16. In the given model, due to alternation of smooth

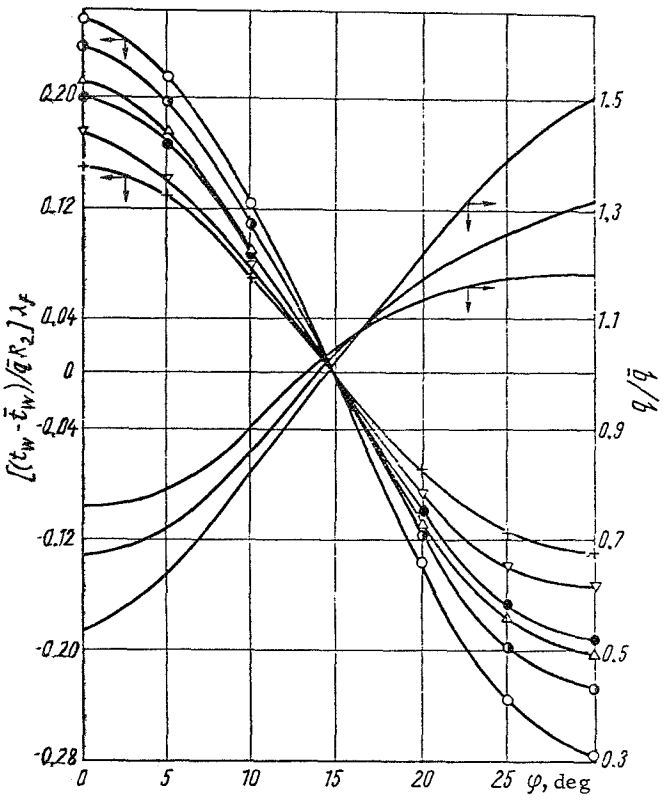

Figure 14. Variation in the Wall Temperature and in the Thermal Fluxes Over the Perimeter of the Center Tube of Model No. 3.

	Pe		Pe
○	22	●	67
◑	33	▽	106
△	63	+	175

and finned tubes, the surface of the center tube can be broken up into three regions with identical heat-transfer conditions (330° < $< \varphi <$ 90°, 210 $< \varphi <$ 330°, $\varphi° < \varphi <$ 210°) (see Fig. 3c). Distributions of temperature and of thermal fluxes averaged over the range 330 $< \varphi <$ 90° are shown in Fig. 15. Temperature maxima in the narrow parts of cells differ depending on whether the neighboring tube is smooth or ribbed. The presence of fins on a neighboring tube for a given cluster geometry produces a certain smoothing of the temperature variation at the center tube.

Figure 16 shows the curve of the maximum variation in the dimensionless temperature as a function of Pe (Re), which shows more pronouncedly than in a cluster of smooth tubes the effect of the coolant velocity on the temperature variation in the center tube. The cause of this are the fins which aid in intermixing the coolant over the cross section of each cell. The intermixing effect becomes greater with an increase in velocity. /193

The values of the Nusselt numbers for the region with stable heat transfer for the center tube of model No. 4 are as follows.

Pe	75	117	178	270	373
Nu	1.1	2.0	2.3	2.9	3.5

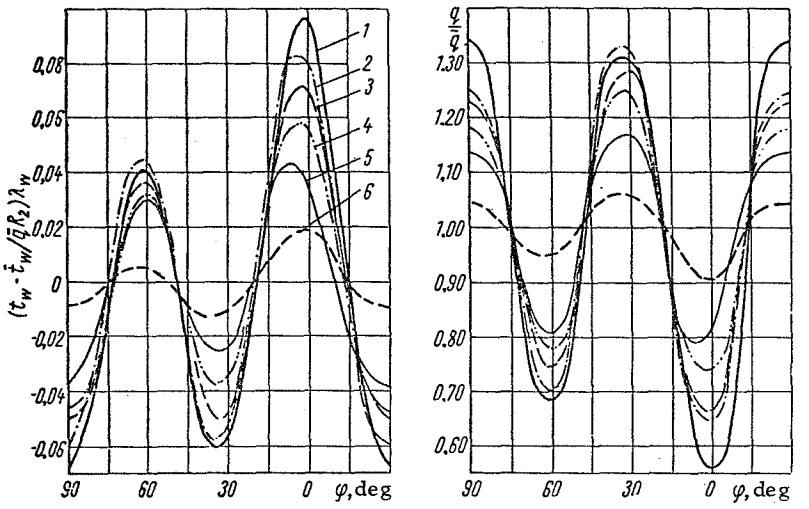

Figure 15. Variation in the Wall Temperature and in Thermal Fluxes over the Perimeter of the Center Tube of Model 4. 1), 2), 3), 4), 5) and 6) are curves for Pe = 75, 117, 178, 270, 373 and 588, Respectively.

Results

1. On the basis of the measured temperature field of models of fuel elements, assembled in hexagonal holders, the following conclusion can be made. The peripheral elements (situated at the flat wall of the shell) can have appreciable temperature variations produced by differences in the geometry of the surrounding spaces. This circumstance must be taken into account in designing liquid-metal cooled reactors.

2. The variation in the wall temperature of peripheral elements is due primarily to the different temperature gains of the coolant in spaces surrounding the fuel elements.

3. Elements situated near a flat wall at a distance equal to the minimum spacing between the fuel elements have a relatively greater temperature variation than elements the distance between which and the flat wall comprises half of the maximum distance between the fuel elements. In both cases the temperature variation depends substantially on the relative spacing of the fuel elements. In tightly-packed clusters (x = 1.04) the temperature variation in the peripheral elements is higher than in the looser clusters (x = 1.15, 1.24).

4. In the loosely-packed clusters the temperature variation in the side elements is appreciably higher than in corner elements. In tightly-packed clusters the variation in the wall temperature of these elements is approximately the same. /194
In both cases the temperature maximum of peripheral elements in turbulent and

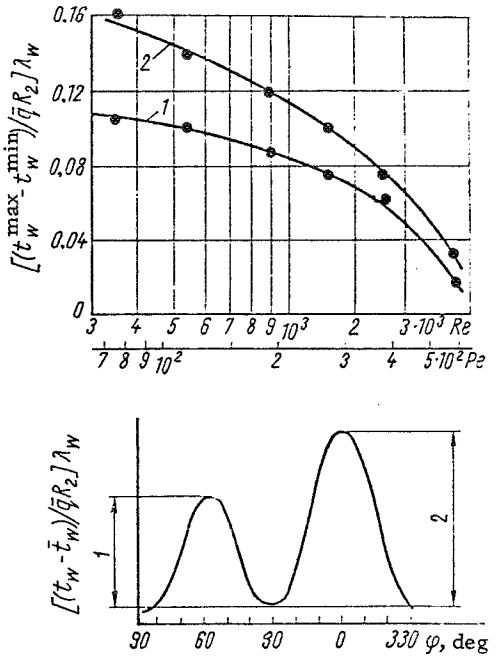

Figure 16. The Maximum [Temperature] Variation in the Center Tube of Model No. 4 as a Function of Re and Pe. 1) and 2) the Heat-Conducting Surface is Facing a Ribbed and Smooth Side Tube, respectively.

laminar flows of the coolant is approximately equal to the maximum temperature of the center fuel elements.

5. In experiments with x = 1.15 we have discovered the effect of redistribution of the coolant flow rates over the cluster's cross section attendant to the transient flow of the coolant. This redistribution can result in the fact that the average wall temperature in the peripheral elements will exceed the average temperature of the center elements.

6. The temperature variations in the walls of side elements become stabilized over the heated length of tight clusters at appreciably higher values of l/d_h than for loosely-packed clusters. The temperature variation in a side tube of the cluster with x = 1.04 does not become stabilized even at a distance of l/d_h · p = 180°.

7. The finning of fuel elements arranged in regular lattices in hexagonal holders reduces the temperature variations in the peripheral elements for the case of turbulent coolant flow. This is not observed for laminar flow.

8. In recalculating the experimental data obtained for specific fuel element designs, one must satisfy the conditions for approximate thermal simulation of fuel elements presented in [4].

REFERENCES

1. Subbotin, V.I., et al.: Teplootdacha v elementakh reaktora, okhlazhdayemykh zhidkim metallom [Heat Transfer in Elements of Liquid-Metal Cooled Reactors]. Report presented at the 3rd International Conference on Peaceful Uses of Atomic Energy, Geneva, 1964.
2. Zhukov, A.V., et al.: Teploobemen pri prodol'nom obtekanii zhidkim metallom razvinutykh puchkov sterzhney [Heat Transfer From Loosely-Packed (Fuel) Rod Clusters To Liquid Metal Flowing in the Axial Direction]. Second Article in Part II of this collection.
3. Ibragimov, M.Kh. and Zhukov, A.V.: Atomnaya energiya, 20, 5, 425 (1966).
4. Ushakov, P.A.: Priblizhennoye teplovoye modelirovaniye tsylindricheskikh teplovydelyayushchikh elementov [Approximate Thermal Simulation of Cylindrical Fuel Elements]. First article in Part II of this collection.

HEAT TRANSFER IN THE INTERTUBULAR SPACE OF LIQUID-METAL HEAT EXCHANGERS

P. L. Kirillov and M. Ya. Suvorov

To calculate the heat transfer coefficient in tube-type heat exchangers one must know the laws governing the transfer of heat in the tubes and in the intertubular space (on axial and transverse flow) of the tube clusters. Heat transfer attendant to the flow of liquid metals in pipes has been studied extensively and at present there are available recommendations on the calculations which agree with one another quite satisfactorily. [On the other hand] very little was done to study the heat transfer attendant to axial flow past tubes, [1-3]. The previously obtained formulas for calculations required checking, since the preceding experiments were performed without checking the purity of the metal or under circumstances where such control was unsystematic. /194 /196

The purpose of the present investigation was in experimental study of heat transfer on axial flow of liquid metal in the intertubular space of a heat exchanger. Here we have determined the dependence of the average heat transfer coefficient on the velocity and on the geometric dimensions of the cluster. To generalize the data obtained, we have used the hydraulic diameter as the characteristic dimension.

The schematic of the stand, consisting of two loops, which was used in the experiments is shown in Fig. 1. In the first (heating) loop the heat-transfer agent is sodium, while in the second loop the coolant is an eutectic sodium-potassium alloy. In the experimental heat exchanger the sodium was piped through the tubes, while the sodium-potassium alloy was pumped through the intertubular space. The sodium was pumped by a centrifugal pump with a frozen-sodium seal. The sodium was pumped through an electric heater and the heat exchanger. This stand was used simultaneously to study the heat transfer of liquid metal in round tubes, for which purpose a special test section was installed. The oxides from the sodium were removed by a cold trap, while the admixture content was monitored by cork-type oxide [content] indicators. The flow rate of the liquid metal was measured by magnetic flowmeters, which were calibrated by a measuring tank. The sodium-potassium alloy was pumped through the circuit by an electromagnetic pump through the experimental heat exchanger and an evaporator. The heat from the evaporator was removed by boiling toluene, the vapor of which condensed in the water-cooled condenser. The alloy circuit was provided by a cold trap, oxide [level] indicator and a tank for calibrating the flowmeters. /19[illegible]

The design of the heat exchangers which were tested on the stand is shown in Fig. 2. The heat exchanger consisted of a cylindrical jacket, with seven tubes placed inside of it and six displacers, welded to the casing. The geometry of the inlet and outlet sections of all the heat exchangers is identical. Only their length and relative spacing were changed, which made it possible to expose the effect of these factors on the average heat transfer (Table 1). The sodium and the sodium-potassium alloy were pumped through the heat exchanger only after both metals

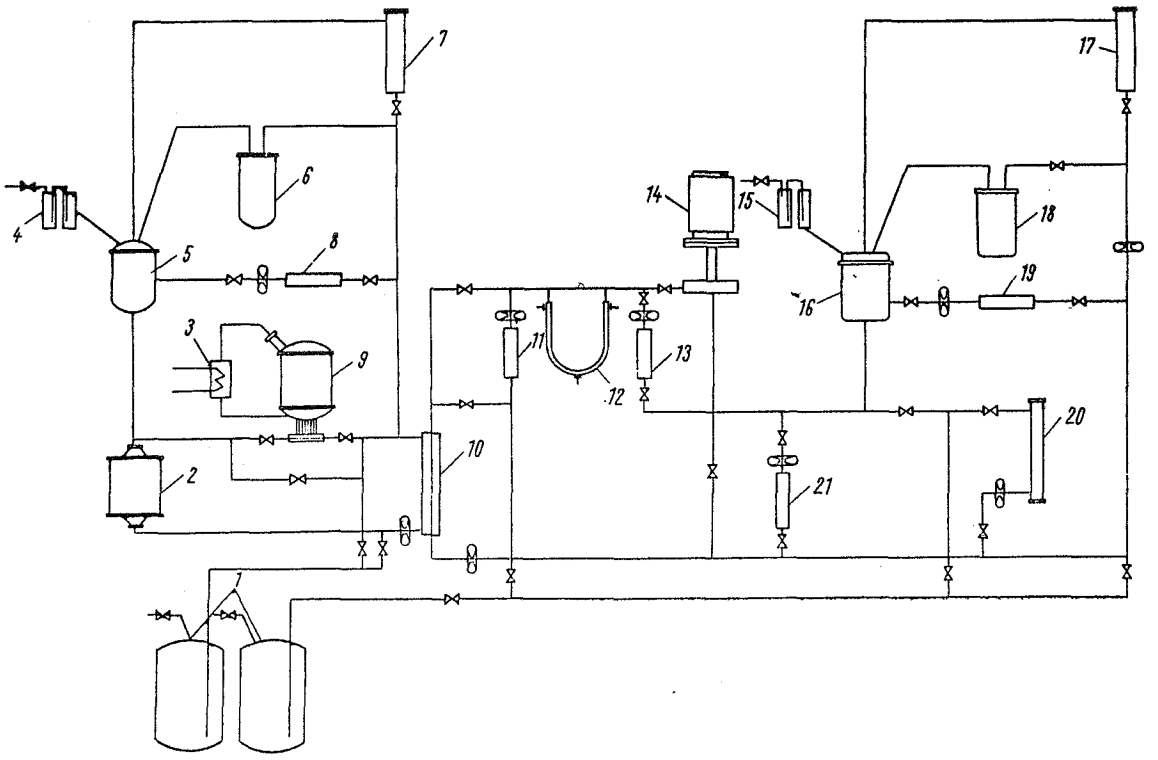

Figure 1. Schematic Diagram of the Experimental Setup (Sodium Circuit). 1) Loading Tanks; 2) Electromagnetic Pump; 3) Condenser; 4) and 15) Vapor Traps; 5) and 16) Breathing Tanks; 6) and 18) Cold Traps; 7) and 17) Measuring Tanks; 8), 11), 13, 19 and 21) Oxide [Content] Indicators; 9) Evaporator; 10) Heat Exchanger; 12) Electric Heating Loop; 14) TsN-280 Centrifugal Pump; 20) Test Section (Tube).

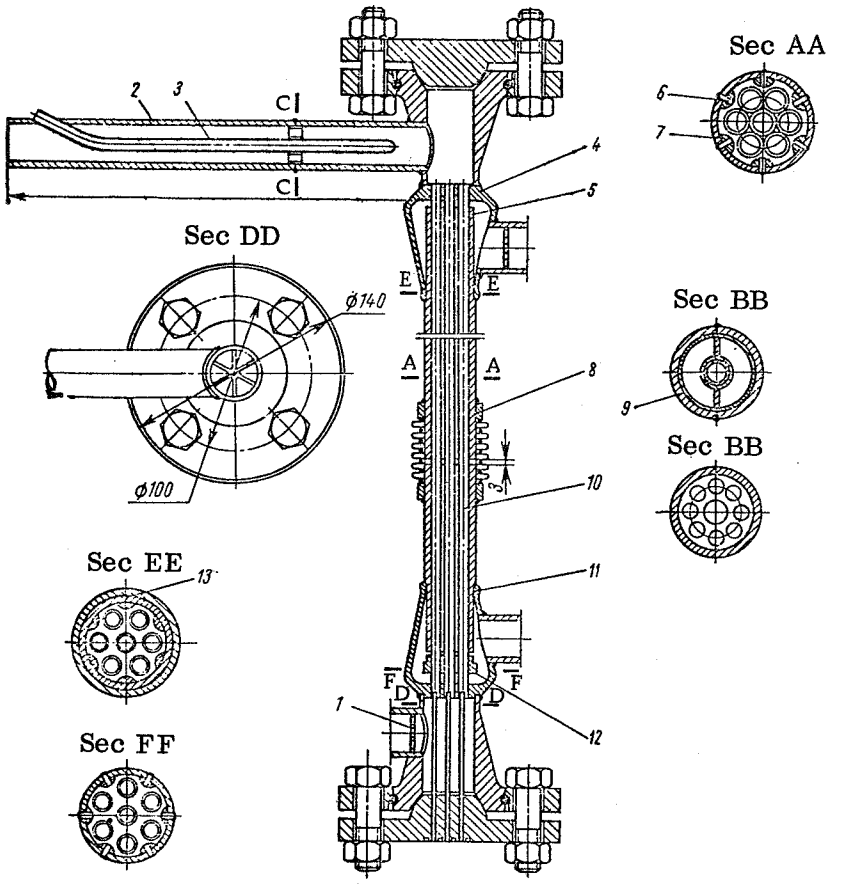

Figure 2. Heat Exchanger. 1) Turbulizer; 2) Connecting Stub; 3) Thermocouple Hood; 4) and 11) Inlet and Outlet Mixing Headers; 5) Casing; 6) and 7) Displacers; 8) Assembled Bellows; 9) Spacing Ring; 10) Tube; 12) Ring; 13) Dowel.

TABLE 1. Basic Geometric Characteristics of the Heat Exchangers

Diameter of tubes, mm	Working length, mm	x	Hydraulic diameter of cluster, mm	L/d_h	Tube material
7.6×0.3	425	1.1	3.57	119	1Kh18N9T
7×0.2	314	1.14	2.62	120	1Kh18N9T
6.8×0.3	500	1.14	2.93	170	EI-211
6.8×0.3	660	1.14	2.93	225	EI-211
7×0.2	514	1.25	4.54	113	1Kh18N9T
7×0.2	765	1.25	4.54	169	1Kh18N9T
7×0.2	1040	1.25	4.54	230	1Kh18N9T
6.8×0.3	460	1.4	7.67	60	EI-211
6.8×0.3	1300	1.4	7.67	170	EI-211

had oxides removed from them by means of cold traps. The oxygen content after trapping was $5 \cdot 10^{-4}$% and $2 \cdot 10^{-3}$% by weight in the sodium and sodium-potassium alloy circuits, respectively. After obtaining a stable thermal state, we have measured the following quantities: 1) flow rates of the sodium and of the sodium-potassium alloy by means of magnetic flowmeters; 2) average temperatures at the inlet and outlet of the heat-transfer agents. The temperatures were measured by chromel-alumel thermocouples with wire diameter of 0.2, placed in capillaries from stainless steel. The thermocouple emf was measured by the R-2/1 potentiometer. /200

On the basis of the measured flow rates and temperatures at the ends of the heat exchanger we have determined the heat transfer coefficient

$$\bar{k}_l = \frac{Q}{\pi \delta t L n} . \tag{1}$$

Since

$$\bar{k}_l = \frac{1}{\frac{1}{\alpha_1 d_{in}} + \frac{1}{2\lambda_w} \ln \frac{d_{out}}{d_{in}} + \frac{1}{\alpha_2 d_{out}}} , \tag{2}$$

the heat transfer coefficient in the intertubular space of the heat exchanger becomes

$$\alpha_2 = \frac{1}{d_{out}\left\{\frac{1}{\bar{K}_l} - \frac{1}{\alpha_1 d_{in}} - \frac{1}{2\lambda_w} \ln \frac{d_{out}}{d_{in}}\right\}} . \tag{3}$$

The coefficient of heat transfer α_1 from the sodium was calculated using the expression for a round pipe

$$Nu_1 = 5 + 0.025 \ Pe_1^{0.8}. \tag{4}$$

In processing the experimental data the characteristic dimension of the intertubular space was the hydraulic diameter for the entire cluster

$$d_h = \frac{4F}{S} . \tag{5}$$

The experimental data are presented in Fig. 3a. Curves which can be described by the expression $Nu_2 - f(Pe_2^{0.6})$ can be drawn through the experimental points.

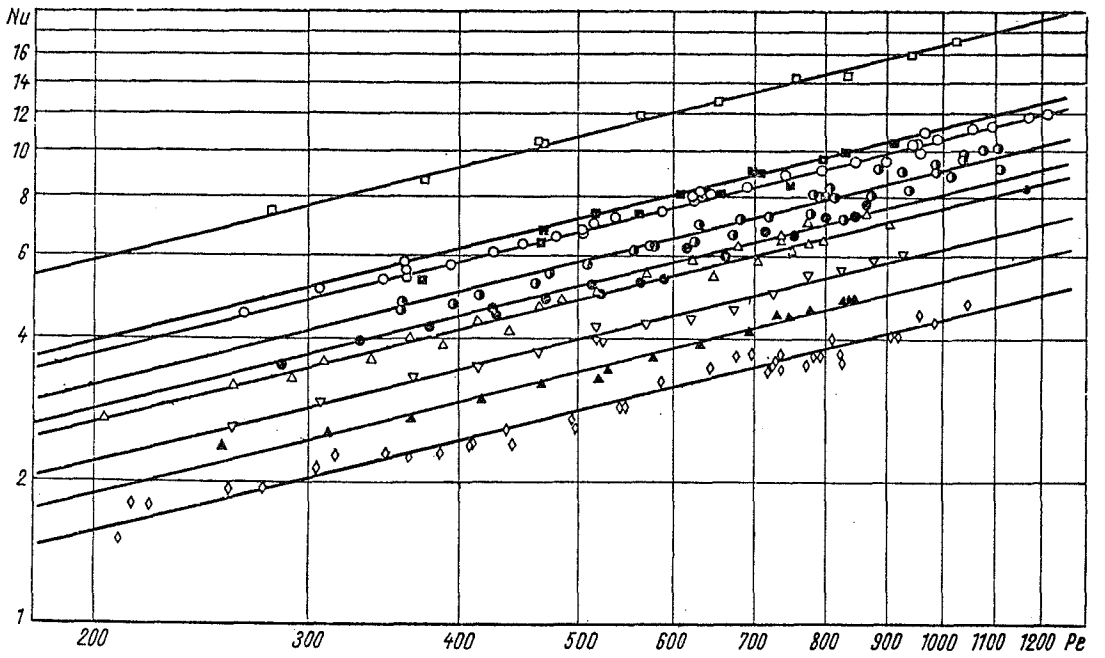

a

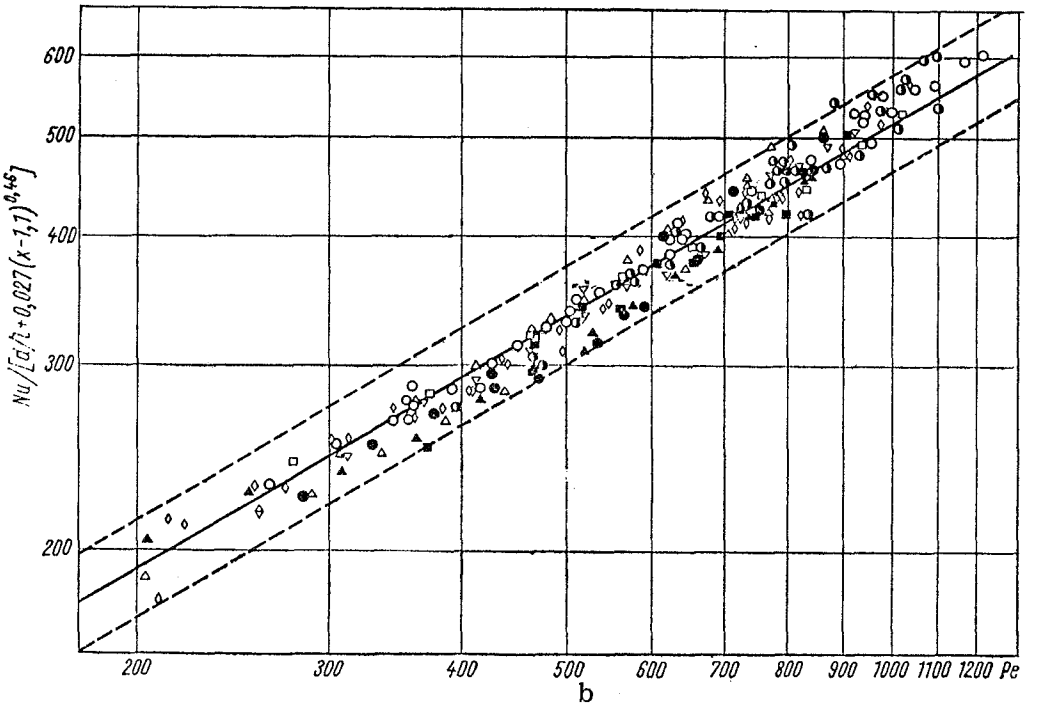

b

Figure 3. Experimental Data in Coordinates $Nu_2 = f(Pe_2)$ (a);

$$\frac{Nu_2}{\left\{\frac{d_h}{L} + 0.027\,(x-1.1)^{0.46}\right\}} = f\,(Pe_2)$$ (b):

	x	l, mm		x	l, mm
◇	1.1	425	△	1.14	314
▽	1.14	500	▲	1.14	660
○	1.25	514	◑	1.25	765
●	1.25	1040	□	1.40	460
■	1.40	1300			

Figure 3a shows that heat transfer depends, in addition, on the relative spacing and on the length of the heat exchanger. To generalize the experimental data, on consideration of these factors, we have selected the following form

$$\mathrm{Nu}_2 = A\left\{\frac{d_h}{L} + B(x-m)^n\right\}\mathrm{Pe}_2^{0,6}, \tag{6}$$

where A, B, m and n are determined graphically. The range within which all the characteristic quantities were varied in tests with all the heat exchangers is given in Table 2.

After the constants are determined, the [above] formula takes on the form

$$\mathrm{Nu}_2 = 8\left\{\frac{d_h}{L} + 0.027(x-1.1)^{0,46}\right\}\mathrm{Pe}_2^{0,6}. \tag{7}$$

Figure 3b displays the experimental data in the coordinates

$$\lg \frac{\mathrm{Nu}_2}{\frac{d_h}{L} + 0.027(x-1.1)^{0,46}} f(\lg \mathrm{Pe}_2).$$

The scatter of experimental points about the average line is ±10%. /202

When operating the heat exchangers we have observed phenomena which requires close attention to the deviation of the actual characteristics of the heat exchangers from their design characteristics. Reference is made here to the reduction in the average heat transfer coefficient in the heat exchanger after prolonged operation, when the oxide content in the sodium increases. The experimental heat exchanger (l = 314 mm) was placed on a stand and operated for four months, the first two weeks of which were spent studying the exchanger's characteristics. During the entire time other experiments were performed at the stand, during which the oxygen content in the sodium circuit varied from $5 \cdot 10^{-3}$ to $5 \cdot 10^{-4}$ [by weight]. After the experiments were performed the stand was disconnected. When it was restarted we have discovered that the trap for removing oxides from the sodium did not operate (it was completely clogged up by the oxides). Nevertheless, we read the heat-exchanger characteristics again and discovered in the process that the heat transfer coefficient has become smaller by a factor of more than two. By increasing the temperature in the circuit and by removing oxides from the metal by a new cold trap the heat transfer coefficient was [then] increased appreciably. However, it still remained by approximately 20% lower than the initial coefficient. We have disconnected then the end flanges of the heat exchanger and washed the tubes by alcohol and water and dried them. The characteristics of the heat exchanger with a surface thus cleaned returned to their initial

TABLE 2. Range of Parameters Under Study

Length, mm	Heat-transfer agent	Velocity, m/sec	Temperature gain, °C	Re·10⁻⁴	Pe	Nu	α_2, kcal/m²-hour-degree	$\bar{k}_l$, kcal/m-hour-degree
425	Na	5.6—13.4	3.7—20.8	8.43—24.65	585—1420	11.1—15.3	—	—
	NaK	2.0—9.9	9—53	1.87—10.92	207—1060	1.5—4.7	9 200—26 100	56—111
314	Na	12	13—15	20.8—24.2	1200	14.2	—	—
	NaK	2.87—12.6	33—120	2.42—10.28	202—914	2.7—7.3	23 100—61 300	111—188
500	Na	12.3—13	16—19	21.8—23.55	1163—1227	14—14.4	—	—
	NaK	3.28—11.8	35—104	3.24—11 6	259—936	2.6—6.0	20 200—45 000	88.5—138
660	Na	11.5—11.6	15.2—18	20—22.8	1090—1112	13.7—13.9	—	—
	NaK	2.61—10.7	38—133	2.61—10.41	203—852	2.15—4.78	16 600—37 000	77.6—123
514	Na	9.5—10	9.7—12	13.6—16	935—980	12.9—13.15	—	—
	NaK	2.0—9.2	16.5—65	2.96—11.35	265—1240	4 62—11.9	21 900—56 000	105—180
765	Na	11.6—12.3	9.3—11	14.99—19.15	961—1280	13.15—14.6	—	—
	NaK	2.69—8.8	18.5—58	3.42—12	359—1130	4.7—9.3	22 400—49 000	106—163
1040	Na	10.4—10.6	14.1—16.2	20.2—22	1050—1082	13.5—13.65	—	—
	NaK	2.38—7.4	11.1—16.8	3.78—11.7	284—876	3.5—7.72	17 400—38 600	90.6—152
460	Na	13.5—13.6	14.1—15.1	24.7—26.42	1278—1297	14.65—14.7	—	—
	NaK	1.4—5.1	25.3—56.5	3.73—13.28	279—1040	7.9—17	24 000—50 000	94—144
1300	Na	12.5—12.7	14—16.6	22.15—24	1178—1200	14.14—1425	—	—
	NaK	1.9—4.6	31—71	4.95—12.2	373—923	5.34—103	15 700—30 400	1.43—112.3

values. Figure 4 shows the variations in Nu during the experiments. A similar picture was also observed when a 1040 mm long heat exchanger was used.

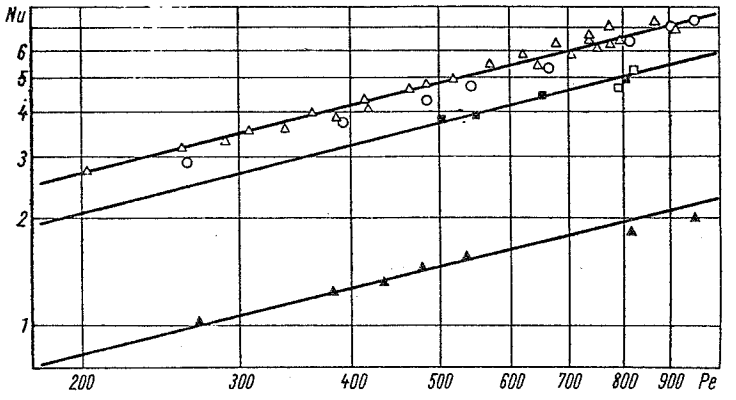

Figure 4. Effect of Impurities in the Metal on the Heat Transfer Coefficient. △ - Pure Metal; ▲ Contaminated Metal; ▪ - After Filtration of Metal, $\tau = 10$ Hours at t = 370°C; □ After Filtration, $\tau = 50$ Hours at t = 250°C and $\tau = 10$ Hours at t = 470°C; ○ - After Washing the Heat Exchanger, Pure Metal.

Results

On the basis of our experiments we can conclude the following. /203

1. The dependence of the heat transfer coefficient on the velocity in the intertubular space can be expressed as

$$\alpha_2 \approx W_2^{0.6} \quad \text{or} \quad \mathrm{Nu}_2 \approx \mathrm{Pe}_2^{0.6}.$$

2. The dimensionless heat transfer coefficient (Nu_2) increases with an increase in the relative spacing of the tubes in the cluster.

3. The average heat transfer coefficient for the intertubular cluster [apparent error] should be space,] becomes stabilized at relative lengths of about 300-400.

4. Until more accurate relationships are obtained, using heat exchangers with a large number of tubes, it is recommended to use the expression

$$\mathrm{Nu}_2 = 8\mathrm{Pe}_2^{0.6}\left\{\frac{d_h}{L} + 0.027\,(x-1.1)^{0.16}\right\},$$

which is valid in the range Pe = 200–1200

$$x = 1.1 - 1.4 \text{ и } L/d_h = 60 - 230;$$

here the oxygen content of the sodium should be $\leq 5 \cdot 10^{-3}$% by weight and in the sodium-potassium alloy it should be $\leq 2.5 \cdot 10^{-3}$% by weight.

5. The sodium oxides, by settling on the heat-exchanger walls, can reduce the heat transfer coefficient several fold.

NOTATION

d_{out} outer diameter of tube

d_{in} inner diameter of tube

d_h hydraulic diameter of cluster

L test length of the tube

F cross sectional area of the cluster

S total wetted perimeter of cluster

x relative spacing

n (this was omitted by translator)

Q_1 quantity of heat given up by the sodium

Q_2 quantity of heat received by the Na-K alloy

δ_t average logarithmic temperature difference

$\overline{k_l}$ average heat transfer coefficient

α_1 coefficient of heat transfer inside the tube

α_2 average coefficient of heat transfer in the intertubular space

w_1 velocity of sodium inside the cluster's tubes

w_2 velocity of the sodium-potassium alloy in the interbular space of the cluster

REFERENCES

1. Borishanskiy, V. M., et al.: In the collection Zhidkiye metally [Liquid Metals], Gosatomizdat, Moscow, 1963.
2. Schwenk, H. C. and Schannon, R. H.: Power, 99, (11), 92 (1955).
3. Brooks, R. D. and Rosenblatt, A. L.: Mech. World and Engng Rec., 75(5), 363 (1953).

ANALYSIS OF THE APPLICABILITY OF AVERAGE HEAT-TRANSFER COEFFICIENTS IN HEAT-EXCHANGER DESIGN

P. A. Ushakov

This article proves analytically that the values of the average heat transfer coefficients for short heat exchangers found by different methods can differ appreciably from one another. It is also proven that, for approximate design calculations for these exchangers it is expedient to use the average heat transfer coefficients determined by means of the mean temperature difference between the wall and the fluid, rather than by integration of local heat transfer coefficients. /204

There exist three methods for finding the average heat transfer coefficients in ducts with q = const, in which the initial sections of thermal and flow stabilization are taken into account. According to the first method the average heat transfer coefficient is determined by means of the mean temperature difference between the wall and the fluid

$$\bar{\alpha}_1 = \frac{q}{\frac{1}{l}\int_0^l (t_w - t_f)\,dx}. \tag{1}$$

Coefficient $\bar{\alpha}_1$ can be used to determine the average temperature of the heat-conducting surface.

Under the second method of averaging one integrates the local heat transfer coefficients

$$\bar{\alpha}_2 = \frac{1}{l}\int_0^l d_{\text{loc}}\,dx = \frac{q}{l}\int_0^l \frac{1}{t_w - t_f}\,dx. \tag{2}$$

Coefficient $\bar{\alpha}_2$ characterizes the average intensity of heat transfer and is not suitable for determining the average temperature of the surface. In general $\bar{\alpha}_1 \neq \bar{\alpha}_2$.

The heat exchanger method ($q \neq$ const) can be used to find some average heat transfer coefficients (third method)

$$\frac{1}{(\alpha_{ef})_1} = \frac{1}{\bar{K}} - \frac{1}{\bar{\beta}_1} - R, \tag{3}$$

$$\frac{1}{(\alpha_{ef})_2} = \frac{1}{\bar{K}} - \frac{1}{\bar{\beta}_2} - R, \tag{4}$$

where $\overline{K}$ is the experimentally determined average heat transfer coefficient

$$\overline{K} = \frac{\bar{q} \ln \frac{\vartheta_2}{\vartheta_1}}{\vartheta_2 - \vartheta_1}, \tag{5}$$

where ϑ_1 and ϑ_2 are the temperature differences between the heat-transfer agents at the inlet and outlet of the heat exchanger, R is the thermal resistance of the wall separating the fluids, $\overline{\beta}_1$ and $\overline{\beta}_2$ are the average heat transfer coefficients found by the first (1) and second (2) methods, respectively. /205

We now show that the method for averaging the heat transfer coefficient K(x) corresponds to the formula

$$\overline{K} = \frac{1}{l} \int_0^l K(x)\, dx. \tag{6}$$

The solution of the heat-balance equation has the form

$$t_1 - t_2 = \vartheta_1 \exp(mp\overline{K}_x x), \tag{7}$$

at x = l

$$\vartheta_2 = \vartheta_1 \exp(mp\overline{K} l),$$

where p is the heat-transfer perimeter, t_1 and t_2 are the temperatures of the fluids in the heat exchanger;

$$m \equiv \frac{1}{C_{p_1}\gamma_1 v_1} - \frac{1}{C_{p_2}\gamma_2 v_2},$$

$$\overline{K}_x = \frac{1}{x} \int_0^x K(x)\, dx; \quad \overline{K} = \overline{K}_{x=l}.$$

we note that $d(x\overline{K}_x) = \overline{K}_x dx + x d\overline{K}_x = \overline{K}_x dx + x d\left(\frac{1}{x}\int_0^x K(x)\, dx\right) = \overline{K}_x dx - \overline{K}_x dx + K(x)dx = K(x)dx$.

Substituting the above into Eq. (7), we get

$$q = \frac{1}{l}\int_0^l (t_1 - t_2)\,K(x)\,dx = \frac{\vartheta_1}{l}\int_0^l \exp(mp\overline{K}_x x)\times$$

$$\times d(\overline{K}_x x) = \frac{\vartheta_1}{mpl}[\exp(mp\overline{K}l) - 1] = \overline{K}\,\frac{\vartheta_2 - \vartheta_1}{\ln\frac{\vartheta_2}{\vartheta_1}}.$$

Thus the coefficient $\overline{\overline{K}}$ obtained in heat-exchanger experiments corresponds to Eq. (6).

For further analysis we now assume that the local heat transfer coefficients in the intertubular space of the heat exchanger and in the cluster of heat-generating rods [fuel elements] of the same geometry (q = const) is the same, i.e., we disregard the effect of variations in q over the length of the heat exchanger on the local heat transfer coefficients. We also must know the distribution functions of the local heat transfer coefficients. We therefore assume that the heat transfer coefficients for counterflow in the intertubular space (8) and in the tubes (9) /206 are described by their corresponding formulas

$$\frac{\alpha}{a} = \frac{1}{1 - \exp[-n(x_0 + x)]}, \tag{8}$$

$$\frac{\beta}{b} = \frac{1}{1 - \exp[-n(l + x_0 - x)]}, \tag{9}$$

where a and b are the stabilized values of heat transfer coefficients, n and x_0 are some constants, and l is the length of the heat exchanger. This form of a function is convenient for mathematical analysis. When $x_0 = 0$ the local coefficients at the inlet sections go to infinity, $\alpha \to \infty$ as $x \to 0$ and $\beta \to \infty$ as $x \to l$. We introduce the following notation: $N = (\alpha/a)_{x=0} = (\beta/b)_{x=l}$ are the relative values of the local heat transfer coefficients at the point where the fluid enters the duct, while $M = (\alpha/a)_{x=l} = (\beta/b)_{x=0}$ are the local heat transfer coefficients at the point where the fluid leaves the duct.

Transforming Eqs. (8) and (9), we get

$$\frac{\alpha}{a} = \frac{1}{1 - \frac{N-1}{N}\exp(-nx)}, \tag{10}$$

$$\frac{\beta}{b} = \frac{1}{1 - \frac{M-1}{M}\exp(nx)}. \tag{11}$$

Specifying values of N and M is equivalent to specification of nl and nx_0 /207

$$nl = \ln\left(\frac{M}{M-1}\frac{N-1}{N}\right);\quad nx_0 = \ln\frac{N}{N-1}.$$

The initial distribution of heat transfer coefficients in a counterflow heat exchanger is shown in Fig. 1 for N = 10, M = 1.02 and N $\to \infty$, M = 1.02. It can be seen that nl changes little as N varies from 10 to ∞.

The local heat transfer coefficients can be found from Eqs. (10) and (11)

$$K(x) = \frac{1}{R + \frac{1}{\beta} + \frac{1}{\alpha}} = \frac{a\exp(nx)}{A\exp(nx) - \frac{a}{b}\frac{M-1}{M}\exp(2nx) - \frac{N-1}{N}}, \tag{12}$$

where A = (1 + Ra + a/b).

According to Eq. (6), the average heat transfer coefficient is determined by integrating Eq. (12)

$$\frac{\overline{K}}{a} = \frac{\ln\Psi}{nl\sqrt{\delta}},$$

$$\Psi = \frac{A+\sqrt{\delta}-2\frac{a}{b}\frac{M-1}{M}}{A+\sqrt{\delta}-2\frac{a}{b}\frac{N-1}{N}}\cdot\frac{A-\sqrt{\delta}-2\frac{a}{b}\frac{N-1}{N}}{A-\sqrt{\delta}-2\frac{a}{b}\frac{M-1}{M}}, \tag{13}$$

it can be seen that always $\delta = A^2 - 4\ a/b\ \frac{M-1}{M}\cdot\frac{N-1}{N} > 0$. The average heat transfer coefficients can be found using Eqs. (1), (2), (10) and (11)

$$\frac{\overline{\alpha}_1}{a} = \frac{q}{\frac{a}{l}\int_0^l (t_w - t_f)\,dx} = \frac{l}{\int_0^l \frac{a}{\alpha}\,dx} = \frac{1}{1 - \frac{N-M}{N\cdot M\ln\left(\frac{M}{M-1}\cdot\frac{N-1}{N}\right)}}, \tag{14}$$

$$\frac{\overline{\alpha}_2}{a} = \frac{1}{l}\int_0^l \frac{\alpha}{a}\,dx = \frac{1}{1 - \frac{\ln\frac{N}{M}}{\ln\frac{N-1}{M-1}}}. \tag{15}$$

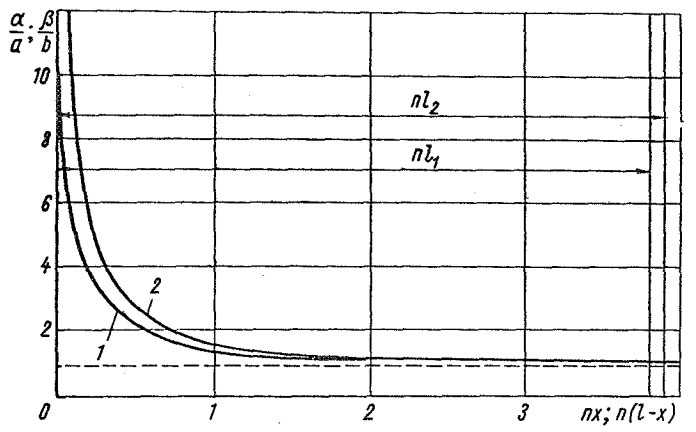

Figure 1. Initial Distribution of Heat Transfer Coefficients Over the Length of a Counterflow Heat Exchanger. 1) N = 10; 2) N → ∞.

In the case at hand we will always have

$$\frac{\bar{\alpha}_1}{a}=\frac{\bar{\beta}_1}{b} \text{ and } \frac{\bar{\alpha}_2}{a}=\frac{\beta_2}{b}.$$

The sought relationship between the average heat transfer coefficients found by different methods [Eqs. (1)-(4)], has the form

$$\varepsilon_1=\left(\frac{\bar{\alpha}}{\alpha_{ef}}\right)_1 = \left(\frac{\bar{\alpha}}{a}\right)_1\left(\frac{a}{\bar{K}}-Ra\right)-\frac{a}{b}, \quad (16)$$

$$\varepsilon_2=\left(\frac{\bar{\alpha}}{\alpha_{ef}}\right)_2=\left(\frac{\alpha}{a}\right)_2\left(\frac{a}{\bar{K}}-Ra\right)-\frac{a}{b}. \quad (17)$$

We recall that subscripts 1 and 2 correspond to the different methods for finding the average heat transfer coefficients. /208

Let us consider some limiting cases. When M → 1 (the heat exchanger length goes to infinity) and bounded values of N the quantities

$$\left(\frac{\bar{\alpha}}{a}\right)_1, \left(\frac{\bar{\alpha}}{a}\right)_2, \left(\frac{\bar{\alpha}}{\alpha_{ef}}\right)_1 \text{ and } \left(\frac{\bar{\alpha}}{\alpha_{ef}}\right)_2$$

go to unity, which is quite understandable from the point of view of physics.

If the thermal resistance of the wall is negligible (Ra = 0), while the heat transfer coefficients for the fluid in the heat-exchanger tubes are much greater than those for the intertubular space (a/b = 0) then, as N → ∞:

1) $(\bar{\alpha}/\alpha_{ef})_1 \to 0$, since $\alpha_{ef}=\bar{K}\to\infty$, while the magnitude of $\bar{\alpha}_1$ is bounded;

2) $(\bar{\alpha}/\alpha_{ef})_2 \to 1$, since $\alpha_{ef}=\bar{\alpha}_2$, although both these quantities go to infinity. /209

If N → ∞, while the values of Ra and a/b do not simultaneously go to zero, then $(\bar{\alpha}/\alpha_{ef})_2 \to \infty$. Thus, the average heat transfer coefficients found by the first method are always bounded, while those found by the second method go to infinity when the local heat transfer coefficients in the initial section go to infinity (when x = 0, N → ∞).

The results obtained on the basis of Eqs. (16) and (17) for M = 1.02 and N = 100 and 10 are shown in Figs. 2a and b. For convenience in comparing these figures the reciprocals of ε_2, i.e., $1/\varepsilon_2$ are also given. It can be seen that in all cases of practical importance (Ra > 0, a/b > 0) the average heat transfer coefficients found by the first method differ much less from α_{ef} than those found by the second method.

It is entirely obvious that the calculations for a heat exchanger can be performed accurately only when one knows the local heat transfer coefficients or by using previously known average ($\bar{\alpha}_1$ or $\bar{\alpha}_2$) and effective [$(\alpha_{ef})_1$ or $(\alpha_{ef})_2$] coefficients.

The question arises as to what will be the errors in calculations for short heat exchangers using average heat transfer coefficients, i.e., using the formulas /210

$$\frac{1}{\bar{K}_1} = R + \frac{1}{\bar{\alpha}_1} + \frac{1}{\bar{\beta}_1};$$
$$\frac{1}{\bar{K}_2} = R + \frac{1}{\bar{\alpha}_2} + \frac{1}{\bar{\beta}_2}.$$

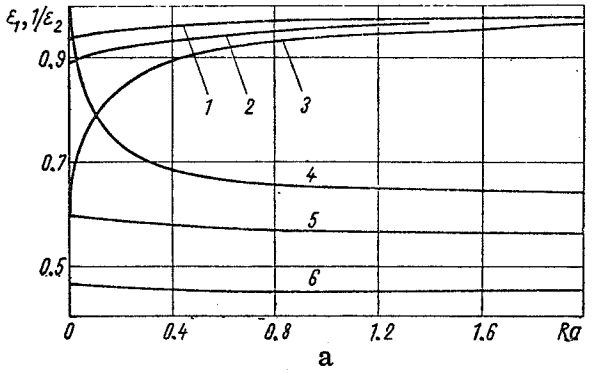

a

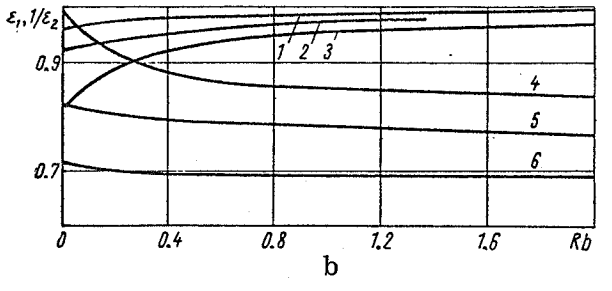

b

Figure 2. Ratio of the Average Heat Transfer Coefficients Determined by Different Methods of M = 1.02 and N = 100 (a) and N = 10 (b). 1), 2) and 3) are Values of ε_1; 4) 5) and 6) are Values of $1/\varepsilon_2$ for a/b = 0, 0.3 and 1, Respectively.

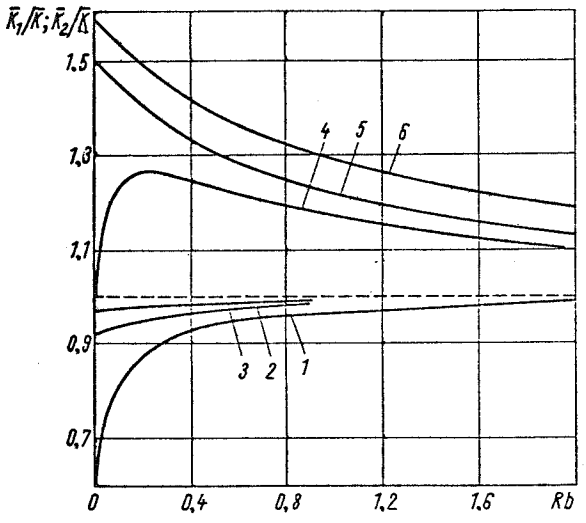

Figure 3. Heat Transfer Coefficients Found by Different Methods for M = 1.02 and N = 100. 1), 2) and 3) are Values of $\bar{K}_1/\bar{K}$; 4), 5) and 6) are Values of $\bar{K}_2/\bar{K}$ for a/b = 0, 0.3 and 1, Respectively.

Comparison of the values of $\bar{K}_1$ and $\bar{K}_2$ with the actual average heat transfer coefficient $\bar{K}$, which was performed using Eqs. (14), (18) and (19), (Fig. 3) shows that heat exchanger calculations using the average heat transfer coefficients $\bar{\alpha}_1$ will result in much smaller errors than calculations using $\bar{\alpha}_2$. An exception are the cases when the relative thermal resistance of the walls (Ra) and the relative heat transfer coefficients (a/b) are at the same time small quantities.

RESISTANCE TO AXIAL FLOW OF FLUIDS PAST ROD CLUSTERS

A. V. Sheynina

Rod clusters in contact with a heat transfer agent flowing along their length /210
are used extensively in all kinds of equipment. It is beyond doubt that the resistance to flow exerted by the clusters and by other intricately-shaped ducts cannot always be calculated using formulas for round tubes and the hydraulic diameter.

Up to present a fair amount of experimental information has been accumulated on the resistance to flow of rod clusters, [1-11]. Articles on the theoretical aspects of this problem have also been published, [12, 13]. As a rule, the experiments were performed in the isothermal flow of water or air. It is proven in [14] and [15] that the flow of liquid metals obeys the same laws as the flow of ordinary fluids (water, air, etc.). The use of ordinary fluids substantially simplifies the performance of experiments. The physical properties of liquid metals depend little on the temperature, hence, the data obtained for isothermal flow of water or air can be used for the isothermal flow of liquid metals.

The available data on the flow resistance of clusters are not always in agreement with one another. Figures 1 and 2 present experimental data for clusters with triangular and square lattices, as well as curves for a round tube constructed on the basis of the Blasius formula.

$$\lambda = 0{,}316 \times \mathrm{Re}^{-0{,}25}, \tag{1}$$

and the Nikuradse formula

$$\lambda = 0{,}0032 + 0{,}221\mathrm{Re}^{-0{,}237}. \tag{2}$$

New data for clusters with relative tube spacing S/d = 1, 1.05 and 1.4 (see /214
Figs. 1 and 2 and Tables 1 and 2) were obtained on a stand (Fig. 3). The working medium was distilled water at 18-80°C. The necessary pressure was produced by the KSM-70 pump with a delivery of 70 m^3/hour at a pressure of 200 m of water. The water flowed through the heat exchanger to a measuring header, consisting of four parallel Venturi tubes with nozzle diameters of 38, 25, 15 and 10 mm. After the measuring header the distilled water was supplied to either the vertical or the horizontal test sections. Then the water was drained to measuring tanks or to the drain tank. The measuring tanks were used for calibrating the flowmeters by the volume method. The equipment and parts of the stand were made from 1Kh18N9T stainless steel. The stand was supplied with distilled water by the ED-2M electric distillation units. The water was heated by electric heaters installed in the supply tank. The water temperature in the stand was measured by copper resistance thermometers combined with an automatically balanced EMV-2 -211A electronic bridge.

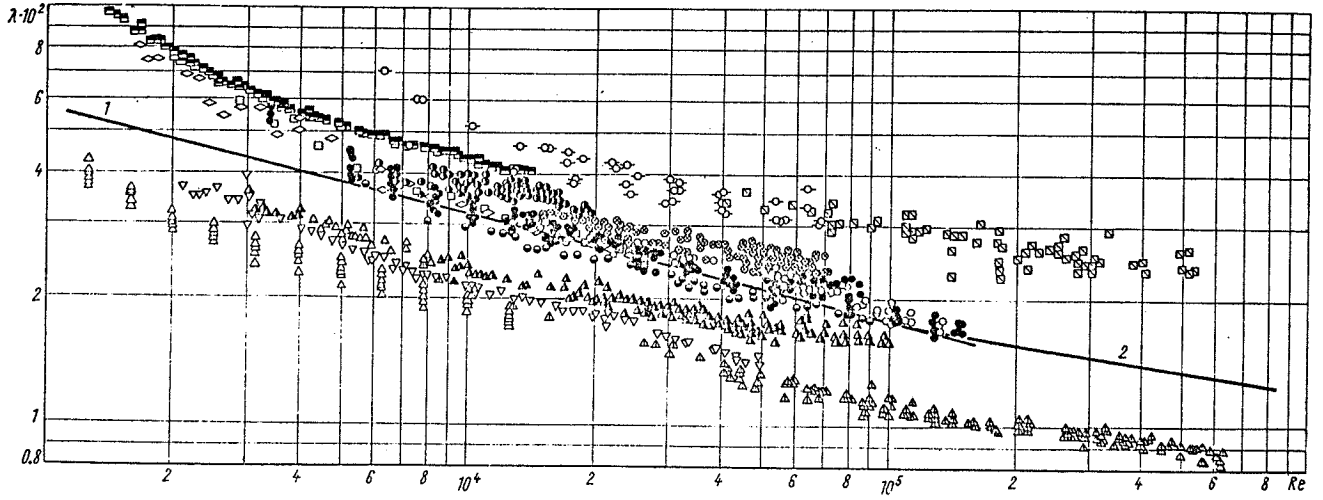

Figure 1. Friction Coefficients for Clusters With a Triangular Lattice. 1) and 2) Denote Curves Obtained From Eqs. (1) and (2); the Legend Used is Given in Table 1.

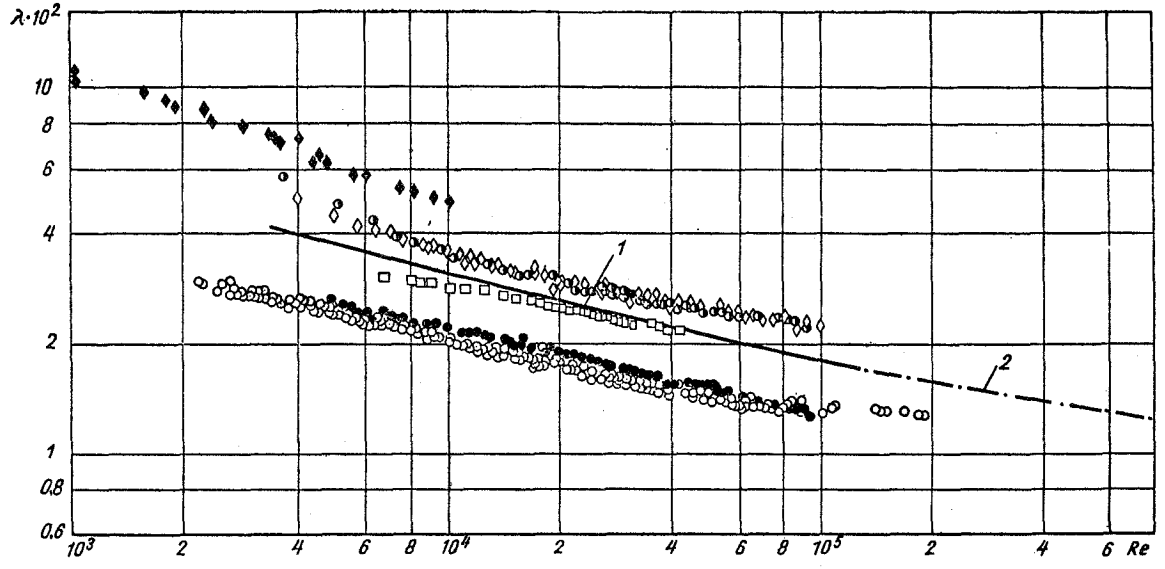

Figure 2. Friction Coefficients for Clusters With a Square Lattice. 1) and 2) Denote Curves Obtained From Eqs. (1) and (2); the Legend Used is Given in Table 1.

TABLE 1. Characteristics of Experimental Clusters With a Triangular Lattice

Reference	$\frac{S}{d}$	N	d	d_{h_∞}	d_{h_M}	L	Working medium	Range $Re \cdot 10^3$	Designations	Cross section of model
[1]	1.0	19	17.6	1.81	1.81	700	Water	1-20	△▽	
[2]	1.0		205	20,9		1800	Water	8-630	△	
[3]	1.015						Air	3-30	□	
	1.05	37	10.0	2.16	2.16	840	Water	3-100	▲	
	1.05	37	14.0	3,02	3,00	1000	Water	3-120	●	
[4]	1.12	19	12.7	4.9	4.9	620	Water	5-100	◒	
[1]	1.13	19	12.0	4.8	5.0	980	Water	14-70	⊗	
[5]	1.19	102	4.7	2,68		1840	Water	0.9-71	▬	
[6]	1.2	19	11.0	6.47		1500	Air	1-40	◇	
[7]	1.2	7	22.0	12.94	11.43	1050	Water	5-20	◑	
	1.4	37	10.0	11.62	11.53	840	Water	12-120	○	
[8]	1.46	37	15.9	19.5	21.5	1220	Water	40-800	■	
[9]	1.76 2.05 2.37	39	19.0	46.2 69,5 98.6		2000	Air	6-70	⊖	

The pressure drop at the Venturi tubes and in the test sections was measured by type DT-50 differential manometers with 1300 mm long tubes. The manometers were filled with mercury, tetrabromoethane, carbon tetrachloride, /216 depending on the magnitude of the pressure to be measured. Pressure drops exceeding 1200 mm of Hg were measured by spring-type comparison manometers. The pressure drops were measured along the length of ducts of models as a function of the average water velocity. It was assumed that the velocity of the latter is uniform over the model's cross section. The experimental data were analyzed by using the hydraulic diameter of an infinite cluster.

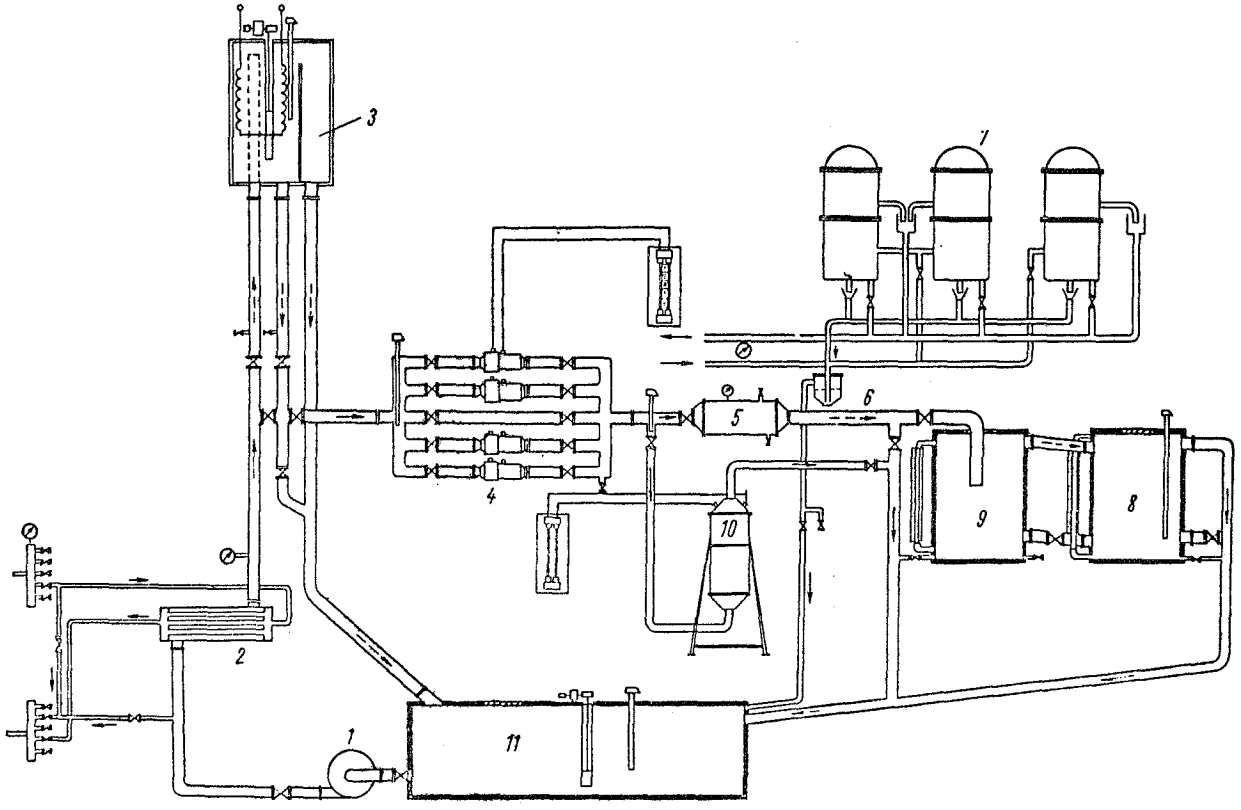

Figure 3. Schematic Diagram of the Experimental Setup. 1) Centrifugal Pump; 2) Heat Exchanger; 3) Delivery Tank; 4) Measuring Header; 5) Damper; 6) Horizontal Test Section; 7) Electric Distillation Units; 8) and 9) Measuring Tanks; 10) Vertical Test Section; 11) Drain Tank.

TABLE 2. Characteristics of Experimental Clusters With a Square Lattice

Reference	$\frac{S}{d}$	N	d	d_{h_∞}	d_{h_N}	L	Working medium	Range $Re \cdot 10^{-3}$	Designations	Cross section of model
[10]	1.0	25	11.4	3.12	3.12	600	Water	2-200	○	
[11]	1.0		48.2	13.2	13.2	3400	Water	5-100	●	
[5]	1.106	100	4.8	2.88		1840	Water	1-10	♦	
[4]	1.12	49	8.45	5.2	4.4			5-100	◑	
[4]	1.2	49	7.92	6.6	5.6			5-100	◊	
[11]	1.31	4	26.6	17.2	32.0	3400	Water	6-40	□	

In order to check the correctness of the measuring method, control experiments were performed using a round pipe. Here use was made of a seamless, round brass tube 30 mm in diameter and 3600 mm long. The obtained values of the friction coefficients were in satisfactory agreement with data for round pipes.

Let us now analyze the experimental data for densely-packed rod clusters, shown in Fig. 4. The experimental data for single ducts formed by the triangular and square closely-packed arrangements [2, 11] are in good agreement with data obtained for closely-packed rod clusters [1] and [10]. The friction coefficients of triangular and square arrays were close to one another. Approximately the same follows from the theoretical calculations of [12] and [13].

It can be seen from Fig. 4 that calculations made on the basis of the Deissler-Taylor method give friction coefficients of densely-packed clusters somewhat on the low side. Calculations made by Buleyev in the region $8000 < Re < 50{,}000$ are in satisfactory agreement with experimental results. The experimental data obtained by the present author lie by 30-40% lower than curves obtained from Eqs. (1) and (2) and they can be approximated by an empirical formula which is valid for triangular and square densely-packed arrays /217

$$\lambda = 0.68\lambda_{fr/pipe} \qquad (3)$$

where $\lambda_{fr/pipe}$ are friction coefficients for round pipes calculated from Eqs. (1) and (2). The experimental data of [11] for a single passage in a dense square lattice are also satisfactorily (to within about 7%) described by Eq. (3).

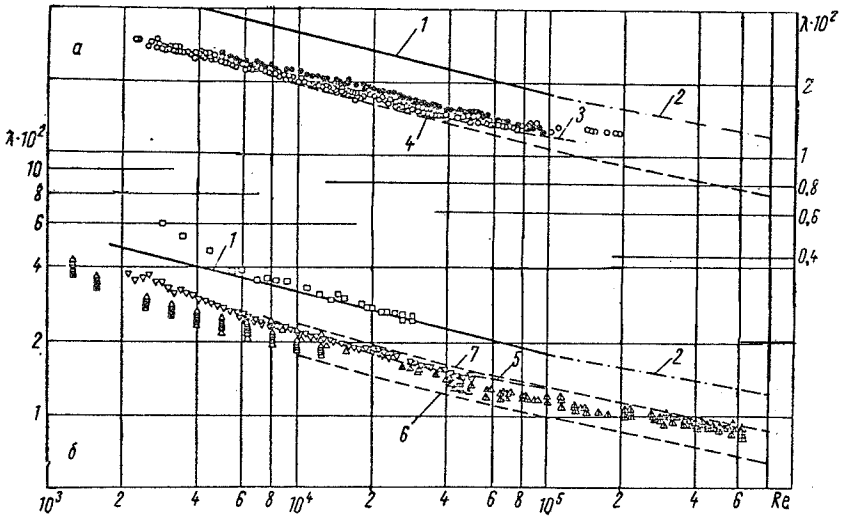

Figure 4. Friction Coefficients for Densely-Packed Rod Clusters. a) Square Lattice; b) Triangular Lattice; 1) and 2) Calculations on the Basis of Eqs. (1) and (2), Respectively; 3) and 5) Curves Obtained by Buleyev, [12] for S/d = = 1; 4), 6) Curves Obtained by Deissler, [13] for S/d = 1; 7) for S/d = 1.02. For the Notation Used see Tables 1 and 2.

The results obtained experimentally by Palmer and Swanson [3] for a single passage of a triangular cluster with S/d = 1.015 lie close to the curve obtained from Eq. (1) for round pipes. It thus follows from the experiments that the friction coefficient becomes greater by about approximately 45% when S/d changes from 1 to 1.015. This appreciable increase in the friction coefficient attendant to a small increase in the space between the rods is also obtained in calculations by the Deissler-Taylor method [13]. Thus, when S/d changes from 1 to 1.02, the value of λ increases by approximately 35%. This effect is produced by a sharp reduction in stagnation zones brought about even by a small increase in the distance between rods.

Let us consider experimental data obtained for two clusters with S/d = 1.05. The first cluster consisted of a bundle of 37 tubes, surrounded by a plane hexagonal displacer. The size of the hexagon was selected so that the hydraulic diameters of the model and the cell be the same. The second cluster has the same number of tubes, but it is surrounded by a specially shaped displacer. The extreme cells of the second cluster have the same cross section as the center cells. The friction coefficient for the cluster with the flat [plane] displacer (Fig. 5) at $Re = (3\text{-}30)\cdot 10^3$ is by approximately 30% lower than for a round pipe. At Re > /218
> 30,000 the experimental points and the curve for the pipe tend to gradually come close to one another. The friction coefficients for the cluster with the specially shaped displacer at $Re = 10^4$ are practically identical with these coefficients for a round pipe.

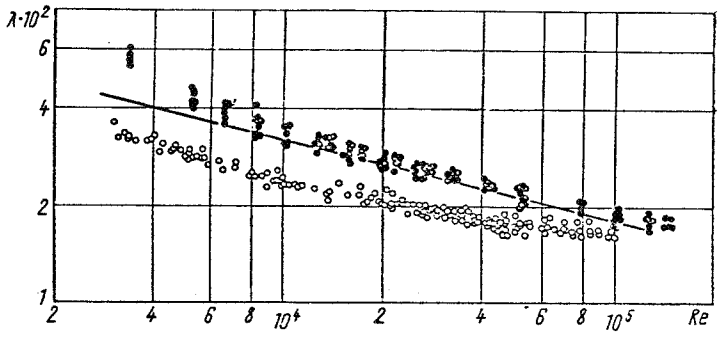

Figure 5. Friction Coefficients in Clusters With a Triangular Lattice, S/d = 1.05. ● - Data for a Cluster With a Specially Shaped Displacer; o - Data for a Cluster With a Rectangular Shell; the Solid Line was Obtained From Eq. (1).

It can be seen from Fig. 5 that the friction coefficients for the two clusters differ appreciably from one another. This can be attributed primarily to the different shape of the cluster cross section, i.e., effect of the shape of the shell.

Figure 6 presents results obtained on measuring the flow resistance of a cluster with S/d ≈ 1.4. In this cluster a bundle consisting of 37 rods was surrounded by a plane displacer. The hydraulic diameter of the model, taking the shell into account is the same as the hydraulic diameter of the center cells. The results thus obtained are compared with those for a cluster with S/d = 1.46, [8]. The resistances of these clusters differ by approximately 50%. In this case, as well as for clusters with S/d = 1.05, the lower coefficient is that for the cluster with the plane hexagonal shell.

Comparing the results obtained by different authors (see Figs. 1 and 2) we can note relationships common to all of them. The friction coefficient of a cluster, when using d_h as the characteristic dimension, depends on the relative lattice spacing S/d, with an increase in which the friction coefficient increases also. The lowest value is observed in dense clusters (S/d = 1).

The experimental results depend also on the effect of the shape of the displacers on the friction coefficients in the clusters. Comparisons were made of data for clusters with close values of S/d and with close number of tubes, but with different shell shapes. The results of this comparison are shown in Fig. 7, where are given the values of the friction coefficient of certain clusters at Re = $= 40 \cdot 10^3$ as a function of S/d. It can be seen from Fig. 7 that the friction coefficients depend on the shape of the shell; here λ of clusters with a plane shell is lower than in clusters with a specially shaped displacer. Thus, analysis of /219
experimental data shows that the resistance of the clusters depends on the shape of the shell. This problem requires special study.

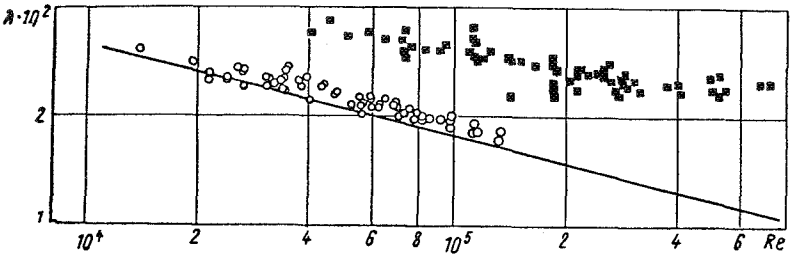

Figure 6. Friction Coefficients in Clusters With a Triangle Lattice, S/d ≈ 1.4. o - Data Obtained by the Present Author for S/d = 1.4; ▪ - for S/d = 1.46, [8]; the Solid Curve was Obtained From Eq. (1).

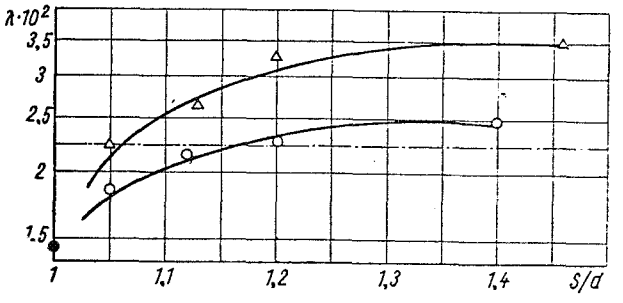

Figure 7. Friction Coefficients in Clusters as a Function of S/d for Re = $40 \cdot 10^3$. o - Data for Clusters With Hexagonal Shells; Δ - With a Specially-Shaped Shell; ● - for a Densely-Packed Cluster; the Dash-Dot Line was Obtained Theoretically for a Round Pipe.

The problems involved in determining the flow resistance of clusters with different spacing devices are more complicated. In these cases the flow resistance is affected by the geometry of the spacing elements proper. The most extensively used and simplest method for spacing the rods are spiral fins. A study was made of the flow resistance of finned clusters, provided with two and four ribs each wound on the outer surface of the rod.

The experimental models consisted of clusters of tubes or rods, surrounded by a specially shaped displacer. The ribs from the surfaces of extreme tubes, facing the displacers, were removed. In analyzing the experimental data the characteristic dimension was the hydraulic diameter of a dimensionless cluster, taking the fins into account. The basic characteristics of the tested cluster are shown in Table 3.

The most complete tests were performed using clusters with a triangular lattice with S/d = 1.05. It was discovered for this spacing that the number of ribs and their lead affect [the friction coefficient]. Clusters with two and four fins were tested. For clusters with four fins the experiments were performed with fin winding leads T = 1400, 300 and 70 mm. The friction coefficients for clusters with T = 1400 and 300 mm differed little from one another (Fig. 8a). The same was observed for clusters with two ribs. For winding leads exceeding 300 mm (T/d > 20), the difference between the friction coefficients of clusters

with and without ribs with S/d = 1.05 is inconsequential and lies within the limits of experimental error (Figs. 8a and b).

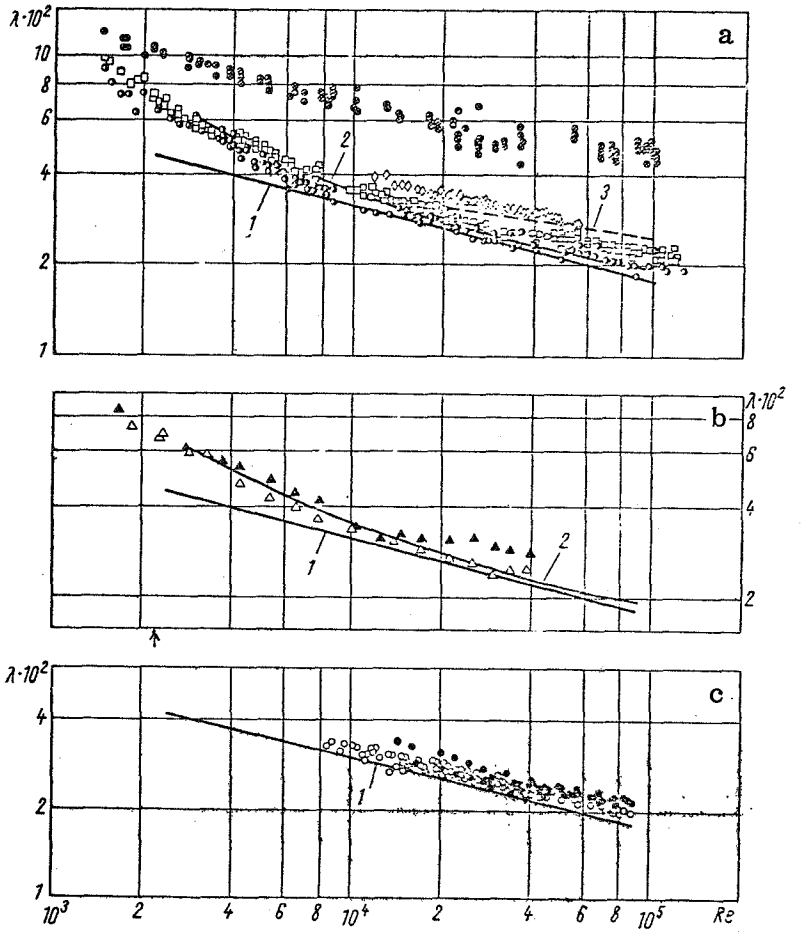

Figure 8. Friction Coefficients for Finned Clusters. 1) Curve Obtained From Eq. (1); 2) S/d = 1.05 (ribless), 3) S/d = 1.1 (ribless), [1]; the Notation is That of Table 3.

Similar results were also obtained before. The experiments were performed with finned clusters with S/d = 1.1 and 1.15. Two clusters with S/d = = 1.1 (see Table 3, rows 1 and 2) had fin winding leads T = 400 and 300 mm. The experimental data for these clusters lie by 10-20% above the Blasius curve for a round tube (Fig. 8c). Changing the fin lead from T = 400 to T = 300 (T < < 20d) did not appreciably affect the friction coefficient. /220

The finned cluster with S/d = 1.15 (Table 3, row No. 8) consisted of 19 tubes 12 mm in diameter. Each tube was equipped by four fins with a winding

TABLE 3. Characteristics of Ribbed Clusters With a Triangular Lattice

Number	$\frac{d+2\delta}{d}$	N	d	$d_{h_{av}}$	n	L	Range of $Re \cdot 10^{-3}$	Designations	T	h_p	Rib shapes
1	1.11	19	12.6	3.9	2	300	40-100	●	300	0.6	
2	1.11	19	12.6	3.9	2	300	8-100	○	400	0,6	
3	1,05	37	14.0	2.88	2	1000	2-100	▲	1400	0.35	
4	1,05	37	14,0	2.88	2	1000	2-100	△	300	0.35	
5	1,05	37	14,0	2.76	4	1000	2-100	◑	1400	0,35	
6	1,05	37	14,0	2,76	4	1000	2-100	□	300	0.35	
7	1,05	37	14,0	2,79	4	600	2-100	⊗	70	0,35	
8	1,15	19	12,0	4,46	4	800	10-50	◊	700	0,9	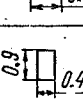

lead of T = 700 mm. The friction coefficient for this cluster is higher than for a round tube by 30%. The results obtained with a ribbed cluster with the same value of S/d are being compared (see Fig. 8a) with data for a smooth cluster (S/d = 1.13) [1].

It can be seen from Fig. 8, that the presence of spacing fins wound spirally, has little effect on the resistance coefficient at T/d < 20, which is also true with respect to the effect of the number of ribs on the magnitude of λ. When the winding lead is reduced to 70 mm (5d) in the cluster with S/d = 1.05, the value of λ has increased by more than a factor of two. /221

The curve of λ as a function of T, obtained for clusters with four ribs at S/d = 1.05, is shown in Fig. 9 in the coordinates $100 \cdot \lambda \, Re^{0.25} = f(T/d)$. It can be seen that, when the winding lead is reduced in a range of from 100 to 20 d, λ almost does not change. A sharp increase in λ is, [however,] observed at low T.

Spacing devices of two more types were also studied. One of them was a "gimlet"-type insert. The experiments were performed with a cluster with S/d = 1.13, with 19 rods 13.6 mm in diameter and 1000 mm long, surrounded /222

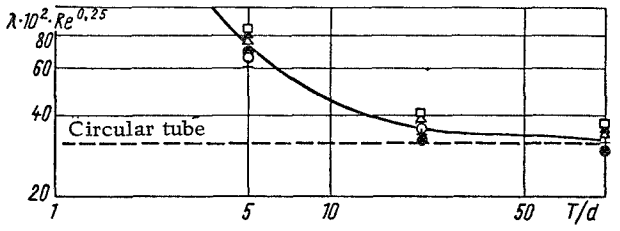

Figure 9. The Friction Coefficient of a Finned Cluster as a Function of the Fin Winding Lead.

Re·10⁻³	10	20	40	60	80	100
notation	○	+	●	△	▲	□

by a specially-shaped displacer. A "gimlet", i.e., a plate 0.8 mm, 3.6 mm in diameter and with a twisting lead P = 30 and 50 mm was placed into each cell of the cluster.

In the second case the spacing device was a steel wire, on which streamlined sleeves, i.e., "beads", were placed at uniform intervals. Up to 30 beads were placed in each cell. The characteristic dimension used was the hydraulic diameter of the model, without taking into account the spacing devices. The resistance coefficient was referred to the arbitrary average velocity of the model without taking into account the thickness of the latter [beads].

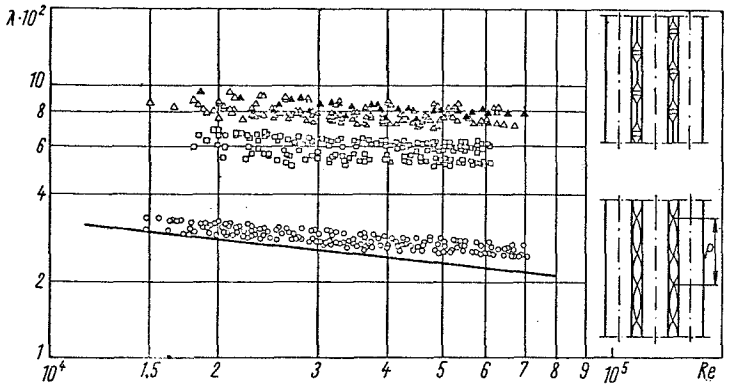

Figure 10. Resistance Coefficient for Clusters With a Triangular Lattice With S/d = 1.13, Provided With Spacing Devices. ○ - Without Spacing Devices; □ - "Bead"-Type Spacer; △ and ▲ "Gimlet"-Type Spacer, P = 50 and 30 mm, Respectively; the Solid Line was Obtained From Eq. (1).

The experimental results which are convenient for practical calculations /223 of hydraulic losses for these two types of inserts, as well as data for a cluster without spacers are presented in Fig. 10. The change in the twisting lead of the gimlet from P = 50 to P = 30 did not appreciably affect the resistance coefficient. The use of the "bead"-type insert increased the flow resistance coefficient twofold, while the use of the "gimlet"-type spacer increased it by a factor of three as compared with the cluster without spacers. In both cases the resistance

coefficient is some arbitrary quantity, since the calculations were performed using an average velocity and hydraulic diameter, calculated without taking the spacing inserts into account. It is difficult to take into account the closing of the cross section by the inserts, since the configuration of the inserts varies over the length of the duct.

REFERENCES

1. Subbotin, V.I., et al.: Atomnaya energiya, 9, Issue 4, 308 (1960).
2. Levchenko, Yu.D., et al.: Raspredeleniye skorostey v yacheyke plotno upakovannogo puchka sterzhney [Velocity Distribution in a Cell Formed by a Densely-Packed Cluster of Rods]. Article immediately following the present one.
3. Palmer, L.D. and Swanson, L.L.: International Development in Heat Transfer, Boulder, London, III, No. 63, 1961-1962.
4. Le Tourneau, B., et al.: Trans. ASME, 79, No. 8, 1751 (1957).
5. Wantland, J.L.: Reactor Heat Transfer Conference of 1956, AEC Report TID, 7529, 525 (1957).
6. Mikhaylov, A.I., et al.: Inzhenerno-fizicheskiy zhurnal, No. 11, 42 (1964).
7. Firsova, E.V.: Inzhenerno-fizicheskiy zhurnal, No. 5, 17 (1963).
8. Miller, P., et al.: A.I. Ch. E. Journal, 2, No. 2, 226 (1956).
9. Salifov, A.P., et al.: Teploenergetika, No. 8, 481 (1954).
10. Ushakov, P.A., et al.: Atomnaya energiya, 13, Issue 2 (1962).
11. Gunn, D.J. and Darling, C.W.: W. Trans. Instn. Chem. Engrs, 41, No. 4, 163 (1963).
12. Buleyev, N.I., et al.: Teplofizika vysokikh temperatur, 2, No. 5, 749 (1964).
13. Deissler, R.G. and Taylor, M.F.: Reactor Heat Transfer Conference of 1956. TID-7529 (1957).
14. Borishanskiy, V.M., et al.: In the collection Zhidkiye metally [Liquid Metals], page 71, Gosatomizdat, Moscow, 1963.
15. Kondrat'yev, N.S.: In the collection Teploperedacha i teplovoye modelirovaniye, page 93. Published by the Academy of Sciences of the USSR, Moscow, 1959.

VELOCITY DISTRIBUTION IN A CELL FORMED BY A DENSELY-PACKED CLUSTER OF RODS

Yu. D. Levchenko, V. I. Subbotin, P. A. Ushakov
and A. V. Sheynina

Experimental study of the velocity distribution in ducts with a nonround cross section are needed for developing reliable methods for calculating the fluid dynamics and heat transfer in various heat exchanger devices, including also nuclear reactors. /223

Dense packing of rods in a triangular lattice makes it possible to develop reactor cores with low porosity with respect to the heat-transfer agent (for example, for fast-neutron reactors). The closeness of the rods creates flow characteristic similar to those in ducts with extended acute corners. Dense packing ($S/d = 1$) is the limiting case of placing rods in a cluster, for which the effects of velocity and temperature variations over the perimeter are most strongly pronounced. /224

Eckert and Irvine [1] have studied the flow in a triangular passage and have discovered a number of peculiar features. In the flow one can observe a nonuniform development of turbulence over the passage's cross section. Transition from laminar to turbulent flow ensues at lower (than in a round tube) Reynolds numbers, calculated on the basis of the hydraulic diameter and the average velocity. In one section of the channel it is possible to have, alongside with a turbulent main body of the flow, regions with laminar flow. Changes in the temperature of heat-conducting walls point to the fact that the turbulent heat transfer is nonisotropic, i.e., heat transfer in the direction of the bisectrix of the angle proceeds with difficulty.

A characteristic feature of ducts with sharp corners was the large length of the fluid-dynamic stabilization section. On the basis of measured velocity distributions in ducts with nonround cross section, I. Nikuradse [2] has suggested the existence of secondary fluid flows.

Of [special] interest for theoretical studies of fluid dynamics in the flow of fluids around rod clusters is work performed by Deissler and Taylor [3] and by Byleyev, [4]. The methods due to Deissler and Taylor are built on simple assumptions, and can be used by any engineer for practical calculations. [On the other hand] for calculations using the three-dimensional model of turbulent transfer developed by Buleyev one must use computers. In the case at hand both methods yield close results, but the future apparently belongs to methods based on more general assumptions than those made by Deissler and Taylor.

Despite the great scientific and practical interest, very little is known about the velocity distributions in ducts with nonround cross section. The staff

of the Physics and Power Institute has performed measurements and calculations of the distribution of velocities and tangential stresses, as well as friction resistance coefficients in a duct simulating a densely-packed rod cluster.

A densely packed rod cluster is the only cluster in which it is possible to isolate an individual cell in the pure form. Hence the studies were not performed with the cluster of rods, but in a duct, specially constructed for this purpose, simulating a cluster of rods. The duct was made from tubes fabricated from 1Kh18N9T steel 219 x 18 mm in diameter. After turning on a lathe to a diameter of 205 x 11 mm with surface finish ∇5 the tube was cut lengthwise into three parts. The sectors [thus obtained] were welded together by argon-shielded arc welding. The air /225
was supplied from a special pump. The experimental stand used for the experiments is described in [5]. The dynamic pressure was measured by a glass Pitot tube 0.20 x 0.12 mm in diameter, placed directly at the duct's outlet. The static pressure was measured through a hole in the duct's wall 0.6 mm in diameter, situated a distance of 35 mm from the outlet flange. This hole, as well as the others, was drilled before the duct was welded together, in order to provide for the maximum possible precision and quality of finish.

Measurement of velocities in the outlet cross section of a duct has a number of advantages. The Pitot tube can be brought to the wall at a distance equal to half its diameter, using the KM-6 cathetrometer [sic] to rigorously control the distance from the wall, to move it easily into any point of the flow, etc.

The dynamic pressure drop was measured by a glass differential manometer filled with alcohol. The alcohol level in the manometer was measured by the KM-6 cathetrometer to within ± 0.05 mm.

The Pitot tubes were made from plain glass, heating it and sharply extruding from tubes 4 mm in diameter. From a large number of tubes which were thus drawn we have picked only those which had a ratio of the inner to the outer diameters of 0.595 to 0.605. These tubes had sufficient rigidity and a relatively moderate inertia. Then these glass capillaries were polished at their ends by fine emery cloth, so that the end of the capillary was made perpendicular to its axis.

The Pitot tube was moved by a coordinate spacing device using micrometer screws with scale divisions of 0.01 mm. The Pitot tube could be moved in mutually perpendicular directions over distances of 100 x 100 x 25 mm. Due to symmetry of the cell produced by triangular packing of the rods, it is sufficient to obtain the velocity distribution in 1/6 of the cross section, however, in order to clarify whether the fluid flow was distributed uniformly, we measured the velocity distribution at $Re = 14.2 \cdot 10^3$ in a region embracing half the cross section.

From the dynamic pressure obtained in each point we have calculated the local velocity

$$U = C\sqrt{\frac{h_1 \cdot 2g}{\gamma_{air}}}, \qquad (1)$$

where $h = h(\gamma_{alc} - \gamma_{air}) = h(802 - \gamma_{air})$ and C is a calibration factor, which was set equal to unity since the Pitot tube was made according to recommendations of [6].

The tangential stress at the wall τ_0 was calculated on the basis of velocities measured by a Pitot tube 0.20 x 0.12 mm in diameter near the wall of the duct assuming that the velocity at the wall is zero and that it increases in the region near the wall in proportion to the distance from the wall; the local tangential stress at the wall can be calculated from the expression /226

$$\tau_0 \simeq \mu \frac{\partial U}{\partial y} \simeq \mu \frac{U}{y}. \qquad (2)$$

Within the limits of a linear velocity distribution along a perpendicular to the wall, i.e., for $\partial U/\partial y = \text{const}$, the value of τ_0 calculated from the above expression does not depend on the distance from the wall. Since only the Pitot tube was placed at large distances, where $\partial U/\partial y \neq \text{const}$, the experimental values of τ_0 were found to be on the low side. Hence the curve showing the distribution of τ_0 over the duct's perimeter was drawn using the values of local tangential stresses calculated from Eq. (2).

In calculating the tangential stress at the wall no corrections were introduced to compensate for the distortion of flow by the Pitot tube, the viscosity of the fluid and the high velocity gradient. Introduction of these corrections, [7] has increased the scatter of the experimental points. The average tangential stresses $\bar{\tau}_0$ thus obtained differed from the $\bar{\tau}_0$ determined using the flow resistance of the passage. It is possible that these corrections are applicable only for large-diameter Pitot tubes and are not suitable for the tubes we have used.

The flow-resistance coefficient was measured using distilled water. The design of the experimental setup is described in [8]. The pressure drop over the length of the passage was measured by differential manometers, in which mercury, tetrabromoethane and carbon tetrachloride were used as the working media. The friction coefficient λ was calculated on the basis of the average velocity, temperature and pressure drop over the length of the passage.

The results of velocity distribution measurements in a passage formed by a closely packed rod cluster are presented in the form of dimensionless isotachs $U/\bar{U}$ in Fig. 1. For the same pressure drop over the length of the passage which was obtained in our experiments, we have calculated the velocity distribution using the Deissler-Taylor method [3]. There were no qualitative differences between the two above distributions, for which reason the calculated velocity distribution is not shown.

Our measurements have shown that the velocity distribution is sufficiently symmetrical, which justifies performance of measurements only in 1/6th of the passage cross section.

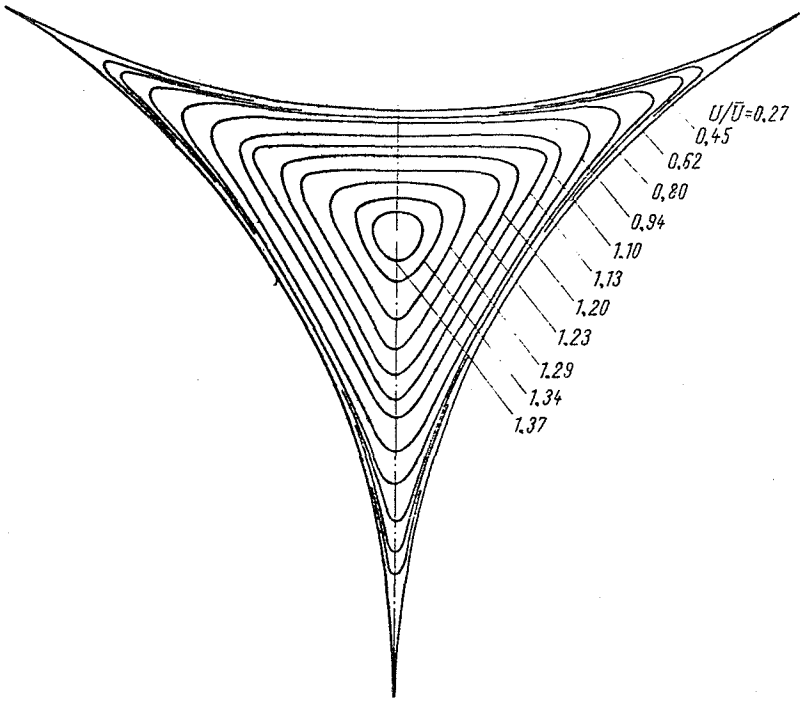

Figure 1. Velocity Distribution (Isotachs) in a Cell Formed by a Rods of a Closely-Packed Cluster (Experiments With Air for Re = 14,200).

For convenience in using the experimental data, Fig. 2 shows the velocity distribution in the form

$$U/\bar{U} = f\,(y/y_{\max}).$$

The parameter [here] is angle φ, measured from the point where the rod are in contact. Judging by Fig. 2, the velocity distribution at small angles comes close to the parabolic, which justifies the assumption of laminar flow in the corners of the cell. This figure also compares the experimental and theoretical results and it also displays previously unpublished results obtained by Buleyev. Calculations using the Deissler-Taylor method yields local velocities in the center on the high side and velocities in the corners of the duct on a low side, which is also obtained when using the Buleyev method. Consequently, the turbulent flow is a duct formed by closely packed rods of a cluster actually occupies a larger area than is shown by theoretical methods. /227

The average velocity obtained from the velocity distribution calculated by the Deissler-Taylor method is by approximately 10% higher than the average velocity determined in experiments for the same value of the pressure gradient $dp/dz = 5.22$ kg/m^2-m.

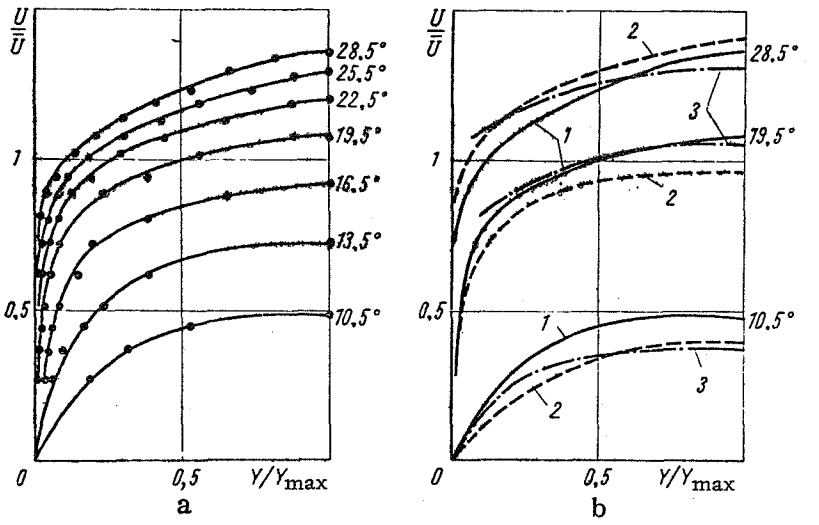

Figure 2. Velocity Distribution Along Normals to the Surface of a Cell Formed by a Densely-Packed Rod Cluster. 1) Experimental Data; 2) Data Obtained Using the Deissler-Taylor Method; 3) Data Obtained Using Buleyev's Method.

Figure 3 displays the velocity distribution over the line of symmetry of the passage (along the bisectrix of an angle) obtained theoretically and experimentally. This figure, as is the case of Fig. 2, shows that the theoretical calculations yield lower values of velocities near a corner of the duct than the experiments. On the other hand, the velocities in the center part of the channel, calculated by the Deissler-Taylor method come out higher than actual.

The results of measurements and calculations show that in a duct produced by a densely-packed rod cluster there exist regions with very low velocities - "stagnation zones", the boundary of which corresponds approximately to an angle $\varphi = 7°$. /229

The velocity distribution in the cell was also measured at $Re = 37,5 \cdot 10^3$ (Fig. 4). The authors were alarmed by the large distortions in the isotachs. Apparently additional work must be done to finally determine the pattern of velocity distribution for a given mode of fluid flow.

Distortion of isotachs are usually attributed to the effect of secondary flows in the fluid, directed along the bisectrix into the corner of the duct. If subsequent studies will confirm the results of preliminary measurements, then the presence of secondary flows in cells formed by closely-packed rod clusters will be proven.

Secondary flows can ordinarily be detected in a fluid by measuring the pressure distribution over the duct cross section. However, due to the fact that the expected pressure drops are small, a special method must be developed for

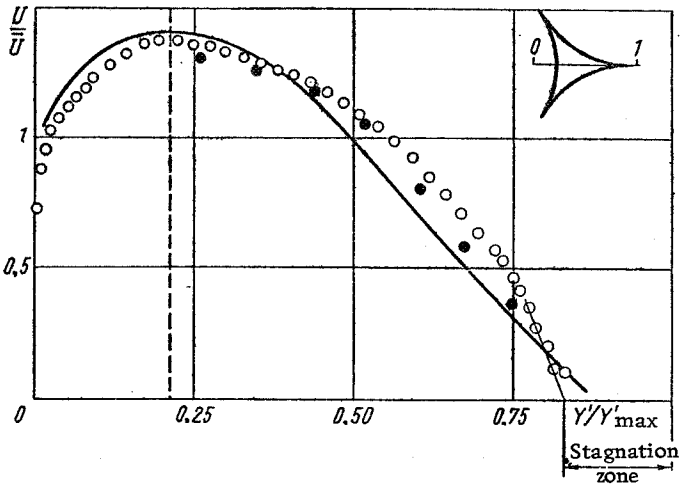

Figure 3. Velocity Distribution Along the Line of Symmetry of a Cell Formed by a Densely-Packed Rod Cluster. o - Experimental Data; • - Calculated by Buleyev; the Solid Line Denotes Curve Obtained by Using the Deissler-Taylor Method.

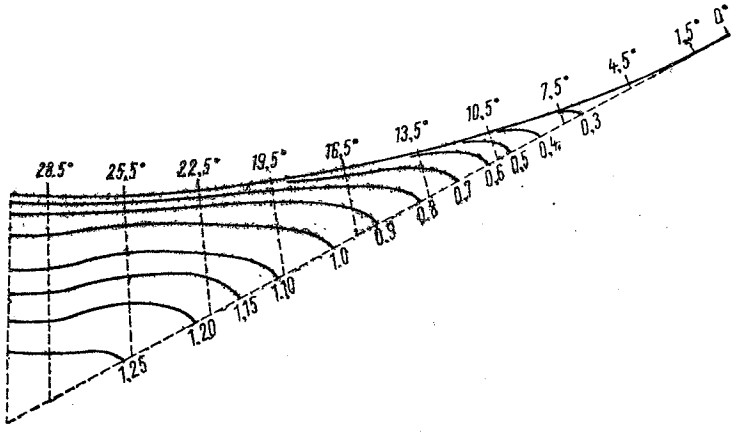

Figure 4. Velocity (Isotach) Distributions in Cells Formed by a Closely-Packed Rod Cluster for Re = 37,500.

measurements of this sort. The authors did not as yet succeed in obtaining satisfactory information using ordinary static pressure probes.

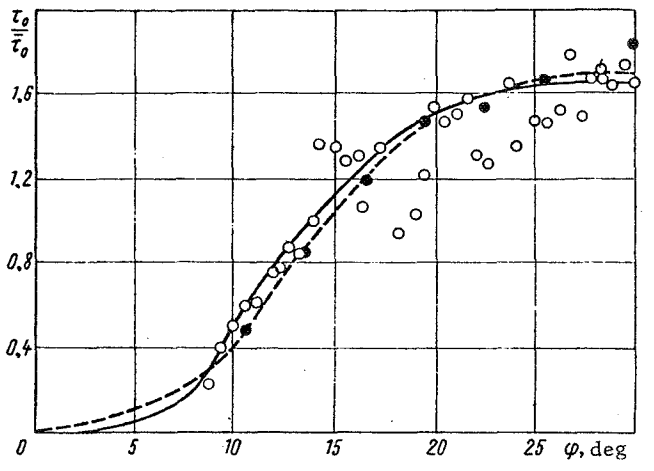

Figure 5. Distribution of Tangential Stresses at a Wall Along the Perimeter of a Cell Formed by a Densely-Packed Rod Cluster for Re = 14,200. o - Experimental Data; ● - Points Calculated Using the Measured Velocity Distribution and the von Kármán Universal Logarithmic Law.

Figure 5 shows in dimensionless coordinates the tangential stress distributions over the duct perimeter; here τ_0 has been calculated on the basis of the measured flow resistance of the duct

$$\bar{\tau}_0 = -\frac{d_h}{4} \cdot \frac{dp}{dz}. \qquad (3)$$

the values of τ_0 for $\varphi < 9°$ were obtained by extrapolation. Integrating experimental curve 1 graphically (see Fig. 5), we have found that

$$\frac{1}{\pi/6} \int_0^{\pi/6} \tau_0/\bar{\tau}_0 = 0.96.$$

Thus, the value of $\bar{\tau}_0$ obtained by measuring the local tangential stresses differs from the value of τ_0 obtained on the basis of the flow resistance by approximately 4%. /231

Figure 6 compares the distribution curves over the perimeter of the passage obtained experimentally and theoretically upon using the Deissler-Taylor and Buleyev's methods. It can be seen that the theoretical methods yield higher-than-actual local tangential stresses in the center and lower-than-actual stresses near the narrow part of the passage. The slight difference between the calculated $\tau_0/\bar{\tau}_0$ obtained by the authors and those taken from [3] is apparently due to subjective errors in graphical solution of the problem and hence is not of importance.

The theoretical method due to Deissler and Taylor is based on the assumption that the distribution along a perpendicular to the wall is governed by the universal logarithmic law. This hypothesis was checked by measuring the velocity distribution and the distribution of tangential stresses at a wall with Re $= 14.2 \cdot 10^3$ The experimental points were plotted in Fig. 7 in coordinates U^+, y^+; here the local values of τ_0 for the applicable angle were substituted into the expressions for these two quantities. The scatter of points near the wall ($y^+ < 30$) is due to the fact that a large contribution in this region is made by errors in determining the distance to the wall. The experimentally obtained velocity distributions along a perpendicular to the wall can in the first approximation be described by Von Kármán's logarithmic law. /232

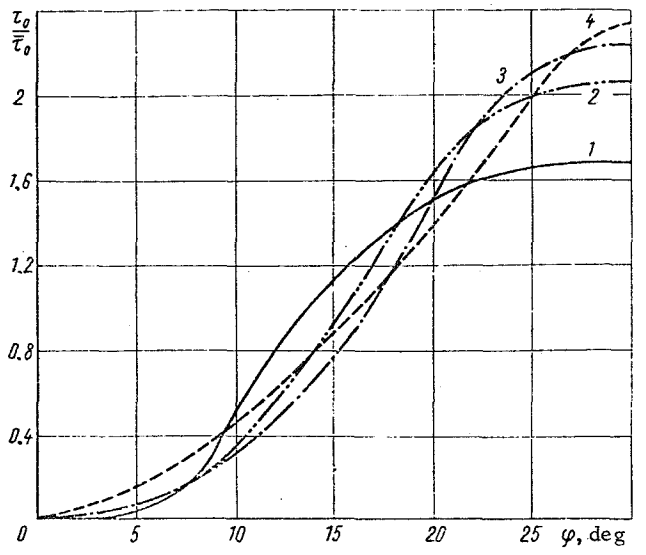

Figure 6. Tangential Stresses Determined Experimentally and Calculated Analytically. 1) Experimental Results for Re = 14,200; 2) Calculated by Buleyev for Re = 9400 and 26,000; 3) Calculated Using the Deissler-Taylor Method for Re = 15,400; 4) Calculations Made by Deissler and Taylor for 20,000 < Re < 900,000, [3].

On the basis of the above considerations we have calculated the distribution of $\tau_0 / \overline{\tau}_0$, the tangential stresses over the perimeter of the duct, making use of velocity distributions away from the wall, obtained experimentally and of Von Kármán's universal law. When $\tau_0/\overline{\tau}_0$ are calculated by this method the errors in measuring velocities and distance from the wall, which are quite appreciable in the region close to the wall, are eliminated. The value of τ_0 was determined from the expression

$$U/\sqrt{\frac{\tau_0}{\rho}} = 5.5 + 5.75 \lg \frac{y \cdot \sqrt{\frac{\tau_0}{\rho}}}{\nu} \quad (4)$$

by substituting the values of velocities at a point in the flow and the distance from the given point to the wall. Equation (4) was solved graphically. The values of τ_0 for given angles φ calculated on the basis of several magnitudes of velocity and corresponding distances from the wall were in good agreement.

The results obtained from Eq. (4) were plotted in Fig. 5. They are in satisfactory agreement with experimentally obtained distributions of τ_0. However, it cannot as yet be claimed that this will also be true for Re > $14.2 \cdot 10^3$. It is possible that for higher Reynolds numbers the suggested secondary flows will affect the distribution of the tangential stresses.

In experiments with distilled water we have measured the pressure drops over the length of the passage and determined the frictional resistance coefficients λ (Fig. 8). When processing these data using the hydraulic diameter the experimental points plotted in logarithmic coordinates lie parallel to the straight lines calculated by the Blasius formula: $\lambda = 0.316\ \mathrm{Re}^{-0.25}$ for Re < 10^5 and by the Nikuradse formula: $\lambda = 0.0032 + 0.221\ \mathrm{Re}^{-0.237}$ for Re > 10^5. The values of the friction coefficient for the passage at hand are lower than those for round tubes by approximately 40%. This is in agreement with results obtained previously in experiments with densely packed rod clusters, [9]. If the diameter of the circle inscribed into a cell formed by the cluster is taken as the characteristic dimension, then the experimental results are in approximate agreement with formulas for round tubes, as is also the case in [9] (see Fig. 8).

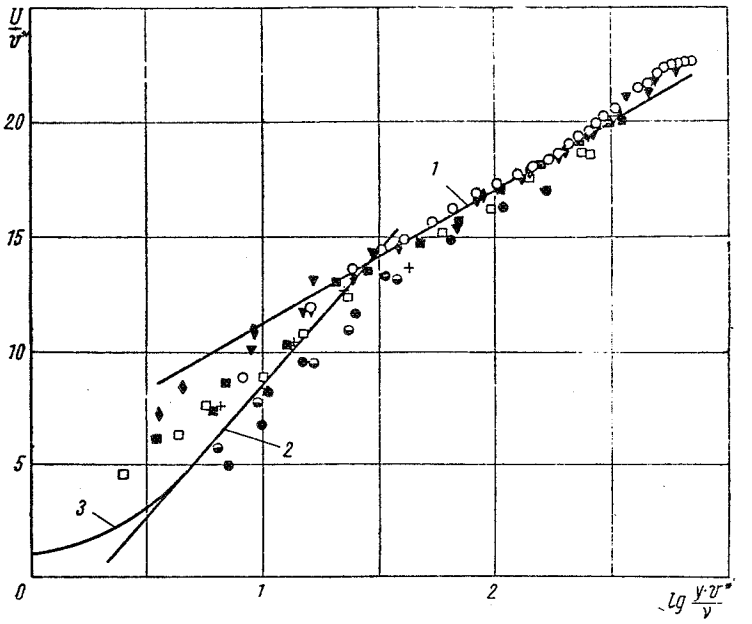

Figure 7. Comparison of Experimental Data on the Velocity Distribution in Cells Formed by a Densely-Packed Rod Cluster With the Universal Logarithmic Law. 1) $U^+ = 5.5 + 5.75 \lg y$; 2) $U^+ = -3.05 + 11.53 \lg y$; 3) $U^+ = y^+$; +, ⊖, ●, □, ■, ◆, ▼ and ○ Were Obtained for $\varphi = 10.5$, 13.5, 16.5, 19.5, 22.5, 25.5, 28.5 and 30°, Respectively.

It can also be seen from Fig. 8 that calculations using the Deissler-Taylor method yield values of the frictional resistance coefficient in densely-packed rod cluster by 7-10% lower [than actual].

In order to find the friction coefficient at $Re = 14.2 \cdot 10^3$, we have used the data on velocity distributions, obtained in experiments with air, from which we calculated the average velocity. The pressure gradient was measured directly in our experiments. In addition we have calculated the friction coefficient using the measured distribution of tangential stresses over the passage's perimeter. As is shown by Fig. 8, the values of friction coefficients found by the different methods are in agreement. The theoretical limiting errors in measuring the velocity distributions comprised about ±2.5% and for the tangential stresses they were about ±10%. The friction resistance coefficients were determined to within approximately ±7%.

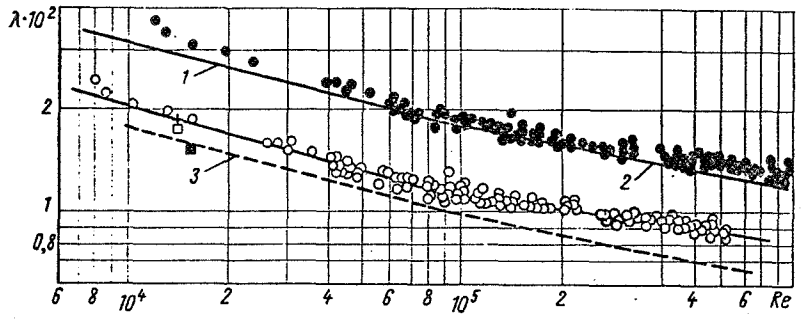

Figure 8. Coefficients of Frictional Resistance for a Cell Formed by a Closely-Packed Rod Cluster. 1) and 2) Were Obtained From Blasius and Nikuradse Formulas for Round Pipes; 3) Represents Calculation of Deissler and Taylor; ○ and ● Denote Experiments Using Water; the Characteristic Dimensions are the Hydraulic Diameter and the Diameter of the Inscribed Circle, Respectively; the Cross Denotes Measurements of Velocity and Pressure Drop Distributions in Air; □ Denotes Measurements of the Velocity and Tangential Stresses Distributions in Air; ■ Denotes Theoretical Results Obtained by the Deissler-Taylor Method.

NOTATION

d diameter of rods in the closely-packed cluster

S distance between rod axes in the cluster

d_h hydraulic diameter of the duct

h dynamic pressure

y distance from the wall, measured along a normal to it

y_{max} distance from the wall along the line of symmetry of the duct, along the normal to the wall

y' distance from the wall in directions parallel to the axis of symmetry of the duct

φ angle, measured from the contact line of the rods

Dimensionless Quantities

λ friction coefficient

$U^+ = \frac{U}{\sqrt{\frac{\tau_0}{\rho}}}$ velocity

$y^+ = \frac{y}{\nu} \cdot \sqrt{\frac{\tau_0}{\rho}}$ distance from wall

REFERENCES

1. Eckert, E.R.G., and Irvine, T.F.: Trans. ASME, v. 82, Series C, No. 2 (1960). /234
2. Nikuradze, I.: Ingenieur-Archiv, 1, 30 (1930).
3. Deissler, R.G. and Taylor, M.F.: Reactor Heat Transfer Conference of 1956, TID-7529 (Pt.-1), Book 2, 416 (1957).
4. Buleyev, N.I.: Teploperedacha [Heat Transfer], page 64. Published by the Academy of Sciences of the USSR, Moscow, (1962).
5. Ibragimov, M.Kh., et al.: Raschet i eksperimental'noye issledovaniye poley skorosti v kanale slozhnoy formy [Calculation and Experimental Study of Velocity Fields in an Intricately-Shaped Passage]. Article immediately following this.
6. Popov, S.G.: Izmereniye vozdushnykh potokov [Air-Flow Measurements]. Gostekhizdat, Moscow (1947).
7. Wuest, W.: Archiv für technisches Messeu, 116, No. 10 (1961).
8. Levchenko, Yu.D., et al.: Gidrodinamika v kol'tsevom zazore s prodol'nymi rebrami [Fluid Dynamics in an Annular Space with Longitudinal Ribs]. Part I of present collection.
9. Subbotin, V.I., et al.: Atomnaya energiya, 10, Issue 4, 308 (1960).

CALCULATION AND EXPERIMENTAL STUDY OF VELOCITY FIELDS IN INTRICATELY-SHAPED PASSAGES

M. Kh. Ibragimov, I. A. Isupov and V. I. Subbotin

Modern heat-engineering facilities and devices use passages of various /234
shapes, in particular, clusters of rods surrounded by a shell. The heat transfer processes in such passages depend substantially on the velocity distribution in the coolant flow. The present article considers the fluid dynamics of a passage formed by a cluster of three round rods, surrounded by a triangular shell. Such a passage combines fluid-dynamic peculiarities in the rod clusters, as well as the effect of the shell on the fluid-dynamic characteristics. The above flow characteristics were determined theoretically and experimentally.

Calculating the Velocity Field and the Friction Resistance Coefficients

Deissler and Taylor [1] have proposed an approximate graphical-analytic method for calculating the velocity fields and the resistance coefficient in intricately-shaped passages. The passage cross section is broken up into a number of areas, bounded by walls and by velocity-gradient lines. Along with assumptions on the existence of hydrodynamic stability and invariability of the physical parameter of the fluid, two basic assumptions are made. It is assumed that, first, the velocity distribution along the normal to the wall in the intricately-shaped passage is describable by the universal law for a round pipe and, second, that no transfer of momentum takes place between the fluid volumes selected in the above manner. The problem is solved by successive approximations.

Deissler and Taylor have used their method for infinite clusters of rods, where the position of the line of maximum velocity is entirely obvious. In the passage under study the position of this line for some parts of the passage can- /235
not be specified, due to the shape of the cross section, which introduces additional difficulties in the calculations.

The calculations were performed for 1/6 of a symmetrical part of the cross section. In order to increase the accuracy in calculating the areas, the part of the cross section under study was magnified eight-fold. The perimeter was broken up into parts equal to the length of arc subtended by 5° angle in the rod. Figure 1 shows the cross section of the passage and the velocity gradient lines in the first approximation. The initial position of the maximum velocity line was taken through points equidistant from the walls. Our experiments show that this assumption is satisfactorily justified.

The calculations were performed for air under the following conditions: $Re = 62 \cdot 10^3$, $r^{++} = 2210$ ($r = d_h/2$), $\Delta l = 3.72$ mm, $P_{bar} = 760$ mm of Hg, and

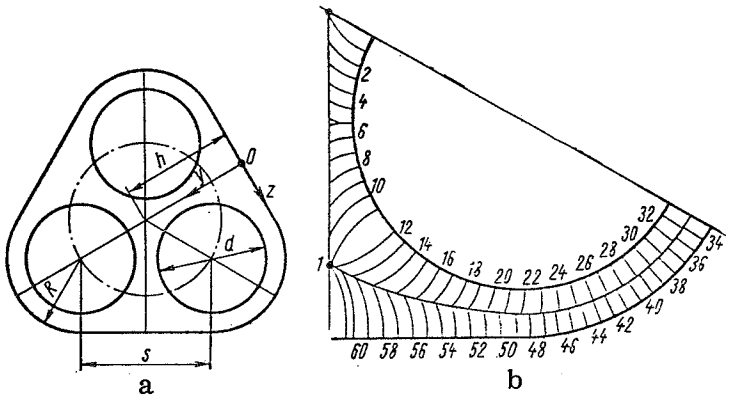

Figure 1. Shape of Passage's Cross Section (a) and Diagram of the Gradients (b).

$t = 20°C$. Parameter r^{++} was selected according to a preliminary estimate of the magnitude of dp/dx, the pressure gradient, on the basis of λ calculated by the Blasius formulas at $Re = 62 \cdot 10^3$. We have assumed that $r = d_h/2$ since, as was shown by calculations, the selected magnitude of the characteristic dimension r does not affect the end results of the calculations.

In [1] the magnitude of r was taken as equal to the rod radius. The calculations were made by specifying values of u^{++} from 9 to 22. The dimensionless velocities $u_i^+ = \frac{u^{++}}{\sqrt{\frac{\Delta A_i}{\Delta l \cdot r}}}$ and distances y_i^+ were calculated for each value of u^{++}.

Use was made here of the universal velocity distribution due to Von Kármán

$$\begin{array}{ll} y^+ \leqslant 5 & u^+ = y^+ \\ 5 < y^+ < 30 & u^+ = 11{,}5 \lg y^+ - 3{,}05 \\ y^+ \geqslant 30 & u^+ = 5{,}75 \lg y^+ + 5{,}5. \end{array} \qquad (1)$$

The values of y_i^+ thus calculated were used to determine distances y_i /236

$$y_i = \frac{y_i^+ \cdot r}{\sqrt{\frac{\Delta A_i}{\Delta l \cdot r}} \cdot r^{++}}.$$

From the midpoints of the corresponding intervals were constructed normals, on which the values of u^{++} were laid off as functions of distance y_i.

In area segments with highly curved boundaries some velocities u^{++} calculated for the given area segments were found to be located in neighboring area segments. The isotach grid thus obtained was compared with the grid of velocity gradients, their mutual orthogonality was estimated visually and the gradient lines were adjusted. It came out in the process of calculations that the maximum velocity line in the wide part of the passage is somewhat displaced toward the rod. To obtain this line more precisely we have made six approximations, while two approximations were thought to be sufficient for the remaining part of the passage.

The isotach grid which was finally obtained was used to calculate the average velocities $u_i^{++} = \frac{\sum_{k=1}^{n} u_k^{++} \cdot \Delta A_k}{\Delta A_i}$ in each elementary area, the average velocity $u_0^{++} = \frac{\sum_{i=1}^{N} u_i^{++} \cdot \Delta A_i}{A_0} = 14.7$ over the passage cross section, the Reynolds number $\mathrm{Re} = \frac{u_0^{++} \cdot r^{++} \cdot d_h}{r} = 65 \cdot 10^3$ and the friction resistance coefficient $\lambda = \frac{2 \cdot d_h}{r \cdot u_0^{++2}} = 0.018$. /237

Figure 2 shows a theoretical velocity distribution in the form of dimensionless isotachs u/u_0. It can be seen that the velocity of the fluid changes substantially over the passage cross section. The point of maximum velocity (1) is displaced by $\delta/y_{max} \sim 12\%$ to the center, while the maximum velocity point in narrow parts (in corners of the passage) is displaced toward the rod by $\delta/y_0 \sim 5\%$.

To determine the validity of the theoretical data obtained and to determine the boundaries of applicability of the Deissler-Taylor method, we have experimentally studied the velocity distribution, the tangential stresses at the wall and the position of the maximum velocity line.

Experimental Study of the Fluid-Dynamic Characteristics of a Passage

The experiments were performed with an air stand, which is schematically depicted in Fig. 3. The air, the flow rate of which was measured by a pre-calibrated normal diaphragm, and the temperature of which was determined by a mercury thermometer with a scale division of 0.1°C, was supplied to the test section by a fan with a nominal delivery of 800 m^3/hour at a pressure of 750 mm of water. The length of the test section is about $50d_h$, the cross section of its passage is shown in Fig. 1a. The inner surfaces of the passage were machined to class six surface finish. The rods could be moved, by screw-type devices, along the bisectrixes of the shell's corners. The length of travel was measured by rulers with verniers.

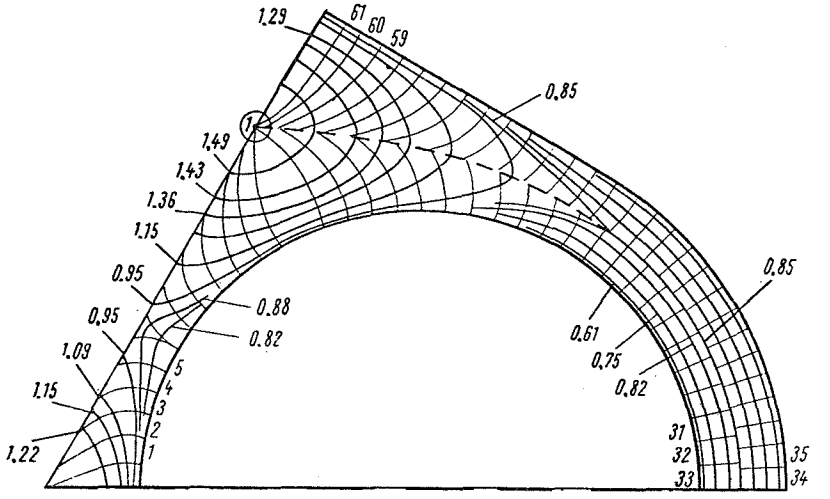

Figure 2. Theoretical (Using the Deissler Method) Distribution of Relative Velocities u/u_0; Re = $65 \cdot 10^3$.

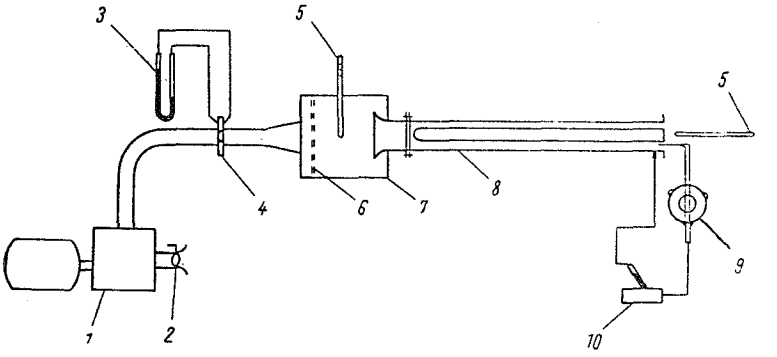

Figure 3. Schematic Diagram of Experimental Setup. 1) Fan; 2) Slide Valve; 3) Differential Manometer; 4) Diaphragm; 5) Thermometer; 6) Mesh; 7) Damping Tank; 8) Experimental Passage; 9) Coordinate Spacer; 10) Micromanometer.

The static pressure was measured in five cross sections of the passage /238
through holes in the shell 0.5 mm in diameter (the ratio of the wall thickness of the shell to the hole diameter was 6). In drilling the holes particular attention was paid to their perpendicularity to the wall and to removal of burrs. Five pickups were made in a cross section located at a distance of 33 mm from the outlet, and these were used for measuring the velocity fields. The remaining cross sections had two pressure pickups each. All the pickups of a given cross section were connected for more reliable pressure measurement.

The local velocities were measured by a total pressure metal tube (Pitot tube) with a working part diameter of 0.45 x 0.15 mm and length of 12 mm, the end of the tube was rounded to a half-spherical shape. The pitot tube was soldered into a reducing tube, serving as a holder, 6 mm in diameter which was fastened in the coordinate spacer, and which could be used to move the holder in four ways: vertically (accuracy of 0.05 mm), horizontally (0.1 mm), rotation in the vertical plane (0.5°) and rotation about the horizontal axis (0.2°).

The velocity distributions were measured in a cross section removed by 10 mm from the outlet end.

The distributions were studied in detail only in 1/6 of a symmetrical part of the cross section. In the remaining parts only control measurements were made, which have shown that the flow in the passage is satisfactorily symmetrical. The velocity distributions were measured along the normals to the flat part of the shell wall (see Fig. 1a, coordinate y) and selectively along normals to the rod surfaces. The pressure drops were measured by a type MMN inclined-tube micromanometer.

The velocity fields were measured in passages of two shapes: with S/d = = 1.15 (Fig. 1a, initial geometry) and when the rods were moved symmetrically to S/d = 1.3. In both cases the Reynolds number was the same and equal to $39 \cdot 10^3$. The flow resistance of the passage was measured in the interval of Reynolds numbers from $18.3 \cdot 10^3$ to $39 \cdot 10^3$ with the rods moved symmetrically by different distances.

The study of tangential stresses at a wall by measuring the velocity distribution in the viscous sublayer requires the use of a thinner Pitot tube and utilization of more sophisticated experimental methods. In our opinion the method presented in [2] is simpler. For the case when the Pitot tube lies on the wall in the dynamic similarity layer, Preston has established a relationship between the tangential stress at the wall and the dynamic pressure difference $P - P_0$, measured by the tube

$$\frac{(P-P_0)\cdot d_t^2}{\rho\nu^2} = F\left(\frac{\tau_0 \cdot d_t^2}{\rho\nu^2}\right), \qquad (2)$$

where F is an empirical function, determined in experiments with a round tube, while d_t is the outer diameter of the Pitot tube. All the corrections made necessary by the large velocity gradient at the wall have been included in this function. Since the dynamic pressure difference $P - P_0$ is quite high, ordinary instruments can be used for these measurements.

In order to be able to use data of [2] care must be taken that the tube, when moved along the perimeter, remains within the limits of the same layer in which the calibration was performed and that the dimensions of the tube be similar to those used in [2]. Hence, we have selected a Pitot tube with a ratio of 0.6 between the inner and outer diameter, when the former is 0.35 mm. The tangential stresses /239

were measured in a section removed by 4 mm from the end of the passage. The method of electric contact was used to determine that the tube was in contact with the wall. Since the experiments have shown that the tangential stresses in symmetrical parts are approximately symmetrical, these measurements were made only in 1/6 of the cross section. The tangential stresses at the wall were measured at $Re = 53.4 \cdot 10^3$ and $35.7 \cdot 10^3$ in the passage with the initial geometry and with the former Reynolds number only in a passage with rods moved into corners up to contact with the shell.

The length of the flow stabilization sections was estimated on the basis of velocity distributions measured at different distances from the inlet. For this purpose slotted holes, through which were introduced Pitot tubes were made in the wall of the shell at distances of $30d_h$ and $40d_h$ from the inlet. After the tube was inserted, the slot was packed. The velocity distributions were measured along two normals to the wall of the shell at $z/h = 0$ and 0.38 in a passage with the rods moved outward ($S/d = 1.3$) at $Re = 39 \cdot 10^3$.

The experimental data were processed as follows. The local velocities were calculated by the formula

$$u = \sqrt{\frac{[(P - P_0) + \delta P_0] \cdot 2}{\rho}},$$

where δP_0 is a correction produced by measuring the total pressure and the static pressure in different cross sections.

We have estimated the effect of the air's humidity and compressibility on the local velocity being calculated. It was shown that these factors, as well as changes in the density of alcohol in the manometer produced by the temperature have little effect. The limiting relative error in measuring the velocity was about ±3%.

To determine the isotachs we have constructed intermediate graphs of $u = f(y)$ for different z. In determining the value of the resistance coefficient λ we have used pressure data obtained with pickups placed at 25, 35 and 50 hydraulic diameters from the inlet. The pressure drop over the length at these distances is satisfactorily approximated by a straight line. The coefficients were calculated by the d'Arcy formula. The limiting relative error in measuring λ was about ±10%.

The tangential stresses at the wall were calculated by a formula presented in [2]

$$\tau_{0i} = \frac{4 \cdot \rho \cdot v^2}{d_h^2} \cdot \sqrt{\frac{2[(P - P_0) + \delta P_0] \cdot d_h^2}{4\rho v^2}} \qquad (3)$$

Using the local tangential stresses τ_{0i}, we found the relative stresses $\bar{\tau}_{0i}$ by graphical integration /240

$$\overline{\tau_{0i}} = \frac{6\left[(\Sigma\tau_{0i}\cdot\Delta l)_{\text{rod}} + (\Sigma\tau_{0i}\cdot\Delta l)_{\text{shell}}\right]}{L_0}. \quad (4)$$

The magnitudes of $\overline{\tau_{0i}}$ were compared with the value of $\bar{\tau}_0$, calculated from the expression

$$\bar{\tau}_0 = \frac{dp}{dx}\cdot\frac{A_0}{L_0}. \quad (5)$$

The limiting error in measuring the tangential stresses was about ±7%.

Figure 4 shows velocity distributions in the form of dimensionless isotachs u/u_0, from which it is seen that there exists a sufficiently large velocity variation over the passage cross section. In the passage with S/d = 1.15 the velocity at the center comprises $u/u_0 = 1.2$, in point 1 it is 1.3, while at the line of maximum velocity in a corner $u/u_0 = 0.96$. When the rods are moved into the corners, the variation becomes greater. The velocity varies particularly at points where the flow narrows down. Thus, for S/d = 1.3 in the center of the passage $u/u_0 = 1.37$, in point 1 it is 1.34, while at the line of maximum velocity in a corner $u/u_0 = 0.55$.

The position of the maximum velocity line in a majority of points agrees satisfactorily with the locus of points equidistant from the wall along a normal. Point 1 deviates most: in a passage with S/d = 1.15 $\delta/y_{0\max} \approx 12\%$, while in a passage with S/d = 1.3 $\delta/y_{0\max} \approx 10\%$. The velocity maximum in this point is very flat and the above deviations are [therefore only] approximate. The de- /241 viation of maximum velocity lines in passages of both forms decreases rapidly along the z coordinate and in the corner this line practically coincides with the midpoint of the space.

Figure 5 shows the friction coefficient as a function of the Reynolds numbers for different rod positions. All the values of λ of the passage under study for any symmetrical positioning of the rods are smaller than those calculated by the Blasius formula. Within limits of scattering of experimental points, the expression λ = f(Re) is parallel to the Blasius curve.

The passage with the most uniform cross section (S/d = 1.15) has the highest flow resistance. Figure 6 shows coefficient λ as a function of S/d for several Re. The reduction in the friction coefficient when the rods are in extreme positions may be attributed to the presence of stagnation zones.

The curve of the friction coefficient in the triangular passage under study at S/d → 1 is in qualitative agreement with data for triangular rod lattices in axial flow.

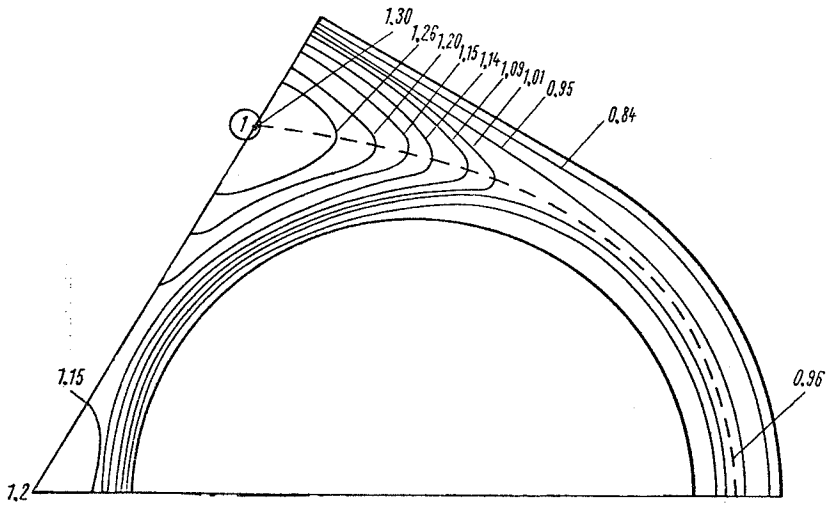

Figure 4. Experimental Distribution of Relative Velocities u/u_0; S/d = 1.15.

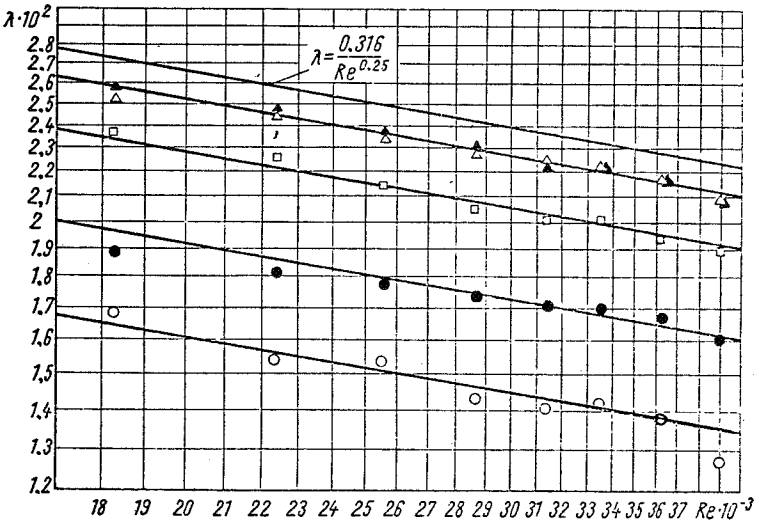

Figure 5. The friction Coefficient as a Function of the Reynolds Number at Different S/d. △, ▲, □, ● and ○ are Points for S/d =1.15, 1.09, 1.01, 1.3 and 1.41, Respectively.

Figure 7 compares the velocity distributions at various distances from the inlet for a passage with S/d = 1.3. The distributions at distances 40 and $30d_h$ from the inlet differ by approximately 13%, while at 50 and $40d_h$ they differed by /243

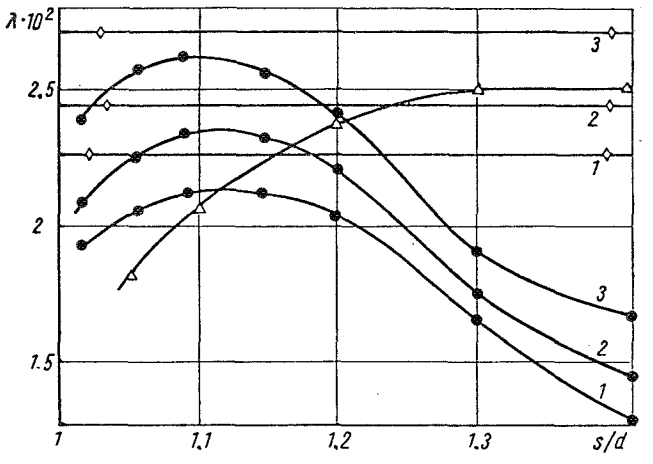

Figure 6. The Friction Coefficient as a Function of S/d. 1), 2) and 3) are Curves for Re = $= 39 \cdot 10^3$, $28.7 \cdot 10^3$ and $18.3 \cdot 10^3$, Respectively; ● Denotes Experimental Values, ◇ Denotes Points Obtained From the Expression $\lambda\ 0.316/Re^{1/4}$; Δ is for a Rod Lattice With $Re = 40 \cdot 10^3$.

not more than 3%. Consequently, at distances of more than $40d_h$ from the inlet the velocity distribution may be regarded as approximately stabilized.

The distributions of tangential stresses at a wall in a passage with the rods placed in various positions is shown in Fig. 8. The tangential stress $\tau_{0i}/\overline{\tau_{0i}}$ varies in a passage with S/d = = 1.15 within the limits of 0.9-1.26, while in a passage with S/d = 1.3 it is within the limits of 0-2.1. The experimental points are not significantly scattered. The values of the average tangential stress at the wall, found by Preston's method ($\bar{\tau}_{0i}$) and those calculated on the basis of the pressure drop ($\bar{\tau}_0$) are in satisfactory agreement with one another. The maximum difference between $\bar{\tau}_{0i}$ and $\bar{\tau}_0$ was 7-15% for the different rod arrangements in the passage. This circumstance shows that Preston's method is suitable for determining the tangential stresses at the wall in such intricately-shaped passages.

The velocity distribution in the passage under study in the coordinates u^+, y^+ is in agreement with the universal velocity distribution. Consequently, the universal velocity distribution is practically applicable also in intricately-shaped passages, if the velocity distribution is measured along a normal to the passage walls. /244

Comparison of Theoretical and Experimental Data

The friction coefficients for $Re = 65 \cdot 10^3$ obtained theoretically by the Deissler-Taylor method and extrapolations of experimental data were found to be in satisfactory agreement. Comparison of velocity fields shows that the theoretically calculated velocities are higher than actual in the wide parts of the cross section and lower than actual in the narrow parts (Fig. 9). The maximum differences in the local velocities comprises about 25%. The distributions were

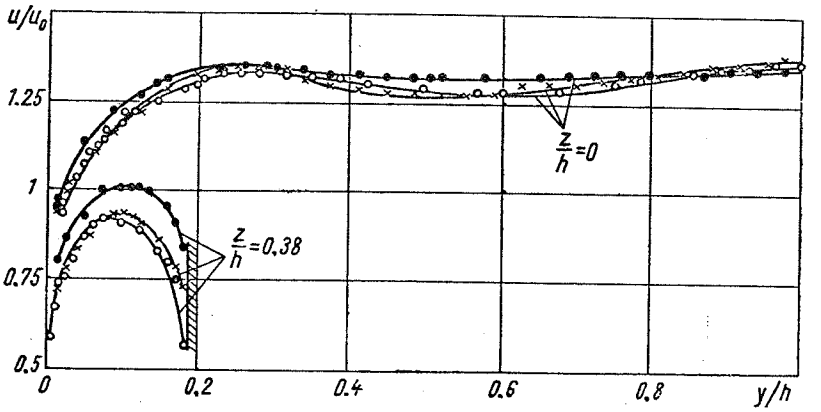

Figure 7. Velocity Distributions at Different Distances From the Inlet, $Re = 39 \cdot 10^3$. ●, × and ○ are for $x/d_h = 30$, 40 and 50, Respectively.

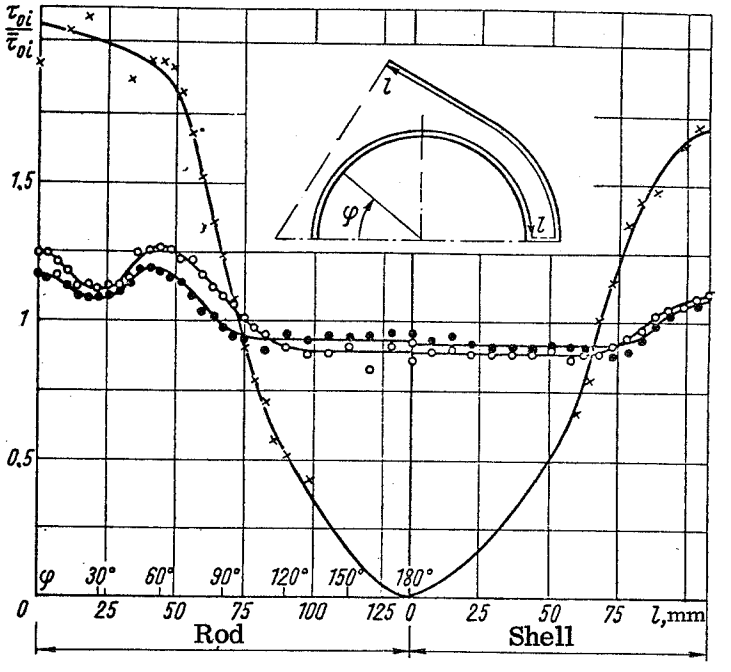

Figure 8. Distribution of Tangential Stresses $\tau_{0i}/\bar{\tau}_{0i}$ Over the Perimeter of the Passage. At S/d = 1.15, $Re = 35.7 \cdot 10^3$ (○); $Re = 53.4 \cdot 10^3$ (●); at S/d = 1.41, $Re = 53.4 \cdot 10^3$ (×).

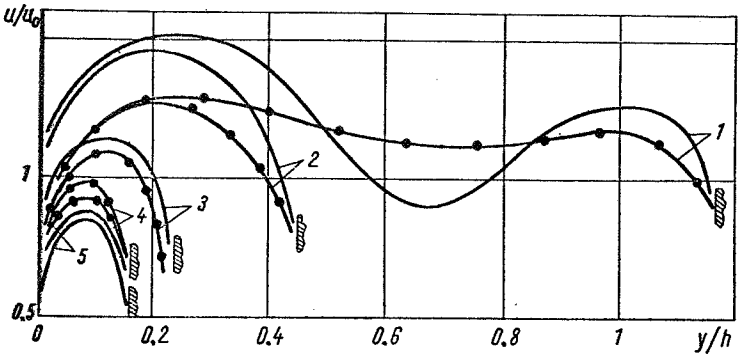

Figure 9. Theoretical (Using the Deissler Method) and Experimental Velocity Distributions. ● - Experimental Data for Re = $39 \cdot 10^3$; the Solid Line was Calculated Theoretically for Re = $65 \cdot 10^2$; 1), 2), 3), 4) and 5) are Curves for z/h = 0, 0.12, 0.31, 0.42 and 0.72, Respectively.

compared for several values of Re, differing from one another ($65 \cdot 10^3$ and $39 \cdot 10^3$), however, it is fully justified due to the fact that the dimensionless velocity distribution depends little on the Reynolds number.

The difference between the theoretical and experimental data is a consequence of the assumptions used in the calculations. As is shown by the experiments, as well by data of [3], the universal velocity distribution in a round pipe describes satisfactorily the velocity distribution even in an intricately-shaped passage. Hence, this assumption is an experimentally proven fact and is beyond doubt. The main source for the above difference is the assumption that there is no transfer of momentum between elementary volumes. The only time when there actually will be no such transfer is that when the momentum transfer is produced by the gradient, when the dimensions of the turbulent eddies (length of the displacement path) is much smaller than the dimensions of the cell and the entire transfer depends on the velocity gradient du/dz.

However, in addition to momentum transfer produced by the [velocity] gradient, there also exists convective transfer of momentum, which is due to the motion of large eddies. Such transfer, naturally, will result in mutual transfer of momentum between the volumes and smoothing out the distribution of τ_0 over the passage's perimeter. Convective transfer of momentum between elementary volumes cannot be eliminated by choosing these volumes along velocity gradient lines, as this is suggested by Deissler and Taylor. Hence, their basic equation of the force balance in an elementary volume

/245

$$\tau_{0i} \cdot \Delta l = -\frac{dp}{dx} \cdot \Delta A_i \qquad (6)$$

is invalid in the case of intricately-shaped passages. It follows from analysis of experimental data, that the greatest imbalance of Eq. (6) is observed in those parts of the passage where the cross section changes appreciably. Hence, the more the distance to the maximum-velocity line varies, the more appreciable is the computed velocity increase [apparent] shown by theoretical calculations. (See Figs. 2 and 10). The [apparent] reduction in velocity in those parts of the cross section where the elementary areas ΔA_i do not change, is produced by a reduction in τ_{0i} in these points.

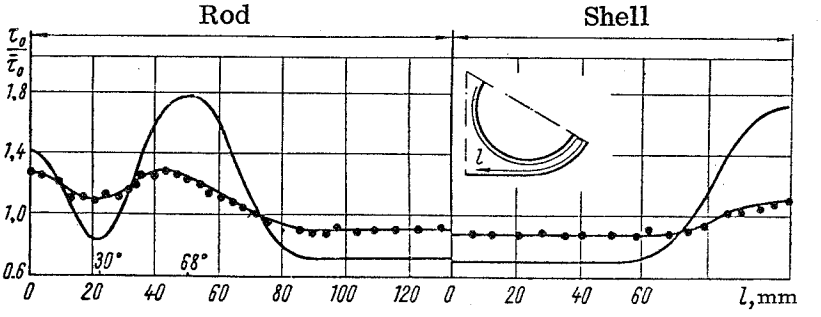

Figure 10. Theoretical (Using the Deissler Method) and Experimental Distributions of Relative Tangential Stresses at a Wall. ● - Experimental Points for Re = 35.7 x 10; the Solid Line was Calculated at Re = $65 \cdot 10^3$.

Figure 10 compares the distribution of tangential stresses τ_{0i} obtained theoretically using the Deissler method, with the experimental distribution. The shape of the theoretical curve of τ_{0i}/τ_{0i} is steeper. The maximum difference in values of τ_0 is about 55%.

Thus, calculations of the velocity field using the Deissler-Taylor method can yield satisfactory results for passages with a moderately variable cross section, when the contribution of the convective momentum transfer is not appreciable.

Simplified Method for Calculating Velocity Fields in Intricately-Shaped Passages[1]

The applicability of the universal velocity distribution for a pipe for calculations involving intricately-shaped passages means that, in order to calculate the velocity fields in such passages it is only necessary to know the tangential stresses at the wall. /246

[1] This method was subsequently refined. See Atomnaya energiya, 21, 2 (1966).

It follows from the assumption that the fluid dynamics in intricately-shaped passages are appreciably affected by convective momentum transfer, that [4]

$$\frac{\tau_0}{\bar{\tau}_0} = f_1 \cdot (1 - e^{-f_2 \cdot \frac{y_0}{\bar{y}_0}}), \tag{7}$$

where f_1 and f_2 are some constants, while $\bar{y}_0$ is the average value of y_0 over the entire cross section of the passage. The above expression shows that for low $y_0/\bar{y}_0$ the variations of y_0 and τ_0 are proportional. In the limit, as $y_0 \to 0$, $\tau_0 \to 0$. As $y_0/\bar{y}_0$ becomes larger the relationship between the variations in y_0 and τ_0 becomes less pronounced, due to the effect of convective momentum transfer by large-scale eddies. /247

Constant f_1 is determined by the norming condition

$$\frac{1}{L_0} \int_{L_0} \frac{\tau_0}{\bar{\tau}_0} dl = 1. \tag{8}$$

The value of f_2 is an empirical quantity, which is related to the shape of the passage cross section. To determine, it is necessary to analyze the experimentally-determined relationship $\tau_0/\bar{\tau}_0 = F(y_0/\bar{y}_0)$ for different passage shapes. Figure 11 shows that experimental points with a scatter of approximately 20% are grouped about two averaging curves. Curve 1 characterizes the distribution of $\tau_0/\bar{\tau}_0$ in a very irregularly shaped passage, while curve 2 corresponds to a more uniform cross section.

The distribution of $\tau_0/\bar{\tau}_0$ depends perceptibly on the overall irregularity in the passage's shape. As a parameter which characterizes this irregularity we can take

$$a = \frac{y_{0\,\max} - y_{0\,\min}}{\bar{y}_0}$$

In a passage with uniform cross section a = 0, in the passages under study a = 2.98 (at S/d = 1.3) and a = 1.39 (for S/d = 1.15). Upon introducing parameter a, f_2 of Eq. (7) takes on the form

$$f_2 = \frac{2.45}{a^{2/3}}. \tag{9}$$

for a passage with a uniform cross section a = 0 and $\tau_0/\bar{\tau}_0 = 1$.

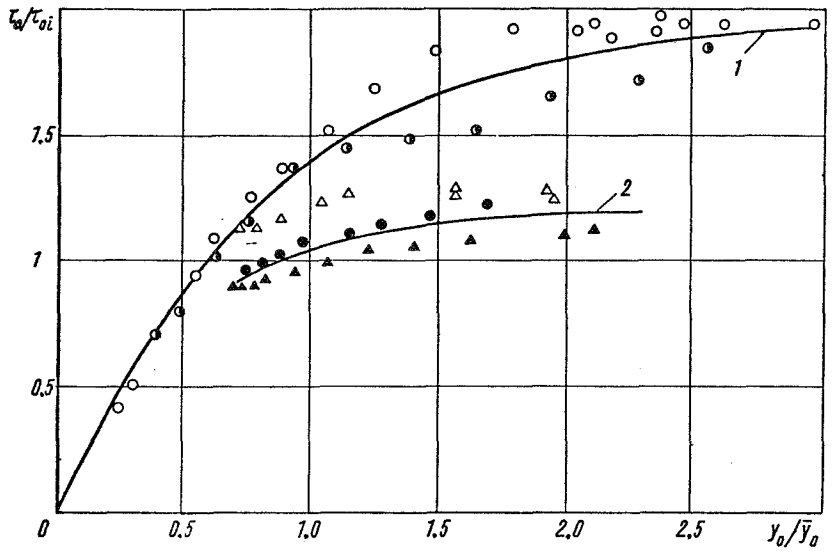

Figure 11. The Relative Tangential Stress $\tau_0/\bar{\tau}_{0i}$ as a Function of $y_0/\bar{y}_0$. ○ - Rod; ◐ - Shell (S/d = 1.41); △ - Rod, φ = = 0-65° (S/d = 1.15); ● - Rod, φ = 65-180; ▲ - Shell.

Comparing values of $\tau_0/\bar{\tau}_0$ obtained experimentally in a passage formed by closely-packed rods, [3], with those obtained using Eq. (7) we see that the theoretically and experimentally obtained values of this ratio are in satisfactory agreement. Parameter a in such a passage is 3.02. The maximum difference, for $y_0/\bar{y}_0 > 0.3$, comprises about 15%. Taking into account the fact that in the passages under study the magnitude of a varied within sufficiently wide limits (from 0 to 3), we can assume that Eq. (7) is valid for calculating $\tau_0/\bar{\tau}_0$ in other intricately-shaped passages formed by various cylindrical and flat surfaces.

Knowing the manner in which the tangential stress varies over the perimeter of a passage, it is possible to recommend a simplified method for calculating the velocity field in hydrodynamically stabilized turbulent flow of a fluid.

1. The maximum velocity line is drawn as the locus of points equidistant from the passage's perimeter, while the latter is broken up into uniform intervals, through the ends of which normals y_{0i} are drawn to the maximum velocity line.

2. The magnitude of $\bar{\tau}_0$ is determined on the basis of the specified flow /249 rate of the fluid through the passage and by selecting a friction coefficient (for example, using the Blasius formulas).

3. Parameters a and $\bar{y}_0$ are determined.

4. The tangential stress distribution is calculated using Eqs. (7)-(9).

5. Successive values of y are specified and the velocity distribution at each normal y_{0i} is calculated, using the universal velocity distribution.

6. The size of elementary areas ΔA_i, formed by the wall, normals y_{0i} and the maximum velocity line is determined.

7. From the isotachs, the average velocity in each elementary area ΔA_i and the average velocity over the passage cross section u_{0p} are calculated by graphical integration.

8. The frictional resistance coefficient is determined as

$$\lambda_p = \frac{8 \cdot \bar{\tau}_0}{\rho \cdot u_{0p}^2} .$$

If the flow rate calculated on the basis of the average velocity differs appreciably from the specified flow rate, then the initial value of $\bar{\tau}_0$ is adjusted (taking into account the λ_p which was obtained) and the calculations are repeated.

Using this method we have calculated the velocity at individual normals in a passage formed by closely-packed rods and in a triangular passage with S/d = 1.3. Figure 12 compares the theoretically and experimentally obtained velocity distributions. The greatest difference between these distributions is about 8% in passages formed by closely-packed rods and about 10% in the triangular passage.

NOTATION

u	average local velocity in direction of the flow, m/sec
u_0	average velocity in the passage
A	passage cross sectional area
ΔA_i	area of i^{th} elementary area
L_0	passage perimeter
d_h	hydraulic diameter $4 \cdot A_0/L_0$

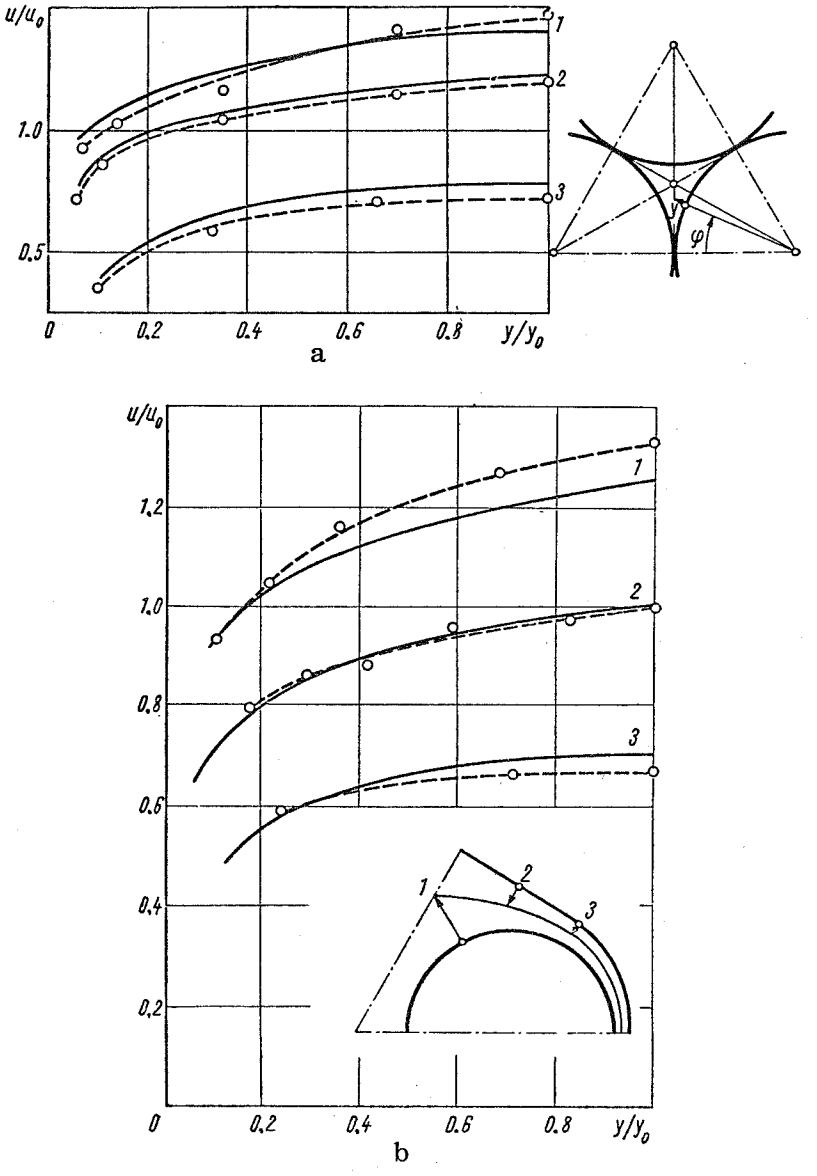

Figure 12. Velocity Distribution in a Passage Formed by Densely-Packed Rods. $Re = 14 \cdot 10^3$, Ref. [3] (a); and in a Passage With S/d = 1.3 With $Re = 39 \cdot 10^3$ (b). o - Experimental Points; the Solid Curves Were Obtained Theoretically; 1), 2) and 3), are for $\varphi = 28.5$, 22.5 and 43.5°, Respectively.

Δl parameter segment

r characteristic dimension

τ_{0i} tangential stress at the wall in the i-th point of the perimeter

τ_0 average tangential stress at the walls of the passage

dp/dx drop in pressure over the length of the passage [pressure gradient]

δ displacement of the position of a point on the maximum velocity line with respect to the position of a point equidistant from the walls

y_i distance along a normal to the wall in an ith elementary area

y_0 distance along a normal from a wall to the maximum velocity line

P total pressure

P_o static pressure.

Dimensionless Quantities

$u^+ = \frac{u}{\sqrt{\frac{\tau_0}{\rho}}}$ velocity /250

$u^{++} = \frac{u}{\sqrt{\frac{-r \cdot dp/dx}{\rho}}}$ velocity parameter

$y^+ = \frac{y \cdot \sqrt{\frac{\tau_0}{\rho}}}{\nu}$ distance

$r^{++} = \frac{\sqrt{\frac{-r \cdot dp/dx}{\rho}}}{} \cdot r$ parameter

REFERENCES

1. Deissler, R. and Taylor, M.: NACA, TN-4384, 1958.
2. Preston, D. R.: Zh.[?] Mekhanika, No. 6 (34) (1955).
3. Levchenko, Yu. D., et al.: Raspredeleniye skorostey v yacheyke plotno upakovannogo puchka sterzhney [Velocity Distribution in a Cell Formed by a Densely Packed Cluster of Rods]. Article immediately preceding this one in the present collection.
4. Ibragimov, M. Kh., et al.: Atomnaya energiya (in print).

PART THREE

BOILING AND CONDENSATION OF METALS

ELECTRONICALLY-HEATED SETUP FOR THE STUDY OF HEAT TRANSFER FROM BOILING METALS BY FREE CONVECTION

A. A. Ivashkevich, A. P. Kudryavtsev, D. M. Ovechkin, D. N. Sorokin, V. I. Subbotin and A. A. Tsyganok

In 1957 Lyon and others [1] have published data on heat transfer from boiling sodium and from a sodium-potassium alloy in a large volume (heat fluxes of approximately up to $0.350 \cdot 10^6$ kcal/m^2-hour). For sodium with heat fluxes of about $0.3 \cdot 10^6$ kcal/m^2-hour the heat transfer coefficient was about $7 \cdot 10$ kcal/m^2-hour-degree. [However], no experimental data has been published on critical heat fluxes q_{cr}. Calculations made using standard relationships which describe experimental data for q_{cr} for ordinary fluids, yield values of the critical thermal flux for sodium, at atmospheric pressure, for example, of from $1.5 \cdot 10^6$ to $10 \cdot 10^6$ kcal/m^2-hour. Hence in working out the methods for performing the experiment being here described particular attention was paid to selection of a method for heating the heat-conducting wall and for measuring the temperature difference between the wall and the fluid [metal]. /251

We have examined various methods for heating the heat-conducting wall for large-volume conditions, and have arrived at the following conclusions.

1. Heating by passing current directly through the test section is impossible due to the electrical conductivity of the metallic heat-transfer agents, while radiant heating can produce thermal fluxes only up to $(1.5\text{-}2) \cdot 10^6$ kcal/m^2-hour.

2. Heat fluxes in excess of 10^7 kcal/m^2-hour can be obtained by using an electric arc or gases passed through an arc (plasmatron), as well as high-frequency heating and heating the boiling alkaline metals by a heat-transfer agent at a temperature higher than that of the metals. However, this creates great technical difficulties such as, for example, stabilization of the heat supply over an extended period of time when heating by the electric arc; corrosion of the heat conducting wall from the hot-gas side when using the plasmatron; determination of the thermal flux when using high-frequency heating, making of a special reliable high-temperature circuit when heating by the heat-exchanger method. /252

3. Electronic heating makes it possible to supply appreciable amounts of power to a relatively moderately-sized surface and thus to obtain high thermal fluxes and to measure them with sufficient accuracy. For example, the thermal fluxes in high-power generator tubes are as high as $86 \cdot 10^6$ kcal/m^2-hour, [2].

In conjunction with this we have selected for our study of critical thermal fluxes and heat transfer from boiling metals the method of electronic heating the heat-conducting wall, which was used previously in experiments using water [3]. The substance of the method consists in the fact that the electrons emitted by the cathode are accelerated by the anode voltage and impinge on the anode. This means that the electrons are stopped in a very thin layer (the thickness of this layer is several microns, even at voltages of about 10 kv), in which the kinetic energy of the electrons is converted into thermal energy.

When determining the power generated at the anode one does not take into account the energy losses due to x-ray radiation and secondary electrons, and it is also assumed that the electrons leave the cathode with zero energy. It has been estimated that the error in determining the anode power produced by the above assumptions is less than 1% for voltages of up to 10 kv. Under electronic heating the surface of the heat-conducting wall facing the cathode is not subjected to oxidation and corrosion even at high temperatures as compared, for example, with arc heating, since it is situated in a vacuum (10^{-5}-10^{-6} mm of Hg). The high-voltage and evacuated system which is needed under this method can be made by selecting standard equipment.

The main part of an electron tube is the cathode. In radio electronics use is made of purely metallic, film and semiconductor cathodes, which may be divided into direct- or indirect-heated devices [4]. In the electron tube used in the study of heat transfer the cathode operates under conditions more difficult than cathode of radio-electronics tubes. In the case at hand the cathode is required to retain its emission properties under a relatively rough vacuum in the tube ($\sim 10^{-4}$ mm of Hg) and operate stably at temperatures in excess of 1300-1500°C, since the temperature of the surface of the heat conducting wall facing the cathode may be as high as that. In addition, the cathode should retain its emission properties under ionic bombardment and on relatively frequent disassembly of the tube. A tungsten cathode satisfies these requirements [4].

The electron tube shown in Fig. 1 consists of a diode, the anode of which (the tube body) is held under ground potential, while adjustable voltage is supplied to the cathode. A removable shell, to the top butt of which is welded a flat working section (header), is fastened to the upper part of the tube body. /253 The inner surface of the header is subjected to electron bombardment and radiant heating by the cathode, which is made from tungsten wire 1 mm in diameter in the form of a flat spiral with an average outer diameter of 38 mm and a distance of 2 mm between loops. The cathode is fastened to molybdenum holders by a molybdenum wire 0.2 mm in diameter over a length of 12-15 mm, the latter is fastened in copper conductors 10, which in their turn are fastened in conductors 25, cemented by the BF-2 glue to an organic-glass insulator. This design of conductors make it possible to center the cathode and to adjust its height position. The cathode is provided by six supports from tantalum foil 0.15 mm thick, which prevents it from sagging. To prevent scattering of the electrons which travel from the cathode to the header, the former is surrounded by a screen made from 0.15 mm thick tantalum sheet and with an inner diameter of 39 mm. The distance between the header /254 and the cathode is approximately 15 mm, while that between the top edge of the screen and the header is about 5-7 mm. To protect the insulator from overheating

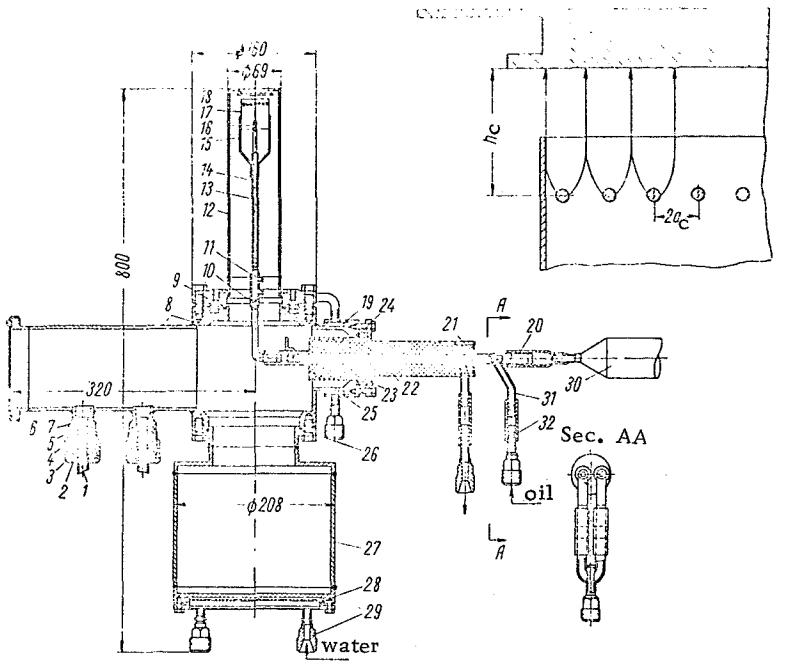

Figure 1. Overall View of the Electron Tube.

1) Measuring Tube; 2) Connector Nut; 3) Pressing Sleeve; 4), 6), 9), 24) and 26) Inserts; 5) Ring; 7) Connecting Sleeve; 8) Housing; 10) Conductor; 11) Screws; 12) Shell; 13) Holder; 14) Insulator; 15) Supporting Bracket of the Screen; 16) Wire, 0.2 mm in Diameter; 17) Screen; 18) Cathode; 19) Cooling Sleeve; 20) Contact 21) Ring; 22) Insulator; 23) Flange; 25) Conductor; 27) Collecting Tank; 28) Cooling Cover; 29) Connecting Sleeve; 30) High-Voltage Cable; 31) Tubular Segment; 32) Sleeve.

the conductor is cooled by transformer oil. A removable container, which serves to catch the metal in case the header breaks down during operation, is fastened to the lower part of the tube body. The individual parts of the tube are packed by vacuum rubber inserts.

The vacuum in the electron tube is measured by the MM-5 and LT-4M pickups. Various types of headers were used in the experiments (Fig. 2). Type I headers were used for the study of critical thermal fluxes. The header temperature was measured by chromel-alumel thermocouples using wires 0.2 mm in diameter, insulated by aluminum oxide. The thermocouples were placed in capillaries from 1Kh18N9T steel 0.5 x 0.1 or 0.8 x 0.15 mm in diameter, which were forced into holes drilled to a depth of about 15 mm. /255

Type I headers are not recommended for the study of heat transfer from boiling fluids, since, for example, headers from stainless steel have a large error due to the fact that it is impossible to determine precisely the position

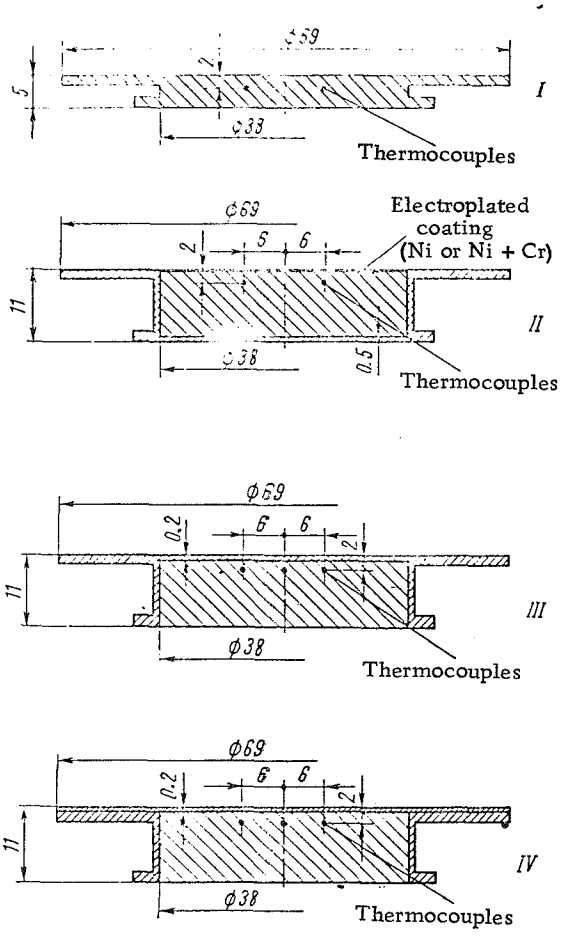

Figure 2. Types of Headers Which are Used.

of the thermocouple bead ($\Delta\delta = \pm 0.4$ mm). For example, for boiling water with $q = 0.63 \cdot 10^6$ kcal/m^2-hour and $\alpha = 31 \cdot 10^3$ kcal/m^2-hour-degree the maximum error in determining the heat transfer coefficient in a single experiment is about 160%. In order to obtain a higher accuracy, it is necessary either to appreciably reduce the error produced by the undeterminacy $\Delta\delta$ in determining the position of the thermocouple bead (which is impossible at present), or to make the headers from materials with a higher thermal conductivity. For this purpose methods were developed and multilayer headers were produced, in which the thermocouples which measure the wall temperature were plotted with copper [5] (see Fig. 2, II, III and IV). Brand M-1 molten copper is poured into a bowl from 1Kh-18N9T steel under a vacuum of 10^{-5} mm of Hg. Before the copper is poured the thermocouples are placed in the bowl. It thus becomes possible to embed several thermocouples into one header. Metallographic examinations have shown that the diffusive coupling between the copper and the 1Kh18N9T steel is satisfactory. Hence, we can regard the thermal contact between the steel and the copper as ideal.

The surface of type II headers was electroplated by a layer of nickel (or nickel followed by chromium) 20-25 micromicrons thick to protect the alkaline metal. The type III header after potting was stoppered from both sides; here steel with a thickness of 0.2 mm was left over at the side facing the heat-transfer agent. Before potting of type IV headers they were topped by a 0.2 mm thick foil from 1Kh-18N9T steel.

In copper-potted headers the error in determining the temperature differences is appreciably smaller as compared with steel headers (which is due to the high thermal conductivity of the copper). In addition, in this case there is practically no distortion of the temperature field, which does not take place when thermocouples are embedded in slot. At high thermal fluxes ($> 1 \cdot 10^6$ kcal/m^2-hour) such headers can operate at approximately the same sodium temperatures as the steel headers.

The electrical system of the tube consists of a high-voltage rectifying device rated at 20 kwt and of measuring instruments. The above rectifying device includes: type ATSK-25 adjustable three-phase autotransformer, the TM20/10 step-up transformer, six type TR15/6 thyratrons connected in the Laryonov circuit, and a filter, consisting of two RL-32.5-0.25 capacitors and of a choke.

The tube heating system was supplied from a specially-made oil-type heating transformer. The heating power was adjusted by an autotransformer. Voltage stabilizers have been included in the tube and thyratron heating circuits. The anode voltage is measured by means of a voltage divider and class 0.5 M 82 multiscale millivotmeter. The anode voltage was monotored by the S-96 electrostatic kilovoltmeter, while the anode current was measured by class 0.5 m 104 multiscale milliameter. All the additional resistances were measured to within ±0.1%. The measuring instruments were protected by R-350 shunts. The heating current and voltage were measured by class 1.5 control-panel instruments in the primary circuit of the heating transformer, since the secondary winding is held at the anode voltage. The rectifier was equipped by operational and protective shunts, which could be used for shutting off the anode voltage and the tube heating. /256

The curve showing the specific emission current j for tungsten as a function of the temperature, constructed on the basis of data of [4] is shown in Fig. 3a. It can be seen that up to a temperature of 2300°K j is practically zero, and that it increases rapidly with a further increase in temperature. In electron tubes used in radio engineering the operating temperatures of tungsten cathodes are within the limits of 2450-2650°K [4]. /257

Electron tubes are capable of operation in the saturation and in the space charge modes. When operating under the saturation mode the anode current is limited by the emissive power of the cathode, which increases with an increase in the temperature, all other conditions remaining equal. If the emission power of the cathode exceeds the anode current, then it is limited by the magnitude of the space charge between the cathode and the anode. In this operating mode the anode current is a function of $U_a^{3/2}$ [4]

$$I_a = 2.33 \cdot 10^{-6} \varkappa F_a \frac{U_a^{3/2}}{h_c^2}, \qquad (1)$$

where h_c is the anode to cathode distance, F_a is the anode surface area, $\varkappa$ is a coefficient which takes into account nonuniformity in the electron bombardment. For a plane electrode system $\varkappa = 1$. For the geometry of our tube (a_c and h_c, see Fig. 1a) the value of $\varkappa$ was close to unity (about 0.98) [4], from which it follows that heat generation by electron bombardment at the surface of the header facing the cathode, under the space charge mode, should be close to uniform. Under the saturation mode the emission current distribution will depend on the cathode temperature.

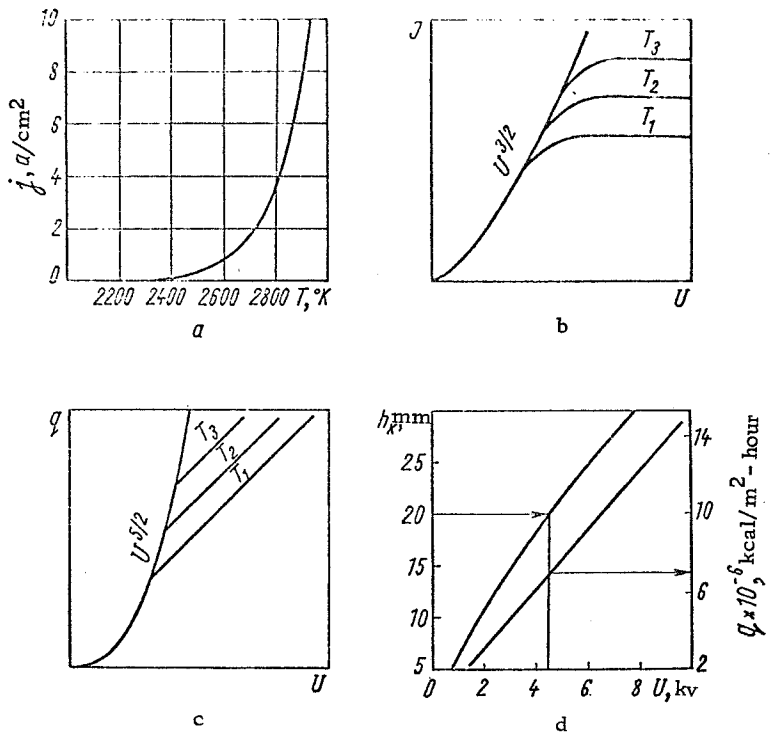

Figure 3. Electron Tube Characteristics.

a) The Specific Emission as a Function of the Temperature for Tungsten; b) Qualitative Dependence of I_a, the Anode Current on the Anode Voltage U_a ($T_{c_1} < T_{c_2} < T_{c_3}$); c) Qualitative Dependence of the Thermal Flux q_a on the Anode Voltage U_a ($T_{c_1} < T_{c_2} < T_{c_3}$); d) Boundary of the Tube's Operating Modes (Saturation and Space Charge) as a Function of h_c.

The specific thermal flux is calculated from the formula

$$q_a = 0.86 \frac{U_a \cdot I_a}{F_h} . \qquad (2)$$

It follows from the above expression and from Eq. (1) that in the space charge mode $q_a \approx U_a^{5/2}$.

Figures 3b and c show the qualitative dependence of I_a and q_a on the anode voltage for operation under the space charge and saturation modes (branches for T_{c_1}, T_{c_2} and T_{c_3}). Figure 3d shows h_c and q_a as a function of U_a for the tube we have used for $I_a = 2$ amps (nominal rectifier current) and $\varkappa = 1$. Figure 3d can be used to estimate the boundary between the space charge and saturation operating modes as a function of the cathode to anode distance. For example, for $h_c = 20$ mm it is possible to operate in the space charge mode at U_a of up to 4.5 kV, producing a thermal flux of approximately up to $7 \cdot 10^6$ kcal/m^2-hour. The cathode heating current and voltage have been calculated by the method presented in [4]. To estimate the variation in the thermal flux at the heat conducting surface produced by possible nonuniform heat generation at the inner surface of the header, we have considered the limiting case of heat generation along a coil ($\varkappa \approx 1/3$), the dimensions of which are equal to those of the cathode's coil. The following assumptions were used in the calculations. /258

1. The header is considered to be an infinite plate, and the spiral distribution is replaced by a stepped distribution. The step lead ($2a_c$) is equal to the cathode coil lead, and the width of the step (b) is equal to the diameter of the cathode wire (see Figs. 1a and 4).

2. The thermal conductivity of the plate and the coefficient of heat transfer from the plate to the fluid are constant. The process of heat transfer in the plate is described by the expression

$$\frac{\partial^2 t}{\partial x^2} + \frac{\partial^2 t}{\partial y^2} = 0 \qquad (3)$$

with the boundary conditions

$$\left(\frac{\partial t}{\partial x}\right)_{x=0} = 0, \quad \left(\frac{\partial t}{\partial y}\right)_{y=0} = -\frac{q(x)}{\lambda},$$

$$\left(\frac{\partial t}{\partial y}\right)_{y=\delta} = -\frac{\alpha(t_{cu} - t_{fl})}{\lambda}.$$

Solving Eq. (3) with the above boundary conditions we get an expression for the thermal flux /259

$$q = \frac{q_0 b}{2a_c} - \lambda \sum_{n=1}^{\infty} \frac{\pi \cdot n}{a_c} \left(A_n e^{\frac{\pi^n}{a_c} y} - B_n e^{\frac{-\pi^n}{a_c} y}\right) \cos \frac{\pi n}{a_c} x. \qquad (4)$$

Figure 4 shows the variability in the thermal flux at the heat conducting surface of the header as a function of the header thickness for different values

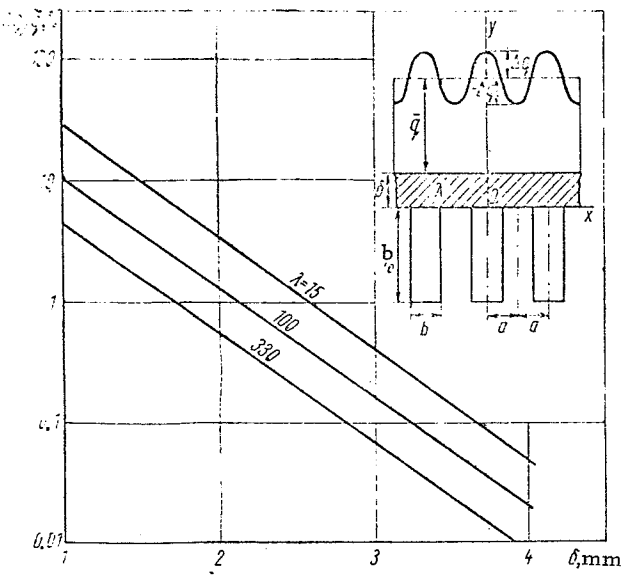

Figure 4. Variability $\Delta q/\bar{q}$ in the Heat Transfer as a Function of Thickness δ and Thermal Conductivity λ of the Material of the Heat Conducting Wall.

of the thermal conductivity, calculated from Eq. (4). It can be seen from the figure that even in this hypothetical case (for headers used in our experiments) the variability in the thermal flux from the heat conducting surface due to the stepped shape of the heat generation curve will be less than 0.1%. These calculations show that the nonuniform generation of heat at the inner surface of the header will be smoothed out at the heat-conducting surface. To eliminate variability in heat generation also at the inner surface, for example, due to lack of uniformity in the cathode temperature when the tube operates under the saturation mode, the work should be performed in the space-charge mode.

We have estimated the thermal flux distribution at the heat-conducting surface of the header as affected by radial heat losses. This process can be described by the expression

$$\frac{\partial^2 t}{\partial r^2}+\frac{1}{r}\frac{\partial t}{\partial r}+\frac{\partial^2 t}{\partial y^2}=0 \qquad (5)$$

with the boundary conditions

$$\left(\frac{\partial t}{\partial y}\right)_{y=0}=-\frac{q_r}{\lambda},$$
$$\left(\frac{\partial t}{\partial y}\right)_{y=\Delta}=-\frac{\alpha(t-t_{fl})}{\lambda}.$$

For headers potted by means of copper the above boundary conditions must be supplemented by the requirement of "matching" at r = R (Fig. 5) /260

$$t_{r=R-0}=t_{r=R+0};$$
$$\lambda_1\left(\frac{\partial t}{\partial r}\right)_{r=R-0}=\lambda_2\left(\frac{\partial t}{\partial r}\right)_{r=R+0}.$$

Equation (5) with the specified boundary and "matching" conditions, and on the assumption that α, t_{fl} and λ are constant, was solved numerically for different

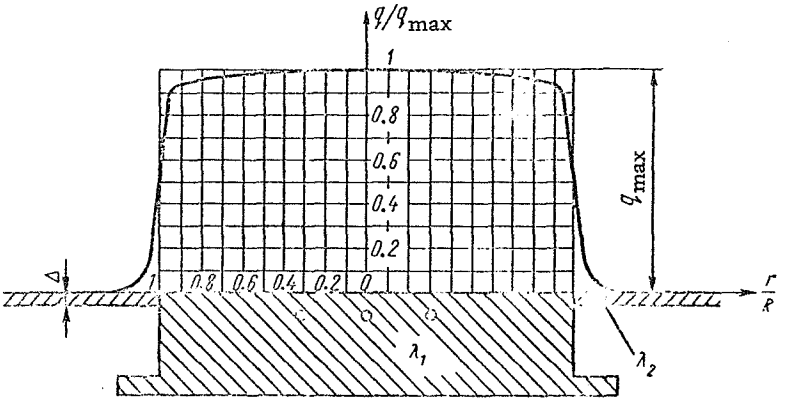

Figure 5. Distribution of the Thermal Flux at the Heat-Conducting Surface of the Header.
Δ - 1 mm; $\alpha = 40 \cdot 10^3$ kcal/m^2-hour-degree; $\lambda_1 = 300$ kcal/m-hour-degree; $\lambda_2 = 15$ kcal/m-hour-degree.

combinations of α, λ and Δ. Figure 5 shows the distribution of the thermal flux at the heat-conducting surface of a header the working part of which is made from copper. It can be seen that the thermocouples which measure the wall temperature are embedded in a region with a uniform flux distribution. Hence, the calculations show that the thermal flux at the heat-conducting surface of a header at the region where the thermocouples are embedded can be regarded as uniform.

To check the operating fitness of the tube we have measured the critical thermal fluxes and the heat transfer from a large volume of boiling water at atmospheric pressure. Two tanks, 70 and 200 mm in diameter were used. Condensers, heated by ordinary water were placed in their upper part. The shell (see Fig. 1, item 7) of the electron tube was inserted from the bottom of the tank. The water, when using these tanks, was maintained at the saturation temperature by auxiliary heaters.

In experiments for measuring q_{cr} the lamp heating was first switched on and then the anode power was increased by increasing the anode voltage. At thermal loads close to the critical the anode power increased in moderate steps (by 2-3% of q) with a holding time at q = const of the order of 2 mins. The production of critical flux was sharply recorded on the EPP-09 potentiometer due to a sharp /261 increase in the temperature difference between the wall and the fluid. Temperature control was set at 100-200°C above the wall temperature preceding the critical flux. After each critical flux has been obtained, the heat-conducting surface of the header was polished by a micronic emery cloth and washed with ethylene alcohol. The salt-content of the water used in the experiments was not monitored.

Figure 6 shows magnitude of critical thermal fluxes from boiling distilled and tap water at surfaces from 1Kh18N9T steel and from copper. The experimental

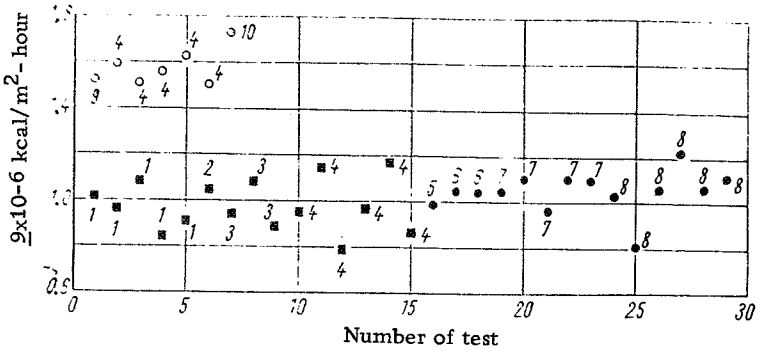

Figure 6. Magnitudes of Critical Thermal Fluxes From a Large Volume of Boiling Water at Atmospheric Pressure.

○ - Ordinary Drinking Water, Surface of 1Kh18N9T Steel; ▪ - Distilled Water, Same Surface; ● - Distilled Water, Copper Surface.

data obtained using different headers agree with one another and with published data, [6] with respect to magnitude of the critical thermal flux, as well as with respect to the scatter of points. The identical numbers next to points show that the experiments were performed with the same header, without dismantling the tube. /262
The volt-ampere characteristics constructed for experiments on q_{cr} shows that the electron tube operated under the space-charge mode. Figure 7 shows an example of the volt-ampere characteristic for experiments on q_{cr} shown in Fig. 6 and designated by numeral 8. It can be seen from Fig. 7 that the volt-ampere characteristic of the tube did not change during the experiments.

The temperature differences over the height of a header were measured in five headers, using thermocouples, in order to determine the thermal flux and to compare it with the flux calculated from Eq. (2) (Fig. 8). We have compared relative, rather than absolute units to eliminate the effect of errors due to imprecise determination of the distance between the thermocouple beads as well as due to errors in the thermal conductivity of the header material. The results presented in Fig. 8 show that the thermal fluxes determined by different methods are in satisfactory agreement.

The feasibility of obtaining high thermal fluxes using the tube was determined by cooling the test section by running water moving in a slot formed by the header and a special jacket. These experiments show that the installation is capable /263
of producing thermal fluxes of about $20 \cdot 10^6$ kcal/m^2-hour. During a short time period (about 5 mins) we have obtained a maximum thermal flux (about $36 \cdot 10^6$ kcal/m^2-hour), but then the anode transformer was overloaded by approximately two-fold.

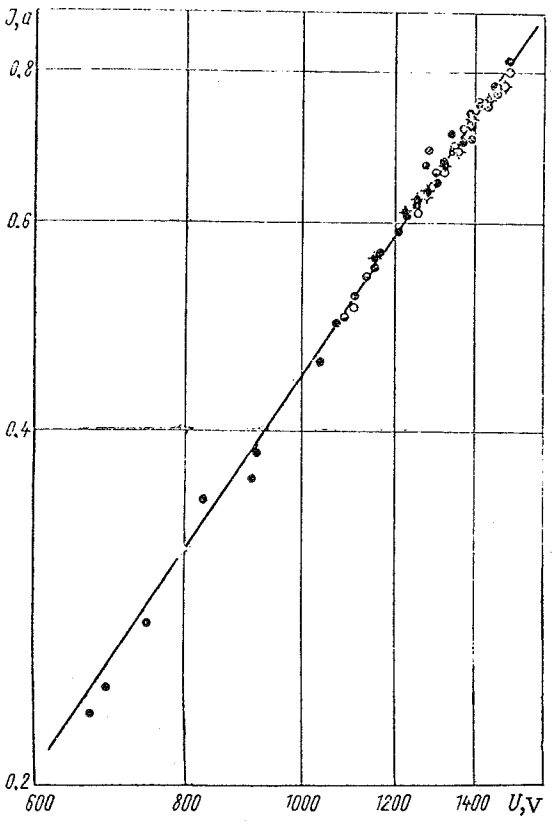

Figure 7. Volt-Ampere Characteristics of the Tube Used in Experiments With Water (Points ● Correspond to Points 8 of Fig. 6).

Headers type II, III and IV (see Fig. 2) were used to perform experiments for measuring the heat transfer coefficient attendant to boiling of a large volume of distilled water, in the process of which we have measured the temperature difference between the wall and the liquid using an R2/1 semiautomatic potentiometer and we have recorded the data using the EPP-09 automatic potentiometer. The experimental results are presented in Fig. 9, which, for comparison, also displays lines obtained from criterial formulas due to Kruzhilin [7] and Kutateladze [8]. These formulas describe satisfactorily the data on heat transfer on nucleate boiling of water at atmospheric pressure. The figure shows that the data we have obtained agree with these formulas. The heat transfer coefficients were calculated from the expression

$$\alpha = \frac{q}{\Delta t},$$

where q is the resultant specific thermal flux, kcal/m^2-hour, while Δt is the temperature difference between the heat conducting surface of the header and the fluid in the container, °C. /264

The resultant specific thermal flux was found as follows

$$q = q_a + q_{heat} + q_{rad};$$

$q_a = 0.86\, U_a I_a / F_h$ is the anode component of the specific thermal flux, where U_a is the anode voltage, V, I_a is the anode current, amps, and F_h is the heat-conducting area of the header, m^2; $q_{heat} = 0.86\, U_{heat} I_{heat} \cdot K \cdot K_1 \varepsilon / F_h$ is the specific thermal flux produced by cathode radiation, where U_{heat} is the heating voltage, V, I_{heat} is the heating current, amps; K is a factor which takes into account that part of the heating power which is radiated to the working surface of the header, K_1 is a factor which takes into account losses in the heating transformer and feeding cable and ε is the emissivity of the header; $q_{rad} = 4.9 \cdot \varepsilon \frac{F_{rad}}{F_h} (T_1/100)^4$

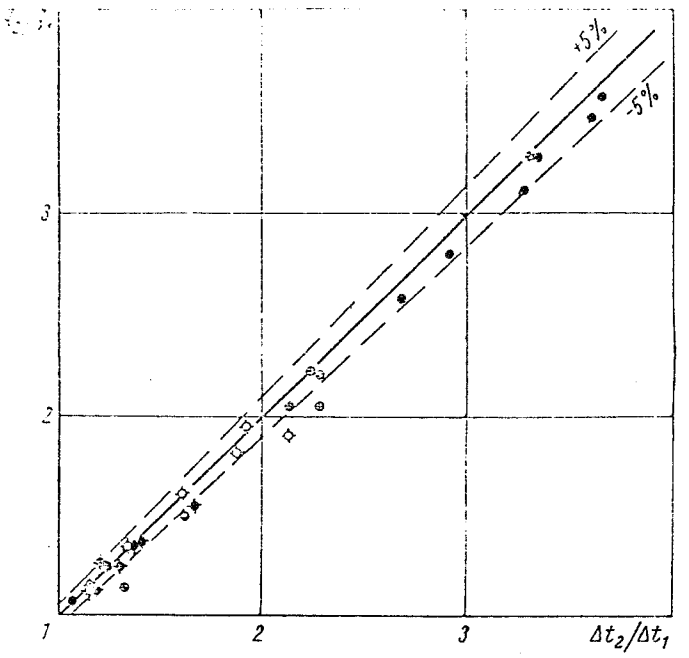

Figure 8. Comparison of the Ratio q_2/q_1 of Thermal Fluxes Calculated From Eq. (2) With the Ratio $\Delta t_2/\Delta t_1$ of the Temperature Differences, Measured Over the Height of the Header and Corresponding to the Above Thermal Fluxes (the Different Symbols Denote Points Obtained With Different Headers).

is the specific thermal flux produced by radiation from the inner surface of the header, where F_{rad} is the radiating surface of the header, m^2, T_1 is the absolute temperature of the radiating surface, °K. In experiments with water we have not taken into account the thermal flux due to radiation from the inner surface of the header, since the surface temperature (T_1) was low.

The temperature difference between the wall and the fluid was calculated as follows

$$\Delta t = \Delta t_m - \Delta t_{cop} - \Delta t_n,$$

where Δt_m is the measured temperature difference between the header and the fluid, degrees; $\Delta t_{cop} = q \frac{\delta_{cop}}{\lambda_{cop}}$ is the temperature difference in the copper layer, degrees; δ_{cop} is the thickness of the copper layer, m; λ_{cop} is the thermal

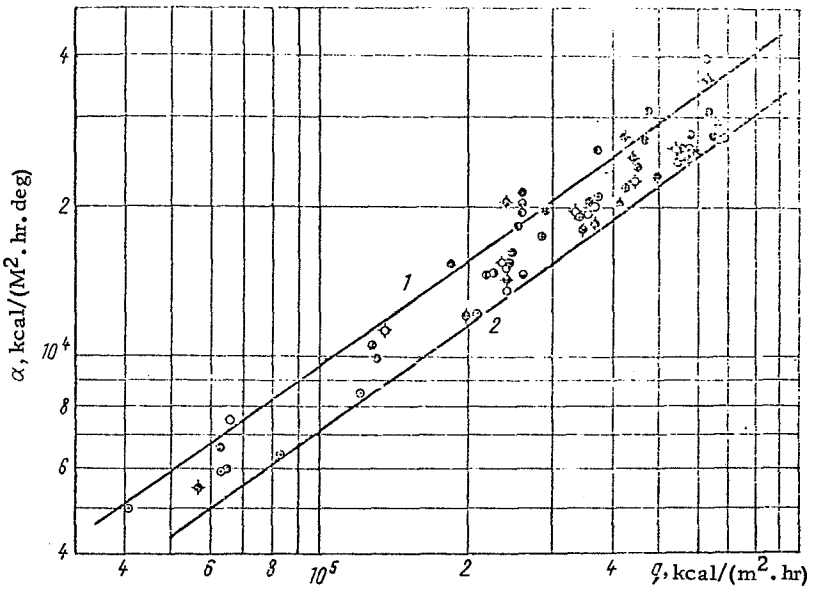

Figure 9. Data on Heat Transfer From a Large Volume of Boiling Distilled Water, P = 1 Atmosphere Absolute (the Different Symbols Denote Points Obtained in Different Series of Experiments).

1) Curve Obtained from the Krushilin Formula; 2) Curve Obtained from the Kutateladze Formula.

conductivity of copper, kcal/m-hour-degree); $\Delta t_n = q \frac{\delta_n}{\lambda_n}$ is the temperature difference in the nickel layer for type II header (see Fig. 2); for type III and IV headers the temperature drop is calculated for a layer of 1Kh18N9T steel; δ is the thickness of the nickel or steel layer, and λ is the thermal conductivity of the nickel or steel, kcal/m-hour-degree.

The limiting relative error of a single measurement of the thermal flux $q = 10^6$ kcal/m^2-hour is $\pm 10\%$. The limiting relative error in determining the heat transfer coefficient $\Delta\alpha/\alpha$ will depend on the magnitude of the thermal flux. For example, for boiling water with $q = 0.2 \cdot 10^6$ kcal/m^2-hour ($q = q_n$) $\Delta\alpha/\alpha \approx \pm 40\%$, while for $q = 0.6 \cdot 10^6$ kcal/m^2-hour $\Delta\alpha/\alpha \approx \pm 25\%$.

When the thermocouples are embedded into a stainless steel wall (type I header, Fig. 2) of the same configuration the limiting relative error will be $\Delta\alpha/\alpha \approx$ $\approx 200\%$, for $q = 0.2 \cdot 10^6$ kcal/m^2-hour and $\Delta\alpha/\alpha \approx 240\%$ for $q = 0.6 \cdot 10^6$ kcal/m^2- /265 -hour.

This example shows that the use of multilayer header, in which the thermocouples are potted with copper (a metal with high thermal conductivity) makes it possible to substantially reduce the error in determining the heat transfer coefficient.

To study heat transfer from metals boiling in a large container we have devised a setup the schematic of which is shown in Fig. 10.

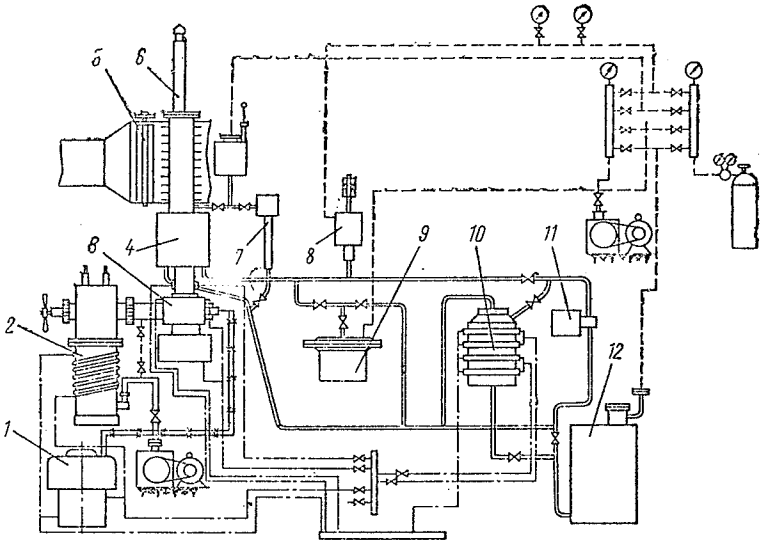

Figure 10. Schematic Diagram of the Setup Used to Study the Transfer of Heat From Alkaline Metals Boiling in a Large Vessel.

1) Gear-Type Oil Pump; 2) Diffusion Pump; 3) Electronic Tube; 4) Working Tank; 5) Air Valve; 6) Movable Thermocouple; 7) Level-Measuring Tank; 8) Pressure Pickup; 9) Distillating Sampler; 10) Cold Oxide Trap; 11) Electromagnetic Pump; 12) Filling Tank.
--------Metal Lines; ------Gas-Vacuum Lines;
---Oil Lines; -----Water Lines.

Figure 11 depicts the design of the operating tank and the movable thermocouple. The electron tube is inserted into the tank from its bottom. The inner surface of the working section (header) is heated, while the heat transfer agent boils at the outer surface. Two holes in the lower part of the working tank serve for filling and draining, as well as for circulating the heat transfer agent through the working tank when removing the oxides. A ribbed air-cooled condenser, used for condensing the heat-transfer agent's vapor, is welded to the upper part of the

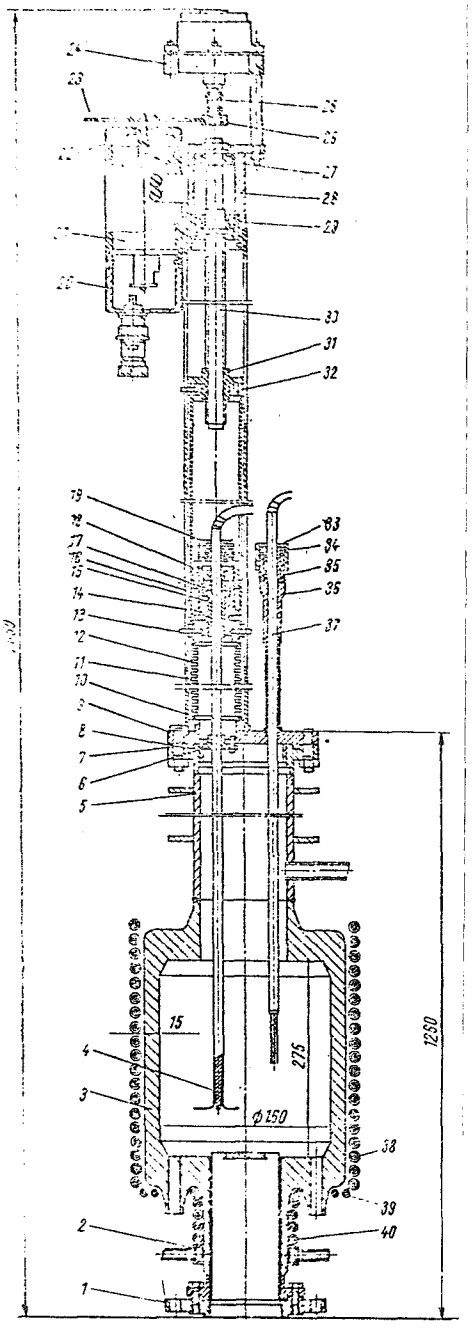

Figure 11. Working Tank With Movable Thermocouple.

1) Shell with Header; 2) Cooling Sleeve; 3) Working Tank; 4) Rod with Thermocouples; 5) Condenser; 6 and 32) Guide Bushings; 7 and 9) Flanges; 8) Copper Gasket; 10 and 15) Bushings; 11) Guiding Tube; 12) Bellows from 1Kh18N9T Steel; 13) Guide Screw; 14) Connecting Stub; 16) Connecting Tube; 17) Siloxane-teflon Packing; 18 and 33) Connector Nut; 19) Graduated Circle; 20) Selsyn Jacke; 21) Selsyn; 22, 27 and 29) Bearings; 23) Gear; 26) Pinion; 24) RD-09 Electric Motor; 25) Coupling Sleeve; 28) Housing; 30) Lead Screw; 31) Nut; 34) Clamping Sleeve; 35) Siloxane-teflon Packing; 36) Connecting Stub; 37) Probe with Stationary Thermocouples; 38, 39 and 40) Electric Heaters.

working tank. The necessary temperature in this tank is maintained by three electric heaters, rated at 14, 3 and 2kW, respectively, supplied from autotransformers.

The movable thermocouple assembly is fastened to the condenser flange. It /267
is packed by gasket from annealed copper or nickel. In the rod's grooves are inserted and metallized four capillaries from 1Kh18N9T steel 0.8 X 0.15 mm in

diameter, in which are placed chromel-alumel thermocouples with alundum insulation (wire diameter 0.2 mm). At the end of the rod the thermocouples are bent away at a right angle from the rod's axis and from one another. The end of the rod can come into direct contact with the surface, in which the capillaries with the thermocouples also come into direct contact with the heat-conducting surface. The end of one of the movable thermocouples is inserted approximately at the center of the heat conducting surface. The movable thermocouples, as well as the thermocouples embedded in the header are connected differentially with the thermocouples held in tube 37.

Tube 16 and rod 4 connected to it are moved vertically by an RD-09 electric motor. Bellows 12, made from 1Kh18N9T steel can be used to move the movable thermocouple over a distance of approximately up to 280 mm, without disturbing the air-tightness of the setup. The position of thermocouples in their vertical motion is determined by a selsyn indicator. The selsyn pickup is connected by a gear and pinion to the shaft of the electric motor.

The receiving selsyn together with a three-arrow position indicator is located at the control panel. It determines the height position of thermocouples to approximately within ±0.3 mm. The angular position of the movable thermocouples is varied manually during the work. The angles of rotation are read from graduated circle 19.

To monitor the temperature over the height of the working tank and the condenser, thermocouples are embedded at appropriate points (not shown in the figure).

All the parts of the stand in contact with the heat-transfer agent are made from 1Kh18N9T steel and are provided with nichrome electric heaters and thermal insulation. The temperature of the subassemblies and pipelines of the setup is monitored by chromel-alumel thermocouples.

REFERENCES

1. Lyon, R. and Foust, A.: Katz D. Chem. Eng. Progr. Symposium Series, v. 51, No. 12, 1955.
2. Hickey, I.: J. Appl. Phys. v. 24, No. 10 (1953).
3. Povarin, P.I. and Kulakov, I.G.: Informatsionnoye pis'mo No. 6. Energeticheskiy Institute AN SSSR [Information Bulletin No. 6. Power Institute of the Academy of Sciences of the USSR]. 1958.
4. Tsarev, B.M.: Raschet i konstruirovaniye elektronnykh lamp [Design and Construction of Electron Tubes]. Gosenergoizdat, Moscow-Leningrad, 1952.
5. Sorikin, D.N., et al.: Byulleten' isobreteniy, No. 18, 1962.
6. Alad'yev, I.T. and Yashnov, V.I.: In the collection Konvektivnaya teploperedacha v dvukhfaznom i odnofaznom potokaky [Convective Heat Transfer in Twin-Phase and Single-Phase Flows]. Energiya Publishing House, Moscow-Leningrad, 1964.
7. Kruzhilin, G.I. and Subbotin, V.I.: In the book Proceedings of the Second International Conference on Peaceful Uses of Atomic Energy. Geneva, 1958.

Doklady sovetskikh uchonykh [Reports by Soviet Scientists], Vol. 2, p. 134, Atomizdat, Moscow, 1959.
8. Kutateladze, S. S.: Osnovy teorii teploobmena [Fundamentals of Heat Transfer Theory]. Mashgiz, Moscow-Leningrad, 1962.

TRANSFER OF HEAT FROM SODIUM BOILING IN A LARGE VESSEL

A. P. Kudryavtsev, D. M. Ovechkin, D. N. Sorokin,
V. I. Subbotin and A. A. Tsyganok

The experiments were performed at flat horizontal sections which were /268
heated (at a diameter of 38 mm) by electron bombardment. Boiling took place at a surface made from 1Kh18N9T steel. The experimental setup and the test sections are described in [1].

In these experiments we measured the temperature difference between the wall and the fluid, pressure and temperature of the sodium in the vessel in the power supplied to the test section, and in a number of experiments also the temperature fields in the sodium, using a movable thermocouple. The indications of thermocouples which read the temperature difference between the wall and the fluid, the fluid temperature and the readings of the movable thermocouple, which was connected differentially with the thermocouple situated in the fluid were continuously recorded by EPP-09 potentiometers (1 sec) and intermittently measured by the R2/1 potentiometer. The oxygen content of the sodium was monitored by the method of distillation at the start and termination of experiments. Before start of tests the working tank was evacuated to a pressure of about 10^{-2} mm of Hg at a temperature of about 300°C.

We have performed three series of experiments (a series denotes a set of experiments performed at one test section without purification and replacement of the heat transfer agent). For convenience in analysis the data of two series of experiments are broken up into subseries by the level of t_s, which were obtained in successive periods of time.

Before starting the experiments of series 1 oxides were removed from the /270
sodium in a cold trap. The oxygen content of the sodium did not exceed 10^{-3}% by weight. In experiments of series 2 and 3 the oxygen content of the sodium was intentionally brought up to approximately 10^{-1}% by weight.

Figure 1 shows the curve of α as a function of time for constant q and t_{fl}. The results of heat-transfer experiments are shown in the form of curves of α plotted against q in Figs. 3, 4 and 6, in which the points are denoted by numerals in accordance with the time sequence in which they were obtained. Figures 2 and 5 display the recordings of the temperature difference between the wall and the fluid for a number of points. The large difference in the values of α in Figs. 3, 4 and 6 for the same q and t_{fl} is not due to experimental error, but to the existence of various heat-removal modes. For example, in Fig. 3 for $q = 0.82 \cdot 10^6$ kcal/m^2-hour one value of α is $15.6 \cdot 10^3$ kcal/m^2-hour-degree, while another is $7.7 \cdot 10^3$ kcal/m^2-hour degree.

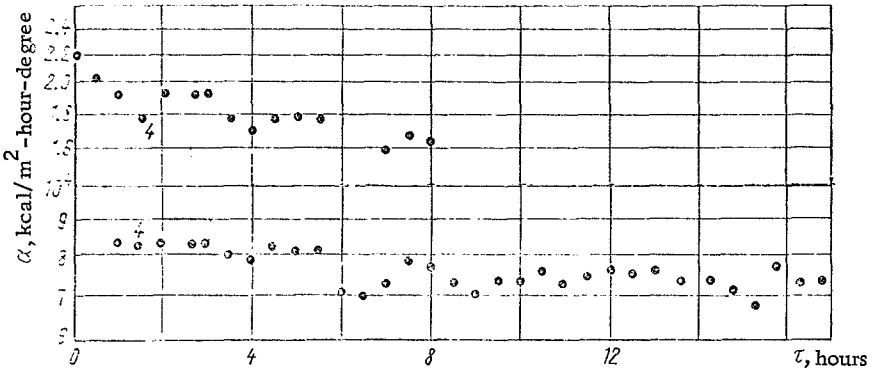

Figure 1. Variation of α in Time (Test Series 1a) for $q = 0.7 \cdot 10^6$ kcal/m^2-hour and $t_{fl} = 690°C$.

Analysis of data presented in Figs. 1, 3, 4 and 6 shows that they can be attributed to the following three modes of heat removal, [2].

1. Heat removal from sodium boiling under fully developed conditions. The wall temperature fluctuations here are moderate or entirely undiscernible (see point 4, of Figs. 4b and 5a). The curve of α as a function of q under this mode is the same (with a power of about 2/3) as for nonmetallic liquids. The data obtained for sodium boiling under the above conditions can be expressed as

$$\alpha = 4q^{2/3}. \qquad (1)$$

The curve obtained using this expression is 1 of Figs. 3, 4 and 6. No discernible dependence of α on P_s was noticed for fully developed boiling of sodium in the pressure range of the tests (about 0.1-1 absolute atmospheres). /271

Figure 7 shows a distribution of temperature in sodium, typical for fully developed boiling, measured by a movable thermocouple which, while at the wall, registered temperature fluctuations with a frequency of about 1 cps, while not temperature fluctuations were recorded away from the wall. The frequency of temperature fluctuations at the surface of a heat-conducting wall attendant to boiling can serve, judging by experiments with water of [3] and [4], as an indicator of a kind of frequency of break-off of vapor bubbles. The measured fluctuation near the heat conducting wall comprises about 50% of the mean temperature difference $\Delta\bar{t}_\alpha$. Temperature fluctuations at the surface of the heat conducting wall with magnitudes commensurable with $\Delta\bar{t}_\alpha$ have also been observed in boiling water, [5] and [6]. The thickness of the boundary layer in sodium boiling under fully developed conditions is about 3-4 mm.

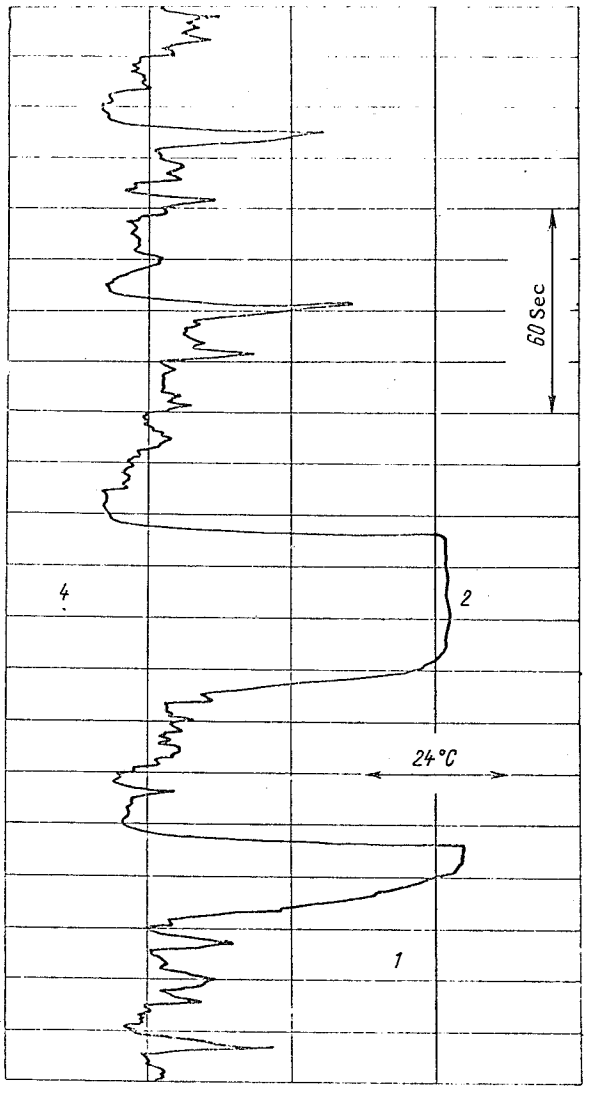

Figure 2. Recording of the Temperature Difference Between the Wall and Fluid for Point 4 of Test Series 1a;
$q = 0.7 \cdot 10^6$ kcal/m^2-hour.
1) $\alpha = 17.7 \cdot 10^3$ kcal/m^2-hour-degree;
2) $\alpha = 8.3 \cdot 10^3$ kcal/m^2-hour-degree.

2. Heat removal by free convection (without boiling) with subsequent dissipation of heat by surface evaporation. Here the sodium temperature at the wall may exceed the saturation temperature by more than 100°C. For example, in our experments (see Fig. 3) there was no boiling at $\Delta t_s \sim 100°$ [$q \approx 0.7 \cdot 10^6$ m^2--hour]. A similar picture was observed in experiments depicted in Fig. 4a. We should note that the relationship between the amount of superheat of the fluid at the heated surface, the thermal flux and the superheating of the fluid in the vessel will depend on the design of the setup.

The heat transfer coefficients for heat removal by free convection for our conditions are in good agreement with the formula

$$\alpha = 95q^{1/3} \qquad (2)$$

(Curve 2 in Figs. 3, 4 and 5). The above expression has been obtained on the basis of experiments with free convection using the same setup, [7]. Here the sodium was held under inert-gas pressure (about 2 absolute atmospheres) and the sodium temperature at the heat-conducting wall was by several hundred degrees lower than t_s. Measurements made by a movable thermocouple at $t_{fl} < t_s$ [7], as well as at $t_{fl} > t_s$ show that, in case of free convection, no temperature fluctuations can be observed at the head-conducting wall (in the laminar region) or away from it. The thickness of the thermal boundary layer (about 15 mm) for convecting heat removal exceeds appreciably that of the boundary layer attendant to developed boiling.

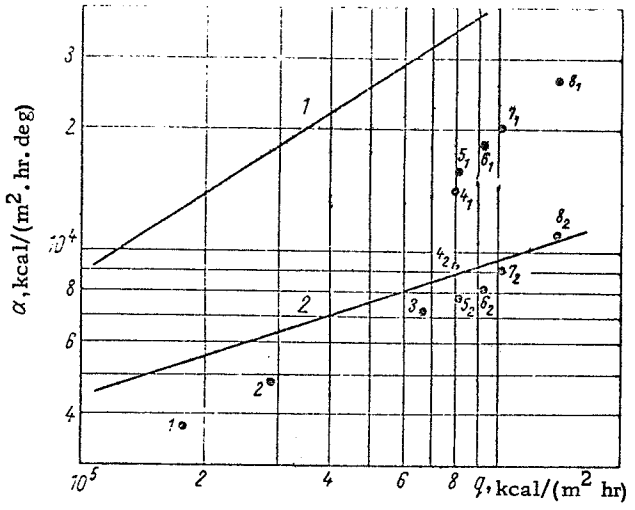

Figure 3. Experimental Data for Series 1b; t_{fl}= 700 12° Co Curve 1 Corresponds to Eq. (1); Curve 2 Corresponds to Eq. (2).

3. Heat removal attendant to unsteady boiling. Under these conditions the removal of heat is accompanied by appreciable temperature fluctuations in the wall (see point 4 in Figs. 1 and 2). The maximum magnitude (Θ_{max}) of fluctuations in the wall temperature is equal to the difference in Δt_α under free convection (without boiling) and attendant to fully developed boiling.

The magnitudes of the heat transfer coefficients for unsteady boiling lie between the values of α for the two preceding heat-removal modes; here the lesser the temperature fluctuations in the heat-conducting wall, the closer the heat transfer coefficients lie to α for developed boiling (Figs. 4 and 5). Experimental data for unsteady boiling cannot be described by a single power law [as could be done for the steady case, DBL], since the heat removal conditions for individual experiments vary appreciably, coming close either to heat removal under developed boiling or by convection without boiling. /273

Analysis of recordings of temperature fields in sodium, temperature differences between the wall and the fluid, as well as direct observations of the boiling of sodium using a special x-ray installation give grounds for assuming the following mechanism for heat transfer by unsteady boiling.

After the first boiling up, large bubbles travel through the volume (seconds or fractions of a second) which absorb the heat of the superheated sodium. As a result of this boiling δt and Δt_α are reduced to magnitudes corresponding approximately to developed boiling (see Fig. 2). As a rule, in the very beginning (from several seconds to several tens of seconds) the formation of vapor bubbles at the heat-conducting surface takes place in the same manner as in developed boiling. Then, at Δt_s which becomes established after the boiling up, the vapor formation center ceases to function and the wall must be superheated more (as compared with developed boiling) in order for a vapor bubble to form in the same vapor-formation center. /274

It is certain to a given degree that several neighboring vapor-formation centers may cease operating simultaneously. The larger the number of neighboring vapor-formation centers which cease to function at a specified Δt_s and

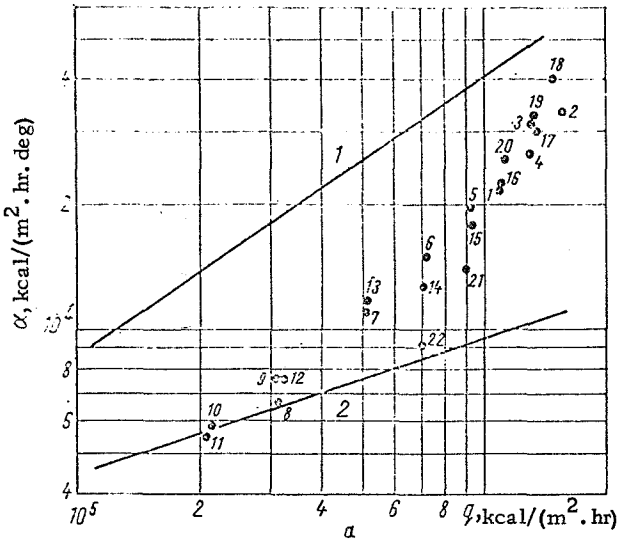

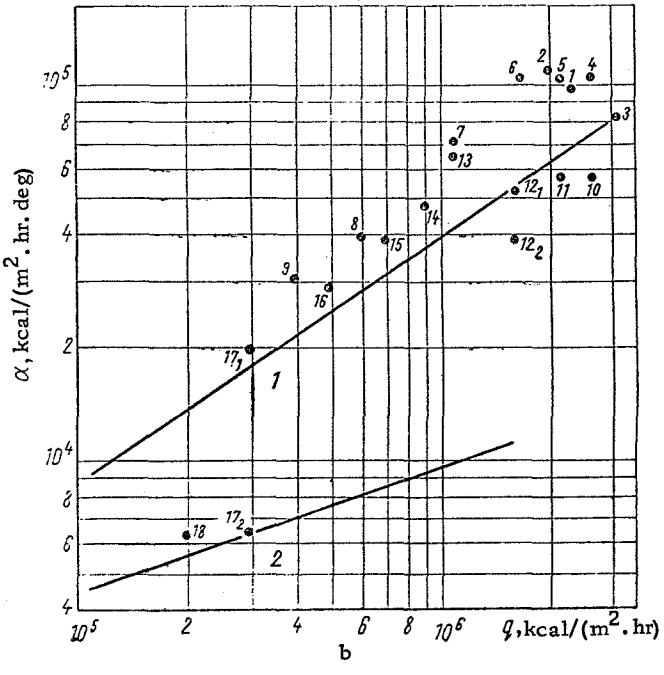

Figure 4. (continued on following page)

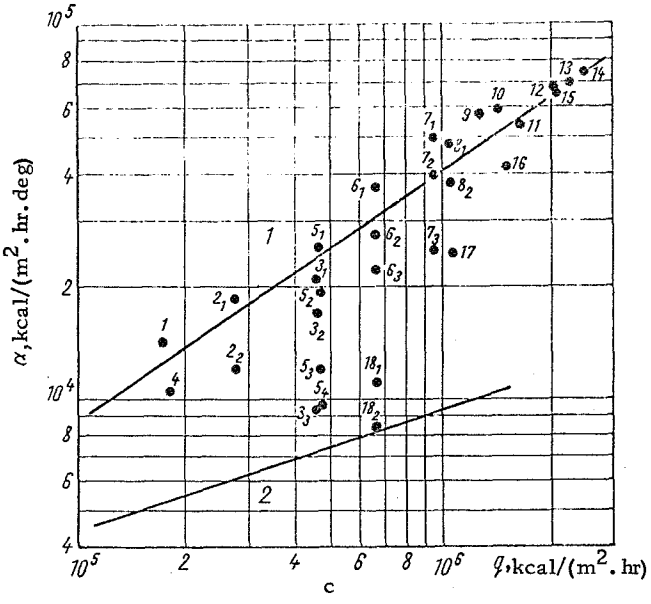

Figure 4. Experimental Data for Test Series 2. a) t_{fl} = 700 ± 12°C (Test Series 2a); b) t_{fl} = 785 ± ± 8°C (Test Series 2b); c) t_{fl} = 860 ± 12°C (Test Series 2c).

and the higher the amount of superheat which is needed to restart them, more will the head-conducting wall be overheated in the given spot.

Analysis of data shows the following.

1. As the thermal flux increases, tendencies appear to transition from convection (without boiling) to unstable boiling (see Fig. 3, point 4), as well as to transition from unstable to fully developed boiling. This is precisely the cause /275 for the "large slope" (> 0.7) of the test data pertaining to unstable boiling (see Fig. 4a).

2. As the sodium temperature rises, the thermal flux at which boiling starts becomes smaller, and the probability of developed boiling increases. For example, in test series 1b boiling started at $q \approx 0.8 \cdot 10^6$ kcal/m^2-hour ($t_{fl} \approx$ ≈700°C), while in series 2c there was boiling at $q \approx 0.2 \cdot 10^6$ kcal/m^2-hour ($t_{fl} \approx$860°C).

3. Increase the time of contact (apparently to certain limits) between the stainless-steel heat-conducting wall and the sodium results, all other conditions remaining equal, in an increase in the thermal flux needed for maintaining the boiling. For example, in test series 1a during the first eight hours we have

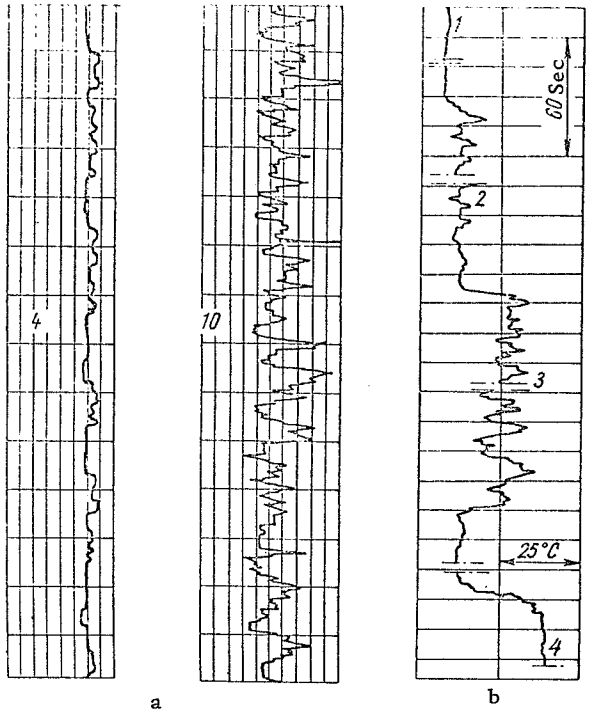

Figure 5. Recording of the Temperature Difference Between the Fluid and the Wall in Test Series 2b (a) and 2c (b).

a) $q = 2.57 \cdot 10^6$ kcal/m^2-hour, $\alpha = 107 \cdot 10^3$ kcal/m^2-hour-degree (Point 4) and $\alpha = 59.7 \cdot 10^3$ kcal/m^2-hour-degree (Point 10); b) $q = 0.47 \cdot 10^6$ kcal/m^2-hour, $\alpha = 25.6 \cdot 10^3$ kcal/m^2-hour-degree, $\alpha = 19.4 \cdot 10^3$ kcal/m^2-hour-degree, $\alpha = 12.1 \cdot 10^3$ kcal/m^2-hour-degree and $\alpha = 9.7 \cdot 10^3$ kcal/m^2-hour-degree (Points 1, 2, 3 and 4, Respectively.

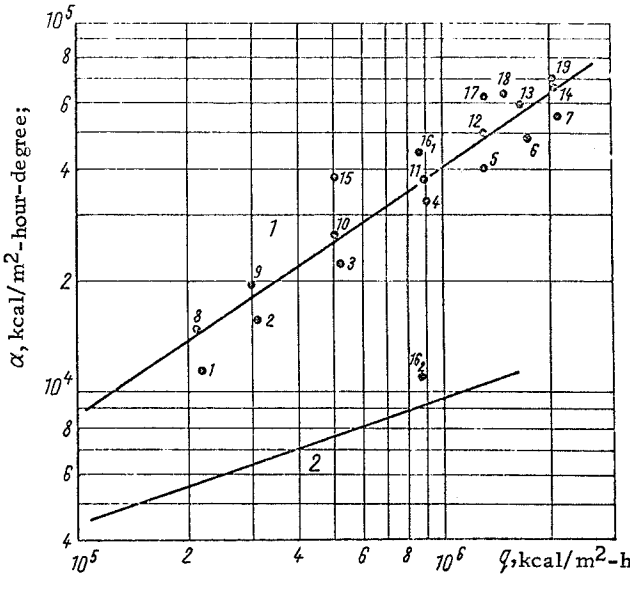

Figure 6. Experimental Data of Test Series 3; $t_{fl} = 700 \pm 12°C$.

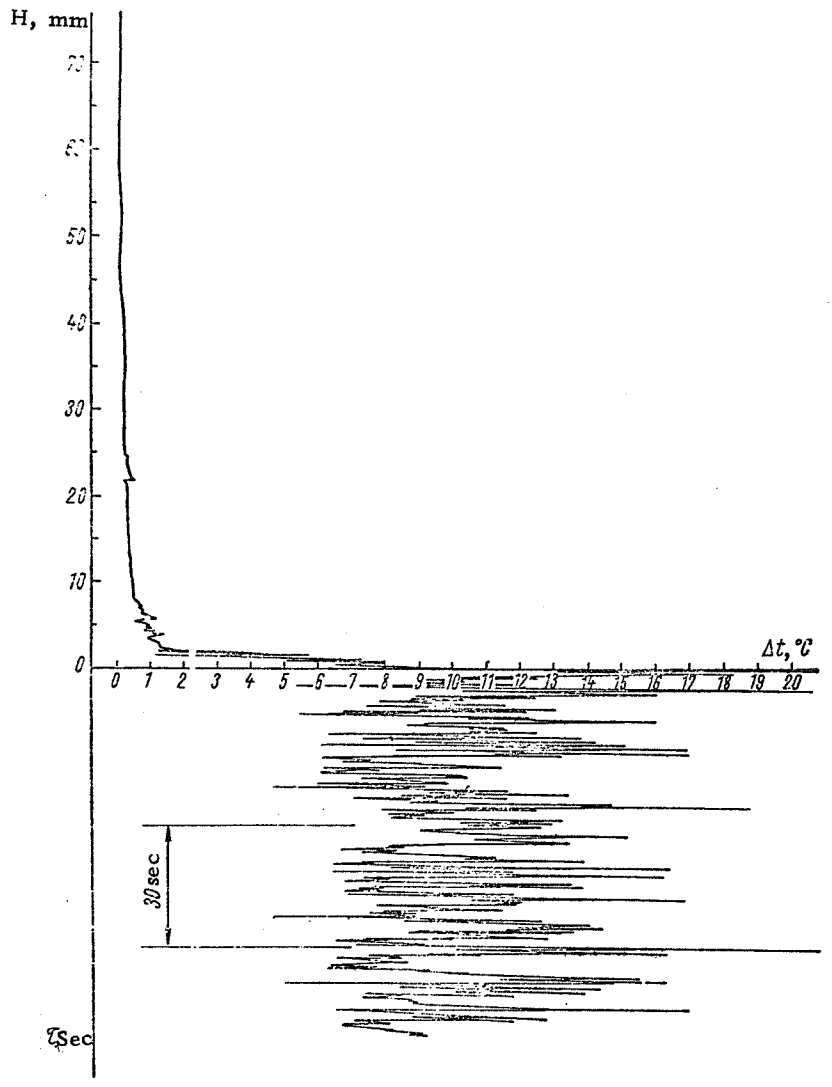

Figure 7. Temperature Distribution in Sodium for Developed Boiling (Point 15, Test Series 2b). $q = 0.7 \cdot 10^6$ kcal/m^2-hour; $\alpha = 38.9 \cdot 10^3$ kcal/m^2-hour-degree.

noticed mutual transitions from unstable boiling to convection (without boiling). During the subsequent nine hours heat removal took place by convection only at the same q and t_{fl}. In test series 2a boiling took place first at $q \approx 0.5 \cdot 10^6$ kcal/m^2-hour, while at the end of the tests there was no boiling at $q \approx 0.7 \cdot 10^6$ kcal/m^2-hour. A similar picture was observed also in series 2c and 3.

4. Within the limits of experimental accuracy no effect of oxygen on heat transfer from boiling sodium was observed (the oxygen content was varied approximately from 10^{-1} to 10^{-3}% by weight).

Measurements of temperature fields in the fluid and in the vapor show that the degree of superheat of the fluid with respect to the vapor depends on the mode of heat removal. For example, for point 14 in Fig. 4c pertaining to developed boiling, the superheat δt comprises about 6°C, while for points 17 and 18 of the same test series, pertaining to unstable heating, it is about 15°C. The superheating of sodium is also manifested by comparison of the experimentally measured sodium pressures and temperature with the expression for the saturation pressure as a function of the temperature given by the formula [8] /277

$$\lg P_{\text{abs. at}} = 4.521 - \frac{5220}{T}. \tag{3}$$

Superheating attendant to boiling is produced by the fact that a part of the supplied heat is given up to the fluid near the heat conducting wall, and then from the fluid it is transmitted by vapor bubbles. If, by analogy with the heat transfer coefficient, we introduce α_{int}, which characterizes the thermal resistance of the boundary layer near the phase interface and the thermal resistance of the phase transition, then we can write an approximate expression for the total amount of supplied heat Q (including the heat supplied by auxiliary heaters)

$$Q = \int_{F_\Phi} \alpha_{\text{int}} \delta t \, dF_\Phi. \tag{4}$$

For Q and P_s = const δt will be the higher, the smaller F_Φ, the phase interface surface and α_{int}. When there is no boiling, the phase interface is only the free surface and δt will be the highest. In the case of boiling δt will be lower, since F_Φ is made larger by the vapor bubbles. Under unstable boiling δt should be higher than for developed boiling. Qualitatively the above is substantiated also by data for water. When water boils under atmospheric pressure the magnitude of δt depends on the surface roughness. The rougher the surface, the lower δt, since a larger number of vapor-formation centers operates at the surface [9].

The magnitude of α_{int} depends on the level of t_s as well as on the admixture content of the sodium, since the latter have an appreciable effect on the thermal resistance of the phase transition. Approximate estimates of α_{int} made on the basis of our measurements show that for a free phase interface for sodium in the range of $P_s \approx 0.1$-1 absolute atmospheres α_{int} is about 10^4 kcal/m^2-hour-degree.

Several experiments on transfer of heat from boiling sodium were performed using test sections from copper, electroplated with nickel or with nickel with chromium (about 20 microns). At temperatures of about 600°C heat removal was accomplished only at unstable boiling or by convection, with subsequent dissipation of heat by evaporation from the free surface. At temperatures above 700°C all the three heat-removal modes exist. However, the electroplated coatings were found to be insufficiently stable to sodium. In certain experiments they broke down and the sodium came into direct contact with the copper, with the result that an excessive rough surface was produced. Only developed boiling of sodium is observed at the copper surface in the temperature range of approximately 700-880°C. The data obtained in these experiments on heat transfer attendant to developed boiling and convection without boiling are in agreement with Eqs. (1) and (2), respectively, while the values of α for unstable boiling lie between the α for developed boiling and for convection. /278

Following are the main features characteristic of sodium boiling in a large vessel at a surface from stainless steel in a pressure range of about 0.1-1 absolute atmosphere.

1. Feasibility of superheating the fluid at the surface by 100-150°C over t_s without taking any special measures. In this case heat removal may be accomplished by convection ($t_{fl} > t_s$) of large thermal fluxes (about 10^6 kcal/m^2-hour) due to high mean temperature differences and the relatively high heat transfer coefficients for sodium.

2. Alongside with ordinary nucleate boiling, unstable boiling may also exist at fluxes of up to q_{cr}, [7] and [10].

3. Instability of heat transfer, consisting in the multiple change of heat-removal modes during a relatively short time period (see Figs. 1-3).

In a number of cases water may also be appreciably superheated at the surface. For example, it is pointed out in [11] that, using a clean glass surface, Harvey superheated water up to 200°C, while Kenrick obtained temperatures of up to 270°C. The wetting contact angle between water and pure glass is zero, [12]. In experiments described in [13], after the system was subjected to a high pressure it was possible to superheat water to about 160°C on a nichrome wire and up to about 150°C on a platinum wire at atmospheric pressure. The boiling up was followed by ordinary nucleate boiling. Reference [14] notes that at very low pressures (for water probably below 0.02 absolute atmospheres) the state of natural convection is followed by the transient mode, without passing through the nucleate boiling mode.

In experiments described in [15-17] pertaining to heat transfer from boiling water and a number of organic fluids in large vessels under low absolute pressures (0.1 absolute atmospheres and below) the same dependence of α on q (about 0.7) was obtained as in the case of $P_s \geq 1$ absolute atm. The study of heat transfer from water boiling on horizontal tubes in a large vessel at pressures of 0.05-2.02 absolute atmospheres and thermal fluxes of (0.013-0.32) 10^6 kcal/m^2-hour

is reflected in [15]. Reference [16] describes experiments on the transfer of heat from boiling water and ethyl alcohol under natural circulation conditions in the range $P_s = 0.125$-1 absolute atmospheres. Reference [17] presents experimental data obtained by Braunlish with a large volume of boiling water ($P_s = 0.09$-1.03 absolute atmospheres) and those due to Kruder for boiling water ($P_s = 0.037$-1.56 absolute atmospheres), methyl ($P_s = 0.08$-1.42 atm abs) and butyl ($P_s = 0.17$-1.41 atm abs) alcohol in a large vessel.

The authors of the present article have performed experiments on the transfer of heat from boiling water in a pressure range of about 0.026-1 atm abs and /279 with thermal fluxes in excess of 10^5 kcal/m^2-hour (surface from 1Kh18N9T steel). The wall thermocouples did not record any temperature fluctuations and boiling at constant q and p_s did not cease. The heat transfer coefficient was proportional to $q^{0.7}$ and $P_s^{0.18}$.

The superheating of water described in [11] and [13] is attributable to conditions of originating of the vapor bubbles. It has been shown in a number of theoretical and experimental works, [11-13] and [18-22] that, when fluids boil on solid surfaces, the vapor bubbles originate in depressions filled with vapor or gas. They primarily originate in depressions with poor wettability. When a bubble is formed in a vapor or gas filled depression, the radius of the depression inlet which is still capable of serving as a vapor-formation center can be estimated from the expression

$$\rho_{min} = \frac{2A\sigma T_s}{r\gamma'' \Delta t_s}. \qquad (5)$$

In the case when the dimensions of vapor nuclei (at $\Delta t_s = 1°C$) are large or when the wettability is good, while there are no gas (vapor) [holding] cavities on the surface, boiling up requires high superheats Δt_s.

There is no basis for the assumption that conditions needed for origination of vapor bubbles for metals are different from those for nonmetallic fluids. For example, in experiments with boiling mercury [23] and [24] the same qualitative picture was obtained with wetted and unwetted surfaces as for water boiling under similar conditions [25]. In both cases when the surface was not wetted the formation of the vapor phase at the heat-conducting surface started at a temperature close to t_s.

Of great importance for boiling is the stability of the vapor-formation center functioning. For example, it is noted in [18] and [21] that the most stable depressions are those with greatest wetting angle.

The appreciable superheats of sodium at the surface, the existence of different modes of heat removal and the instability of heat transfer attendant to

boiling which were observed in our experiments ($P_s \approx 0.1$-1 abs atm) can be explained, on the basis of presently utilized concepts about the origination of vapor bubbles, by the following main causes.

1. As was already noted in [26], the vapor nuclei of sodium superheated by 1°C are large. For example, at $P_s = 1$ abs atm and the same Δt_s, ρ_{min}, the radius of the first nucleus, calculated from Eq. (5) is ten-fold greater for sodium than for water. Experiments with sodium were performed on surfaces on which water boiled at $\Delta t_s = 5°C$ (atmospheric pressure). If it is assumed that the same vapor- or gas-filled depressions serve as vapor formation centers for sodium also, then according to Eq. (5) they should have corresponding to them superheats of $\Delta t_s = 200°C$ at $t_s = 700°C$ and $\Delta t_s = 78°C$ at $t_s = 800°C$. However, these values of Δt_s are higher than experimental values, particularly than those for developed /280
boiling. It, therefore, may be assumed that relatively larger depressions were the [actual] vapor formation centers. At surfaces not specially machined the size distribution of the depressions should be close to normal and the number of "large" depressions, which are the predominant vapor-formation centers may be relatively low.

However, this factor alone does not suffice for explaining the experimental data we have obtained. For example, in test series 3 at $t_{fl} \simeq 700°C$ and $\Delta t \simeq 23°C$ (point 8) the fluid was boiling, while in test series 2c the boiling ceased temporarily (point 18) at a higher temperature ($t_{fl} \simeq 860°C$) and $\Delta_t \simeq 100°C$. The value of ρ_{min} calculated from Eq. (5) for point 8 of test series 3 exceeded by approximately 20-fold the ρ_{min} for point 18 in test series 2c. The increased value of ρ_{min} alone does not suffice to account for the existance of developed and unstable boiling under identical pressures at surfaces with the same finish.

2. The heated surface is wetted satisfactorily by the sodium. According to available data, metal surfaces are wetted satisfactorily by alkaline metals at temperatures of about 500°C and above [27].

Sodium is capable of reducing oxides of metals, if the free energy of the system becomes lower as a result of the reaction

$$M_nO_m + 2mNa \longrightarrow mNa_2O + nM$$

(here M denotes a metal). The temperatures at which our experiments were performed (about 700-900°C) are such that sodium reduces oxides of nickel, molybdenum and iron. The rate of oxide reduction depends on the surface material and the temperature level, however we are not aware of quantitative data on this. Apparently the satisfactory wettability of metals by sodium at temperatures above 500°C is due to the reduction of oxide films, which is substantiated by experiments concerned with wettability of oxides of certain metals by sodium (the extreme wetting angle in this case being about 110-140°C) [28].

When the oxide film of a surface is reduced, the latest parts of the latter to undergo such a reaction will, most probably, be the oxides in the depressions. As the wettability is improved, the magnitude of the superheat Δt_s needed for initial boiling up and the probability of existence of unstable boiling should increase. These tendencies were proven experimentally.

When boiling sodium (and other metals) one must determine whether the sodium reduces the oxide films at the heat-conducting surface (nongetter surface or, conversely, the material of the heat-conducting surface reduces the oxides of the sodium (getter-type surface). Zirconium and titanium can serve as examples of getter materials for sodium. Boiling of sodium at getter and nongetter surfaces may differ appreciably due to the difference in the wettability of these surfaces. All the discussions of this article pertain to nongetter surfaces.

3. High thermal conductivity of sodium. High thermal conductivity promotes superheating of the fluid in the entire volume, on one hand, and increases the time needed for superheating the fluid at the heat-conducting surface after break-off of the bubble on the other hand. The latter increases the probability that the vapor remaining in the depression after the bubble breaks off will be replaced by fluid. The time needed for superheating this fluid, estimated on the assumption that the latter is superheated only due to thermal conductivity, is by approximately 20-fold greater for sodium (700-900°C) than for water (100°C), if q and Δt in both cases are the same. This also proves that the frequency of vapor bubble breakoff from boiling sodium should be lower than in the case of water. The same opinion was expressed above on the basis of the measured frequency /281
of temperature fluctuations in developed boiling, determined by a movable thermocouple situated at the wall.

Thus, the relative large size of the depressions which serve as vapor-formation centers for sodium at $P_s \approx 0.1$-1 abs atm and the good wettability of the latter are responsible for the high Δt on initial boiling up, as well as (together with the high thermal conductivity) for the instability in the functioning of the vapor-formation centers.

The low values of α_{int} at the free surface of the liquid metal aid in the existence of unstable boiling in sodium. The fluid in the vessel can be appreciably superheated only at low α_{int} at the free surface. The magnitude of Δt_s on boiling is reduced due to a reduction in Δt_α, as well as of δt. The difference in Δt_s for heat removal by free convection without boiling the heat removal with boiling (q = const) can depend appreciably on the δt attendant to convection without boiling. The larger the ration $\delta t/\Delta t_s$, the more probable it is that boiling will cease.

The depression in the functioning of the vapor-formation centers, and the subsequent cessation of boiling could also have been affected by the pressure surge accompanying the boiling up. However, comparing the recording of temperature differences between the wall and the fluid and the experimentally observed time during which the pressure surge took place, we came to the conclusion that this effect is either entirely absent or insignificant.

In closing, let us consider the effect of the oxygen content of sodium on heat transfer on boiling.

If the oxygen content is within the limits of solubility at boiling temperatures, then the sodium reduces the oxide film on the surface of the construction materials noted above. In conjunction with this it may be assumed that the oxygen content of the sodium (within the limits of solubility) should not appreciably affect heat transfer attendant to boiling, which is also substantiated by our experiments. If, however, the oxygen content of the sodium exceeds the solubility at the given temperature, then the oxides may become deposited on the heating surface and thus affect the heat transfer on boiling.

The subject of heat transfer from sodium boiling in a large vessel is treated in [29 - 32]. In [29] and [32] the experiments were performed in a wide range of thermal fluxes. These data are, as a whole, in satisfactory agreement with those obtained by us. In [30] and [31] the experiments were performed with low thermal fluxes and the data thus obtained lie above our data and the data of [29] and [32]. It should be noted that at low thermal fluxes appreciable errors in determining the heat transfer coefficient are possible due to instability of the boiling process as well as in the determination of the mean temperature difference. /282

NOTATION

t_s - saturation temperature, °C

t_w - temperature of heat conducting surface, °C

Θ_{max} - maximum magnitude of the fluctuation in the temperature difference between the fluid and the wall, °C,

P_s - saturation pressure

α_{int} - heat transfer coefficient at the fluid-vapor interface

r - heat of vaporization

F - surface of the heat conducting surface

F_Φ - area of the interface

$A = 1/427$ - thermal equivalent of work

REFERENCES

1. Ivashkevich, A. A., et al.: Ustanovka s elektronnym obogrevom dlya issledovamiya teploobmena pri kipenii metallov v usloviyakh svobodnoy konvektsii

[Electronically-Heated Setup for the Study of Heat Transfer from Boiling Metals by Free Convection]. First article of Part III of this collection.
2. Subbotin, V.I., et al.: USSR report No. 328, Proceedings of the Third International Conference on the Peaceful uses of Atomic Energy, Geneva, 1964, v. 8, N.Y., 1965.
3. Rogers, T. and Mesler, R.A.: I. Ch. E. Journal, v. 10, No. 5, 656 (1964).
4. Torikai, K.: Report of Japan No. 580. Proceedings of the Third International Conference on the Peaceful uses of Atomic Energy, Geneva, 1964, v. 8, N.Y., 1965.
5. Moore, F.D. and Mesler R.B.A.: I Ch. E. Journal, v. 7, No. 4, 620 (1961).
6. Hsu, Y.Y., et al.: Trans. ASME, Ser. C, No. 3, 254 (1961).
7. Kudryavtsev, A. P., et al.: Eksperimental'noye issledovaniye teplootdachi ot horizontal'noy ploskoy poverkhnosti k natriyu pri svobadnoy konvektsii [Experimental Study of Heat Transfer from a Horizontal Flat Surface to Sodium by Free Convection] Part I or II of present collection.
8. Makansi, M.M., et al.: J. Phys. Chem., 50, 40 (1955).
9. Jakob, M. and Fritz, W.: Forschung Gebiete Ingenieur, 2 (434), 1931.
10. Kudryavtsev, A.P., et al.: Eksperimental'noye issledovaniye kriticheskikh teplovykh potokov pri kipenii natriya v bol'shom ob"yeme [Experimental Study of Critical Thermal Fluxes in Sodium Boiling in a Large Vessel]. Article immediately following the present.
11. Paese, D.C. and Blinks, L.R.: J. Phys. Colloid. Chem., 51, No. 2, 556 (1947).
12. Harvey, E.N., et al.: J. Appl. Phys., 18, No. 2, 162 (1947).
13. Sabersky, R.H. and Gates, C.W.: Jet Propulsion, 25, No. 2, 67 (1952).
14. Schorck, V.E. and Lienhard, I.H.: Trans. ASME, Ser. C, v. 85, No. 3, 261 (1963). /283
15. Minchenko, F.P. and Firsova, E.V.: Article in the collection Voprosy teplootdachi i gidravliki dvukhfaznykh sistem [Problems of Heat Transfer and Fluid Flow of Two-Phase Systems]. Gosenergoizdat, Moscow, 1961.
16. Kolach, G.A. and Vvedenskiy, Yu.G.: Trudy Moskovskogo energeticheskogo instituta. Issure 48, 1963.
17. Kutateladze, S.S. and Borishanskiy, V.M.: Spravochnik po teploperedache [Heat-Transfer Handbook]. Gosenergoizdat, Moscow-Leningrad, 1958.
18. Bankoff, S.G.: Trans. ASME, 79, No. 4, 735 (1957).
19. Corty, C. and Foust, A.S.: Chem. Engng Progr. Sympos., Ser. 51, No. 17, 1 (1955).
20. Hsu, Y.Y.: Trans. ASME, Ser. C, v. 84, No. 3, 18 (1962).
21. Griffith, P. and Wallis, I.: Chem. Engng Progr. Sympos., Ser. 56, No. 90, 49 (1960).
22. Clark, H.B., et al.: Chem. Engng Progr. Sympos., Ser. 55, No. 29, 103 (1959).
23. Lozhkin, A.N. and Kanayev, A.A.: Binarnyye ustanovki [Binary Devices]. Mashgiz, Leningrad, 1946.
24. Bonilla, C.F., et al.: Chem. Engng Progr. Sympos., Ser. v. 53, No. 20 (1957).
25. Averin, K.Ye.: Izvestiya AN SSSR, OTN, No. 3 (1954).
26. Deyev, V.I. and Solov'yev A.N.: Inzhenerno-fizicheskiy zhurnal, No. 6 (1964).

27. Balzhiser R. E., et al.: Nuclear Science Abstracts, v. 1, No. 9, Abstracts 14033 (1964).
28. Bradhurst, D. H. and Buchanon, A. S.: P. zn. Khimiya, Ref. 116543 (1962).
29. Noyes, R. S.: Trans. ASME, Ser. C, 85, No. 2, 125 (1963).
30. Lyon, R., et al.: Chem. Engng Progr. Sympos., Ser. v. 51, No. 7, 41 (1955).
31. Borishanskiy, V. M., et al.: Atomnaya eneriya, 19, Issue 2, 191 (1965).
32. Petukov, B. S., et al.: Third International Heat Transfer Conference, Vol. V. Chicago, August 7, 1966.

EXPERIMENTAL STUDY OF CRITICAL THERMAL FLUXES IN SODIUM BOILING IN A LARGE VESSEL

A. P. Kudryavtsev, D. M. Ovechkin, D. N. Sorokin,
V. I. Subbotin and A. A. Tsyganok

Up to present very little was published on critical thermal fluxes in metals /283
boiling in a large vessel. A study [1], was made of the dependence of the critical thermal flow in a large volume of magnesium boiling on horizontal tube on the magnesium concentration in the mercury. As the magnesium concentration in the mercury increased, the critical flux also increased and reached a maximum for a magnesium content of about 0.03% by weight. In the pressure range under study (1-10 abs atm) no dependence of the thermal flux on the pressure was observed.

Reference [2] describes the study of critical thermal fluxes in boiling potassium in a large volume at a horizontal tube in a pressure range of 0.007-1.55 abs atm (the magnitude of the critical flux at atmospheric pressure was $1.63 \cdot 10^6/m^2$-hour). Temperature fluctuations in the volume were observed, as well as super- /284
heating of the potassium above the saturation temperature. Reference [3] cites an empirical equation describing these experimental data

$$q_{cr} = 1.66 \cdot 10^6 \cdot P_s^{0.165}, \quad (1)$$

where P_s is in kg/cm^2.

Noyes [4] has studied critical thermal fluxes in sodium boiling under conditions of natural convection at horizontal molybdenum and stainless steel tubes under pressures of about 0.03-0.07 kg/cm^2. On the basis of these experimental data, as well as for data obtained by McAdams for water and some other organic fluids, Noyes supplements the equation for the boiling crisis under natural convection conditions, obtained on the basis of the fluid-dynamics concept of crisis, [5], by the factor $Pr^{-0.245}$.

$$q_{cr} = 0.144 r \gamma'' \left(\frac{\gamma - \gamma''}{\gamma''}\right)^{1/2} \left(\frac{g^2 \sigma}{\gamma}\right)^{1/4} Pr^{-0.245}. \quad (2)$$

According to the author, this equation is valid for sodium also at higher pressures, as well as for other metals.

We have performed seven series of experiments at a flat horizontal surface heated by electron bombardment at a radius of 38 mm. The heat conducting surface

was placed in a working tank from 1Kh18N9T steel 165 mm in diameter. The heat was removed from the condenser by air. The temperature of the heat-conducting wall was measured by chromel-alumel thermocouples, with wires 0.2 mm in diameter which were covered by aluminum oxide and placed in a protective capillary 0.8 x 0.15 mm in diameter made from 1Kh18N9T steel. The capillaries were placed into holes 0.85 mm in diameter drilled in the wall. The sodium temperature was also measured by chromel-alumel thermocouples (wire diameter 0.5 mm), placed in a sleeve.

The temperature difference between the fluid and the wall and the sodium temperature were continuously recorded on the EPP-09 automatic potentiometers, in which 1 sec is needed for the carriage to traverse the entire scale. The crisis was recorded on the basis of a sharp increase in the temperature difference between the wall and the fluid. The [power] supply was shut off by end switches, with which the potentiometers were provided.

The first five test series were performed using a surface from the VZh-98 alloy, the sixth series was conducted on a molybdenum surface, while the surface for the seventh series was made from 1Kh18N9T steel. After the first crisis was obtained, the load was increased rapidly (approximately up to 80% of the critical load) and then the power supply was increased by steps of approximately 3%. The setup and the methods used for performing experiments for measuring q_{cr} are described in detail in [6].

As was already pointed out [7], sodium boiling under natural convection conditions in a pressure range of about 0.1-1 abs atm can proceed by two modes.

1. Developed boiling mode, under which only insignificant fluctuations in the wall temperature are recorded by the thermocouples.

2. Unstable boiling mode, under which these temperature fluctuations may /285
be very high (for example, at $q \approx 10^6$ kcal/m^2-hour the fluctuations may be as high as 70°C). Depending on the boiling mode preceding the initiation of the crisis, the magnitude of q_{cr} may differ.

Figure 1 shows examples of recorded temperatures of the molybdenum wall before and during the crisis for points 4 and 8. For point 4 the temperature fluctuations before the crisis were appreciably greater than those for point 8. The magnitude of the critical thermal flux for point 4 is by approximately 60% lower than q_{cr} for point 8, although the pressure (P_s) in both cases was approximately the same. In our experiments on heat transfer from a copper surface the thermal fluxes exceeded the q_{cr} presented in the present article and no crisis ensued at all, although the sodium pressure in both cases was the same.

The difference in the values of q_{cr} brought about by the mode of boiling (developed and unstable boiling) preceding the crisis can be attributed to the fact that the probability of onset of the boiling crisis is the higher, the larger the vapor bubbles or the vapor regions at the heat conducting wall. This point of view /286
can be supported by data for water and organic fluids, for which q_{cr} increases

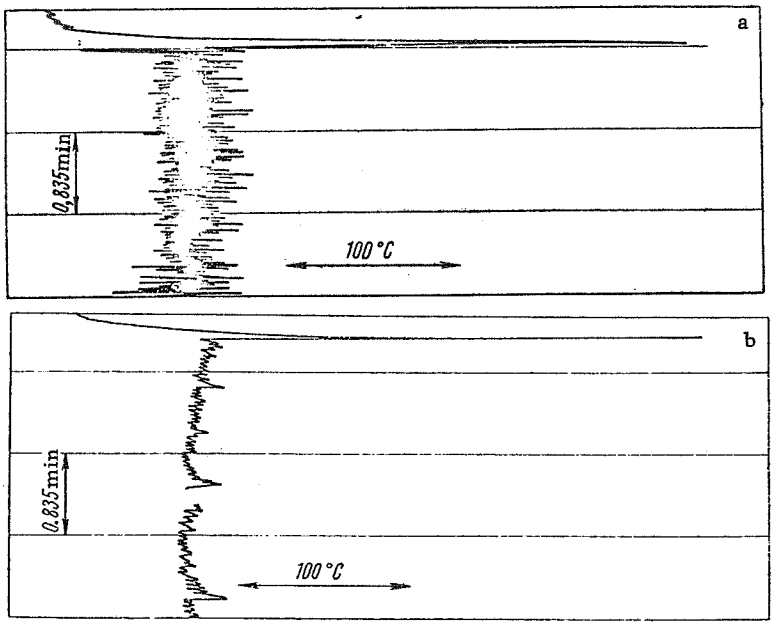

Figure 1. Record of the Temperature of a Molybdenum Wall Before and During the Crisis for Point 4 (a) and Point 8 (b) of Fig. 2.

with underheating [?] of the fluid to t_s and with an increase in the pressure (up to 1/3 P_{cr}). This can be attributed to the fact that with an increase in the underheating and in P_s the maximum diameter of bubbles situated at the wall decreases although the number of vapor-formation centers increases with an increase in P_s (for a constant thermal flux).

Figure 2 shows values of q_{cr} obtained in boiling sodium. The level of critical thermal fluxes can, with a scatter of 30%, be described by the formula

$$q_{cr} = (1.5 + 1.3P_s) \cdot 10^6, \tag{3}$$

where P_s is in atmospheres. The above empirical expression (line 4) can be used only in the range of pressures $1.5 \cdot 10^{-2}$-1.2 abs atm. Experimental points obtained by Noyes [4] are in good agreement with the above expression. However, on the whole, the agreement between Eqs. (2) and (3) is much worse (see Fig. 2). Figure 3 also displays lines obtained from criterial formulas of [5] and [8], which described experimental data on q_{cr} for water and organic fluids boiling in a large vessel

$$\frac{q_{cr}}{r\sqrt{g\gamma''\left(1+\frac{\gamma''}{\gamma}\right)}\sqrt[4]{\sigma(\gamma-\gamma'')}} = 0.14, \tag{4}$$

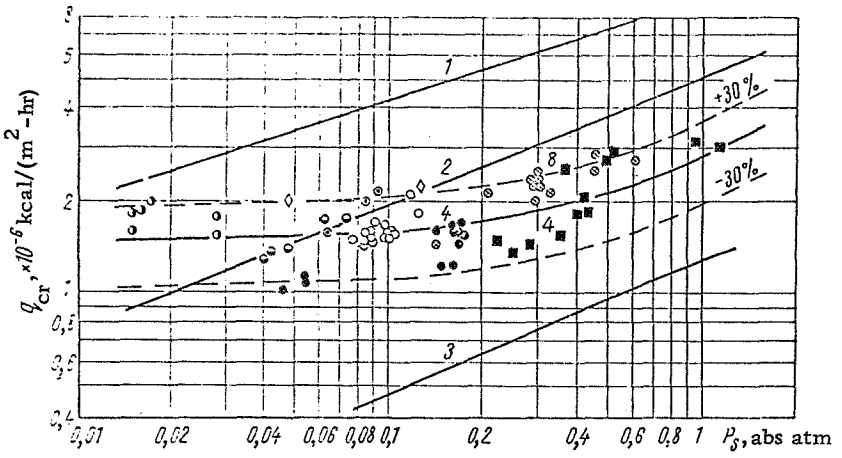

Figure 2. Experimental Data on Critical Thermal Fluxes:
○, ◇, ⊗, ◑, ⊙ and — [sic] - the VZh-98 alloy; ■ - molybdenum; ● - 1Kh18N9T steel; ⊖ - data of [4].

Curves	Obtained for the formula
1	5
2	2
3	4
4	3

$$q_{cr} = 4700 \frac{T_s^{0.32} \sigma^{0.21} \lambda^{0.4} (r\gamma'')^{0.36} (\gamma - \gamma'')^{0.48}}{\lambda^{0.31} C_p^{0.08} \mu^{0.14}}. \quad (5)$$

In our calculations we have used the values of λ, C_p and ν from [9], while r and γ'' were taken from [10] and γ from [11]. The values of σ were calculated from the expression /287

$$\sigma = 200.12 - 9.833 \cdot 10^{-2} t,$$

presented in [11]. The values of P_s were obtained from the formula

$$\lg P_{atm} = 4.521 - \frac{5220}{T_s}, \quad (6)$$

also from the above reference.

As can be seen from Fig. 2, the Noyes formula [2] (should be (2), DBL) [line 2] agrees with Eq. (3) only in a relatively narrow pressure range (about 0.025-0.1 atm abs), and a difference of about a factor of two is observed at extremes of the pressure range under study. The values of q_{cr} calculated from Eq. (4) [line 3] lie by approximately a factor of three lower than the experimental

data, while those calculated from Eq. (5)[line 1] lie by approximately a factor of three above the latter.

Formula (4) is based on the fluid dynamics theory of the boiling crisis and satisfactorily expresses the manner in which q_{cr} depends on P_s for water and organic fluids. The fact that this formula does not agree with the experimentally obtained values of q_{cr} does not mean that the nature of the crisis attendant to the boiling of metal does not obey the laws of fluid dynamics. It is possible that in boiling metals, due to their high thermal conductivities, a substantial part of the heat from the heat-conducting surface is transferred by the fluid even at thermal fluxes close to the critical. This may be one of the factors responsible for the disagreement between experimentally obtained q_{cr} for sodium and those given by Eq. (4).

It can be seen from Fig. 2 that points obtained on the surface made from the VZh-98 alloy have a scatter of less than 30%. If an averaging line is drawn through these points, then its slope will be approximately the same as the slope of the line obtained from Eq. (1) which describes experimental data for potassium. On the other hand, the slopes of lines 1, 2 and 3 are much greater. However, the available data still do not suffice to obtain a generalized expression for q_{cr} as a factor of P_s, as well as for determining the laws governing the effect of the surface on q_{cr} in boiling metals.

REFERENCES

1. Korneyev, M.I.: Teploenergetika, No. 4 (1955).
2. Balzhiser R.E., et al.: Nuclear Science Abstracts, 18, No. 9, 14033 (1964).
3. Brooks, R.D. and Bonilla, C.F.: Nucleonics, 22(3), 43 (1964).
4. Noyes R.C.: Trans. ASME, 85(2) (1963).
5. Kutateladze, S.S.: Osnovy teorii teploobmena [Fundamentals of the Heat Transfer theory]. Mashgiz, Moscow, 1962.
6. Ivashkevich, A.A., et al.: Ustanovka s elektronnym obogrevom dlya issledovaniya teploobmena pri kipenii metallov v usloviyakh svobodnoy konvektsii [Electronically-Heated Setup for the Study of Heat Transfer from Boiling Metals by Free Convection]. First article of Part III.
7. Subbotin, V.I., et al.: Report No. 328, presented to the 3rd International Conference on Peaceful Uses of Atomic Energy, Geneva, 1964.
8. Kruzhilin, G.N. and Subbotin, V.I.: In the book Proceedings of the Second International Conference on Peaceful Uses of Atomic Energy. Geneva, 1958. Doklady sovietskikh uchenykh [Reports by Soviet Scientists], Vol. 2, page 134, Atomizdat, Moscow, 1959. /288
9. Vargaftik, N.B.: Spravochnik po teplofizicheskim svoystvam gazov i zhidkostey [Handbook of Thermophysical Properties of Gases and Liquids]. Fizmatgiz, Moscow, 1963.
10. Volyak, L.D.: Inzhenerno-fizicheskiy zhurnal, No. 3 (1962).

11. Zhidkometallicheskiye teplonositeli [Liquid-Metal Heat-Transfer Agents]. Collection of articles translated from English under the editorship of A. Ye. Sheyndlin, Foreign Literature Publishing House, Moscow, 1958.

MEAN TEMPERATURE DIFFERENCE IN LOW-PRESSURE VAPOR GENERATORS AND CONDENSERS

P. L. Kirillov

During the last few years the need has arisen for low-pressure vapor generators. In particular, a number of projects [1] and [2], use is made of vapor generators for obtaining mercury or potassium vapor, which is then directed into a turbine. The vapor pressure at the turbine inlet can be from several tenths of an atmosphere to several atmospheres. Here the flow resistance of the vapor generator is comparable with the absolute presssure of the vapor at the outlet. This produces an unusual distribution of the mean temperature of the heated heat-transfer agent (it is cooled, despite the fact that heat is supplied to it). The temperature distribution of the vaporized heat transfer agent (saturation temperature) along the length is determined by the changes in pressure which, in their turn, depend on the flow rate and on the vapor content at each section. This picture is observed in vapor generators operating at any pressure, but the drop in the saturation temperature, produced by a reduction in pressure usually does not exceed several degrees and may be disregarded in calculations. At low pressure the temperature of the heat-transfer agent may drop by several tens of degrees, which is appreciable. /288

According to the above, the temperature of the heat transfer agent over the length and the mean temperature pressure will not obey the exponential distribution, meaning that the ordinary expression for the log mean temperature difference is no longer valid. The purpose of the present paper is to obtain a new expression for the log mean temperature difference under these conditions.

For the elementary heat transfer surface in a vapor generator we, as usual, have the following equations (Fig. 1)

$$dQ = \bar{k}\,(t_1 - t_2)\,df, \tag{1}$$

$$dQ = -c_1 G_1\,dt_1 = G_2\,dq_2 \quad \text{(for straight flow)}. \tag{2}$$

$$dQ = -c_1 G_1\,dt_1 = -G_2\,dq_2 \quad \text{(for counterflow)}. \tag{3}$$

Here $dq_2 = di_2 + wdw/g$. We restrict ourselves to low velocities, such that $wdw/g \ll di_2$. /289

It is obvious that one can assume a constant $\bar{k}$ for each vapor-generator section only approximately. However, the manner in which the heat-transfer

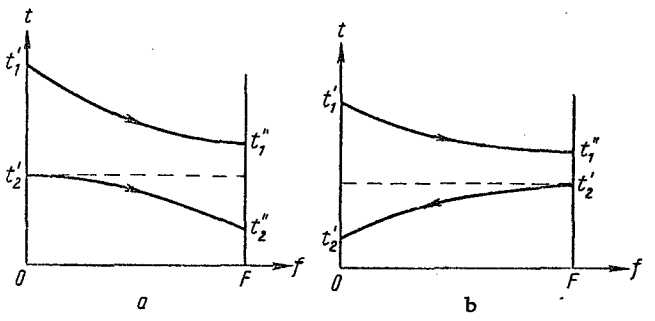

Figure 1. Temperature Variation in the Vaporizing Part of the Vapor Generator.

a) for Straight Flow; b) for Counterflow.

coefficient varies over the length, particularly, due to changes in the coefficient of heat transfer to the two-phase flow, is so complicated, that analytical calculation in which k appears as a function of length are as yet difficult to perform. In addition, the relationship $\alpha(l)$ has not been as yet studied in all the regions of the flow and the available experimental data do not suffice for constructing an analytical formula, hence,

$$\overline{k} = \frac{1}{F}\int_0^F k\,df. \tag{4}$$

The validity of the above expression, which is not generally obvious, was proven in [3].

The change in the enthalpy di_2 will be found from known thermodynamic relationships (see [4])

$$di = T\,ds + Av\,dp, \tag{5}$$

$$T\,ds = c_x\,dT + r\,dx, \tag{6}$$

$$c_x = c' + x\left(\frac{dr}{dT} - \frac{r}{T}\right), \tag{7}$$

$$dp = \frac{r}{AT}\frac{1}{v'' - v'}\,dT. \tag{8}$$

Substituting Eqs. (6)-(8) in Eq. (5), setting $v' \ll v''$, and disregarding changes in the latent heat of vaporization, we will get for our case /290

$$di = -c'\,dt + r\,dx. \tag{9}$$

The above expression can also be obtained from a T-s diagram.

$$i_2 = i_1 + r_2\,dx;\quad i_3 = i_1 - c'\,dt + r_3 x_3;$$
$$di = i_3 - i_2 = -c'\,dt + r_3 x_3 - r_2 x_2 = -c'\,dt + r\,dx + x\,dr, \tag{10}$$

whence, if we disregard changes in r, we get Eq. (9). Substituting farther this expression into Eqs. (2) and (3), we get

$$dt_1 = -\frac{dQ}{c_1 G_1}, \tag{11}$$

$$-dt_2 = \pm \frac{dQ}{c_2 G_2} - \frac{r\,dx}{c_2}. \tag{12}$$

Now

$$dt_1 - dt_2 = -\left(\frac{1}{c_1 G_1} \mp \frac{1}{c_2 G_2}\right) dQ - \frac{r\,dx}{c_2}.$$

Substituting $dQ = \bar{k}\Delta t_x\,df$, we get

$$d(\Delta t_x) = -\left(\frac{1}{c_1 G_1} \mp \frac{1}{c_2 G_2}\right) \bar{k}\Delta t_x\,df - \frac{r\,dx}{c_2}. \tag{13}$$

Here the minus sign pertains to straight flow, while the plus sign is for counterflow. Denoting further $\left(1/c_1G_1 \mp 1/c_2G_2\right)\bar{k} = n$, $\left(-\frac{r}{c_2}\frac{dx}{df}\right) = m(f)$, we arrive at the expression

$$\frac{d(\Delta t_x)}{df} + n\Delta t_x = m(f). \tag{14}$$

the solution of which is

$$\Delta t_x = e^{-nf}\left[\int m(f)\,e^{nf}\,df + t\right]. \tag{15}$$

We assume in the first approximation that the vapor content varies linearly over the length, then dx/df = const and

$$m(f) = -\frac{r}{c_2}\frac{dx}{df} = \text{const}. \tag{16}$$

From Eq. (15) we get that

$$\Delta t_x = Ae^{-nf} - \varphi, \tag{17}$$

where

$$\varphi = -\frac{r}{c_2 n}\frac{dx}{df}.$$

It is easy to see that, when dx and $\varphi = 0$, Eq. (17) yields an exponential temperature distribution over the length and reduces to the ordinary expression for the log mean temperature difference.

For straight flow we get (see Fig. 1a) /291

$$\Delta t_x(F) = t_1'' - t_2'' = \Delta t'' = Ae^{-nF} - \varphi, \tag{18}$$

whence

$$A = (\Delta t'' + \varphi)\, e^{nF}, \tag{19}$$

$$\Delta t' = (t_1' - t_2') = A - \varphi. \tag{20}$$

Equating Eqs. (19) and (20), we get

$$\ln \frac{\Delta t' + \varphi}{\Delta t'' + \varphi} = nF. \tag{21}$$

Let us now find the mean temperature difference for the entire straight-flow vapor generator

$$\overline{\Delta t} = \frac{1}{F}\int_0^F \Delta t_x\, df = -\frac{A}{nF}(e^{-nF} - 1) - \varphi. \tag{22}$$

After Eqs. (19) and (21) are substituted here and simple transformations are made, we get

$$\overline{\Delta t} = \frac{\Delta t'' - \Delta t'}{\ln \frac{\Delta t'' + \varphi}{\Delta t' + \varphi}} - \varphi. \tag{23}$$

For counterflow (see Fig. 1b), we have

$$t_1' - t_2'' = A - \varphi, \tag{24}$$

$$t_1'' - t_2' = Ae^{-nF} - \varphi, \tag{25}$$

whence we get an expression similar to Eq. (21)

$$\ln\frac{t_1'-t_2''+\varphi}{t_1''-t_2'+\varphi}=nF, \tag{26}$$

and the average temperature difference

$$\overline{\Delta t}=\frac{(t_1'-t_2'')-(t_1''-t_2')}{\ln\frac{t_1'-t_2''+\varphi}{t_1''-t_2'+\varphi}}-\varphi. \tag{27}$$

The above expression and Eq. (23) can be written in the general form

$$\overline{\Delta t}=\frac{\Delta t_б-\Delta t_м}{\ln\frac{\Delta t_б+\varphi}{\Delta t_м+\varphi}}-\varphi, \tag{28}$$

where

$$\varphi=-\frac{r}{c_2\left(\frac{1}{c_1G_1}\mp\frac{1}{c_2G_2}\right)\bar{k}}\frac{dx}{df}. \tag{29}$$

The minus sign is for straight flow, while the plus sign is for counterflow.

The processes taking place in condensers are similar (Fig. 2). For an elementary heat transfer surface in this case we have /292

$$dQ=\bar{k}_1(t_1-t_2)_x\,df, \tag{30}$$

$$dQ=-G_1\,di_1=c_2G_2\,dt_2 \text{ (for straight flow)}, \tag{31}$$

$$dQ=-G_1\,di_1=-c_2G_2\,dt_2 \text{ (for counterflow)}. \tag{32}$$

Examining Eqs. (5)-(8) or a T-s diagram for our case, as this was done above, we get

$$di_1=-c_1\,dt_1-r\,dx. \tag{33}$$

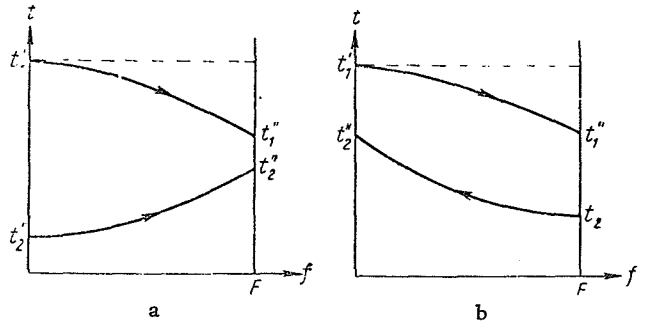

Figure 2. Temperature Variation in a Condenser.
a) for Straight Flow; b) for Counterflow.

Substituting this expression in Eqs. (31) and (32), we write

$$dt_1 = \frac{dQ}{c_1 G_1} - \frac{r\,dx}{c_1}, \tag{34}$$

$$dt_2 = \pm \frac{dQ}{c_2 G_2}, \tag{35}$$

$$d(t_1 - t_2)_x = \left(\frac{1}{c_1 G_1} \pm \frac{1}{c_2 G_2}\right) \overline{k}_1 (t_1 - t_2)_x\, df - \frac{r\,dx}{c_1} \tag{36}$$

or

$$\frac{d(\Delta t_x)}{df} - \left(\frac{1}{c_1 G_1} \pm \frac{1}{c_2 G_2}\right) \overline{k}_1 \Delta t_x = -\frac{r\,dx}{c_1\,df}. \tag{37}$$

Denoting here

$$m_1(f) = -\frac{r}{c_1}\frac{dx}{\partial f}, \quad n_1 = -\left(\frac{1}{c_1 G_1} \pm \frac{1}{c_2 G_2}\right) \overline{k}_1,$$

we arrive at an equation, entirely analogous to Eq. (14)

$$\frac{d(\Delta t_x)}{df} + n_1 \Delta t_x = m_1(f). \tag{38}$$

Solving it in the method presented above, we get an expression for the log mean temperature difference in the condenser

$$\overline{\Delta t} = \frac{\Delta t_б - \Delta t_м}{\ln \frac{\Delta t_б + \varphi_1}{\Delta t_м + \varphi_1}} - \varphi_1, \tag{39}$$

where /293

$$\varphi_1 = \frac{r}{c_1} \frac{1}{\left(\frac{1}{c_1 G_1} \pm \frac{1}{c_2 G_2}\right) \overline{k}_1} \cdot \frac{dx}{df}. \tag{40}$$

The plus sign pertains to straight flow, while the minus sign is for counterflow.

REFERENCES

1. Proceedings of 1962 High-Temperature Liquid-Metal Heat Transfer Technology Meeting, BNL-756, N. Y., 1962.
2. Davis, H. L.: Nucleonics, 22(3), 34 (1964).
3. Ushakov, P. A.: Analiz primenimosti srednikh koeffitsientov teploobmena dlya rascheta teploobmennikov [Analysis of the Applicability of Average Heat Transfer Coefficients for Heat-Exchanger Design]. Part II of present collection.
4. Vukalovich, M. P. and Novikov, I. I.: Tekhnicheskaya termodinamika [Engineering Thermodynamics]. 3rd edition. Gosenergoizdat, Moscow-Leningrad, 1962.

TRANSFER OF HEAT FROM CONDENSING SODIUM VAPOR

N. B. Bakulin, M. N. Ivanovskiy, V. P. Sorokin,
V. I. Subbotin and B. A. Chulkov

The experimental study of heat transfer from condensing vapors of pure alkaline metals is made difficult by the aggressiveness of the latter, the high temperature level and the need to measure high heat transfer coefficients under the above conditions. Small admixtures of noncodensing gases, vapor of metals with low boiling temperatures or contaminant deposition on the condenser wall can result in appreciable distortions. Instability of vapor formation under certain vapor-generator operation mode makes measurements difficult. /293

It is known that steel surfaces are well wetted by sodium and that it undergoes film condensation. Due to the high thermal conductivity of liquid sodium (60-80 w/m-degree), the condensate film creates a low thermal resistance R_f to the transfer of heat to the condenser wall. Under these conditions heat transfer is appreciably affected by the following boundary conditions:

1) The temperature difference between the vapor and the condensate needed for bringing about the phase transition results in the appearance of resistance R_{ph} to the phase transition;

2) When the vapor contains noncondensing gases or other admixtures, a diffusion resistance R_d arises in the vapor near the condensate surface;

3) Contaminant deposits on the condenser wall create a thermal contact resistance R_c. The total thermal resistance attendant to condensation is [thus] composed of the above resistances ($R = R_f + R_{ph} + R_d + R_c$). The contribution made by a given resistance to the total resistance depends on the specific conditions of condensation. /294

At present very little has been published on the transfer of heat from condensing sodium vapor [1-3]. The heat transfer coefficients obtained in [1] and [2] are appreciably lower than those which can be attributed to the thermal resistance of the condensate film. The measurements in [1] were performed at vapor temperatures of 630-870°C and with temperature differences of 2.7-4.1°C between the vapor and the wall; the heat transfer coefficients were 65-75 kW/m^2-degree, i. e., less than 20% of the theoretical coefficients, which take into account only the resistance of the condensate film. No reasons are given for obtaining low (as compared with those calculated by the Nusselt theory) heat transfer coefficients.

To analyze the effect of boundary conditions on heat transfer attendant to condensation of pure "stationary" sodium vapor, we have performed experiments

on a setup described in [4]. Using a movable thermocouple 0.5 mm in diameter, we have measured the temperature fields in the vapor, in the liquid sodium filling the condenser's bath and in the condenser wall, under steady thermal conditions. To measure the wall temperatures, the movable thermocouple was lowered into a narrow (1.2 mm) vertical slot milled in the condenser. The thermal fluxes were calculated on the basis of the measured temperature gradients in the condensate and at the condenser wall. The readings of thermocouples (as a function of the position of the thermocouple probe) for several characteristic thermal modes are shown in Fig. 1. By examining the temperature field in liquid sodium and at the wall it is possible to determine the presence or absence of a temperature jump at the liquid-wall interface, i.e., on the magnitude of R_c. In the temperature range /295
under study (up to 520°C), no R_c was found between pure sodium and 1Kh18N9T steel. The table gives experimentally obtained values of temperature jumps at the vapor-liquid interface, as well as the heat transfer coefficients $\alpha_{ph} = 1/R_{ph}$, calculated on the basis of these jumps. Figure 2 displays experimental values of α_{ph} as a function of the temperature of the saturated vapor. It can be seen /296
from the figure that α_{ph} in the range of parameters under study increases highly with a rise in the vapor temperature and at 480°C it is about 50 kw/m-degree.

Experimental Data on Condensation of Pure Sodium Vapor

Vapor Temperature C	Temperature Jump, C	Thermal Flux kw/m^2	Heat Transfer Coefficient kw/m^2 - degree.		Condensation Factor
			6 Theoretical	7 Experimental	
512.0	1.8	186	71	103	1.18
483.5	3.1	157	50.1	50.7	0.99
481.0	3.6	152	48.0	42.3	0.94
462.0	3.5	131	34.2	37.4	1.04
464.5	3.4	130	35.9	38.3	1.03
433.5	5.3	117	17.6	22.1	1.11
412.5	7.6	99	12.1	13.0	1.04
412.5	7.4	106	12.1	14.3	1.07
391.0	12.3	108	7.7	8.8	1.07
387.5	14.1	114	7.2	8.1	1.06
384.0	17.3	120	6.5	6.9	1.03
401.5	8.5	91	9.5	10.7	1.06
431.5	4.1	84	18.9	20.5	1.04
431.0	4.0	72	18.2	18.0	0.99
445.0	3.3	77	24.3	23.3	0.98
445.0	3.2	81	24.3	25.3	1.02
461.0	2.3	86	33.4	27.3	0.90
461.0	2.2	77	33.2	35.0	1.03
411.0	7.1	84	11.7	11.8	1.00
473.0	2.5	98	41.5	38.8	0.97
899.0	<1.5	195	4170	>130.0	—

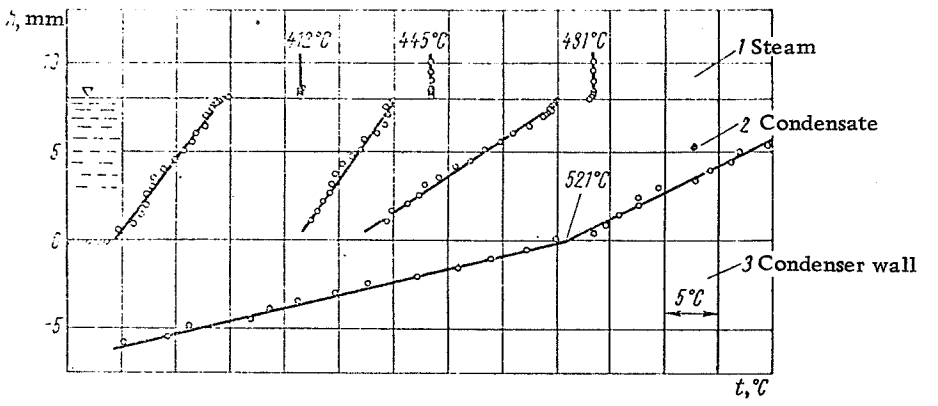

Figure 1. Temperature Fields Measured in Condensing Sodium.

1) Steam; 2) Condensate; 3) Condenser wall.

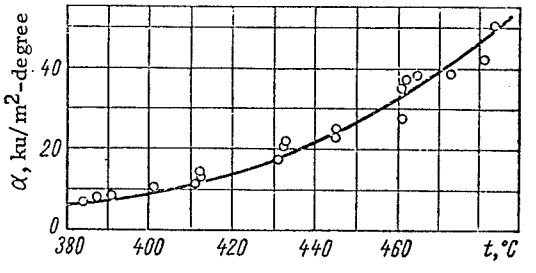

Figure 2. Heat Transfer Coefficients Calculated on the Basis of Measured Temperature Jumps at the Vapor-Liquid Interface and Thermal Flux. The Curve Represents Values of α_{ph} Calculated From Eq. (3) With f = 1.

Examination of the phase transition process from the point of gas kinetics makes it possible to obtain theoretical relationships for α_{ph}. The resultant mass flux can be related to the temperature and pressure under phase transition conditions by the well-known Hertz-Knudsen formula, which is precisely what was done in [5], but, as is shown [6-8], this formula does not take into account the increase in resultant mass flux produced by the convective motion of the vapor along the normal to the phase interface. When the condensation factors are close to unity, disregard of the convective velocity of the steam produces large errors. The most general expression for the resultant mass flux attendant to phase transition was obtained in [6]

$$G = \frac{1}{(1/f - 1/2 - v/4c)} \left\{ \frac{P_0}{(2\pi g R T_0/M)^{1/2}} - \frac{P}{(2\pi g R T/M)^{1/2}} \right\}. \quad (1)$$

A correction for the effect of the vapor velocity was obtained in [6]; when considering the average molecular velocity it is

$$\frac{1/f}{1/f - 1/2 - v/4c}$$

In [7] this problem is considered in more detail for the particular case of $v/c \ll 1$. On the assumption that the velocity distribution of the molecules evaporating from the fluid is Maxwellian, the same results were obtained as in [6], i.e., the correction is $2/(2 - f)$. Approximate consideration for the case of $v/c \gg 1$ of [8] yields a correction of about $1.7/(2 - f)$. For the case of v close to c the solution was inconclusive and the calculations are performed by successive approximations.

Using Eq. (1) we can write a formula for α_{ph} for vapor condensation at the condensate surface

$$\alpha_{ph} = \frac{q}{T_0 - T} = \frac{r + c_p''(T_0 - T)}{(1/f - 1/2 - v/4c)(T_0 - T)} \left\{ \frac{P_0}{(2\pi g R T_0/M)^{1/2}} - \frac{P}{(2\pi g R T/M)^{1/2}} \right\}. \quad (2)$$

In the case of T_0 close to T and $v/c \ll 1$, we can simplify Eq. (2) and write

$$\alpha_{ph} = \frac{2f}{2 - f} \left(\frac{r^2 M}{2\pi g R T_0} \right)^{1/2} \left\{ \left(\frac{dP}{dT} \right)_{T_0} - \frac{P_0}{2T_0} \right\}. \quad (3)$$

In this case α_{ph} for condensation does not depend on the thermal flux and is a function of the vapor pressure (temperature) only.

Using experimental data on temperature jumps at the vapor-condensate interface attendant to condensation of sodium and Eqs. (2) and (3), we can calculate f for sodium. The results of these calculations are presented in the table and in Fig. 3. The physical parameters for sodium vapor in the calculations were taken from [9]. As can be seen from Fig. 3, the experimental points for f thus found are close to unity in the entire temperature range. This result is in agreement with the generally held view that the condensation factors for liquid and solid metals, in which the vaporizing molecules are identical with the condensating ones should be unity. However, the experiments which served as the basis for this opinion were performed at low pressures and low phase transition rates. The data obtained by the present authors give grounds for the assumption that f for pure sodium in the pressure range covered in the experiments does not depend on the pressure and is equal to unity. /297

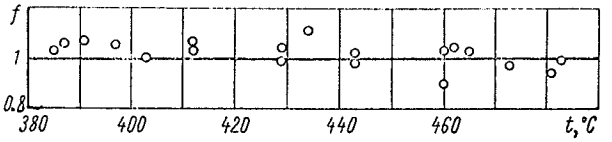

Figure 3. Condensation Factors Calculated on the Basis of Experimental Data.

The thermal resistance of the phase transition on condensation of sodium can be calculated from formulas of the gas kinetic theory setting f = 1. When there are not diffusion and thermal contact resistances and the pressures are not too low, the moderate resistance of the transition results in a high rate of heat transfer from condensing vapor of pure sodium.

Although the experiments were performed on condensation of "stationary" vapor, i.e., when the vapor did not move along the surface of condensation, the thermal resistance of the phase transition will be the same also in the case of moving vapor. The motion of the vapor along the surface of condensation does not affect α_{ph}, since the longitudinal velocity of vapor in a vapor layer near to the surface of condensation with a thickness of the order of a mean molecular path is zero, or is a priori known to be less than the velocity of thermal motion of molecules.

We wish to note that heat transfer from condensing vapors of alkaline metals, i.e., potassium [4] and sodium, is one of the high-rate processes of heat transfer. Heat transfer coefficients under appropriate pressures and high-rate condensate removal can be as high as 50 kw/m^2-degree and higher. However, as was pointed out by the present authors in [4], even small admixtures of noncondensating gases and other contaminants can appreciably reduce the rate of heat transfer. The problems of thermal resistance of the phase transition and the condensation factors that were here considered may be of interest not only for condensation of metals, but also in the study of processes of vacuum distillation, boiling, flow of metal vapors through a nozzle, and other phenomena related to phase transformations.

NOTATION

f - condensation factor /298

v - convective velocity of the vapor in the direction normal to the condensation surface

c - average thermal velocity of vapor molecules

R - universal gas constant

M - molecular weight

T_0, P_0 - temperature and pressure of vapor above the condensate, °C

T, P - temperature at the condensate surface and the saturated vapor pressure corresponding to this temperature, °C

α_{ph} - coefficient of heat transfer attendant to phase transition

G - mass flux attendant to phase transition

REFERENCES

1. Misra B. and Bonilla C.: Chem. Engng. Progr. Sympos, Ser. 52 (18), 7-21 (1956).
2. Roth, L. T.: Proceeding of 1962 High-Temperature Liquid-Metal Heat Transfer Technology Meeting, BNL-756, N. Y., 1962, 276.
3. Noyes, R. C.: See p. 97 of Ref. [2] above.
4. Subbotin, V. I., et al.: Teplofizika vysokikh temperatur, No. 4, 617 (1964).
5. Silber, R. C.: Engineering, 161, No. 5 (505).
6. Rish, R.: Helv. phys. acta, 6, 132 (1933).
7. Kucherov, R. Ya. and Rikenglaz, L. E.: Doklady AN SSR, 133, No. 5, page 1130, 1960.
8. Zwick, S. A.: J. Appl. Phys., 31, No. 10, 1735 (1960).
9. Vargaftik, N. B.: Spravochnik po teplofizicheskim svoystvam gazov i zhidkostey [Handbook of Thermophysical Properties of Gases and Liquids]. Fizmatgiz, Moscow, 1963.

PART FOUR

TECHNIQUES OF WORK WITH LIQUID METALS

CORROSION RESISTANCE OF CONSTRUCTION MATERIALS TO SODIUM

V. V. Zotov, B. A. Nevzorov and Ye. V. Umnyashkin

Sodium and the eutectic alloy of sodium and potassium are the most extensively used liquid-metal coolants. /299 An important problem in their use is the selection of construction materials with sufficient resistance to corrosion in nonisothermal flow, satisfactory mechanical properties (ultimate strength, relative elongation, etc.) at elevated temperatures, moderate thermal expansion coefficient as well as with good workability i.e., ease of rolling, welding, etc.

In the study of corrosive action of sodium on various metals extensive use is made of vial tests under isothermal conditions. Since it is impossible to determine the actual rates of certain processes (mass transfer, solubility, effect of nonmetal admixtures in the liquid metal, etc.) the vial tests are of value only for qualitative determination of the corrosion resistance of the material in the given liquid-metal coolant. In tests in containers (vertical and inclined) the temperature drops produce convection flows of the liquid metals, which increases the rates of all corrosion processes. Directed flow of the coolant exists in loops with temperature drops. In this case the flow velocities of the liquid-metal coolant depend on the temperature difference and can be calculated. Nevertheless, results of corrosion tests obtained in nonisothermal containers and convection loops cannot be used with sufficient reliability in the design of equipment. Various rotary-type test machines (with and without interchange of the liquid metal) are also unable to produce the needed results. And only results of corrosion tests obtained by testing materials in circuits with forced circulation can be used with confidence for /300 design purposes since the circulation loops afford the main parameters, i.e., specified coolant temperature and temperature drop, necessary flow velocities of the liquid metal, nonmetallic admixture content of the latter, as well as a specific ratio of the coolant volume to the surface area washed by the flow.

Several kinds of corrosion interaction with the liquid metals are observed when testing materials in circulation loops. The main kind of corrosion for steels and alloys in liquid metals is by solution of the solid-phase components in the liquid metal. The atoms of the solid substance may dissolve uniformly over the entire washed surface. In this case the solution effect removes the entire surface layer and no corrosion interaction zones are observed. If, however, the individual components of the alloy are dissolved selectively, then corrosion zones may form on the surface in contact with the liquid metal due to the appearance of porosity, disintegration and pitting in the surface layer. Frequently corrosion interaction has a clearly expressed intercrystalline character, i.e., when the corrosion proceeds along the grain boundaries. Intercrystalline corrosion in a liquid sodium medium can extend, for certain metals, to a sufficiently great depth, which in the final count results in an appreciable reduction in the ultimate strength and in the relative elongation. The rate of such corrosion is sometimes appreciable,

since, while [only] individual atoms are carried away by the liquid metal on uniform solution, in intercrystalline corrosion entire crystals may be removed from the surface of the constructional material. The dissolved components and the corrosion products are carried by the liquid metal into cooler parts of the device, where they settle out of the solution and crystallize on wall of pipelines, heat exchangers and other units, due to supersaturation attendant to the temperature reduction. This process is called thermal mass transfer or mass transfer due to a temperature gradient. Deposition of the transferred metal particles and corrosion products can result in partial or total stoppering up of ducts.

Another kind of mass transfer is also observed, i.e., concentration mass transfer, which may take place under isothermal conditions. It comes about in the case when several metals with different solubilities are in contact with the liquid metal and when these metals interact with one another, forming intermetallic compounds, nitrides, carbides or solid solutions. Concentration mass transfer is dangerous from the point of view of reducing the plasticity properties of the metal, since the latter may become embrittled due to the formation of various compounds.

The rate of corrosion processes may be affected by the following factors: /301
test temperature, temperature gradient in the system, cyclical temperature changes, ratio of the liquid-metal volume to the surface area of the system, purity of the liquid metal, its rate of flow, state of the metal surface (quality of finish, protective coatings, etc.), state of the material (heat treatment, presence of internal stresses, grain size, etc.), number of different metals in contact with the same liquid metal, chemical composition of the materials of construction, duration of tests, etc.

Chemical Nature of Oxygen in Liquid Sodium

The corrosion resistance of pure metals, as well as of structural steels and alloys exposed to the atmosphere and immersed in electrolytic solutions depends to a large extent on the protective properties of passive films which are oxidic in nature. Many investigators believe that also in sodium the corrosion resistance of materials depends to a certain extent on the chemical stability of their oxidic films. By this attribute all the metallic materials can be divided into three classes.

The first class is made up of stainless steel and nickel, i.e., materials the oxides or compound oxides of which have a chemical stability in sodium smaller than or close to the stability of sodium oxide.

The second class embraces materials, the oxides or compounds oxides of which are more stable than sodium oxide. Here the oxides of these metals are well coupled to the base; zirconium is presented as an example of these.

The third class contains materials the oxides of which are more stable than sodium oxide, but they are poorly coupled with the base, these are, for example, niobium, vanadium, uranium, beryllium, etc.

As a rule, breakdown of the oxide films results in the disappearance of the potential barrier, and thus, in an increase in the rate of corrosion. It is shown in [1] that the passive film on pure chromium and on the surface of austenitic stainless steels is retained in sodium up to 500-540°C, and it breaks up rapidly when the temperature is made higher. It is thus obvious that corrosion of stainless chromium and chromium-nickel steels in sodium up to 500°C depends to a given extent on the passive film, while on further increase in the temperature the steel displays its true corrosion resistance, not screened by films which act as potential barriers.

Many investigators point to the fact that at temperatures above 500°C the corrosion rate of construction materials in sodium (dissolution, frontal and intercrystalline corrosion) is determined primarily by the oxygen content of the sodium [1-5]. This is proven experimentally. For example, Bruch [5] has shown /302
that in sodium flowing at 0.4 m/sec at 450°C the rate of dissolution of iron increases 16 fold when the oxide content is increased from 0.01 to 0.04% by weight. Hempel [6] presents data on the corrosion rate of molybdenum in sodium containing 0.01 and 0.05% of oxygen by weight at 705°C. In the first case the corrosion rate is equal to a weight loss by the specimens of the order of 0.00014 milligrams/ /cm^2-hour, while in the second case it is 0.0111 milligrams/cm^2-hour.

It is shown in [5] that the presence of oxygen in sodium reduces the temperature at which intercrystalline corrosion starts in stainless steel. Thus brand 304 steel was subjected to initial intercrystalline corrosion to a depth of one-two grains when held for 2500 hours at 300°C in sodium with an 0.8% oxygen content by weight. Precisely the same corrosion effect was observed in specimens of this steel brand when tested in sodium with 0.003% of oxygen by weight at 710°C for 3000 hours.

The above facts, which could be continued, show that, when the oxygen content of sodium is increased, the structural materials are subjected to corrosion failure at a high rate due to the additional development of some chemical process.

Published data are available on this problem. Horsley [7], referring to [8] has shown experimentally that when heating sodium containing 5 and 10% of oxygen by weight in iron crucibles at 800°C for seven days ferrites with compositions $Na_2O \cdot FeO$ and $(Na_2O)_2 \cdot FeO$ are formed on the wall (this was shown by x-ray analysis). When using sodium with a lower oxygen content (0.005, 0.01 and 0.16% by weight) no ferrite containing films were discovered on the crucible walls. Nevertheless, Horsley has suggested that the intensifying effect of oxygen on metal corrosion in sodium consists in the formation of chemical compounds such as ferrites, which are highly soluble in sodium.

Harbourn [9], and Weeks and Klamut [10] in examining the problem of mass transfer came to the conclusion that oxidation of metal (for example, of iron)

$$Fe + Na_2O \rightarrow 2Na + FeO; \qquad (1)$$

may take place in the hotter part of the circulation system. It is assumed that in the cooler part of a nonisothermal circulating system the ferric oxide is reduced by the sodium, yielding the metal

$$FeO + 2Na \rightarrow Fe + Na_2O. \quad (2)$$

Hence, the transported masses consist of sintered highly-dispersed iron powder.

To clarify the detail the mechanism of the accelerating effect of oxygen on corrosion of structural materials in sodium it is interesting to examine the chemical nature of the oxygen dissolved in the sodium. Analyzing elementary physiochemical processes of corrosion it was decided on theoretical considerations that partial dissociation of sodium oxide in the liquid sodium into ions is possible and /303 a suggestion was made that the active form which accelerates the corrosion of metals in sodium are the negative oxygen ions. To check this assumption experimentally, direct current was passed through oxygen-containing liquid sodium. This method was used previously for a number of important studies for determining the nature of hydrogen, carbon and sodium dissolved in liquid copper and steel [11], as well as of carbon in hard steels [12-15].

U-shaped vessels with two hollow spheres at the ends, into which molybdenum electrodes were soldered, were made from Pyrex. The vessels were filled under vacuum with sodium, containing from 0.03 to 0.07% of oxygen by weight. The filled and soldered vessels were held in a furnace at 300 ± 5°C and simultaneously with this 2 amps of direct current was passed through them for 1-6 hours. After termination of the experiments the sodium (1.7 grams) held in the anode and cathode spheres was analyzed chemically for oxygen. Results of eight experiments are shown in Table 1, from which it can be seen that in all cases the oxygen was transported

TABLE 1. Results of Chemical Analysis for Oxygen and Certain Theoretical Data on Electron Transfer of Oxygen in Sodium at 300°C (With a Current of 2 amps).

Experiment No.	Test duration hours	Before experiment		After experiment				By what factor has the oxygen content in the anode spheres increased as compared with cathode spheres	Quantity of oxygen transported to anode per 1 amp-hour milligrams
				Anode spheres		Cathode spheres			
		10^2% by wt.	milligrams	10^2% by wt.	Milligrams	10^2% by wt.	Milligrams		
1	1	2.4	0.4	3.2	0.55	1.6	0.27	2	0.07
2	2	4.7	0.8	6.3	1.07	3.1	0.53	2	0.07
3	2	3.85	0.65	6.1	1.03	1.6	0.27	3.8	0.09
4	6	5.65	0.96	10.5	1.78	0.86	0.14	12	0.07
5	4	6.4	1.08	9.3	1.58	3.5	0.60	2.7	0.06
6	3	3.75	0.64	6.5	1.1	1	0.17	6.5	0.07
7	4	4.35	0.74	7.6	1.3	1.1	0.18	7	0.07
8	5	7	1.19	9.8	1.7	4.2	0.72	2.3	0.05

only to the anode vessels (to the positive pole); here the amount of oxygen transported per 1 amp-hour was practically constant. Thus the experimental results show that, at the low oxygen solubilities in sodium at 300°C, negatively-charged oxygen ions travel to the anode.

It stands to reason that at a higher temperature not only the solubility [16] but the electrical transfer of oxygen ions in the sodium should increase. Experiments were performed at 600°C in steel tubes 12 mm in diameter, with a wall thickness of 0.4 mm and length of 180 mm for 2 and 4 hours. At the middle of each tube was placed a steel tube segment, which served as an oxygen source. /304

The tubes were filled under vacuum with sodium containing $6\text{-}8 \cdot 10^{-3}$% of oxygen by weight, welded up and held in a furnace while direct current at the rate of 10 amps was passed through them [17, 18]. After termination of the experiment the tubes were frozen and their anode and cathode ends were cut off under vacuum. Without removing them from the vacuum chamber, the cut off ends of the tubes were analyzed chemically for the oxygen content (Table 2). A control test without passing of current showed that at 600°C the inner glass tube interacted with the sodium and enriched it with oxygen from 0.008% by weight (starting content) to 0.10-0.11% by weight (by a factor of 13.75 during 4 hours).

TABLE 2. Results of Chemical Analysis for Oxygen and Some Theoretical Data on Electron Transfer of Oxygen in Sodium at 600°C.

Test number	Conditions	Oxygen content in the ends of tubes, % by weight		Oxygen transported to the anode per 1 amp-hour	
		anode (+)	cathode (-)	% by wt.	milligrams
1 (four tubes)	600°C, 10 a, 2 h	0.32	0.0045	0.0157	1.943
2 (four tubes)	600°C, 10 a, 4 h	0.87	0.0037	0.0216	2.674
3 (two tubes)	600°C, without current, 4 hours (control test)	0.11	0.1	—	—

Experiments in which current was passed show that appreciable amounts of oxygen are carried only to the positive poles of tubes. In experiment No. 1, 1.943 milligrams were passed per 1 amp-hour, while in experiment No. 2, 2.674 milligrams of oxygen were carried over. This difference can be attributed to the time difference and to the fact that sodium oxide was supplied by the glass tubes into sodium not yet saturated with oxygen. The experiments at 300-600°C have shown that transport of negatively charged oxygen ions is observed to the positive pole; here 30 times more oxygen is carried at 600°C. This leads to the conclusion that

the oxygen dissolved in the sodium is in the ion state. But since molarization takes place simultaneously with the dissociation, we must use the balance equation

$$Na_2O \rightleftarrows 2Na^+ + O^{-2}. \quad (3)$$

Apparently, sodium oxide exists in sodium in the stable form as colloidal and other particles. Most probably the molecular solution of sodium oxide exists in negligible concentrations, disappears entirely with an increase in temperature due to displacement of the equilibrium to dissociation. The dissociation is caused by the fact that the neutral atoms of sodium (the solvent) are capable of lightly deforming the outside shell with the valence electron when interacting with the ion lattice of the sodium oxide. As a result of the formation of induced dipoles, the sodium atoms solvate the ions of the sodium oxide and thus weaken the forces of attraction between them. Final dissociation takes place by means of the thermal energy of the medium [19]. On these assumptions the oxygen ion should have the form of the solvated complex

/305

$$[-Na_m + O]^{-2},$$

where m is the number of atoms of sodium solvates with induced dipoles.

Postulation of the existence of oxygen in ionic form in liquid sodium makes possible a new approach in clarifying the corrosion mechanism. For example, the accelerating effect of oxygen on the process of dissolution of steels in liquid sodium can be attributed to the fact that reactions with the participation of most chemically active ionic form of oxygen (for dissolution of iron) take place in the diffusion layer at the interface

$$Fe^0 + O^{-2} \rightarrow FeO + 2e^-, \quad (4)$$

$$2Na^+ + 2e^- \rightarrow 2Na^0. \quad (5)$$

These reactions should have high rates. Quantitatively they are limited only by the rate of supply of oxygen ions. Each act of formation of ferric oxide disturbs the solubility equilibrium at the given temperature and a corresponding number of iron ions is transferred from the lattice to the diffusion boundary layer. Subsequently the ferric oxide molecules move away from the boundary layer by diffusion (stage which controls the total dissolution rate) and, by virtue of changes in the concentration, are reduced by sodium according to the reaction

$$FeO + 2Na \rightarrow Fe + Na_2O. \quad (6)$$

The above mechanism for the corrosion of iron with participation of oxygen ions is somewhat similar to processes observed on homogeneous catalysis with

formation of intermediate chemical compounds. In our case ferric oxide serves as such a compound.

Corrosion Resistance of Ferritic-Pearlitic Chromium Steels

Austenitic chromium-nickel steels are sufficiently corrosion resistant in sodium up to temperatures of 650-700°C. But, due to their relatively low thermal conductivity and high thermal expansion coefficient, these steels can crack under alternating thermal loads. Hence, it is of great interest to examine the corrosion resistance of ferritic-pearlitic nonnickel steels, the chemical composition /306
of which is shown in Table 3. The steels were tested in a sodium stand at temperature of 500, 600 and 700°C, in sodium flowing at 5 and 12 m/sec and containing 2-5% of oxygen by weight. Upon metallographic examination of the specimens after holding in the above sodium flows, no corrosion interaction zones were observ- /307
ed in the overwhelming majority of steels. Only in the EP-78, EP-79, 1Kh1MFS and 12KhMF steels was there observed an elevated corrosion of grain boundaries in the surface layer at the surface to a depth of 10-20$\mu\mu$ at 600°C. But the quantity of the pearlitic component in the majority of the tested steels decreased appreciably (as compared with the starting composition) as early as at 500°C, while steels such as EP-78, EP-79, 1Kh2M, 12KhMF and 12Kh2MFSR practically completely lost their carbon at 600°C, which is also substantiated by chemical analysis (Table 4). Only the EI-802 steel retained its starting structure when held for long /308
time periods in sodium at 700°C. The carbon content of the EI-531 and EI-802 steels, as shown by chemical analysis, practically did not change. Changes in the weight of specimens of all the pearlitic-class steels tested per unit time were practically insignificant and varied within the limits of 0-0.0003 milligrams/cm^2-hour, depending on the test temperature.

TABLE 3. Chemical Composition of Pearlitic and Chromium Steels

Steel brand	Element content, % by weight						
	C	Si	Cr	Mo	V	Nb	W
12KhMF	0.11	0.20	1.03	0.25	0.20	—	—
EP-79	0.16	0.83	1.10	0.36	0.22	0.33	—
EP-78	0.13	0.52	1.16	0.50	0.20	—	—
1Kh1M1FS	0.15	0.52	1.20	1.03	0.26	—	—
12Kh2MFSR	0.14	0.53	1.76	0.56	0.24	—	—
1Kh2M2F	0.14	0.95	2.19	1.54	0.32	—	—
1Kh2M	0.15	0.08	2.25	0.99	—	—	—
EI-531	0.17	0.57	2.51	0.65	0.31	0.64	—
1Kh5MS	0.14	1.54	6.32	0.70	—	—	—
EI-802	0.14	0.10	11.6	0.67	0.42	0.30	0.30
EI-993	0.20	0.38	12.4	0.52	0.31	0.52	0.59
EP-38	0.17	1.33	13.6	0.78	0.41	0.37	—

TABLE 4. Decarbonization of Pearlitic and Chromium Steels in a Flow of Sodium (Flow Velocity of 5 m/sec)

Steel brand	Test time, hours	Carbon content, % by weight			
		Starting	After holding in sodium at the temperature, °C		
			500	600	700
12KhMF	2000	0.11	0.06	0.03	—
EP-79	2000	0.16	0.1	0.09	—
EP-78	2000	0.13	0.06	0.05	—
1Kh1M1FS	2000	0.15	0.06	0.09	—
12Kh2MFSR	2000	0.14	0.08	0.02	—
1Kh2M2F	2000	0.14	0.1	0.1	—
1Kh2M	1800	0.15	0.1	0.06	—
EI-531	1800	0.17	0.17	0.14	—
1Kh5MS	2000	0.14	0.14	—	—
EI-802	6500	0.14	—	0.13	0.13
EI-993	6500	0.2	—	—	0.14
EP-38	6500	0.17	—	—	0.05

The mechanical properties of steels tested in sodium (Table 5) differ noticeably from the properties of the same steels held at the same temperature in a container with argon ("without a medium"). The mechanical properties of EI-531 and EI-802 steels practically did not change when they were tested in a sodium flow at temperatures of 600 and 700°C. The above shows that changes in the structure of ferritic-pearlitic chromium steels and in their mechanical properties on holding in a sodium flow takes place as a result of decarburization of these steels, the rate of which at a given temperature depends on their alloying-element content (chromium, niobium, canadium and tungsten), which binds the steels carbon into stable carbides. The higher the quantity of carbide-forming elements, the stronger is the carbon bound in complex carbide compounds and the more stable all the properties of steel subjected to liquid sodium.

The carbon content of the steel should not exceed the quantity needed for formation of stable carbides with the carbide-forming elements added to the steel. In the opposite case the steel gives up the excess carbon which will be carried by the sodium flow to other sections of the appâratus where, as a result of this, part and components made from austenitic stainless steels may become carbonized, which may result in embrittlement and failure. Thus, the EI-993 steel contains in the initial state somewhat more carbon than the EI-802 steel (0.20 and 0.14%, respectively), while the content of other elements is approximately the same. When tested at 700°C in the flow of sodium for 6500 hours the EI-993 steel lost the entire excess carbon, and in the final count it only retained as much of it as contained in the EI-802 brand. If, however, excess carbide-forming elements are added to the steel, this can impair the workability of the steel (ease of rolling, welding, etc.). Experiments show that high-chromium pearlitic steels, for example, EI-802, 1Kh13 and others also tend to carbonization in the flow of sodium if the latter is contaminated by hydrocarbons to some degree. Carbonization

takes place to a great depth and the plasticity of steel then is highly reduced, which can result in failure of components.

TABLE 5. Mechanical Properties of Ferritic-Pearlitic Steels Tested in a Sodium Flow (Velocity of 5 m/sec)

Steel brand	Temperature, °C	Time, hours	After holding without a medium		After testing in sodium	
			σ_u, kg/mm^2	δ, %	σ_u, kg/mm^2	δ, %
12KhMF	500	2000	51	21	38	29
	600	2000	51	25	29	39
EP-79	500	2000	59	27	51	27
	600	2000	59	25	43	36
EP-78	500	2000	60	21	45	29
	600	2000	52	26	39	36
1Kh1M1FS	500	2000	67	16	52	18
	600	4000	55	17	40	35
12Kh2MMFSR	500	3600	60	25	52	21
	600	3600	55	29	37	33
1Kh2M2F	500	2000	67	16	63	15
	600	4000	65	14	53	26
1Kh2M	500	1800	44 *	30 *	41	31
	600	1400	44 *	30 *	34	38
EI-531	500	1800	46 *	27 *	46	27
	600	1400	46 *	27 *	44	28
1Kh5MS	500	3600	82	20	78	19
	600	3600	74	19	66	22
EI-802	500	2000	51	25	48	24
	600	2000	52	24	46	25
	700	4000	49	22	45	22
EI-993	500	3600	91	17	93	13
	600	3600	87	17	77	17
	700	2500	57	22	59	21
	700	6500	57	22	57	24
EP-38	500	3600	91	17	93	13
	600	3600	90	18	77	18
	700	2500	68	12	68	13
	700	6500	68	12	67	12

NOTE: The asterisk denotes the mechanical properties of steels in the initial state, i.e., after heat treatment; σ_u is the ultimate strength of steel and δ is the relative elongation.

It can be claimed on the basis of the above data that corrosion processes in ferritic-pearlitic steels held in sodium are practically independent of the flow velocity in the velocity range at hand (5-12 m/sec).

No erosion-type failures were observed in steel specimens tested at flow velocities of 12 m/sec.

Corrosion Resistence of Austenitic Stainless Steels

Austentic stainless steels are capable for prolonged operation in sodium at /309
temperatures up to 650-700°C; they are sensitive to the oxygen content of the sodium. At oxygen contents of up to $5 \cdot 10^{-3}$% by weight [these] steels are not subject to appreciable corrosion failures. However, at higher concentration corrosion is observed with predominance of intergranular corrosion (Table 6).

TABLE 6. Chemical Composition of Stainless Austenitic Steels Which Were Tested

Steel brand	Alloying Element, % by weight							
	C	Si	Cr	Ni	Nb	Mo	Ti	W
1Kh10N10T	0.06	0.43	17.5	10.3	—	—	0.45	—
EI-448	0.08	0.51	16.5	12.5	—	2.01	0.52	—
EI-211	0.06	2.6	19.1	14	—	—	—	—
EI-888	0.07	3.9	13.3	14	0.6	—	—	—
EI-847	0.07	0.26	15.6	15	0.7	3.04	—	—
EI-844	0.02	0.46	15.1	15.1	—	3.05	—	—
EI-854	0.09	0.35	14	15.7	1	—	—	—
EI-850	0.02	4.36	11.8	16	0.53	—	—	—
EI-403	0.08	0.88	17.9	16.3	1.22	1.22	—	—
EI-851	0.11	0.27	13.8	19.1	1	—	—	2.34
EP-71	0.03	0.26	21.6	21.5	—	—	1.2	1.29
EP-148	0.1	0.27	21.5	24.1	1.07	2.62	—	1.4

Austenitic stainless steels can become highly carburized when the sodium is contaminated by carbon-containing compounds or when the liquid metal is simultaneously in contact with carbon or pearlitic steels. Here their plasticity is sharply reduced. Consequently, use should be made of proper combinations of materials in order to avoid [excessive] oxygen content in the system and contamination of the liquid sodium by hydrocarbons.

In our experiments we have discovered transport of nitrogen from the gas atmosphere to the surface of the austenitic steel. When nitrogen was used as a protective gas for the sodium, we have observed nitriding of the ducts of our setup which were made from 1Kh18N10T steel. The setup operated with an isothermal flow of sodium at a temperature of 450°C for one year. Metallographic ex- /310
amination of the inner surface of ducts showed a narrow (10 micromicrons) light strip with a high hardness. Structural analysis by x-rays showed presence of chromium nitrides on the surface. A similar light band was also observed on specimens from 1Kh18N10T steel, tested on the stand in isothermal flow of sodium at 400°C during 1800 hours. A two-phase structure is observed from the surface to a depth of 5 micromicrons consisting of nitrogen-saturated ferrite, chromium nitrides and austenite. The specimens increased insignificantly in weight due to the nitriding.

Here the ultimate strength of the steel did not change, but the plasticity reduced appreciably. While in the initial state the relative elongation of the steel was 44%, then after testing in sodium flow it dropped to 34%. The above examples show that it is not permissible to use nitrogen as a protective gas for sodium, since this can result in embrittlement of the elements of apparatus due to nitriding. It may be assumed that at temperatures higher than 400 and 450°C the 1Kh18N10T steel would have been nitrided to a greater extent.

Chronium-nickel stainless steels in the form of tubular or flat tension specimens were tested at temperatures of 600 and 700°C in sodium flowing at 5 and 12 m/sec with an oxygen content of $3 \cdot 10^{-3} - 7 \cdot 10^{-3}$% by weight. It can be seen from Table 7 that the weight of all the austenitic steels was reduced in the tests. As was shown experimentally, the tendency of these steels to mass transfer becomes apparent when corrosion tests are made in a flow of liquid sodium starting with 600°C. When testing at this temperature the specimens changed their weight very little (0.0008 milligrams/cm^2-hour), while in tests at 700°C the rate of weight loss increased to about 0.0030 milligrams/cm^2-hour (experiment time 4000 hours). The reduction in the weight of specimens serves as grounds for the conclusion that austenitic steels have a greater tendency to the transfer of mass than ferritic-pearlitic steels, which is due to their nickel content which has an appreciably higher solubility in sodium than iron and chromium.

Metallographic analysis of austenitic steels shows corrosion interaction of intercrystalline character (high corrosion of grain boundaries). At 600°C it was observed primarily only in those specimens of these steels which were tested in sodium containing $7 \cdot 10^{-3}$% of oxygen by weight, and it is absent at oxygen concentrations of $3\text{-}4 \cdot 10^{-3}$% by weight. In the case of the higher oxygen content, the depth of intercrystalline interaction of EI-211, 1Kh18N10T and EI-448 steels at 600°C is as high as 70-150 micromicrons during 5100 hours. Specimens from 1Kh18N10T steel tested in sodium at 700°C for 6500 hours had an appreciably smaller depth of corrosion (20-30 micromicrons) due to the lower oxygen content of the sodium, while no corrosion interaction zones were observed in specimens from EL-211 steel. The test results show that the corrosion resistance of austenitic steels depends to a large extent on the oxygen content of the sodium. All the tested steels of this class are sufficiently corrosion resistant materials in the flow of liquid sodium at temperatures up to 700°C, if the oxygen content does not exceed $5 \cdot 10^{-3}$% by weight.

The mechanical properties of austenitic chromium-nickel steels tested at 600°C in sodium differed little from the properties of the starting material (after quench hardening) and from the properties of the same steels held at the same temperature in an inert-gas atmosphere. /311

At 700°C practically all the austenitic steels exhibit aging tendencies to one or another degree, which produced some increase in the ultimate strength (σ_u) and a reduction in the relative elongation (δ). Here the mechanical properties of specimens tested in sodium are on the level of properties of specimens held in argon. This means that processes which bring about the changes in mechanical /312

TABLE 7. Results of Corrosion Testing and Changes in Mechanical Properties of Austenitic Chromium-Nickel Steels in a Flow of Sodium (Velocity 5 m/sec)

Steel brand	Temperature, °C	Time, hours	Maximum depth of corrosion, microns	Oxygen content of sodium, % by wt.	After holding without medium		After testing in sodium	
					σ_u kg/mm^2	δ, %	σ_u kg/mm^2	δ, %
1Kh18N10T	600	1500	50	7	69	31	70	26
	600	5100	100	7	69	31	75	25
	700	2500	20—30	4	66	19	67	27
	700	6500	20—30	4	66	19	70	26
EI-448	600	1500	80	7	69	20	75	13
	600	5100	150	7	69	20	75	15
EI-211	600	1500	30	7	58	30	67	27
	600	5100	70	7	58	30	64	24
	700	2500	0	4	46	4	59	5
	700	6500	0	4	46	4	58	5
EI-888	700	2500	0	4	73	25	68	30
	700	6500	20—30	4	73	25	70	30
EI-847	600	2000	0	3—4	62	45	56	43
	600	4000	0	3—4	—	—	—	—
	700	4000	20	4	69	32	68	32
EI-844	600	2500	0	5	55	28	56	36
	600	5500	0	5	54	32	58	24
EI-854	600	2500	40	5	57	24	56	27
	600	5500	60	5	55	26	56	17
EI-850	600	2500	50	5	76	28	74	30
	600	5500	80	5	66	16	70	17
EI-403	600	2000	0	3—4	69	39	61	38
	700	4000	30	4—5	72	29	73	28
EI-851	600	2500	50	5	57	27	58	25
	600	5500	50	5	53	15	58	21
EP-71	600	4000	—	3—4	94	23	93	23
	700	4000	15	4—5	79	18	82	23
EP-148	600	4000	—	3—4	71	28	70	31
	700	4000	15	4—5	79	20	79	20

properties are not related to the corrosive action of the sodium. The plastic properties drop most appreciably in the EI-211 steel, due to intensive separation of the secondary phase at 700°C not only along grain boundaries but also in the grain proper. In the 1Kh18N10T, EI-847 and EI-888 steels the separation of new phase components takes place primarily along grain boundaries.

X-ray diffraction studies of steel tested in sodium as well as held in argon, show that the composition of phases precipitated in the process of aging is different for each steel brand and is related to the alloying components. For EI-847 steel which has a high molybdenum content, the precipitate was the Fe_3Mo intermetallic compound (Laves' phase). The EI-888 steel contains about 4% of silicon

and hence, a substantial amount of the complex intermetallic compound $Ni_2(Cr, Fe)Si$ is precipitated in this steel in the process of aging.

The amount of TiC in the structure of the 1Kh18N10T steel increased and, in addition, a noticeable quantity of the sigma phase appeared. Thus, examination of the mechanical properties, microstructure and data of x-ray diffraction analysis show that all the austenitic steels are structurally unstable to some extent at 700°C, but the majority of them retain satisfactory mechanical properties even after exposure of 6500 hours.

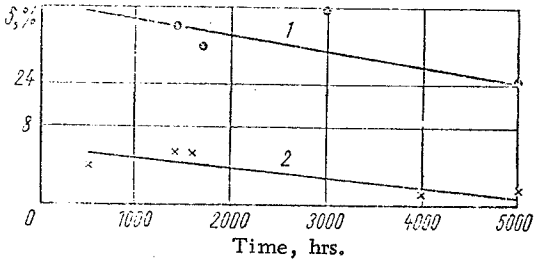

Figure 1. Relative Elongation of EI-211 Steel Tested in Flow of Sodium at 600°C as a Function of the Test Time and of the Oxygen Content of the Sodium.

1) at $5 \cdot 10^{-3}$% by Weight;

2) at $4 \cdot 10^{-3}$% by Weight.

Intercrystalline corrosion interaction with sodium reduces the plasticity of austenitic steels. Figure 1 shows the change in the relative elongation of the EI-211 steel as a function of the testing time at 600°C and of the oxygen content of the sodium. Despite some scatter of the experimental points it can be seen that the plasticity of austenitic steels depends appreciably on the oxygen content of the sodium.

No effect of the rate of the liquid sodium (12 m/sec) on the corrosion or erosion of stainless chromium-nickel steels was observed. /313

Corrosion Resistance of Heat-Resistant Alloys With a Nickel Base

Work with liquid sodium at high temperatures requires materials with high heat resistance. Nickel-base alloys such as Nimonic are heat resistant up to temperatures of 850-900°C. We have tested the following nickel-base alloys in the flow of sodium: EI-437b, EI-559A and Kh20N60M5V10Yu2T2 and, for comparison, we have also tested the EI-211 stainless chromium-nickel steel containing about 14% of nickel by weight (Table 8). The corrosion tests were performed at sodium temperatures and velocities of 700-930°C and 2 m/sec. The oxygen content of the sodium was maintained at $6 \cdot 10^{-3}$% by weight or less by a cold trap. The testing time at each temperature was 300 hours.

The results of these experiments are shown in Fig. 2. The experimental data point to a sharp increase in the rate of mass transfer for Nimonic-type alloys at temperatures above 800°C. The rate A of mass transfer in the temperature range of the test can be expressed by the formula

$$K = K_0 \cdot e^{-\frac{Q}{RT}}, \qquad (7)$$

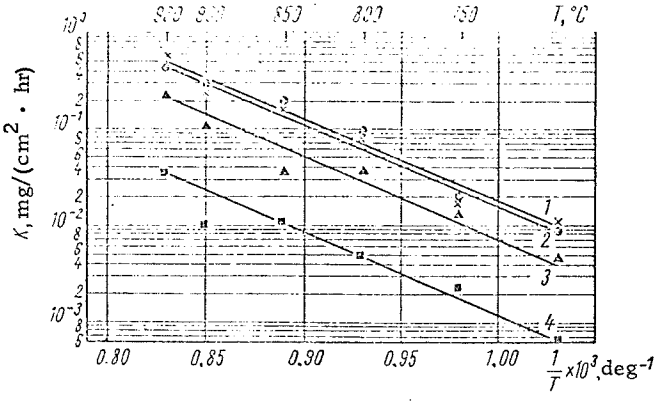

Figure 2. The Rate of Mass Transfer (K) as a Function of the Temperature (T, °K).

1) The EI-437b Alloy; 2) The Kh20N60M5V10-Yu2T2 Alloy; 3) The EI-559A Alloy; 4) EI-211 Steel.

where K is the rate of mass transfer, milligrams/cm^2-hour; K_0 is a coefficient, constant for a given material, which takes into account the effect of various factors on the mass transfer, milligrams/cm^2-hour, R is the universal gas constant, which is 1.987 cal/gram-atom-degree, T is the temperature, °K, and Q is the heat of dissolution, cal/gram-atom (in the graph this is the tangent of the slope of line in K to axis 1/T). /314

The K_0 and Q calculated on the basis of experimental data are shown in Table 9. The magnitudes of Q are very close for all the materials tested and apparently are characteristic of lattices with gamma structures, since we have here the dissolution of nickel-containing materials. The products of mass transfer after the EI-437b alloy has been held in a flow of sodium at 880°C for 190 hours contained 21.5% by weight of chromium, 72.0% by weight of nickel and 0.93% by weight of titanium. Initially the EI-437b alloy was composed of 77% by weight of nickel, while after the test the nickel content dropped to 59% by weight. Consequently, as they became dissolved from the surface of the alloy, the nickel atoms, by diffusion from the inner volume of alloy (which is shown by layer-by-layer chemical analysis) again were supplied to the surface, where they were dissolved by the sodium, etc. This mechanism of leaching out of nickel from alloys may continue for a long time with attendant constant reduction in the nickel content. The calculated heat of dissolution Q is an average for the individual components of the alloy. /315

All the tested materials can be arranged by their readiness to dissolution and to mass transfer in the following order: EI-211 steel, the EI-559A, Kh20N-60M5V10Yu2T2 and EI-437B alloys. It can be seen from this that the rate of mass transfer is directly proportional to the nickel content. Addition of aluminum to nickel-base alloys reduced the mass transfer rate. As is shown experimentally, the EI-559 alloy is more prone to mass transfer than the EI-559A alloy, although the nickel content in the former is even somewhat lower than in the latter; however, the aluminum content of the EI-559A alloy is higher, due to which it is less subjected to mass transfer in sodium than the EI-559. The EI-827 Nimonic-type alloy with a high nickel content (74% by weight) exibited very high corrosion resistance to the transfer of mass in sodium also due to its elevated aluminum content. Aluminum binds the nickel into the stable Ni_3Al compound and thus reduces its diffusion mobility and consequently also the tendency to dissolution in sodium.

The mass transfer rate is not only a function of the temperature but also of the test time. Figure 3 shows that K, the mass transfer rate increases with an

TABLE 8. Chemical Composition of Nickel-Base Heat-Resistant Alloys and of the EI-211 Steel

Material	Content of alloying elements, % by weight								
	C	Si	Cr	Ni	Mo	Al	Fe	Ti	W
EI-437b	0.05	0.38	20.6	75	—	0.35	0.43	2.54	—
Kh20N60M5V10Yu2T2	0.1	—	20	60	5.0	2.3	—	1.3	10
EI-559	0.1	0.5	18.2	55.9	—	2.3	23	—	—
EI-559A	0.02	0.5	16.6	57.8	—	3.3	21	—	—
EI-827	0.07	0.4	10	74	6.0	4.3	--	—	5.0
EI-211	0.16	2.4	20.6	13.8	—	—		—	—

NOTE: The EI-437b, Kh20N60M5V10Yu2T2 and EI-827 alloys contain about 0.01% by weight of boron.

1) Material; 2) Content of Alloying Elements, % by Weight 3) EI; 4) KHZON6OM5VIOYU212

TABLE 9. Magnitudes of K_0 and Q for the Materials Tested

Material	$K_0 \times 10^{-5}$ mg/(cm^2 · hr)	Q, cal/gram-atom
EI-437b	79.52	39 900
Kh20N60M5V10Yu2T2	80.05	40 000
EI-559A	52.65	40 800
EI-211	9.93	41 100

1) Material; 2) Milligrams/cm^2- hour; 3) Q, cal/gram atom; 4) EI-4376; 5) KH2ON6OM5VIOYU2; 6) EI-559A; 7) EI-211

increase in the holding time, i.e., the longer the test the higher the loss of weight per unit time. And only for the EI-211 steel is the rate of mass transfer constant at 930°C. The experiments have shown that mass transfer is reduced appreciably with improved finish of the surfaces washed by the liquid metal. Nickel has a higher solubility in sodium than other components of structural materials. Due to the difference in the dissolution rates of the alloy base and of its alloying components, the surface in contact with the sodium obviously increases, due to the appearance of rough spots and hence, the rate of mass transfer also increases. Since an increase in the surface results in increasing the mass transfer rate, then the working surfaces of components and elements in contact with liquid sodium should have a high finish.

All the experimentally studied nickel-base alloys are, to one degree or another, prone to mass transfer. The dissolved components are carried by the sodium from the hot to the cooler zone, where they are saturated and precipitate. This process is highly dangerous, since the transfer products which form are capable of accumulating in the cold zone of the device and to plug up the liquid-metal passages. The transported masses start to precipitate on the walls of the stand's ducts when the /316

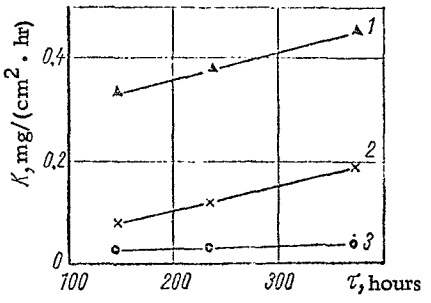

Figure 3. The Rate of Mass Transfer (K) as a Function of the Holding Time (τ) at 930° for the Following Nickel-Base Alloys.

1) Kh20N60M5V10Yu2T2; 2) EI-559A; 3) EI-211 steel.

liquid metal's temperature is reduced by as little as 20-30°C and move along the duct surfaces up to temperature zones of 600°C (for a test temperature of 630°C). Numerous experiments show that thickest layers of the transfer products form at points of reduction in duct cross sections (or in slots), where the rate of flow of the liquid metal is increased appreciably. Residues of the transferred mass are sintered to metal walls at temperatures of 600°C and above and are held there very strongly, while at temperatures below 600°C they are quite loose and are poorly bound to the base.

Corrosion Resistance of Refractory Metals

Refractory metals such as molybdenum, niobium, etc., can be used as structural materials with liquid sodium. Corrosion studies of molybdenum and niobium specimens, tested in a flow of sodium at 5 m/sec and with an oxygen content of $4 \cdot 10^{-3}$% by weight during 3600 hours at 600 and 700°C show that molybdenum has satisfactory corrosion resistance under these conditions, while the niobium specimens failed practically completely as early as at 600°C. The molybdenum had an insignificant weight gain. Similar results were obtained when testing in a sodium flow at 930°C. The molybdenum specimens increased insignificantly in weight, while the niobium specimens, even if they did not fail during the test (300 hours), exhibited a very high rate of weight loss (about 0.1 milligrams/$/cm^2$-hour).

A large number of tests performed with molybdenum in liquid sodium heated to up to 1050°C have verified its high corrosion resistance. Results of studies show that the corrosion resistance of molybdenum does not depend on the rate of flow of the liquid metal in the velocity range under study (0.2-2.5 m/sec). When the oxygen content of the sodium was held to $2 \cdot 10^{-2}$% by weight, no embrittlement of molybdenum specimens was observed and their mechanical properties at the end of the test remained on the initial level. In all cases a slight increase in the weight of molybdenum specimens was observed, which apparently is due to the formation, at the surface, of an intermetallic molybdenum-nickel compound such as MoNi (the ducts and other components of the stand were made from the EI-211 chromium-nickel steel). Metallographic analysis did not show any corrosion zones on molybdenum specimens held in a flow of sodium at 600, 700 and 930°C. /317

The corrosion resistance of niobium depends on the oxygen content of the liquid metal (Fig. 4). The rate of corrosion of niobium in sodium flowing at 2 m/sec at 900° C as a function of the oxygen content can be described by the expression (in the range of up to $4 \cdot 10^{-2}$% oxygen by weight)

$$K = 172 \cdot 10^{-5} \cdot e^{84.3 \cdot X}, \quad (8)$$

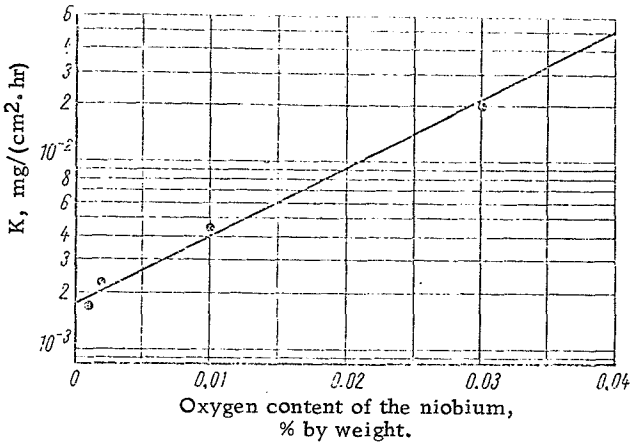

Figure 4. The Corrosion Rate for Niobium as a Function of the Oxygen Content of Sodium at 900°C.

where X is the oxygen content of the sodium, % by weight. Prolonged (3600 hours) testing of niobium even at 600°C and with an oxygen content of $4 \cdot 10^{-3}$% by weight results in total failure of the specimens.

Absence of a corrosion zone in niobium specimens (which lost up to 80% of their thickness) points to the fact that interaction with oxygen results in the formation of very loose, poorly bound niobiates, which were practically completely washed off by the flow of the liquid metal. Only at the surface of individual specimens was there observed a corrosion layer up to 15 micromicrons deep, which consisted of niobium oxides in very poor bound with the base metal.

The strength of niobium specimens tested at 900°C for 300 hours is reduced sharply, while their relative elongation increases, which points to start of crystallization. Metallographic tests also show that niobium undergoes partial recrystallization in the process of tests, which starts usually from the specimen surface.

The rate of flow of the liquid sodium affects the corrosion resistance of niobium. After testing at 900°C in liquid sodium flowing with velocities of 0.2 (in convection loops), 1.0 and 2.5 m/sec (in a circuit) the rates of weight loss by the /318 niobium (for the same oxygen content) were 0.04, 0.06 and 0.10 milligrams/cm^2-hour, respectively. Obviously, when the flow rate of liquid sodium is increased, a larger quantity of dissolved oxygen arrives at the surface of niobium specimens, which is the factor responsible for the increased corrosion rate. In addition, the increase in the sodium flow velocity should promote a more rapid removal of the loose products of corrosion which form on the niobium surface.

Comparatively prolonged use of niobium in liquid sodium coolant requires that the oxygen content of the coolant be held below $1 \cdot 10^{-3}$% by weight.

REFERENCES

1. Manly W. D.: Corrosion, 12, No. 7, 46-52 (1956).
2. Epstein, L.: In the book: Proceedings of the International Conference on Peaceful Uses of Atomic Energy, Geneva, 1955 (US Publishers McGraw-Hill for Pergamon Press, or vice versa).

3. Hofman, E. E. and Manly, W. D.: Problems in Nuclear Engineering, Lond., 1957.
4. Evans, J. W.: Nuclear Engineering, 4, No. 5, 35 (1957).
5. Bruch, E. G.: Nuclear Metallurgy, 4, No. 2, 20 (1956).
6. Hempel, C. A.: Corrosion, v. 14, No. 12 (1958).
7. Horsley, G. W.: J. Iron and Steel Inst. No. 1, 182 (1956).
8. Kelman, Z. R., et al.: Resistance of Materials to Attack by Liquid Metals. USA, 1950.
9. Harbourn, B.: Corros. Prevent. and Control., v. 5, No. 1 (1958).
10. Weeks, J. R. and Klamut, C. J.: Corrosion of Reactor Materials, v. 1, p. 105, 1962, International Atomic Energy Agency, Vienna.
11. Rabkin, M. A.: Zhurnal prikladnoy khimii, XXX, 5, 791 (1957).
12. Prosvirnin, V. I.: Vestnik metallopromyshlennosti, 12 (1937).
13. Lebedev, T. A. and Guterman, V. M.: Trudy TsNIITMASh, II, 1948.
14. Romadin, K. L.: Trudy Voyenno-vozdushnoy inzhenernoy Akademii im. Zhukovskogo. Issue 157, 1947.
15. Babikova, Yu. F. and Gruzin, P. L.: Fizika metallov i metallovedeniye [Physics of Metals and Metals Science]. Issue 5, page 255. Metallurgizdat, Sverdlovsk, 1957.
16. Zhidkometallicheskiye teplonositeli (natriy) [Liquid-Metal Heat-Transfer Agents (sodium)]. Collection of articles under the editorship of A. Ye. Sheyndlin. Foreign Literature Publishing House, Moscow, 1959.
17. Nevzorov, B. A.: Zhurnal fizicheskoy khimii. Issue 3, XXXV (1961).
18. Nevzorov, B. A.: Nature of Oxygen in Liquid Sodium. In the transactions of the Conference: Corrosion of Reactor Materials, Vol. 2. International Atomic Energy Agency, Vienna, 1962.
19. Nekrasov, B. V.: Kurs obshchey khimii [A Course in General Chemistry]. Goskhimizdat, Moscow, 1954.

DETERMINATION OF THE OXYGEN CONTENT OF SODIUM AND OF THE SODIUM-POTASSIUM ALLOY BY VACUUM DISTILLATION

I. B. Dmitryeva, F. A. Kozlov and E. K. Kuznetsov

Determination of the oxygen content of sodium and of sodium-potassium alloys is one of the more difficult problems of analysis. The method most extensively used is that of mercury extraction, which is based on separation of oxides from metals by transforming it into an amalgam [1]; however, the sensitivity of this method which is 0.01% of oxygen by weight does not satisfy the exacting requirements which are at present being put to purification as well as to content-control of heat transfer agents. The method for determining the oxygen content of conventionally used liquid-metal coolants deserving most attention is that of vacuum distillation, [2], the substance of which consists in separating the metal from its oxides under a vacuum, which is possible due to the great difference in their vapor pressures. /318 /319

Studies performed under laboratory conditions show that increasing the sensitivity of the above method requires increasing the sample weight which is taken for analysis, and reducing possible contamination of the sample in the process of taking it and in preparation for analysis. In order to do this, various versions of distilling samplers have been devised, which can be used for taking a sample of the coolant (weighing 100 grams) directly from the circuit and to analyze it by the vacuum distillation method. The samples are taken rapidly, the time needed for this being not more than a minute and a half, which eliminates the possibility of redistribution of oxides during sampling. The fact that sampling and analysis are made by the instrument means that the sample will not be contaminated when it is prepared for analysis. For the sodium-potassium alloy this method of analysis for oxygen is more expedient, since, due to the fact that this alloy is liquid at room temperature, it is difficult to take a sample for analysis in a different vessel.

Designs of distilling samplers are shown in Fig. 1. The device shown in Fig. 1b can be used to take sequential samples at intervals from several minutes to several hours with subsequent simultaneous distillation of all the four samples. This device consists of three valves and a vacuum chamber. That part of it which is shut off by the valves is the vessel from which the samples are taken. In order that the metal should not get spilled when pouring the sample into the cup held in the vacuum chamber, a special tube has been provided. It is necessary to carefully remove the alkaline metal from the vacuum chamber's surface, in order to eliminate additional contamination when taking the following sample. To make the valve more accessible for washing, the tube is removable. The specified distillation temperature is maintained by an adjustable-heat furnace, and is monitored by thermocouples. The vapors of liquid-metal coolants condense on the surface of a baffle plate, which prevents the vapor from getting into the vacuum line, and at the lower flange. The device is split into two parts so that the cup with the residue can be removed after the distillation. The system is made airtight by a vacuum-rubber gasket.

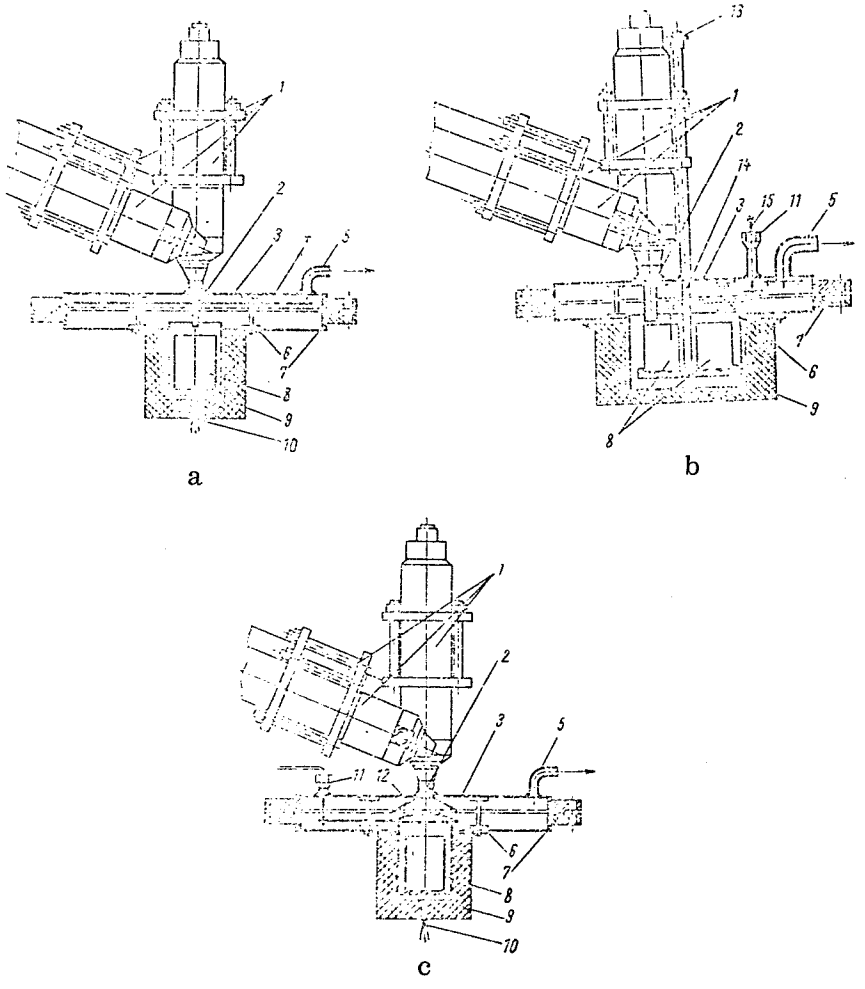

Figure 1. Designs of Distilling Samplers for Work With Sodium (a and b) and With Sodium-Potassium Alloy (c).

1) Liquid-Metal Valves; 2) Drain Tube; 3) Vacuum Chamber Casing; 4) Baffle Plate; 5) Line to Vacuum Pump; 6) Thrust Pieces; 7) Packing; 8) Sampling Cup; 9) Furnace; 10) Thermocouple; 11) Packing; 12) Rotary Baffle Plate; 13) Cup Position Indicator; 14) Rotary Bar; 15) Movable Level Gage.

Keeping in mind the specifics of work with the sodium-potassium alloy, the above device has been equipped with a rotary baffle plate, which is placed into the cover of the vacuum chamber through the packing and with a funnel, which protects /320 the cup from metal which may fall into it from condensation surfaces.

Experimental method. Before the vacuum chamber is assembled, its inside surfaces and the cup are throughly washed with distilled water and alcohol and are

dried. After assembly the chamber is washed with argon and evacuated to a residual pressure of $1 \cdot 10^{-2}$ mm of Hg. Before sampling the cup is degassed at 500-550°C. Simultaneously with this the rate of flow of the metal through the sampler is adjusted to 1500 liters/hour.

The device operates under the same temperature mode before the metal is /321
pumped through the sampler as well as during this. The sodium was continuously circulated through the cold trap. The cold trap temperature varied within not more than ±5% of that specified. The sodium was circulated through the distilling sampler for not less than 30 minutes.

Before taking each sample the plugging up temperature was determined not less than twice, using a cock-type oxide-level indicator. The samples were taken only as long as the differences in the plugging up temperature did not exceed 10°C; when this happened the temperature of the still furnace was lowered, the circulation was shut off and, when it was determined that there is no flow, the sample was drained, after which the furnace was put on and the specified temperature established. The vacuum pump operated continuously during the distillation; after the latter was finished the furnace was shut off, the distillation device was cooled, the system was filled with argon and the chamber was dismantled.

To determine the quantity of oxides in the distillation residue the inner surface of the cup was washed with 100 milliliters of distilled water in 10 milliter portions at room temperature. The solution thus obtained was titrated by sulfuric acid in the presence of a mixed indicator and the oxygen content of the sodium was determined. The sample weight was found by collecting the condensate and weighing it; the error in weight due to loss of metal and additional oxidation of it in the air did not exceed 5%, which was verified experimentally.

When four samples were distilled simultaneously, the weight of sodium collected in each cup was determined. For this purpose the sodium temperature during sampling was determined and, using a level gage (see Fig. 1b) the quantity of sodium in the cup was measured.

Experimental results. Selection of the distillation conditions is a decisive factor in obtaining the required precision for a given method. These conditions should ensure complete removal of the metal from the sample and not permit appreciable vaporization of the oxides. On the assumption that the oxides, after the metal is removed from the sample, are held under the equilibrium pressure of dissociation and that the gas behaves as an ideal gas, we have estimated the possible oxide losses from a nickel cup 40 mm in diameter during one hour. It was found that in a 100 gram sample the oxide losses by evaporation reduce the results by 10^{-5}, 10^{-4} and $7 \cdot 10^{-4}$% by weight for temperatures of 500-600°C, respectively.

The distillation conditions were selected at temperatures of 500, 550 and 600°C with a distillation time of 1 to 40 hours, the oxygen concentration varied here from 0.0005 to 0.02% by weight (Table 1). When the samples are distilled (at temperatures of 500 and 550°C) for 3-6 hours, the reproducilibity of results is satisfactory, which is proven experimentally. When this time was increased /322
(to 25-40 hours at temperatures of 500°C and to about 10 hours at temperatures

TABLE 1. Results of Experiments for Selecting the Distillation Conditions

500° C			550° C			600° C		
Plugging up temperature, °C	Distillation time, hours	Oxygen content, % by weight	Plugging up temperature, °C	Distillation time, hours	Oxygen content, % by weight	Plugging up temperature, °C	Distillation time, hours	Oxygen content, % by weight
218	3	2.3	286	5	5.7	285	1	4.7
222	3	1.9	283	5	5.3	284	3	3.1
225	3	1.9	286	7	4.6	284	5	2
212	4	1.4	282	10	4.6	289	7	1
212	4	1						
205	40	1.4	330	3.5	10			
			319	3.5	8.9			
234	5	5.9	314	5	9.6			
281	7	4.2	315	6	9			
286	10	3.8	325	7.5	7.7			
335	3.5	20	338	10	8.1			
338	3.5	19						
335	3.5	14						
336	6.5	19						
335	7.5	16						
335	10	11						
330	25	7.2						
336	40	6.9						

of 550°C), the quality of results became poorer. This can apparently be attributed to partial vaporization of the metal oxides, as well as interaction between the latter and the cup's material and diffusion into the walls. When the distillation time was 25-40 hours the inner surface of the cup became covered by a blackish-green film, which did not dissolve in water. At 600°C the oxygen content of the sample became smaller in proportion to the distillation time.

On the basis of the results obtained and of the theoretical data, we have selected the following distillation conditions for subsequent tests: temperature 500-550°C, time 5 hours, residual pressure $1 \cdot 10^{-2}$ mm of Hg.

When distilling the alloy, the rotary baffle plate was covered for one hour before the end of distillation, with the result that no alloy drops fell into the cup when the sampler was dismantled.

When using the four-cup sampler, the samples taken first are stored for a prolonged time in the vacuum chamber. To check for further oxygen contamination of the metal [due to the storage time, DBL], we have made special experiments, which show that metal held in a cup under a vacuum of 10^{-2} mm of Hg for 9 hours, did not become oxidized.

The duration of one analysis was 8 hours when using distilling samplers with /323
one cup and 2-3 hours when a four-cup device was used. The amount of oxygen removed from the sampler by vacuum distillation was determined by comparing

the quantity of oxygen added to the sample to that found in the sample after distillation. Here measures were taken to hold the natural oxygen content of the sample to a minimum. It was equal to the concentration which is provided by a cold trap with an inside temperature of 110°C (0.0003-0.0005% by weight).

The oxygen introduced into the liquid metal was measured as follows: before making the analysis a specified quantity of the alkaline solution of sodium hydroxide was placed in the nickel cup; this solution was made to evaporate at 100°C and was finally dried at 150-200°C. The cup with the residue was placed in the vacuum chamber and a sample of the liquid metal was taken from it. In order that the hydroxide should interact with the metal and that the oxides should become distributed over the entire volume of the sample, the latter was held for 2-3 hours at 150°C and only then was the distilling device operated under distillation conditions. These conditions and the subsequent analysis were identical to those described above. Addition of oxygen to the sample by this method yields oxides and a hydride. The latter dissociates under distillation conditions and is removed from the sample.

The alkali hydroxides which are added to the sample should be prevented from being lost or being transformed into carbonates, they also should be dehydrated. We have performed special tests which show that, under the vaporization and drying conditions we have used, no hydroxide losses took place. On the average 7% of the hydroxide became carbonated when vaporizing in air.

When performing the "oxygen put in - oxygen found" experiments the cup /324
was not degased, since this can result in loss of the hydroxide. Therefore, we have performed experiments to determine the control-test value for a degased nickel cup, which, on the average, was $5 \cdot 10^{-4}$% of oxygen by weight, when calculated for a 100 gram sample. The oxygen content of the sodium poured into the cup was determined by a cock-type oxide indicator. On the average the percentage of oxide loss from the sample calculated on the basis of the data of these experiments was 14% (Table 2).

TABLE 2. Results of "Oxygen Added - Oxygen Found" Tests

Starting quantity of oxygen, grams $\times 10^{-4}$	Oxygen added, grams $\times 10^{-3}$	Total amount of oxygen, grams $\times 10^{-3}$	Quantity of oxygen found, grams $\times 10^{-3}$	Oxygen lost, %
5	39	39.5	33.7	15
6	39	39.6	34.7	12
4	39	39.4	32.0	19
6	7.8	8.4	7.0	17
6	7.8	8.4	7.0	17
6	1.56	2.26	2.0	11
3	1.56	1.86	1.4	21
4	1.58	1.98	1.6	19
8	0.84	1.64	1.6	2.0
4	0.78	1.18	1.1	7.0
7	0.78	1.48	1.4	5.0

To determine the control test value it is necessary to use the distilling sampler to take and analyze a sodium sample with zero oxygen content. We could not do this, and hence, the control-test value was determined as the quantity of oxides which form on the surface of the cup when it is held in sodium vapor under the distillation conditions used by us.

The use of the four-cup distillating sampler (see Fig. 1b) made it possible to determine the control-test value for several cups from different metals simultaneously:

Nickel (x 10^{-4}% by weight)	3.7	0.69	4.7	6.6	3.5	2.2	3.8	1.8
Molybdenum (x 10^{-4}% by weight)	1.3	1	0	0.68	1.2	1.8		

The lowest control-test value is given by a molybdenum cup $(1.0 \pm 0.4) \cdot 10^{-4}$% by weight, and a nickel cup $(3.4 \pm 1.4) \cdot 10^{-4}$% by weight, calculated for a sample of 100 grams.

Thus, the minimum oxygen concentration determined by the distilling sampler is $(2\text{-}5) \cdot 10^{-4}$% by weight when using nickel cups and about $1 \cdot 10^{-4}$% by weight when using molybdenum cups. The increase in sensitivity is limited by the control-test value.

The distillation method can be used to determine oxygen concentrations in the range of $1 \cdot 10^{-4} - 5 \cdot 10^{-2}$% by weight.

REFERENCES

1. Pepkowitz, Z. P. and Judd, W. C.: Analyt. Chem. 22, No. 10, 1283 (1950).
2. White, I. C.: Nucl. Sci. Abstrs, 15, 8290 (1957).

THE COCK-TYPE INDICATOR AS AN INSTRUMENT FOR DETECTING ADMIXTURES IN SODIUM

F. A. Kozlov, E. K. Kuznetsov and V. I. Subbotin

A large volume of work has been performed lately for developing a device /324
for continuous sampling and monitoring of admixtures in liquid sodium [1], and [2]. These devices are at present undergoing experimental assimilation and have not as yet come into extensive practical use. It is precisely for this reason that /325
the cock-type indicator described in [3-5] is practically the only one and the most reliable instrument which is used extensively in liquid-metal facilities; it can be used for rapid (30 minutes) and remote determination of the admixture content of the coolant. The operating principle of this indicator is based on the ability of the admixtures precipitating from a solution to plug up passages.

The instruments include a special device with a small passage, a heat exchanger for cooling the liquid metal, adjusting valve or a special pump for establishing the required rate of flow through the instrument, a flowmeter, and thermocouple for determining the temperature of the liquid metal flowing through narrow holes. It is used to determine the oxygen content of sodium and of the sodium-potassium alloy; it can also be used to determine other admixtures the solubility of which changes with the temperature.

Dependence of Readings of the Cock-Type Oxide-Content Indicator on the Main Parameters

Theoretical analysis. The cock-type indicator does not record the precipitation of the first crystals of the oxide, but the time when the resistance of the device due to oxide precipitation increases to such an extent that the flow rate of sodium through the device is reduced from the starting value Q_0 to some quantity Q_1. In general we can write

$$Q_1 = aQ_0,$$

where $0.97 < a < 1$.

The time needed for precipitating the required quantity of oxides (τ_{st}) depends on the design of the instrument and conditions of experiment. The experiment is performed with constant reduction of the temperature of the metal flowing through the hole. When the flow rate drops to Q_1, the plugging up temperature (t_{st}), which is lower than the saturation temperature (t_s) by Δt, is read. Obviously, for a given rate of temperature reduction in the washer $dt/d\tau = \text{const}$

$$t_s = t_{pl} + \tau_{pl}\frac{dt}{d\tau} = t_{pl} + \Delta t. \qquad (1)$$

Let us consider how Δt depends on the main parameters of the instrument and experimental conditions. We shall assume that:

1) The pressure drop in the instrument during the experiments remains constant and is determined from the d'Arcy formula;

2) The entire resistance of the instrument is concentrated in the holes where the sodium flow has the lowest temperature and where are precipitated the oxides which increase the flow resistance of the instrument;

3) The instrument has n holes with diameter d_0 and length l;

4) The flow of sodium through the holes is turbulent and the resistance coefficient is determined by the Blasius law, while the oxide flow per unit surface per unit time is given by the expression [6] /326

$$j = \frac{\xi}{2} \frac{M_{Na_2O} \cdot \gamma_{Na} \cdot \bar{w} \cdot Z}{\varepsilon \cdot 100 M_0 \cdot Pr_D^{3/4}}; \quad (2)$$

5) The flow does not contain crystallization centers moving together with the sodium.

To reduce the flow rate of metal through the instrument from Q_0 to Q_1, the passage cross section must be reduced by some quantity S'. Using the d'Arcy relationship and the Blasius law, it is easy to show that

$$S' = 0.785 \cdot d_0^2 \cdot [1 - a^{11/11}]. \quad (3)$$

With consideration given to local resistances (narrowing and widening of flow)

$$S' = 0.785 \cdot d_0 \left[1 - \sqrt{\frac{\zeta_2}{\zeta_1}} \cdot a \right], \quad (4)$$

where ξ_1 and ξ_2 are the total resistances of the holes for flow rates Q_0 and Q_1.

The flow resistance in the instrument is [actually] concentrated not only in the holes, where the plugging up takes place, hence, S' should be greater than calculated by Eqs. (3) or (4). This can be taken into account by introducing the factor $\varphi > 1$. The larger the resistances other than those of the holes, the greater φ. It is obvious that

$$S' l \gamma_{Na_2O} = \int_0^{\tau_{pl}} \pi d l j \, d\tau = \frac{\pi \gamma_{Na} \cdot M_{Na_2O} l}{\varepsilon \cdot 100 M_0 \cdot Pr_D^{3/4}} \int_0^{\tau_3} \sqrt{\frac{\zeta}{2}} \cdot \bar{w} \, dZ \, d\tau$$

or, making use of the fact that

$$\sqrt{\frac{\zeta}{2}} \approx \frac{K}{(\bar{w}d)^{0.1}},$$

$$\text{and } \bar{w}d = \frac{4Q_0}{\pi dn}, \tag{5}$$

we get

$$S' = \pi K_1 \int_0^{\tau_{pl}} \left(\frac{Q_0}{d}\right)^{0.9} Z\, d\tau, \tag{6}$$

where

$$K_1 = \frac{\gamma_{Na} \cdot M_{Na_2O} \cdot K}{100 \cdot \gamma_{Na_2O} \cdot M_0 \cdot \varepsilon \cdot Pr_D^{3/4} \cdot n^{0.9} \left(\frac{\pi}{4}\right)^{0.9}}. \tag{7}$$

During time τ_{pl} the flow rate through the instrument changes little, and hence, we can write /327

$$S = \pi \cdot K_1 \bar{Q}^{0.9} \int_0^{\tau_{pl}} \frac{Z}{d^{0.9}} \cdot d\tau. \tag{8}$$

In order to evaluate the integral in the above expression we must know the manner in which the supersaturation and the size of the holes vary with time. The change in time in the supersaturation is determined by the oxygen solubility in the sodium as a factor of the temperature and of the rate of temperature drop in the holes. This relationship is found to be cumbersome. But if it is assumed that the sodium temperature does not go below the saturation temperature by more than 50°C, then in this temperature range the solubility of oxygen as a function of the temperature can be written in the form

$$C_s = C - \frac{dC_s}{dt}(t_s - t), \tag{9}$$

where dC_s/dt for each oxygen concentration in the sodium has a different value. Making use of the fact that the temperature reduction proceeds at a constant rate, we get from Eq. (9) the dependence of supersaturation on the time

$$Z = \frac{dC_s}{dt} \cdot \frac{dt}{d\tau} \cdot \tau. \tag{10}$$

The change in the hole size due to oxide deposition can be found from

$$-d(d) = K_1 \frac{Q_{Na}^{0.9} \cdot Z}{d^{1.9}} \cdot d\tau, \tag{11}$$

which was obtained from conditions of materials balance making use of Eqs. (2), (5) and (7). Integration of (11) within the limits of d_0 - 0 and 0 - τ, respectively, yields

$$d = \left(d_0^{2.9} - \frac{2.9}{2} \cdot K_1 \bar{Q}^{0.9} \frac{dC}{dt} \cdot \frac{dt}{d\tau} \cdot \tau^2 \right)^{1/2.9}. \tag{12}$$

Substituting the above expression and Eq. (10) into (8), integrating and transforming using Eqs. (1) and (3) and the fact that $\bar{Q} = Q_0/2(1 + a)$, we get

$$\Delta t \simeq 8.7 \sqrt{\frac{M_0 \gamma_{Na_2O} d_0^3 \varphi \varepsilon n \, Pr_D^{3/4} \frac{dt}{d\tau} \left\{ 1 - \left[1 - \frac{1}{2}(1 - a^{14/11}) \right]^{\frac{2.9}{2}} \right\}}{M_{Na_2O} \gamma_{Na} Q_0 \sqrt{\xi} \cdot \frac{dC}{dt}(1 + a)}}. \tag{13}$$

In deriving the above no consideration was given to reduction in the supersaturation due to deposition of oxides on the surfaces of the heat exchanger and the pipeline connecting the heat exchanger with the washer. If we take into account the fact that under actual conditions the sodium flow at these sections is laminar, then it can be shown that reduction in the supersaturation due to deposition at these sections will be higher, the greater the value of the expression /328

$$\frac{dC}{dt} \cdot \frac{dt}{d\tau} \cdot \frac{S^{2.8} (1 + a)^{2.8}}{S_f^{1.8} Q^{3.8}}. \tag{14}$$

Approximate estimates show that the reduction is supersaturation for oxide indicators in which the pipeline connecting the heat exchanger with the washer is not longer than 0.2 m, while the heat exchanger does not have branched out surface, is insignificant. Under other conditions this effect may be substantial, which must be taken into account when designing the device.

Obviously the [postulated] absence of crystallization centers moving together with the sodium will produce an additional reduction in the supersaturation and will subsequently result in lower-than-actual readings.

It can be seen from Eq. (13) that, in order to make smaller the difference between actual conditions and the instrument's readings, it is necessary to reduce the dimensions of the holes in which the oxides are deposited and also the

rate at which the temperature is reduced at the washer, and to increase the rate of flow of the sodium through the instrument. It also follows from this expression that in order to maintain Δt constant when the oxygen content is decreased (reduction in dC/dt) it is necessary to either increase the sodium flow rate through the instrument or to reduce the cooling rate.

Experimental results. One of the designs of cock-type indicators used is shown in Fig. 1. The characteristics of holes and heat exchangers of [a number of] indicators are shown in the Table.

TABLE. Characteristics of Holes and Heat Exchangers of Oxide Indicators

Instrument number	Holes			Heat exchange		
	Dimensions	Number	Total area, mm^2	Tube diameter, mm	Passage cross section, mm^2	Design
1	1 × 1	16	16	30 × 2.5	0.00049	Rubber tube
2	1 × 1	16	16	55 × 3	0.00188	» »
3	0.52 × 0.52	34	~9.2	55 × 3	0.00188	» »
4	0.24 × 0.31	34	~2.5	55 × 3	0.00188	» »
5	0.29 × 0.32	64	6	31 × 2.5	0.00106	Two-pass coil
6	0.31 × 0.34	16	1.7	31 × 2.5	0.00106	Same as above
7	0.52 × 0.52	16	4.3	31 × 2.5	0.00106	» »
8	0.87 × 0.87	16	12	31 × 2.5	0.00106	» »
9	1 × 0.75	12	9	20 × 2	0.0002	Single-pass cell
10	0.52 × 0.52	34	9.2	20 × 2	0.0002	Same as above

In performing the experiment we have worked out the following method for determining the stopping up temperature. Before starting the test, when the temperature of the liquid metal in the device was at maximum (400-500°C) the holes were washed with sodium (flow rate of 1 m^3/hour) for 15-20 minutes. The experiment was started only when the flow rate of sodium through the device for the given pressure drop became constant. After washing the holes, the washer was lowered, the required flow rate of sodium was established; the fan is started 5-10 minutes later and, adjusting the air flow rate, the required rate of metal temperature reduction in the holes was selected. The tests were run either until the flow of metal through the device ceased entirely, or until the flow rate became 0.1-0.2 of the initial quantity. /329

The dependence of the instrument's readings on the sodium flow rate was studied using nine washers in various combination with heat exchangers (see Table). For each instrument it was read not less than with two oxygen contents in the sodium. The absolute level of oxygen concentration in the sodium varied from $2.5 \cdot 10^{-2}$% by weight ($t_{pl} \approx 400$°C) to $6 \cdot 10^{-4}$% by weight ($t_{pl} \approx 150$°C). The flow rate of sodium through the device was varied from 10 to 800 liters/hour.

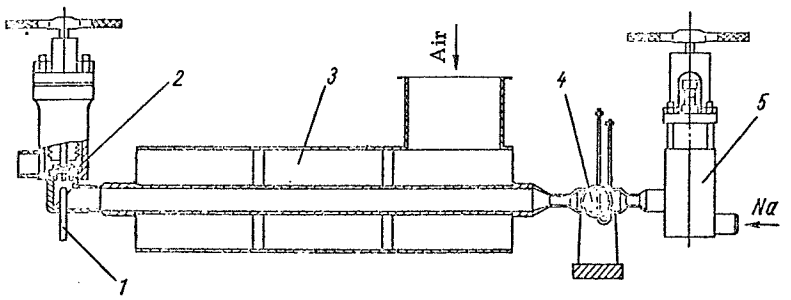

Figure 1. Design of a Cock-Type Oxide Indicator.

1) Thermocouple Pocket; 2) Main Valve; 3) Heat Exchanger; 4) Flowmeter; 5) Adjusting Valve.

If, in the case of large sodium flow rates, the heat exchanger capacity did not suffice to reduce the temperature to the required level, the temperature in the circuit had to be lowered. Here the temperature drop in the heat exchanger was not less than 70°C. Some results obtained in experiments for determining the dependence of the instrument's reading on the metal flow rate through it, are presented in Fig. 2.

A fact common to all the experiments is that, when the flow rate of sodium is reduced below a certain level, the instrument readings become lower and unstable. Here the lower the oxygen concentration in the sodium, the higher the flow rate at which the instrument starts giving unstable readings. Reduction of hole size for the same heat exchanger design and with the oxygen concentration of sodium remaining constant also results in increasing the flow rates at which the instrument readings are lower than actual. /330

Figure 3 presents results characterizing regions of unstable (I) and stable (II) operation of indicators; the points show the flow rate of sodium through the instrument for which the indicators give lower than actual readings for the given oxygen content of the sodium. It can be stated that region I is a region which the reduction in the readings is a quantity which is clearly recorded in experiments. According to this approach [which is based upon Eq.(13)]. one would expect that in the transition from region I to region II, the flow rate would increase with o- reduction in the oxygen concentration in the sodium or upon an increase in the hole size.

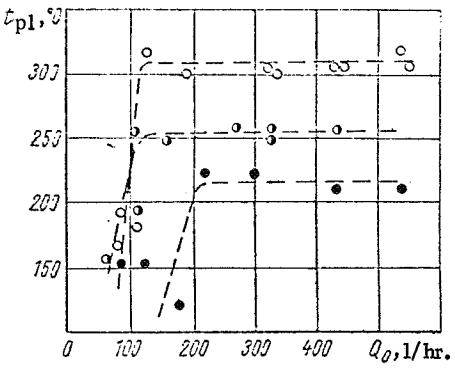

Figure 2. Readings of Indicator No. 5 as a Function of the Metal Flow Rate.

Similar behavior was observed experimentally. Quantitative comparison of experiments shows that, when the oxygen content is reduced from 0.01 to 0.0005% by weight, in order for the instrument to

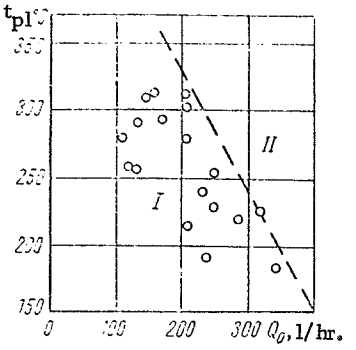

Figure 3. Regions of Unstable (I) and Stable (II) Operation of Indicator No. 5.

operate reliably it is necessary to increase the flow rate by a factor of 3.2; in our experiments the flow rate has to be increased 2-3 fold. [Thus] the dependence on the hole size is less sharply expressed in the experiments than was expected.

When comparing experimentally- and theoretically-obtained data consideration should be given to instability of results for determining the transition boundary between regions I and II. In our opinion this is due to the statistical character of oxide deposition in holes and to some instability of parameters such as the rate of cooling, distribution of flow resistance in the device among the holes and the adjusting valve. When the sodium flow rate through the device is reduced or when the hole size is increased, the portion of the resistance devolved upon the adjusting valve increases. This should have resulted in a higher φ and, consequently, also in a higher rate of reduction in the instrument's reading with a reduction in the flow rate than it would follow from Eq. (13). /331

It should be noted that data obtained in these experiments cannot be used to judge about the difference between the saturation and plugging up temperatures for the stable operation region. Clarification of this problem requires either accumulation of more statistical data or performance of special experiments.

The experiments for determining the dependence of the indicator's readings on the size of holes, rate of temperature reduction at the washer, which are described below, were performed with flow rates for which the instrument's operation was stable (see Fig. 3, region II).

The dependence of the instrument's readings on the hole size was studied by comparing two instruments simultaneously connected to the circuit. Here the oxygen concentration was maintained at the specified level. The plugging up temperature was determined at least twice for each instrument and then averaged. Comparisons were made for instruments 4 and 10, 9 and 2, 5 and 7, 3 and 9 (see the table); the averaged ratios of plugging up temperatures were 1.08, 1.03 and 1, respectively. It can be seen that indicators with smaller holes yields higher plugging up temperatures, i.e., the smaller the hole, the lesser the difference between the plugging up temperature determined by the instrument and the saturation temperature. As the oxygen concentration in sodium was made larger, the differences in the indicators' reading became smaller. For example, when comparing readings of indicators 4 and 10 in the range of t_{pl} = 155-200°C, the indicators with smaller holes give readings higher by 11%, while in the ranges 200-280, 280-320, 320-360 and 360-390°C the readings were higher by 10, 8, 6 and 4% respectively.

Using average ratios of plugging up temperatures and assuming that

$$\frac{t^2_{pl}}{t^9_{pl}} \cdot \frac{t^9_{pl}}{t^3_{pl}} = \frac{t^2_{pl}}{t^3_{pl}}, \qquad (15)$$

we have calculated the ratios of t^2_{pl}, t^3_{pl}, t^4_{pl}, t^5_{pl} and t^9_{pl} to t^4_{pl}. This ratio as a function of the hole size is shown in Fig. 4. It can be seen that, as the hole size is made larger, the instrument reads lower.

The dependence of the instrument's readings on the rate of reduction of the temperature of the metal flowing through the holes was studied for instruments 1, 2, 3 and 9. The oxygen content of the sodium was varied from 0.004 to 0.026% by weight. The experiments with each instrument were performed for two oxygen concentrations. The rate of temperature reduction was from 0.3 to 37°C per minute. Within limits of experimental error no dependence of the instruments' readings on the rate of temperature reduction of the metal flowing through the holes was observed in this range of concentrations.

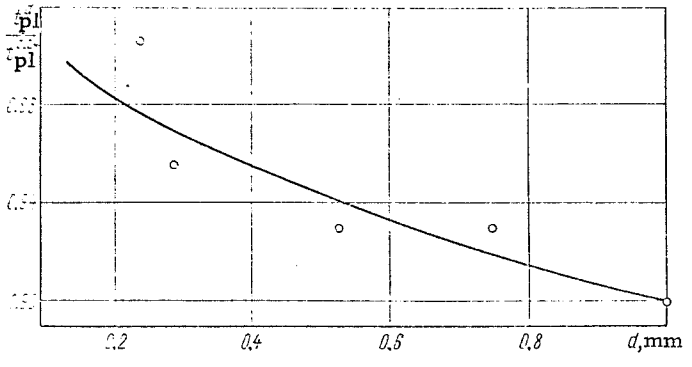

Figure 4. Readings of a Cock-Type Oxide Indicator as a Function of Hole Dimensions.

At the same time experiments performed in region I (see Fig. 3) with different rates of temperature reduction at the washer have shown that, when the rate of temperature reduction is made smaller, /332
the difference between the actual oxygen content and the instrument's readings is reduced. Moreover, in experiments far from the interface between the regions in cases when the temperature of the sodium flowing through the holes was reduced by 10-15°C below the saturation temperature, a gradual reduction in the flow rate due to deposition of oxides on the holes, was also observed.

Considering experimental results and the possibility of occasional variations in the flow rate of metal through the instrument, it can be said that in measurements with cock-type indicator it is undesirable to have a higher rate of temperature reduction than 10°C/min, since this can result in a random error in determining the plugging up temperature.

The dependence of the plugging up temperature which is determined by the cock-type oxide indicator on the hole size made it necessary to perform calibrating tests.

Calibrating a Cock-Type Oxide Indicator

The No. 4 oxide indicator (see table) was calibrated by two methods: 1) comparing the stopping up temperature with the temperature inside the cold trap which has operated for a prolonged period at constant temperature and 2) determining the oxygen concentration in the sodium by a distilling sampler, [7].

Calibration by the first method is based on the experimental and logical fact that, when the liquid metal circulates for a long time through the cold trap, its oxygen concentration will be determined by the temperature conditions of the trap. During the experiment the temperature in the trap was maintained at the specified level to within ±10°C.

After the entire sodium was passed through the cold trap at least five times the plugging up temperature determined by the oxide indicator was practically constant and, within limits of experimental error (±10%) was in agreement with the temperature in the cold trap.

The use of the second calibration method was as follows. With the oxygen /334
concentration in the circuit and the circulation [rate] of the sodium through the sampler constant, the plugging up temperature was measured at least twice by the indicator and it was averaged. Immediately after the last reading was taken on the oxide indicator, a sample was taken and analyzed (Fig. 5).

The scatter of experimental data on oxygen concentration in excess of 1.10^{-3}% by weight, as compared with the average, did not exceed 30%. This scatter becomes larger at higher concentrations, which may be attributed to the fact that the value of the control test, which determines the sensitivity of the method is, at low concentrations, commensurable with the natural oxygen content of the sodium. It is obvious that, within the above limits of accuracy in determining the plugging up temperature and in determining the oxygen content of the sodium, the relationship which is obtained represents the solubility of oxygen in sodium as a function of temperature. Analyzing it by the method of least square, we get

$$\lg C_s = 1.14 - \frac{1910}{T}. \qquad (16)$$

Comparison of results obtained by the present authors with those of other workers shows that in temperature ranges below 280°C the former yield a higher oxygen solubility in sodium than the latter. In the temperature range 140-190°C the present results are close to those of [4, 8-10]; in the range of 250-390°C data of [5, 8, 11-13] are practically identical. At hight temperatures [6] and [11] give oxygen solubilities exceeding data by the present authors 3 and 4 fold, while data of [12] and [13] at these temperatures are in agreement with the present data.

The relationships presented in [9] and [10] apparently reflect the results of the same experimental work [4]. However, the results in it were obtained by a cock indicator with larger holes (1.27 mm), which should give oxygen solubilities in sodium on the high side (an indicator with such holes gives a lower plugging up temperature than an indicator with 0.24 mm holes, by more than 8%).

The results which were obtained show that the cock-type oxide indicator is a quite complicated instrument, something which is not reflected in published work. The instrument's indications depend on many parameters. Among them we must note the flow rate of sodium through the instrument devolved upon one hole. It was shown that when the flow rate through the instrument is reduced below a certain

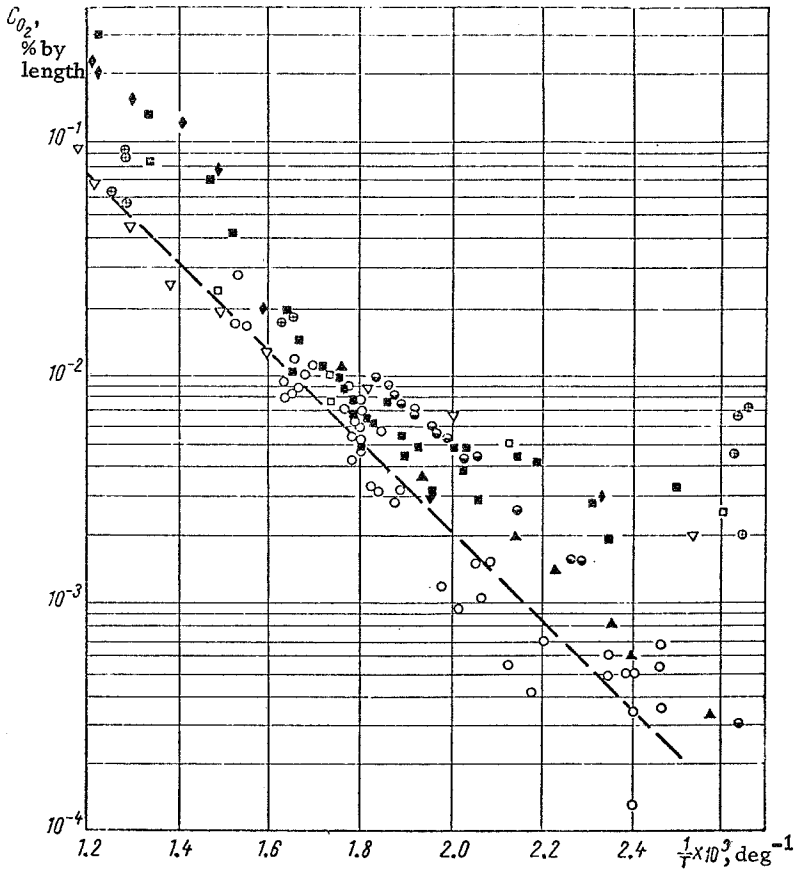

Figure 5. Calibrating a Cock-Type Oxide Indicator.

NOTATION: □ and ◆ - [5]; ⊕ - [12]; ◒ - [8]; ■ - [10]; ▲ - [7]; ▽ - [11]; ○ and — are for data obtained by the present authors.

value the latter gives lower than actual readings. The larger, the holes, the higher the metal flow rate which is needed for stable operation. For an indicator with holes of 0.87 x 0.87 mm it is about 600 liters/hour. /335

Experimental studies show that, as should have been expected on the basis of theoretical analysis, even when the flow rate of sodium is high, the instrument's readings depend on the hole size. A device with holes of 0.24 x 0.31 mm gives readings on the average by 10% lower than an instrument with hole size of 1 x 1 mm.

It follows from theoretical analysis that, in order to reduce the error, one should strive when designing the instrument that the flow resistance be concentrated in the holes, while the length of sections, washed with sodium whose temperature is below the saturation temperature, their surface and volume should be held to a minimum.

Calibration of the instrument with holes of 0.24 mm by the first method has shown that, for large sodium flow rates, the plugging up temperature agrees, within the ±10°C of experimental error, with the saturation temperature. This circumstance made is possible to refine the relationship governing the temperature dependence of oxygen solubility in sodium.

NOTATION

M - molecular (atomic) weight

D - coefficient of diffusion

Δt - negative deviation in the instrument's readings, °C

j - rate of flow of sodium oxide per unit surface per unit time

C_s - concentration of oxygen in the sodium, corresponding to the solubility at the given temperature

$Z = C - C_s$ - supersaturation

d_0 - diameter of holes in the instrument

ξ - integral resistance coefficient

a - factor which takes into account stability of flow rate through the instrument and the sensitivity of the secondary instrument

φ - factor taking into account the distribution of flow resistances in the instrument

$Pr_D = \nu/D$ - diffusion Prandtl number

τ - time

ε - some constant approximately equal to unity

n - number of holes in instrument

S - surface [area]

S_f - passage area

V - volume of section up to the washer washed with the supersaturated solution

REFERENCES

1. Blake, L. R.: J. of the Brit. Energy Conf., 6, 1 (1961).
2. Blake, L. R. and James, A. R.: Nucleonics, 19, 5, 66 (1961).
3. Brugeman, W. H.: A. I. Ch. E. Journal, 2, 153 (1956).
4. Grey, I. L.: Nucleonics, 14, 10, 34 (1956).
5. Zhidkometallicheskiye teplonositeli [Liquid-Metal Heat-Transfer Agents]. Translated from English under the editorship of A. Ye. Sheyndlin, Foreign Literature Publishing House, Moscow, 1958.
6. Levich, V. G.: Fiziko-khimicheskaya gidrodinamika [Physio-chemical Fluid Flow] [??]. Fizmatgiz, Moscow, 1959.
7. Dmitriyeva, N. B., et al.: Article preceding this in the present collection. /336
8. Allen, J.: Nucl. Engng, 7, 76, 352 (1962).
9. Sidjel [??] S., et al.: Proceedings of the International Conference on Peaceful Uses of Atomic Energy, Geneva, 1955. Technology and Engineering Series. Published in the US by McGraw-Hill for Pergamon Press or vice versa.
10. Evans, J. W.: Nucl. Engng, 4, 35, 59 (1959).
11. McIntosh, A. B. and Bagley, K. Q.: The Journal British Nuclear Energy Conference, 3, 1, 15 (1958).
12. Williams, D. D., et al.: J. Phys. Chem. 63, 1, 78, (1954).
13. Bannykh, Z. S. and Fefelova, I. V.: In Trudy Ural'skogo khimicheskogo instituta. Issue 5, Goskhimizdat, Leningrad, 1957-1958.

EFFECT OF ADMIXTURES ON THE ELECTRIC RESISTANCE OF MOLTEN LITHIUM

M. N. Arnol'dov, M. N. Ivanovskiy, V. I. Subbotin and B. A. Shmatko

A number of publications have appeared lately which deal with experimental /336
determination of the electrical resistivity of molten lithium [1], [2]. The deviations between the results of these references exceed the total experimental error, which may be caused by differences in the chemical composition of the lithium specimens used.

The basic (quantitatively speaking) admixtures of molten lithium, which interact with it are: nitrogen, oxygen and hydrogen (from vapor in the air). The quantity of admixtures in the lithium depends on the specific experimental conditions and may turn out to be a random quantity. The admixtures are a source of additional (admixture-caused) electric resistivity.

Consideration of the electric resistivity of lithium as a function of the admixture content is of interest also from another point of view. It helps in understanding the physical nature for the origin of admixture-caused electric resistance as a whole and in liquid metals in particular.

Attempts have been made to explain the experimental data on the effect of metallic admixtures on the electric resistivity of some molten alkaline metals, based on the development of the well-known Linde law [3], [4]. The authors of [5], using and developing the work of Friedel and others, [6], have calculated the magnitude of the electric resistance of molten lithium containing potassium and sodium admixtures.

The effectiveness of theoretical calculations is appreciably reduced due to the inavailability of experimental data on which to base the calculations, in particular, due to inavailability of data on the dependence of the partial volumes dissolved in the lithium on the concentration of these volumes. Of great importance is the magnitude of the charge of the admixture ion in the lithium. We have measured /337
the electric resistivity of molten lithium as a function of the temperature and of the concentration of the oxygen, nitrogen and hydrogen dissolved in it.

Chemical-thermodynamics calculations show that the oxygen, nitrogen and hydrogen exist in lithium at temperatures of 200-350°C mainly in the form of an oxide, nitride and hydride of lithium, respectively. The existence of admixtures such as lithium hydroxide or carbonate under these conditions is impossible from the point of view of thermodynamics.

The measuring tube into which the lithium being tested was poured, was made from 1Kh18N9T steel with an inner diameter of 7.95 mm and a wall thickness of 0.25 mm. Before the lithium was poured, its electric resistance in the entire

range of temperatures being studied was measured. Thermostatic control of the measuring tube was obtained by a thermostat with a boiling Dowtherm®. The electrical resistance of the tube with the lithium, which was poured into it, was measured by a double d–c bridge. The lithium used in the test was ordinary, with the following composition:

Element						
Composition	O_2 $1\cdot10^{-2}$			N_2 $1\cdot10^{-2}$	C $5\cdot10^{-4}$	H_2 $3\cdot10^{-2}$
Element	Na	K	Ca	Be	Mg	Ag
Composition	$5\cdot10^{-1}$	$8\cdot10^{-3}$	$6\cdot10^{-3}$	$<10^{-3}$	$3\cdot10^{-3}$	$3\cdot10^{-4}$
Element	Cu	Ti	Ni	Fe	Mn	Ba
Composition	$3\cdot10^{-3}$	$3\cdot10^{-3}$	$2\cdot10^{-3}$	$1\cdot10^{-3}$	$1\cdot10^{-4}$	$1\cdot10^{-2}$
Element	Al	Zr	Cr	Si		
Composition	$3\cdot10^{-2}$	$3\cdot10^{-4}$	$3\cdot10^{-2}$	$4\cdot10^{-2}$		

The admixture content in the lithium was measured by introducing gaseous oxygen, nitrogen and hydrogen beneath the surface of molten lithium in a special tank. In order to rapidly obtain equilibrium concentrations of the admixtures under test and to [then] hold it constant, the lithium was continuously circulated from the tank into the tube and back. The quantity of the admixtures added was determined by measuring their pressure in a tank with known volume, from which the gaseous admixture was supplied to the lithium tank. The quantity of the admixtures added and results of chemical analysis of lithium for the content of the given admixture were systematically compared. Differences in the quantities compared did not exceed the error inherent in chemical analysis and the measurement of the admixture quantities added.

The obtained dependence of the electric resistivity of lithium on the content /338
of nonmetallic admixtures (Fig. 1) can be used to explain the differences in experimental data obtained by various investigators who, most probably, made measurements with lithium with different composition and content of admixtures. It follows from Fig. 1 that the dependence of the electric resistivity of lithium on the admixture content can be satisfactorily described by a linear formula, which is in agreement with the general viewpoint of the theory of admixture-caused resistance at low admixture concentrations. Unfortunately, the total inavailability of data on the dependence of the specific volumes of admixtures and their partial pressures on the admixture temperature and concentration makes it impossible to process the data we have obtained in the manner that this was done in [3-5].

It is remarkable that the electric resistivity of lithium depends on the oxygen content much less than on the nitrogen and hydrogen contents only in the case when all these admixtures are nonionized. In the opposite case the oxygen ion, which has a larger charge than the hydrogen ion, should produce a larger admixture-caused resistance. Apparently, here the latter is not determined by the difference in the ionic charges of the admixtures and of the solvent metal, but rather in the

difference in dimensions of the admixture and solvent atoms. This difference produces a nonuniform charge density in the volume of the metal, which is precisely the cause for electron scattering which produces the admixture-caused electric resistance [4]. The absence of nitrogen and hydrogen ions in lithium at temperatures up to 350°C, or, more precisely, their negligible content, is shown by the following: the magnitudes of the admixture-caused electric resistivity do not depend on the temperature, i.e., the Matthiessen rule is satisfied.

Figure 2 shows the electric resistivity of lithium as a function of the temperature for different nitrogen and hydrogen concentrations. The differences between the resistivities of contaminated and pure metals for a given temperature /339
is the admixture-caused electric resistivity. As can be seen from Fig. 2, the resistivity lines as a function of temperature for different admixtures are mutually parallel, which shows that the Matthiessen rule is satisfied.

The portion of admixtures which is ionized in the lithium depends on the temperature. Hence, if the admixture-caused resistivity is found not to be temperature dependent, this means that the lithium contains no ionized nitrogen or hydrogen.

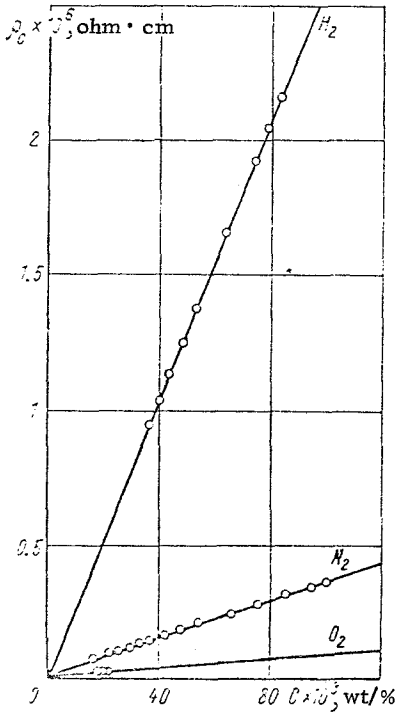

Figure 1. The Electric Resistivity of Lithium at 300°C as a Function of the Oxygen, Nitrogen and Hydrogen Content.

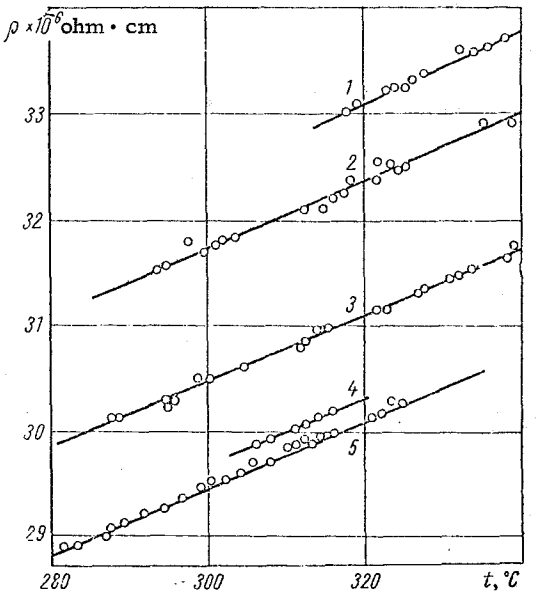

Figure 2. Electric Resistivity of Lithium as a Function of the Temperature for Different Nitrogen and Hydrogen Contents.

1), 2) and 3) Changes in Nitrogen Content; 4) and 5) Changes in Hydrogen Content.

It should also be noted that the relationships expressed by Figs. 1 and 2 remained unchanged also for a measuring tube held, together with the lithium, at 300°C for 800 hours.

REFERENCES

1. Fridman, J. F., et al.: J. Chem. Phys., 34, No. 3 (1961).
2. Solov'yev, A. N., et al.: Zhurnal prikladnoy mekhaniki i tekhnicheskoy fiziki. 1, No. 1 (1963).
3. Blatt, F.: Phys. Rev., 108, 285 (1951).
4. Green, B.: Phys. Rev., 4, 126 (1962).
5. Shpil'rayn, E. E. and Savchenko, V. A.: Teplofizika vysokikh temperatur, 3, No. 1, 1965.
6. Friedel, J.: Philos. Mag., 7, 43, 153 (1952).

THE USE OF HOT TRAPS FOR REMOVING OXYGEN FROM SODIUM

F. A. Kozlov and E. K. Kuznetsov

INTRODUCTION

One of the main problems arising in using liquid sodium as a reactor coolant is that of keeping its oxygen content to a minimum. The required degree of purification is determined by the construction materials used in the facility, the working temperature, facility design and other factors. At present extensive use is made of two methods of oxygen removal: purification by cold and hot traps (getter purification). Both methods differ from one another radically by the nature of phenomena on which their operation is based, and also by the minimum concentration of oxygen which is obtained by using these methods. /340

The solubility of oxygen in sodium drops with a reduction in the temperature, which is the basic method for oxygen removal by the cold-trap method. The minimum possible sodium temperature in cold traps is limited by the 100-150°C level, hence, the minimum oxygen concentration produced by these devices is $(1-.5)\cdot 10^{-3}$ % by weight, [1-3].

The getter purification method uses the ability of some substances to reduce sodium oxides to pure sodium. The higher the reaction temperature, the higher the reaction rate. This method ensures a higher degree of oxygen removal than the cold-trap method. Consequently, if the oxygen concentration in the sodium should be below that produced by cold traps, the hot trap should be used.

The problems which must be resolved when removing oxygen and other admixtures by a hot trap are: selection of the getter material, study of the laws governing the interaction between the getter and the sodium's admixtures, determination of the maximum oxygen concentration produced by the [given] getter, selection of the hot trap design, developing techniques for obtaining and maintaining the specified oxygen concentration in the sodium using the hot traps [1, 3-6].

The condition characterizing the ability of a metal to reduce sodium oxide to pure sodium is the reduction in the free energy of reaction

$$n\mathrm{Na_2O} + b\mathrm{Me} \rightarrow \mathrm{Me_bO_n} + 2n\mathrm{Na}. \qquad (1)$$

Figure 1 shows the free energy needed for formation of stoichiometric oxides of various metals as a function of the temperature, [7]. It can be seen that a number of metals can be used as getters. However, it is most practical to use zirconium and its alloys with titanium, since, when reacting with oxygen, these form a dense film bound to the basic metal of the oxide. The interaction of zirconium /341

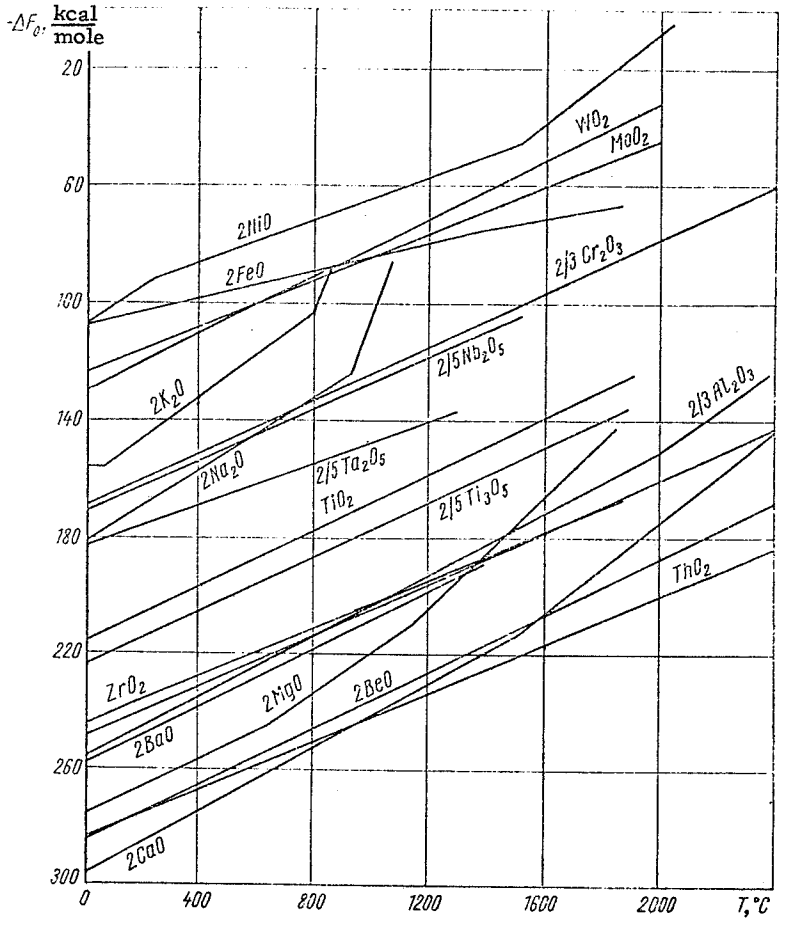

Figure 1. The Free Energy of Oxide Formation (per 1 Gram-Mole of Oxygen).

with oxygen is described in [5] and [6]. It was shown experimentally that the increase in the weight of zirconium can be described by an equation such as

$$\frac{\Delta P}{S} = A \cdot \tau^n \cdot \exp\left(-\frac{B}{T}\right) = k \cdot \tau^n. \qquad (2)$$

However, the available data are insufficient for resolving the above problems. /342
[For this reason] we have performed experiments to clarify the laws governing oxygen removal by hot traps with a zirconium getter.

Interaction Between Zirconium and Sodium-Held Oxygen

In our experiments we have used arc-molten zirconium iodide foil 0.1, 0.5 and 0.8 mm thick. Specimens of the needed size were placed in special chambers which were cut into the circulation circuit of the installation. The chambers were constructed so that it was possible to test the specimens at three different sodium velocities. Before starting the test the sodium was pumped through the specimen chambers for 8-35 hours at temperatures not above 350°C, simultaneously removing oxygen from it by a cold trap. When the oxygen concentration in the circuit dropped to 0.001-0.0005% by weight, the temperature in it was raised, and then the specimens were tested for a specified time.

In the course of experiments the oxygen content of the sodium was maintained at the specified level by continuously pumping the sodium through the cold trap, the temperature inside of which was 110-140°C. The constancy of oxygen concentration in the circuit was monitored by a cock-type oxide indicator. A number of specimens was tested in sodium purified by a hot trap.

After terminating the experiments the chambers were cut out, the sodium residues were dissolved in ethyl alcohol, the foil was washed with water and dried and then its weight gain was determined. Control experiments showed that this kind of processing does affect the accuracy of weight gain determination. Individual specimens were replaced in the chambers for continuation of test, after the weight gain has been determined. We have performed 113 experiments at 510-1100°C. The time during which the specimens were held in sodium varied from 15 to 435 hours, while the sodium velocity was from 0.05 to 5.7 m/sec.

In calculating coefficients A, B and n of Eq. (2) we have used only those data for which the weight gain in the roughly purified sodium was less than 17% of the total weight gain in the tests. A part of the tested specimens was subjected to chemical, metallographic and x-ray diffraction analysis.

Dependence of the Weight Gain of Zirconium Specimens on the Time of Holding in Sodium

For zirconium specimens tested in sodium (constant temperature) k of Eq. (2) is constant. Then, analyzing the experimental results in the form

$$\lg\left(\frac{\Delta P}{S}\right) = f(\lg \tau),$$

which get a straight line (Fig 2). In this method of data analysis, we have used the method of least squares to determine the power n for temperatures of 540, 560 and 620°C, the average value of which was 0.51. /343

Dependence of Weight Gain of Zirconium Specimens on the Temperature

In the study of temperature dependence of the weight gain in zirconium the temperature range was extended to 1100°C. However, due to failure of the zirconium foil [at high temperatures] we could only determine the weight gains of specimens tested at 720°C. The experimental data, which are treated in the form $\lg\left(\frac{\Delta P}{S\tau^{0.51}}\right) = f(1/T)$ are shown in Fig. 3. As expected, within limits of experimental error, they lie on a straight line, the equation of which, found by the method of least squares, has the form

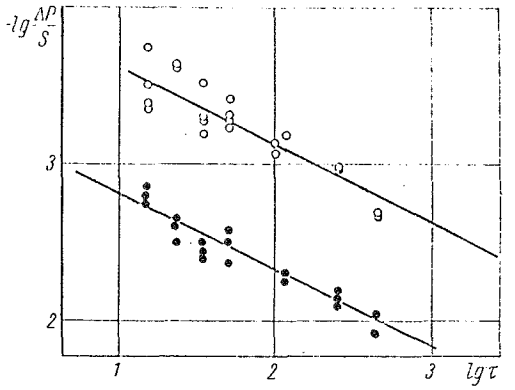

Figure 2. Weight Gain of the Zirconium as a Function of the Holding Time in Sodium.

○ — $\lg\left(\frac{\Delta P}{S}\right) = -4.187 + 0.54 \lg\tau$ for 540°C;
● — $\lg\left(\frac{\Delta P}{S}\right) = -3.318 + 0.50 \lg\tau$ for 620°C.

$$\lg\left(\frac{\Delta P}{S\tau^{0.51}}\right) = 4.253 - 6800 \cdot \frac{1}{T}. \qquad (3)$$

Changing to Eq. (2), we get

$$\frac{\Delta P}{S} = 1.8 \cdot 10^4 \tau^{0.51} \exp\left(-\frac{15700}{T}\right). \qquad (4)$$

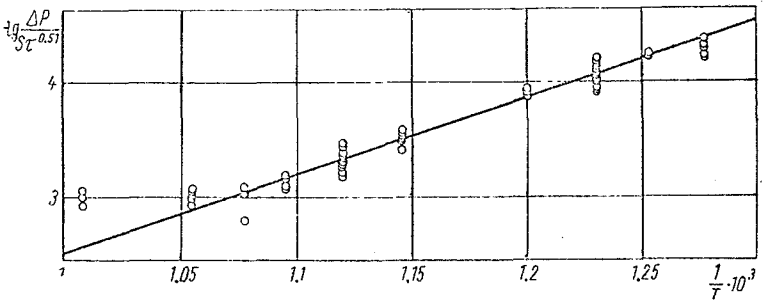

Figure 3. Weight Gain of Zirconium as a Function of the Temperature.

We now consider the results obtained by testing 0.1 mm thick zirconium specimens at temperatures above 650°C in more detail. The weight gains of the specimens at these temperatures are lower than those which were expected on the basis of Eq. (4). This reduction may be due to two factors: increase in the rate of mass transfer for zirconium with an increase in the temperature of the sodium, washing the specimens, and reduction in the rate of zirconium penetration /344

by the oxygen, due to the reduced oxygen concentration gradient. For these reasons in calculating n in Eq. (2) we did not take into account results obtained at 675°C and above.

Dependence of the Weight Gain of Zirconium Specimens on the Oxygen Concentration and on the Sodium Velocity

To clarify the qualitative dependence of the weight gain of zirconium specimens on the oxygen concentration of the sodium, the latter were tested at three different velocities of sodium, which was purified by a hot trap. The tests were run at 620°C for 115 hours (Fig. 4). In sodium purified by a hot trap the weight gains of the zirconium were found to be 2.5-3 fold smaller as compared with those obtained in sodium purified by a cold trap. When the velocity was reduced from 0.2 to 0.02 m/sec the weight gain became smaller by a factor of more than 2.3. We did not succeed in precisely measuring the oxygen content of the sodium in this experiment. It is only known that it was less than 0.0003% by weight.

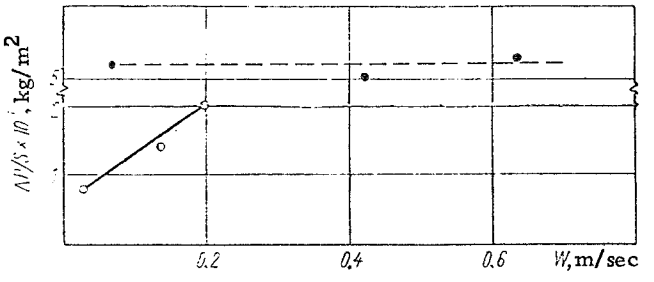

Figure 4. The Weight Gain of Zirconium as a Function of the Sodium Velocity.

● - Oxygen Removed from the Sodium by a Cold Trap; ○ - Oxygen Removed from the Sodium by a Hot Trap.

Changes in the Chemical Composition of Specimens Subsequent to Holding in Sodium

Chemical analysis of zirconium specimens held in sodium showed that, within limits of experimental error, the weight gain of the zirconium is determined by oxygen absorption. No systematic relationships for variations in concentrations of elements such as carbon, nitrogen, hydrogen, iron, chromium, sodium, copper, aluminum, etc., was discovered. At temperatures below 620°C no stable concentration of nickel in the specimens was observed, while at temperatures higher than this the nickel concentration was higher than for the starting zirconium. /345

X-ray Diffraction and Metallographic Analyses of Zirconium Specimens Subsequent to Testing

X-ray diffraction was used to analyze the starting zirconium and specimens 0.1 mm thick tested at temperatures of 540, 560, 600, 675 and 720°C for 250 hours. Analysis of the x-ray pictures showed that specimens tested at 600 and 675°C

contain on their surface a layer of ZrO_2. No zirconium oxides were found on specimens tested at 540-560°C.

On specimens 0.8 mm thick, held in sodium at temperatures of 620 and 720°C for 432 and 250 hours, respectively, metallographic analysis has discovered a zirconium oxide film about 0.1 mm thick. The oxide film increases sharply the microhardness of the specimen surfaces, which may become as high as 800 kg/mm^2.

The grain size of crystals of specimens tested in sodium increase in size on raising the temperature and extending the holding time. It should be noted that the absorbed oxygen increases the brittleness of the zirconium. From this point of view the permissible weight gain per unit surface for zirconium sheets 0.1 mm held in sodium purified by a cold trap is about 4%.

Change in the Electric Resistivity of Zirconium Subsequent to Holding in Sodium

The resistance of the starting zirconium and of specimens held in sodium was measured by the R-329 double bridge. The experimental data were reduced to 0°C. It was assumed in the calculations that the temperature coefficient of electric resistivity does not depend on the oxygen concentration and is equal to $4.4 \cdot 10^{-3}/°C$ [8] (Fig. 5). The differences between the electric resistivities of the zirconium-oxygen alloy and the zirconium oxidized in sodium purified by a cold trap are apparently due to nonuniform distribution of oxygen over the specimen cross section.

The electric resistivity of specimens from hot traps is in better agreement with data of [8]. This can be attributed to the fact that the above zirconium was held longer in sodium with a lower oxygen concentration than the specimens tested in sodium purified by a cold trap. Under these conditions the rate of oxygen diffusion into the sodium exceeds the rate of formation of the surface oxide layer /346 and, consequently, the oxygen absorbed by the zirconium is more uniformly distributed over the specimen cross section, forming a structure to zirconium-oxygen alloys. It is obvious that for this very reason the zirconium in hot traps is more brittle than in cold trap purified sodium.

Removal of Oxygen From Sodium by Hot Traps

On the basis of the above results we have constructed and tested several hot traps, in which zirconium foil 0.1 and 0.3 mm thick was used as the getter (Fig. 6). These traps were tested in sodium circuits with a metal volume from 0.05 to 0.2 m^3 at 550-670°C. The test time varied between 100 and 1150 hours, the flow rate of the sodium through the hot traps was 1-2.5 m^3/hour. The sodium purity was monitored by a distilling sampler [9].

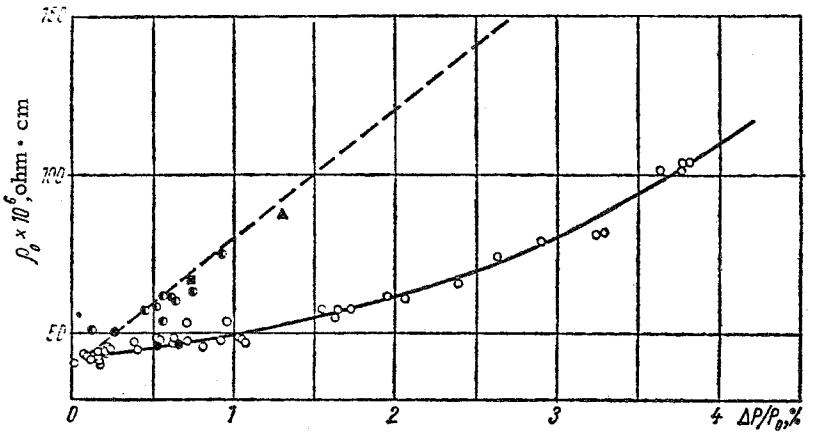

Figure 5. Electric Resistivity of Zirconium as a Function of the Oxygen Concentration in Sodium.

○ – Zirconium Held in Sodium Purified by a Cold Trap; ● – Purified by a Hot Trap; ◐, ■ and ▲ Zirconium from Different Hot Traps; the Dashed Line Reflects Data of [8].

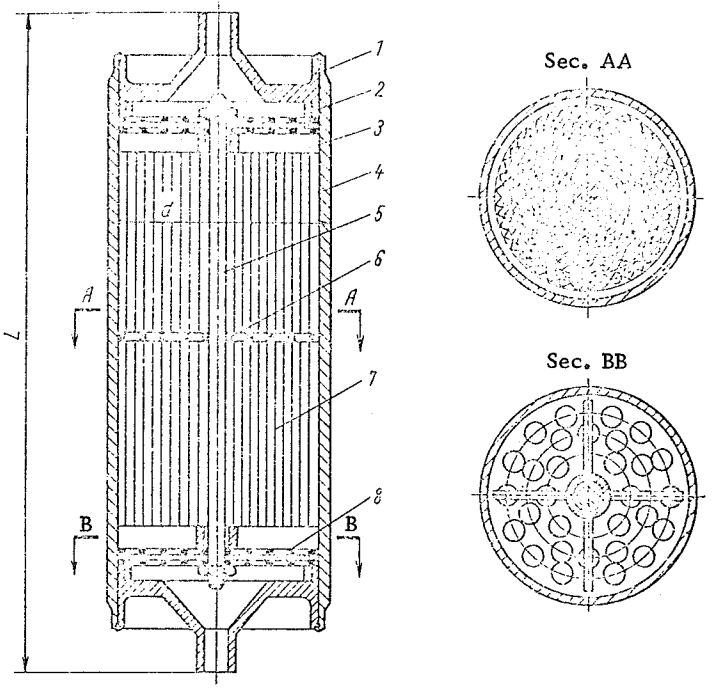

Figure 6. Section Through a Hot Trap.

1) Reducing Cover; 2) Thrust Ring; 3) Packing Ribs; 4) Trap Casing; 5) Pin; 6) Grid; 7) Zirconium; 8) Mesh.

Figure 7 shows the manner in which the oxygen concentration in the closed circulation circuit varied as the sodium was purified by a cold and hot trap. Similar results were obtained in other experiments in which oxygen was removed from sodium by hot traps. A characteristic phenomenon encountered in these experiments is the increase in the oxygen content of the sodium after the cold trap is shut off and the temperature is increased. This is due to the following factors.

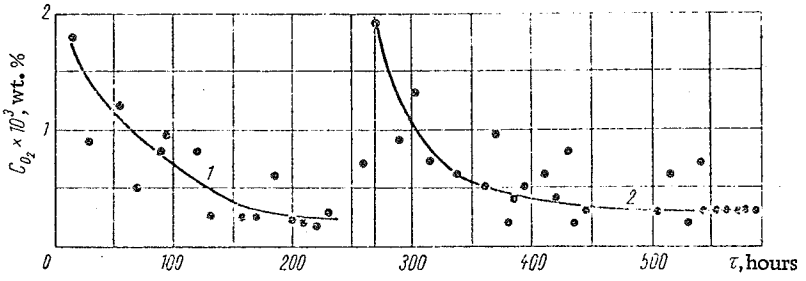

Figure 7. Change in Oxygen Concentration in a Circuit When the Sodium is Purified by a Cold (1) and Hot (2) Traps.

A rise in the temperature increases the solubility of oxygen in the sodium, /348
and the rate of dissolution and speeds up the diffusion processes. Hence, oxygen from remote corners of the circuit, from walls of expansion tanks and the structural metal is absorbed by the circulating sodium.

Analyzing the sodium for oxygen using a distilling sampler (see Fig. 7) we see that after purification the oxygen content of the sodium remains approximately on the same level of $(2-5) \cdot 10^{-4}$% by weight. However, these numbers do not reflect the actual oxygen concentration produced by the hot traps, but point only to the limiting sensitivity of the distilling sampler. Hence, the results of these experiments cannot be used to judge about the maximum oxygen content of sodium purified by hot traps. The above is verified by the fact that the weight gain of the zirconium held in sodium purified by a hot trap and the weight gain of zirconium from the hot traps is by several factors lower than that of specimens tested in sodium purified by a cold trap.

The following results were obtained with respect to the mechanical strength of the zirconium foil.

1. Zirconium foil 0.1 mm thick (weight gains of 1.5-2%) becomes so brittle that it can no longer be used.

2. In 0.1 mm thick foil tested for 1000 hours at 650-670°C the oxide film peeled and the foil proper failed. Foil 0.3 mm thick tested under the same conditions lost part of its initial elasticity, but it still could be used.

Estimating Equilibrium Oxygen Concentrations in Sodium

It was pointed out above that only those materials can be used as getters in which the free reaction energy (ΔF) described by Eq. (1) becomes lower. This condition is necessary, but not sufficient. The second requirement which is presented to a getter is providing the required oxygen concentration in the liquid metal. Exact calculations based on the law of mass action require knowledge of the activity coefficients for the sodium-held and getter-held oxygen, as well as the solubilities of the getter proper, as well as of its oxide in sodium [10, 11]. These data are either inavailable or incomplete. [Therefore] we give below estimates of the equilibrium concentrations of oxygen, on some assumptions.

For the reaction described by Eq. (1) we write

$$K_a = \frac{a_{Na}^{2n} \cdot a_{Me_bO_n}}{a_{Me}^{b} \cdot a_{Na_2O}^{n}} = \exp\left(-\frac{\Delta Z}{RT}\right).$$

Making use of the fact that the change in the isobaric potential ΔZ for reactions proceeding at constant volume is practically equal to ΔF [10], and that $a_{Na_2O} = C_{Na_2O}/C^*_{Na_2O}$ [11], we get /349

$$C_{Na_2O} = C^*_{Na_2O} \cdot \sqrt[n]{\frac{a_{Na}^{2n}}{\exp\left(-\frac{\Delta Z}{RT}\right)}} \cdot \sqrt[n]{\frac{a_{Me_bO_n}}{a_{Me}^{b}}}.$$

Assuming further that the solubility of the getter and of its oxide in sodium is zero (the reaction is heterogeneous) and the activity of the sodium (the reaction proceeds with excess sodium) is equal to unity, we have

$$C_{Na_2O} = C^*_{Na_2O} \cdot \exp\left(\frac{\Delta F}{RTn}\right). \qquad (5)$$

The following can be concluded from the results tabulated above. The greatest degree of oxygen removal can be obtained by using thorium, uranium and a zirconium-titanium alloy as getter materials. The degree of oxygen removal is reduced with an increase in temperature. The lowest equilibrium oxygen concentrations in sodium are obtained at temperatures of about 400°C and lower, but then the reaction rate becomes lower. Hence, the temperature at which a hot trap should be operated should be in the range of 550-650°C. Oxides of construction materials (FeO, NiO and others) should become reduced in sodium even when the oxide content of the latter is above the permissible.

TABLE. Equilbrium Concentrations of Sodium Oxides for Different Getters, Calculated From Eq. (5).

Reaction	c_{Na_2O} (mole fractions)		
	400° C	600° C	800° C
$Zr + 2Na_2O \rightleftarrows ZrO_2 + 4Na$	$1.3 \cdot 10^{-15}$	$7.2 \cdot 10^{-13}$	$3.9 \cdot 10^{-11}$
$Ti + 2Na_2O \rightleftarrows TiO_2 + 4Na$	$1.3 \cdot 10^{-10}$	$9.1 \cdot 10^{-9}$	$1.1 \cdot 10^{-7}$
$Nb + 2Na_2O \rightleftarrows NbO_2 + 4Na$	$4.3 \cdot 10^{-5}$	$8.5 \cdot 10^{-5}$	$1.5 \cdot 10^{-4}$
$\frac{4}{5} Ta + 2Na_2O \rightleftarrows \frac{2}{5} Ta_2O_5 + 4Na$	$4.2 \cdot 10^{-6}$	$1.15 \cdot 10^{-5}$	$1.8 \cdot 10^{-5}$
$Th + 2Na_2O \rightleftarrows ThO_2 + 4Na$	$4.3 \cdot 10^{-21}$	$4.4 \cdot 10^{-17}$	$1.2 \cdot 10^{-14}$
$U + 2Na_2O \rightleftarrows UO_2 + 4Na$	$9.7 \cdot 10^{-17}$	$9.5 \cdot 10^{-14}$	$5 \cdot 10^{-12}$

Calculation and Design of Hot Traps

The calculation and design of a hot trap are closely related to the system in which it is to operate. If the materials from which the facility is made present rigorous requirements to the coolant purity, then the hot trap must maintain the oxygen concentration on a level which is permissible from the point of view of corrosion of these materials, If this is not necessary, then the rate of oxygen removal from the coolant should be such that its concentration should not increase above the saturation concentration at the lowest coolant temperature in the given facility.

The following must be known when the determining factor in a given system is the rate of corrosion of construction materials: the manner in which the corrosion rate depends on the temperature, the time and the oxygen concentration; the permissible time of contact between the structural material and the oxygen-containing sodium, and the dependence of this time on the oxygen's temperature and concentration. Many of these data are not known at present. Hence, the calculation techniques will not be presented for a specific facility.

The purpose of these calculations is determining the quantity of getter material needed for obtaining the required hot-trap output and for ensuring the stable operation of the latter and of the facility as a whole during a specified time period. In performing these calculations one must, in addition to starting data (they are determined by the system which is to be served by the trap) select the getter material, the hot trap temperature, the geometric size of the getter and other parameters.

Selection of a Getter and Operating Parameters

Zirconium foil can be used as a getter for removing oxygen from sodium. On the basis of experimental data and of thermodynamic calculations, we assume a temperature range of 550-650°C for the zirconium getter. The lower temperature limit

is bound by the rate of absorption of oxygen by the zirconium (below 550°C the reaction rate is reduced appreciably), while the upper limit is limited by the increase in the mass transfer of zirconium [6].

The velocity of sodium flowing through the trap is taken so that the flow in the cells formed by the foil is turbulent. Calculations show that for a hydraulic diameter of cells of about 10^{-3} m the velocity of sodium in the latter should be 0.6 m/sec. If the parameters of the facility (sodium flow rate, pressure drop) or design considerations require that the veolocity in the trap be lower, this can be done, but then consideration should be given to the possible reduction in the oxygen absorption by zirconium.

The thickness of the zirconium foil is determined by the total weight gain of zirconium per unit surface for the entire time of trap operation. The total weight gain should be such that no oxide films, which subsequently peel, form on the zirconium surface and that the foil does not become too brittle. The weight gain per unit area satisfying these conditions will be called the normally permissible weight gain.

It can be seen from the above that the maximum weight gain permissible per /351
unit area is a function of parameters such as foil thickness, operating temperature, oxygen concentration in the sodium, etc., i.e.,

$$\left(\frac{\Delta P}{S}\right)_{\max} \quad f(T, C, \delta). \tag{6}$$

At present the form of the above equation is not known precisely, and it has to be determined experimentally. On the basis of general considerations and of some experimental data it can be expected that the maximum permissible weight gain will basically depend on the foil thickness, meaning that it should increase as δ is made larger. It is shown experimentally that when using foil $1 \cdot 10^{-4}$ m thick the maximum permissible weight gain is limited by 2% or to approximately 0.006 kg/m^2.

Assuming that $(\Delta P/S)_{max}$ is proportional to the foil thickness and disregarding the dependence on the oxygen concentration of the sodium and on the temperature, Eq. (6) can be written in the form

$$\left(\frac{\Delta P}{S}\right)_{\max} \approx 66 \cdot \frac{\delta}{K_1}, \tag{7}$$

where we shall assume that $K_1 = 1.3$ when $\delta = 3 \cdot 10^{-4}$ m and that $K_1 = 1$ when $\delta = 1 \cdot 10^{-4}$ m.

Making use of Eq. (4) we can write

$$\delta = 2.73 \cdot 10^2 \cdot \text{op}^{0.51} \cdot K_1 \cdot K_2 \cdot \exp\left(-\frac{15\,700}{T}\right). \quad (8)$$

Depending on the sodium content and on the behavior of flow in the hot trap (turbulent or laminar flow), the value of K_2 varies from 1 to 0.25-0.5. No analytical expression has been found to relate K_2 to the oxygen concentration. It is only known on the basis of experimental data that $K_2 = 1$ when the oxygen concentration is 0.0005-0.001% by weight, and $K_2 = 0.25$-0.6 when the sodium is purified by a hot trap.

Calculating the Weight of Zirconium Without Consideration of the Rate of Its Interaction With Oxygen

The minimum quantity of zirconium needed for removing the specified quantity of oxygen from the sodium can be calculated from the reaction equation

$$Zr + O_2 \rightarrow ZrO_2.$$

However, in this case the entire zirconium is transformed into an oxide, which apparently cannot be obtained in practice. Hence, the calculations should be performed using data on the maximum permissible weight gains per unit surface. /352

The total amount of oxygen to be removed by a hot trap can be expressed as

$$P_{O_2} = \frac{m \cdot K_3 (C_{in.} - C_{fin}) P_{Na}}{100}. \quad (9)$$

Making use of the above expression, we can write the weight of the zirconium in the form

$$P_{Zr} = \frac{m \cdot K_3 \delta \cdot \gamma_{Zr} (C_{in.} - C_{fin}) P_{Na}}{200 \left(\frac{\Delta P}{S}\right)_{max}}. \quad (10)$$

It was taken into account in deriving the above that $S = 2P_{Zr}/\gamma_{Z_r}\delta$.

It should be noted that calculations for a hot trap using Eq. (10) can be performed only when the rate of oxygen removal is not of importance.

Calculating the Weight of Zirconium for a Given Rate of Oxygen-Zirconium Reaction

We calculate the weight of zirconium from Eq. (4). In this case we must make certain assumptions, which are not entirely verified by experimental data.

1. The rate of reaction between zirconium and oxygen is independent of the sodium velocity.

2. Intermixing of the sodium in the circuit is ideal.

3. The concentration of oxygen in the sodium which at a given instant is in contact with zirconium in the hot trap is constant.

The equation of material balance for oxygen in a closed system for an infinitesimal time interval has the form

$$-K_3 \cdot P_{Na} \cdot dC = G(C - C')\, d\tau, \tag{11}$$

while for the sodium flowing through the hot trap it is expressed as

$$\frac{G(C - C')\, d\tau}{100} = \frac{Sd\left(\frac{\Delta P}{S}\right)}{K_4}. \tag{12}$$

We shall assume that the oxygen concentration at the hot trap outlet is not zero ($C' \neq 0$). Solving Eqs. (11) and (12) we then have

$$-K_3 P_{Na}\, dC = \frac{100}{K_4} \cdot S \cdot d\left(\frac{\Delta P}{S}\right). \tag{13}$$

We calculate d(ΔP/S) using the expression

$$\frac{\Delta P}{S} = K_2 A \cdot \tau^n \exp\left(-\frac{B}{T}\right) = k \cdot K_2 \tau^n. \tag{14}$$

Two cases will be considered.

1. The rate of reaction between zirconium and oxygen in the sodium when /353
$C < 0.001\%$ by weight is expressed by the average value of K_2. Then

$$-dC = \frac{100 \cdot k \cdot K_2 n \cdot S}{K_3 \cdot K_4 \cdot P_{Na}} \cdot \tau^{n-1}\, d\tau. \tag{15}$$

Integrating the above expression from C_{in} to C_{fin} and from $(\tau_{op} - \tau_0)$ to τ_{op}, respectively, and recalculating for the weight of zirconium, we get

$$P_{Zr} = \frac{K_3 K_4 \cdot \delta \cdot \gamma_{Zr} (C_{in.} - C_{fin}) \cdot P_{Na}}{200 \cdot k \cdot K_2 \cdot [\tau_{op}^n - (\tau_{op} - \tau_0)^n]} . \quad (16)$$

2. When the rate of reaction between zirconium and oxygen is a function of the latter's concentration we have

$$d\left(\frac{\Delta P}{S}\right) = \frac{\partial\left(\frac{\Delta P}{S}\right)}{\partial \tau} \cdot d\tau + \frac{\partial\left(\frac{\Delta P}{S}\right)}{\partial C} \cdot dC.$$

We perform our calculations on the assumption that $K_2 = C/C_0$ when $C \leq C_0$. Finding $(\Delta P/S)$ for this case, substituting its value into Eq. (13) and integrating, we get

$$P = \frac{K_3 K_4 \delta \cdot \gamma_{Zr} (C_{in.} - C_{fin}) \cdot P_{Na}}{200 \cdot K_0 [C_{fin} \cdot \tau_p^n - C_{in.} \cdot (\tau_p - \tau_0)^n]} , \quad (17)$$

where

$$K_0 = \frac{k}{C_0} .$$

It is obvious that Eq. (17) has a physical meaning only when $C_{fin} \cdot \tau_{op}^n > C_{in}(\tau_{op} - \tau_0)^n$ and $C_{in} < C_0$. When $C_{in} > C_0$, then the weight of the zirconium must be determined by simultaneously solving Eqs. (16) and (17).

When the oxygen content of the sodium flowing through the hot trap is appreciable, the zirconium placed at the trap inlet will have a larger weight gain than that situated far from the inlet. On the assumption that the weight gain due to absorption of oxygen from the sodium is described by Eq. (14) and that $K_2 = C/C_0$, while the concentration of oxygen at the trap inlet is C_0, we have obtained an expression which can be used to estimate the specific weight gain of zirconium foil situated at distance y from the trap inlet, during time τ

$$\frac{\Delta P}{S} = n \cdot A \cdot \exp\left(-\frac{B}{T}\right) \cdot \int_0^{\tau} \tau^{n-1} \exp(-X) \cdot d\tau, \quad (18)$$

where

$$X = \frac{100 \cdot n \cdot A \cdot \exp\left(-\frac{B}{T}\right)}{C_0} \cdot \frac{y \cdot \tau^{n-1} S}{G}.$$

Design of Hot Traps

The required quantity of zirconium foil is placed in the hot-trap housing in the form of stacks. One of the placing methods possible is alternating corrugated and noncorrugated foil sheets. Here it can be assumed that the cells formed by the foil are equilateral triangles with side length b. Then the volume $V_{h.t.}$ of a hot trap can be calculated from the formula /354

$$V_{h.t.} = S_{h.t.} L_{h.t.} = P_{Zr} \frac{\left(b + \frac{\delta}{2}\right)^2}{2\sqrt{3}\delta b \gamma_{Zr}}. \quad (19)$$

The total section of the hot trap ($S_{h.t.}$) for a given sodium flow rate through it can be found from

$$S_{h.t.} = \frac{G\left(b + \frac{\delta}{2}\right)}{3600\sqrt{3}\nu \mathrm{Re}_{cr}\left[1 + \frac{2\sqrt{3}\delta}{(b + \delta/2)}\right]}. \quad (20)$$

The inlets of hot traps using zirconium foil must be provided with special devices, which would be able to hold the particles which are not soluble in sodium, which form in it. The latter can appear due to failure of zirconium by embrittlement and due to peeling of the oxide film from the zirconium surface. If stainless steel mesh is used for this purpose, then their design should be as follows: the flow resistance should be made as low as possible; deposition of mechanical particles should not rapidly increase the latter. In addition, to prevent the zirconium foil stacks from failing under their own weight and by dynamic loads of the flow, special dividing grids should be placed between the stacks.

NOTATION

$\Delta P/S$ - increase in the weight of zirconium per unit surface

P - weight

τ - time of contact between zirconium and sodium

τ_{op} - total operating time of the hot trap

τ_0 - time needed for one purification of sodium at the end of the hot trap's operating life

δ - thickness of zirconium sheet

G - flow rate of sodium

C - oxygen content of sodium

C_0 - minimum oxygen content of sodium for which no reduction is observed in the rate of oxygen absorption

C_{Na_2O} - equilibrium concentration of Na_2O in sodium /355

$C^*_{Na_2O}$ - saturation concentration of Na_2O in sodium

A, B, n - coefficients of equation describing the weight gain of zirconium

K_2 - coefficient which takes into account reduction in the weight gain of zirconium when the oxygen concentration is reduced to below C_0 and the flow turbulence in the hot trap is lessened

K_3 - coefficient which takes into account the oxygen flowing in from dead-end and other sections of the circuit

K_4 - coefficient which takes into account the incompleteness of washing the zirconium surface by sodium

K_a - thermodynamic equilibrium constant

REFERENCES

1. Hinze, R. B.: Nucl. Engng., 5, 48, 225 (1960).
2. Faris, F., Johnson, D., et al.: In the book Proceedings of the Second United Nations International Conference on Peaceful Uses of Atomic Energy, Geneva, 1958.
3. Allen, J.: Nucl. Engng., 7, 76 352 (1962).
4. Bawman, F. and Cubicciotti, D. A.: J. Ch. E. Journal, 2, 2, 173 (1956).
5. Carter, R. L., et al.: Proceedings of the Second United Nations International Conference on the Peaceful Uses of Atomic Energy, held in Geneva. V. 7, Reactor Technology, Geneva United Nations, 1958, p. 72.
6. Davis, M. and Draycott, A.: Proceedings of the Second United Nations International Conference on the Peaceful Uses of Atomic Energy, held in Geneva. V. 7, Reactor Technology, p. 94, Geneva, 1958.

7. Yeremenko, V. N.: Titan i yego splavy [Titanium and Its Alloys]. Published by the Academy of Sciences of the Ukrainian SSR, Kiev, 1960.
8. Tsirkoniy [Zirconium]. Collection of articles, Part II. Translated from English under the editorship of V. A. Alekseyev. Foreign Literature Publishing House, Moscow, 1955.
9. Dmitriyeva, I. B., et al.: Second article, Part IV of present collection.
10. Karapet'yants, M. Kh.: Khimicheskaya termodinamika [Chemical Thermodynamics]. Goskhimizdat, Moscow-Leningrad, 1953.
11. Distefano, J. R. and Hoffman, E. E.: Atomic Energy Review, 2, 1, 3-34 (1964).

MAXIMUM PERMISSIBLE LEAKAGE IN A SODIUM-TO-WATER STEAM GENERATOR

N. N. Ivanovskiy and F. A. Kozlov

The use of sodium as the coolant in large nuclear power stations makes /355
it necessary to develop efficient and reliable sodium-to-water steam generators. At present the greatest promise is held out by a single-wall generator, [1], which ensures higher economy and simplicity than the two-wall design. However, water leakages in the single-wall device is more dangerous, since then the water gets into the sodium. One of the major problems which this creates is that of removing the products of interaction with water from the so- /356
dium. According to [2], the reaction between water with sodium, on excess of the latter, can be written as

$$4Na + H_2O \rightarrow Na_2O + 2NaH. \quad (1)$$

Accumulating in the sodium the products of reaction can interfere with the heat transfer between the water and sodium, stopping up of the circuit's ducts, as well as increased corrosion of construction materials. Hence, the water must be continuously removed from the sodium by a cold trap. As was shown in [3], this device is capable of removing the products of interaction between water and sodium from the latter.

Only a part of the liquid metal is circulated through the trap. Hence, depending on the amount of leakage, a given concentration of products of interaction is established in the sodium. Reliable operation of a facility requires that all the admixtures be in the dissolved state at operating temperatures. This condition serves as a limit on the amount of leakage above which the facility will be in danger of failure. To determine this maximum leakage we shall now derive an equation which could be used to calculate the change in the oxygen content of the sodium with time, in the presence of oxygen sources and drains in the system.

It is shown in [3] that in cases when the minimum temperature in the system, when water gets into sodium, exceeds 220°C, the sodium oxides will primarily pass into the crystalline phase. Hence, the calculations can be based on the quantity of oxygen which gets into sodium in the form of H_2O, while the maximum permissible concentration could be the solubility of oxygen in sodium at minimum sodium temperature in the wall.

On the condition that intermixing in the system is ideal, the equation of material balance for the oxygen in sodium has the form

$$P_{Na}\, dC = (G_1 - G_2)\, d\tau. \quad (2)$$

In our case the oxygen is removed by a cold trap. Assuming that the oxygen concentration of the sodium passing through the cold trap is reduced to C', we have

$$G_2 = G_t \ (C - C'). \tag{3}$$

Then Eq. (2) will become

$$P_{Na}\, dC = [G_1 - G_t \ (C - C')]\, d\tau. \tag{4}$$

Integrating the above expression for $\tau = 0$ and C = C', we get

$$C = C' + \frac{G_1}{G_t}\left(1 - e^{-\frac{\tau G_t}{P_{Na}}}\right). \tag{5}$$

Under these conditions the maximum oxygen content of the sodium will be /357

$$C_{max} = C' + \frac{G_1}{G_t}, \tag{6}$$

it is reached during a time

$$\tau \geqslant \frac{5P_{Na}}{G_t}. \tag{7}$$

Changing to the size of the maximum permissible leakages, we have

$$G_{H_2O} = 1.12 G_t \ (C_{max} - C'). \tag{8}$$

Using Eqs. (7) and (8) for a specific case it is possible to calculate the maximum permissible leakage of a sodium-to-water steam generator, as well as the time for reaching the maximum concentration in the circulating sodium.

It can be seen from Eq. (8) that the duration of operation of a steam generator with a leak will be determined by the thoroughput of the cold trap and by the magnitude of the leakage. In order that the system be capable of prolonged operation with large leakages, cold traps with high thoroughput and capacity must be designed.

NOTATION

P_{Na} - weight of sodium in facility

G_t - flow rate of sodium through cold trap

G_1 - influx of oxygen into sodium by water leakage

G_2 - oxygen removed from sodium by the cold trap

C - oxygen content of sodium after τ hours of leakage of steam generator, parts by weight

C' - oxygen content of the sodium at cold-trap outlet, parts by weight

G_{H_2O} - maximum permissible leakage of steam generator

REFERENCES

1. Poplavskiy, V. M., et al.: Teploenergetika, No. 7 (1966).
2. Ivanovskiy, N. N. and Kozlov, F. A.: Atomnaya Energiya, 17, 5 (1964).
3. Subbotin, V. I., et al.: Atomnaya Energiya, 19 (3), 298 (1965).

SOME PROBLEMS OF OPERATION AND DESIGN OF LIQUID-METAL LOOPS

A. V. Drobyshev, V. A. Kurov and I. T. Filipov

The extensive experience accumulated up to now in work with alkaline metals has not been sufficiently illuminated in available publications [1-4]. Liquid metal loops are extensively used in the study of compatibility between the materials of construction and the liquid metal, in the study of heat transfer and fluid dynamics, as well as in testing fuel elements and their mockups outside the reactor. /357 /358

The construction material specimens are tested in liquid-metal filled vessels, placed on stationary and rotating supports. Installations with a wide range of possibilities for this purpose are loops with natural and forced coolant circulation (Figs. 1 and 2). The stands are used for prolonged tests at constant coolant temperature and velocity.

Arrangements used for the study of thermal-flow dynamics which have test sections of complex design equipped with a larger number of temperature, pressure, flow rate, etc., pickups [5], are frequently made as multi-loop circuits which, as a rule, operate in a wide flow-rate and temperature range (Fig. 3). Mockups of fuel elements are tested in similar arrangements, where integrated data on the specimen behavior can be obtained. To obtain the required number of thermal cycles (thermal shocks) in a short period of time, use is made of specially designed setups (Fig. 4). The fuel-element mockup is placed in a sodium-filled vessel, which was induction heated by the LA-107 generator and water cooled; cycle duration is 41 secs.

We shall here consider only loops with forced coolant circulation (see Fig. 3), since they include all the equipment of simpler loops and, in addition, they also have special equipment such as metal-to-metal high-temperature heat exchangers [6], etc. The majority of experiments was performed in setups with capacities not above 250 liters and liquid-metal flow rates of not more than 20 m^3/hour. These setups should operate stably and reliably when the flow rate is varied from zero to nominal. In setting up the thermal balance of the system (nominal operating mode) one must know precisely the entire assortment of tubing from which the circuit is made. Even insignificant deviations of diameters have an appreciable effect on redistribution of temperatures and velocities of the liquid metal over the entire circuit. Due to this it is always useful to have an excess-capacity heater and higher-than-specified pressure head. The tendency to reduce the loop volume and to provide for excess pump head capacity has lead to the use of centrifugal pumps with $n_s < 50$ [7], however, it was found [8] that the operating reliability of electromagnetic pumps is higher. As a rule, the major part of the pressure head which is developed by the pump is used up at the test section (Fig. 5). Hence, the heat-exchanger apparatus of experimental /360

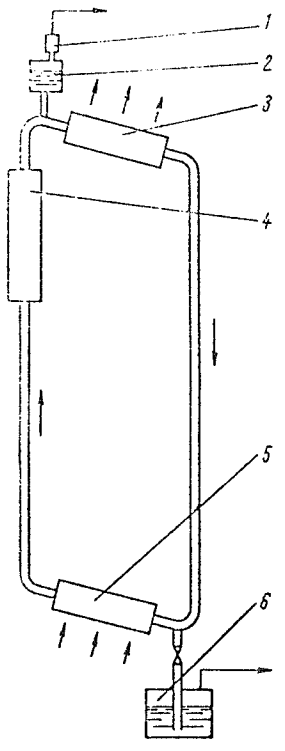

Figure 1. Schematic of a Natural-Circulation Loop.

1) Vapor Trap; 2) Compensating Tank; 3) Cooler; 4) Test Section; 5) Heater; 6) Drain Tank.

setups is not the most efficient from the point of view of compactness and of minimum volume of the alkaline metal, as compared with, for example, slot-type heat exchangers but has an acceptable flow resistance of the ducts.

Auxiliary Systems

Preparing the heat-transfer agent. The sodium is supplied from the plant in special 100 liter containers, and its oxygen content is up to 0.05% by weight. Depending on the test conditions, the sodium can be used without distillation, as well as with preliminary distillation. In the second case the metal is heated until it melts and is poured into an evaporating tank. Distillation takes place at 550-560°C with a continuously operating pre-evacuation pump. The sodium vapor condenses in a condensing tank. The eutectic sodium-potassium alloy is prepared in a special installation with a proportioning device [10]. /361

The admixture content of the heat-transfer agent is monitored by samplers indicators and other devices, which are installed on the bypass lines of the loop. The samples are taken by distilling samplers [11] or using sections which are first frozen and then removed [for analysis]. Satisfactory checking precision is provided by the indication method, which is based on the stopping up of narrow passages at a specific flow rate and temperature.

Oxygen and nitrogen are removed from the heat transfer agent during operation by cold [13] and hot [14] oxide traps. Under maximum conditions the oxygen content of the liquid metal is held to $1 \cdot 10^{-3}$% by weight when using the cold and $1 \cdot 10^{-4}$% by weight when using the hot traps.

The gas-and-vacuum system is used for filling the setup with the liquid metal, for maintaining the operating pressure, sampling and for testing the airtightness of the arrangement. Vacuuming is performed through a compensating tank and a vapor trap (Fig. 6). The diameter of the pipeline connecting the trap to the tank should be at least 70 mm. The vapor trap is a pipe 120 mm in diameter, with welded inclined baffles and a layer of stainless chips. In vacuum systems of setups with liquid-metal volumes of 50-500 liters use is made of tubes 30-40 mm in diameter and not more than 3 m long (from the header to the vessel), and of the VN-1 and VN-2 pumps. Tubes 10-20 mm in diameter were used in the gas systems. /362

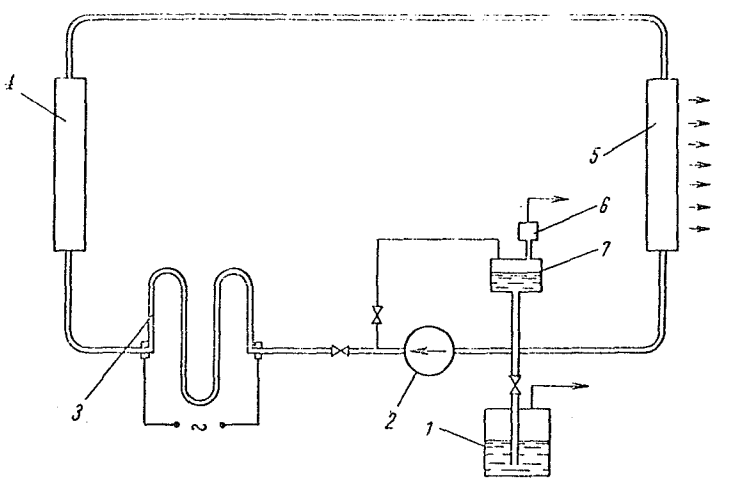

Figure 2. Recuperator-Less Loop.

1) Drain Tank; 2) Pump; 3) Heater; 4) Test Section; 5) Cooler; 6) Vapor Trap; 7) Compensating Tank.

Instrumentation. Standard membrane-type manometers are used as pressure pickups. Compensating pressure pickups have also been developed (Fig. 7). The level is measured by contact level meters (pin-type, automotive spark plugs, etc.,), which are based on closing an electric circuit by the liquid metal, or potentiometer-type gages [16]. The temperature was measured by standard thermocouples, as well as by microthermocouples.

Equipment Layout and Safety Measures

The experimental setups are located in bays or halls. The designer must take into account convenience in operation, installation and dismantling of equipment, location of instrumentation pickups, shutoff and regulating valving, placing preheaters and thermal insulation and safety requirements. Extensive pipeline length increases the liquid-metal volume, flow resistance and heat losses to the surroundings. More rigorous layout requirements are presented to setups with centrifugal pumps with frozen-sodium seals. In this case the pump is placed on a platform at a height of 2-2.5 m. The pump seal should be at the elevation of the maximum liquid-metal level in the compensating tank, since [otherwise] metal may spill into the premises or gas may be sucked into the pump chamber. The compensating tank should contain enough metal to completely fill the equipment situated above the maximum level. A drainless cold oxide trap may be placed at any level. The distilling sampler should also be placed in a safe and convenient place, since it has to be used during the setup's operation. The still should be rigidly supported, so that, when the latter is disassembled, the metal drops suspended from the screen will not drop into the cup and thus distort the measurements. The oxide indicators and the measuring tank are placed on the setup's platform. Heat exchangers, test section, coolers, heater,

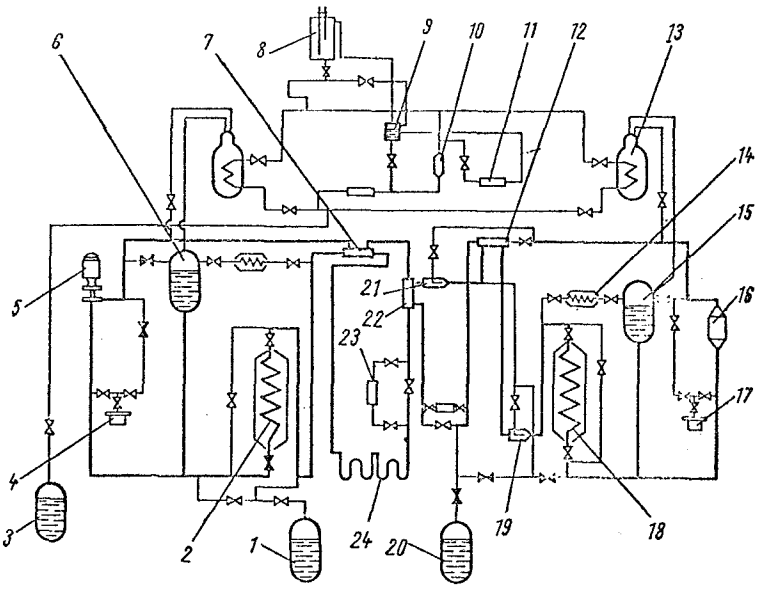

Figure 3. Diagram of a Three-Loop Arrangement.

1) Drain Tank of First Loop; 2) Cooler of First Loop; 3) Drain Tank of Third Loop; 4) Distilling Sampler; 5) Pump of First Loop; 6) Compensating Tank of First Loop; 7) Recuperator of First Loop; 8) Measuring Tank; 9) Compensating Tank of Third Loop 10) Pump of Third Loop; 11) Cold Oxide Trap; 12) Recuperator of Second Loop; 13) Cold Oxide Trap; 14) Oxide indicator; 15) Compensating Tank of Second Loop; 16) Pump of Second Loop; 17) Distilling Sampler; 18) Cooler of Second Loop; 19) Mixing Header; 20) Drain Tank; 21) Mixing Header; 22) Loop-to-Loop Heat Exchanger; 23) Hot Oxide Trap; 24) Heater.

hot traps, etc., are placed at elevation eliminating formation of gas pockets and providing for completer draining of metal. The drain tank is placed in the lowest point of the loop. For convenience in operating the setup and to reduce its height, the drain tank is usually placed in a pit (Fig. 8); the pipelines are inclined at 3-5°. Expensive equipment (transformers, vacuum pumps) should not be placed beneath pipelines and equipment with liquid metal. The setup platform should be rigidly fastened to permanent walls to eliminate vibrations. To protect the service personnel from possible accidents, the high-temperature sections should be placed in inert-gas chambers. All the equipment beneath the setup platform is covered by movable shields. /363

Pans should be placed at zero elevation to collect metal which may spill during an accident and to localize a possible fire. Water may be used at alkaline-metal setups only when absolutely necessary. The water pipelines are laid below the platform and are insulated. The drain lines of the loop are maintained at a temperature higher than the melting temperature of the metal, and are remotely controlled by electrically-driven valves. The remaining valves

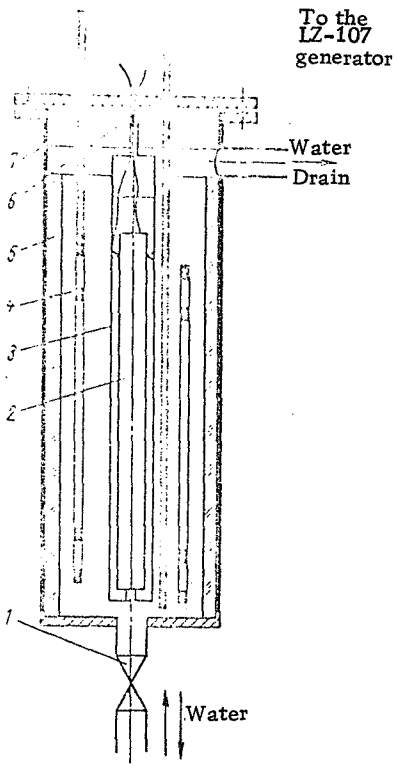

Figure 4. Schematic Diagram of a Setup for Thermal-Shock Testing of Specimens.

1) valve; 2) specimen; 3) vessel with metal; 4) inductor; 5) insulation; 6) level gage and thermocouples; 7) casing.

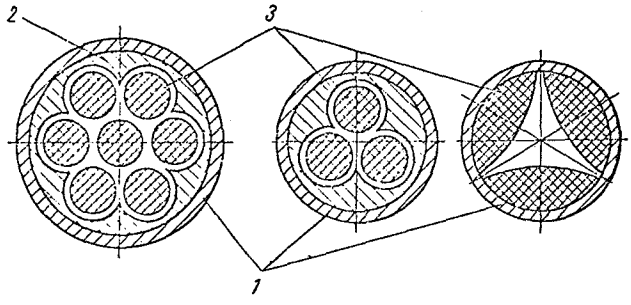

Figure 5. Sections Through Test Sections of a Setup.

1) casing; 2) spacer; 3) specimens.

are manually operated. The stand is supplied by a signalling and blocking system. When metal leakage is discovered, the electric supply is shut off and the valves of drain lines are opened. The main heater is also shut off automatically when the temperature of the heat-transfer agent and supply busbars increases above the permissible value, when there is no liquid metal flowing, no water in the busbars and when the pump stops suddenly.

Accidents were previously caused by nichrome heaters, wound onto pipelines and supplied with current at 220 V. When using small-diameter tubing the porcelain buses [insulators] cracked and the heaters were short-circuited

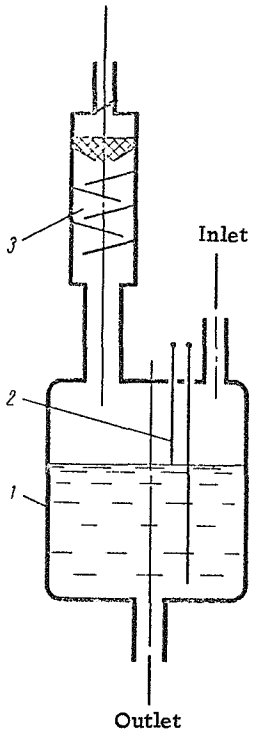

Figure 6. Joining a Gas-and Vacuum Line to the Loop.

1) Compensating Tank; 2) Level Gage; 3) Vapor Trap.

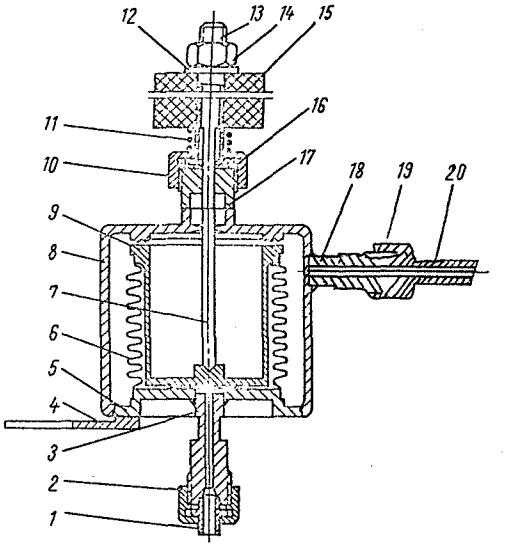

Figure 7. Section Through a Compensating Manometer.

1, 2 and 3) Liquid-Metal Inlets; 4) Fastening Plate; 5) Cover; 6) Bellows 7) Core; 8) Casing; 9) Bellows Joint; 10) Connector Nut; 11) Spring; 12) Washer; 13) Rod; 14) Nut; 15) Spool; 16) Sleeve; 17) Connecting Pipe; 18, 19 and 20) Gas Inlets.

by the pipeline. Two methods are now used to prevent this, one which consists in using separating transformers, and the other in reducing the voltage to approximately 48 V by type OSU-100/0.5 transformers. Accidents are also caused by centrifugal pumps with frozen-sodium shaft seals. The sodium in the space between the casing and the shaft is frozen by process water. During operation bicarbonates are deposited on the walls of the cooling jacket, which interferes with removal of heat and thus leads to splatter of metal. [To remedy this the sodium-held] admixtures are periodically removed by a 20% solution of nitric acid. Accidents also happened when the main heater and pump blocking system were not connected (the heater was supplied with 15,000 amps of current and, when the pump jammed, it burned instantaneously), as well as due to defects in the construction materials, i.e., microcracks, micropores, pealing, etc. Accidents may also be produced by manufacturing defects, such as low quality of joint welding; usually these are discovered during the run-in period.

The cost of developing an experimental loop for heat engineering studies /364 at maximum temperature of 500°C can be broken up as follows: 1) design work 7%; 2) cost of construction materials 6%; 3) standard process equipment 18%;

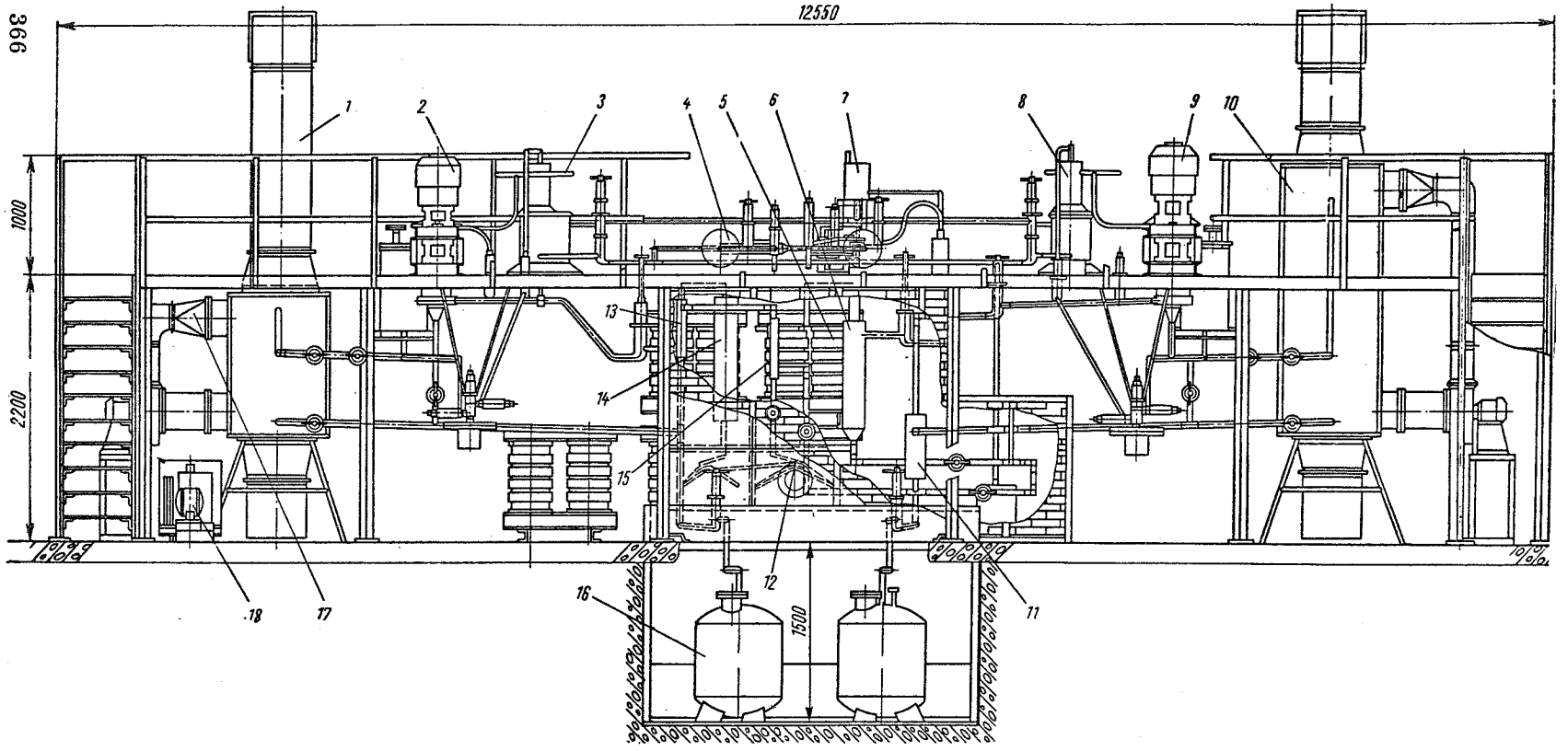

Figure 8. Equipment Layout for a Three-Loop Setup.

1) Cooler; 2) Pump of First Loop; 3 and 8) Cold Oxide Traps; 4) Hot Oxide Trap; 5) Transformer; 6) Mixing Header; 7) Compensating Tank; 9) Pump of Second Loop; 10) Cooler; 11) Heat Exchanger; 12) Heat; 13) Recuperator; 14) Inter-Loop Heat Exchanger; 15) Test Section; 16) Drain Tank; 17) Cooler Heating System; Vacuum Pump.

4) standard electrical equipment 12%; 5) instrumentation 12%; 6) making non-standard process equipment 27%; 7) process equipment installation 7%; 8) electrical equipment installation 6%; 9) adjustment of electrical equipment and of instrumentation 5%.

REFERENCES

1. Balandin, Yu. F. and Markov, V. G.: Konstruktsionnyye materialy dlya ustanovok s zhidkometallicheskim teplonositelem [Construction Materials for Facilities Using Liquid-Metal Heat-Transfer Agents]. Sudpromizdat, Leningrad, 1961.
2. Andreyev, P. A., et al.: Zhidkometallicheskiye teplonositeli yadernykh reaktorov [Liquid-Metal Coolants of Nuclear Reactors]. Sudpromgiz, Leningrad, 1959.
3. Zhidkometallicheskiye teplonositeli (natriy i natrievo-kalievyye splavy) [Liquid-Metal Coolants (Sodium and Sodium-Potassium Alloys)]. Collection of articles translated from English under the editorship of A. V. Sheyndlin. Foreign Literature Publishing House, Moscow, 1953.
4. Kutateladze, S. S., et al.: Zhidkometallicheskiye teplonositeli [Liquid-Metal Heat-Transfer Agents]. Atomizdat, Moscow, 1958.
5. Zhukov, A. V., et al.: Part II of present collection.
6. Kurov, V. A. and Menshikov, V. F.: Article of present collection immediately following this.
7. Kuznetsov, V. A., et al.: Atomnaya Energiya, 7, 11 (1959).
8. Marin, N. I., et al.: Present collection, Part IV.
9. Kays, W. M. and London, A. L.: Compact Heat Exchangers, The National Press, Palo Alto, California, 1955.
10. Sittig, M.: Natriy [Sodium]. Gosatomizdat, Moscow, 1961. [Most likely a translation].
11. Dmitrieva, I. B., et al.: Second article, Part IV of present collection.
12. Kozlov, F. A., et al.: Article following [11] in present collection.
13. Kozlov, F. A., et al.: Teplofizika vysokikh temperatur, 3, No. 1, 154 (1965).
14. Kozlov, F. A. and Kuznetsov, E. K.: Part IV of present collection.
15. Turchin, N. M. and Shumskiy, R. V. [sic].: Article following [6] in present collection.
16. Kirillov, P. L., et al.: Atomnaya energiya, 9, 3 (1960).

HEAT EXCHANGERS OF EXPERIMENTAL LIQUID-METAL LOOPS

V. A. Kurov and V. F. Men'shikov

No systematized material on the above topic has been published in the Soviet Union. In the publications available [1] and [2], primary attention is paid to problems of heat transfer and practically no consideration is given to design and operation of heat exchangers. In the present paper we are considering the design and operation of heat exchangers for sodium and its alloys [3]. These are primarily coolers (metal-to-water, metal-to-air), interloop heat exchangers, recuperators[1] and mixing devices. /364 /365

An efficient heat exchanger should satisfy the following requirements:

1) Reliable operation of facilities under all conditions (sometimes with a changed heat-transfer surface) during the specified time of operation, sufficient strength safety factor at the given rates of temperature variations (startup and shutoffs);

2) inspection and contaminant removal in shortest time;

3) uniform distribution of heat-transfer agent flow (no stagnation zones, gas pockets, etc.);

4) is provided with facilities for complete draining of heat transfer agents;

5) is accessible for the necessary quality control on manufacture.

The requirements produced by the physical and chemical properties of the heat transfer agents are well known [4].

As a rule, the designer is limited by the above requirements. However, among heat exchangers satisfying these requirements preference is given to those with the highest efficiency and with lower power consumption for pumping the liquid metal [5]. The above requirements are satisfied by conformance to the following conditions.

1. The velocity of the liquid metal in the supply stubs is specified as equal to (or smaller than) its velocity in the working section of the heat exchanger. Otherwise it is necessary to make a tapered stub with a taper angle of 15° or to place equalization sections into the inlet chambers, to equalize the flow velocity over the cross section. /366

---

[1] The term recuperators is used here to designate heat exchangers, in the cavities of which only one heat-transfer agent flows all the time.

2. When the heat transfer agent flows into the intertubular space perpendicular to the tubes a baffle and uniform distribution of the liquid metal over the inlet cross section are provided.

3. To prevent nonproductive flow of the heat transfer agent, spacers are provided between the casing and the tube cluster.

4. To increase the rate of heat transfer, baffles are placed in the intertubular space (for flow across the tubes).

5. In order to make the tube cluster more rigid (to eliminate vibrations), the tubes are spaced by screens, which can serve simultaneously as baffles.

6. When the heat-transfer surfaces are coiled, comb-shaped spacers are used.

In cooler shown in Fig. 1 is provided with a device for uniformly distributing the flow over the tubes when the inlet angle of the chamber is more than 30°. Experience shows that without use of such devices heat transfer does not take place over the entire surface. Table 1 lists types of heat exchangers.

Metal-to-Water Coolers

The use of water for cooling the above heat transfer agents involves operating difficulties, but makes it possible to develop a small-size device. The heat transfer surface always has two air-tight walls (made from tubes of different diameter) and an adjustable intermediate space. The latter makes it possible to reduce the thermal stresses in the walls which are particularly high when water is let into a heated up loop. To ensure acceptable heat transfer coefficients the intermediate space is filled by an interlay from an alloy such as Wood's metal, graphite powder, gas, etc. The intactness of walls is monitored by changes in pressure in the intermediate space and, in case of a gas interlayer, also by closing of an electric circuit by the liquid metal which penetrates the wall. /368

It is practically impossible to adjust the capacity by varying the water flow rate, since the outlet temperature is limited, hence, adjustment is obtained by changing the surface of heat transfer by the following techniques: /369

1) Sectioning;

2) Moving the water-shell casing.

3) Changing the level of interlayer. This method is preferable, since it makes it possible to obtain smooth heat removal in a wide range.

When making such a cooler, particular attention is paid to provisions for checking the welded seams connecting the tubes to tube headers and of the latter to the casings. On the basis of operating experience we recommend the use

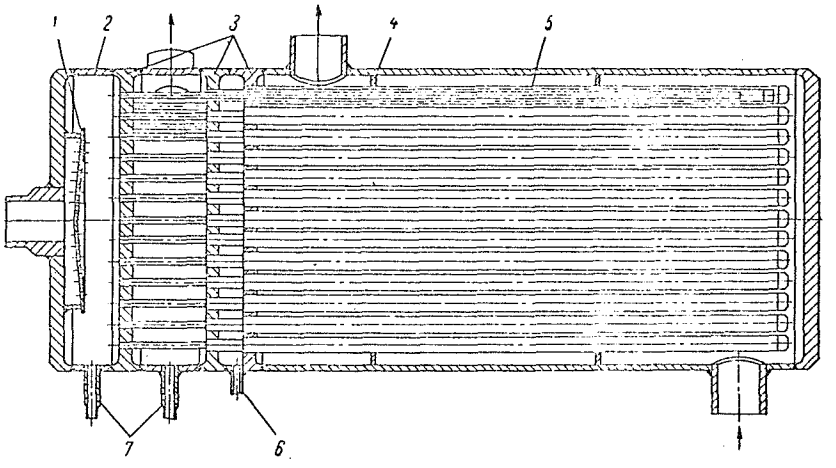

Figure 1. Metal-to-Water Cooler.

1) Flow Equalization Section; 2) Inlet Chamber; 3) Tube Header; 4) Casing; 5) Bayonet Tube; 6) Connecting Stub of Intermediate Cavity; 7) Draining Stub.

TABLE 1. Heat Exchanger Types

	Recuperative										Dir. cont.	
	Without intermediate layer						W/intermediate layer					
	Coil-type	2 tube	Shell-and-tube				2 tube	Shell-and tube		Built-in cooler		
			U-shaped	With moving rings	With bellows	Rigid	Lenticular compensator		W/bayonet tubes			
		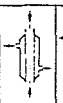							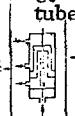		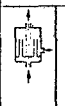	
1.M/M	+	+	+	+	+	+					+	+
2.M/G	+											
3.M/W							+	+	+	+		

Remarks
1) M/M-Inter-loop Metal-to-metal heat exchanger's and recuperators
2) M/G-Metal-air cooler
3) M/W-Metal-water cooler

of heat exchangers shown in Fig. 2 (for a surface of $< 1\,m^2$) and in Figs. 1 and 3 (for a surface of $> 1\,m^2$).

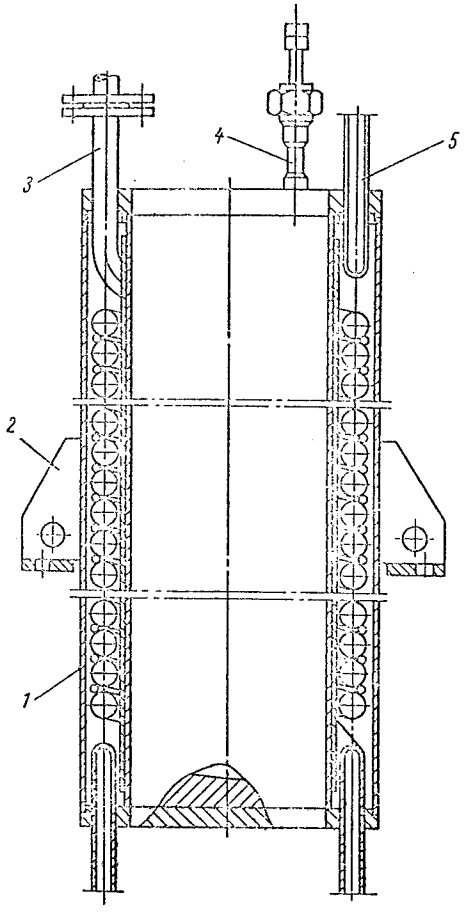

Figure 2. Metal-to-Water Cooler.

1) Casing; 2) Support; 3) Metal-Carrying Coil; 4) Level Gage; 5) Water-Carrying Coil.

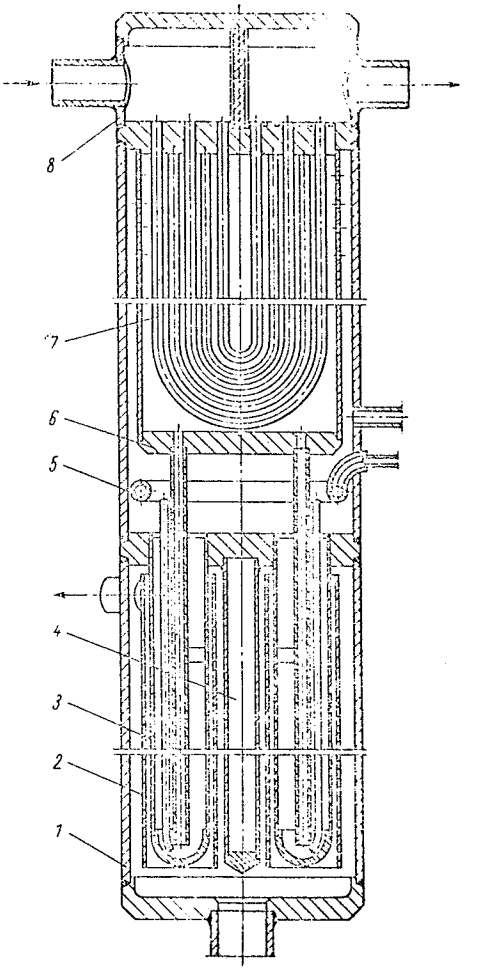

Figure 3. Metal-to-Water Cooler.

1) Casing; 2) Jacket; 3) Shell; 4) Spacer; 5) Drain System; 6) Condenser Jacket; 7) Condenser; 8) Inlet (Outlet) Water Chamber.

Metal-to-Air Coolers

The main advantages of metal-to-air heat exchangers as compared with water cooled apparatus is the ability of adjusting the heat removal within a wide range and greater operating safety. They can also be modified to provide for preheating. Their disadvantage is the large size. Use is made of coolers with surfaces of $< 3\,m^2$ and $> 3\,m^2$ (Fig. 4).

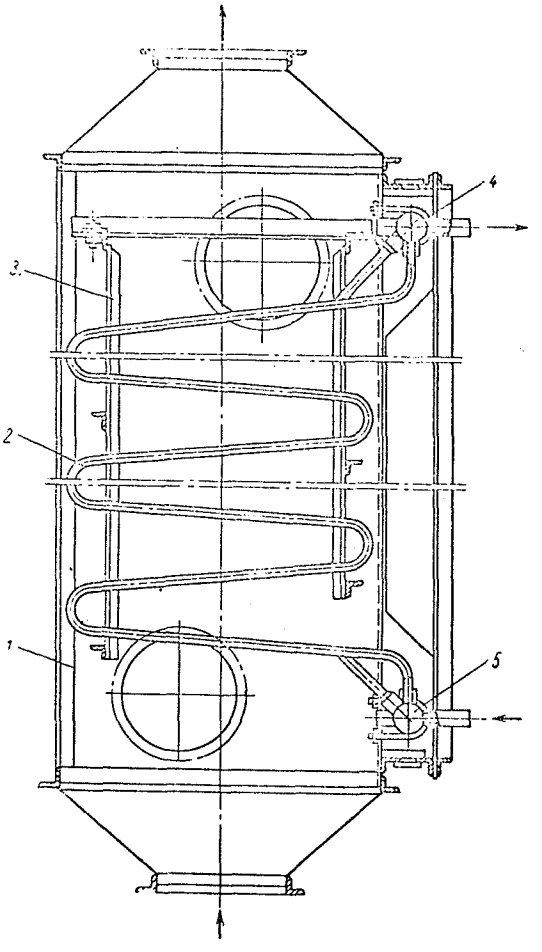

Figure 4. Metal-to-Air Cooler.

1) Jacket; 2) Coils; 3) Spacing System; 4) Oultlet Header; 5) Inlet Header.

Inter-Loop Metal-to-Metal Heat Exchangers and Recuperators

While the purpose served by coolers and interloop heat exchangers is obvious, the inclusion of recuperators in loop arrangements requires some clarification. Recuperators are thermal bridges between the hot and cold branches of the same loop (Fig. 5), which make it possible to reduce the power consumption in the heater and to provide, for a given heat-transfer agent flow rate, the specified maximum and minimum temperatures in the loop. If we disregard heat losses in the loop, then

$$N_h^r = N_h - N_r,$$

where N_h^r is the power consumption in a recuperator-equipped loop, N_h is the power consumed by the heater in a recuperator-less loop and N_r is the recuperator rating. The inclusion of a recuperator in a loop reduces the required cooler surface. Coolers are structurally more complicated than recuperators and, in addition, they have a lower heat-transfer coefficient. The apparent increase complication of the loop layout [actually] results in increasing the total heat-transfer surface and increases the safety in operating the circuit. /370

The mean temperature difference between the cold and hot branches of the recuperator, which is determined by the heater, may be as high as 200°C (heating to 500°C) for steady-state operation. The high temperature levels and large mean temperature differences require close attention to finishing of structural components which are related to uniform distribution of flows over the cross section and to compensation of thermal expansion. To protect the tubes from the effect of transverse flow, the section of the tube cluster ahead of the inlet stub is protected by a baffling device (Fig. 6), which serves as a continuation of the casing.

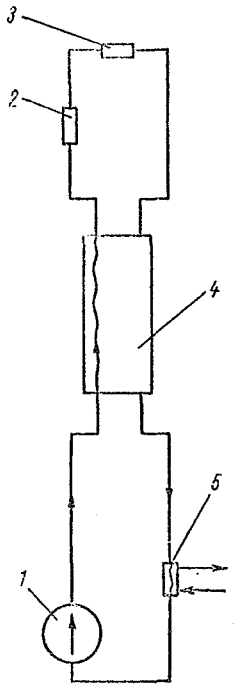

Figure 5. Schematic Diagram of a Recuperator-Equipped Loop.

1) Pump; 2) Heater; 3) Working Section; 4) Recuperator; 5) Cooler.

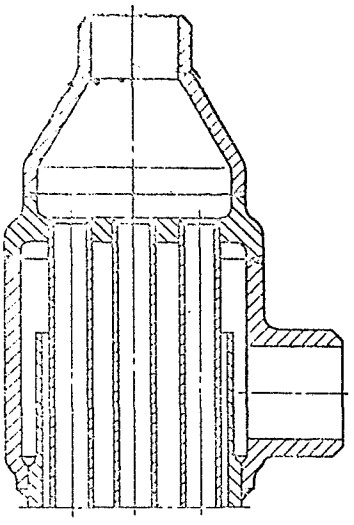

Figure 6. Baffling Device Which is a Continuation of the Casing.

In recuperators (Fig. 7) the ring serves as continuation of spacers of all shapes, and also serves for distributing the flow uniformly over the cross section of the intertubular space. /371

The tubes are connected to the tube lattice by welding only. Tubes with wall thicknesses of more than 1 mm and with a diameter of up to 30 mm are connected by flashing off the edge of the hole in the tube header, while when the wall thickness is less than 1 mm, this is done by flashing off the "whisker" in the tube header. Both methods produce a strong and tight joint when the tubes are made to conform to the hole diameters. In both cases it is possible to have high tube cluster densities, i.e., spacing of 1.2 d and even less.

The thermal stresses are reduced by creating a stagnant zone of the heat-transfer agent, using a screen, while in tubes this is obtained by lining and covering (see Fig. 1). The difference in thermal expansions in the straight tubes and in the casing was compensated by placing several bellows on the tube cluster (see Fig. 7 and Table 1). To compensate for thermal expansions of different (not welded together) construction materials in recuperators, the tube cluster was placed into the casing on packing rings. Leakages between different spaces comprised less than 1% of the heat-transfer agent flow rate. /373

Nonconformance to the above requirements results in breakdowns. For example, the recuperator shown in Fig. 8 failed as a result of improper flow distribution between the tubes.

Rigid-design recuperators are usually made in the manner shown in Fig. 9. Use is also made of recuperators with compensation on the heat-transfer surface of less than 0.5 m^2 (Fig. 10) and more than 0.5 m^2 (see Fig. 7 and Table 2).

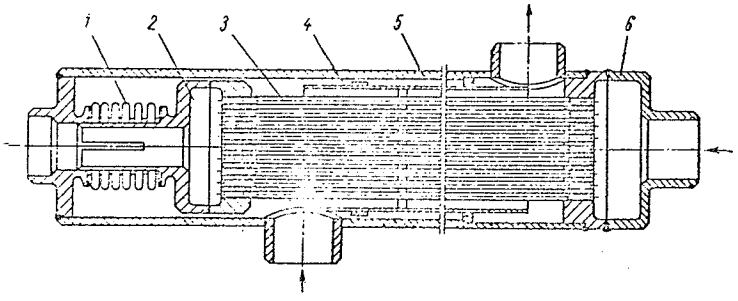

Figure 7. Schematic Diagram of a Recuperator With a Compensating Bellows.

1) Bellows; 2) Movable Chamber; 3) Tube; 4) Spacer; 5) Casing; 6) Chamber.

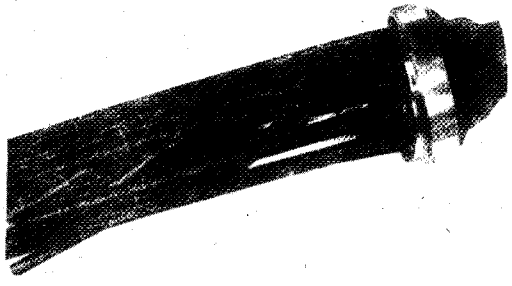

Figure 8. Recuperator After Failing.

Mixers are used in loops for:

1) Heating the entire volume of the heat transfer agent to the specified temperature, provided that only a part of the flow, which is heated to a higher temperature, passes through the heater.

2) Reducing the heat-transfer agent temperature ahead of the recuperator. We have used tubular-type and double-tube type recuperators (Figs. 11 and 12).

TABLE 2. Fitness of Materials of Construction at Different Temperatures

Material	Temperature, °C	Heat-transfer agent	Velocity, m/sec	Oxygen content, %	Time of operation, hours	State
1Kh18N10T	650	Na	2	$2 \cdot 10^{-3}$	4500	Continues to operate
1Kh18N10T	600	K	2	—	2000	Same as above
1Kh18N9T	250 350	Na—K		—	7000	Same as above

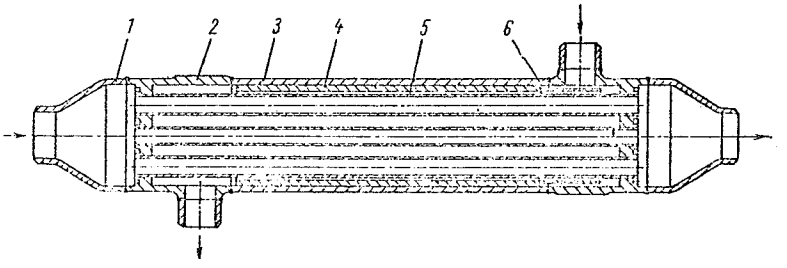

Figure 9. Schematic of a Recuperator.

1) Chamber; 2) Tube-Header Chamber; 3) Casing; 4) Spacer; 5) Tube; 6) Baffling Device.

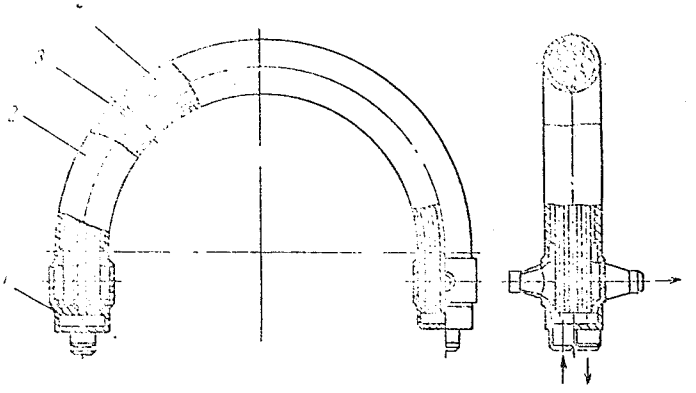

Figure 10. Schematic of a Recuperator.

1) Chamber; 2) Casing; 3) Star-Shaped Spacer; 4) Tube.

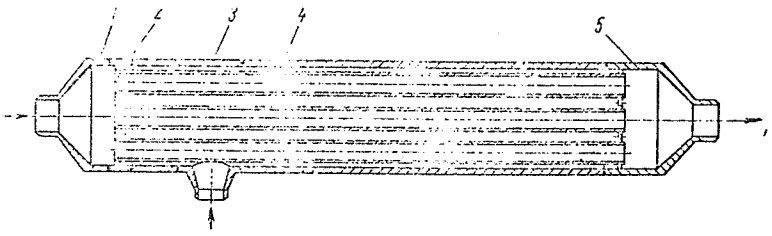

Figure 11. Schematic of a Tubular-Type Mixer.

1) Chamber; 2) Tube Header; 3) Casing;
4) Tube; 5) Chamber.

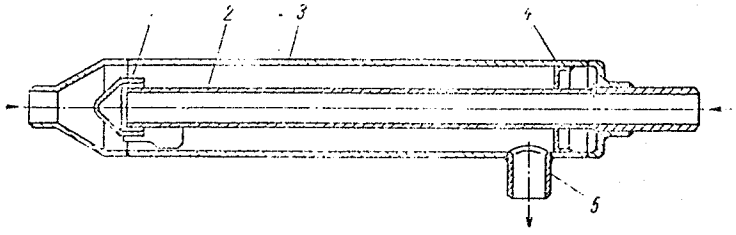

Figure 12. Schematic of a Double-Tube Mixer.
1) Cap; 2) Tube; 3) Casing 4) Ring; 5) Connecting Stub.

REFERENCES

1. Kutateladze, S.S., et al.: Zhidkometallicheskiye teplonositeli [Liquid-Metal Heat-Transfer Agents]. Atomizdat, Moscow, 1958.
2. Zhidkometallicheskiye teplonositeli [Liquid-Metal Heat-Transfer Agents]. Collection of articles translated from English under the editorship of A.V. Sheyndling. Foreign Literature Publishing House. Moscow, 1953.
3. Drobyshev, A.V., et al.: Article immediately preceding this one in the present collection.
4. Chechetkin, A.V.: Vysokotemperaturnyye teplonositeli [High-Temperature Heat-Transfer Agents]. Gosenergoizdat, Moscow, 1962.
5. Andreyev, M.M., et al.: Teploobmennaya apparatura energicheskikh ustanovok [Heat-Transfer Devices of Power Facilities]. Mashgiz, Moscow, 1963.

STUDY OF VELOCITY FIELDS BY THE ELECTROMAGNETIC METHOD

N. N. Turchin and R. V. Shumskiy

Processes of heat transfer are closely related to the fluid dynamics of the heat transfer agent. The velocity fields are studied experimentally primarily by means of Pitot tubes and of thermoanemometers. At present these devices cannot be used in liquid metals. The high electrical conductivity of the latter makes it [however] possible to determine local velocities by measuring the electric potentials which are generated when the liquid moves in a magnetic field. The feasibility of using the electromagnetic method is clarified in [1-3], which consider a round tube for which the distribution of potentials in axisymmetric flow was obtained analytically. The experimental data are in good agreement with the calculations. /374

The present article also presents results of experiments with a round tube, but it considers a more general case of the motion of a fluid in the annulus formed by two coaxial tubes with an arbitrary [thermal] conductivity of the walls. It is assumed that the velocity distribution is axisymmetric [$v_r = v_0 = 0$, $v = v_z(r)$], and that it does not change in a homogeneous magnetic field which is sufficiently large so that edge effects can be disregarded; the secondary induced field is negligible. Determination of the potential in some point M (Fig. 1) reduces to solving the following system of differential equations (the subscripts denote the region for which the equations are written) /375

$$\nabla^2 U_1 = 0, \tag{1a}$$

$$\nabla^2 U_2 = B_0 \frac{\partial v}{\partial r} \sin\Theta, \tag{1b}$$

$$\nabla^2 U_3 = 0. \tag{1c}$$

The general form of solution for each of the above is

$$U_1 = (A_1 r + C_1 r^{-1}) \sin\Theta, \tag{2a}$$

$$U_2 = \left(B_0 r^{-1} \int_{r_2}^{r_3} vr\, dr + A_2 r + C_2 r^{-1} \right) \sin\Theta, \tag{2b}$$

$$U_3 = (A_3 r + C_3 r^{-1}) \sin\Theta. \tag{2c}$$

Using the boundary conditions (equality of potentials and equality of the normal components of the flux at the interface) and solving simultaneously Eqs. (2), we can determine the coefficients of these equations. Then the potential field in the fluid will be expressed as

$$U_2 = B_0 \sin\Theta \left[r^{-1} \int_{r_2}^{r_1} vr\,dr + \frac{1}{2} v_0 \left(1 - \frac{d_2^2}{d_3^2}\right) \frac{(D_3 - 1)\,r}{(D_3 + 1)(1 - D)} + \right.$$
$$\left. + \frac{1}{2} v_0 \frac{D}{1 - D} \cdot \frac{r_3^2 - r_2^2}{r} \right], \tag{3}$$

where

$$D = \frac{d_2^2}{d_3^2} \frac{(D_3 - 1)(D_1 - 1)}{(D_3 + 1)(D_1 + 1)}; \quad D_3 = \frac{\sigma_2}{\sigma_3} \frac{1 + d_3^2/d_4^2}{1 - d_3^2/d_4^2};$$

v_0 is the average flow velocity and σ is the electrical conductivity of the medium. The flow rate is determined by the total potential difference measured at the outer surface of tubes between points a, and b with coordinates $r = r_4$, $\Theta = \pm \pi/2$

$$\delta U_3 = B_0 v_0 (d_3 - d_2) \frac{2\,\frac{d_3 + d_2}{d_4}}{\left[\left(1 + \frac{d_3^2}{d_4^2}\right) + \frac{\sigma_3}{\sigma_4}\left(1 - \frac{d_3^2}{d_4^2}\right)\right]} \cdot [1 - D]^{-1} \tag{4}$$

or points a', b' with coordinates $r = r_1$, $\Theta = \pm \pi/2$

$$\delta U_1 = B_0 v_0 (d_3 - d_2) \frac{\frac{d_1}{d_2}\left(1 + \frac{d_3}{d_4}\right)}{\left[\left(1 + \frac{d_1^2}{d_2^2}\right) - \frac{\sigma_1}{\sigma_2}\left(1 - \frac{d_1^2}{d_2^2}\right)\right]} \cdot \frac{D}{1 - D}. \tag{5}$$

It is easy to show that, when $d_2 = 0$, Eq. (4) becomes identical with the expression for a round tube presented in [4]. /376

It is also of interest to present a formula for the flow resistance. In the case of a passage with conducting walls, electromagnetic forces appear in the fluid and they slow down the motion. The addition flow resistance which is thus produced is equal to [5]

$$\text{grad } P = K \sigma_2 v_0 B_0^2,$$

where the deceleration coefficient for an annular space

$$K = \frac{(D_3 - 1)^{-1} + \frac{d_2^2}{d_3^2}(D_1 + 1)^{-1}}{(D_3 + 1)(D_3 - 1)^{-1} - \frac{d_2^2}{d_3^2}(D_1 - 1)(D_1 + 1)^{-1}},$$

$$D_1 = \frac{\sigma_2}{\sigma_1} \frac{1 + d_1^2/d_2^2}{1 - d_1^2/d_2^2}.$$

From Eq. (3) we [now] can get an expression for the potential field in a round pipe in the form

$$U_2 = \frac{1}{2} B_0 \sin\Theta (\bar{v}_r + Cv_0) r; \tag{6}$$

here $\bar{v}_r$ is equal to the average velocity in a passage cross section of radius r. /377
The value of C varied from +1 when $\sigma_w = 0$ to -1 for $\sigma_w = \infty$. When the tube size is selected properly, C may become zero (when $\sigma_w/\sigma_{fl} = 1 + d_3^2/d_4^2/1 - d_3^2/d_4^2$).

Thus the potential at each point is not determined by the local velocity, but rather by the average velocity in a cross section whose radius is equal to the current radius of the point proper. The potential will determine the local velocity only in a homogeneous velocity distribution. In other cases the local velocities can be determined on the basis of the diagram of potentials, using Eq. (3). Figure 2 shows such a diagram for different values of C and Re. In turbulent flow the potential diagrams [curves] lie close to one another and when the Reynolds number is varied from ∞ to 10^4 the signal increases on the average by 10-20% /378
depending on the value of C.

The quantity which depends more substantially on the velocity is the potential gradient (Fig. 3). Differentiating Eq. (6) over the radius, we get

$$\frac{dU_2}{dr} = \frac{1}{2} B_0 \sin\Theta [v_r - \bar{v}_r + Cv_0], \tag{7}$$

where v_r is the local velocity. The probe for measuring grad U should be provided with two electrodes situated at a distance of $\Delta r \ll r_0$ from one another. Using this kind of probe it is possible to simultaneously measure the potential diagram and the gradient. Then it is easy to get from Eqs. (6) and (7) that

$$\frac{U_2}{r} + \frac{dU_2}{dr} = B_0 \sin\Theta \left(\frac{1}{2} v_r + Cv_0\right). \tag{8}$$

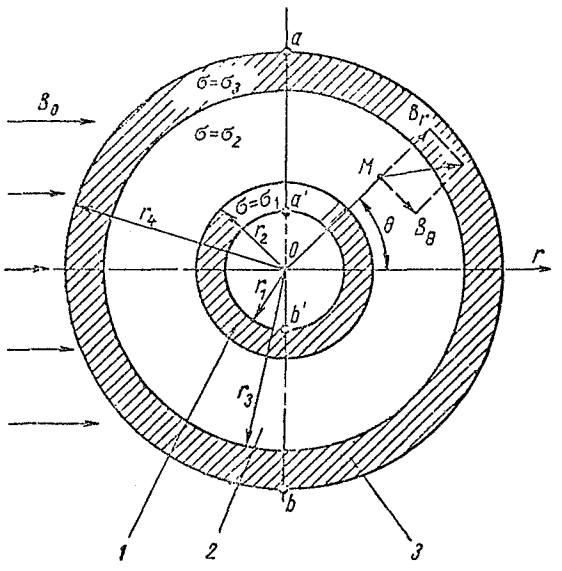

Figure 1. Geometry of Passage.

1) Region of the Inner-Tube Wall; 2) Fluid Region; 3) Region of the Outer-Tube Wall.

Reference [3] presents results of experiments for measuring the velocity distribution by both methods. The electrode was a metal capillary, inside which passed an insulated wire, welded at its end to the capillary. In this case it is impossible to say with certainty that the signal measured is equal to the potential in the fluid point in contact with the junction. The velocity distribution in a flow of the sodium-potassium alloy, flowing in a stainless steel tube with an inside diameter of 36 mm, was measured by a probe with two molybdenum wires 0.2 mm in diameter. The electrodes were soldered to the probe by means of a glass end piece; the distance between them was 0.9 mm (Fig. 4). The magnet can be moved along the tube, which makes it possible to measure the potential distribution in the cross section at the tube elevation and along the magnetic field (Figs. 5 and 6). The potential diagrams obtained in a homogeneous magnetic field at $Re = 7.8 \cdot 10^3$, are shown in Fig. 6b. The experimental points lie between the curves for the above Reynolds number and for a Reynolds number going to infinity, respectively. It is difficult to determine the Reynolds number to which the experimentally obtained potential diagram corresponds. As can be seen from the figure, the straight line about which the experimental points are clustered has a higher slope than the calculated curve for $Re = 7.8 \cdot 10^3$. It can be concluded from this that either the velocity distribution in the magnetic field has become less steep, or that this effect is due to measurement errors. The velocity distribution should become reconstructed after entering the magnetic field by a certain distance. /379

In the given experiment the potential curves measured in a homogeneous magnetic field at a distance of 10 r_0 from one another were found to be the same (the data obtained in the plane with $l = 540$ are not shown in Fig. 6). The curves along the magnetic field obtained in other experiments performed for a range of Reynolds numbers from $3.76 \cdot 10^3$ to $3.04 \cdot 10^4$ and in a range of magnetohydrodynamic interaction parameters from 0.36 to 148. Apparently, the flattening in the velocity distribution, if any, was of the order of magnitude of the experimental error. In addition, as was shown above, the potential curve depends little on the Reynolds number of turbulent flow. Hence, it is practically very difficult to use it for determining the shape of the velocity distribution.

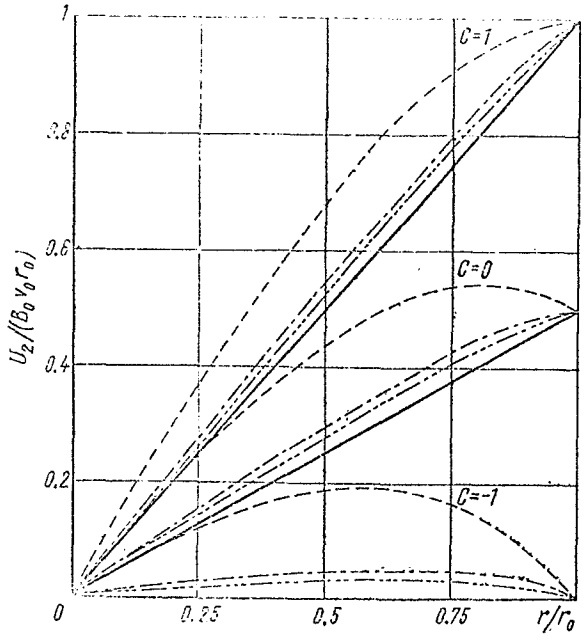

Figure 2. Diagrams of Potentials in the Fluid Flow.

---Laminar Flow; -.-.-Re= $7.5 \cdot 10^3$;

-...- Re = $7.5 \cdot 10^4$; —— Re = ∞ .

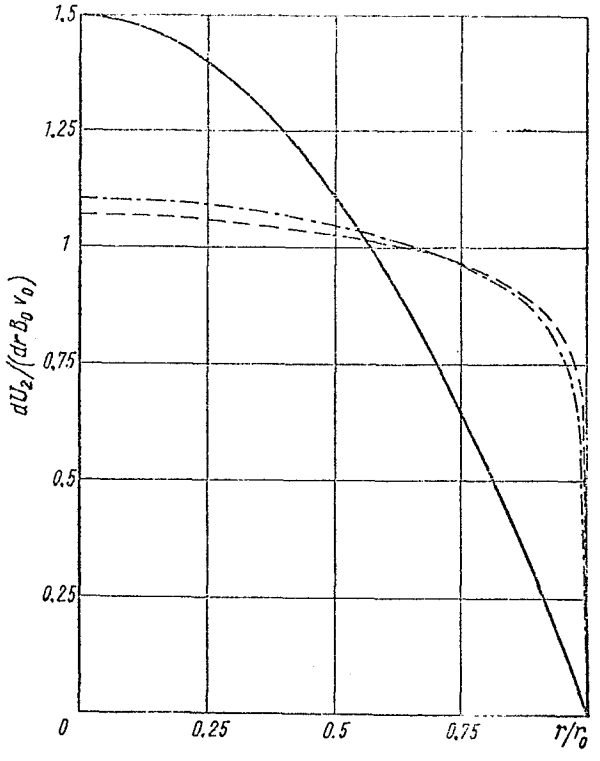

Figure 3. Diagram of the Potential Gradient in the Flow of Fluid. The Solid Line Pertains to Laminar Flow; the Dash-Dot Line is for Re = $7.5 \cdot 10^3$, and the Dashed Line is for Re = $7.5 \cdot 10^4$.

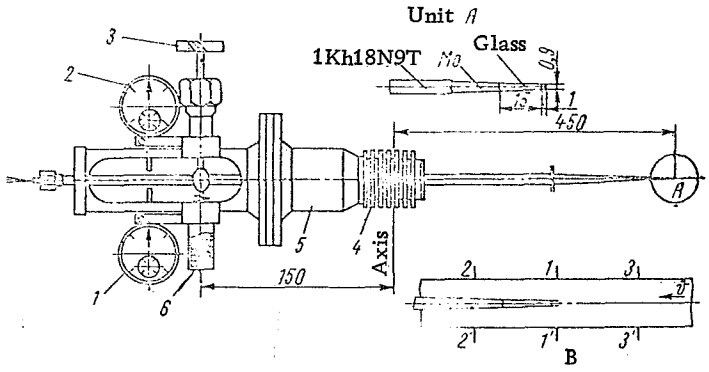

Figure 4. Design of Probe.

1 and 2) Micrometers; 3) Microscrew; 4) Bellows; 5) Centering Plane; 6) Spring; B) Position of Probe in Tube Relative to the External Electrodes.

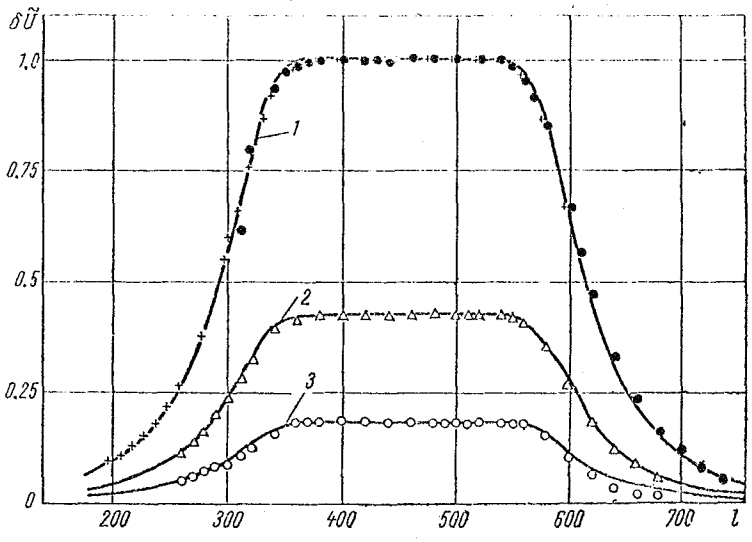

Figure 5. Diagrams for the Potentials $\delta \cdot \tilde{U}$ Along a Tube ($Re = 2.5 \cdot 10^4$, $M = 786$).

● and + – Outside of the Tube at Electrodes 1–1' and 3–3', Respectively; ○ and Δ – in the Fluid at a Distance $r/r_0 = 0.445$ and 0.885, Respectively; 1) Magnetic Induction $B(l)/B_0$; 2) Curve of $\delta\tilde{U} = B(l)r/B_0r_0$.

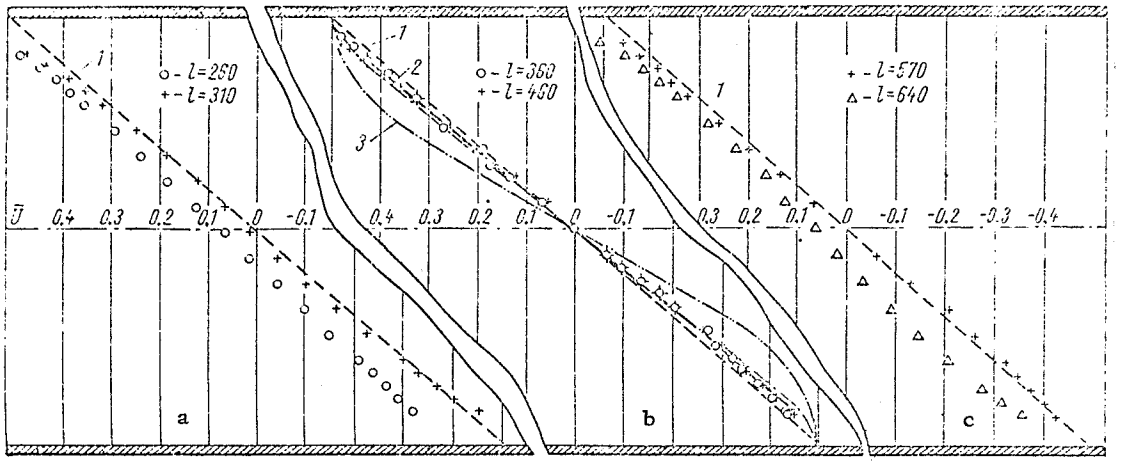

Figure 6. Curves of Potentials Over the Height of the Tube ($Re = 7.8 \cdot 10^3$, $M = 577$).

a) At the End Section of the Magnetic Field; b) in the Homogeneous Field; c) at the Starting Section of the Magnetic Field; ---, -.- and -..- are Curves Calculated for $Re = \infty$, $Re = 7.8 \cdot 10^3$ and for Laminar Flow, Respectively.

We did not succeed in experimentally obtaining a relationship which would reliably describe the change in grad U over the tube height, using two electrodes to measure the signal. The experimental data were highly scattered. Changes in the effective distance between the electrodes were also observed. If we denote the latter by Δr, the signal measured at the electrodes by ΔU and the total signal which measured outside of the tube by δU, we can show that for a linear potential curve /381

$$\Delta r = m \frac{\Delta U}{\delta U} r_0,$$

where m is a constant, depending on the tube parameters. The ration $\Delta U/\delta U$ was measured with the probe in the same position (it was in the center), varying either the induction while holding the velocity constant, or conversely, varying the velocity at constant induction. It was found that in the first case Δr remained almost constant, while in the second case it diminished (table).

The potential difference between electrodes 2-2'' (see Fig. 4) is calculated from Eq. (4) for an annulus. According to calculations, the value of the signal here should have been by 1.5% higher than between electrodes 3-3', which was verified experimentally. /382

It was noted in [6] that the edge effects practically do not affect the magnitude of the signal at the magnetic field boundaries. It can be seen from Fig. 5

that also in the present experiments the potential field at the outer wall of the tube, as well as in the fluid flow proper follows changes in the magnetic field.

Values of Δr

$V_0 = 0{,}357$ m/sec = const									
B, gauss	1300	2370	4670	5820	5830	5985	6415	7520	7650	8120
δU, mV	1.5	2.65	5.15	5.76	6.41	6.62	7.05	8.25	8.42	9.2
ΔU, mkV	17.5	33.5	71.5	86	86	88.5	91	114	114	125
Δr, mm	0.42	0.455	0.5	0.54	0.485	0.48	0.465	0.5	0.49	0.49
$B = 5780$ gausses = const										
v_0, m/sec	0.121	0.263	0.56	0.667	0.85	1.03	1.09	1.25		
δU, mV	2.16	4.68	9.05	11.87	15.2	18.28	19.55	22.2		
ΔU, mkV	8.5	32	77	110	137	215	200	230		
Δr, mm	0.141	0.246	0.306	0.334	0.324	0.41	0.37	0.373		

REFERENCES

1. Kolin, A. J.: Appl. Phys., 15, 151 (1944).
2. Williams, E.: Proc. Phys. Soc., A, 42, 469 (1930).
3. Gushchin, G. I., et al.: Voprosy magnitnoy gidrodynamiki [Problems of Magnetohydrodynamics]. Published by the Academy of Sciences of the Latvian SSR, Riga, 1963.
4. Turchin, N. M.: Teplofizika vysokikh temperatur, 1, 118 (1963).
5. Turchin, N. M.: Magnitnaya gidrodinamika, 1, 147 (1965).

ELECTROMAGNETIC A-C PUMP FOR LIQUID METALS RATED AT 120 m^3/hour

Ye. M. Avilova, T. V. Doktorova, N. I. Marin
and V. A. Povsten'

The development of a pump for liquid metals with an output of 120 m^3/hour /382
completes the task of designing a series of electromagnetic volute pumps, work on which was performed for the last several years in the Physics and Power Institute.[1] The design of this pump is generally similar to that of other pumps of this series, but differs by a number of features (Fig. 1).

The stator consists of the casing with a stack of iron, assembled from 0.5 mm thick electrical steel sheets, pressed into it. The iron stack has 72 slots into which are placed a three-phase winding with organic silicon insulation. The heat is removed from the stator by water flowing in a jacket welded to the casing. The cooled wedge-shaped copper inserts limit the thermal flow at the projecting parts of the winding from the liquid-metal side.

The triple-start screw-thread shaped passage for the liquid metal is formed by two welded shells, to the outer of which were welded ribs along a spiral. The inner shell protects the armature from the liquid metal and serves to close the magnetic circuit. Guiding devices, consisting of tapered sections and ribs, /383
welded to them along a spiral, are welded to the ends of the shells. The spiral angle may vary from 30° to 90°. These devices serve to smoothly change the velocity and direction of the liquid metal.

The thermal resistance between the stator and the liquid metal is produced by an air gap, in which are placed very thin corrugated metal screens, which reduce the thermal radiation.

Unlike other pumps of the series, this one is made with an airtight casing, /384
which prevents the liquid metal from penetrating the premises on failure of the 1.5 mm thick outer shell.

The pump was tested with sodium in order to refine its parameters, as well as to expose and eliminate design shortcomings. The testing setup consisted of a circulating loop, the flow rate of sodium in which was measured by a magnetic flow meter, connected to the PSRI-01 secondary instrument, the pressure was measured by the MEM-3 manometric pickup, connected to the EPVI-14 secondary instrument, the temperature of the stator winding was determined by chromel-kopel thermocouples, placed in a capillary from 1Kh18N9T steel

---

[1] Avilova, Ye. M., et al. Magnitnaya gidrodinamika, 1, 110 (1965).

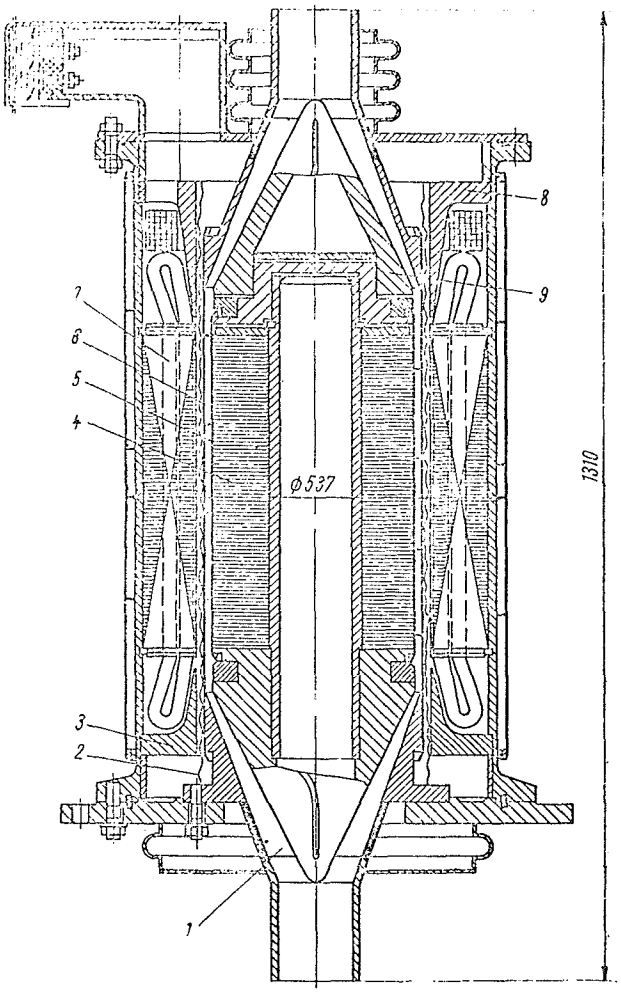

Figure 1. General View of Pump.

1 and 9) Guiding Devices; 2) Screen; 3 and 8) Wedge-Shaped Copper Inserts; 4) Armature; 5 and 6) Passage-Forming Shells; 7) Stator.

0.8 x 0.1 mm in diameter. The pump was thus operated for 2500 hours with sodium at 330°C; the winding temperature here did not exceed 130°C. The permissible winding temperature for prolonged operation is 180°C. The design delivery of the pump is 150 m^3/hour in which case the sodium flows through the pump at 10 m/sec. The tests showed that the pump operates noiselessly and stably at deliveries of 40-120 m^3/hour. When the output is increased above 120 m^3/hour, i.e., when the sodium velocity is increased to 8 m/sec, the pump becomes noisy with the noise increasing with a further increase in the delivery rate; the noise intensity could be reduced only by increasing the argon pressure in the expansion tank of the loop. The pump was operated at its top design speed only for a short time, with the argon pressure maintained at 0.9-1 kg/cm^2, but even this could not entirely eliminate the noise. Prolonged operation with intensive noise is undesirable, since the noise is apparently produced by vibration of the thin walls of the metal passages. This operating mode is regarded as difficult. The noise can be produced by separation of the metal stream at the pump inlet. Consequently, it should be assumed that 120 m^3/hour is the top delivery rate for this pump. /385

The pump was also unstable at deliveries of 30-40 m^3/hour. The flow variables of the pump's operation fluctuated. The instability of operation at these flow rates and, consequently, at high slip, depends on the instability of electric contact resistances between the spiral ribs of the passage and the liquid metal, the effect of which increases with an increase in the slip. When the pump is first started, and the liquid metal does not as yet sufficiently wet the ribs, an increase in the electric contact resistance in fact reduces the head. However, the resistance is reduced appreciably after as little as several hours of operation. The head developed by the pump increases and remains stable on further operation (Fig. 2).

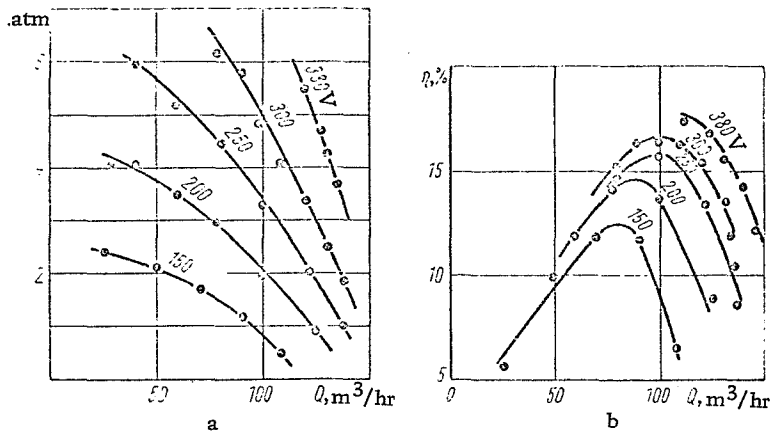

Figure 2. The Pressure (a) and Efficiency (b) as a Function of the Delivery Rate for Different Applied Voltages and for a Sodium Temperature of 720°C.

As can be seen from Fig. 2a, for a given applied voltage, a reduction in the liquid-metal flow rate is accompanied by an increase in the head. However, this also increases the stator current, which, as is known, depends on the applied voltage, slip (flow rate) and the electrical conductivity of the liquid metal. Due to limitations imposed by heating of the windings, the current cannot exceed 250 amps, hence, the pump can operate with maximum output $(Q \times H)_{max}$ at different flow rates only when it is supplied through a voltage regulator. Figure 3 shows the dependence of the output on the flow rate at maximum current of 250 amps and at 450°C. This characteristic makes it possible to establish optimal operating mode for the pump. For the above sodium temperature the pump has the greatest output for a flow rate of 115 m^3/hour, the head then being 5.2 kg/cm^2. The power consumption at maximum output is 97 kw, the voltage is 350V, efficiency 17.5% and the power factor is 0.64. /386

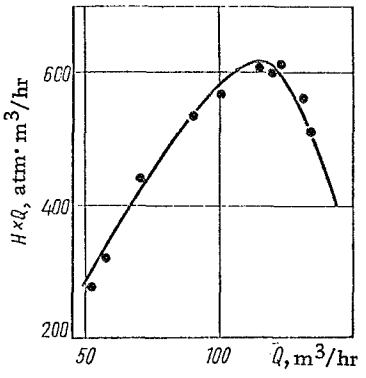

Figure 3. Delivery as a Function of Sodium Flow Rate at 250 amps and Sodium Temperature of 720°.

The fact that the characteristics depend on the sodium temperature is due to changes in its electrical conductivity. When the latter increase, the stator current must be limited by lowering the

*Delivery and output here are head x flow rate of metal.

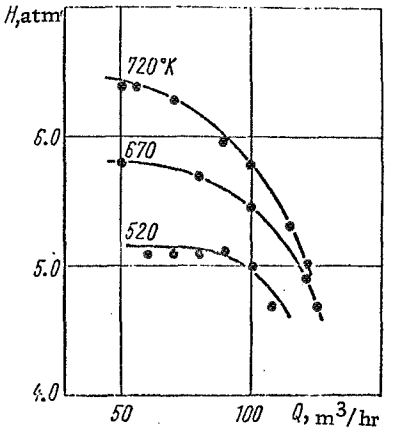

Figure 4. Head as a Function of the Flow Rate at 250 amps and Different Sodium Temperatures.

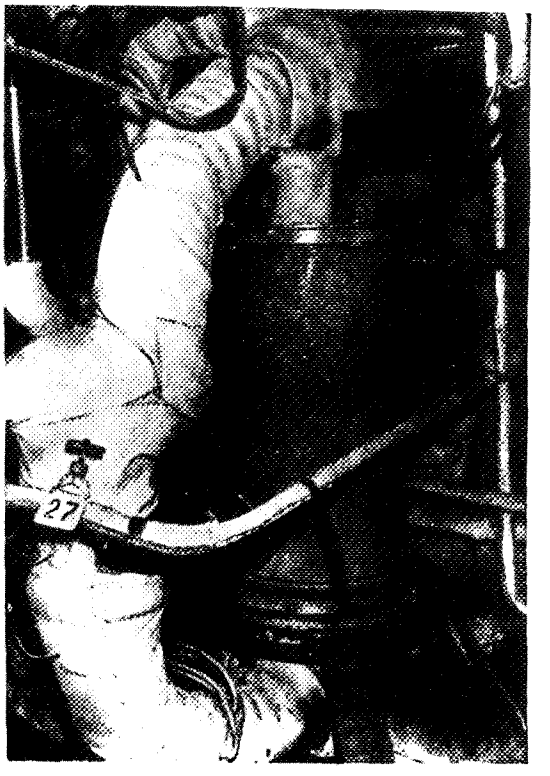

Figure 5. General View of the Pump Operating at a Thermophysical Stand.

supplied voltage which, for the same flow rate, reduces the head, since the induction of the magnetic field drops (Fig. 4). At present the pump operates successfully at a thermophysical stand (Fig. 5), circulating sodium at 200-250°C. The sodium flow rate at this stand does not exceed 120 m^3/hour. It can be regulated smoothly by varying the voltage supplied to the pump.

ELECTROMAGNETIC SCREW PUMP FOR PUMPING OF LIQUID METALS

Ye. M. Avilova, Ye. L. Ivanter, N. I. Marin and V. A. Povsten'

Ordinary d-c pumps must be supplied from current sources of 2000-10,000 amps and above, which is very inconvenient under laboratory conditions and hence, limits their use. [On the other hand] d-c pumps must be used in studies where fluctuations in the liquid-metal flow rates are not permissible. Since laboratory setups usually require only moderate metal flow rates, great promise is held by d-c electromagnetic pumps with a screw-shaped flow passage which, when built with a multiwinding cross section can be built to use only moderate amounts of current (100-200 amps). These pumps can be supplied from moderately-sized standard rectifiers. The flow rate of metal through such a pump is 2 cm^3/sec, the pressure when pumping sodium and using 200 amps of current is 1.3 kg/cm^2 and the working temperature of the liquid metal may be as high as 500°C (Fig. 1).

The pressure developed by the pump varies somewhat depending on the kind of metal pumped. At low flow rates it depends primarily on the electrical conductivity of the liquid metal. The higher this conductivity, the higher the pressure produced. The magnetic flux produced by the exciter winding penetrates the liquid metal flowing through the pump. The d-c current passed through the liquid metal along the pump axis interacts with the magnetic field of the exciter winding. As a result the liquid metal is set into rotational motion which is transformed into translation by the spiral passage. Here the pump delivery pressure is equal to the sum of pressures produced in the individual windings of the passage. The magnetic field induced by the current flowing through the liquid metal is compensated by a return conductor, made in the form of a cylinder from St. 3 steel. It is kept in electric contact with the working section along a tapered surface using a pressing flange. Due to the moderate current use, the working part of the pump is made as a single entity with the current supplying conductors. It consists of two coaxial stainless-steel shells. The inner shell has cut into it a spiral passage for the liquid metal with a cross section of 4 x 4 mm^2, the passage wall thickness is 0.8 mm and the passage has 15 windings. Small air gaps serve as electric insulation between the working part and the return conductor and magnetic system. The magnetic system is formed by the outer cylindrical magnetic circuit (St. 3), inner core, lower flange and gasket, the latter used for pump-assembly purposes. The total nonmagnetic gap of the system is 10 mm. /388

The pump has independent excitation (64 V, 1 amp), which ensures smooth pressure adjustment by varying the magnetic flux, the exciter winding is a tapped coil, made from PNSDK high-temperature conductor wire 0.83/1.08 in diameter. If the pump must be preheated, the [tapped] sections are connected parallel to a standard [50 cycle] power source. Heating here takes place by eddy currents in /389 the magnetic system and walls of the flow part.

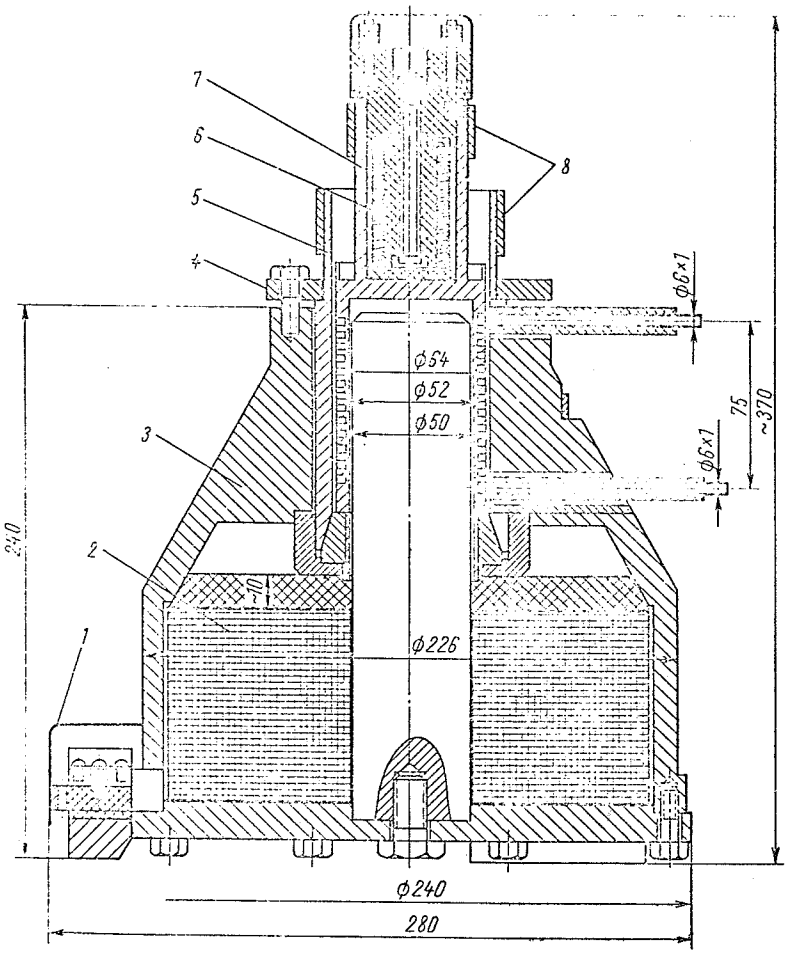

Figure 1. Design of an Electromagnetic Volute Pump.

1) Terminal Block; 2) Exciter Winding; 3) Magnetic System; 4) Pressing Flange; 5) Return Conductor; 6) Heater; 7) Flow Section; 8) Current Buses.

The 200 watt flow section heater, which is a nichrome-wire spiral placed in a ceramic holder, is used to compensate for the temperature reduction of the liquid metal flowing through the pump.

The pump was tested at a stand using an In-Ga-Sn alloy with specific weight of 6.5 grams/cm^3 and electric resistivity of $30 \cdot 10^{-6}$ ohm-cm. The relationships shown in Figs. 2 and 3 were obtained at liquid metal temperatures of 20°C.

After testing the pump was installed in a small loop in which it circulated an alloy of the same composition.

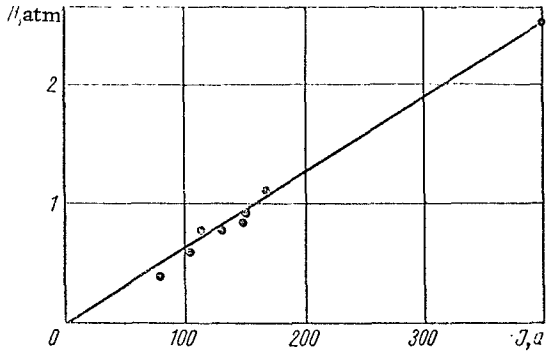

Figure 2. Pressure Developed by the Pump as a Function of the Current Flow in Flow Section at Zero Flow Rate and With Constant Excitation.

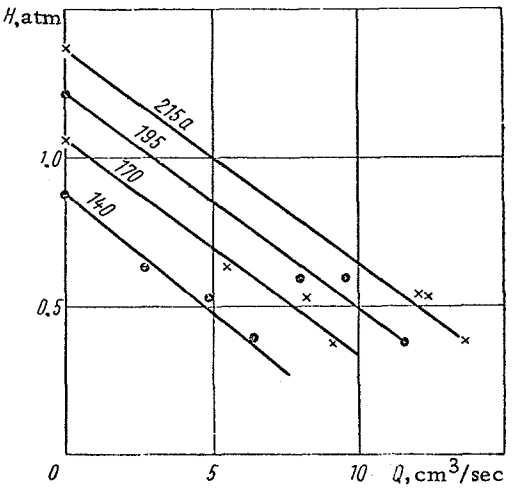

Figure 3. Pressure Developed by the Pump as a Function of the Flow Rate for Different Current Consumption at the Flow Section and With Constant Excitation.

It should be remembered when operating the pump that the liquid-metal loop to which the pump is connected, is held under the operating voltage of the latter, which does not exceed 1 V. The current dissipated in a long loop with a small diameter is low. However, in the case of large diameters and short loops, the flow section of the pump should be made with an electric tap in the center, which will divide it into two parallel branches. Here the ends of the loop will be at approximately the same potentials and thus current leakage into the loop will be prevented. In addition, when pumping liquid metals at temperatures of 700-800°C, to facilitate electrical insulation, it is easy to make the pump with series excitation. The copper winding of the exciter can be protected by an inert gas, as well as by chromium plating its surface. /390

The successful operation of this pump, feasibility of usage for pumping metals at 700-800°C, the moderate current consumption and the simplicity of design and manufacture show that a d-c volute pump is a convenient device for pumping liquid metals under laboratory conditions.

HYDROSTATIC BEARINGS IN SODIUM PUMPS

N. N. Aristarkhov, Yu. Ye. Bagdasarov, Yu. L. Kulikov,
Ye. N. Larin, M. S. Pinkhasik, A. A. Rineyskiy
and B. S. Tymosh

A major problem in designing a sodium pump is the selection of the pump bearing. /390 Although it is pointed out in [1] that in a cold-trap equipped loop it is possible to use ordinary roller and ball bearings, such pumps are not available at present. This may be in part due to difficulties in selecting materials, as well as due to the fact that the liquid metal, despite the use of filters, may contain a large quantity of oxides, which has a detrimental effect on the operation of rolling-contact bearings.

Hydrodynamic as well as hydrostatic bearings can be used for work with sodium. The difference between them consists in the manner in which pressure is obtained in the carrying layer of the fluid. In a hydrodynamic bearing the lift in the layer dividing the rubbing surface is produced by the fluid captured by the rotating shaft and delivered into the radial clearance. The required shaft lift is produced on certain combinations of the clearance size, shaft rpm and fluid viscosity. Due to the low viscosity of sodium, the hydrodynamic bearings must be made with very small clearances, and if the sodium contains solid particles (for /391 example, oxides), then this may result in failure of the bearings, which was actually observed [2].

In the hydrostatic bearing the external load is produced by the fluid pressure in the bearing layer and may be made independent of the shaft rpm by supplying the fluid by an auxiliary pump. These bearings are extensively used in the chemical industry [3]. They also operate in fluids with poor lubricating properties and containing solid particles. The clearance of such a bearing is selected upon due consideration of the size of the solid particles and the expected operational eccentricity of the pump shaft. By the method of fluid supply to the bearing chambers hydrostatic bearings are divided into throttle- and slot-type. The operating principle for any of these two types consists in the following: when the shaft is deflected by unbalanced forces, the pressure in the chambers to which /392 the shaft has come closer increases and that in the oppositely-located chambers decreases, thus producing a restoring force which returns the shaft to the initial position. Thus, the rubbing surfaces in these bearings are separated by the layer of fluid. The operating principle of an elementary hydrostatic bearing is shown in Fig. 1.

Attempts due to use a throttling hydrostatic bearing in sodium pumps did not produce positive results. The throttling holes were plugged up by oxides and the bearing just became a simple sliding-contact bearing. After obtaining negative results with three throttling hydrostatic bearings, we have decided that /393 they should not be used, at least in moderate-delivery pumps (up to 200 m^3/hour).

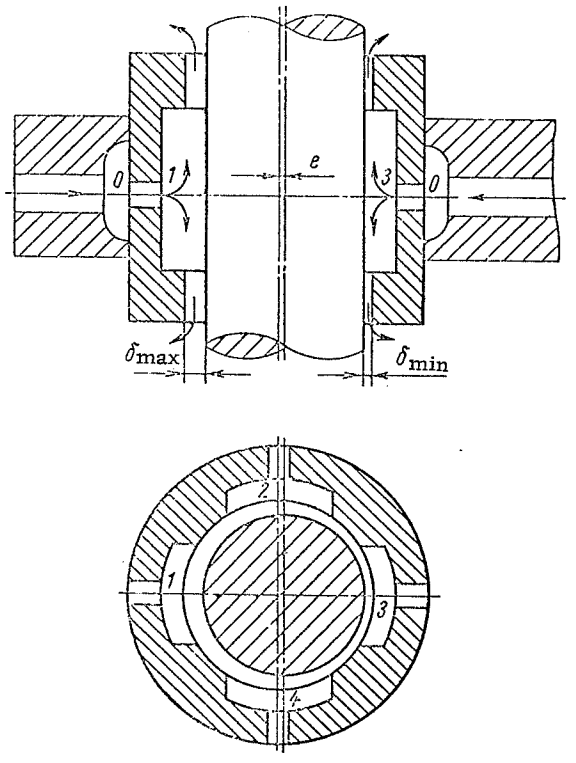

Figure 1. Schematic Diagram of a Throttling Hydrostatic Bearing, Where 1, 2, 3 and 4 are the Lift-Producing Chambers.

A slot-type hydrostatic bearing is shown in Fig. 2. The fluid from the pump flows through slots between the shaft and the sleeve into holes, from which it is directed into oppositely-situated chambers through spiral passages. The pressure in the bearing's chambers varies according to changes in the inlet and outlet clearances. Thus, for example, when the shaft moves to the right, the pressure in the right chamber increases not only due to reduction in clearance 7, at the outlet of this chamber, but also due to increase in the size of clearance 1 at the inlet of this chamber. Here the pressure in the left carrying chamber is reduced with an increase in clearance 3 at its outlet and to reduction in clearance 9 at the inlet into the opposite opening. Since during operation the clearances at the inlet and outlet increase simultanously, the relationship between throttling of the fluid at the inlet and outlet, as well as the carrying capacity of the bearing, remain unchanged. Consequently, the rate of flow of the fluid to the bearing will increase with increased wear of the journals. Direct flow of fluid between the carrying and regulating chambers is prevented by an annular groove, which is located between these chambers and which is connected to the low-pressure chamber by special holes. The slot-type bearing has still another property for operation with alkaline metals. Unlike the throttling bearing, almost the entire pressure drop in the slot-type bearing takes place in the clearance between the stationary sleeve of the bearing and the rotating sleeve, which appreciably reduces the danger of stopping up this clearance by oxides. The flow cross sections of holes for internal supply of the liquid metal to the carrying chambers may be quite large. The conditions of operation of the rubbing pairs in liquid metals are those of a combined effect of the load, high temperature and medium. When the sodium contains oxygen, metallic compounds may form with materials which can result in failure of the surface layer.

The operating conditions of a hydrostatic bearing become much more complicated when sodium is supplied to it from the delivery line of its pump. In this case on starting, stopping and when operating at low pump rpm, the bearing will operate with dry or semidry friction. This circumstance presents strict requirements to materials from which the rubbing pairs of bearings are made. At present there is no single approach to selection of these materials, due to lack of

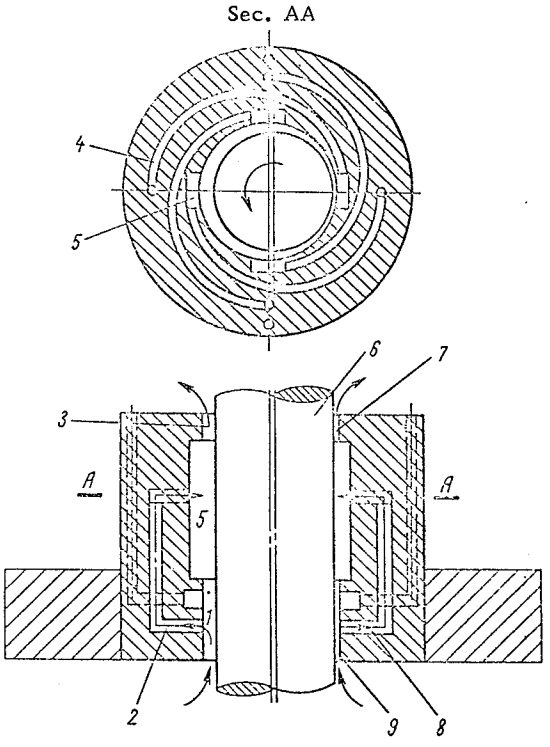

Figure 2. Schematic Diagram of a Hydrostatic Bearing With Mutually Reversible Slot Throttling.

1 and 9) Sodium Passages of Bearings; 2 and 8) Radial Sodium-Supply Passages; 3 and 7) Discharge Clearances; 4) Spiral Passages for Leading Sodium in the Carrying Chambers; 5) Carrying Chambers of Bearing; 6) Pump Shaft.

sufficient experimental data. Some preliminary data on the operating endurance of rubbing-pair materials were obtained using laboratory pumps [2]. It was established that the service life of an RF-1 steel - beryllium bronze pair is reduced sharply when the temperature of the pumped metal is increased to 400°C. Cast iron paired with RF-1 steel failed at temperatures of 200-400° C. A pair made of RF-1 steel - EI-229 steel operated for about 300 hours at liquid-metal temperature of 400°C. Some recommendations on the selection of rubbing-pair materials are presented in [4]. /394

Below are presented experimentally obtained data on the operating endurance of a hydrostatic bearing with self-reversing slot throttling for different oxygen contents of the sodium, shaft rpm and sodium temperatures (table). The experiments were performed at an experimental setup (Fig. 3).

The hydrostatic bearing was placed on a pump (Fig. 4), which was driven by an electric motor rated at 36 kW. The motor has three windings, thus providing three steps of rpm adjustment. The pump and motor shafts were coupled by a sliding adapter, while the torque is transmitted by a spline. The composite shaft thus produced has two ball bearings and one (lower) hydrostatic bearing, with the liquid sodium supplied to it from the delivery line of the pump along a pipe provided by a magnetic flowmeter.

The design of the bearing is shown schematically in Fig. 2. It is made from Kh18 steel, the shaft is made from 4Kh13 steel with a nominal shaft diameter of 55 mm, bearing clearance of 0.35 mm and 12 carrying chambers. The bearing and shaft were heat treated as follows: heating to 650°C, hardening with final heating in salt bath to 1020°C and oil-bath cooling to 290°C, temper hardening at 290°C and air cooling. The hardness of working surfaces after heat treatment was 52-55 RH.

In the process of tests the operation of the bearing was monitored on the basis of flow rate of sodium through it, by the power consumption of the pump, /395

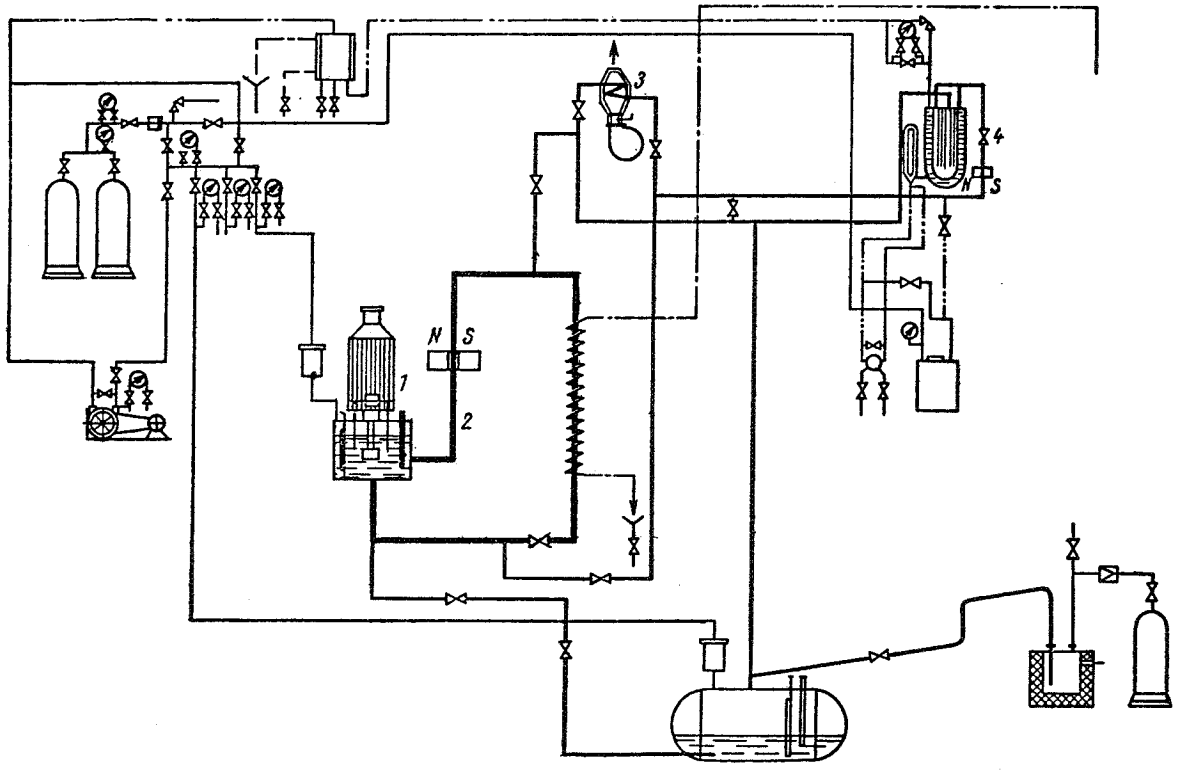

Figure 3. Schematic Diagram of a Pump Stand.

1) Pump with an Output of up to 150 m^3/hour and Pressure of 3 kg/cm^2;
2) Main Loop; 3) Oxide Indicator; 4) Cold Trap.

Characteristics of Various Stages of the Study

Stage No.	Sodium temperature, °C	Oxygen content of loop, % by weight	Pump pressure kg/cm^2	Pump delivery	Test time, hours	No. of starts and stops	Sodium flow rate in the bearing, m^3/hour	
							At beginning of test stage	At end of stage
I	330	0.01 0.02	5	100	1100	36	6.5	8.7
II	330	0.025	5	100	123	110	8.7	9.0
III	300—350	0.04	0.6	40	450	6	2.5	2.9
IV	530—550	0.007	5	100	120	4	9.7	9.5

TABLE Concluded

Radial wear of working journals of the shaft, mm					Radial wear of working journals of the bearing				
1	2	3	4	5	1	2	3	4	5
0.045	0.035	0.04	0.065	0.04	0.043	0.015	0.006	0.013	0.001
0.085	0.0125	0.025	0.03	0.025	0.048	0.026	0.031	0.015	0.001
0.085	0.09	0.04	0.07	0.04	0.044	0.504	0.051	0.08	0.022
0.01	0.08	0.02	0.07	0.02	0.23	0.23	0.262	0.204	0.164

as well as by periodic listening to the bearing's operation. After the pump is started up, constant flow rate of sodium through the bearing and the loop is immediately established. Periodic listening to the operating pump shows that the bearing operates smoothly without side noise. The sodium flowed to the bearing at a rate exceeding the design value by 2-2.5 m^3/hour.

It was noted toward the end of the first test stage that when the pump operated with a closed delivery flap, ambient noise was heard in the vicinity of the hydrostatic bearing. It could have been expected that [direct] contact takes place between the shaft and the bearing, although the pump pressure increased in this

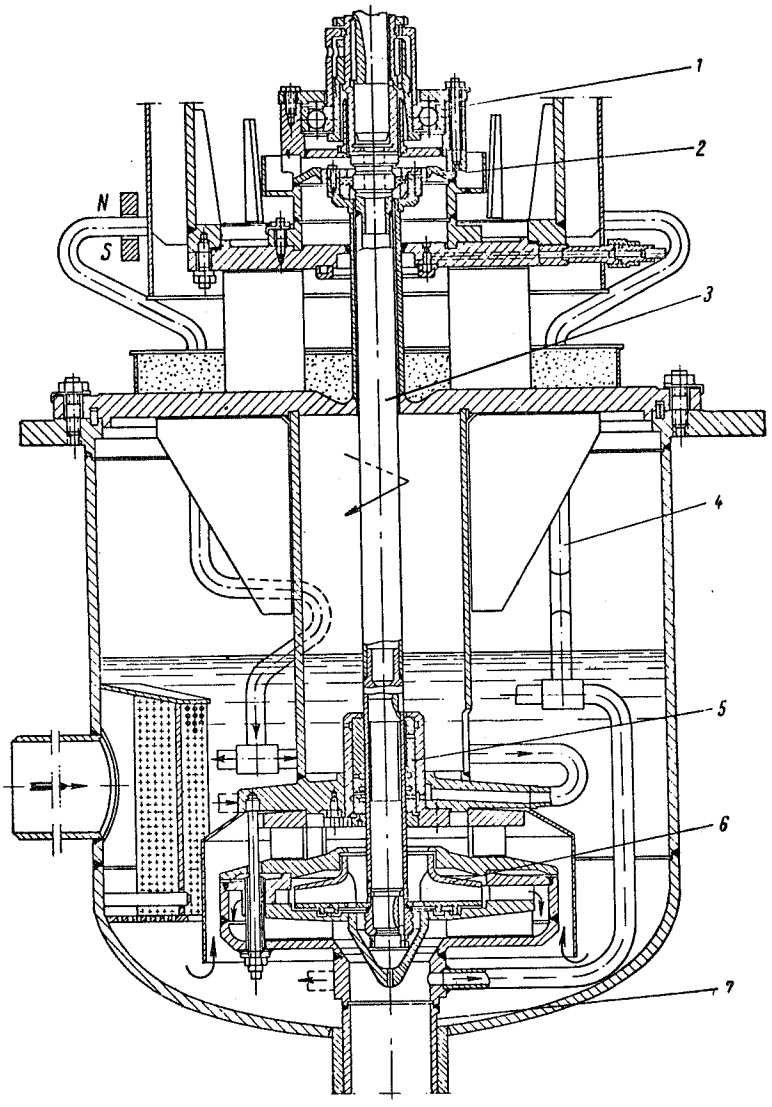

Figure 4. Pump With a Hydrostatic Bearing (the Upper Part of the Electric Motor is Not Shown).

1) Center Ball Bearing; 2) Polyfluoroethylene Packing; 3) Pump Shaft; 4) Sodium-Supply Lines to the Bearing; 5) Hydrostatic Bearing; 6) Impeller; 7) Delivery Pipe.

mode from 5 to 6 kg/cm^2 as compared with the nominal pressure, should have aided in improving the operating conditions for the bearing. Upon analysis we have arrived at the following hypothesis. It is possible that, when the rate of flow of sodium through the bearing is increased, it loses its vibration stability, and this in turn, breaks down the continuity of the fluid film and the shaft comes into [direct] contact with the bearing. It is probable that a region exists in which

the bearing operates properly. We have also considered another case: short-duration operation of the bearing without sodium supply through it (the sodium supply lines to the bearing were "frozen"), also with the pump delivery flap closed. The bearing operated without ambient noise. At the first stage the pump was started up and operated for 5-10 sec six times without supplying sodium to the bearing. External inspection of the rubbing pairs after 1100 hours of operation showed that their surface was smooth without scratches. The shaft was /398
worn concentrically at all the working journals, the bearing also increased; here the wear of the latter was eccentric relative to the center lines. Figure 5 shows characteristics of the pump, measured at the start and end of the first test stage. The flow rate of sodium through the bearing increased toward the end of the tests, which is due to the increased clearances through which the sodium flowed, produced by wear. The pump characteristic did not change after the 1100 hours of operation. The radial wear of the rubbing pairs of the bearing for this and all the subsequent stages is presented in the table.

The second stage consisting in study of operating endurance of the bearing on cyclical stops and starts. The cycles were repeated after 60 minutes. The pump was started up 1-4 minutes after stopping. It was noted that after each start the flow rate of sodium through the bearing was first somewhat higher than before stopping and, over 10-15 minutes it gradually took on a value close to the initial magnitude (Fig. 6). The rate of flow of sodium through the bearing increased from cycle to cycle. No defects, except for wear of working surfaces was discovered when the bearing was dismantled.

The third stage consisted in the study of operating endurance of the bearing at 1/3 of the nominal shaft rpm. It should be noted that the bearing was designed for a pressure of 5 kg/cm^2, hence, the results of this stage should be regarded as qualitative [only].

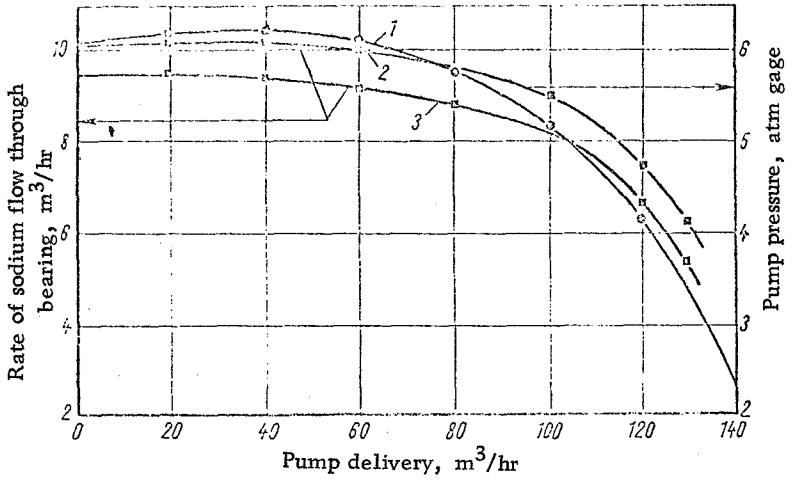

Figure 5. Characteristics of the Bearings at the 1st Stage.

1) Pump Pressure; 2) Rate of Flow of Sodium through the Bearing at the End of Tests; 3) Same as Above at the Beginning of Test.

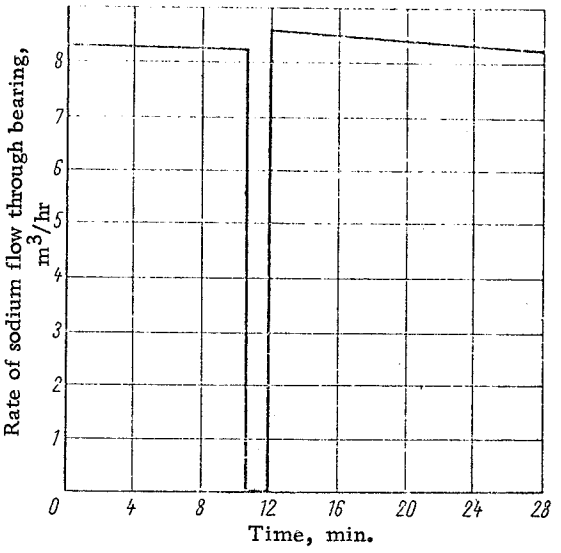

Figure 6. Rate of Flow of Sodium Through a Hydrostatic Bearing on Starting and Stopping.

After the pump was started up, /400 the bearing operated smoothly, without ambient noise. The electric system for heating the outer part of the sodium supply lines to the bearing operated unsatisfactorily. After 24 hours the temperature on the outer part of the pipe dropped to 140°C and flow of sodium through the bearing ceased (Fig. 7). Reheating the entire system to 470°C and starting the pump did not yield satisfactory results - sodium did not flow through the bearing. It was discovered on disassembling the pump that the sodium supply lines to the bearing were chocked by oxides. External inspection and blow down by gas showed that the inner sodium communications holes in the bearing are free of sodium compounds. No wear of rubbing pairs was observed during this time (Fig. 8). Inspection of the bearing after operation at reduced shaft rpm showed that the surface of the rubbing pairs is smooth without scratches or dents.

At the fourth stage we have investigated the operating endurance of the bearing at sodium temperatures of 530-550°C in order to determine the durability of the rubbing pairs of the bearing. Comparison of the bearing characteristics obtained at the start and end of this state (Fig. 9) shows that the rate of flow of sodium through the bearing decreased toward the end of this stage. After the pump was disassembled we have discovered, in addition to additional wear, also metal peeling. Some holes for supplying sodium to the carrying chambers were partially covered over by local galling of steel. No peeling or visible workhardening were observed. It is possible that the plugging up of holes by galling is responsible for reducing the flow of sodium through the bearing. Control checks of the shaft /401 wear showed that part of the shaft situated outside the bearing, as well as journals situated in the bearing sleeve had their diameter increased from 54.78 to 54.90 mm. Metallographic analysis showed that the shaft hardness dropped from 55 and 36 RH. Changes in the shaft diameter are due to structural transformations in the steel. The high shaft wear at this stage is apparently attributable to the reduction in the steel hardness. No corrosion interaction between the metal and the liquid sodium was observed (Fig. 10).

When the bearing operates at low rpm the wear of rubbing pairs is at maximum. We note that the conditions under which the bearing operates at this stage are very difficult (the pump pressure dropped nine-fold and reached 0.6 kg/cm^2). Under these conditions the continuity of the fluid film preventing the rubbing pairs

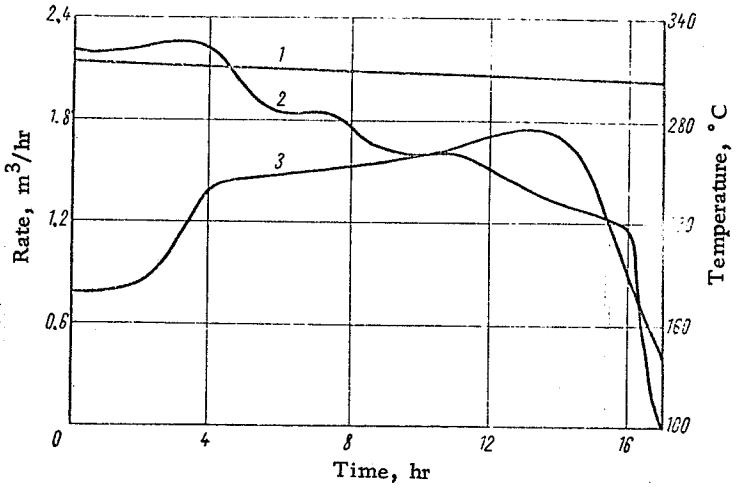

Figure 7. Change in the Rate of Flow of Sodium Through a Hydrostatic Bearing When the Sodium Supply Lines are Chocked by Oxides.

1) Sodium Temperature in the Loop; 2) Rate of Flow of Sodium through Bearing; 3) Temperature on the Surface of the Outer Part of the Sodium Supply Line to the Bearing.

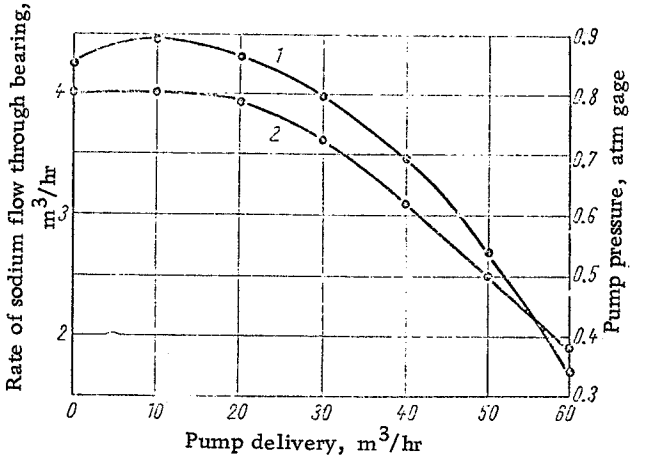

Figure 8. Characteristics of the Pump and Hydrostatic Bearing at the 3rd Test Stage.

1) Pump Pressure; 2) Rate of Flow of Sodium through the Bearing.

from direct contact may be disturbed. In addition, the bearing is divided into 12 chambers, which practically prevents the formation of a fluid wedge when the bearing ceases to operate as a hydrostatic bearing.

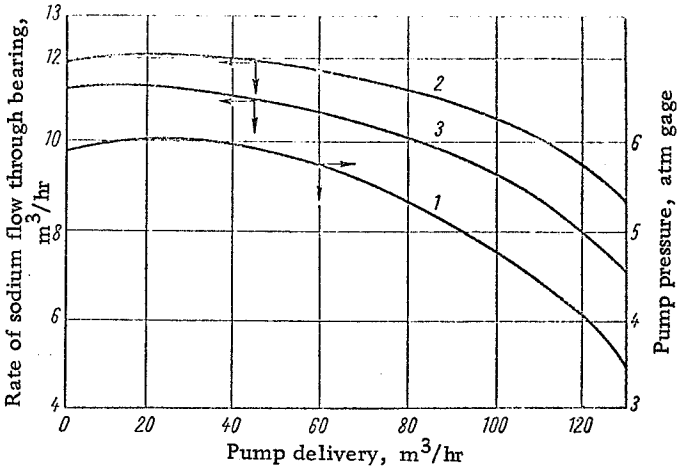

Figure 9. Bearing Characteristics at the 4th Stage.

1) Pump Pressure; 2) Rate of Flow of Sodium through the Bearing at Start of Tests; 3) Same as Above at End of Tests.

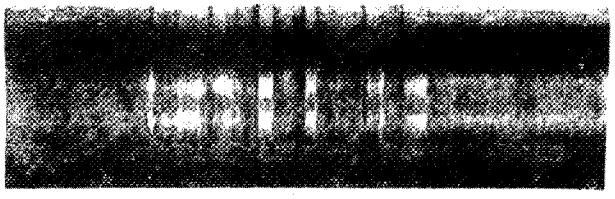

Figure 10. Working Part of the Pump Shaft.

Our studies should be regarded as qualitative, since the wear could have been affected by the frequent disassembly and assembly of the bearing. Additional experiments are needed to finally establish the character of wear of the rubbing pairs and the effect of the bearing's design on the magnitude of wear. It can, however, be concluded on the basis of our experiments that the operating endurance of a slot-type hydrostatic bearing in sodium pumps is satisfactory. The rubbing pairs we have used can be used in hydrostatic bearings for liquid-sodium temperatures of up to 400°C.

REFERENCES

1. Palmer, R. and Platt, A.: Fast-Neutron Reactors. [Translated from English and] published by Atomizdat, Moscow, 1963.

2. Kirillov, P. L., et al.: Atomnaya energiya, 7, Issue 1 (1959).
3. Chernousov, N. P.: Novyye konstruktsii germeticheskikh khimiko-tekhnologicheskikh mashin [New Designs of Leakproof Machines for the Chemical Industry]. Kimicheskoye mashinostroyeniye, No. 1 (1959).
4. Reactor Handbook, v. IV. Engineering. N. Y. Interscience publishers, 1964.

FLOWMETER FOR MEASURING LARGE LIQUID-METAL FLOWS

N. L. Loginov

Permanent-magnetic flowmeters are extensively used to measure the flow of liquid metal, since their design is simple and reliable; they can withstand elevated temperatures and aggressive media, are convenient to use and are sufficiently accurate. These characteristics make these flowmeters suitable for use in liquid-metal cooled nuclear power facilities. However, the use of the general arrangement for magnetic flowmeters (pipeline, placed between the magnet poles) in larger power facilities, using large-diameter pipelines, for example, of 200 mm and above, is difficult, since in this case the weight, size and cost of the magnetic system becomes very high.

The device considered in this paper is a flowmeter which operates by measuring the velocity in one point of the flow. Such an instrument is moderate in size as compared with the pipeline; it is intended for measuring liquid-metal flow /403 rates from 50 to 1000 m^3/hour in a pipeline 300 mm in diameter.

The design of the pickup shown in Fig. 1 includes an all-turned casing from 1Kh18N9T steel, installed on the pipeline by welding [thus] keeping the loop leak- /404 proof. Inside the casing is placed a holder with the field-producing magnet, also made from 1Kh18N9T steel. The magnet is made from the Magnico alloy with directional crystallization. The maximum magnetic induction in the outer plane of the casing bottom for the given pickup is 840 gausses. The magnet can be used at metal temperatures of up to 450-500°C; it is fastened by a pin in a slot in the holder. Two stainless steel electrodes are installed on the same holder, and they are insulated from the latter by asbestos-cement inserts. The working ends of the electrodes are sharpened and bear on the casing bottom at a distance of 18 mm from one another. Stainless-steel conductors, used for carrying away the signal are welded to the free ends of the electrodes. The electrodes contact the pickup's bottom due to the fact that the holder is pressed by a nut and pin. The ends of the latter enter slots in the housing and keep the holder at a fixed position.

The pickup is designed so that, if necessary, its entire inner part may be removed for inspection or repair without disturbing the airtightness of the working loop. Figure 1 shows the directions of the magnetic and electric fields. The pickup is installed on the operating pipeline is such a manner that its bottom is located at the pipeline axis, i.e., in a region with a uniform velocity distribution.

Figure 2 shows a distribution of the magnetic induction vector component perpendicular to the pickup's bottom as a function of the distance from the magnet butt, obtained by the IMI-3 instrument. The highest point of the graph corresponds to the position of the outer surface of the pickup bottom. The figure shows that the magnetic induction drops almost to zero at a distance of about 50 mm from the bottom. It can thus be expected that the presence of moving metal

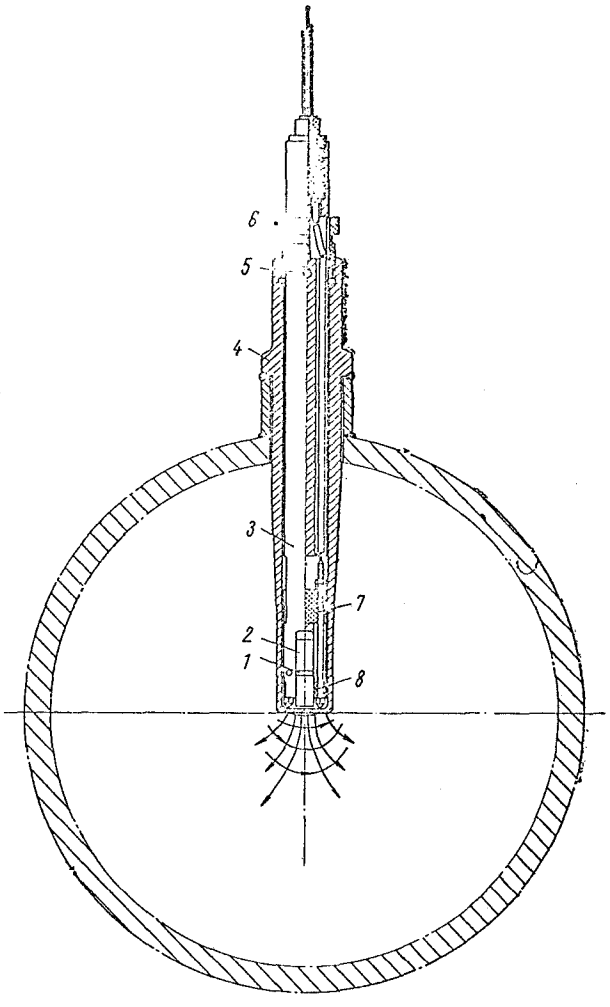

Figure 1. Design of Pickup and its Installation on an Operating Pipeline.

1) Magnet-Fastening Pin; 2) Magnet; 3) Holder; 4) Single-Piece Turned Casing; 5) Pin; 6) Nut; 7 and 8) Asbestos-Cement Insert.

at distances of more than 50 mm will not appreciably affect the pickup's sensitivity. Consequently, it can be calibrated on pipelines about 100 mm in diameter, which can be done using laboratory liquid-metal setups.

It can be assumed that in facilities with a larger diameter the pickup's readings are proportional to the velocity of metal at the pipeline axis. Knowing this velocity it is also possible to calculate the rate of flow of metal through

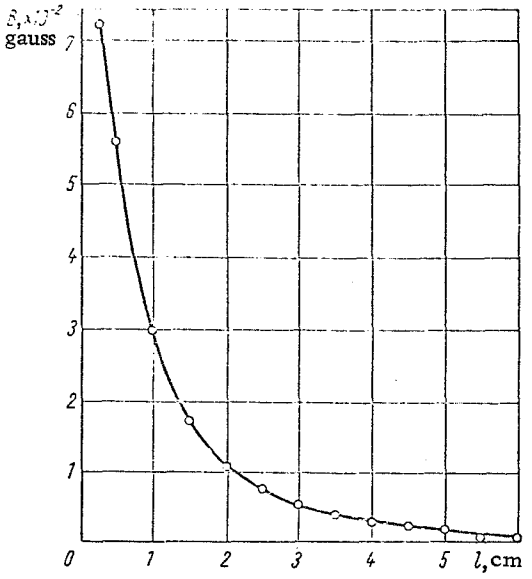

Figure 2. The Component of the Magnetic Induction Vector Perpendicular to the Pickup Bottom as a Function of the Distance.

the pipeline. Hence, the results of calibration are represented in the form of dependence of the output signal on the velocity, rather than the flow rate.

For calibration the pickup was installed on a sodium loop with a 103 mm diameter pipeline, which was equipped with an ordinary magnetic flowmeter calibrated by the volume method and used as a standard. The pickup emf was measured by a R-2/1 semiautomatic potentiometer.

The rate of flow of metal through the pipeline was determined by the "standard" magnetic flow meter, then the average velocity in the cross section where the pickup was located was calculated and a curve showing the output signal of the pickup as a function of the velocity was constructed. The results of calibration are shown in the table. The output signal of the pickup is not too large but in the operating velocity range (0.2-3 m/sec) it is sufficient for measurements, for example, using the EPP-09 potentiometer with the 0-1 millivolt scale.

Results of Flowmeter Calibration

Flow rate, m^3/hr	Velocity, m/sec	EMF, mV	Flow rate, m^3/hr	Velocity, m/sec	EMF, mV
5.90	0.252	0.046	28.20	1.205	0.276
9.60	0.410	0.084	29.20	1.250	0.287
11.50	0.493	0.102	29.00	1.200	0.280
13.35	0.570	0.127	30.60	1.310	0.305
16.50	0.708	0.158	34.40	1.470	0.344
22.30	0.955	0.212	34.40	1.470	0.350
35.50	1.520	0.350	42.00	1.800	0.428
25.85	1.100	0.258	49.40	2.100	0.490

TIME NEEDED FOR MELTING CYLINDRICAL [METAL] VOLUMES

V. M. Selivanov, N. M. Trebina and V. I. Sharypin

INTRODUCTION

Melting and solidification of metals is accompanied by changes in their state of aggregation, which has a perceptible effect on the temperature field and on the melting time of the metal. The melting time of metals cannot be determined analytically since the surface at which melting takes place changes position. This problem was solved by various methods in [1-7]. Dusinberre [6] and Eyres [7] have proposed a method for solving this problem using an analog computer. Baxter [3], who resorted to this technique, has generalized results on the melting of bodies with an initial temperature equal to the melting temperature for boundary conditions of the 1st and 3rd kinds. The present paper presents generalizing results for the melting of cylindrical volumes with an initial temperature different from the melting temperature for different heat-transfer conditions at the metal surface (boundary conditions of the 1st, 2nd and 3rd kinds). /406

Statement of Problem

It is required to describe the process of melting of a cylindrical body with specified thermophysical parameters and initial temperature t_0. The following are the assumptions made:

1) the material is a pure substance, i.e., melting takes place at a single specific temperature;

2) the density of the substance does vary on changes in the state of aggregation;

3) no heat is lost from the ends of cylinders;

4) the thermophysical properties of both phases (liquid and solid) are the same and do not depend on the temperature.

Solution of the Problem

A schematic depicting the melting of a cylindrical body is shown in Fig. 1. The presence in the cylinder of liquid and solid phase regions, a moving boundary between them and complex conditions at the phase interface makes it necessary

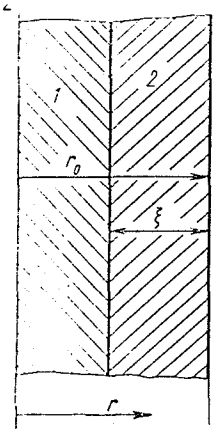

Figure 1. Schematic Showing the Melting of a Cylindrical Body With Liquid (1) and Solid (2) Phases.

to describe the temperature field of the cylinder by two equations (one for each phase). We now write an equation for the thermal conductivity for a cylinder of infinite length with constant physical properties /407

$$\gamma C \cdot \frac{\partial t}{\partial \tau} = \frac{\lambda}{r} \cdot \frac{\partial}{\partial r} \cdot \left(r \cdot \frac{\partial t}{\partial r} \right) \quad (0 < r \leqslant r_0, \ \tau > 0). \tag{1}$$

It is possible to obtain a single equation applicable to both phases. We introduce new variables, i.e., the enthalpy and specific flux. The enthalpy

$$J(t) = \int_0^t C \, dt \quad \text{or} \quad \frac{dJ(t)}{dt} = C \tag{2}$$

The specific flux

$$\Phi(t) = \int_0^t \lambda \cdot dt \quad \text{or} \quad \frac{d\Phi(t)}{dt} = \lambda. \tag{3}$$

In order that Eq. (1) be applicable in the entire region $0 \leq r \leq r_0$ it is necessary to make allowances for the fact that, in the process of reaching the melting temperature, the heat supplied is expended not only for heating up, but also for melting. This can be done by supplementing Eq. (1) by the expression

$$\lim_{\varepsilon \to 0} \int_{-\varepsilon}^{\varepsilon} c \, dt = \int_{-0}^{+0} c \, dt = \rho. \tag{4}$$

After substitution of new variables into Eq. (1) and reducing it to the dimensionless form, we get

$$\frac{\partial J^*}{\partial \tau^*} = \frac{\partial^2 \Phi^*}{\partial r^{*2}} + \frac{1}{r^*} \cdot \frac{\partial \Phi^*}{\partial r^*} \quad (0 < r^* \leqslant 1, \ \tau^* > 0)$$

The initial condition is $J^*(r^*, 0) = J^*_{i0}$, while the boundary conditions at the surface are

$$t^*(1, \tau^*) = t^*_n - \text{I kind};$$

$$\frac{\partial \Phi^*(1, \tau^*)}{\partial r^*} = q \cdot \frac{cr_0}{\lambda \rho} = +K^* - \text{II kind};$$

$$\frac{\partial \Phi^*(1, \tau^*)}{\partial r^*} = -Bi\,[t^*(1, \tau^*) - t^*_m] - \text{III kind}.$$

The relationship between the dimensionless parameters is shown in Fig. 2. Let us now consider the case of J* and t*. From the mathematical point of view it is immaterial how this relationship will be plotted in coordinates t* (J*). On practical considerations this is done in the manner shown in Fig. 2a. This position of the zero point makes it possible to solve Eq. (5) on an analog computer at $t_{ml} = 0$ for melting and solidification, which follows from the relationships obtained for the dimensionless temperature and enthalpy. The slope in the positive quadrant, which is unity, appreciably facilitates analysis of data obtained from temperature fields in the melting body, since [then] J* = t*. In Fig. 2a the enthalpy J* = -1 attendant to melting corresponds to the solid phase at the melting temperature, while J* = 0 corresponds to the liquid phase at the same temperatures. The intermediate values of J* correspond to a two-phase system and show the part devolved upon the solid phase. If J* > 0, then the liquid phase is superheated relative to the melting temperature. Similar considerations can be presented by analyzing the graphical relationships $\Phi^*(J^*)$ and $\Phi^*(t^*)$ (see Figs. 2b and 2c) To solve Eq. (5) on an analog computer it is necessary to [first] obtain from it a difference-differential equation. In the case of a cylinder it is most expedient to divide the radius into equal segments relative to r^{*2}, so that each layer so cut out would have the same energy store. Substituting $Z^* = r^{*2}$ into Eq. (5) and replacing the variables of the complex function, we get

/408

$$\frac{\partial J^*}{\partial \tau^*} = 4Z^* \frac{\partial^2 \Phi^*}{\partial Z^{*2}} + 4 \frac{\partial \Phi^*}{\partial Z^*} \quad (0 < Z^* \leqslant 1,\ \tau^* > 0). \tag{6}$$

We shall consider the enthalpy only in (n + 1)-discrete zones, situated at distance $Z^* = i/n$ (i = 0, 1, 2, ..., n) from the center, at equal intervals. We get (n + 1) differential equations

$$\left.\begin{aligned} &\frac{dJ_0^*}{d\tau^*} = 4n\,(\Phi_1^* - \Phi_0^*) \\ &\frac{dJ_i^*}{d\tau^*} = 2n\,[(2i+1)\,\Phi_{i+1}^* - 4i\cdot\Phi_i^* + (2i-1)\cdot\Phi_{i-1}^*]. \end{aligned}\right\} \tag{7}$$

For $i = n$

a) boundary conditions of the 1st kind

$$\Phi_n^* = t_c^* = t_n^*;$$

b) of the 2nd kind

$$\frac{dJ_n^*}{d\tau^*} = 8n^2\,(\Phi_{n-1}^* - \Phi_n^*) + 2\,(2n+1)\cdot K^*;$$

c) of the 3rd kind

$$\frac{dJ_n^*}{d\tau^*} = 8n^2\,(\Phi_{n-1}^* - \Phi_n^*) - 2\,(2n+1)\cdot Bi\,(t_n^* - t_c^*).$$

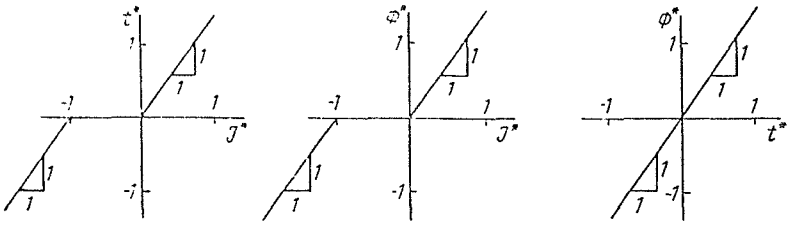

Figure 2. Functional Relationship Between Dimensionless Parameters.

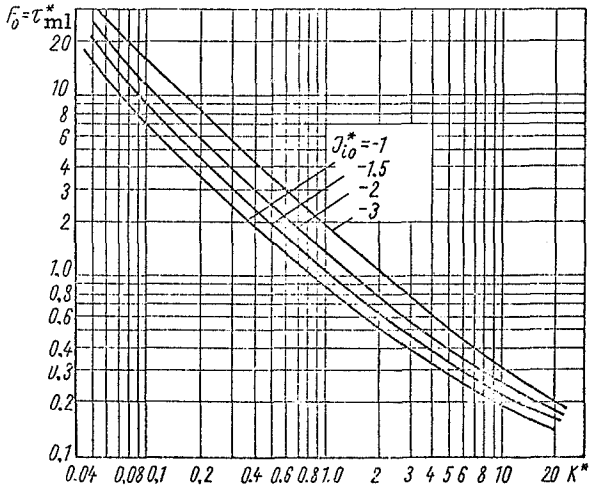

Figure 3. Nomogram for Calculating the Melting Time for Cylindrical Volumes Heated by a Constant Thermal Flux.

The above system of equations was solved on the EMU-10 analog computer, and nomograms were constructed on the basis of results obtained. The initial enthalpy was calculated from the expression /409

$$J^*_{i0} = \frac{C(t_0 - t_{ml})}{q} - 1.$$

The melting time is found from

$$\tau_{ml} = \frac{\tau^* \cdot r_0^2}{a}.$$

The nomograms of Figs. 4 serve to calculate the melting times for cylinders for boundary conditions of the 1st and 3rd kinds. Each nomogram is constructed for specific boundary conditions. When Bi = ∞ (boundary conditions of the 1st kind) it is necessary to assume that the surface temperature t^*_s is equal to the temperature of the medium t^*_m. The nomograms shown in Figs. 3 and 4 can be used to determine the time for melting cylindrical volumes of substances in which the initial enthalpy is

$$J^*_{i0} = \frac{C(t_0 - t_{ml})}{\rho} - 1 \geqslant -3.$$

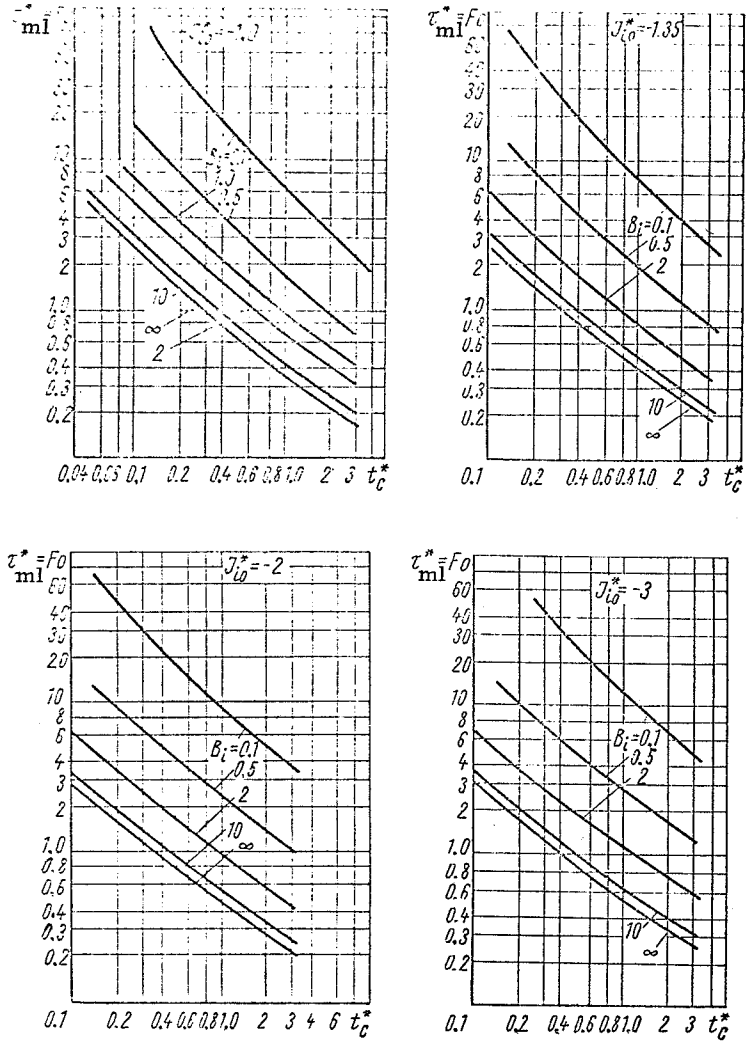

Figure 4. Nomograms for Calculating the Melting Time of Cylindrical Volumes Under Boundary Conditions of the 1st and 3rd Kind.

NOTATION

r - current radius of cylinder

r_0 - radius of cylinder

ξ - depth of molten layer

t_{ml} - melting temperature, °C

t_s - surface temperature, °C /411

t_m - temperature of the heating medium, °C

ρ - latent melting temperature

τ - time

J - enthalpy

ϕ - specific flux

q - thermal flux density

α - heat transfer coefficient

$$r^* = \frac{r}{r_0}; \quad J^* = \frac{J}{\rho}; \quad \Phi^* = \frac{\Phi}{\gamma \cdot a \cdot \rho}; \quad t^* = \frac{C(t - t_{ml})}{\rho};$$

$$F_0 = \tau^* = \frac{a\tau}{r_0^2}; \quad Bi = \frac{\alpha \cdot r_0}{\lambda}; \quad Z^* = r^{*2}.$$

REFERENCES

1. Veynik, A.I.: Teoplobmen mezhdu slitkom i izlozhnitsey [Transfer of Heat Between An Ingot and Its Mold]. Metallurgizdat, Moscow, 1959.
2. Veynik, A.I.: Priblizhennyy raschet protsessov teploprovodnosti [Approximate Calculation of Heat-Conduction Processes]. Gosenergoizdat, Moscow-Leningrad, 1959.
3. Baxter, D.S.: In the book Transactions of ASME. Translated from English, 84, series C, No. 4, p. 55. Foreign Literature Publishing House Moscow, 1962.
4. Carslaw, H.S. and Jaeger, I.C.: Oxford University Press. Lond., 1947. pp. 71, 227.
5. London, A.L. and Sebah, R.A.: Trans. ASME, v. 65, p. 771 (1943).
6. Dusinberre, G.M.: Trans. ASME, v. 67, p. 703 (1945).
7. Eyres, N.R.: Philos. Trans. Roy. Soc., v. 240A, 1946, 1-57.

FROZEN SODIUM SEALS

A. V. Drobyshev, Yu. I. Likhachev and I. M. Saratov

INTRODUCTION

At present much attention is given to the development of shaft packings. /411
Experiments have shown that frozen sodium seals in combination with a special packing gland can compete with bellows- and membrane-type packings, and in some cases have certain advantages over them. The main advantage of these packings is the unlimited height of rise and the feasibility of use with any shaft, rod, etc., diameter. The leak through this kind of seal is exceedingly small, only about 2-3 grams per day in a rotating shaft, When used with a valve, flap, etc., rod no leakage is observed at all [1, 2].

To obtain approximate values of the torque and axial load in these seals it is necessary to solve the problem of deformations and stresses in a pliable annular layer, included between two rigid cylindrical surfaces. In addition, one /412
must know the mechanical properties of the packing material at operating temperatures. To obtain these data we have made a special device which can be used to test sodium specimens at different temperatures. The tests were performed on a UM-1800 machine with variable rate of stress application. The characteristics of the mechanical properties of sodium which were obtained can be used to determine the expected torque for a rotating shaft, as well as the shearing force for the case of a sliding shaft (rod).

Study of a Frozen-Sodium Seal

We consider two kinds of packings glands with frozen sodium seals. In the first case the rod rotates over angle φ under the action of a force couple with moment M, while in the second case it is imparted an axial displacement δ by force P (Fig. 1). The main purpose here is to obtain relationships between M and φ and between P and δ. We now consider the strain in an annular layer of the packing contained between perfectly rigid cylindrical surfaces of a rod (r = = a) and the packing gland housing (r = b).

The Rod is Loaded by a Force Couple

The packing material passes the elastic and elastoplastic strain stage quite rapidly and hence, creep at these stages can be disregarded. Making use of the axial symmetry of the problem and the sufficiently extended rod length, we can regard all the components far from the ends as functions of r only, in which case

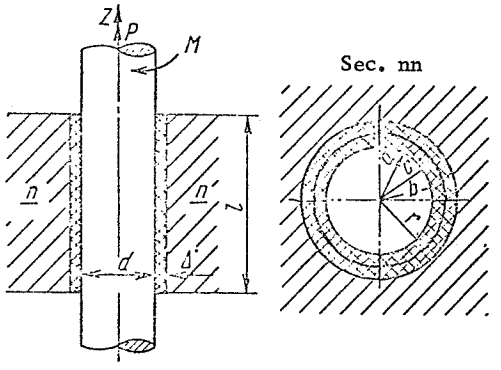

Figure 1. Calculating Scheme of Frozen Sodium Seal.

$\gamma_{z\Theta} = \gamma_{r\Theta} = 0$. Since strain in the axial direction is restricted, the axial displacements $u_z = 0$. /413

Elastic stage of packing deformation. At the start of load application the packing material undergoes elastic straining and its state is defined by the following equations. Equilibrium equations

$$\frac{\partial \sigma_r}{\partial r} + \frac{\sigma_r - \sigma_\Theta}{r} = 0, \tag{1}$$

$$\frac{\partial \tau_{r\Theta}}{\partial r} + \frac{2\tau_{r\Theta}}{r} = 0. \tag{1a}$$

Geometric relationships

$$\varepsilon_r = \frac{\partial u_r}{\partial r}, \quad \varepsilon_\Theta = \frac{u_r}{r}, \quad \varepsilon_z = \frac{\partial u_z}{\partial z} = 0, \tag{2}$$

$$\gamma_{r\Theta} = \frac{\partial u_\Theta}{\partial r} - \frac{u_\Theta}{r}. \tag{2a}$$

Physical relationships

$$\varepsilon_r = \frac{1}{E}[\sigma_r - \mu(\sigma_z + \sigma_\Theta)], \quad \varepsilon_\Theta = \frac{1}{E}[\sigma_\Theta - \mu(\sigma_z + \sigma_r)],$$
$$\varepsilon_z = \frac{1}{E}[\sigma_z - \mu(\sigma_r + \sigma_\Theta)], \tag{3}$$

$$\gamma_{r\Theta} = \frac{\tau_{r\Theta}}{G}, \tag{3a}$$

where μ, E and G is Poisson's ratio, Young's modulus and the modulus of rigidity.

We must satisfy the boundary conditions

$$r = a, \quad u_r = 0, \quad \tau_{r\Theta} = \tau = \frac{M}{2\pi a^2 l}, \tag{4}$$

$$r = b, \quad u_r = u_\Theta = 0. \tag{5}$$

The solution of system of Eqs. (1)-(3) is known, [3]

$$\left.\begin{aligned} &\bar{\sigma}_r = B + \frac{A}{r^2};\ \bar{\sigma}_\Theta = B - \frac{A}{r^2};\\ &\bar{\sigma}_z = 2\mu B;\ \bar{\tau}_{r\Theta} = \frac{C}{r^2};\\ &\bar{u}_r = \frac{1+\bar{\mu}}{E}\left[B(1-2\mu)r - \frac{A}{r}\right];\\ &\bar{u}_\Theta = Dr - \frac{C}{2Gr}, \end{aligned}\right\} \tag{6}$$

(the bar denotes components of the elastic stage). Satisfying boundary conditions (4) and (5), we get

$$\bar{\tau}_{r\Theta} = \frac{\tau a^2}{r^2},\ \bar{\gamma}_{r\Theta} = \frac{\tau a^2}{Gr^2},\ \bar{u}_\Theta = \frac{\tau a^2}{2Gb^2}\left(r - \frac{b^2}{r}\right). \tag{7}$$

The remaining components are zero. The angle of rotation of the rod is

$$\varphi = \frac{u_\Theta(a)}{a} = \frac{M}{4\pi G a^2 l}\left(\frac{a^2}{b^2} - 1\right). \tag{8}$$

The elastic deformation terminates by appearance of plastic strain near the rod surface, when the von Misses yield criterion is satisfied /414

$$N(a) = \frac{\sigma_T}{\sqrt{3}} = \tau_T, \tag{9}$$

where

$$N = \frac{1}{\sqrt{6}}\sqrt{(\sigma_r - \sigma_\Theta)^2 + (\sigma_z - \sigma_\Theta)^2 + (\sigma_r - \sigma_z)^2 + 6(\tau_{r\Theta}^2 + \tau_{rz}^2 + \tau_{z\Theta}^2)} \tag{10}$$

is the total tangential stress; σ_t is the yield strength of the material of the packing at the given temperature. The torque for which plastic strain starts is

$$M_T = 2\pi a^2 l \tau_T. \tag{11}$$

Here the angle of twist of the shaft

$$\varphi_T = \frac{\tau_T}{2G}\left(\frac{a^2}{b^2} - 1\right). \tag{12}$$

The elastoplastic stage of strain in the packing. If the material of the packing can be workhardened, then there appears a certain zone of plastic deformations $a \leq r \leq c$, alongside with the elastic zone $c < r \leq b$, which is retained. This zone continues to be described by Eqs. (6), while Eqs. (1), (1a), (2) and (2a) remain valid in the plastic zone, while the physical relationships, according to the theory of small elastoplastic deformations, have the form [4]:

a) condition of incompressibility of the material

$$\varepsilon_r + \varepsilon_\Theta + \varepsilon_z = 0; \tag{13}$$

b) condition of similitude and coaxiality of the strain and stress deviators

$$\frac{\varepsilon_i - \varepsilon_j}{\sigma_i - \sigma_j} = \frac{\gamma_{ij}}{2\tau_{ij}} \quad (i,\ j = r,\ z,\ \Theta); \tag{14}$$

c) power law for the workhardening

$$\Gamma = K \cdot N^n, \tag{15}$$

where

$$\Gamma = \sqrt{\frac{2}{3}} \sqrt{(\varepsilon_r - \varepsilon_\Theta)^2 + (\varepsilon_z - \varepsilon_\Theta)^2 + (\varepsilon_r - \varepsilon_z)^2 + \frac{3}{2}(\gamma_{r\Theta}^2 + \gamma_{z\Theta}^2 + \gamma_{rz}^2)} - \tag{16}$$

is the shearing-strain, while K and n are coefficients characteristic of a given material at the specified temperature, which are determined experimentally. In torsional tests of thin-walled tubes

$$N = \frac{M}{2\pi R^2 \delta}, \text{ and } \Gamma = R \cdot \alpha,$$

where M is the moment twisting the tube, R, δ and α are the average radius, thickness and the angle of twist per unit length of the tube, respectively (Fig. 2). /415
It is also required that components σ_r, $\tau_{r\Theta}$, u_r and u_Θ at the boundary between regions r and c be continuous. Solving Eq. (1a) and satisfying boundary condition (4), we get for the plastic region

$$\tau_{r\Theta} = \frac{a^2 \tau}{r^2}. \tag{17}$$

Equations (2) and (13) yield

$$u_r = \frac{A_1}{r}, \quad \varepsilon_\Theta = -\varepsilon_r = \frac{A_1}{r^2};$$

using boundary condition (4), we get

$$u_r = \varepsilon_\Theta = \varepsilon_r = 0, \tag{18}$$

from which, together with Eq. (14) it follows that $\sigma_r = \sigma_\Theta$, and further from Eq. (1) we have

$$\sigma_r = \sigma_\Theta = B_1.$$

Since $\varepsilon_z = 0$, $\sigma_z = 1/2(\sigma_r + \sigma_\Theta)$, hence,

$$\sigma_r = \sigma_\Theta = \sigma_z = B_1. \tag{19}$$

From the above expression and from Eqs. (10), (16) and (18) we have

$$N = \tau_{r\Theta}, \quad \Gamma = \gamma_{r\Theta}. \tag{20}$$

Condition $N(c) = \tau_T$ is satisfied at the boundary of the plastic region ($r = c$), whence it follows

$$c = a\sqrt{\frac{\tau}{\tau_T}}. \tag{21}$$

From Eqs. (2), (15) and (20) we get

$$\frac{du_\Theta}{dr} - \frac{u_\Theta}{r} = \frac{Ka^{2n}\tau^n}{r^{2n}},$$

solving which we get

$$u_\Theta = -\frac{Ka^{2n}\tau^n}{2nr^{2n-1}} + D_1 r. \tag{22}$$

Using Eq. (5) and the condition that the components are continuous at boundary r = c, we will get for the components of the elastic region the same expressions (7), while for the plastic region

$$\left.\begin{aligned} \sigma_r = \sigma_\Theta = \sigma_z = 0, \\ u_\Theta = \frac{K}{2n}\left(\tau_T^n - \tau^n \frac{a^{2n}}{r^{2n}}\right) r + \frac{\tau a^2 - \tau_T b^2}{2Gb^2} r, \end{aligned}\right\} \tag{23}$$

the angle of twist of the rod is

$$\varphi = \frac{K}{2n}\left[\tau_T^n - \frac{M^n}{(2\pi a^2 l)^n}\right] + \frac{1}{2G}\left(\frac{M}{2\pi b^2 l} - \tau_T\right). \tag{24}$$

If c = b, then the plastic region extends over the entire packing, in which case /416
the rod is loaded by the moment

$$M_0 = 2\pi b^2 l \tau_T, \tag{25}$$

and its angle of twist

$$\varphi_0 = \frac{K\tau_T^n}{2n}\left(1 - \frac{b^{2n}}{a^{2n}}\right). \tag{26}$$

In the case of a packing made from an ideal elastoplastic material [see Fig. 2 (dashed line)], it fails at M_T such that an annular plastic hinge is formed on the rod surface and its further twist proceeds without an increase in the moment [see Fig. 4 (horizontal line)].

Plastic deformation of the packing. Application to the rod of moment $M > M_0$ results in further development of plastic deformations over the entire cross section of the packing. This stage of deformation may take place quite a long time, hence, in addition to instantaneous strain, one also must take into account creep strain. We now consider this stage of deformation, using the following relationships between the stresses and the rates of strain [5-6]:

a) conditions of elastic change in the volume

$$\xi_r^p + \xi_\Theta^p + \xi_z^p = 0, \quad \xi_r^c + \xi_\Theta^c + \xi_z^c = 0; \tag{27}$$

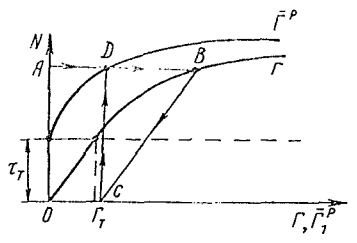

Figure 2. The Stress-Strain Diagram of the Packing Material N = f(Γ) and the Method for Reconstructing it into an N = = f($\bar{\Gamma}^p$) Diagram. The Straight Line BC is Parallel to the Initial Segment of Curve N = f(Γ).

b) conditions of similititude and coaxiality of stress deviators and of rates of plastic and creep strains

$$\frac{\xi_i^p - \xi_j^p}{\sigma_i - \sigma_j} = \frac{\eta_{ij}^p}{2\tau_{ij}}; \quad \frac{\xi_i^c - \xi_j^c}{\sigma_i - \sigma_j} = \frac{\eta_{ij}^c}{2\tau_{ij}} \quad (i, j = r, \Theta, z); \tag{28}$$

c) disregarding plastic components, the rates of strain are now composed from the rates of plastic strain and of creep strain

$$\xi_i = \xi_i^p + \xi_i^c, \qquad \eta_{ij} = \eta_{ij}^p + \eta_{ij}^c \qquad (i, j = r, \theta, z); \tag{29}$$

d) assuming that workhardening is governed by a power law, we shall regard N, the total tangential stress, as being related to the measure of plastic strain $\bar{\Gamma}^p$ in the following manner

$$\bar{\Gamma}^p = K_1 (N - \tau_T)^{n_1}, \tag{30}$$

where $\Gamma^p = \int H^p \, dt$ is defined as an integral taken over the entire straining path, of the intensity of the plastic shear strain rate

$$H^p = \sqrt{2}\sqrt{(\xi_r^p)^2 + (\xi_\theta^p)^2 + (\xi_z^p)^2 + 2[(\eta_{r\theta}^p)^2 + (\eta_{z\theta}^p)^2 + (\eta_{rz}^p)^2]}, \tag{31}$$

K_1 and n_1 are coefficients characteristic of the given material at the specified temperature, which must be determined experimentally. Using the Γ - N diagram thus obtained it is possible to construct a curve of $\bar{\Gamma}^p$, making use of the fact that $\bar{\Gamma}^p = R\alpha - N/G$ (see Fig. 2);

e) we assume that the intensity of the creep shear strain rate H^c is a power-law function of the total tangential stress N /417

$$H^c = K_c(t) \cdot N^m, \tag{32}$$

where $K_c(t)$ and m are some time function and a coefficient, which are determined experimentally. The value of H^c is defined by a relationship similar to (31),

but the creep strain rates ξ^c and η^c are used instead. We now write the known relationships between the rates of strain, components of the rates of displacement and the displacements

$$\xi_r = \frac{\partial V_r}{\partial r}; \quad \xi_\Theta = \frac{V_r}{r};$$
$$\xi_z = \frac{\partial V_z}{\partial z}; \tag{33}$$

$$\eta_{r\Theta} = \frac{\partial V_\Theta}{\partial r} - \frac{V_\Theta}{r}; \tag{33a}$$

$$V_r = \frac{du_r}{dt}, \quad V_\Theta = \frac{du_\Theta}{dt},$$
$$V_z = \frac{du_z}{dt}; \tag{33b}$$

the equilibrium Eqs. (1) and (1a) are now written for the current coordinates (r, Θ, z) of points of the packing. Boundary conditions (4) and (5) remain the same. Solving Eq. (1a) with boundary condition (4) yields

$$\tau_{r\Theta} = \frac{a^2}{r^2}\tau(t), \tag{34}$$

where $\tau(t) = M(t)/2\pi a^2 l$ and M(t) is a function of time (Fig. 3). Due to the fact that deformation in the axial direction is constrained and that the material of the packing is [was assumed to be] incompressible, we can use Eqs. (4) and (5) to write

$$u_z = u_r = 0, \tag{35}$$

consequently,

$$V_r = V_z = \xi_r = \xi_\Theta = \xi_z = 0. \tag{36}$$

Usings Eqs. (1), (10), (28), (29) and (36) we can show that

$$\sigma_r = \sigma_\Theta = \sigma_z = B(t), \quad N = \tau_{r\Theta}. \tag{37}$$

From the above and from Eqs. (27) and (28) we get

$$\xi_i^p = \xi_i^c = 0, \qquad (i = r, \Theta, z), \tag{38}$$

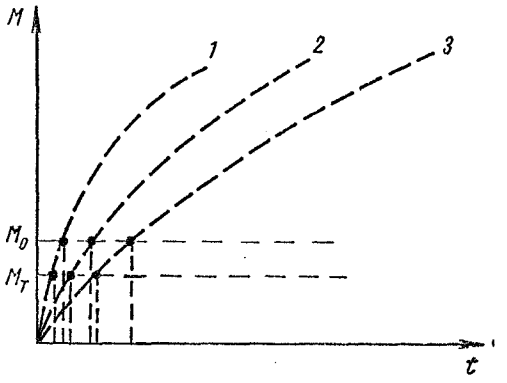

Figure 3. Change in the Moment Twisting the Rod with Respect to Time for Different Loading Rates $V_1 > V_2 > V_3$ (1, 2 and 3, Respectively).

i.e.,

$$H^p = \eta^p_{r\Theta}, \qquad H^c = \eta^c_{r\Theta}. \tag{39}$$

Using the above expression and Eqs. (29) and (33), we get /418

$$\frac{\partial V_\Theta}{\partial r} - \frac{V_\Theta}{r} = H^p(r, t) + H^c(r, t),$$

solving which together with Eq. (5), we get

$$V_\Theta = r\int_b^r \frac{H^p(x, t)}{x}\,dx + r\int_b^r \frac{H^c(x, t)}{x}\,dx. \tag{40}$$

In the general case

$$V_\Theta = \frac{du_\Theta}{dt} = \frac{\partial u_\Theta}{\partial t} + \frac{\partial u_\Theta}{\partial r}\frac{dr}{dt} + \frac{\partial u_\Theta}{\partial \Theta}\frac{d\Theta}{dt} + \frac{\partial u_\Theta}{\partial z}\frac{dz}{dt}.$$

Since r and z are constant in time, while

$$u_\Theta = u_\Theta(r, t),$$

then

$$\frac{dr}{dt} = \frac{dz}{dt} = \frac{\partial u_\Theta}{\partial \Theta} = 0, \text{ i.e., } \frac{du_\Theta}{dt} = \frac{\partial u_\Theta}{\partial t},$$

whence

$$u_\Theta = \int_0^t V_\Theta(r, y)\,dy, \tag{41}$$

here integration is performed over the entire loading path from t = 0 to some t. Using Eqs. (40) and (41) and making use of the fact that r is constant in time, we write

$$u_\Theta = r\int_b^r \frac{dx}{x}\int_0^t H^p(x, y)\,dy + r\int_b^r \frac{dx}{x}\int_0^t H^c(x, y)\,dy, \tag{42}$$

where $\int_0^t H^p(x, y)\, dy = \bar{\Gamma}^p$ is a measure of the plastic deformation accumulated over the entire straining path from t = 0 to t. For sufficiently developed strains $\bar{\Gamma}^p$ - N and Γ - N are almost identical and we can replace Eq. (30) by Eq. (15). Using the latter equation together with Eqs. (32), (34) and (37), we get from Eq. (42)

$$u_\Theta = -\frac{Ka^{2n}\tau^n}{2nr^{2n-1}}\left(1-\frac{r^{2n}}{b^{2n}}\right) - \frac{a^{2m}}{2mr^{2m-1}}\left(1-\frac{r^{2m}}{b^{2m}}\right)\int_0^t \tau^m(y)\,K_c(y)\,dy. \tag{43}$$

The angle of twist of the rod is

$$\varphi = -\frac{u_\Theta(a)}{a} = -\frac{KM^n(t)}{2^{n+1}\pi^n l^n n a^{2n}}\left(1-\frac{a^{2n}}{b^{2n}}\right) - \frac{1}{2^{m+1}\pi^m l^m m a^{2m}}\times \left(1-\frac{a^{2m}}{b^{2m}}\right)\int_0^t M^m(y)\,Kc(y)\,dy. \tag{44}$$

The first term in the last expression defines the contribution to the rod's angle of twist by instantaneous strains and does not depend on the manner in which the twisting moment varies with time. The second term defines the contribution made by creep and depends on the manner in which moment M(t) changes with time. Consequently, the relationship φ - M in the given case is not unique for different M(t) (Figs. 3 and 4). /419

Rod Loaded by an Axial Force

We now consider the elastic and elastoplastic stage of loading, without consideration of creep strain. Making use of the axial symmetry and the large length of the rod, all the components away from the ends can be regarded as functions of r only, in which case $\gamma_{r\Theta} = \gamma_{z\Theta} = u_\Theta = 0$.

Elastic stage of load application to rod. To solve this problem we use the equilibrium Eq. (1) and the equation

$$\frac{\partial \tau_{rz}}{\partial r} + \frac{\tau_{rz}}{r} = 0, \tag{45}$$

relationship (2) and the condition

$$\gamma_{rz} = \frac{\partial u_z}{\partial r}, \tag{46}$$

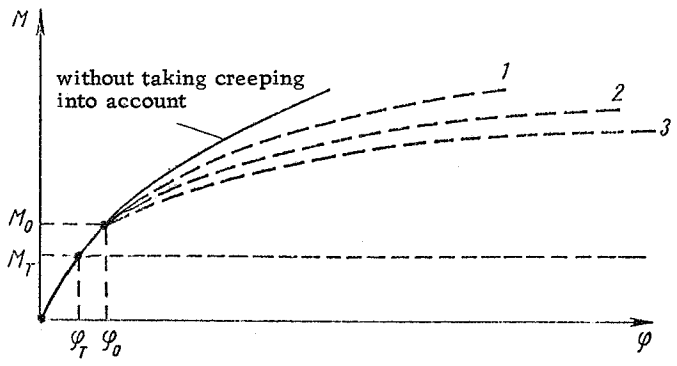

Figure 4. The Moment Twisting the Rod as a Function of the Latter's Angle of Twist; Curves 1, 2 and 3 Correspond to Different Rates of Changes in Moment M of Fig. 3.

Eqs. (3) and the expression

$$\gamma_{rz} = \frac{\tau_{rz}}{G}. \tag{47}$$

The boundary conditions to be satisfied are

$$r = a, \quad u_r = 0, \quad \tau_{rz} = \tau = \frac{P}{2\pi a l}, \tag{48}$$

$$r = b, \quad u_r = u_z = 0. \tag{49}$$

Solving Eq. (45) and satisfying condition (48), we have /420

$$\bar{\tau}_{rz} = \frac{\tau a}{r}. \tag{50}$$

Using the above expression and Eqs. (46) and (47), making use in the process of Eq. (49), we get

$$\bar{u}_z = -\frac{\tau a}{G} \ln \frac{b}{r}. \tag{51}$$

The solution of systems (1), (2), (3) is known, [7]

$$\left.\begin{gathered}\bar{u}_r = Ar + B/r, \quad \bar{\varepsilon}_\Theta = A + B/r^2, \quad \bar{\varepsilon}_r = A - B/r^2, \\ \bar{\sigma}_r = E\left[A(1+\mu) - \frac{B}{r^2}(1-\mu-2\mu^2)\right], \\ \bar{\sigma}_\Theta = E\left[A(1+\mu) + \frac{B}{r^2}(1-\mu-2\mu^2)\right], \\ \bar{\sigma}_z = 2\mu(1+\mu)EA.\end{gathered}\right\} \tag{52}$$

Using Eqs. (48) and (49), we get

$$\bar{u}_r = \bar{\varepsilon}_r = \bar{\varepsilon}_\Theta = \bar{\sigma}_r = \bar{\sigma}_\Theta = \bar{\sigma}_z = 0. \tag{53}$$

The axial displacement of the rod

$$\delta = u_z(a) = -\frac{P}{2\pi lG}\ln\frac{b}{a}. \tag{54}$$

Plastic deformations appear on the rod surface at the load

$$P_T = 2\pi a l \tau_T. \tag{55}$$

The rod displacement attendant to this is

$$\delta_T = -\frac{\tau_T a}{G}\ln\frac{b}{a}. \tag{56}$$

Elastoplastic stage of load application to the packing. On further application of load $P > P_T$ to a packing made from workhardening material there appears a zone $a \leq r \leq c$ of plastic deformations, along which is also retained zone $c \leq r \leq b$ of elastic deformation. Equations (50) and (52) are still valid in the latter zone; the behavior in the plastic region continues to be governed by Eqs. (1), (2), (45) and (46), while the physical relationships, according to the theory of small elastoplastic displacements are expressed by Eqs. (13)-(15). In addition to satisfying Eqs. (48) and (49) it is also required that components σ_r, τ_{rz}, u_r and u_z be continuous at $r = c$, i.e., at the boundary of the plastic region.

Equation (50) remains valid for the plastic region. Using Eqs. (2) and (13), we get

$$u_r = \frac{A_1}{r}, \quad \varepsilon_\Theta = -\varepsilon_r = \frac{A_1}{r^2}. \tag{57}$$

Satisfying the continuity condition and the boundary conditions for component u_r, /421 we get that $A_1 = A = B = 0$, i.e.,

$$\begin{cases} u_r = \varepsilon_r = \varepsilon_\Theta = \overline{u}_r = \overline{\varepsilon}_r = \overline{\varepsilon}_\Theta = \overline{\sigma}_\Theta = \overline{\sigma}_r = \overline{\sigma}_z = 0, \\ \Gamma = \gamma_{rz}. \end{cases} \tag{58}$$

It follows from Eqs. (1), (14) and (58) that $\sigma_r = \sigma_\Theta = \sigma_z = B_1$, i.e.,

$$N = \tau_{rz}. \tag{59}$$

At the boundary of the plastic zone $N(c) = \tau_T$, whence

$$c = \frac{a\tau}{\tau_T}. \tag{60}$$

Using Eqs. (15), (46), (50), (58) and (59), we get the expression

$$\frac{du_z}{dr} = \frac{K\tau^n a^n}{r^n},$$

solving which together with the condition that u_z is continuous at the boundary of the plastic zone yields

$$u_z = -\frac{K\tau_T^{n-1} a\tau}{n-1}\left(\frac{a^{n-1}\tau^{n-1}}{r^{n-1}\tau_T^{n-1}} - 1\right) - \frac{\tau a}{G}\ln\frac{b\tau_T}{a\tau}. \tag{61}$$

The axial displacement of the rod

$$\delta = u_z(a) = -\frac{K\tau_T^{n-1}}{2\pi l\,(n-1)}\left[\frac{P^n}{(2\pi a l\tau_T)^{n-1}} - P\right] - \frac{P}{2\pi lG}\ln\frac{2\pi lb\sigma_T}{P}. \tag{62}$$

Plastic strain proceeds over the entire cross section of the packing (c = b) at the load

$$P_0 = 2\pi bl\tau_T, \tag{63}$$

the displacement of the rod attendant to this

$$\delta_0 = -\frac{K\tau_T^n b}{n-1}\left[\left(\frac{b}{a}\right)^{n-1} - 1\right]. \tag{64}$$

The carrying ability of a packing made from an ideal elastoplastic material is exhausted when plastic deformations appear on the surface of the rod, hence, here the load on the rod cannot exceed P_T (horizontal line in Fig. 6).

Plastic deformation of the packing. When a load $P > P_0$ is applied to the rod, plastic straining takes place over the entire cross section of the packing. We now consider this loading stage so as to include the effect of creep of the material of the packing. For this we use the physical relationships (27) and (32). The equilibrium Eqs. (1) and (45), Eqs. (33) and (33b) and boundary conditions (48) and (49) retain their validity. Instead of Eq. (33a) we have

$$\eta_{rz} = \frac{\partial V_z}{\partial r}, \tag{65}$$

solving the above equation together with boundary condition (48), we get /422

$$\tau_{rz} = \frac{a}{r}\tau(t),$$

where

$$\tau(t) = \frac{P(t)}{2\pi a l}. \tag{66}$$

For an incompressible material, making use of conditions (48) and (49) away from the ends

$$u_r = 0,$$

consequently

$$V_r = V_\theta = \xi_r = \xi_\theta = \xi_z = 0. \tag{67}$$

It can be shown further that

$$\sigma_r = \sigma_\theta = \sigma_z = B(t), \quad N = \tau_{rz}, \tag{68}$$

$$\xi_i^p = \xi_i^c = 0, \quad (i = r, \theta, z), \tag{69}$$

$$H^p = \eta_{rz}^p, \quad H^c = \eta_{rz}^c. \tag{70}$$

Using Eqs. (29), (65) and (70), we write

$$\frac{\partial V_z}{\partial r} = H^p(r,\ t) + H^c(r,\ t),$$

whence, making use of (49) we have

$$V_z = \int_b^r H^p(x,\ t)\,dx + \int_b^r H^c(x,\ t)\,dx.$$

In general,

$$V_z = \frac{du_z}{dt} =$$

$$= \frac{\partial u_z}{\partial t} + \frac{\partial u_z}{\partial r}\frac{dr}{dt} + \frac{\partial u_z}{\partial \Theta}\frac{d\Theta}{dt} + \frac{\partial u_z}{\partial z}\frac{dz}{dt}.$$

Since Θ and r are constant in time and

$$u_z = u_z(r,\ t),\ \text{то}\ \frac{dr}{dt} = \frac{dz}{dt} = \frac{\partial u_z}{\partial z} = 0,$$

i.e., $V_z = \partial u_z/\partial t$, whence

$$u_z = \int_b^r dx \int_0^t H^p(x,\ y)\,dy + \int_b^r dx \int_0^t H^c(x,\ y)\,dy,$$

where $\int_0^t H^p(x, y)dy = \overline{\Gamma}^p$ is the plastic deformation accumulated over the entire straining path from t = 0 to t. Using Eqs. (15), (32), (66) and (68) for sufficiently developed deformations, we get /423

$$u_z = -\frac{Ka^n\tau^n(t)}{(n-1)\,b^{n-1}}\left(\frac{b^{n-1}}{r^{n-1}} - 1\right) - \frac{a^m}{(m-1)\,b^{m-1}} \times$$

$$\times \left(\frac{b^{m-1}}{r^{m-1}} - 1\right) \int_0^t K_c(y)\,\tau^m(y)\,dy. \qquad (71)$$

The axial displacement of the rod

$$\delta = u_z(a) = -\frac{KP^n(t)\,b}{(n-1)(2\pi bl)^n}\left(\frac{b^{n-1}}{a^{n-1}}-1\right)-$$

$$-\frac{b}{(m-1)(2\pi bl)^m}\left(\frac{b^{m-1}}{a^{m-1}}-1\right)\int_0^t K_c(y)\,P^m(y)\,dy. \qquad (72)$$

The first term here represents the contribution of instantaneous strains, while the second accounts for the creep strain and depends highly on the manner in which force P varies with time. Figures 5 and 6 show curves of P as a function of time and the corresponding δ - P curves.

Results Obtained by Analyzing Stress-Strain Diagrams for Sodium

It follows from the above that the force needed for moving the movable parts of frozen seals can be calculated on the basis of stress-strain diagrams for the heat-transfer agent. The available equipment can be used most conveniently for determining stress-strain diagrams under tensile loads. The large size of specimens, low loads, rapid corrosion in air are the main experimental difficulties when working with sodium.

The mechanical properties of the sodium were determined on specimens specially cast in a split metal chill mold. To increase coupling with the sodium, the butt parts of the chill mold had a rough screw threading on their inner surface; they served as end pieces for the specimen and the load was applied to them (Fig. 7). /424

The sodium specimens were tested in a somewhat modified UM-1800 machine. To increase the sensitivity of the load indicator, the sodium specimen was connected directly to the machine's electrotensometric dynamometer. The machine can produce several rates of deformation, which was utilized. The mechanical properties of sodium as a function of the temperature were obtained by heating the sodium specimens in a bath filled with VM-4 preliminary -vacuum oil (Fig. 8).

The sodium was tested in tension at three straining rates $\dot{\varepsilon} = 0.6$, 2.5 and 7.2 hour^{-1} and temperature of 20°C, as well as at four temperature levels (14, 20, 42 and 76°C) with a straining rate $\varepsilon = 7.2$ hour^{-1}. The changes in the ultimate strength σ_b, yield strength $\sigma_{0.2}$, and the relative elongation at rupture δ, as a function of one of the parameters ($\dot{\varepsilon}$, or T) is shown in Figs. 9 and 10. /425

The region of uniform straining in sodium specimens tested in tension is, as can be seen from Fig. 11, moderate and comprises 3-8%. The conduct of the test segment of the specimen under load differs from that of other materials. The round cross section of the specimens of plastic materials retains its shape up to /426

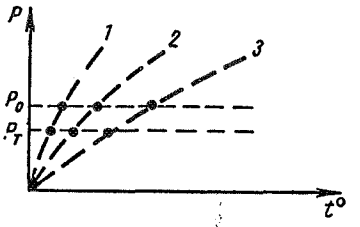

Figure 5. Variation in the Tensile Load Applied to a Rod in Time for Different Loading Rates $V_1 > V_2 > V_3$ (1, 2 and 3, Respectively).

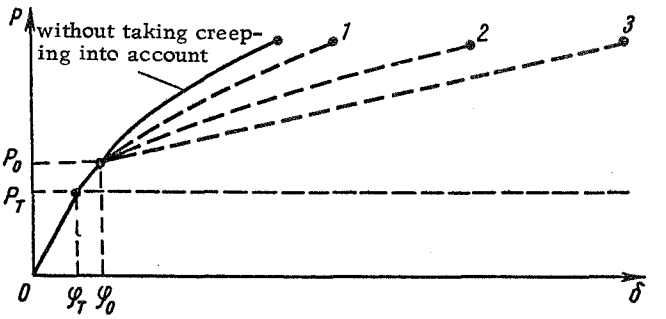

Figure 6. The Load Applied to the Rod as a Function of the Rod's Displacement. Curves 1, 2 and 3 Correspond to the Different Rates of Variation in P Shown in Fig. 5.

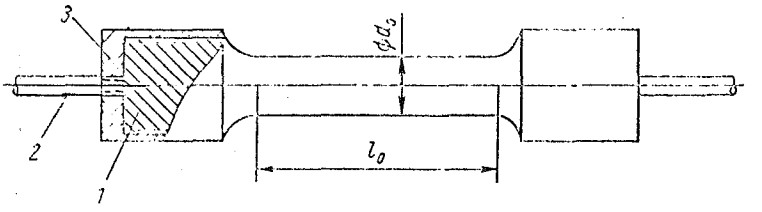

Figure 7. A Tensile Sodium Specimen.

1) Sodium; 2) Pull rod; 3) Aluminum End Piece of the Specimen (Design Length of Specimen 1_0 = 100 mm; Design Diameter d_0 = 22 mm).

failure, while the cross section of a round cast sodium specimen loaded above the ultimate strength changes, taking on outlines which are not uniform over the test length of the specimen (Fig. 12).

The methods for calculation require that the experimental results be plotted and used in the form of S - Ψ load diagrams (where S is the true stress and Ψ is the relative narrowing down [necking down]). However, it can be seen from our description of the experiment that it is impossible to obtain such a diagram for the segment starting with the ultimate strength and continuing to the point of failure. Hence, to construct the N(Γ) diagram the initial segment of the stress - strain diagram in the above coordinates was approximated by a power law extended past the ultimate strength [segment], [6] and [7]. In addition, calculations were performed on the assumption that past the ultimate strength point the material of the packing is workhardened insignificantly and its stress-deformation

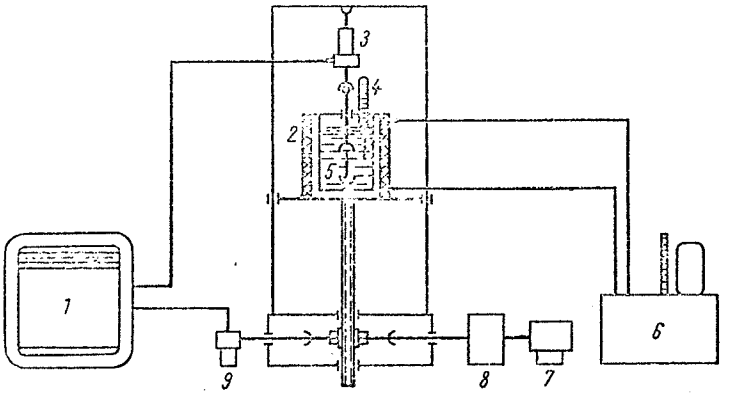

Figure 8. Schematic of Setup for Tensile Testing of Sodium Specimens.

1) Electronic Potentiometer; 2) Liquid Bath; 3) Dynamometer; 4) Thermometer; 5) Specimen; 6) Thermostat; 7) Motor; 8) Reducing Gear; 9) Pickup Selsyn.

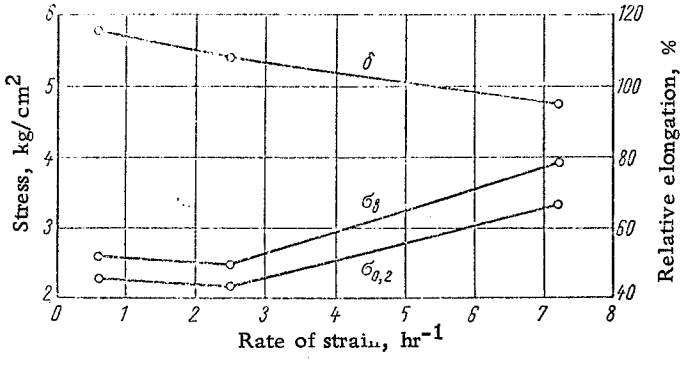

Figure 9. Mechanical Properties of Sodium in Tension as a Function of the Straining Rate at 20°C.

axis (Fig. 13, dashed lines). The N(Γ) diagrams reconstructed on the basis of the load diagrams P (Δl) are shown in Fig. 13.

The experimental results show that resistance to deformation increases with an increase in the [loading] rate and reduction in temperature. The forces needed for moving the movable parts of a frozen seal will change correspondingly. Hence, the starting data for computations should be obtained at deformation rates and temperatures close to those encountered under actual conditions. /427

The temperature range in the tensile test covers the temperatures observed in operating frozen sodium seals. The range of deformation rates is relatively small.

Data for steel tested with variations in the rate of straining show that resistance to deformation can increase by 2-3 fold when the rate is changed by an order of 6-8 [8].

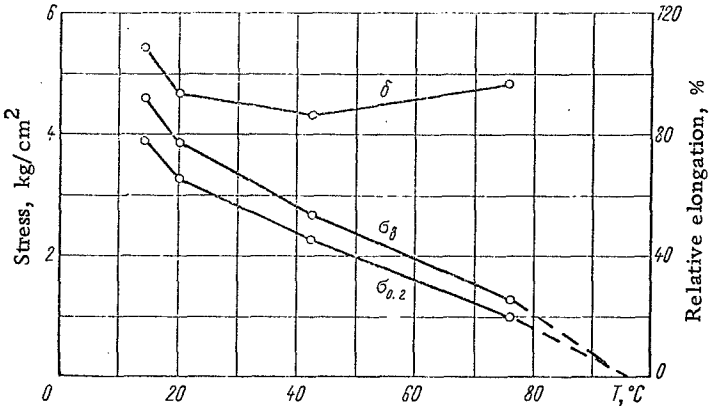

Figure 10. Mechanical Properties of Sodium in Tension as a Function of the Test Temperature for a Straining Rate of 7.2 hour^{-1}.

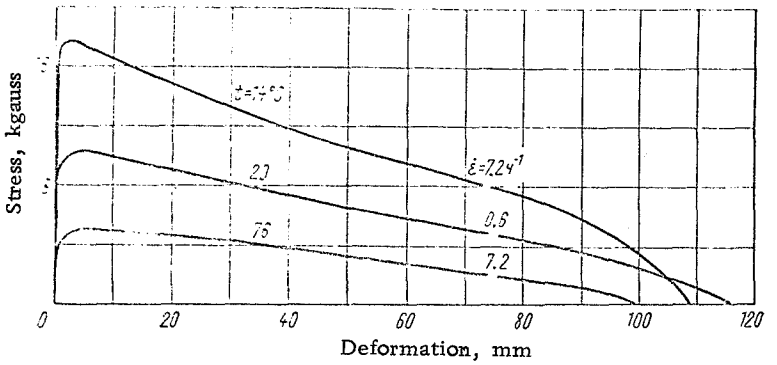

Figure 11. Load - Deformation Diagram for Sodium Specimens (Design Length of Specimen l_0= 100mm, its Diameter d_0 = 22 mm).

Figure 12. Shape of Sodium Specimen After Failure.

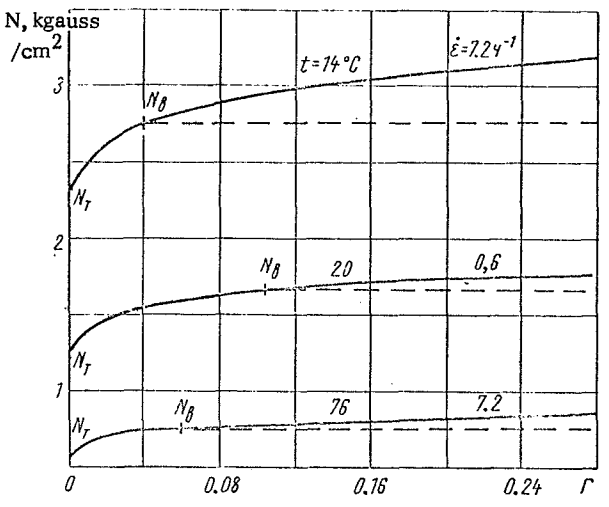

Figure 13. Stress-Strain Diagrams for Sodium for Different Temperatures and Loading Rates.

Using data obtained in tensile tests of sodium one must take into account the increase in the resistance to straining at deformation rates higher than those used in these tests.

Below we present calculation of moving forces using a stress-strain curve for sodium obtained at T = 14°C and $\varepsilon = 7.2$ hour^{-1}. The most accurate diagrams can be obtained in torsion tests of thin-walled tubular specimens tested at load rates close to those encountered in practice. A special facility is being designed for this purpose.

Results of calculations. /428
Analysis of stress-strain curves of the material of the packing obtained in tensile tests at 14°C yields the following constant of the yield curve in Eq. (15)

$$K = 1.509 \cdot 10^{-7} \text{ (cm}^2\text{/kg)}, \quad n = 11.85.$$

Yielding starts at stresses of $N_T = 2.25$ kg/cm^2. Assuming that the modulus of rigidity G is approximately equal to 1000 kg/cm^2, we get that $\Gamma = 0.225 \cdot 10^{-2}$.

We have calculated the twisting moments, forces and the corresponding angles of twist and displacements without taking into account creep of the material for a frozen seal with the following dimensions: a = 19 mm, b = 20 mm, l = 120 mm for torsion and a = 18 mm, b = 18.25 mm and l = 180 mm for axial displacement. The results obtained are

$$M_T = 612 \text{ kg·cm}; \quad \varphi_T = 1.097 \cdot 10^{-4}; \quad P_T = 457 \text{ kg}; \quad \delta_T = 5.50 \cdot 10^{-5} \text{ cm}$$
$$M_0 = 678 \text{ kg·cm}; \quad \varphi_0 = 2.238 \cdot 10^{-4}; \quad P_0 = 465 \text{ kg}; \quad \delta_0 = 6.02 \cdot 10^{-5} \text{ cm}.$$

If it is assumed that the material of the seal is not workhardened past the /429
ultimate strength $\Gamma > \Gamma_B$ (see Fig. 13), then the ultimate twisting moment and axial force can be found as

$$M_{\max} = 2\pi a^2 l N_b, \; P = 2\eta a l N_b,$$

where N_b is tangential stress at the instant when the cylindrical specimen ceases to yield in an orderly manner. For sodium at 14°C we have $N_b = 2.75$ kg/cm^2. Calculations yield $M_{max} = 750$ kg-cm, $P_{max} = 560$ kg. Figures 14 and 15 show the twisting moment as a function of the angle of twist of the shaft and the axial force as a function of the rod's displacement.

Study of the Characteristics of Frozen-Sodium Seals

At present many centrifugal pumps in operation use frozen-sodium seals. Their shaft rpm are as high as 3000 and the sodium temperature in the snail-case housing is 750°C. The maximum diameter of shafts of high-temperature pumps is 40 mm [9].

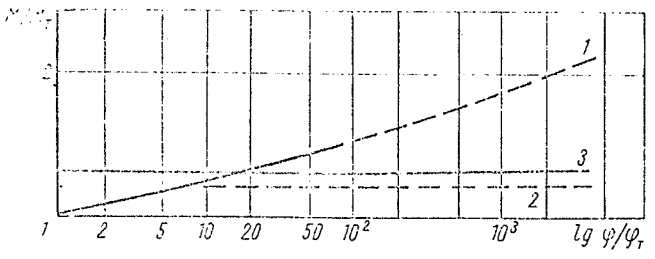

Figure 14. The Twisting Moment as a Function of the Rod's Angle of Twist for a Frozen-Sodium Seal.

1) Calculated Assuming Power-law Workhardening; 2) Calculated Assuming No Workhardening after Necking; 3) Experimentally Obtained Curve.

To determine the power losses due to friction a special installation was constructed which is shown schematically in Fig. 16. Unlike a pump, this installation did not have an impeller; it used a d-c motor rated at 1.6 kW to obtain variable rpm.

The first experiments were made with water. The power lost by fluid friction at different rpm was determined. The power was compared with the pump operating with and without water, whereupon the installation was dried and filled with sodium. The power was then measured with sodium let in at the freezing section, at the same rpm. The results obtained (with water and sodium) make it possible to establish that fluid friction exists in the clearance between the shaft and the housing [10]. Calculations were performed to determine the thickness of the fluid film. Use was made of the formula [11]

$$\Delta P = \xi \frac{C}{2\delta} \gamma \frac{W^2}{2q}. \qquad (73)$$

We transform this expression

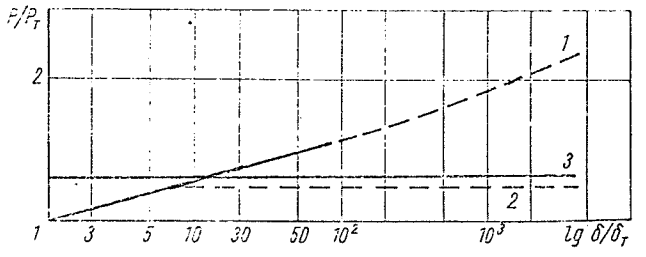

Figure 15. Axial Force on a Rod as a Function of the Axial Displacement for a Frozen-Sodium Seal (for Curve Legend see Fig. 14).

where Q is the flow rate, m^3/hour;

$$\xi = \frac{96}{R_e} = \frac{96\nu}{2w\delta} = \frac{96\nu\pi D}{2Q}.$$

Substituting these values into Eq. (73), we get

$$\Delta P = \frac{96\nu\pi De\gamma Q^2}{4\delta Q\pi^2 D^2\delta^2 2q} = \frac{48Q l\nu\gamma}{4\delta^3 q\pi D}.$$

Substituting the appropriate numerical values, we get /430

$$\delta = \sqrt[3]{\frac{48\nu\gamma Q}{4\Delta P g\pi D}} = \sqrt[3]{\frac{48\cdot 75\cdot 10^{-3}\cdot 940\cdot 1{,}8\cdot 10^{-7}}{4\cdot 1\cdot 10^5\cdot 9{,}8\cdot 3{,}14\cdot 4\cdot 10^{-2}}} =$$

$$= \sqrt[3]{\frac{4{,}8\cdot 7{,}5\cdot 9{,}4\cdot 1{,}8\cdot 10^{-6}}{4\cdot 6\cdot 10^2\cdot 9{,}8\cdot 3{,}14\cdot 4}} = \sqrt[3]{\sim 5\cdot 10^{-8}} = 1{,}7\cdot 10^{-5}\ \text{m}.$$

Thus, the thickness of the film of liquid sodium in the clearance between the housing and the shaft is about 15-20 micromicrons. This calculation should be regarded as a qualitative estimate.

The power lost in fluid friction does not exceed 1%, by absolute magnitude, of the power needed for pumping the metal and depends primarily on the pump shaft rpm. This relationship, determined experimentally, is parabolic (Fig. 17). Reference [6] presents a formula for calculating the fluid-friction power loss in sliding-contact bearings of the segment-type

$$\Delta N = 10KSn\sqrt{Sn\mu\gamma C_p\Delta t}. \qquad (74)$$

It is also possible to determine the friction power using the known Newton formula /431

$$F = -\mu S\frac{dw}{d\delta}. \qquad (75)$$

This formula can be transformed to the form

$$\Delta N = \frac{10\mu\omega^2 lD^3}{120\delta}. \qquad (76)$$

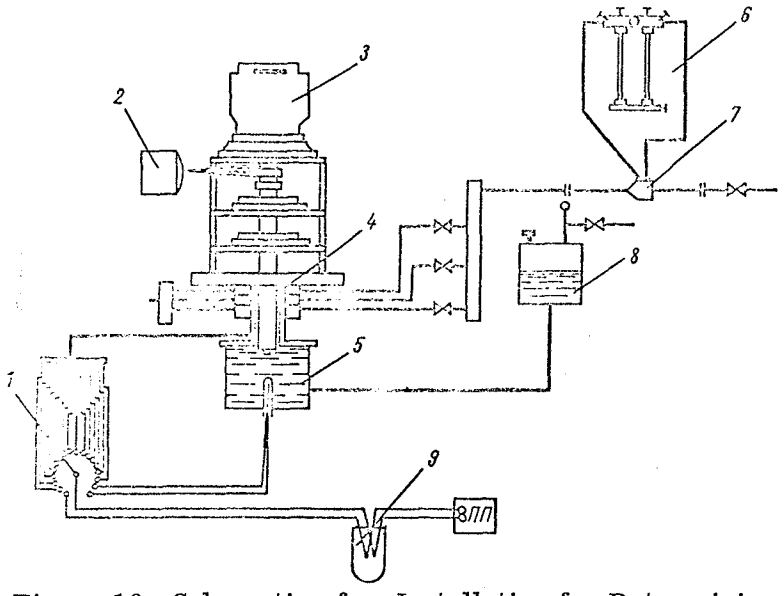

Figure 16. Schematic of an Installation for Determining the Properties of a Frozen-Sodium Seal for a Rotating Shaft.

1) Multipoint Switch; 2) Stroboscope; 3) d-c Motor; 4) Seal under Test; 5) Test Volume; 6) Differential Manometer; 7) Venturi Nozzle; 8) Expansion Tank; 9) Dewar's Flask.

which is done as follows: we assume that the distribution of the peripheral velocity is linear

$$F = \mu\pi DH\frac{W}{d}, \tag{77}$$

on the other hand,

$$W = \frac{\pi Dn}{60}, \tag{78}$$

then

$$F = \mu\pi DH\frac{\pi Dn}{60\delta}, \tag{79}$$

we define M at the shaft

$$M = FR = F\frac{D}{2}, \tag{80}$$

$$\Delta N = 10MW, \tag{81}$$

where W is the angular velocity.

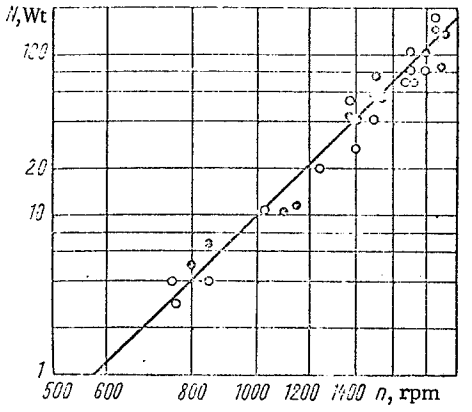

Figure 17. Power Lost in Friction in a Packing Seal, where ○ is Water and ● is Sodium.

Substituting these quantities into Eq. (75), we will get a quantity expressing the fluid-friction power in the clearance between the shaft and pump housing. Comparing experimental data with results obtained by calculations a divergence of 30% is found in the region of high n. But these differences are not of principal importance, since, as was shown, the absolute value of the power lost in friction does not exceed 1%. These differences may apparently be attributed to the surface finish, since it is precisely at high shaft rpm that these exert their effect.

To determine the starting torque in frozen-sodium seals use was made of the installation shown in Fig. 16; in which a lever with a DS-0.2 dynamometer replaced the electric motor. When the sodium in the seal is liquid, the torque needed for rotating the shaft was, as expected, practically zero. Reduction in the sodium temperature to below that of solidification sharply increased the required torque. In experiments to determine the tangential stress for sodium in the frozen-sodium seal the temperature was measured over the height of the valve, which made it possible to determine the size of the shaft surface which is in contact with the solidifying sodium. It was found that the tangential stress depends on the temperature and on the starting shaft rpm. It was also established that increasing the sodium pressure in the loop from 0 to 12 kg/cm^2 does not affect the torque of the friction coefficient. /432

For seals for which calculations were performed above it was found in experiments that $M_{max} = 800$ kg-cm or $M_{max}/M_T = 1.3$ and $P_{max} = 600$ kg or $P_{max}/P_T = 1.3$. Comparison of M_{max} and P_{max} obtained experimentally and theoretically shows that they agree satisfactorily (see Figs. 14 and 15).

CONCLUSIONS

1. A method was developed for calculating the startup forces of frozen metal (such as Na, K, etc.) seals.

2. Stress-strain diagrams for sodium were obtained for different straining rates and different temperatures.

3. Characteristics of several designs of frozen-sodium seals were studied experimentally. Comparison of experimental and theoretical results shows satisfactory agreement.

REFERENCES

1. Kirillov, P. L., et al.: Atomnaya energiya, 7, 11, (1959).
2. Zhidkometallicheskiye teplonositeli [Liquid-Metal Heat-Transfer Agents]. Collection of articles, translated from English under the Editorship of A. Ye. Sheyndlin. Foreign Literature Publishing House, Moscow, 1959.
3. Kristianovich, S. A., et al.: Nekotoryye voprosy mekhaniki sploshnoy sredy [Certain Problems of Mechanics of a Continuous Medium]. Published by the Academy of Sciences of the USSR. Moscow-Leningrad, 1938.
4. Il'yushin, A. A.: Plastichnost' [Plasticity]. Fizmatgiz, Moscow, 1948.
5. Hill, R.: The Mathematic Theory of Plasticity. Oxford University Press. 1950.
6. Kachanov, L. M.: Teoriya polzuchesti [Theory of Creep]. Fizmatgiz, Moscow, 1960.
7. Timoshenko, S. P.: Theory of Elasticity. McGraw-Hill Book Company, Inc. 1934.
8. Nadii, A.: Theory of Flow and Fracture of Solids. McGraw-Hill Book Company, Inc., 1950.
9. Shaposhnikov, N. A.: Mekhanicheskiye ispytaniya metallov [Mechanical Testing of Metals]. Mashgiz, Moscow-Leningrad, 1954.
10. Golubev, A. I.: Sovremennyye uplotneniya vrashchayushchikhsya valov [Present-Day Packings of Rotating Shafts]. Mashiz, Moscow, 1962.
11. Drobyshev, A. V. and Turchin, N. M.: Atomnaya energiya, 10, 386 (1961).
12. Loytsyanskiy, L. G.: Mekhanika zhidkostey i gazov [Mechanics of Liquids and Gases]. Gostekhizdat, Moscow, 1957.
13. Ayzenshteyn, A. I.: Tsentrobezhnyye nasosy dlya neftyanoy promyshlennosti [Centrifugal Pumps for the Petroleum Industry]. Gostoptekhizdat, Moscow, 1957.

APPENDICES

I. CALCULATIONS OF HEAT TRANSFER IN LIQUID METALS

These recommendations were compiled by analyzing data obtained in SSSR and in foreign countries up to 1 January 1966. /433

The formulas presented below are recommended for convective heat transfer calculations for liquid metals containing admixtures below the limit of solubility at the given temperature. They can be used without reservations when the liquid metal is heated. When it is cooled and in the cases when the admixtures precipitate from solution, depending on the specific contamination conditions and other factors which are at present difficult to assess quantitatively, the impurities may settle on the heat-transfer surfaces and thus reduce the heat transfer coefficient several fold.

These cases require separate examination. This remark does not pertain to boiling and condensation processes. It should be remembered in the calculations that at the beginning (at 200°C sometimes for several hundred of hours) the heat transfer coefficient of the heat-transferring surface may be by a factor of 3-5 lower the design values until wetting of the wall is achieved.

1. Convective Heat Transfer

Round Tube

Theoretical formula	Range of appliability and boundary conditions	Accuracy, %
$Nu = 5 + 0.025\ Pe^{0.8}$ (A1)	$3 \cdot 10^3 < Re < 10^6$ $0.004 < Pr < 0.04$ $l/d > 30$ $q_w = const$	15
$Nu = 4.36$ (A2)	$Re < 2.3 \cdot 10^3$	10

Formula (1) yields local heat transfer coefficients and is valid for the region of steady-state heat transfer, i.e., far from the tube inlet and from the start

of the heated section. To find the average heat transfer coefficient in short tubes ($5 < l/d < 30$) we must introduce the correction[1]

$$\varepsilon_l = 1.7\left(\frac{d}{l}\right)^{0.16} \tag{A.3}$$

Studies[2] show that ε_l is a function of not only l/d, but also of the Peclet number, and on the extent of contamination of the tube wall.

Formula (2) is applicable to the case when axial flow of heat over the fluid and the wall are small and the effect of natural convection can be disregarded. When axial flow of heat is taken into account, then the heat transfer coefficient calculated from Eq. (2) should be multiplied by the correction factor ψ, which is found from the expression

$$\frac{1}{\psi} = 1 + 4\frac{4.36}{\mathrm{Pe}^2}(1+\varphi)\left(1 - \frac{1+\varphi}{\mathrm{Pe}L}\right), \tag{A.4}$$

where

$$\varphi = \frac{F_w\lambda_w}{F_f\lambda_f}.$$

Longitudinal flow of heat through the fluid and the walls of the heat exchanger change the temperature fields, which should be taken into account in calculating the mean temperature drop in the heat exchanger. For equal water equivalents of the liquid metal, the theoretical temperature drop in the heat exchanger

$$\Delta t = \Delta t_0 \frac{1 + \frac{1+\varkappa}{\mathrm{Pe}\cdot L}\left[1 - \frac{\sqrt{1 + 4\omega\frac{\varkappa}{(1+\varkappa)^2}}}{1+\omega}\right]}{1+\omega}, \tag{A.5}$$

where

$$\omega = \frac{4Kd}{\lambda_f \mathrm{Pe}^2}(1+\varkappa+\varphi), \qquad \varkappa = \frac{F_1\lambda_1}{F_f\lambda_f}, \qquad \varphi = \frac{F_w\lambda_w}{F_f\lambda_f},$$

---

[1] Kutateladze, S. S. Osnovy teorii teploobmena [Fundamentals of the Theory of Heat Transfer], Mashgiz, Moscow-Leningrad, 1962.

[2] Subbotin, V. I., et al. Atomnaya Energiya, 13, No. 2 (1962).

Δt_0 is the temperature drop between the heat-transfer agents at infinite distance from the heat exchanger; K is the heat transfer coefficient; d is the tube diameter or the equivalent diameter; F_w, F_f and F_1 are the cross sectional area of the wall, of the liquid metal in the tube and of the liquid metal in the intertubular space, respectively.

Rectangular Duct

Conditions	Formula	Range of applicability	Accuracy, %
Heating from one side, qw = const	$Nu = 4.9 + 0.0175\ Pe^{0.8}$ (A 6)	$4 \cdot 10^2 < Pe < 4 \cdot 10^3$, $\frac{a}{b} > 5$	±15
Heating from two sides, qw = const	$Nu = 10 + 0.025\ Pe^{0.8}$ (A 7)	$4 \cdot 10^2 < Pe < 4 \cdot 10^3$, $\frac{a}{b} > 5$	±20

It should be remembered, in calculating heat transfer in rectangular ducts, /435 that the wall temperature is not uniform over the duct's cross section. The difference between the wall temperature and the average temperature of the heat transfer agent for corners of ducts can be by 40-50% higher than for their centers. In all cases of utilization of Eqs. (A.6) and (A.7) the size of the heat-transferring part facing the liquid-metal flow should not exceed the duct's dimensions.

Concentric and Eccentric Annular Ducts

Conditions	Formula	Range of applicability	Accuracy, %
Heating from one side, qw = const e = 0	$Nu = 5 + 0.02\ Pe^{0.8}$ (A 8)	$250 < Pe < 7.5 \cdot 10^3$ $1.0 < \frac{d_2}{d_1} < 2.0$	±15
Heating from one side, qw = const e = 0.5	$Nu = 0.016\ Pe^{0.9}$ (A 8a)	$40 < Pe < 600$ $\frac{l}{d} \geqslant 100$	±25
Heating from two sides, qw = const e = 0	$Nu = 10 + 0.025\ Pe^{0.8}$ (A.9)	$300 < Pe < 4 \cdot 10^3$ $1.05 < \frac{d_2}{d_1} < 2.0$	±25

Formulas (A.8) and (A.9) are applicable only for a symmetrical annulus. In an eccentric annulus heat transfer becomes inhomogeneous to a large extent over the angular dimension as well as over the length. The heat transfer sometimes is not stabilized at all in the case of large Peclet numbers. A certain role is played by the wall thickness and its thermal conductivity. Estimates can be obtained from Eq. (A.8a) for an internally heated annular duct with a wall thickness of 15 mm made from 1Kh18N9T steel.

Rod and Tube Cluster

Conditions	Formula	Range of applicability	Accuracy, %
Continuous rods packed closely in a triangular lattice	$\mathrm{Nu}=0{,}15\left(\frac{\lambda_w}{\lambda_f}\right)^{0{,}2}\mathrm{Pe}^{0{,}3+0{,}04\sqrt{\frac{\lambda_w}{\lambda_f}}}$ (A10) *	$80<\mathrm{Pe}<600$; $0{,}7<\frac{\lambda_w}{\lambda_f}<16{,}5$	±20
Rods arranged in a triangular array with spacing x	$\mathrm{Nu}=0{,}58\,(1{,}1x^2-1)^{0{,}55}\mathrm{Pe}^{0{,}45}$ (A11) *	$400<\mathrm{Pe}<4\cdot10^3$; $1{,}1<x<1{,}5$	±20
Continuous packing of continuous rods in a rectangular array	$\mathrm{Nu}=0{,}6+0{,}013\,\mathrm{Pe}^{0{,}7}$ (A12)	$10^2<\mathrm{Pe}<2\cdot10^3$; $0{,}5<\frac{\lambda_w}{\lambda_f}<20$; $\frac{l}{d_r}>50$	±20
Intertubular space of counterflow heat exchangers	$\mathrm{Nu}=8\left[\frac{d_r}{l}+0{,}027\times(x-1{,}1)^{0{,}16}\right]\mathrm{Pe}^{0{,}6}$ (A13)	$200<\mathrm{Pe}<1200$; $60<\frac{l}{d_n}<260$; $1{,}1<x<1{,}4$	±15

Techniques of Heat Transfer Calculations in Rod Clusters, Arranged in a Triangular Array (Axial Flow) for $1 \le x \le 1.75$ and $1 < \mathrm{Pe} < 4000$. /436

1. For each specified spacing x Nu_{st} and Nu_{sq} is found from Fig. A.1.

2. Knowing the dimensions and thermal conductivities of fuel elements, it is possible to calculate the parameters

$$\Lambda_0=\frac{\lambda_w-\lambda_0}{\lambda_w+\lambda_0};\quad \xi=\frac{R_1}{R_2};\quad \frac{\lambda_w}{\lambda_f}.$$

[1]Here α is the heat transfer coefficient, averaged over the angle at a section away from the inlet $\alpha = \bar{q}/\bar{t}_w - t_f$.

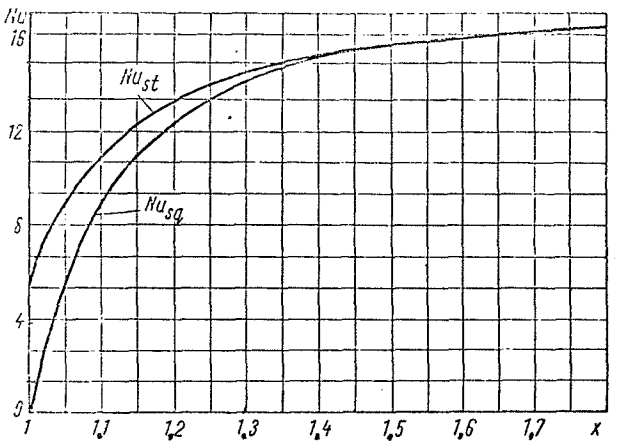

Figure A.1.

Figure A.2 is then used to find $\Psi = f(\Lambda\xi^{12})$.

3. Then one finds

$$Nu_s = \Psi (Nu_{st} - Nu_{sq}) + Nu_{sq}. \quad (A.14)$$

4. Figures A.3 and A.4 are used to find f_1 and f_2.

5. Then $Nu = f_1 Nu_s +$ /438
$+ f_2 Pe$ is calculated, where Nu is a value averaged over the perimeter and calculated as

$$Nu = \frac{\bar{q} d_n}{(\bar{t}_w - \bar{t}_f)\lambda_f}.$$

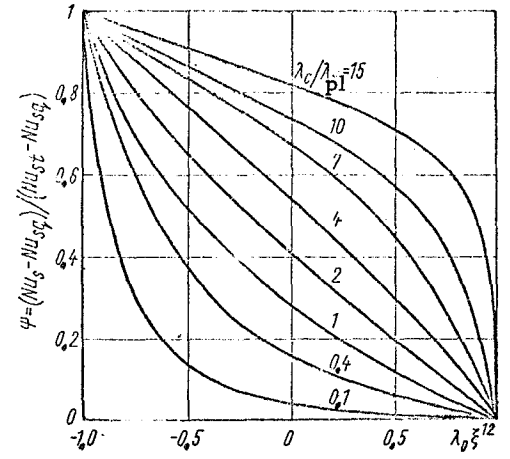

Figure A.2.

6. Using Fig. A.5 the maximum temperature variation over the perimeter of fuel elements is determined for the given Ψ and x

$$t_w^{max} - \bar{t}_w = \frac{\Psi \bar{q} R_2}{\lambda_f}.$$

Condensation of Pure Vapor /440

Thermal resistance to heat transfer is composed of two parts: of the thermal resistance of the condensate film and of the thermal resistance of phase transition

$$\frac{1}{\alpha} = R = R_{ml} + R_{ph} \quad (A.20)$$

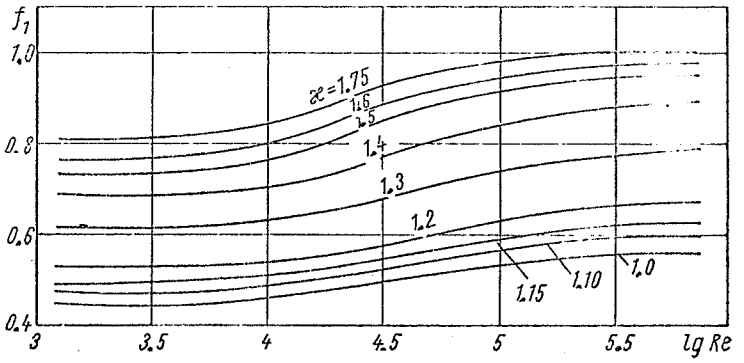

Figure A.3.

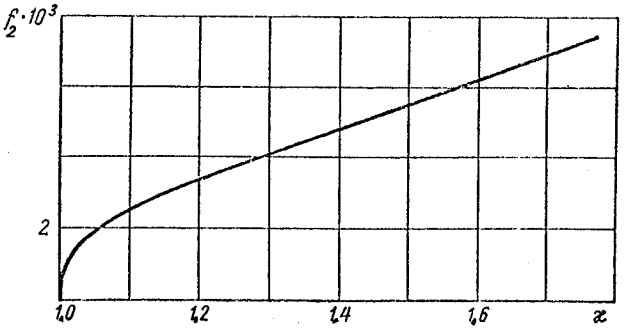

1. Thermal resistance of the condensate film.

a) Laminar flow $Re_{ml} = 4G/g\mu < 1600$, with R_{ml} calculated as for ordinary fluids. Corrections are needed for $r/C_p\Delta T_{ml} < 50$.[1]

b) Turbulent flow for $Re_{ml} = 4G/g\mu > 1600$; with R_{ml} found from Fig. A.6 for a given Re.

[1] Labuntsov, D.A., Teploenergetika, 12, 47 (1956).

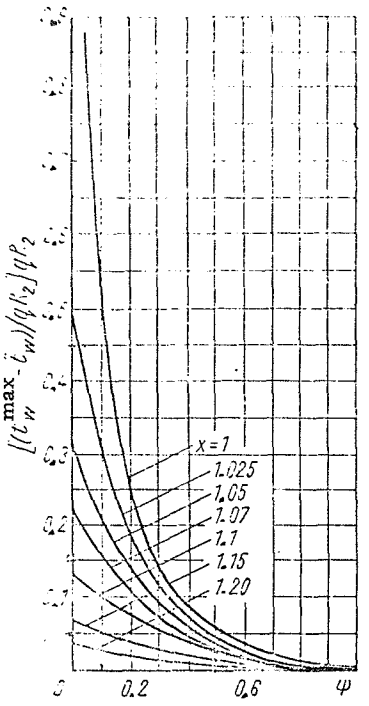

Figure A.5.

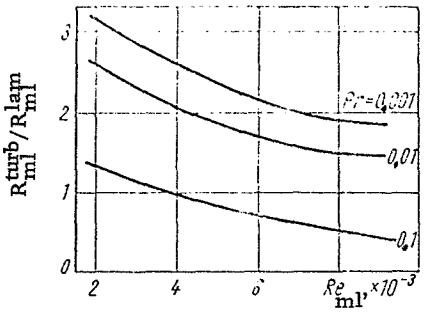

Figure A.6

2. Thermal resistance of the phase transition.

$$\frac{1}{R_{ph}} = \frac{2r}{A\sqrt{\frac{2\pi RT_s}{M}}}\left[\frac{r}{T_s(v''-v')} - \frac{P_s}{2T_s}\right] \qquad (A.21)$$

Tranverse Flow Past Tubes

Formula	Range of applicability	Accuracy, %
$Nu = Pe^{0.5}$ (II.15)	$10^2 < Pe < 4\cdot10^3$ $\frac{s_1}{d} = 1.2$ $1.1 < \frac{s_2}{d} < 1.5$ $\frac{l}{d} \sim 10$	±30

Natural Convection

Conditions	Formula	Range of applicability	Accuracy, %
Horizontal cylinder	$Nu = 0{,}53\ (GrPr^2)^{1/4}$ (A16)	$10 < GrPr^2 < 10^4$	±15
Horizontal plastic	$Nu = 0{,}35\ (GrPr)^{1/3}$ (A17)	$2.5 \cdot 10^3 < GrPr^2 < 3 \cdot 10^5$	±25

Combined Free and Forced Convection in a Round Tube

Formula	Range	Accuracy, %
$Nu = A\,(Pr)\,Z^{1.4}$, (A18) where $A = 0.34$ and $Pr = 0.005$ $A = 0.24$ and $Pr = 0.02$	$\frac{l}{d} = 5$ $3 < Pe < 150$ $10 < Z < 30$	±25

2. Transfer of Heat Attendant to Changes in the State of Aggregation

Boiling

Conditions	Formula	Range of applicability	Accuracy, %
Horizontal surface of a large volume	$\alpha = 4q^{2/3}$ (A19)	0.1 atm p 1.2 atm, 10^5 kcal/(m^2 · hr) q q_{cr}	± 30 for sodium and potassium

Critical Thermal Fluxes

Conditions	Formula	Range of utilization	Accuracy, %
Horizontal surface of a large volume	$q_{cr} = (1.5 + 1.3\,p) \cdot 10^6$ kcal/(m^2 · hour) (A22)	For sodium 0.015 atm $\leq p \leq$ 1.2 atm	±30
	$q_{cr} = 1.7\,p^{0.12} \cdot (10^6$ kcal/(m^2 · hour) (A23)	For potassium 0.03 atm $\leq p \leq$ 1.4 atm	±25

NOTATION

A - 1/427

B - height of retangular duct

d_1 and d_2 - major and minor diameters of the annulus

$d_h = 4F/P$ - hydraulic diameter of duct

F - cross sectional area of duct

l - duct length

$L = l/d_h$ - relative length of duct

P - perimeter

R - universal gas constant

S_1 and S_2 - spacing along the front and into the depth of a cluster with flow transverse to tubes

ε_e - correction factor for shorttubes

$Z = \frac{d}{2}\sqrt[4]{\frac{g\beta\frac{t_{in}-t_{out}}{l}}{\nu a}}$ - dimensionless parameter, reflecting the effect of natural convection.

II. CORROSION RESISTANCE AND TEMPERATURE LIMIT OF UTILIZATION OF CERTAIN CONSTRUCTION MATERIALS IN A SODIUM FLOW

1. Pearlitic Chromium Steels

/441

Steel	Temperature limit of utilization	Loss of carbon, %, at 600°C after 2000 hours in sodium flow, of the quantity of carbon in a surface layer 1 mm thick [1,2]	Steel	Temperature limit of utilization	Loss of carbon, %, at 600°C after 2000 hours in sodium flow, of the quantity of carbon in a surface layer 1 mm thick [1,2]
EI-802	700	5[3]	1Kh1M1FS	450	40
EI-993	600	5—20	EP-79	450	45
EP-38	600	5—20	1Kh2M	450	60
1Kh5MS	550	5—20	EP-78	450	60
EI-531	500	20	12KhMF	450	75
1Kh2M2F	450	30	12Kh2MFSR	450	85

[1] Construction materials can be arbitrarily divided into those with good corrosion resistance in sodium at the given temperature and an operating time of 2000 hours, if the carbon loss does not exceed 10%; into materials with satisfactory resistance if the carbon loss comprises 10-30%, and into materials with poor resistance on carbon losses of above 30%.

[2] The experimental data were obtained for an oxygen concentration in the sodium of $(2-5)\cdot 10^{-3}$% by weight.

[3] Carbon loss after 6500 in sodium flow.

2. Nickel-Containing Steels and Alloys, Refractory Metals

Material class	Material[1]	Temperature limit of utilization, °C, for 5000 hours work	Rate of corrosion mg/(cm^2.hr), in a flow of sodium at 700°C with an oxygen content of (3-5).10-3 % [by weight]
Stainless austenitic steels	EI-211	800	0,0006
	EI-854	700	~0,0007
	EP-71	700	0,0008
	EP-148	700	0,001
	EI-847	700	0,002
	EI-403	700	0,003
	1Kh18N10T	700	0,003—0,004
	EI-888	700	0,003—0,004
	EI-448	700	0,003—0,004
	EI-844	700	0,003—0,004
	EI-850	700	0,003—0,004
	EI-851	700	0,003—0,004

TABLE (concluded)

Material class	Material[1]	Temperature limit of utilization, °C, for 5000 hours work	Rate of corrosion mg/(cm^2.hr), in a flow of sodium at 700°C with an oxygen content of (3-5) 10^{-3}% [by weight]
Nickel-base allows	EI-827	800	0.003 - 0.004
	EI-559A	700	0.004
	EI-559	700	~0.006
	Kh20N60M5V10Yu2T2	700	0.008
	Molybdenum	700	0.0095
Refractory metals	Niobium	1100	0[3]
		1000	0.0025[3]

[1]By their corrosion resistance in sodium, the construction materials can be divided into those with good corrosion resistance at the given temperature if the rate of corrosion does not exceed 0.0010 milligrams/cm^2-hour; into those with satisfactory corrosion resistance, if their corrosion rate lies in the range from 0.0010 to 0.0100 milligrams/cm^2-hour.

[2]The oxygen content of the sodium should be of the order of 10^{-4}% by weight.

[3]Rate of corrosion at 900°C.

Translated for the National Aeronautics and Space Administration by Scripta Technica, Inc., NASw-1694.

ABSTRACTS

Study of Heat Transfer in Liquid Metals in Round Pipes (V. D. Talanov and P. A. Ushakov) 1

This paper presents experimental heat transfer data for mercury and sodium-potassium alloy in stainless steel and copper tubes, respectively. Empirical dimensionless equations proposed by previous investigators were found to correlate well with the experimental data. The data showed the thermal contact resistance to be negligible under the experimental conditions, provided the oxides of the liquid metal are in the dissolved state.

Heat Transfer with Liquid Metal in a Vertical Pipe with Low Peclet Numbers (N. A. Ampleyev, P. L. Kirillov, V. I. Subbotin and M. Ya. Suvorov) 8

The paper presents an attempt to clarify the cause for disagreement in heat transfer data at low Peclet numbers obtained by previous investigators. Difference from previous equations is attributed, in part, to natural convection effects, end heat losses, entrance conditions. Absence of thermal resistance effects was confirmed and the effect of l/D is studied.

Heat Transfer of Sodium and a Sodium-Potassium Alloy in Short Vertical Pipes by Combined Convection (L. G. Volchkov, M. K. Gorchakov, P. L. Kirillov and F. A. Kozlov) 28

Under the experimental conditions, the combined convection heat transfer was found to be appreciably higher than in forced convection only. In short ducts, the length was shown to have little effect on heat transfer, although the effect remains unclear. The temperature field is shown to agree with theoretical predictions based on the stabilized laminar flow problem.

Taking into Account Longitudinal Heat Flows when Measuring the Average Temperature of Fluids in Pipes and Heat Exchanges for Low Peclet Numbers (M. K. Gorchakov) 40

The author presents a relationship between the actual average temperature of the fluid and its theoretical value in tubes at constant heat fluxes and in double pipe heat exchangers with identical flow rates in both passages. An evaluation is made of the effects of shape of velocity profile, channel geometry, longitudinal heat conduction, and nonuniformity of heat flux.

Statistical Characteristics of Turbulent Temperature Fluctuations in Fluid Flows (V. P. Bobkov, M. Kh. Ibragimov and V. I. Subbotin) 53

The article presents experimental data on certain statistical characteristics of temperature fluctuations in turbulent flow of various fluids with highly different thermal conductivities (water, mercury, lead). The

intensity of temperature fluctuations, spatial correlation coefficients, scales of temperature disturbance, correlation coefficients, probability distribution and channel radii are considered in evaluating the various effects on heat transfer and flow.

Statistical Characteristics of Temperature Fluctuations in Heat Exchanger Walls Attendant to High Thermal Fluxes (M. Kh. Ibragimov, V. I. Merkulov and V. I. Subbotin) 71

The authors present some statistical characteristics, intensity and cross-correlation function, of temperature fluctuations in the wall of a double pipe heat exchanger with the same agent (liquid metal) flowing through each duct, but at a different temperature. Experimental equipment and collected data are described and analyzed.

Heat Transfer in Turbulent Flow of Fluids in Square Ducts (M. Kh. Ibragimov, Yu. M. Rabotyashnik, G. I. Sabelev, V. I. Sidirov and V. I. Subbotin) 82

Results of a heat transfer study in a square duct with water and mercury are presented. The temperature fields in the wall and in the fluid have been obtained as well as the statistical characteristics of turbulent temperature fluctuations. The inapplicability of equations for round pipes to square ducts is demonstrated. The effect of secondary flows on heat transfer is experimentally determined. Correction factors for square ducts are presented.

Fluid Dynamics in an Annular Space with Longitudinal Ribs (Yu. D. Levchenko, V. I. Subbotin, P. A. Ushakov and A. V. Sheynina) 100

Results of an experimental heat transfer study with narrow annuli, both concentric and eccentric, are presented. Experimental test section construction and collected data are given. The applicability of previously recommended calculation methods for velocity distribution and friction factors is shown.

Effect of Eccentricity on Heat Transfer to Liquid Metals in Annular Spaces (V. I. Subbotin, V. D. Talanov and P. A. Ushakov) 108

The paper describes the effect of spacing ribs and eccentricities on the temperature field of the surface of the heat-conducting tube cooled by liquid metal (NaK) flowing in a narrow annulus. Close agreement with other experimental data for eccentric, but ribless, annuli is demonstrated.

Transfer of Heat in Turbulent Flows of Fluids in Annular and Plane Spaces (N.I. Buleyev, V.A. Mosolova and L.D. Yel'tsova) 120

Calculations of temperature fields and heat transfer coefficients for turbulent flow in annular and plane spaces are presented. Use is made of integral approximations for turbulent coefficients of thermal conductivity. The calculated heat transfer coefficients for several fluids are compared with the available experimental data.

Experimental Study of Heat Transfer From a Flat Horizontal Surface to Sodium by Free Convection (A.P. Kudryatsev, D.M. Ovechkin, D.N. Sorokin, V.I. Subbotin and A.A. Tsyganok) 130

The experimental study was carried out to compare the level of heat transfer in boiling and in free convection of liquid metals. Experimental data were correlated satisfactorily by equations previously proposed by other authors. A different set of heat transfer equations applies for turbulent and laminar free convection regions.

Approximate Thermal Simulation of Cylindrical Fuel-Element Rods (P.A. Ushakov) 136

The author uses dimensional analysis and other analytical tools to arrive at methods of simulation of thermal conditions of fuel rods in liquid-metal cooled nuclear reactors. The presented methods are successfully used in simulation of actual reactor cores.

Heat Transfer From Loosely-Spaced [Fuel] Rod Clusters to Liquid Metal Flowing in the Axial Direction (A.V. Zhukov, V.I. Subbotin and P.A. Ushakov) 149

The present article considers experimental heat transfer data obtained with fuel rod clusters to liquid metal in longitudinal (axial) flow past the rods. It is assumed that temperature variation over rod perimeter is small and that the heat transfer coefficients depend little on rod geometry, jacket thickness, thermal conductivity of the fissionable material and of the jacket. Empirical equations are derived and data are compared with existing correlations.

Experimental Study of Temperature Fields of Fuel Elements, Using Models (A.V. Zhukov, L.K. Kudryatseva, Ye.Ya. Sviridenko, V.I. Subbotin, V.D. Talanov and P.A. Ushakov) 170

Results of an experimental heat transfer study with simulated fuel elements are presented and analyzed. Hexagonal housings were used and the peripheral elements were found to undergo appreciable temperature variations. These temperature variations are analyzed for different packing modes. Transient coolant flow was also studied with the attendant effects on rod temperature. Tinning with fuel elements is considered in turbulent and laminar flow.

Heat Transfer in the Interbular Space of Liquid-Metal Heat Exchanges (p. L. Kirillov and M. Ya. Suvorov) 190

The paper presents the data of an experimental heat transfer study with axial flow of a liquid metal coolant. The correlation for average heat transfer coefficient as a function coolant velocity and cluster geometry has been obtained. Effect of tube oxidation on heat transfer has been studied and analyzed.

Analysis of the Applicability of Average Heat-Transfer Coefficients in Heat-Exchanger Design (P. A. Ushakov) 200

This paper compares different available methods of obtaining average heat transfer coefficients for short heat exchangers. It is shown that it is preferable to employ average heat transfer coefficients calculated on the basis of average temperature difference between the wall and the fluid, to the use of integrated values of local heat transfer coefficients.

Resistance to Axial Flow of Fluids Past Rod Clusters (A. V. Sheynina) 207

Experimental data on friction factors for flow through rod clusters are presented, analyzed and compared with existing correlations. Different types of clusters and configurations were studied. The effect of different spacers and inserts is discussed.

Velocity Distribution in a Cell Formed by a Densely-Packed Cluster of Rods (Yu. D. Levchenko, V. I. Subbotin, P. A. Ushakov and A. V. Sheynina) 220

The paper presents a thorough analysis of an experimental study of velocity distribution in ducts with noncircular cross-section. Both velocity and shear stress as well as friction factors in ducts simulating a densely-packed rod bundle.

Calculation and Experimental Study of Velocity Fields in Intricately-Shaped Passages (M. Kh. Ibragimov, I. A. Isupov and V. I. Subbotin) 231

The present article considers the fluid dynamics of a passage formed by a cluster of three round rods surrounded by a triangular shell. Such duct combines the fluid flow characteristics of rod clusters as well as exposes the effect of the shell on the fluid flow. These characteristics were studied experimentally and considered theoretically.

Electronically-Heated Setup for the Study of Heat Transfer From Boiling Metals by Free Convection (A. A. Ivashkevich, A. P. Kudryavtsev, D. M. Ovechkin, D. N. Sorokin, V. I. Subbotin and A. A. Tsyganok) 248

The authors present a discussion of an experimental study of electronically heated system for pool boiling of liquid metals. Very high heat fluxes which can be easily measured were obtained.

Transfer of Heat From Sodium Boiling in a Large Vessel (A. P. Kudryavtsev, D. M. Ovechkin, D. N. Sorokin, V. I. Subbotin and A. A. Tsyganok) 265

Boiling studies with sodium were carried out at flat horizontal plates heated by electron bombardment. The heaters were made of stainless steel. Comparison of pool boiling data obtained in previous experiments shows generally satisfactory agreement. Effect of dissolved oxygen on heat transfer is considered.

Experimental Study of Critical Thermal Fluxes in Sodium Boiling in a Large Vessel (A. P. Kudryavtsev, D. M. Ovechkin, D. N. Sorokin, V. I. Subbotin and A. A. Tsyganok) 281

Data of an experimental burnout study with liquid sodium on flat horizontal surface are presented. The obtained data and data of other researchers are still too scarce, in the opinion of the authors, to allow the derivation of an empirical generalized correlation.

Mean Temperature Difference in Low-Pressure Vapor Generators and Condensers (P. L. Kirillov) 287

The paper studies the behavior of liquid metal vapors as a heat transfer medium. A new expression for the log mean temperature difference is obtained for both parallel and counterflows.

Transfer of Heat From Condensing Sodium Vapor (N. B. Bakulin, M. N. Ivanovskiy, V. P. Sorokin, V. I. Subbotin and B. A. Chulkov) 294

The paper analyzes the effect of boundary conditions on heat transfer in condensation of pure "stationary" sodium vapor. The temperature field in the vapor in the liquid metal and the wall were measured. The effect of noncondensing gases and other contaminants is considered.

Corrosion Resistance of Construction Materials to Sodium (V. V. Zotov, B. A. Nevzorov and Ye. V. Umnyashkin) 300

This papers reviews the available data on corrosion resistance of materials of construction to liquid sodium. The chemical nature of oxygen in liquid sodium is analyzed and classified. Corrosion resistance of ferritic-pearlitic chromium steels as well as that of austenitic stainlesss steels is presented and discussed at various thermal and flow conditions. Also, alloys with a nickel base and refractory metals are grouped and classified.

Determination of the Oxygen Content of Sodium and of the Sodium-Potassium Alloy by Vacuum Distillation (I. B Dmitryeva, F. A. Kozlov and E. K. Kuznetsov) 318

An experimental method for determining oxygen content in liquid sodium is presented. Apparatus for performing the measurements is described as well as analysis of the obtained results.

The Cock-Type Indicator as an Instrument for Detecting Admixtures in Sodium (F. A. Kozlov, E. K. Kuznetsov and V. I. Subbotin) 324

The special indicator for detecting admixtures in liquid metals is described. The operation, construction, calibration and other aspects of the instrument are given in great detail. Experimental data obtained with the instrument by different investigators are plotted and compared.

Effect of Admixtures on the Electric Resistance of Molten Lithium (M. N. Arnol'dov, M. N. Ivanovskiy, V. I. Subbotin and B. A. Shmatko) 336

The effect of admixtures, such as nitrogen, oxygen and hydrogen, on the electrical resistivity of liquid lithium is described. The temperature dependences of the admixture concentration and type of admixture are presented.

The Use of Hot Traps for Removing Oxygen From Sodium (F. A. Kozlov and E. K. Kuznetsov) 340

The paper gives a thorough description of theoretical and practical aspects of the use of hot traps for oxygen removal from sodium. The reaction of zirconium cladding with the oxygen is considered as a function of time of exposure, temperature, concentration, liquid metal velocity, changes in chemical composition. Methods of testing the cladding by x-ray diffraction and metallographic analysis are described along with the changes in its electrical resistivity.

Maximum Permissible Leakage in a Sodium-to-Water Steam Generator (N. N. Ivanovskiy and F. A. Kozlov) 357

The paper presents a set of conditions for calculating the maximum permissible leakage in a liquid sodium steam generator. Safety factors are considered.

Some Problems of Operation and Design of Liquid-Metal Loops (A. V. Drobyshev, V. A. Kurov and I. T. Filipov) 360

Operation and design problems of liquid metal loops operating with forced coolant circulation are described. Auxiliary systems, instrumentation, safety measures, equipment layout and costs are included in the brief review.

Heat Exchangers of Experimental Liquid-Metal Loops
(V. A. Kurov and V. F. Men'shikov) 368

The paper presents design criteria and operating procedures for heat exchangers associated with liquid metal loops. Liquid-metal-to-water coolers, liquid-metal-to-air coolers, as well as liquid metal-to-liquid-metal exchangers and recuperators are described.

Study of Velocity Fields by the Electromagnetic Method
(N. N. Turchin and R. V. Shumskiy) 377

The present paper presents experimental data on velocity field in a round tube and an annular channel. Data for laminar and turbulent flows are given and other parameters, such as end effects, are considered.

Electromagnetic A-C Pump for Liquid Metals Rated at
120 m^3/hour (Ye. M. Avilova, T. V. Doktorova, N. I. Marin
and V. A. Povsten') 385

The physical features, design characteristics and performance data for a 120 m^3/hr electromagnetic A-C pump for circulating liquid metals are presented.

Electromagnetic Screw Pump for Pumping of Liquid Metals
(Ye. M. Avilova, Ye. L. Ivanter, N. I. Marin and V. A. Povsten') 389

The design features and operating characteristics of an electromagnetic screw pump are given. The pump is well suited for laboratory-scale tests with liquid metals.

Hydrostatic Bearings in Sodium Pumps (N. N. Aristarkhov,
Yu. Ye. Bagdasarov, Yu. L. Kulikov, Ye. N. Larin,
M. S. Pinkhasik, A. A. Rineyskiy and B. S. Tymosh) 392

The design of hydrostatic bearings for sodium pumps is considered. Operating principles of the bearings, temperature resistance, pressure, wear and noise were tested in a sodium loop. Creep was also considered at temperatures up to 400°C.

Flowmeter for Measuring Large Liquid-Metal Flows
(N. L. Loginov) 403

The device described in this paper is a flowmeter which operates by measuring the velocity at one point in the flow. The size of the instrument is moderate in comparison with the size of the pipeline. It is intended for operation at 50-1000 m^3/hour of a liquid metal flowing in a pipeline 300 mm in diameter. Other operating parameters are also given.

Time Needed for Melting Cylindrical [Metal] Volumes
(V. M. Selivanov, N. M. Trebina and V. I. Sharypin) 406

The paper presents theoretical data and nomograms for calculating the time needed for melting of metal cylinders, starting at a temperature below the metal melting temperature. Cases of constant temperature, constant heat flux and constant heat transfer coefficient are considered (boundary conditions of the first, second and third kind, respectively).

Frozen Sodium Seals (A. V. Drobyshev, Yu. I. Likhachev and I. M. Saratov) 412

The paper presents the results of a thorough engineering study of frozen liquid metal seals. A method for calculating the startup forces of such seals is given. Stress-strain diagrams for sodium are given for different strain rates and different temperatures. Characteristics of several designs of frozen-sodium seals were studied. Comparison of theoretical and experimental data shows satisfactory agreement.

Appendix I
Calculations of Heat Transfer in Liquid Metals 437

This appendix presents recommendations for calculating heat transfer to liquid metals based on world-wide data published up to January 4, 1966. Equations are given for convective heat transfer in round tubes, rectangular ducts, concentric and eccentric annuli, rod and tube clusters. Equations for condensation of liquid metal vapor are presented. Combined free and forced convection are given.

Appendix II
Corrosion Resistance and Temperature Limit of Utilization of Certain Construction Materials in a Sodium Flow 446

This appendix gives tables of corrosion resistance to liquid metals of pearlitic chromium steels and nickel-containing steels and alloys as well as refractory metals.